CONF-9309310--

PROCEEDINGS

Joint DOE/NSF Workshop on

FLOW OF PARTICULATES AND FLUIDS

September 29 - October 1, 1993

Statler Hotel
Ithaca, New York

U.S. Department of Energy
Pittsburgh Energy Technology Center

National Science Foundation

MASTER

DISTRIBUTION OF THIS DOCUMENT IS UNLIMITED

DISCLAIMER

This report was prepared as an account of work sponsored by an agency of the United States Government. Neither the United States Government nor any agency thereof, nor any of their employees makes any warranty, express or implied, or assumes any legal liability of responsibility for the accuracy, completeness or usefulness of any information, apparatus, product, or process disclosed, or represents that its use would not infringe privately owned rights. Reference herein to any specific commercial product, process, or service by trade name, trademark, manufacturer, or otherwise, does not necessarily constitute or imply its endorsement, recommendation, or favoring by the United States Government or any agency thereof. The views and opinions of authors expressed herein do not necessarily state or reflect those of the United States Government or any agency thereof.

This report has been reproduced directly from the best available copy.

Copies of this report are available from the National Technical Information Service, U.S. Department of Commerce, Springfield, VA 22161.

FOREWORD

These proceedings are the result of the Fifth DOE-NSF Workshop on fundamental research in the area of particulate two-phase flow and granular flow. The present collection of twenty contributions from universities and national laboratories is based on research projects sponsored by either the Department of Energy or the National Science Foundation.

These papers illustrate some of the latest advancements in theory, simulations, and experiments. The papers from the Workshop held September 29 - October 1, 1993 have been separated into three basic areas: experiments, theory, and numerical simulations. A list of attendees at the workshop is included at the end of the proceedings.

We would like to thank all those involved in the organization of this workshop and especially the participants of the workshop for their contribution in preparing this volume.

Sean I. Plasynski
William C. Peters
Mike C. Roco

TABLE OF CONTENTS

THEORETICAL SESSION

NUMERCIAL SESSION

EXPERIMENTAL SESSION

THEORETICAL SESSION

DENSE, COLLISIONAL, NEARLY STEADY, NEARLY FULLY DEVELOPED FLOWS DOWN INCLINES

J. T. Jenkins
Department of Theoretical and Applied Mechanics
Cornell University, Ithaca, NY 14853 USA

ABSTRACT

In preparation for the the development of a hydraulic theory for particulate flows that involve particle collisions throughout their depth, we analyze a flow down an incline that is dense, one dimensional, nearly steady, and nearly fully developed. Because we employ more realistic boundary conditions at the base of the flow, the analysis is slightly more complicated than that of Savage (1983); because we restrict our attention to dense flows, it is somewhat simpler than that of Richman & Marciniec (1990).

THEORY

We first consider rapid flows of a granular material consisting of identical, nearly elastic, frictionless spheres of mass m and diameter σ. The familiar coefficient of restitution e characterizes the energy lost to the component of velocity normal to the surface of two colliding spheres. Although we restrict our attention to nearly elastic collisions of identical, frictionless spheres, we anticipate that the many features of the flow involving irregular particles of different sizes interacting through frictional, inelastic collisions are captured by this idealized system.

The mean fields of interest are the mass density ρ, the product of m and the mean number n of spheres per unit volume; the mean velocity $\mathbf{u}$ about which the actual particle velocity fluctuates; and the granular temperature T that measures the energy per unit mass of the velocity fluctuations.

The balance laws for mass, linear momentum, and the fluctuation energy have the familiar local forms:

$$\dot{\rho} + \rho \, \nabla \cdot \mathbf{u} = 0 \, , \tag{1}$$

where an overdot indicates a time derivative following the mean motion;

$$\rho \, \dot{\mathbf{u}} = \nabla \cdot \mathbf{t} + n \, \mathbf{F} \, , \tag{2}$$

where **t** is the symmetric stress tensor and **F** is the external force on a sphere; and

$$\frac{3}{2}\rho\,\dot{T} = -\nabla\cdot\mathbf{Q} + \mathrm{tr}\,(\mathbf{t}\cdot\nabla\mathbf{u}) - \gamma\,, \tag{3}$$

where **Q** is the flux of translational energy, tr denotes the trace of a tensor, and γ is the rate at which the energy of the translational fluctuations is dissipated in collisions in a unit volume.

The hydraulic analyses will be based upon a flow in the x-y plane that is rectilinear,nearly steady, and nearly fully developed. The x-component u of the velocity, the density ρ, and the granular temperature T depend upon x, y, and t. The base of the flow is taken to be at y = 0, the upper surface of the flow is given by y = H(x,t), and the x-axis is assumed to be inclined at an angle ϕ from the horizontal. We assume that the flow is long and thin, so that variations in the y-direction are much more intense than those in the x-direction, and that the time necessary to adjust to a steady solution across the flow is more rapid than the characteristic times for change along the flow. In the analysis across the flow, the acceleration along the flow is ignored, the pressure is taken to be hydrostatic and the dependence on x and t enters only through that of the upper surface. In this case, (1) is satisfied identically and the x- and y-components of (2) require that the shear stress $S \equiv t_{xy}$ and the pressure p satisfy

$$\frac{\partial S}{\partial y} - \frac{\partial p}{\partial x} = -\rho\, g \sin\phi \tag{4}$$

and

$$\frac{dp}{dy} = -\rho\, g \cos\phi\,, \tag{5}$$

where g is the gravitational acceleration. Then, with $Q \equiv Q_y$, (3) reduces to

$$-\frac{dQ}{dy} + S\,\frac{du}{dy} - \gamma = 0\,. \tag{6}$$

The mean shear stress working through the gradient of the mean velocity is the source of the fluctuation energy, while the inelastic collisions dissipate it. At any point in the flow at which there is an imbalance in the rates of production and dissipation, there is a transport of fluctuation energy to or from neighboring points in the flow.

We restrict our attention to dense flows with a distinct upper surface in which the volume fraction $\nu \equiv n\pi\sigma^3/6$ is around 0.5. In this case, collisions between particles rather than the flight of particles between collisions are responsible for the fluxes of momentum and energy. In addition, in the expressions for the fluxes derived in the kinetic theory, we retain only those contributions to the collisional fluxes that dominate in the dense limit. Then, with the assumptions that the spheres are nearly elastic, we write the dispersive pressure p and the shear stress S as the high-volume-fraction limits of expressions provided by Chapman & Cowling (1970, Sec. 16.41) for frictionless, elastic spheres:

$$p = 4 \rho G T , \tag{7}$$

where (Carnahan & Starling, 1979)

$$G \equiv \nu (2 - \nu) / 2 (1 - \nu)^3 ; \tag{8}$$

and

$$S = \frac{2}{5} J \kappa \frac{du}{dy} , \tag{9}$$

where $J \equiv 1 + \pi/12$ and

$$\kappa \equiv (4 / \pi^{1/2}) \rho \sigma T^{1/2} G . \tag{10}$$

Upon expressing κ in terms of p, we obtain a simple relation between the velocity gradient and the temperature:

$$\frac{du}{dy} = \frac{5 \pi^{1/2}}{2 J} \frac{T^{1/2}}{\sigma} \frac{S}{p} . \tag{11}$$

We adopt the corresponding expression for the flux of fluctuation energy (Chapman & Cowling 1970, Sec. 16.42) that is, in the dense limit, given by

$$Q = - M \kappa \frac{dT}{dy} , \tag{12}$$

where $M \equiv 1 + 9\pi/32$.

The rate of decrease of fluctuation energy per unit volume is (Jenkins & Savage, 1983)

$$\gamma = 6 \kappa T (1 - e) / \sigma^2, \tag{13}$$

Boundary conditions are derived based upon the collisional exchange of momentum and energy at the boundary. Here we will consider a bottom boundary that is a surface to which particles are rigidly attached, called a bumpy boundary. The bumpiness of the boundary is characterized by an angle θ that measures the average depth that a flow particle can penetrate between wall particles. A boundary consisting of a plane on which spheres identical to those of the flow have been close-packed has a value of θ near $\pi/6$ (Jenkins & Askari, 1993).

At a bumpy boundary, the particles of the boundary are arranged differently than particles in the flow. Consequently, in order to balance the component of linear momentum parallel to the surface of the boundary, the flow must slip with respect to the boundary. We denote the magnitude of the slip velocity by v. Then, at the bottom boundary,

$$v = \left(\frac{\pi}{2} \right)^{1/2} f T^{1/2} \frac{S}{p}, \tag{14}$$

where the slip coefficient f depends only on the bumpiness of the boundary. For small values of θ (Jenkins & Askari, 1993),

$$f(\theta) \doteq \frac{2}{\theta^2} - \frac{5 \pi}{24 J} + \frac{25 \pi + 300\sqrt{2} - 7 J}{360 J} \theta^2 . \tag{15}$$

In general, collisions between the particles of the flow and the boundary dissipate energy, and the rate D of dissipation per unit area is given in terms of the boundary coefficient of restitution e_w by

$$D = (2 / \pi)^{1/2} (1 - e_w) h T^{1/2} p \tag{16}$$

where h depends only on the bumpiness,

$$h(\theta) \doteq 1 + \frac{1}{4} \theta^2 . \tag{17}$$

Then the balance of energy at a bumpy boundary requires that the flux of fluctuation energy from the flow plus the rate of working of the shear stress through the slip velocity equals the rate of collisional dissipation. Consequently, at the bottom boundary,

$$-Q + S\,v = D\,; \tag{18}$$

or with (12), (14), and (16),

$$\sigma \frac{dT}{dy} = -2\,b_0\,T\,, \tag{19}$$

where

$$b_0 \equiv \frac{1}{\sqrt{2}\,M}\left[\frac{\pi}{2} f \left(\frac{S}{p}\right)^2 - (1 - e_w)\,h\right]. \tag{20}$$

The boundary condition is applied at the position of the center of a flow particle that touches the point on the boundary that project furthest into the flow.

The integral of (5) is

$$p(y) = g \cos\phi \int_y^H \rho(\xi)\,d\xi\,, \tag{21}$$

where we have assumed that p vanishes at y = H. Because the function G(v) varies far more rapidly with v than v itself, we ignore the variation of ρ with y in (21) and replace it by its average value. Then

$$p(y) = \bar{\rho}\, g \cos\phi\,(H - y)\,, \tag{22}$$

and, upon using this when integrating (4),

$$S(y) = \bar{\rho}\, g \cos\phi\,(\tan\phi - H')\,(H - y)\,, \tag{23}$$

where we have assumed that S vanishes at the free surface in such a way that

$$\frac{S}{p} = \tan\phi - H'\,. \tag{24}$$

We employ (11), (12), and (13) in the balance of fluctuation energy (6) and replace κ by $\sigma p/(\pi T)^{1/2}$ wherever it occurs and use (22) to write p as a function of y. The resulting equation for w is most conveniently expressed in terms of the independent variable $s \equiv (H - y) / \sigma$:

$$\frac{d^2 w}{d s^2} + \frac{1}{s}\frac{dw}{ds} - k^2 w = 0 , \tag{25}$$

where

$$k^2 \equiv \frac{1}{M}\left[3(1-e) - \frac{5\pi}{4J}\left(\frac{S}{p}\right)^2 \right]. \tag{26}$$

At the upper surface, s = 0, we require that

$$\frac{dw}{ds} = 0 . \tag{27}$$

The solution of (25) consistent with this is

$$w(s) = w_0 \frac{I_0(ks)}{I_0(kH)} , \tag{28}$$

where w_0 is the value of the fluctuation velocity at the base of the flow and I_0 is the associated Bessel function of order zero.

When the bottom boundary is bumpy and the flow is steady and fully developed, (19) requires that at $s = H/\sigma$,

$$\frac{I_1(kH/\sigma)}{I_0(kH/\sigma)} = \frac{b_0}{k} . \tag{29}$$

This is the relationship between the depth of the flow and the inclination of the base in this simple situation. In an unsteady and/or developing flow, this relationship is only approximately satisfied.

In Figure 1 we show the variation of the height of a steady, fully developed flow over a range of stress ratios for realistic values of the coefficients of restitution and boundary bumpiness. In this situation, the height of the flow is determined by the stress ratio and is independent of the rate of flow. In Figure 2 we show profiles of the fluctuation velocity, normalized by its value at the base, for several values of the stress ratio. The fluctuation velocity decreases with height and, as the height of the flow increases, the fluctuation velocity at its top approaches zero.

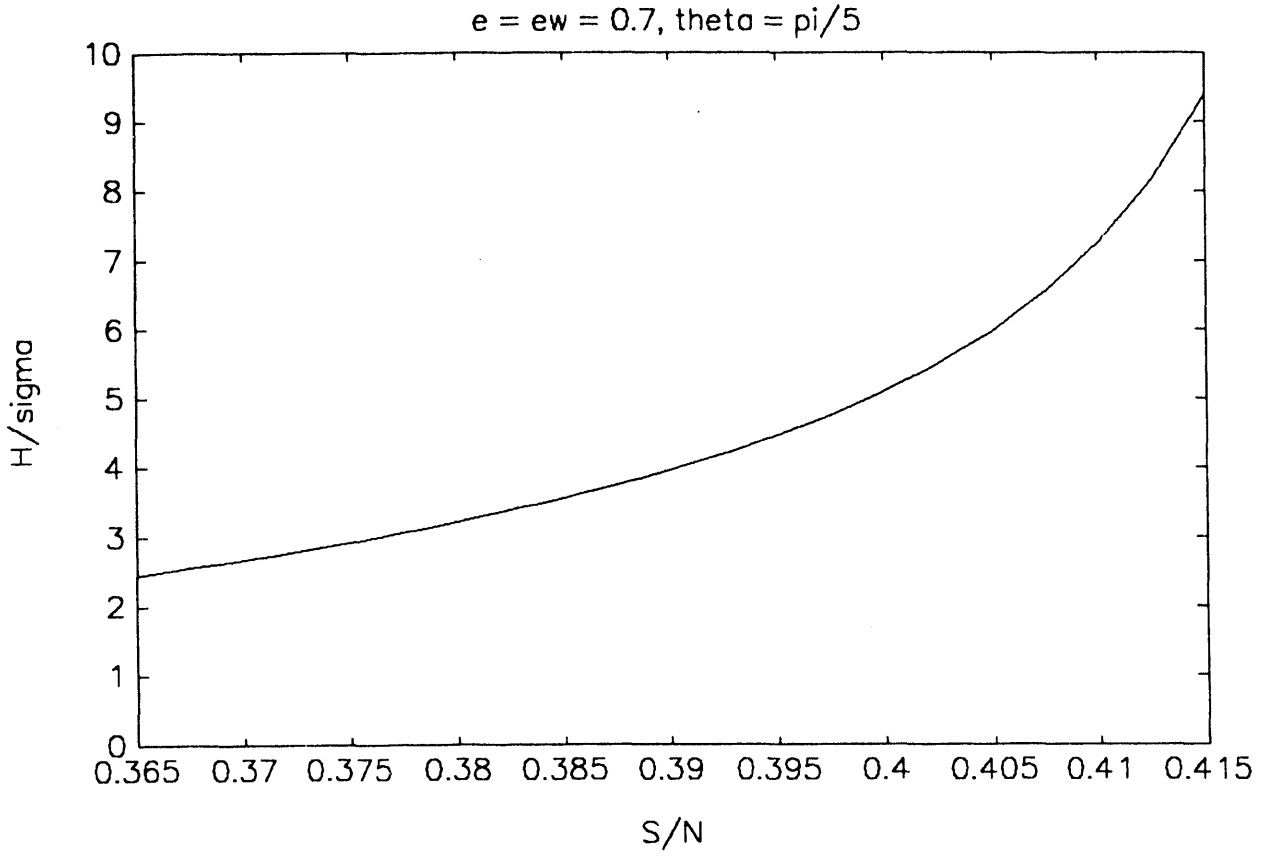
e = ew = 0.7, theta = pi/5
H/sigma
S/N
0
1
2
3
4
5
6
7
8
9
10
0.365
0.37
0.375
0.38
0.385
0.39
0.395
0.4
0.405
0.41
0.415

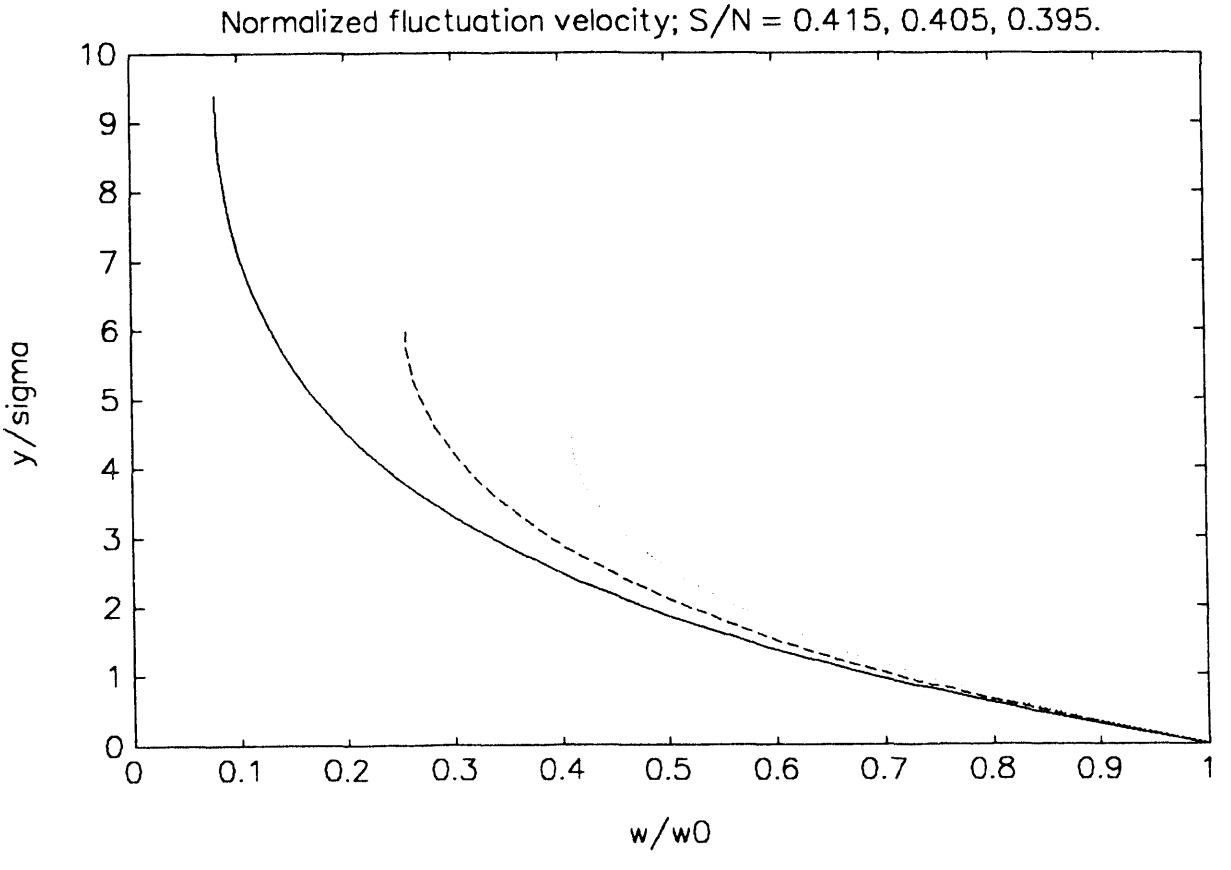
Normalized fluctuation velocity; S/N = 0.415, 0.405, 0.395.
y/sigma
w/w0
0
1
2
3
4
5
6
7
8
9
10
0
0.1
0.2
0.3
0.4
0.5
0.6
0.7
0.8
0.9
1

The velocity is determined by integrating (11) and using the value (14) for the slip velocity at the base of the flow:

$$u(y) = \left(\frac{\pi}{2}\right)^{1/2} w_0 \left(f + \frac{5}{\sqrt{2}\, J} \frac{1}{k\, I_0(kH)} \int_{k(H-y)/\sigma}^{kH/\sigma} I_0(\xi)\, d\xi \right) \frac{S}{p} . \tag{30}$$

In particular, the velocity $U \equiv u(H)$ at the free surface is given in terms of the height of the flow and the stress ratio by

$$U = \left(\frac{\pi}{2}\right)^{1/2} w_0 \left(f + \frac{5}{\sqrt{2}\, J} \frac{1}{k\, I_0(kH)} \int_{0}^{kH/\sigma} I_0(\xi)\, d\xi \right) \frac{S}{p} . \tag{31}$$

In Figure 3 we show profiles of the mean velocity normalized by the fluctuation velocity at the bottom of the flow for the three values of the stress ratio. The remarkable feature of these profiles is their linearity. In Figure 4 we show the variation of the velocity at the top of the flow, normalized by w_0, versus the stress ratio.

The variation of the volume fraction through the height of the flow may be obtained by combining equations (7) and (22):

$$G(\nu) = \frac{1}{4} \frac{\sigma g}{U^2} \left(\frac{U}{w_0}\right)^2 \left(\frac{w_0}{w}\right)^2 \frac{(H - y)}{\sigma} . \tag{32}$$

When the velocity U of the free surface is known, equation (32) may be inverted to determine $\nu(y)$. Of course, ν must everywhere be large enough to justify our restriction to dense flows. Given U and S/p, w_0 is determined in terms of them by (31); so the solution is complete.

A more natural parametrization may obtained by eliminating $U^2/\sigma g$ in favor of the volume V of material above a unit area of the base:

$$V \equiv \int_0^H \nu(y)\, dy = V\left(\frac{U^2}{\sigma g}, \frac{S}{p}\right) . \tag{33}$$

Then, for a given stress ratio, the volume flux Q,

$$Q \equiv \int_0^H \nu(y)\, u(y)\, dy = Q\left(\frac{U^2}{\sigma g}, \frac{S}{p}\right) , \tag{34}$$

may be expressed in terms of V by eliminating $U^2/\sigma g$ between (33) and (34).

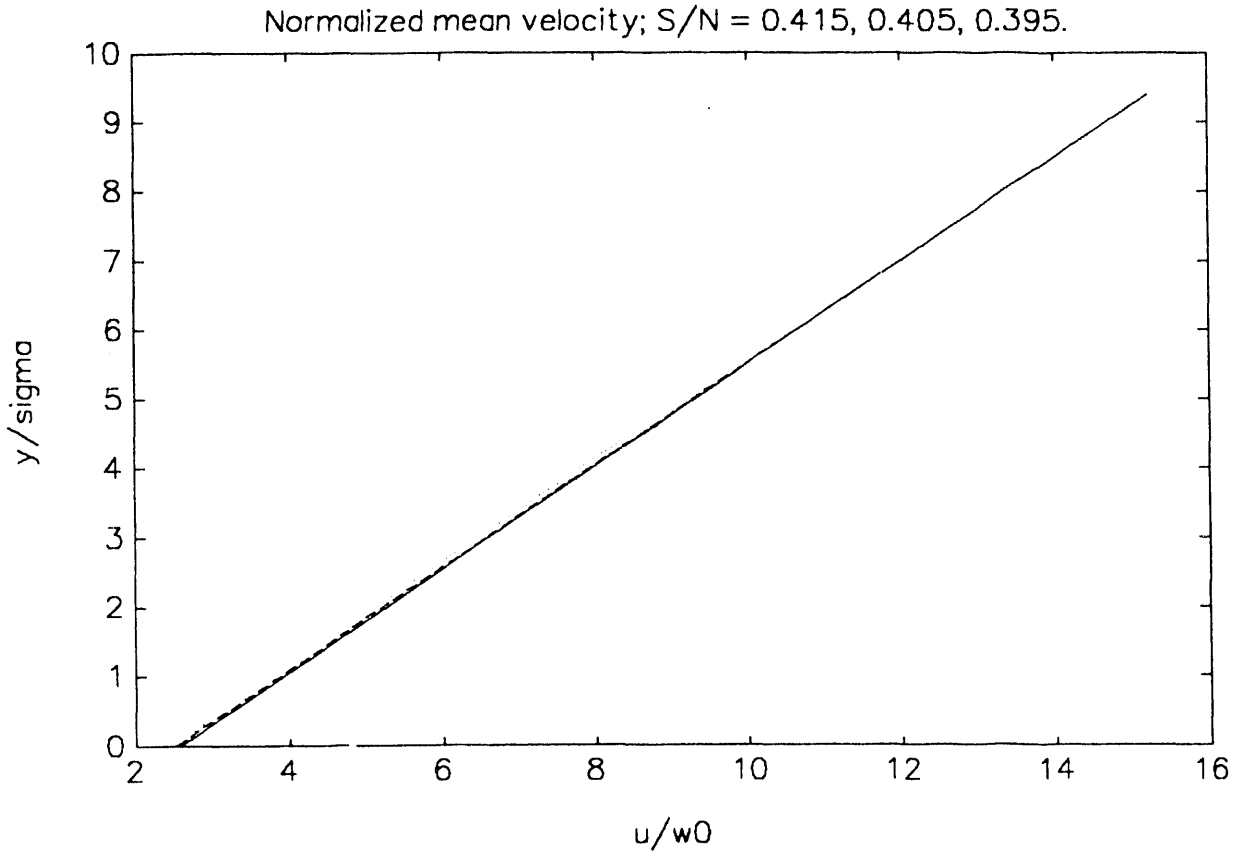
Normalized mean velocity; S/N = 0.415, 0.405, 0.395.
y/sigma
u/w0
0
1
2
3
4
5
6
7
8
9
10
2
4
6
8
10
12
14
16

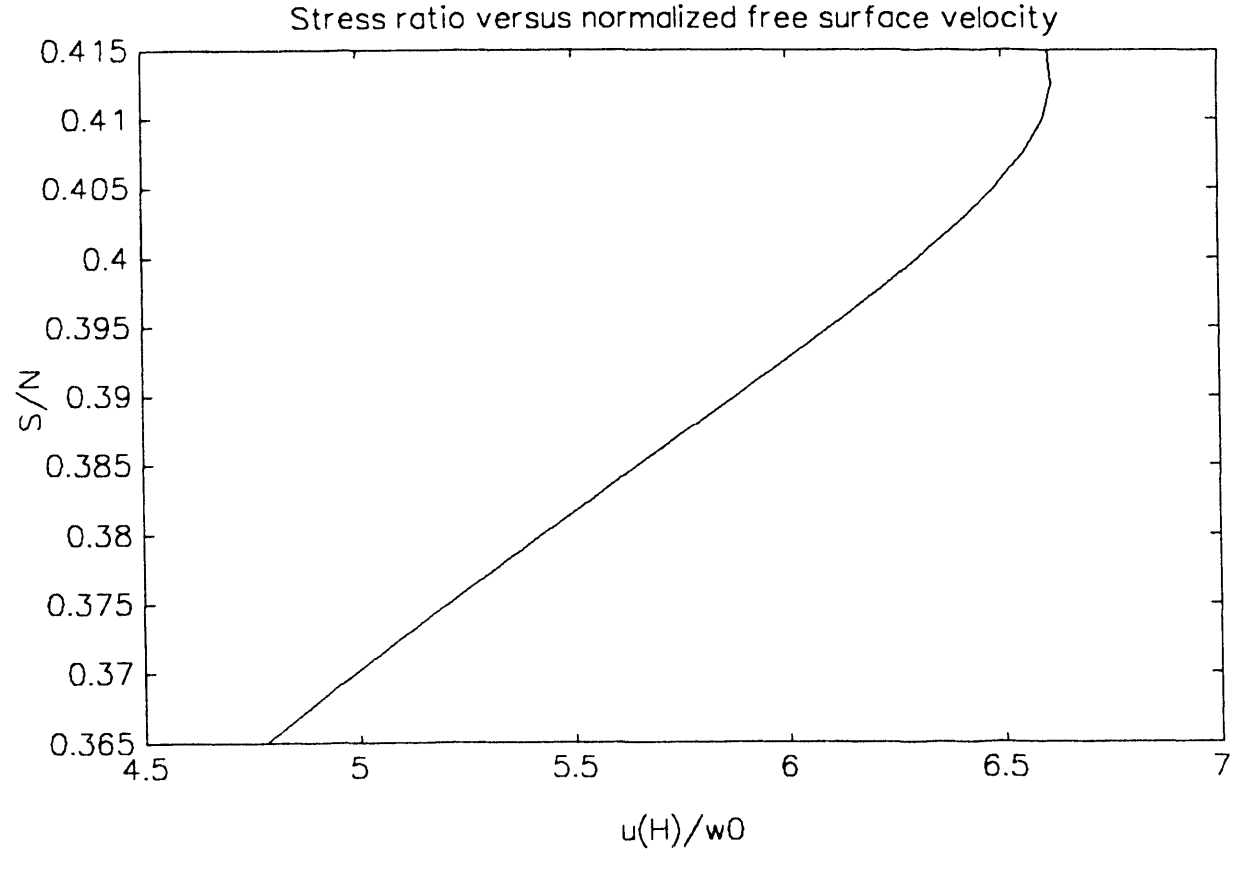
Stress ratio versus normalized free surface velocity
S/N
u(H)/w0
0.365
0.37
0.375
0.38
0.385
0.39
0.395
0.4
0.405
0.41
0.415
4.5
5
5.5
6
6.5
7

ACKNOWLEDGEMENT

This research was supported by the Department of Energy as part of the Granular Flow Advanced Research Objective.

REFERENCES

Carnahan, N.F. and K. Starling (1979) "Equations of state for non-attracting rigid spheres," J.Chem. Phys. 51, pp. 635-636.

Chapman, S. and T.G. Cowling (1970) The Mathematical Theory of Non-Uniform Gases, Third Edition, Cambridge University Press, Cambridge.

Jenkins, J.T. and E. Askari (1993) "Rapid shear flows of frictional spheres driven by identical bumpy, frictional boundaries," (in preparation).

Richman, M.W. and R.P. Marciniec. (1990) "Gravity-driven granular flows of smooth inelastic spheres down bumpy inclines," J. Appl. Mech. 57, pp. 1036-1043.

Savage, S.B. (1983) "Granular flows at high shear rates," In Theory of Dispersed Multiphase Flow. (R.E. Meyer, Ed.) Academic Press, New York, pp. 339-358.

The Growth of Disturbances in Fluidized Beds: Capturing Gas and Liquid Behavior in a Single Framework

K. Anderson, Y. Kevrekidis, S. Sundaresan, & R. Jackson
Department of Chemical Engineering, Princeton University
Princeton, NJ 08544

The last thirty years have seen numerous attempts to develop appropriate governing equations for dense suspensions of solid particles. The exact solution of the problem involves the solution of the complete Navier-Stokes equations for the fluid along with the Newtonian equations of motion for each particle. The dramatic increase in the computational power available to engineers and scientists may one day make such solutions practical, but that day has not yet arrived. Hence, those concerned with the mechanics of dense suspensions such as fluidized beds have approached the problem by volume averaging the exact equations over regions large compared to the particle spacing, but small compared to the size of the flow.

The ability to solve these equations has been limited to special cases. Consequently, the applicability of the proposed equations of motion remained in question. At the time of their development, solution of the equations was limited to an analysis of the stability of the uniformly fluidized state, performed by linearizing the equations for small deviations from uniformity, and approximate solutions for bubble motion in gas fluidized beds. Early analyses indicated that the equations predicted small disturbances would grow an order of magnitude faster in a gaseous suspension than in a similar liquid suspension, and this has been confirmed experimentally [2, 5].

Gaseous and liquid suspensions exhibit dramatically different behavior. Both are unstable [7]. In liquid suspensions waves develop which later buckle and are destroyed. By contrast, gaseous suspensions are characterized by the formation of voids containing few or no particles. These regions are called bubbles in fluidized beds because of their similarity to bubbles found in gas-liquid flows. It has been known for many years that the equations of motion also have approximate solutions which represent bubbles [3, 8]. One dimensional analyses [6] have shown that upon becoming unstable the volume averaged equations have fully developed traveling wave solutions.

The elusive question has remained whether the proposed equations of motion can distinguish between the observed behavior of the two systems. This question can only be resolved by examining the two- or three-dimensional dynamic predictions of the proposed equations of motion. It is to this end that the present work has been addressed.

Equations of Motion

We use here the equations of motion developed by Anderson and Jackson [1]. Beginning with the Navier-Stokes equation for the fluid and the equation of motion of a single particle, governing equations were developed by volume averaging. If ϕ, $\mathbf{u}$, and $\mathbf{v}$ represent the volumetric concentration of particles and the average velocities of the fluid and solid phases, respectively, then the equations of motion may be written:

$$\nabla \cdot [(1-\phi)\mathbf{u} + \phi\mathbf{v}] = 0 \tag{1}$$

$$\frac{\partial \phi}{\partial t} + \nabla \cdot [\phi\mathbf{v}] = 0 \tag{2}$$

$$\rho_f \frac{\partial \mathbf{u}}{\partial t} + \rho_f \mathbf{u} \cdot \nabla \mathbf{u} = -\nabla p - \mathbf{F} + \nabla \cdot \mathbf{E}_f + \rho_f \mathbf{g} \tag{3}$$

$$\begin{aligned} \rho_s \phi \frac{\partial \mathbf{v}}{\partial t} + \rho_s \phi \mathbf{v} \cdot \nabla \mathbf{v} \;=\; & -\nabla p^s + \mathbf{F} + \nabla \cdot \mathbf{E}_s \\ & + \phi(\rho_s - \rho_f)\mathbf{g} \\ & + \rho_f \phi \frac{\partial \mathbf{u}}{\partial t} + \rho_f \phi \mathbf{u} \cdot \nabla \mathbf{u} \end{aligned} \tag{4}$$

Several terms result from the volume averaging process and must be defined further. The interaction of the two phases is represented by the term $\mathbf{F}$. Physically this term includes drag and virtual mass effects. The drag is represented by the Richardson-Zaki relation (1954) originally developed for sedimentation and fluidization. Virtual mass effects arise from the relative

acceleration of the two phases. Together then, the interphase interaction is taken to be:

$$\mathbf{F} = \beta(\phi)(\mathbf{u} - \mathbf{v}) + \rho_f C(\phi)\frac{d}{dt}(\mathbf{u} - \mathbf{v}) \tag{5}$$

where the drag coefficient $\beta(\phi)$ is given by

$$\beta(\phi) = \frac{(\rho_s - \rho_f)g}{u_t}\frac{\phi}{(1-\phi)^{n-1}} \tag{6}$$

The dynamic stresses $\mathbf{E}_f$ and $\mathbf{E}_s$ represent the resistances of the fluid and the particle assembly to shear. Though the behavior in all likelihood is not Newtonian for these systems, they will be assumed to be so in the interests of simplicity, since our goal is to find the simplest adequate form of the equations. The stresses are thus represented by:

$$\mathbf{E}_f = \mu_f\{\nabla\mathbf{u} + \nabla\mathbf{u}^T - \frac{2}{3}\mathbf{I}\nabla\cdot\mathbf{u}\} \tag{7}$$

$$\mathbf{E}_s = \mu_s(\phi)\{\nabla\mathbf{v} + \nabla\mathbf{v}^T - \frac{2}{3}\mathbf{I}\nabla\cdot\mathbf{v}\} \tag{8}$$

The fluid viscosity is taken to be that of the pure fluid, while the solids viscosity is assumed to be a function of solids concentration. The functional form is suggested by kinetic theory arguments for granular flows:

$$\mu_s(\phi) = \frac{a\phi}{1-(\phi/\phi_{cp})^{1/3}} \tag{9}$$

Finally, the particle pressure, p^s, represents the resistance of the particle assembly to normal stresses. Several forms have been suggested in the literature, all of which require that this pressure diverges as the material becomes close packed. The form chosen here was suggested by Hernandez and Jiminez:

$$p^s(\phi) = (\rho_s - \rho_f)g d_p\, C_0^2\, \phi^3 \exp\left(\frac{m\phi}{(\phi_{cp}-\phi)}\right) \tag{10}$$

With these constitutive models, the set of equations is closed. We emphasize that we have chosen the same closure expressions for all fluidized beds, both liquid and gas, since our goal has been to test the physics of the equations using as simple a system of equations as possible.

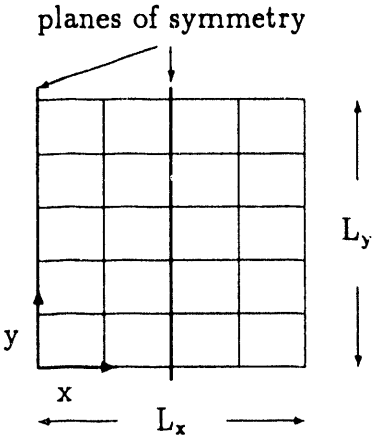

Figure 1: Periodic Cell

Model Formulation

In order to eliminate the effects of the boundary conditions on the results, we have limited the analysis to periodic solutions in an unbounded fluidized bed. The equations are solved in a rectangular cell which is repeated periodically in both the horizontal and vertical directions. Since there is then symmetry across the midline, the domain for computations may be reduced to one half of the cell. This domain is shown in Figure 1.

The equations are discretized spatially using the finite element method, chosen because of the flexibility offered in proceeding to other geometries and imposing boundary conditions. In the finite element method, the domain is subdivided into quadrilateral elements, and the independent variables are approximated over the element as polynomial functions. The volume fraction and the fluid and solids velocity components are approximated as biquadratic functions, while the pressure is treated as bilinear. The different orders for the variables are chosen to eliminate spurious pressure modes which arise from a poor choice for the pressure basis functions.

The equations are integrated over each element using Galerkin's method. The system is thus reduced to a set of nonlinear ordinary differential equations. An implicit Euler step is used for the time propagation for stability considerations. After specifying an initial condition, the system of equations is then integrated forward in time. The initial conditions for these simulations are small sinusoidal perturbations of the uniformly fluidized bed, obtained

	Gas Bed	Liquid Bed
Particle phase		
particle size	200 μm	1 mm
density	2.2 g/cm^3	2.2 g/cm^3
viscosity	7.6 poise	3 poise
Fluid phase		
density	0.0013 g/cm^3	1 g/cm^3
viscosity	0.0181 cp	1 cp
Particle pressure		
m	0.3	0.3
C_0	0.5	0.5
other quantities		
terminal velocity	142 cm/s	14.3 cm/s
drag index	4.35	3.65
stability limit	0.58	0.445
ϕ_0	0.57	0.43
λ_y max	π cm	2.25 cm

Table 1: Physical Properties and Parameters

by solution of the linearized equations. More complex initial conditions may be constructed by the Fourier synthesis of a solution from such components.

Values of the physical parameters used in the calculations are given in Table 1. For the gaseous suspension, we consider 200 μm glass beads fluidized by air. By contrast, the liquid system is 1 mm glass beads fluidized by water. The particle sizes were chosen to represent typical values used by investigators, and for which the observed behavior has been well characterized. In particular, 200 μm glass beads are of such a size that the gas bubbles that form are surrounded by a region of circulating gas usually called the "bubble cloud".

The code is tested intially against the predictions of linear stability theory. Small perturbations of the uniform bed travel at the speeds predicted from linear theory. As the mesh is refined, the growth rates also converge to those

predicted from the linear theory. Coarse meshes result in the wave being more stable than the theory predicts, thus these errors are not catastrophic. An additional, important check for the equations is obtained by posing the eigenvalue problem. It is found that the eigenvalues of the algorithm converge to the values predicted analytically from the linear stability analysis as the grid is refined.

Growth of One-Dimensional Waves

For both gaseous and liquid suspensions, linear stability predicts the fastest growing disturbance to be a one-dimensional wave traveling upwards through the bed. Our analysis of the system of equations thus proceeds from this fastest growing wave. In general we consider cell sizes of the dominant wavelength and integer multiples thereof. By restricting the number of elements in the lateral direction, the solution can be constrained to be one-dimensional.

For the parameters in Table 1, the gas fluidized bed becomes unstable at a particle volume concentration of 57.8%. We consider a bed of uniform void fraction 57% which is just on the unstable side of this limit. Figure 2 shows the development of the wave of dominant wavelength for the air fluidized bed. A sinusoidal disturbance develops swiftly and smoothly into a nonlinear wave with a sharp front and smooth tail traveling upwards through the bed at a speed of 18.7 cm/s. The time for development is a few seconds. By computing the eigenvalues of the algorithm for the fully developed one-dimensional wave, it is shown to be stable to additional one dimensional disturbances. Finally, it should be noted that this fully developed wave is robust and is achieved from a variety of initial conditions.

If we double the size of the cell, our previous solution still satisfies the equations, but now with two periods of the wave contained in the box, as shown in Figure 3. The two period wave is unstable, and when it is perturbed by a small increment of the unstable eigenfunction, the two waves coalesce. The coalescence is oscillatory and is pictured is Figure 4. The final form of the coalesced wave is identical to that obtained by beginning with a single sinusoid in the larger box, whose smooth development is shown in Figure 5. The nonlinear wave in the longer box possesses similar features to that in the smaller box, but it is deeper and the front is sharper.

The final example of one-dimensional growth in an air fluidized bed is

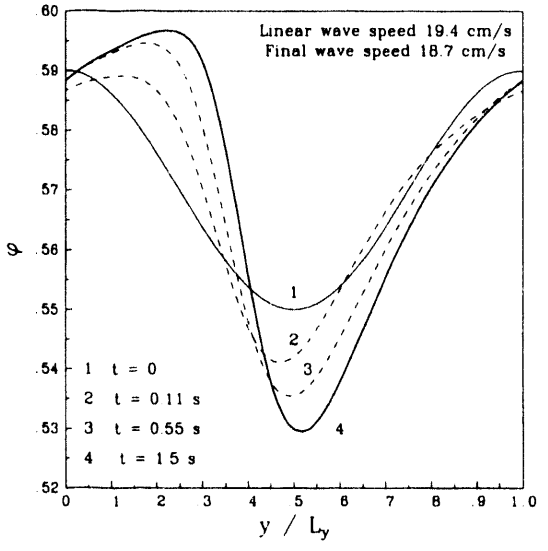

Figure 2: Development of the fastest growing 1D wave in an air fluidized bed

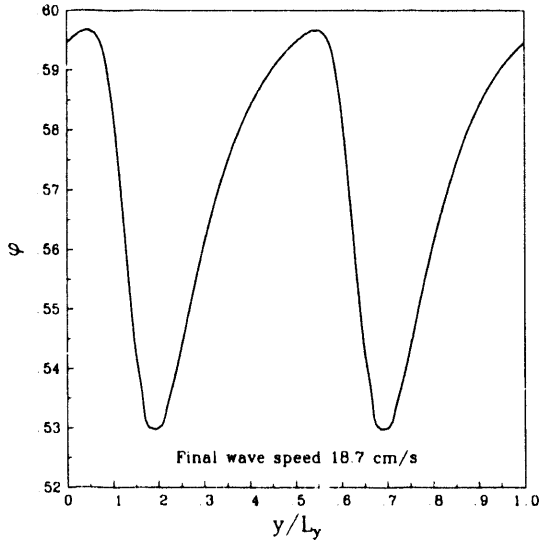

Figure 3: The fastest growing 1D wave in larger box in an air fluidized bed

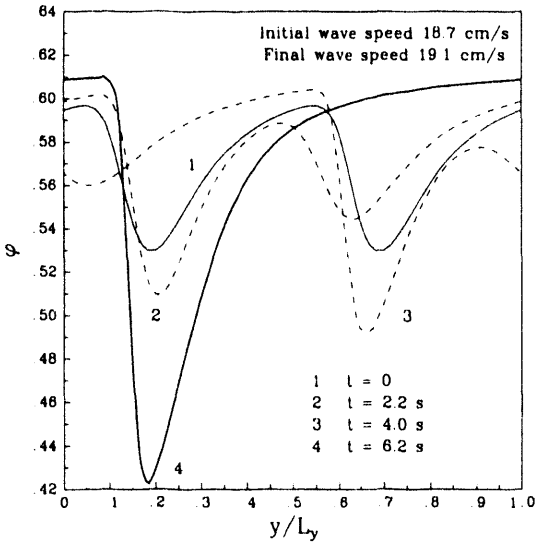

Figure 4: Coalescence of the π cm 1D wave in an air fluidized bed

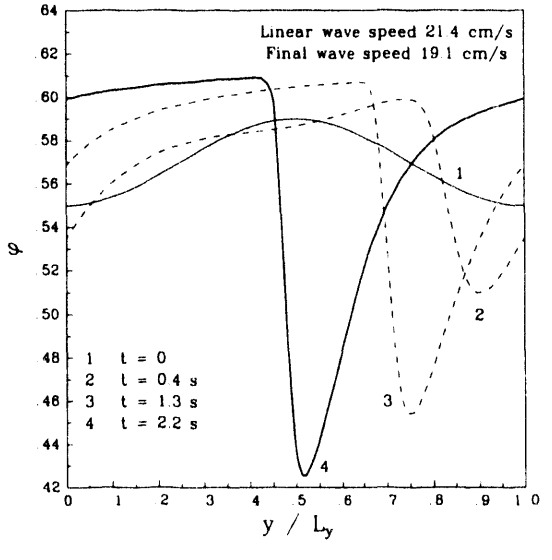

Figure 5: Development of the 2π cm wave in an air fluidized bed

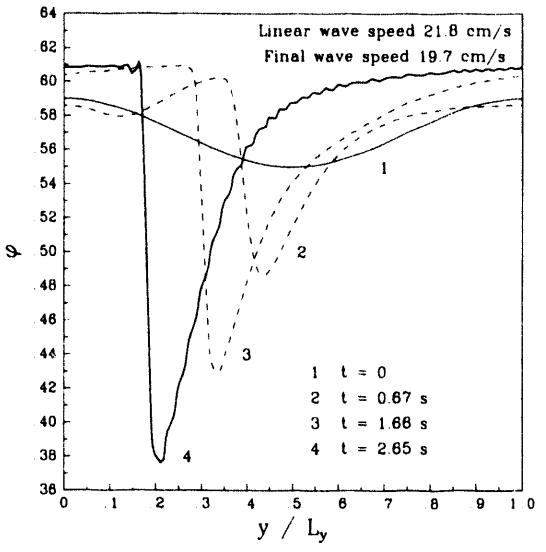

Figure 6 Development of the 3π cm 1D wave in an air fluidized bed

for a box of height 3π cm, three times the wavelength of the fastest growing wave. As shown in Figure 6, the sinusoidal disturbance grows smoothly into a nonlinear wave of the sort seen thus previously, but it is deeper. in general, only the longest possible wavelength for a given box is stable. Smaller wavelengths tend to coalesce.

For liquid suspensions the qualitative behavior is much the same. Development of the fastest growing wave and one of twice that wavelength are shown in Figures 7 and 8, respectively. The absence of sharp fronts is due to the fact that the bed is stable to much lower density for the same parameters as for the gas bed. When densities are not near the close packed limit the wave fronts are not so steep. The primary difference between the one dimensional behavior of gas and liquid systems is the much slower growth seen in the latter. In liquid fluidized beds, the wave travels many wavelengths before becoming fully developed. However, there is no indication of qualitative differences in the types of one-dimensional structures seen in gaseous and liquid suspensions.

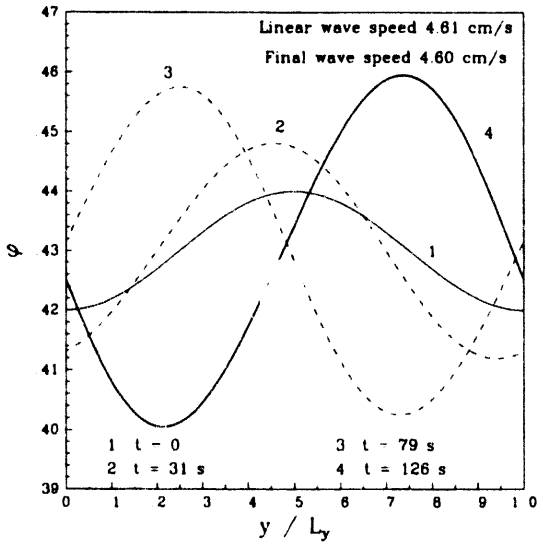

Figure 7: Development of the fastest growing wave in a water fluidized bed

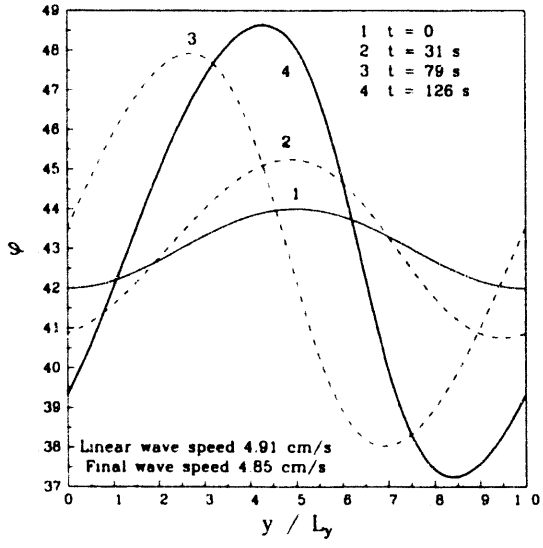

Figure 8: Development of the 4.5 cm 1D wave in a water fluidized bed

Growth of Two-Dimensional Disturbances

The longest wavelength fully developed one-dimensional wave for a given box size is stable to one-dimensional disturbances. However as the box width is increased and the mesh refined laterally, the one dimensional wave loses stability in the lateral direction. The eigenvalue representing this unstable perturbation of the one-dimensional wave is always real. For both gas and liquid fluidized systems, the one-dimensional wave is perturbed in the direction of the dominant instability and integrated forward in time.

For the one-dimensional wave shown in Figure 6, the fastest growing lateral disturbance corresponds to a lateral wavelength two thirds that in the axial direction. The initial perturbation is shown in Figure 9. Figures 10 through 12 show the subsequent development of the density field and the streamlines for both phases. The perturbed wave becomes a void, resembling in many respects a bubble in a gas fluidized bed. The circulating vortex in the fluid and the flow of solids around the void are characteristic of bubbles. The velocity of rise in the rest frame also corresponds well with that to be expected for a bubble of this size. The hole has a solids concentration of roughly 10%, whereas actual bubbles are nearly particle free. We thus hesitate to call the void a true bubble, but in structure it certainly resembles one, and development continues if the integration is prolonged.

The two-dimensional development of the perturbed wave in the liquid suspension is shown in Figures 13 to 17. We begin with the fully developed one-dimensional wave from Figure 8. The fastest growing lateral disturbance of this wave has a wavelength equal to the axial one. The initial growth is similar to that in the gas bed, and is nearly as rapid. An incipient void begins to form and circulation appears in the fluid. Beyond this point, however, the behavior of the two systems diverges. The velocity in the liquid vortex is sufficient to lift the particles from the dense region below, resulting in circulation in the solids phase as well as the fluid. Particles lifted from the dense region behind the void fill the incipient hole whose remnants accelerate upwards through several wavelengths and destroy the structure which had developed to this point. The picture is thus completely different from that seen in gaseous suspensions. The behavior bears a resemblance to the theory of maximum stable bubble size in fluidized suspension proposed by Davidson over thirty years ago [4]. It is also the first indication that the volume averaged equations of motion predict qualitatively different behavior for gaseous

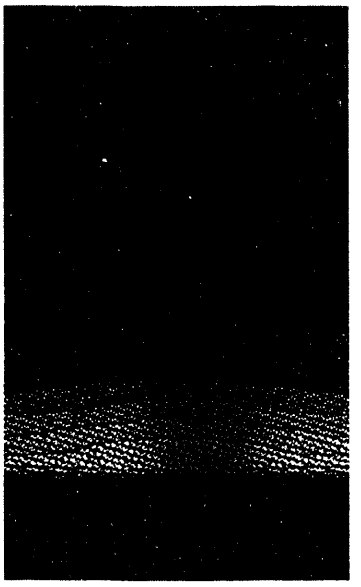

Figure 9: 2D perturbation of the 3π cm wave in an air fluidized bed

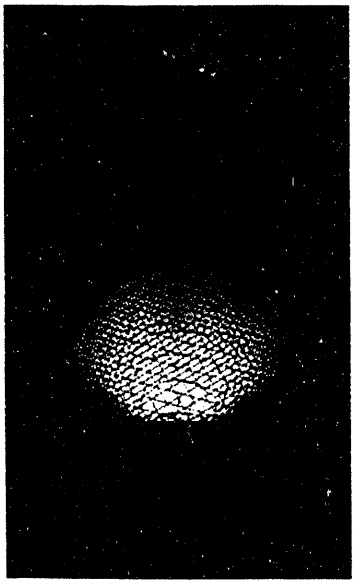

Figure 10: 2D growth of the 3π cm wave in an air fluidized bed, $t = 0.52$ s

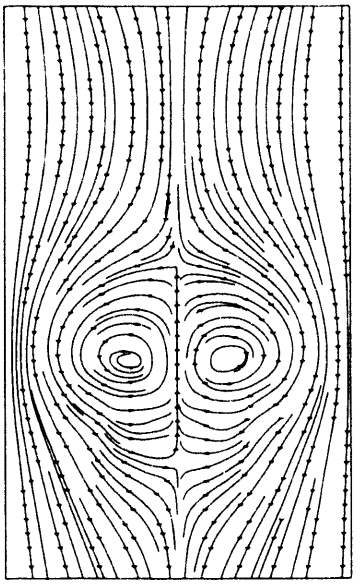

Figure 11: fluid streamlines for the 3π cm wave, t = 0.52 s

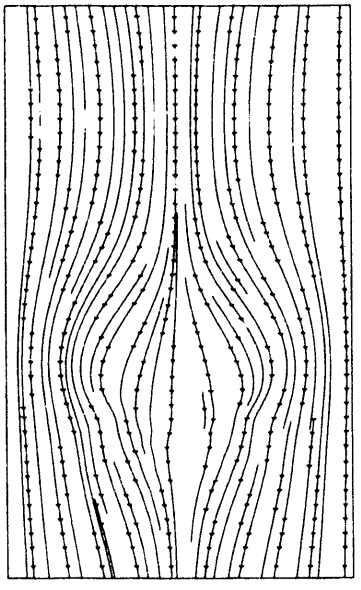

Figure 12: solids streamlines for the 3π cm wave, t = 0.52 s

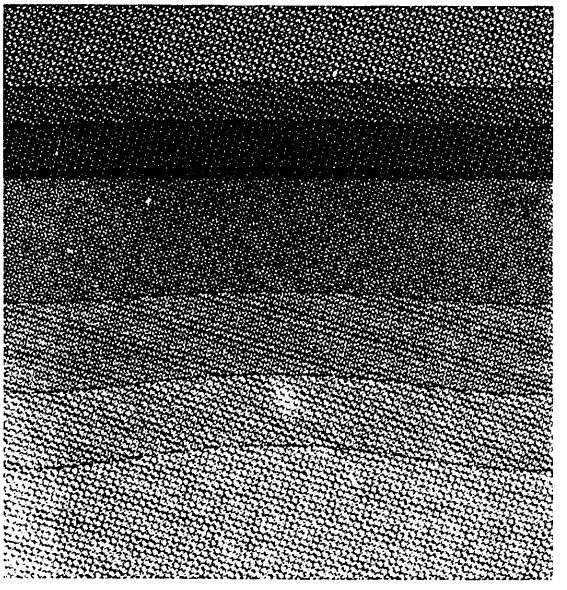

Figure 13: 2D perturbation of the 4.5 cm wave in a water fluidized bed

and liquid suspensions.

Conclusions

The volume averaged equations of motion for small particles suspended in a fluid have been studied with the simplest set of constitutive closures, to explore the extent to which they represent observed behavior. A finite element code has been developed to examine the predictions of the system of equations, and it has been tested against analytical results. With confidence in the code established, we have proceeded to follow the growth of one and two dimensional disturbances in gaseous and liquid suspensions.

In both systems one-dimensional disturbances grow into similar structures. The time scales of this growth are very different for the two, but this difference is in agreement with observed behavior. These one-dimensional waves become unstable against pertrubations with lateral structure, with the instability again taking the same form in both systems. The initial two-dimensional development is identical in both systems; a void forms and recirculation appears in the fluid. Finally, in the last stages of development, the incipient void in the gaseous suspension continues to grow smoothly into

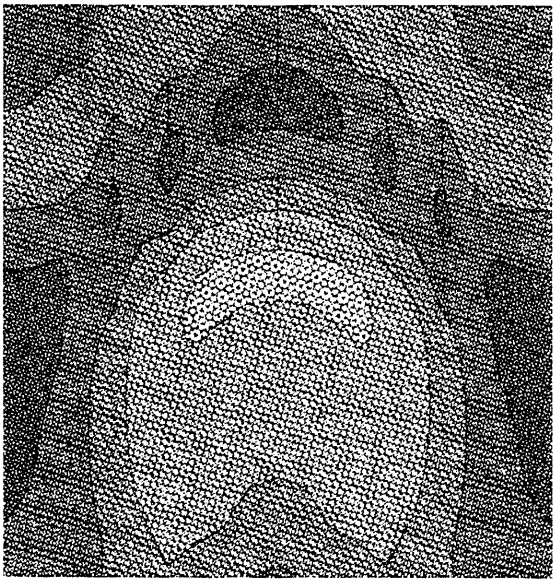

Figure 14: 2D growth of the 4.5 cm wave in a water fluidized bed, t = 1.1 s

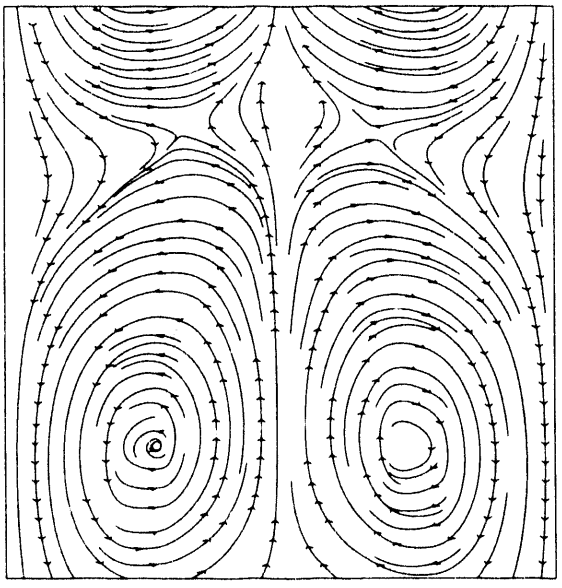

Figure 15: fluid streamlines for the 4.5 cm wave, t = 1.1 s

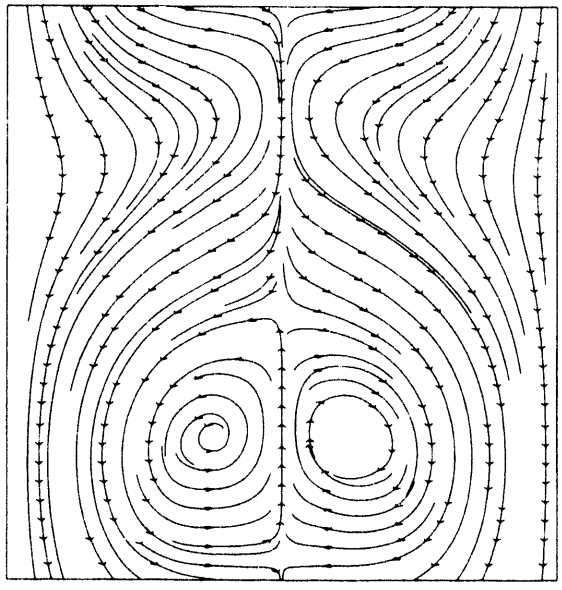

Figure 16: solids streamlines for the 4.5 cm wave, t = 1.1 s

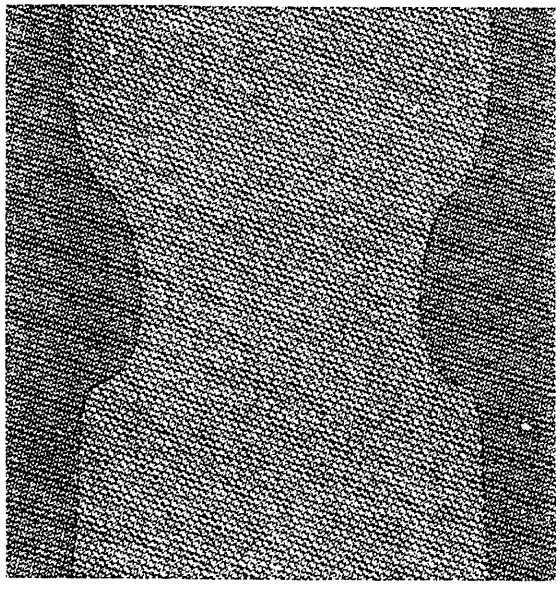

Figure 17: the 4.5 cm wave in a water fluidized bed, t = 3.1 s

a bubble-like structure, while that in the liquid suspension is destroyed as particles are lifted by the liquid vortex to fill the void. This is the first evidence that the volume averaged equations of motion represent the observed difference in behavior between typical gas and liquid fluized beds.

References

[1] Anderson, T.B. and R. Jackson, *I/EC Fundamentals*, **6**:527-539 (1967).

[2] Anderson, T.B. and R. Jackson, *I/EC Fundamentals*, **8**:137-144 (1967).

[3] Davidson, J.F., *Trans. Inst. Chem. Eng.*, **39**:320 (1961).

[4] Davidson, J.F. and D. Harrison, "Fluidised Particles", (p. 84) Cambridge University Press (1963).

[5] El-Kaissy, M.M. and G.M. Homsy, *Int. J. Multiphase Flow*, **6**:305-318 (1980).

[6] Ganser, G.H. and D.A. Drew, *Int. J. Multiphase Flow*, **16**:447-460 (1990).

[7] Jackson, R., *Trans. Inst. Chem. Eng.*, **41**:12-21 (1963).

[8] Jackson, R., *Trans. Inst. Chem. Eng.*, **41**:22-28 (1963).

GRAVITY-DRIVEN FLOWS OF SMOOTH, INELASTIC SPHERES DOWN BUMPY INCLINES

Mark W. Richman and Richard E. Martin

Mechanical Engineering Department
Worcester Polytechnic Institute
Worcester, Massachusetts 01609

Abstract

In this paper, we employ a kinetic theory to analyze steady, fully developed, gravity-driven flows of identical, smooth, highly inelastic spheres down bumpy inclines. We treat the solid fraction, mean velocity, and components of the full second moment of fluctuation velocity as mean fields. In addition to the balance equations for mass and momentum, we treat the balance of the full second moment of fluctuation velocity as an equation that must be satisfied by the mean fields. However, in order to simplify the resulting boundary value problem, we retain fluxes of second moments in its isotropic piece only. The constitutive relations for the stresses and and collisional source of second moment depend explicitly on the second moment of fluctuation velocity, and the constitutive relation for the energy flux depends on gradients of granular temperature, solid fraction, and components of the second moment. We obtain numerical solutions that are free of stress and energy flux at the tops of the flows, satisfy momentum and energy balances at the bumpy base, and are most easily parameterized in terms of the granular temperature at the tops of the flows. To each such temperature there corresponds a value of mass hold-up and mass flow rate. For fixed coefficients of restitution, boundary bumpiness, and angle of inclination, we calculate the variation of mass flow rate with mass hold-up, and for a prescribed value of mass hold-up we calculate the profiles of solid fraction, mean velocity, normal components of the second moment, and normal stresses.

Balance Equations and Constitutive Relations

We are concerned here with steady, fully developed, gravity-driven flows of identical, smooth, highly inelastic spheres down bumpy inclines. The diameter of each sphere is σ, the mass density of each is ρ_p, and the coefficient of restitution between them is e. In what follows, e need not be close to unity. The vertical acceleration due to gravity is g, and the angle

Presented at the Annual Joint NSF/DOE Workshop on Flow of Particulates and Fluids, Ithaca, New York, September 30 - October 1, 1993.

between the incline and the the horizontal is ϕ. We introduce an x_1-x_2-x_3 Cartesian coordinate system such that x_1 measures distance along the incline parallel to the flows, and x_2 measures distance above the incline perpendicular to the the flows. The flows are infinitely extended in the x_1- and x_3-directions.

The mean fields of interest in these granular flows are the solid fraction ν, the only non-zero velocity component u_1, the granular temperature T, and the components A_{11}, A_{22}, A_{33}, and A_{12}, of the *deviatoric* part of the second moment of particle fluctuation velocity. Their dimensionless counterparts ν, $u \equiv u_1/(\sigma g)^{1/2}$, $\tau \equiv T/\sigma g$, $a_{11} \equiv A_{11}/\sigma g$, $a_{22} \equiv A_{22}/\sigma g$, $a_{33} \equiv A_{33}/\sigma g$, and $a_{12} \equiv A_{12}/\sigma g$ depend on the dimensionless coordinate $y \equiv x_2/\sigma$ only. Their variations with y are governed by the x_1- and x_2-components of the balance of momentum, the balance of energy, and the x_1-x_1, x_2-x_2, x_3-x_3 and x_1-x_2 components of the balance of second moment.

Under these circumstances, the balance of mass is satisfied identically. If P_{ij} are the components of the pressure tensor, then in terms of their dimensionless counterparts $p_{ij} \equiv P_{ij}/\rho_p \sigma g$, the x_1- and x_2-components of the balance of momentum are,

$$p_{12}' = \nu \sin\phi \quad , \tag{1}$$

and

$$p_{22}' = -\nu \cos\phi \quad , \tag{2}$$

where primes denote differentiation with respect to y. The x_3-component of the balance of momentum demonstrates that p_{32} does not vary with y. The balance of energy is the isotropic part of the balance of the full second moment of fluctuation velocity. If Q_2 is the x_2-component of the energy flux, Γ is the rate of energy dissipation due to inelastic collisions, and their dimensionless counterparts are $q \equiv 2Q_2/\rho_p(\sigma g)^{3/2}$ and $\gamma \equiv -2\Gamma/\rho_p \sigma^{1/2} g^{3/2}$, then the balance of energy is,

$$q' = \gamma - 2p_{12}u' \quad . \tag{3}$$

The remaining equations are obtained from the deviatoric part of the balance of full second moment. In addition to the components P_{ij} of the pressure tensor, these equations involve the components Q_{ijk} and χ_{ij} of the flux and collisional source of the deviatoric part of the second moment. If the spatial gradients of Q_{ijk} are small compared to χ_{ij}, then, in terms of the dimensionless source components $\gamma_{ij} \equiv \chi_{ij}/\rho_p \sigma^{1/2} g^{3/2}$, the resulting approximate equations for a_{11}, a_{22}, and a_{12} are the x_1-x_1 deviatoric component of the balance of second moment,

$$\frac{4}{3} p_{12} u' = \gamma_{11} \quad ; \tag{4}$$

the x_2-x_2 deviatoric component of the balance of second moment,

$$\frac{-2}{3} p_{12} u' = \gamma_{22} \quad ; \tag{5}$$

and the x_1-x_2 component of the balance of second moment,

$$p_{22} u' = \gamma_{12} \quad . \tag{6}$$

The x_3-x_3 deviatoric component of the second moment equation determines a_{33}, and to within a minus sign is given by the sum of equations (4) and (5).

In what follows, we employ the constitutive theory derived by Richman and Martin [1993]. The constitutive relation for the shear stress p_{12} is given in terms of the solid fraction ν, the granular temperature τ, and the second moment component a_{12} by,

$$p_{12} = -2(1+e)\nu G\tau \left[\frac{2}{5\sqrt{\pi\tau}} u' - H \frac{a_{12}}{\tau} \right] \quad , \tag{7}$$

in which $G(\nu)$ is equal to $\nu(2-\nu)/2(1-\nu)^3$ and $H(G)$ is equal to $2[1+5/4(1+e)G]/5$. The normal pressure p_{11} is given in terms of ν, τ, and the deviatoric component a_{11} of second moment by,

$$p_{11} = 2(1+e)\nu G\tau \left[F + H \frac{a_{11}}{\tau} \right] \quad , \tag{8}$$

in which $F(G)$ is equal to $[1+1/2(1+e)G]$. Similarly, the remaining normal pressures p_{22} and p_{33} are given by,

$$p_{22} = 2(1+e)\nu G\tau \left[F + H \frac{a_{22}}{\tau} \right] \quad , \tag{9}$$

and

$$p_{33} = 2(1+e)\nu G\tau \left[F + H \frac{a_{33}}{\tau} \right] \quad . \tag{10}$$

Differences between the normal stresses result from corresponding differences between a_{11}, a_{22}, and a_{33}.

The energy flux q is related to gradients of τ, a_{22}, and ν according to the relation,

$$q = \frac{-4(1+e)\nu G\tau^{1/2}}{\pi^{1/2}} (\kappa\tau' + \lambda\tau\nu' + \eta\, a_{22}') \quad , \tag{11}$$

in which the coefficients $\kappa(\nu, e)$, $\lambda(\nu, e)$, and $\eta(\nu, e)$ are given by,

$$\kappa = \left\{ 1 + \frac{9\pi(1+e)(2e-1)}{4(49-33e)} \left[1 + \frac{5}{3(1+e)^2(2e-1)G} \right] \left[1 + \frac{5}{6(1+e)G} \right] \right\} \quad , \tag{12}$$

$$\lambda = \frac{-9\pi e(1-e)}{4(49-33e)} \frac{d(\ln \nu G)}{d\nu} \left[1 + \frac{5}{6(1+e)G} \right] \quad , \tag{13}$$

and

$$\eta = \frac{2}{5} \left\{ 1 + \frac{25\pi(3e+1)(\beta+\alpha)}{24(3-e)(49-33e)} \left[1 + \frac{1}{(1+e)(\beta+\alpha)G} \right] \left[1 + \frac{5}{6(1+e)G} \right] \right.$$

$$\left. + \frac{5\pi\xi}{24(3-e)} \left[1 + \frac{1}{(1+e)\xi G} \right] \left[1 + \frac{5}{6(1+e)G} \right] \right\} \quad , \tag{14}$$

where $\beta \equiv (49-33e)[-6(1+e)/5+4(1+e)^2/3]/14(3e+1)$, $\alpha \equiv [-4/5-9(1+e)/5+2(1+e)^2/3]$, and $\xi \equiv [-4/5+6(1+e)/5+4(1+e)^2/21]$. If gradients of a_{22} are ignored and e is set equal to 1, then expression (11) reduces to the expression for the energy flux in assemblies of nearly elastic spheres obtained by Jenkins and Richman [1985].

The remaining constitutive quantity is the collisional source of second moment of fluctuation velocity. In it, we retain terms linear in a_{11}, a_{22}, a_{33}, a_{12}, and u'. In addition, we retain just those nonlinear terms that guarantee that, in the tensoral form of the balance of of second moment, the collisional contribution to the stress is multiplied only by the rate of strain. In this manner, the isotropic piece of the source of second moment is approximated by,

$$\gamma = \frac{-24\nu G(1-e^2)\tau^{3/2}}{\pi^{1/2}} \quad . \tag{15}$$

The corresponding result obtained by Jenkins and Richman [1985] may be obtained by replacing $(1-e^2)$ by 2(1-e) in expression (15). The deviatoric parts of

the x_1-x_1 and x_2-x_2 components of the source of second moment are given in terms of ν, τ, a_{11}, a_{22}, a_{12}, p_{12}, and u' by the constitutive relations,

$$\gamma_{11} = \frac{-24\nu G(1+e)(3-e)\tau^{3/2}}{5\pi^{1/2}} \frac{a_{11}}{\tau} + (p_{12} - \nu a_{12})u' \quad , \tag{16}$$

and

$$\gamma_{22} = \frac{-24\nu G(1+e)(3-e)\tau^{3/2}}{5\pi^{1/2}} \frac{a_{22}}{\tau} - (p_{12} - \nu a_{12})u' \quad , \tag{17}$$

where p_{12} is given by equation (7). Similarly, the x_1-x_2 component of the source of second moment is,

$$\gamma_{12} = \frac{-24\nu G(1+e)\tau^{3/2}}{5} \left\{ \frac{(3-e)}{\pi^{1/2}} \frac{a_{12}}{\tau} - \frac{(2-e)}{4} \frac{u'}{\tau^{1/2}} \right\} + [(p_{22} - p_{11}) - \nu(a_{22} - a_{11})] \frac{u'}{2} \quad , \tag{18}$$

where p_{11} and p_{22} are given by equations (8) and (9). Constitutive relations (16), (17), and (18) have no counterparts in the theory of Jenkins and Richman [1985] for nearly elastic spheres.

In order to reduce the number of equations in the governing system, we employ constitutive relation (16) to eliminate γ_{11} from balance (4) to obtain,

$$\frac{a_{11}}{\tau} = \frac{-5\pi^{1/2}}{24\nu G(1+e)(3-e)\tau} \left[\frac{1}{3} p_{12} + \nu a_{12} \right] \frac{u'}{\tau^{1/2}} \quad , \tag{19}$$

and constitutive relation (17) to eliminate γ_{22} from balance (5) to obtain,

$$\frac{a_{22}}{\tau} = \frac{-5\pi^{1/2}}{24\nu G(1+e)(3-e)\tau} \left[\frac{1}{3} p_{12} - \nu a_{12} \right] \frac{u'}{\tau^{1/2}} \quad . \tag{20}$$

Equations (19) and (20) and constitutive relation (7) demonstrate that the deviatoric components a_{11} and a_{22} are sums of terms proportional to $(u')^2$ or to products of a_{12} and u'. These nonlinear terms were neglected by Jenkins and Richman [1985]. Consequently, they predicted that, for flows of nearly elastic spheres, the components a_{11}, a_{22}, and a_{33} all vanish. In that approximation, the constitutive equations (8), (9), and (10) simplify and guarantee that the normal pressures p_{11}, p_{22}, and p_{33} are all equal.

Finally, we employ constitutive relation (18) to eliminate γ_{12} from balance (6) to obtain,

$$\frac{a_{12}}{\tau} = \frac{-\pi^{1/2}(3e-1)}{12(3-e)}\left[1+\frac{5}{2(1+e)(3e-1)G}\right]\frac{u'}{\tau^{1/2}} \quad , \tag{21}$$

where we have neglected terms that are cubic in u', a_{12}, and products of u' and a_{12}. If equation (21) is employed to eliminate a_{12} from constitutive relation (7) and e is set equal to 1, then the resulting expression for the shear stress is identical to that obtained by Jenkins and Richman [1985].

Boundary Conditions

With appropriate conditions applied at the free surface and base of the incline, equations (1), (2), (3), (7), (9), (11), (15), (19), and (20) determine the variations with y of p_{12}, p_{22}, q, τ, γ, u', ν, a_{12}, and a_{22}. Although the location of the free surface is not known, the stresses and the energy flux each vanish there; i.e.

$$p_{12} = 0 \quad \text{and} \quad p_{22} = 0 \quad , \tag{22}$$

and

$$q = 0 \quad . \tag{23}$$

Because the stresses both vanish at the top of the flow, ν may be eliminated between equations (1) and (2) to demonstrate that $p_{12}/p_{22}=-\tan\phi$.

If ν is equal to 0 and τ is not, then according to constitutive relation (9) the normal stress condition at the top of the flow is automatically satisfied. Near the top of the flow, therefore, ν is small, the normal stress may be approximated by

$$p_{22} = \nu(\tau + a_{22}) \quad , \tag{24}$$

and because the ratio p_{12}/p_{22} is everywhere equal to $-\tan\phi$, the shear stress may be approximated by

$$p_{12} = -\nu(\tau + a_{22})\tan\phi \quad . \tag{25}$$

Furthermore, if equations (21) and (25) are employed to eliminate a_{12} and p_{12} from constitutive relation (7), then we find that near the top of the flow, u' is given approximately by,

$$u' = \frac{24(3-e)(1+e)(\tau+a_{22})\tan\phi}{5\pi^{1/2}\tau^{1/2}}\nu \quad . \tag{26}$$

With u' given by equation (26), the lowest order approximation of equation (7) dictates that,

$$a_{12} = -(\tau + a_{22}) \tan\phi \quad , \tag{27}$$

and with p_{12}, u', and a_{12} given by equations (25), (26), and (27), balance (20) yields,

$$1 + \frac{a_{22}}{\tau} = \frac{-3/2 + \sqrt{9/4 + 6\tan^2\phi}}{2\tan^2\phi} \quad . \tag{28}$$

For small values of ν and prescribed values of τ and ϕ, equation (28) fixes a_{22}, equations (24) and (25) fix p_{22} and p_{12}, and for prescribed values of e, equation (26) fixes u'. As ν approaches zero, so too do the stresses p_{22} and p_{12} and the velocity gradient u'. However, in the same limit the components a_{22} and a_{12} of second moment each approach *nonzero* limits that depend only on the inclination angle ϕ and the local value of τ.

Of interest also are the limiting behaviors of the gradients τ', ν', a_{12}' a_{22}' and u" as ν approaches zero. By differentiating approximations (24) and (28) with respect to y, for example, we find that

$$\nu' = \frac{-\nu\cos\phi}{f(\phi)\,\tau} - \frac{\nu\tau'}{\tau} \quad , \tag{29}$$

where $f(\phi)$ is given by the right-hand-side of equation (28), and

$$a_{22}' = [f(\phi) - 1]\,\tau' \quad . \tag{30}$$

If these are employed to eliminate ν' and a_{22}', then constitutive relation (11) for the energy flux demonstrates that τ', and therefore ν' and a_{22}', each approach zero with ν. Simple differentiation of approximations (26) and (27) with respect to y then demonstrates that both u" and a_{12}' approach zero in the same manner.

At the base of the incline (i.e. y=0), the rate **M** at which momentum is supplied to the flows by inelastic collisions between flow particles and the base must balance the traction vector at the base. Furthermore, the difference between the rate $-M_1u_1$ at which energy is supplied by slip work and the rate D at which it is absorbed by inelastic collisions between flow particles and the base must balance the energy flux at the base.

The transfer rates **M** and D depend on the geometry and dissipative nature of the incline. Here we focus on inclines that are flat surfaces to which identical, smooth, hemispherical particles of diameter d are randomly

attached at an average distance s apart. In order to prevent flow particles from colliding with the flat part of the boundary, the maximum allowable value of s/d is $-1+(1+2\sigma/d)^{1/2}$. When a flow particle collides with a boundary particle the distance between their centers is $\delta\equiv(\sigma+d)/2$, and the energy dissipated is fixed by the coefficient of restitution e_w between them. A measure of the bumpiness of the boundaries is the angle $\theta\equiv\sin^{-1}(d+s)/(d+\sigma)$, which increases from 0 to $\pi/2$ as the boundaries evolve from perfectly flat to extremely bumpy.

We employ the general expressions for **M** and D obtained by Richman and Martin [1993] for assemblies of inelastic spheres that interact with bumpy boundaries described above. The expression for **M** involves an unknown factor that accounts for excluded volume and particle shielding at the boundary. If we first employ the balance between the x_2-components of **M** and the traction vector to write the unknown factor in terms of p_{22}, a_{22}, τ, and θ, then the balance between the x_1-components of **M** and the traction vector determines the slip velocity u(0) according to,

$$\frac{u}{\tau^{1/2}} = \frac{-\pi^{1/2}}{2^{1/2}I}\left[1+\frac{a_{22}}{\tau}\left(1-\frac{3}{4}\sin^2\theta\right)\right]\frac{p_{12}}{p_{22}} + \frac{\delta}{\sigma}\frac{(2I-\sin^2\theta)}{2I}\frac{u'}{\tau^{1/2}} + \frac{\pi^{1/2}}{2^{3/2}I}\frac{a_{12}}{\tau} \quad , \qquad (31)$$

where $I(\theta)\equiv 2[2\csc^2\theta(1-\cos\theta)-\cos\theta]/3$. Furthermore, the energy flux at the boundary is determined by,

$$q = 2\left\{-p_{12}u - \frac{2^{3/2}}{\pi^{1/2}}(1-e_w)\csc^2\theta(1-\cos\theta)\left[1+\frac{a_{22}}{\tau}\left(1-\frac{3}{4}\sin^2\theta\right)\right]^{-1}\tau^{1/2}p_{22}\right\} \quad . \qquad (32)$$

Conditions (22), (23), (31), and (32) are the five conditions needed to complete the set of equations (1), (2), (3), (7), (9), (11), (15), (19), and (20). We provide a detailed description of the solution procedure in the following section.

Solution Procedure

The shear stress constitutive relation (7), the normal stress constitutive relation (9), and the x_2-x_2 and x_1-x_2 deviatoric components (20) and (21) of the balance of second moment determine ν, u', a_{12}, and a_{22} as functions of τ, p_{12}, and p_{22}. *In principle,* these functions may be employed to eliminate ν from the momentum equations (1) and (2), ν and u' from the energy equation (3) in which γ is replaced by expression (15), and ν, τ, ν', and a_{22}' from the energy flux constitutive equation (11). The four equations that result are first order ordinary differential equations that determine $\tau(y)$, $p_{12}(y)$, $p_{22}(y)$, q(y), and therefore $\nu(y)$, u'(y), $a_{12}(y)$, and $a_{22}(y)$ to within four constants of integration. These four constants and the dimensionless depth L (measured in particle diameters) are determined by the shear and normal stress conditions (22), the

energy flux conditons (23) and (32), and by prescribing a nonzero value τ^* of τ at the top of the flow. The mass hold-up corresponding to this choice of τ^* may be calculated according to its definition,

$$m_t = \int_0^L \nu dy \quad . \tag{33}$$

The component $a_{11}(y)$ is then determined algebraically by equation (19), the component $a_{33}(y)$ is simply the sum $-(a_{11}+a_{22})$, and the stresses $p_{11}(y)$ and $p_{33}(y)$ are fixed by their constitutive relations (8) and (10). Finally, by direct integration of u'(y), the profile u(y) may be found to within a fifth constant that is determined by the momentum flux condition (31), and the mass flow rate may be calculated according to its definition,

$$\dot{m} = \int_0^L \nu u dy \quad . \tag{34}$$

Unfortunately, it is not possible in closed form to eliminate ν, u', a_{12}, and a_{22} from equations (1), (2), (3), and (11). Consequently, in the numerical integration of these equations, at each spatial location at which τ, p_{12}, and p_{22} are known it is necessary to invert the nonlinear algebraic equations (7), (9), (20), and (21) to determine the corresponding values of ν, u', a_{12}, and a_{22}. In order to avoid this difficulty, we actually *raise* the order of the system by differentiating equations (7), (9), (20), and (21) with respect to y. In this manner, the four resulting equations and the energy flux constitutive relation (11) may be written in matrix form:

$$[C]\{L\} = \{R\} \quad , \tag{35}$$

in which the components of the five dimensional vectors {L} and {R} are:

$$L_1 = \tau' , \qquad L_2 = \nu' , \qquad L_3 = a_{22}' , \qquad L_4 = a_{12}' , \qquad L_5 = u'' ; \tag{36}$$

and

$$R_1 = \frac{-\sin\phi}{2(1+e)G} , \quad R_2 = \frac{-\nu\cos\phi}{2(1+e)} , \quad R_3 = \frac{-\pi^{1/2}q}{4(1+e)\nu G\tau^{1/2}} , \quad R_4 = \frac{\nu u'\sin\phi}{3} , \quad R_5 = 0 . \tag{37}$$

The components of the 5x5 coefficient matrix [C], which are given explicitly in the Appendix, depend on various combinations of the unknowns τ, p_{12}, ν, u', a_{12}, and a_{22}. The momentum equations (1) and (2), the energy equation (3)

in which γ is replaced by expression (15), and the matrix equation (35) are eight first order equations for τ, p_{12}, p_{22}, q, ν, u', a_{12}, and a_{22} that may be solved by straightforward numerical integration. The first and second rows of equation (35) are the differentiated forms of the shear stress relation (7) and the normal stress relation (9); the third row is the energy flux relation (11); and the fourth and fifth rows are the differentiated forms of the x_2-x_2 component (20) and the x_1-x_2 component (21) of the balance of second moment.

For fixed values of e, e_w, σ/d, s/d, and ϕ, we employ a fourth order Runge-Kutta technique to integrate equations (1), (2), (3), and (35) from the top of the flow, where p_{12}, p_{22}, and q vanish and τ is equal to its prescribed value W^2. Because, at the top of the flow, p_{22} vanishes and τ does not, ν must vanish there. However, we have seen in the previous section that under these circumstances the gradients τ', ν', a_{12}', a_{22}', and u" also vanish. Moreover, equations (1), (2), (3) and (15) demonstrate that when ν is equal to zero, so to are p_{12}', p_{22}', and q'. Integrations initiated when ν=0 therefore yield no spatial variations in p_{12}, p_{22}, q, τ, ν, a_{12}, a_{22}, and u'. This indicates that the theory predicts that the flows are infinitely deep and that p_{12}, p_{22}, q, τ, ν, a_{12}, a_{22}, and u' each approach their values at the top of the flow asymptotically from the base. To overcome this difficulty, we follow Oyediran et. al. [1992] and set ν equal to 10^{-6} at the top of the flow, which is equivalent to relaxing very slightly the normal stress condition there. Then with $\tau=W^2$, q=0, and a_{22}, a_{12}, u', p_{12}, and p_{22} given by equations (28), (27), (26), (25), and (24), the integration produces spatial variations as it proceeds toward the base. We have also initiated the integrations with several other combinations of ν and q between 10^{-5} and 10^{-7}, and in each case obtained results that were indistinguishable from those based on $\nu=10^{-6}$ and q=0.

For any value of W^2, the depth L is the distance from the point at which the integrations are initiated to the location at which the basal energy flux condition (32) is satisfied. When condition (32) is satisfied, the variations $p_{12}(y)$, $p_{22}(y)$, q(y), $\tau(y)$, $\nu(y)$, $a_{12}(y)$, $a_{22}(y)$, and u'(y), and the mass-hold-up are completely determined. With the slip velocity fixed by condition (31), the variation u(y) may then be determined by direct integration of u'(y), and the mass flow rate is fixed by its definition (34). The process of finding solutions is complicated only by the fact that there are a great variety of parameter values (e, e_w, σ/d, s/d, and ϕ) and initial values W^2 for which condition (32) can not be satisfied; under these circumstances the theory predicts that no steady, fully-developed flows can be maintained.

Results and Discussion

In this section, we present a sample of the results obtained from the solution procedure described above. In two previous papers, Richman and Marciniec [1990] and Oyediran et.al. [1992] employed a theory for nearly elastic particles, focused much of their attention on flow particles with e=.8, and

boundaries with e_w=.95, σ/d=1/2, and s/d=-1+$2^{1/2}$, and found that steady, fully developed flows could be maintained at inclinations roughly between ϕ=19° and 21.5°. In order to focus on flows more inelastic than these, we simply double their value of (1-e) by taking e=.6, and do not alter their values of e_w, σ/d, and s/d. We find that for these more dissipative flows, the theory for highly inelastic particles predicts that the range of inclinations for which steady, fully developed flows may be maintained is raised to roughly between 20° and 26°. In all that follows, we take an intermediate inclination of ϕ=23° near the upper limit of the range.

In the left-hand panel of Figure 1, we show the variations of flow rate $\dot{m}$ with the value W of $\tau^{1/2}$ at the top of the flow. In in the right-hand panel, we eliminate W and show the corresponding variation of $\dot{m}$ with mass hold-up m_t. The lowest value (.158) of W shown on the curve in the left-hand panel is the minimum value at which the solid fraction throughout the flow is everywhere less than .65. The largest value (.990) of W shown on the curve is the maximum value that yields a mass hold-up m_t that is greater than unity. As W decreases from its maximum to its minimum value, the flows become less thermalized, more massive, faster, more shallow, and more dense. The flow rate increases because both the mass and the speed increase. For the parameters used here, there is only one flow for each flow rate.

In Figure 2, we plot the profiles of ν, $w \equiv \tau^{1/2}$, and u for m_t=4, and $\dot{m}$=103.2, and W=.498. In Figure 3, we plot the corresponding profiles of $k_{11}^{1/2} \equiv (\tau+a_{11})^{1/2}$, $k_{22}^{1/2} \equiv (\tau+a_{22})^{1/2}$, and $k_{33}^{1/2} \equiv (\tau+a_{33})^{1/2}$, and p_{11}, p_{22}, and p_{33}. Solid dots on the profiles indicate the location (y=13.47) below which ninety-nine percent of the mass is contained. Within the flows, the rate at which energy is dissipated by inelastic collisions is greater than the rate at which it is supplied by gravity. For this reason, the boundary must supply energy to the flow, and the energy flux must be positive at the boundary. Interestingly, in the case shown here the gradients of τ and ν make positive contributions to the energy flux at the boundary while the gradient of a_{22} actually makes a negative contribution.

The left-hand panels of Figures 2 and 3 demonstrate that near the top of the flow, the solid fraction is small, the components k_{22} and k_{33} are nearly equal, and both are less than k_{11}. As y decreases from about 15 to 9.4, the solid fraction increases dramatically from 0 to its maximum value .39, k_{22} rapidly approaches k_{11}, and both are greater than k_{33}. As y decreases from 9.4 to 0, the solid fraction gradually decreases from its maximum value to .15 at the boundary, k_{22} gradually approaches k_{33}, and both are less than k_{11}. Except near the top of the flow, where the solid fraction, velocity gradient, and normal stresses each vanish, the variations of the differences between p_{11}, p_{22}, and p_{33} with depth follow from the behaviors of k_{11}, k_{22}, and k_{33}. These variations are due primarily to variations in solid fraction and have been observed in the numerical simulations of homogeneous shearing by Walton and Braun [1986], Campbell [1989], and Hopkins and Shen [1992].

Acknowledgements

The authors are grateful to the Pittsburgh Energy Technology Center of the U.S. Department of Energy for its support of this work through contract DE-AC22-91PC90185.

References

Campbell, C.S., 1989, The Stress Tensor for Simple Shear Flows of a Granular Material, J. Fluid Mech., Vol. 203, pp. 449-473.

Hopkins, M.A., Shen, H.H., 1992, A Monte Carlo Solution for Rapidly Shearing Granular Flows Based on the Kinetic Theory of Dense Gases, Vol. 244, pp. 477-491.

Jenkins, J.T., Richman, M.W., 1985, Grad's 13 Moment System for a Dense Gas of Inelastic Spheres, Arch. Rat. Mech. Anal., Vol. 87, pp. 355-377.

Oyediran, A.A., Richman, M.W., Martin, R.E., Alexandrou, A.N., 1992, Granular Flows Down Bumpy Inclines, accepted in Acta Mech.

Richman, M.W., Martin, R.E. ,1993, A Theory for Flows of Identical, Smooth, Highly Inelastic Spheres, in preparation.

Walton, O.R., Braun, R.L., 1986, Stress Calculations for Assemblies of Inelastic Spheres in Uniform Shear, Acta Mech., Vol. 63, pp. 73-86.

Appendix

Here we provide the elements of the 5x5 coefficient matrix [C] of equation (35). The subscripts on the elements of [C] are unrelated to the x_1-x_2-x_3 coordinate directions.

The first row of equation (35) is the differentiated form of shear stress relation (7). The coefficients are,

$$C_{11} = \frac{u'}{5\sqrt{\pi\tau}} \quad , \qquad C_{12} = -a_{12}\frac{dH}{dv} - \frac{p_{12}}{2(1+e)(vG)^2}\frac{d(vG)}{dv} \quad , \tag{A1}$$

and

$$C_{13} = 0 \quad , \qquad C_{14} = -H \quad , \qquad C_{15} = \frac{2\tau^{1/2}}{5\pi^{1/2}} \, . \tag{A2}$$

The second row of equation (35) is the differentiated form of the normal stress relation (9). The coefficients are,

$$C_{21} = vGF \, , \quad C_{22} = \tau\frac{d(vGF)}{dv} + a_{22}\frac{d(vGH)}{dv} \, , \quad C_{23} = vGH \, , \tag{A3}$$

and C_{24}=C_{25}=0. The third row of equation (35) is the energy flux relation (11). The coefficients are,

$$C_{31} = \kappa \quad , \qquad C_{32} = \lambda\tau \quad , \qquad C_{33} = \eta \quad , \tag{A4}$$

and C_{34}=C_{35}=0. The fourth row of equation (35) is the differentiated form of the x_2-x_2 deviatoric component (20) of the balance of second moment. The coefficients are,

$$C_{41} = \frac{-12(1+e)(3-e)vGa_{22}}{5\sqrt{\pi\tau}} \, , \quad C_{42} = \frac{-24(1+e)(3-e)\tau^{1/2}a_{22}}{5\pi^{1/2}}\frac{d(vG)}{dv} + a_{12}u' \, , \tag{A5}$$

and

$$C_{43} = \frac{-24(1+e)(3-e)vG\tau^{1/2}}{5\pi^{1/2}} \quad , \qquad C_{44} = vu' \quad , \qquad C_{45} = va_{12} - \frac{1}{3}p_{12} \, . \tag{A6}$$

The fifth row of equation (35) is the differentiated form of the x_1-x_2 component (20) of the balance of second moment. The coefficients are,

$$C_{51} = \frac{6(3\text{-}e)a_{12}}{\pi^{1/2}(3e\text{-}1)\tau^{3/2}} \ , \quad C_{52} = \frac{5u'}{2(1+e)(3e\text{-}1)G^2}\frac{dG}{dv} \ , \quad C_{53} = 0 \ , \qquad \text{(A7)}$$

and

$$C_{54} = \frac{-12(3\text{-}e)}{\pi^{1/2}(3e\text{-}1)\tau^{1/2}} \ , \qquad C_{51} = -\left[\ 1 + \frac{5}{2(1+e)(3e\text{-}1)G}\ \right] \ . \qquad \text{(A8)}$$

Figure Captions

Figure 1: The variations of $\dot{m}$ with W and m_t for e=.6, e_w=.95, $\sigma/d=1/2$, $s/d=-1+2^{1/2}$ and $\phi=25^o$.

Figure 2: The variations of v, w, and u with y for e=.6, e_w=.95, $\sigma/d=1/2$, $s/d=-1+2^{1/2}$ and $\phi=25^o$, when m_t=4.

Figure 3: The variations with y of $k_{11}^{1/2}$, $k_{22}^{1/2}$, and $k_{33}^{1/2}$; and the variations with y of p_{11}, p_{22}, and p_{33} for e=.6, e_w=.95, $\sigma/d=1/2$, $s/d=-1+2^{1/2}$ and $\phi=25^o$, when m_t=4.

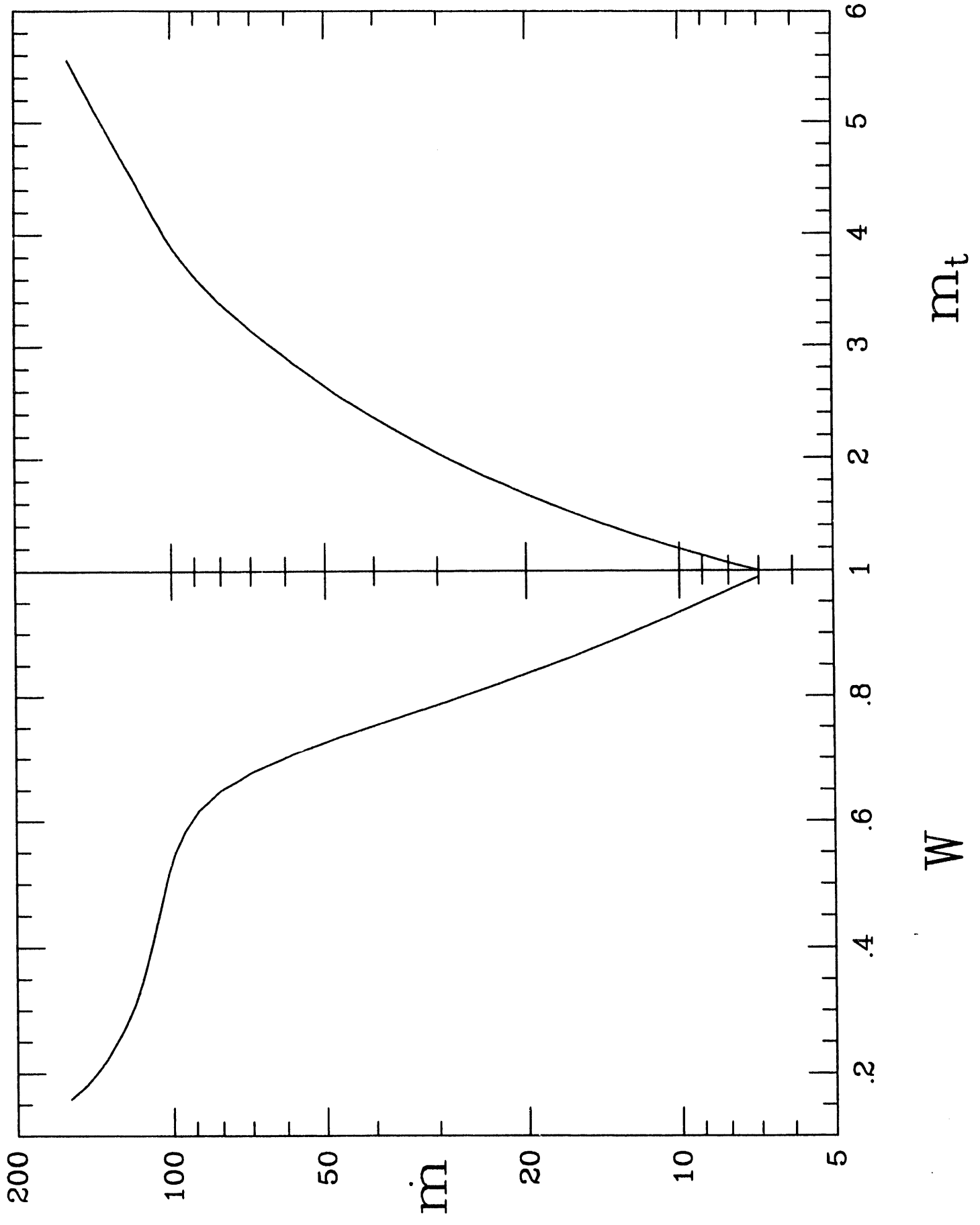

Figure 1: The variations of $\dot{m}$ with W and m_t for e=.6, e_w=.95, $\sigma/d=1/2$, $s/d=-1+2^{1/2}$ and $\phi=25^o$.

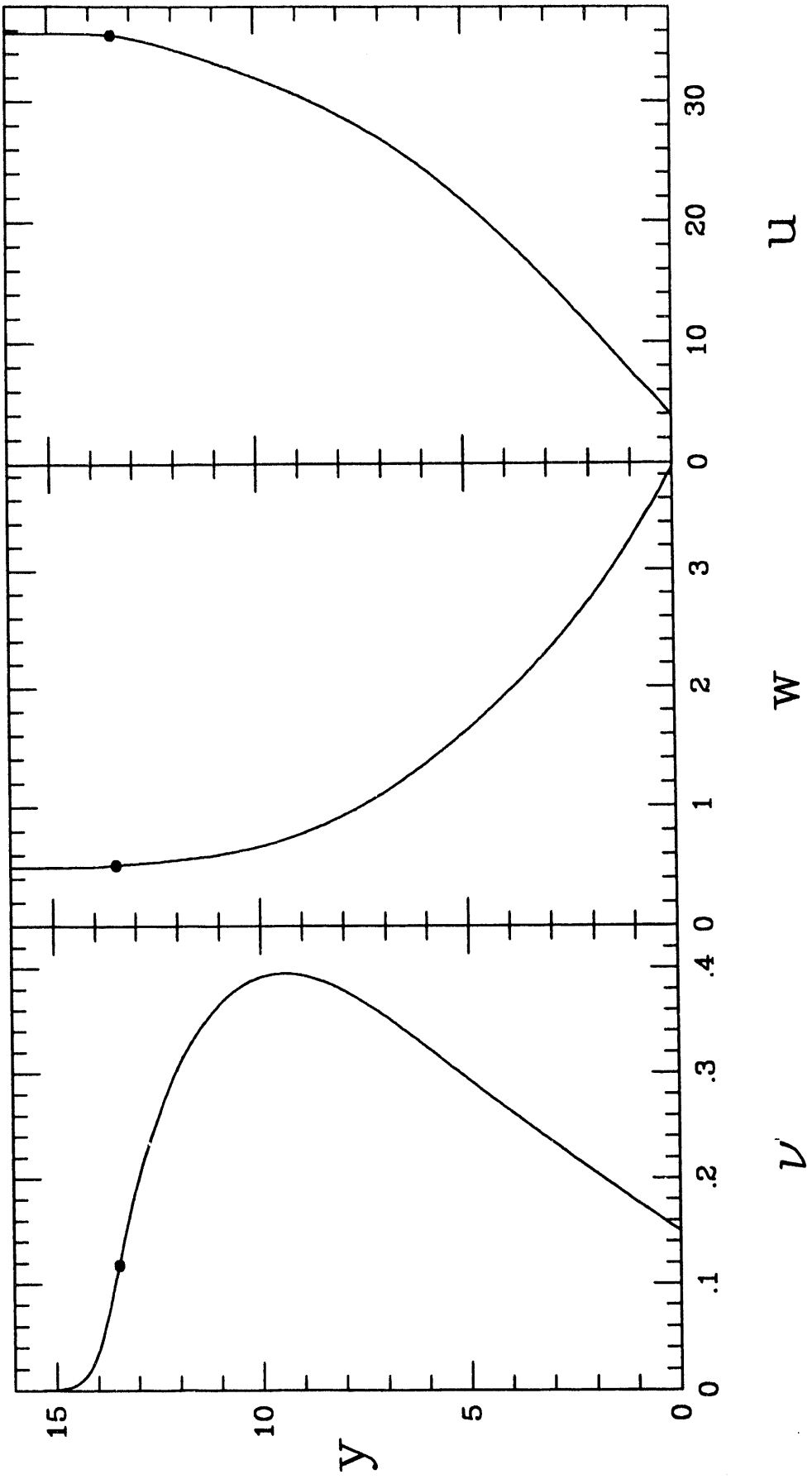

Figure 2: The variations of v, w, and u with y for e=.6, e_w=.95, $\sigma/d=1/2$, $s/d=-1+2^{1/2}$ and $\phi=25^\circ$, when $m_t=4$.

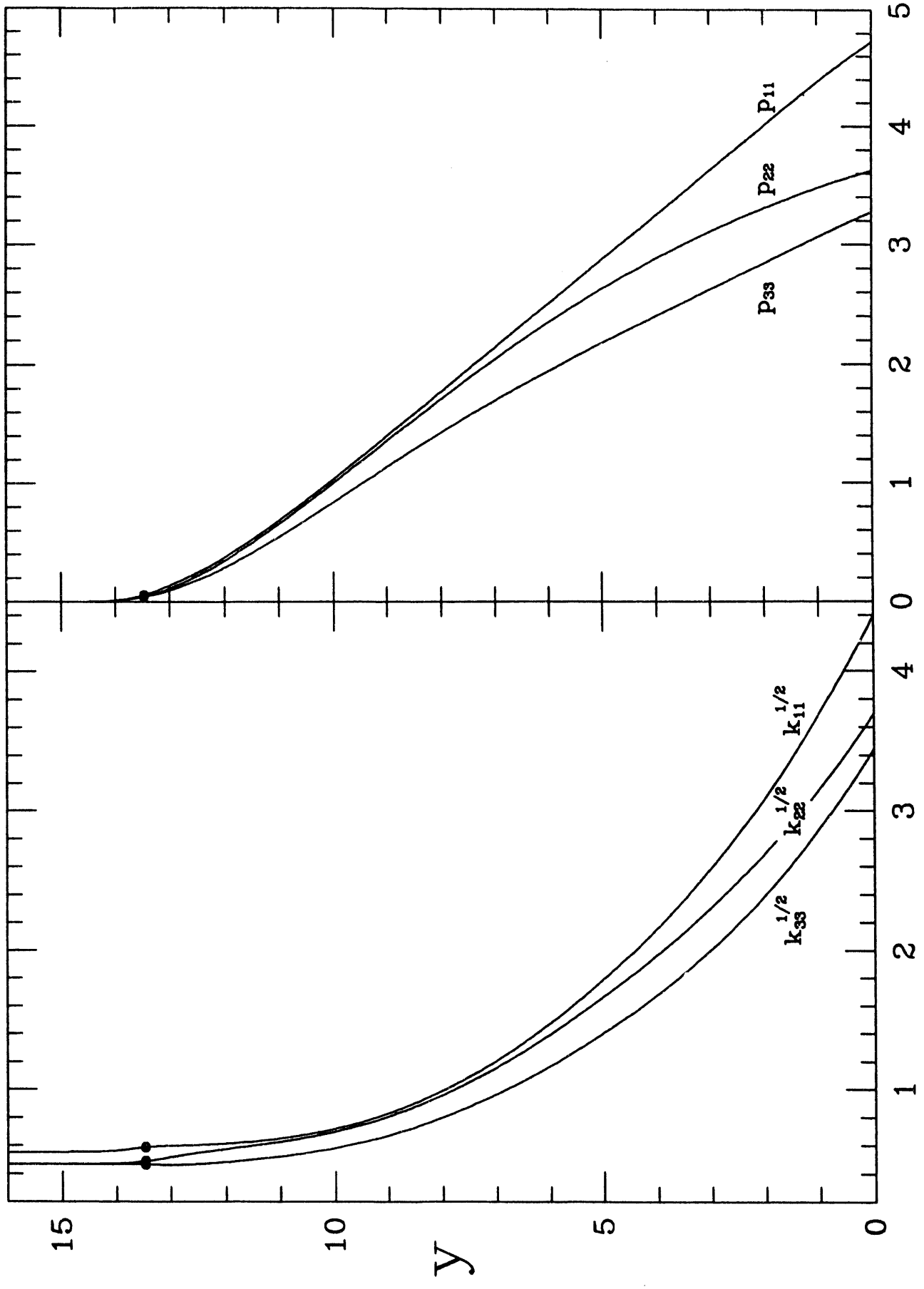

Figure 3: The variations with y of $k_{11}^{1/2}$, $k_{22}^{1/2}$, and $k_{33}^{1/2}$; and the variations with y of p_{11}, p_{22}, and p_{33} for e=.6, e_w=.95, $\sigma/d=1/2$, $s/d=-1+2^{1/2}$ and $\phi=25^o$, when $m_t=4$.

DISPERSE FLOWS: EFFECTIVE EQUATIONS AND PARTICLE STRESS

A. Prosperetti, D.Z. Zhang, and H. Bulthuis
Department of Mechanical Engineering
The Johns Hopkins University
Baltimore USA

The purpose of this paper is to briefly describe a new method for the derivation of averaged equations for disperse multiphase flow and to demonstrate its flexibility by application to a variety of systems such as potential flow, viscous flow, heat convection, thermocapillary flow, and others. First the main components of the method will be recalled briefly omitting proofs that can be found in Zhang (1993), Zhang and Prosperetti (1993a, b), and Bulthuis, Prosperetti, and Sangani (1993).

1 The basic tools

We envisage a system consisting of discrete particles and a suspending continuous phase. To obtain effective equations we perform an average over an ensemble of realizations of the system, each one consisting of the same number N of particles arranged in a different configuration $\mathcal{C}^N$. The word configuration is used here in a broad sense to denote the full set of variables necessary to describe the system. For example, for rigid particles in potential flow a configuration is specified by the set of positions and velocities of the particles so that

$$\mathcal{C}^N \equiv \mathbf{y}^{(1)}, \mathbf{y}^{(2)}, \ldots, \mathbf{y}^{(N)}, \mathbf{w}^{(1)}, \mathbf{w}^{(2)}, \ldots, \mathbf{w}^{(N)}. \tag{1}$$

Here $\mathbf{y}^{(\alpha)}$ and $\mathbf{w}^{(\alpha)}$ are the position and velocity of the α-th particle, with $\alpha = 1, \ldots, N$. In the case of spherical bubbles the set of radii and radial velocities of the bubbles must be added to specify $\mathcal{C}^N$. For rigid non-spherical particles one needs a set of vectors to specify orientation and angular velocity, and so on. For simplicity, in the following, we shall only indicate explicitly the variables listed in (1), extensions and adaptations to other cases being straightforward.

The probability of any specific configuration is specified by a probability distribution $P(N;t)$. The particles are assumed to be identical and therefore a convenient normalization of P is

$$\int d\mathcal{C}^N \, P(N;t) = N!, \tag{2}$$

where the integration is over all the variables of $\mathcal{C}^N$, and over the appropriate range for each one. The action of boundaries and macroscopic quantities (e.g., an imposed pressure gradient) is assumed to be deterministic and is not included in P.

The volume fractions $\beta_{C,D}$ of the continuous and disperse phase are given by

$$\beta_{C,D} = \frac{1}{N!} \int d\mathcal{C}^N \, \chi_{C,D}(\mathbf{x};N) \, P(N;t), \tag{3}$$

where $\chi_{C,D}$ is the characteristic, or indicator, function of the phases. For example, $\chi_D(\mathbf{x};N) = 1$ when the point $\mathbf{x}$, given that the system has the configuration $\mathcal{C}^N$, is inside a particle. The particle boundary is

assumed to have zero measure so that $\chi_C + \chi_D = 1$ and, as a consequence, $\beta_C + \beta_D = 1$. For equal rigid spheres of radius a one has

$$\chi_D(\mathbf{x};N) = \sum_{\alpha=1}^{N} H(a - |\mathbf{x} - \mathbf{y}^\alpha|) = 1 - \chi_C(\mathbf{x};N), \tag{4}$$

with H the Heaviside distribution. With this expression the definition (3) gives

$$\beta_D(\mathbf{x},t) = \int_{|\mathbf{x}-\mathbf{y}|\le a} d^3y\, n(\mathbf{y},t), \qquad n(\mathbf{y},t) = \int d^3w\, P(\mathbf{y},\mathbf{w};t)\,. \tag{5}$$

Here $P(1;t) \equiv P(\mathbf{y},\mathbf{w};t)$ is the single-particle probability density function obtained from $P(\mathcal{C}^N,t)$ by integration over $N-1$ particle coordinates and n is the particle number density.

Let $f_C(\mathbf{x},t;N)$ be any flow quantity pertaining to the continuous phase. Its *phase ensemble* average is defined by

$$< f_C > (\mathbf{x},t) = \frac{1}{N!\beta_C} \int d\mathcal{C}^N\, \chi_C(\mathbf{x};N)\, P(N;t)\, f_C(\mathbf{x},t;N)\,. \tag{6}$$

A similar definition is used for the conditional average $< f_C >_1 (\mathbf{x},t|1) \equiv < f_C >_1 (\mathbf{x},t|\mathbf{y},\mathbf{w})$ i.e. the average over all the configurations such that one particle center occupies the position $\mathbf{y}$ with velocity $\mathbf{w}$.

An advantage of this type of average is that the quantity to be averaged does not have to be defined in both phases. An example is pressure, which is an ill-defined quantity for a rigid particle. A disadvantage is that differentiation and averaging do not commute,

$$\nabla(\beta_C < f_C >) = \beta_C < \nabla f_C > + \int_{|\mathbf{x}-\mathbf{y}|=a} dS_y\, \mathbf{n} \int d^3w\, P(1;t) < f_C >_1 (\mathbf{x},t|1)\,. \tag{7}$$

$$\begin{aligned} \nabla^2(\beta_C < f_C >) &= \beta_C < \nabla^2 f_C > + \nabla \cdot \int_{|\mathbf{x}-\mathbf{y}|=a} dS_y \mathbf{n} \int d^3w P(1;t) < f_C >_1 \\ &+ \int_{|\mathbf{x}-\mathbf{y}|=a} dS_y\, \mathbf{n} \cdot \int d^3w P(1;t) < \nabla f_C >_1\,. \end{aligned} \tag{8}$$

In order to obtain a relation for the time derivative one needs the evolution equation for P which is

$$\frac{\partial P}{\partial t} + \sum_{\alpha=1}^{N} \left[\nabla_{\mathbf{y}^\alpha}(\mathbf{w}^\alpha P) + \nabla_{\mathbf{w}^\alpha}(\dot{\mathbf{w}}^\alpha P)\right] = 0\,, \tag{9}$$

where the dot denotes the time derivative. With this it is easy to prove that

$$\frac{\partial}{\partial t}(\beta_C < f_C >) = \beta_C < \frac{\partial f_C}{\partial t} > - \int_{|\mathbf{x}-\mathbf{y}|=a} dS_y \int d^3w\, \mathbf{w}\cdot\mathbf{n}\, P(1,t) < f_C >_1\,. \tag{10}$$

By using the kinematic boundary condition at the particle surface one finds

$$\frac{\partial(\beta_C < f_C >)}{\partial t} + \nabla \cdot (\beta_C < f_C \mathbf{u}_C >) = \beta_C < \frac{\partial f_C}{\partial t} + \nabla \cdot (f_C \mathbf{u}_C) >\,. \tag{11}$$

Thus, though not commuting, averaging and convective differentiation satisfy a simple relation that plays a central role in the derivation of the averaged equations.

In dealing with the disperse phase it is more useful to use a different kind of average. Let $g_D^{(\alpha)}$ be a quantity pertaining to the α-th particle as a whole, such as velocity, radius, position, etc. The definition is

$$\overline{g_D}(\mathbf{x},t) = \frac{1}{n(\mathbf{x},t)} \int d^3w\, P(\mathbf{x},\mathbf{w};t)\, g^{(1)}(\mathbf{x},\mathbf{w},t)\,. \tag{12}$$

This definition recognizes the fact that the most compact description of the particles is obtained in terms of global attributes rather than field quantities. An example is velocity for the case of rigid particles. Since a velocity field is well defined at each point of each particle, one could introduce an average $< \mathbf{u}_D >$ similar to that used for the continuous phase. However, in this way, the essential simplification that arises from the rigidity constraints would be lost. Our approach is instead to introduce an average velocity of the particle centers

$$\overline{\mathbf{w}}(\mathbf{x},t) = \frac{1}{n(\mathbf{x},t)} \int d^3w\, P(\mathbf{x},\mathbf{w};t)\, \mathbf{w}\,, \tag{13}$$

and, by a similar relation, of their angular velocities if needed. Other advantages are apparent. Consider, for example, rotating homogeneous, smooth, rigid, spherical particles in potential flow. In this case the rotational degree of freedom is clearly irrelevant, although it is easy to show that

$$< \mathbf{u}_D > = \overline{\mathbf{w}} + \frac{1}{5}a^2 \left[\nabla \times \overline{\Omega} + \frac{1}{n}(\nabla n \cdot \nabla \overline{\mathbf{w}} + \nabla n \times \overline{\Omega}) + \nabla^2 \overline{\mathbf{w}} + O(a^2) \right] , \tag{14}$$

where $\overline{\Omega}$ is the average of the angular velocity vector. An equation of motion phrased in terms of $< \mathbf{u}_D >$ must therefore be more complex than one based on $\overline{\mathbf{w}}$ because it must contain terms that cancel the effect of rotation. Furthermore, with the definition (12), one can average the equation of motion $\mathbf{F} = m\dot{\mathbf{w}}$ of the particles directly with no need to introduce information about the particle-material constitutive relation.

This approach is clearly applicable to particles completely described by a finite number of attributes. It may not be as advantageous in the case of an infinity of degrees of freedom, such as deformable drops with internal flow, although it could readily be extended to deal with this case as well. The definition (12) is appropriate for quantities $g_D^{(\alpha)}$ that, as the velocity $\mathbf{w}$, only depend on the variables of the α-th particle. It is not difficult to generalize the result to cover other situations.

It is easy to show for such particle-centers averaged quantities that

$$\frac{\partial}{\partial t}(n\,\overline{g_D}) + \nabla \cdot (n\,\overline{\mathbf{w}\, g_D}) = n\,\overline{\frac{\partial g^{(1)}}{\partial t}}\,, \tag{15}$$

where the time derivative in the right-hand side is taken following the motion of the particles.

2 Applications

In all the examples to be described below the continuous phase is assumed to be incompressible. In this case, by setting $f_C = 1$ in (11), its average continuity equation is readily found to be

$$\frac{\partial \beta_C}{\partial t} + \nabla \cdot (\beta_C \mathbf{u}_C) = 0\,. \tag{16}$$

For the disperse phase we have a balance equation for the number density given by

$$\frac{\partial n}{\partial t} + \nabla \cdot (n\overline{\mathbf{w}}) = 0\,. \tag{17}$$

Although, as shown by (5), β_D does not exactly equal n times the particle volume v, the error in assuming this equality is of order $(a/L)^2$, where L is the macroscopic length scale, and we shall disregard it. This is one aspect of what we refer to as *the small-particle approximation*. With this approximation, then, for rigid particles we find a relation analogous to (16). For spherical bubbles (which here, for simplicity, are taken to have the same radius and radial velocity) we have instead

$$\frac{\partial \beta_D}{\partial t} + \nabla \cdot (\beta_D \overline{\mathbf{w}}) = 4\pi n a^2 \dot{a}\,. \tag{18}$$

We now give some examples. The equations of motion of the continuous phase are obtained by averaging the appropriate exact microscopic equations (e.g. the Euler or Stokes equations) by using the rules (7), (8), and (11). As shown e.g. by Eq. (7), this procedure introduces integrals containing the conditionally averaged fields with one particle held fixed. This is the guise under which the fundamental problem of closure, common to all averaging methods, arises in the present context. In the dilute limit – i.e., to order β_D – the difficulty is bypassed by observing that the conditionally averaged field is required with $O(1)$ accuracy only. To this accuracy, it is found that this field satisfies a *closed* set of equations that can be solved explicitly. In essence this step involves solving the problem of one particle immersed in an external field consisting of the first two terms of the Taylor series of the unconditionally averaged fields around the particle center. In one case – thermocapillary flow – the contribution of the conditionally averaged field can be eliminated in terms of other quantities and exact results can be obtained. In the case of linear potential flow at finite volume fraction, we use direct numerical simulation to close the equations.

For the disperse phase, we average the particle equation of motion directly using the relation (15). For simplicity, we write $\mathbf{u}_C$, $\mathbf{w}$ in place of $< \mathbf{u}_C >$, $\overline{\mathbf{w}}$. Occasionally, however, we restore the averaging symbol where necessary for clarity.

In most of the examples we consider the dilute case in the sense that the results are only correct to $O(\beta_D)$.

2.1 Rigid particles in potential flow

For equal homogeneous, rigid, spherical particles in an inviscid liquid, at low volume fractions, the continuous phase equation of motion is

$$\begin{aligned}
\rho_C \beta_C & \left[\frac{\partial \mathbf{u}_C}{\partial t} + (\mathbf{u}_C \cdot \nabla)\mathbf{u}_C\right] + \beta_C \nabla p_C \\
= & -\frac{1}{2}\rho_C \left[\beta_D \left(\frac{\partial \mathbf{u}_C}{\partial t} + \mathbf{u}_C \cdot \nabla \mathbf{u}_C - \frac{\partial \mathbf{w}}{\partial t} - \mathbf{w} \cdot \nabla \mathbf{w}\right) + \nabla \cdot (\beta_D \mathbf{M}_D)\right] \\
- & \frac{1}{2}\rho_C \beta_D (\nabla \times \mathbf{u}_C) \times (\mathbf{w} - \mathbf{u}_C) + \beta_C \rho_C \mathbf{g} \\
+ & \nabla \cdot (\beta_C \rho_C \mathbf{M}_C + \beta_D \mathbf{T}_C) .
\end{aligned} \tag{19}$$

In this equation the first group of terms in the right-hand side will be recognized as the effect of the added mass interaction between the phases (see e.g. Landau & Lifshitz 1959; Auton *et al.* 1988). The last term represents the effect on added mass of the fluctuations of the particle velocity,

$$\mathbf{M}_D = \overline{\mathbf{w}}\,\overline{\mathbf{w}} - \overline{\mathbf{w}\mathbf{w}} . \tag{20}$$

Alternatively, one may refer to $\mathbf{M}_D$ as the Reynolds stress of the particle phase. The next line of (19) contains the lift and the body forces. In the last line $\mathbf{M}_C$ is the Reynolds stress of the continuous phase, which can be shown to be given by

$$\begin{aligned}
\mathbf{M}_C = & -\frac{1}{20}\beta_D [3(\mathbf{u}_C - \mathbf{w}) \cdot (\mathbf{u}_C - \mathbf{w})\mathbf{I} + (\mathbf{u}_C - \mathbf{w})(\mathbf{u}_C - \mathbf{w})] \\
& + \frac{1}{20}\beta_D [3(Tr\mathbf{M}_D)\mathbf{I} + \mathbf{M}_D] .
\end{aligned} \tag{21}$$

Of particular interest is the non-isotropic stress $\mathbf{T}_C$ given by

$$\mathbf{T}_C = \frac{1}{5}\rho_C \left\{\left[2(\mathbf{u}_C - \mathbf{w})^2 \mathbf{I} - \frac{9}{4}(\mathbf{u}_C - \mathbf{w})(\mathbf{u}_C - \mathbf{w})\right]\right\} - \frac{2}{5}\rho_C (\mathrm{Tr}\,\mathbf{M}_D) + \frac{9}{20}\mathbf{M}_D , \tag{22}$$

where $\mathbf{I}$ is the identity tensor. Although $\mathbf{T}_C$ in appearance seems to be a sort of momentum flux due to the relative motion of the phases and the particle velocity fluctuations, it will be seen in the next example that

it actually behaves as a genuine stress tensor in the continuous phase. It may be observed that this is the correct form of a term that is sometimes introduced in averaged equations models by writing $\nabla[(p_S - p_C)\beta_D]$ (see e.g. Prosperetti & Jones 1974) or, less correctly, $(p_S - p_C)\nabla\beta_D$, in which p_S is interpreted as the average pressure of the surface of the particles. In such models, on the basis of potential flow past a sphere, the difference $p_S - p_C$ is usually equated to $-\frac{1}{4}\rho_C(\mathbf{u}_C - \mathbf{w})^2$ which is just the trace of $\mathbf{T}_C$.

For the disperse phase the momentum equation is

$$\begin{aligned}\rho_D\beta_D & \left[\frac{\partial \mathbf{w}}{\partial t} + (\mathbf{w}\cdot\nabla)\mathbf{w}\right] + \beta_D\nabla p_C \\ = & \frac{1}{2}\rho_C\left[\beta_D\left(\frac{\partial \mathbf{u}_C}{\partial t} + \mathbf{u}_C\cdot\nabla\mathbf{u}_C - \frac{\partial}{\partial t}\mathbf{w} - \mathbf{w}\cdot\nabla\mathbf{w}\right) + \nabla\cdot(\beta_D\mathbf{M}_D)\right] \\ + & \frac{1}{2}\rho_C\beta_D\,(\nabla\times\mathbf{u}_C)\times(\mathbf{w}-\mathbf{u}_C) + \rho_D\nabla\cdot(\beta_D\mathbf{M}_D) + \beta_D\rho_D\mathbf{g}\,. \end{aligned} \tag{23}$$

Here again in the right-hand side we find the added mass and lift forces with opposite sign to the continuous-phase equation, although there is no term analogous to $\mathbf{T}_C$.

It should be explicitly noted that this equation does not contain a "particle pressure," but that the particles move responding to the continuous-phase pressure. This is the correct physical picture that could not be as easily recovered by averaging the local equation for the particle material rather than the fundamental equation for the motion of the particles as a whole.

In the present dilute limit, these equations coincide with those obtained by Wallis (1991).

2.2 Massless bubbles in potential flow

Let us now turn to the case of equal spherical bubbles in potential flow. The continuous-phase momentum equation now takes the form

$$\begin{aligned}\rho_C\beta_C & \left[\frac{\partial \mathbf{u}_C}{\partial t} + (\mathbf{u}_C\cdot\nabla)\mathbf{u}_C\right] + \beta_C\nabla p_C \\ = & -\frac{1}{2}\rho_C\left[\left(\frac{\partial \mathbf{u}_C}{\partial t} + \mathbf{u}_C\cdot\nabla\mathbf{u}_C - \frac{\partial \mathbf{w}}{\partial t} - \mathbf{w}\cdot\nabla\mathbf{w}\right) + \nabla\cdot(\beta_D\mathbf{M}_D)\right] \\ + & \frac{1}{2}\rho_C n\dot{v}(\mathbf{w}-\mathbf{u}_C) + \frac{1}{2}\rho_C\beta_D\,(\nabla\times\mathbf{u}_C)\times(\mathbf{w}-\mathbf{u}_C) + \beta_C\rho_C\mathbf{g} \\ + & \nabla\cdot(\beta_D\mathbf{T}_C + \beta_C\rho_C\mathbf{M}_C)\,. \end{aligned} \tag{24}$$

The added mass interaction is now augmented by a term due to the time dependence of the bubble volume v, and $\dot{v} = 4\pi a^2\dot{a}$ with

$$\dot{a} = \frac{\partial a}{\partial t} + \mathbf{w}\cdot\nabla a\,. \tag{25}$$

This effect can readily be interpreted in terms of the familiar single-bubble results of potential flow. The stress tensor $\mathbf{T}_C$ is now defined by

$$\begin{aligned}\mathbf{T}_C = & \rho_C\left\{\left[\frac{2}{5}(\mathbf{u}_C-\mathbf{w})^2 - a\ddot{a} - \frac{3}{2}\dot{a}^2\right]\mathbf{I} - \frac{9}{20}(\mathbf{u}_C-\mathbf{w})(\mathbf{u}_C-\mathbf{w})\right\} \\ & - \frac{2}{5}\rho_C(\mathrm{Tr}\,\mathbf{M}_D) + \frac{9}{20}\mathbf{M}_D\,, \end{aligned} \tag{26}$$

and the Reynolds stress is given by

$$\begin{aligned}\mathbf{M}_C = & -\beta_D\left[\dot{a}^2 + \frac{3}{20}(\mathbf{u}_C-\mathbf{w})\cdot(\mathbf{u}_C-\mathbf{w})\right]\mathbf{I} - \frac{\beta_D}{20}(\mathbf{u}_C-\mathbf{w})(\mathbf{u}_C-\mathbf{w}) \\ & + \frac{1}{20}\beta_D[3(Tr\mathbf{M}_D)\mathbf{I} + \mathbf{M}_D]\,, \end{aligned} \tag{27}$$

where

$$\ddot{a} = \left(\frac{\partial}{\partial t} + \mathbf{w}\cdot\nabla\right)\left(\frac{\partial a}{\partial t} + \mathbf{w}\cdot\nabla a\right). \tag{28}$$

Since the bubbles are taken to be massless, the inertia of the disperse phase is negligible and the momentum equation is

$$\begin{aligned}\beta_D\nabla p_C &= \frac{1}{2}\rho_C\beta_D\left[\frac{\partial \mathbf{u}_C}{\partial t} + \mathbf{u}_C\cdot\nabla\mathbf{u}_C - \frac{\partial \mathbf{w}}{\partial t} - \mathbf{w}\cdot\nabla\mathbf{w}\right] - \frac{1}{2}\rho_C\nabla\cdot(\beta_D\mathbf{M}_D)\\ &- \frac{1}{2}\rho_C n\dot{v}(\mathbf{w}-\mathbf{u}_C) - \frac{1}{2}\rho_C\beta_D\,(\nabla\times\mathbf{u}_C)\times(\mathbf{w}-\mathbf{u}_C) + \beta_D\rho_C\mathbf{g}.\end{aligned} \tag{29}$$

For the case of bubbles there is another equation for the radial motion. This is obtained by averaging the normal stress balance across the bubble surface and is found to be, in the present dilute limit,

$$a\,\ddot{a} + \frac{3}{2}\dot{a}^2 = \frac{1}{\rho_C}\left[p_B - \frac{2\sigma}{a} - p_C - \frac{1}{3}Tr\mathbf{T}_C\right], \tag{30}$$

where σ is the surface tension coefficient and p_B the pressure inside the bubble. In a simple model this quantity could be specified for example by an isothermal or adiabatic relation. The appearance in this equation of the trace of $\mathbf{T}_C$ underscores the physical meaning of this quantity as an additional stress in the liquid due to the relative motion of the phases.

2.3 Particle stress in potential flow

We now consider the case of rigid spherical particles, again in potential flow, from a different viewpoint. Initially we do not assume a dilute system, but derive a result of general validity. Throughout this section the averaging symbols are restored.

Write the equation of motion of the generic particle as

$$\begin{aligned}m\dot{\mathbf{w}} &= -\int_{|\mathbf{x}-\mathbf{z}|=a} dS_z\,\mathbf{n}\,p_C(z,t;N)\\ &= \rho\int_{|\mathbf{x}-\mathbf{z}|=a} dS_z\,\mathbf{n}\left(\frac{\partial\phi}{\partial t} + \frac{1}{2}\mathbf{u}_C\cdot\mathbf{u}_C\right) + \mathbf{f}^c,\end{aligned} \tag{31}$$

where $\mathbf{f}^c$ is the force due to collisions with other particles, and body forces have been disregarded for simplicity. In terms of the impulse

$$\mathbf{J} = -\rho\int_{|\mathbf{x}-\mathbf{z}|=a} dS_z\,\mathbf{n}\,\phi, \tag{32}$$

this equation takes the form

$$m\dot{\mathbf{w}} + \dot{\mathbf{J}} \equiv \dot{\mathbf{p}} = \rho\int_{|\mathbf{x}-\mathbf{z}|=a} dS_z\,\mathbf{n}\cdot\left(\frac{1}{2}u_C^2\mathbf{I} - \mathbf{u}_C\mathbf{u}_C\right) + \mathbf{f}^c. \tag{33}$$

Upon averaging according to (12) we have

$$n\left[\frac{\partial\overline{\mathbf{p}}}{\partial t} + \overline{\mathbf{w}}\cdot\nabla\overline{\mathbf{p}}\right] + \nabla\cdot n\left[(\overline{\mathbf{w}\mathbf{p}} - \overline{\mathbf{w}}\,\overline{\mathbf{p}})\right] = -\nabla\cdot\left[\sigma^k + \sigma^p\right] + \mathbf{F}^c. \tag{34}$$

Here $\mathbf{F}^c = n\overline{\mathbf{f}^c}$ and the other terms in the right-hand side are the kinetic and potential parts of the particle stress, σ^k and σ^p respectively. The former is similar to a Reynolds stress and is given by

$$\sigma^k = -n(\overline{\mathbf{w}\mathbf{p}} - \overline{\mathbf{w}}\,\overline{\mathbf{p}}). \tag{35}$$

The latter one is of greater interest. It may be written in the form

$$\sigma^p = \rho\beta_C \langle \mathbf{u}_C\mathbf{u}_C\rangle - \frac{1}{2}\rho\beta_C \langle \mathbf{u}_C \cdot \mathbf{u}_C\rangle \mathbf{I} + \rho \int d^3w\, P(\mathbf{x},\mathbf{w};t) \int_{|\mathbf{x}-\mathbf{y}|=a} dS_y\, \mathbf{s} \left\langle (\mathbf{n}\cdot\mathbf{u}_C)\mathbf{u}_C - \frac{1}{2}u_C^2\mathbf{n}\right\rangle_1 (\mathbf{y},t|\mathbf{x},\mathbf{w}) . \tag{36}$$

This result is of general validity and holds also for non-homogeneous, dense mixtures. It can be shown that it coincides with a recent result of Sangani and Didwania (1993) after the latter is suitably corrected. The derivation by the present method is much simpler than that given by these authors.

Up to $O(\beta_D)$ included, σ^p is independent of the particle configuration and is found to be given by

$$\sigma^p \simeq \beta_C\rho_C\left(<\mathbf{u}_C><\mathbf{u}_C> - \frac{1}{2}<\mathbf{u}_C>\cdot<\mathbf{u}_C>\mathbf{I}\right) + \beta_D\rho_C\left[\overline{\mathbf{w}}<\mathbf{u}_C> + \frac{1}{2}<\mathbf{u}_C>(<\mathbf{u}_C> - \overline{\mathbf{w}}) + <\mathbf{u}_C>\cdot\left(\frac{1}{2}\overline{\mathbf{w}} - <\mathbf{u}_C>\right)\mathbf{I}\right] . \tag{37}$$

The divergence of this expression can be proven to be identical to the number density multiplied by the force on a single sphere moving with velocity $\mathbf{w}$ in a flow with a uniform rate of strain, $\mathbf{u}_C + \mathbf{x}\cdot\nabla\mathbf{u}_C$,

$$\nabla\cdot\sigma^p = \frac{3}{2}\beta_D\rho_C(\overline{\mathbf{w}} - <\mathbf{u}_C>)\cdot\nabla<\mathbf{u}_C> + O(\beta_D^2) . \tag{38}$$

It can be shown that Eq. (34), with σ^p given by this relation, is identical to the result obtained by eliminating the pressure gradient between Eqs. (19) and (23) and dropping the lift force contribution.

The derivation of an explicit expression valid to higher order in β_D requires some assumption on the particle configuration. Results for periodic particle arrangements are given in Bulthuis *et al.*(1993).

2.4 Linear potential flow

Consider now the case of equal rigid spheres in linear potential flow. This model would be appropriate, for instance, for the case of small-amplitude oscillations or for incipient motion started from rest. We assume that the suspension is homogeneous or weakly homogeneous, in the sense that the results are accurate up to terms containing the first derivatives of β_D included.

On the basis of general arguments of Continuum Mechanics, such as Galilean invariance, isotropy, transformation properties under time-reversal, and others it is possible to show that the two momentum equations must have the form

$$\rho_C\frac{\partial\mathbf{u}_C}{\partial t} + \nabla p_C = \frac{1}{2}\rho_C\beta_D C\frac{\partial}{\partial t}(\mathbf{w}-\mathbf{u}_C) + \rho_C\mathbf{g} , \tag{39}$$

$$\rho_D\frac{\partial\mathbf{w}}{\partial t} + \nabla p_C = \frac{1}{2}\rho_C\beta_C C\frac{\partial}{\partial t}(\mathbf{u}_C-\mathbf{w}) + \rho_D\mathbf{g} . \tag{40}$$

The coefficient $C \equiv C(\beta_D, \rho_D/\rho_C)$ is the same in both equations and needs to be determined. A priori, the only information available is that it depends on the volume fraction and the ratio of the densities. It may be shown that this coefficient is related to Wallis's exertia E by $E = \frac{1}{2}\beta_D C$. If the well-known approximation of Zuber (1964) to the added mass coefficient is valid, then $C = 1$.

In Zhang and Prosperetti (1993a) the coefficient C is obtained by carrying out direct numerical simulations and averaging over the ensemble of simulations. The results indicate that C remains equal to 1 within $\pm 10\%$ for volume fractions as large as 30% and any density ratio. For $\rho_D < \rho_C$ this range of near constancy extends up to $\beta_D = 50\%$. The maximum deviation from 1 does not exceed 20% all the way to the close-packing limit.

2.5 Stokes flow

In the case of a dilute suspension of rigid spherical particles in Stokes flow the continuous-phase momentum equation is found to be

$$\begin{aligned}\beta_C \nabla p_C &= \nabla \cdot \left\{ \mu_C \left[1 + (\frac{3}{2}\alpha + 1)\beta_D \right] [< \nabla \mathbf{u}_C > + (< \nabla \mathbf{u}_C >)^T] \right\} \\ &+ \frac{9}{2}\frac{\beta_D}{a^2}\mu_C(\mathbf{w} - \mathbf{u}_C) + \beta_C \rho_C \mathbf{g}\,, \end{aligned} \tag{41}$$

where

$$\alpha = \frac{\mu_D + \frac{2}{5}\mu_C}{\mu_D + \mu_C}\,. \tag{42}$$

The same equation expressed in terms of $\nabla < \mathbf{u}_C >$, rather than $< \nabla \mathbf{u}_C >$, takes the form

$$\begin{aligned}\nabla p_C &= \nabla \cdot \left\{ \mu_C \left[1 + (\frac{3}{2}\alpha + 1)\beta_D \right] [\nabla \mathbf{u}_C + (\nabla \mathbf{u}_C)^T] \right\} \\ &+ \frac{3\mu_C^2}{5(\mu_C + \mu_D)} \nabla \cdot [(\mathbf{w} - \mathbf{u}_C)(\nabla \beta_D) + (\nabla \beta_D)(\mathbf{w} - \mathbf{u}_C)] \\ &+ \frac{3\beta_D \mu_C}{a^2} \frac{\mu_C + \frac{3}{2}\mu_D}{\mu_C + \mu_D}(\mathbf{w} - \mathbf{u}_C) + \beta_C \rho_C \mathbf{g}\,. \end{aligned} \tag{43}$$

The term in the second line vanishes identically for rigid particles, but not for drops. It is therefore seen that, when expressed in this form, the equation acquires a non-Newtonian structure.

To reduce the equation to a form from which the well-known Einstein viscosity correction is apparent, we need to express the strain tensor in terms of the mean volumetric flow rate

$$\mathbf{u}_m = \beta_D \mathbf{w} + \beta_C \mathbf{u}_C\,. \tag{44}$$

The result is

$$\begin{aligned}\nabla p_C &= \nabla \cdot [\mu_E [\nabla \mathbf{u}_m + (\nabla \mathbf{u}_m)^T] \\ &+ \frac{3}{a^2}\beta_D \mu_C \frac{\mu_C + \frac{3}{2}\mu_D}{\mu_C + \mu_D}(\mathbf{w} - \mathbf{u}_C) + \beta_C \rho_C \mathbf{g}\,, \end{aligned} \tag{45}$$

where

$$\mu_E = (1 + \frac{5}{2}\beta_D)\mu_C\,, \tag{46}$$

as expected (see e.g. Landau & Lifshitz 1959).

The disperse phase momentum equation is

$$\rho_D \left(\frac{\partial \mathbf{w}}{\partial t} + \mathbf{w} \cdot \nabla \mathbf{w} \right) = -\nabla p_C - \frac{9}{2}\frac{\mu}{a^2}(\mathbf{w} - \mathbf{u}_C) + \beta_D \rho_D \mathbf{g}\,. \tag{47}$$

2.6 Heat conduction

We now turn to a different problem, that of steady heat conduction in a composite consisting of a matrix with thermal conductivity K_C and equal spherical inclusions with thermal conductivity K_D.

In the dilute limit the procedure described at the beginning of this section, in this case, leads to

$$\nabla \cdot (D_E \nabla T_m) + \frac{3\beta_D D_C}{a^2}(T_D - T_C) = 0\,, \tag{48}$$

where D_E is the effective diffusivity of the medium given by (see e.g. Jeffrey 1973)

$$D_E = \left[1 + \frac{3\beta_D(K_D - K_C)}{K_D + K_C}\right] D_C \,, \tag{49}$$

and

$$T_m = \beta_D T_D + \beta_C T_C \,, \tag{50}$$

is the mean temperature. In (49) $D_C = K_C/(\rho_C C_{pC})$, with C_{pC} the continuous-phase specific heat, is the thermal diffusivity. The last term of (48) shows that the particles act as heat sources or sinks for the continuous phase.

The corresponding disperse-phase equation is

$$\frac{3\,\beta_D\,K_C}{a^2\,C_{pD}\,\rho_D}(T_D - T_C) - \frac{\beta_D}{C_{pD}\,\rho_D}\dot{q}_D = 0 \,. \tag{51}$$

Here $\dot{q}_D$ is the volumetric heat source in the particles. If this quantity vanishes, then, from this equation, $T_C = T_D$, so that (48) takes the more conventional form

$$\nabla \cdot (D_E \nabla T_C) = 0 \,. \tag{52}$$

2.7 Convection at low Re, large Pe numbers

We now add, to the problem of the previous section, the effects of flow at low Reynolds, large Péclet numbers. Using the results of Acrivos & Taylor (1962) for the heat transfer from a particle immersed in a linear temperature gradient, it is possible to show that the averaged energy equation for the continuous phase can be written as

$$\begin{aligned} \frac{\partial(\beta_C T_C)}{\partial t} &+ \nabla \cdot (\beta_C T_C \mathbf{u}_C) \\ &= \frac{1}{\rho_C\,C_{pC}} \nabla \cdot (K_E \nabla T_m) + \frac{3\,\beta_D\,D_C}{a^2}\left(1 + \frac{Pe}{4}\right)(T_D - T_C) \\ &- \frac{3}{16}\nabla \cdot [\beta_D (T_D - T_C)(\mathbf{w} - \mathbf{u}_C)] \,, \end{aligned} \tag{53}$$

where the particle Péclet number is defined by

$$Pe = \frac{2a|\mathbf{w} - \mathbf{u}_C|}{D_C} \,, \tag{54}$$

and the effective thermal conductivity K_E is given by $\rho_C C_{pC} D_E$, with D_E as in (49). The last term in (53) is due to the slip between the disperse phase at temperature T_D and the continuous phase at temperature T_C. Qualitatively, therefore, its origin lies in the same physical process that, at the molecular level, is responsible for ordinary conduction in a fluid. Not surprisingly, therefore, it appears as the divergence of a vector. The last term in the second line, on the other hand, is similar to the distributed heat source effect described before in connection with Eq. (48), modified however by the convectively enhanced heat exchange between the particles and the fluid.

The averaged energy equation for the disperse phase is

$$\frac{\partial}{\partial t}(\beta_D\,T_D) + \nabla(\beta_D\,\mathbf{w}\,T_D) = -\frac{3\,\beta_D\,K_C}{a^2\,C_{pD}\,\rho_D}\left(1 + \frac{Pe}{4}\right)(T_D - T_C) + \frac{\beta_D}{C_{pD}\,\rho_D}\dot{q}_D \,. \tag{55}$$

2.8 Thermocapillary flow

Consider a bubble in an infinite expanse of fluid, in which a uniform, constant temperature gradient **H** far from the bubble is imposed. Let the surface tension of the interface between the bubble and the fluid be σ. Assume that σ decreases linearly with the temperature T, and that the bubble is spherical with radius a. Young *et al.* (1959) found that in this case the bubble moves with the velocity

$$\mathbf{U} = -\frac{a}{2\mu_C}\frac{d\sigma}{dT}\mathbf{H}, \tag{56}$$

under the assumption of low Reynolds number

$$R = \frac{\rho_C\, aU}{\mu_C}, \tag{57}$$

and small Marangoni number

$$Ma = \frac{aU}{\alpha} = -\frac{d\sigma}{dT}\frac{a^2 H}{2\,\mu_C\, D_C}. \tag{58}$$

After scaling the velocity by U, temperature by $a\,H$, and lengths by a, Acrivos *et al.* (1990) showed that the temperature and velocity field for the liquid in the suspension of bubbles can be written as

$$T = \mathbf{h}\cdot\mathbf{x} + \phi, \qquad \mathbf{u}_C = -\nabla\phi, \tag{59}$$

where $\mathbf{h}$ is the dimensionless temperature gradient $\mathbf{h} = \mathbf{H}/H$, and ϕ satisfies the Laplace equation. They showed that in this suspension each bubble has the same dimensionless velocity

$$\mathbf{w} = \mathbf{h}. \tag{60}$$

We shall only use nondimensional quantities in the following analysis.

The averaged liquid velocity can be written in terms of ϕ by using (59) as

$$\beta_C\,\mathbf{u}_C(\mathbf{x},t) = -\frac{1}{N!}\int \chi_C\,(\nabla\phi)\,P(N,t)\,d\mathcal{C}^N, \tag{61}$$

and the average heat flux is

$$\begin{aligned}\mathbf{Q}_C &= \beta_C\nabla T_C(\mathbf{x},t) = \frac{1}{N!}\int(\mathbf{h}+\nabla\phi)\,\chi_C\,P(N,t)\,d\mathcal{C}^N \\ &= \beta_C\,\mathbf{h} + \frac{1}{N!}\int \chi_C\,\nabla\phi\,P(N,t)\,d\mathcal{C}^N.\end{aligned} \tag{62}$$

The averaged mixture velocity is

$$\begin{aligned}\mathbf{u}_m &= \beta_D\mathbf{w} + \beta_C\mathbf{u}_C \\ &= \beta_D\,\mathbf{h} - \frac{1}{N!}\int \chi_C\,\nabla\phi\,P(N,t)\,d\mathcal{C}^N,\end{aligned} \tag{63}$$

and the relative velocity is

$$<\mathbf{u}_D> - <\mathbf{u}_m> = \beta_C\,\mathbf{h} + \frac{1}{N!}\int \chi_C\nabla\phi P(N,t)d\mathcal{C}^N, \tag{64}$$

which equals the right-hand side of (62). Since the bubbles are non-conducting, the mixture heat flux $\mathbf{Q}_m$ is the same as the averaged heat flux in the continuous phase. Thus we have

$$\mathbf{w} - \mathbf{u}_m = \mathbf{Q}_C = \mathbf{Q}_m = K_E\,\nabla <T_m>. \tag{65}$$

The last step follows from the definition of effective conductivity. We have thus provided a very simple - but rigorous - proof of the relation recently found by Acrivos *et al.* (1990) generalizing it at the same time to the case in which a gradient of the volume fraction is present. For a uniform bubble distribution, it can be easily shown that $\nabla <T_C> = \mathbf{h}$.

It is clear that this result does not hinge on the assumption of dilution but is valid for any concentration.

3 Conclusions

We have described a number of problems to which the approach to averaging that we have developed has been successfully applied. While in some cases the results coincide with known ones, others are original. In addition, due to the inherent greater simplicity of the method, errors in earlier results have readily become apparent.

The main advantages of this method appear to be the following:

1. *Systematicity*: In all of the examples described, the same procedure has been applied. There is no need to use a different approach for potential problems or for the highly viscous case, as is often necessary with other approaches. Furthermore, at least in the dilute limit, closure relations arise naturally from the formalism with no need for *ad hoc* hypotheses.

2. *Flexibility*: Not only the method has been applied to a wide variety of problems, but both analytical and numerical closure techniques have been demonstrated. A third possibility, that we have not yet developed but that appears to be potentially useful, is that of approximate closures of the "effective medium" kind.

Acknowledgments

The present study has been supported by NSF and DOE under grants CTS-8918144 and DE-FG02-89ER14043 respectively.

References

ACRIVOS, A., JEFFREY, D.J., and SAVILLE, D.A. 1990 Particle migration in suspensions by thermocapillary or electrophoretic motion. *J. Fluid Mech.* **212**, 95-110.

ACRIVOS, A. and TAYLOR, T. 1962 Heat and mass transfer from single sphere in Stokes flow. *Phys. Fluids* **5**, 387-394.

AUTON, T.R., HUNT, J.C.R., and PRUD'HOMME, M. 1988 The force exerted on a body in inviscid unsteady non-uniform rotational flow. *J. Fluid Mech.* **197**, 241-257.

BULTHUIS, H., PROSPERETTI, A., and SANGANI, A.S. 1993 "Particle stress" in disperse two-phase potential flow. *J. Fluid Mech.*, submitted.

JEFFREY, D.J. 1973 Conduction through a random suspension of spheres. *Proc. Roy. Soc.* **A335**, 355-367.

LANDAU, L. and LIFSHITZ, E. 1959 *Fluid Mechanics*, Pergamon.

PROSPERETTI, A. and JONES, A.V. 1984 Pressure forces in disperse two-phase flows. *Int. J. Multiphase Flow* **10**, 425-440.

SANGANI, A.S. and DIDWANIA, A.K. 1993 Dispersed phase stress tensor in flows of bubbly liquids at large Reynodls numbers. *J. Fluid Mech.* **248**, 27-54.

WALLIS, G.B. 1991 The averaged Bernoulli equation and macroscopic equations of motion for the potential flow of a two-phase dispersion. *Int. J. Multiphase Flow* **17**, 683-695.

YOUNG, N.O., GOLDSTEIN, J.S., and BLOCK, M.J. 1959 The motion of bubbles in a vertical temperature gradient. *J. Fluid Mech.* **6**, 350-356.

ZHANG, D.Z. 1993 Ensemble Phase Averaged Equations for Multiphase Flows. Doctoral dissertation, Department of Mechanical Engineering, Johns Hopkins University.

ZHANG, D.Z. and PROSPERETTI, A. 1993a Averaged equations for inviscid disperse two-phase flow. *J. Fluid Mech.*, in press.

ZHANG, D.Z. and PROSPERETTI, A. 1993b Averaged equations for bubbly flows. *Phys. Fluids A*, submitted.

ZUBER, N. 1964 On the disperse two-phase flow in the laminar regime. *Chem. Eng. Sci.* **19**, 897-917.

STABILITY ANALYSIS FOR THE FLOW OF GRANULAR MATERIALS DOWN AN INCLINED PLANE

K. R. Rajagopal and R. Gudhe
Department of Mechanical Engineering
University of Pittsburgh
Pittsburgh, PA 15261

INTRODUCTION

The comprehensive survey by Boyle and Massoudi (1989) discusses the various constitutive equations that have been used to model the flow of granular materials. Here, we are interested in the stability of flow down an inclined plane, of granular materials that are modeled according to the constitutive relation of Jenkins and Richman (1985, 1986). The kinetic theory approach to modeling has been applied to granular materials by various investigators [cf. Ogawa, Umemura & Oshima (1980), Shen (1981), Jenkins & Savage (1983), Ahmadi & Shahinpoor (1983a, 1984), Lun, et al. (1984), Ahmadi and Ma (1986), Ma and Ahmadi (1985, 1988), Jenkins and Richman (1985, 1986), Johnson and Jackson (1987), and Boyle and Massoudi (1989)]. Details of many of these models can be found in the review article by Boyle and Massoudi (1989).

GOVERNING EQUATIONS

We shall assume that the stress tensor governing the flow of granular materials down an inclined plane is given by [cf. Richman and Marciniec (1990)].

$$\mathbf{P} = \{ 4 \rho G F T \} \mathbf{1} - 2 \mu E \hat{\mathbf{D}} \tag{1}$$

Where,

$$F(\nu) = 1 + \frac{1}{4G} \tag{2}$$

$$E(\nu) = 1 + \pi \frac{(1+5/8G)^2}{12} \tag{3}$$

$$G(\nu) = \frac{\nu\,(2-\nu)}{2\,(1-\nu)^3} \tag{4}$$

$$\mu = \frac{8\,\sigma\,\rho\,G\,T^{1/2}}{5\,\pi^{1/2}} \tag{5}$$

In the above equation $\mathbf{P}$ denotes the Cauchy Stress, ν the volume fraction of the solid, $\hat{\mathbf{D}}$ denotes the deviatoric part of stretching tensor $\mathbf{D}$ associated with the solid motion and T the granular temperature.

Consider the flow of granular material modeled by the above model based on a kinetic theory like approach, down an inclined plane (cf. Figure 1) due to the action of gravity [cf. Savage (1979), Johnson and Jackson (1987), Johnson, et al. (1990), Hui, et al. (1984), Richman and Marciniec (1990), Hutter, et al. (1986a, b)]. In this problem we

consider steady one dimensional flow of incompressible granular materials (*i.e.* ρ_p = constant) down an inclined plane, where the angle of inclination is α. The governing equations of motion are the conservation of mass, momentum, and a pseudo energy equation. The conservation of mass is

$$\frac{\partial \rho}{\partial t} + div(\rho \mathbf{u}) = 0, \tag{6}$$

where $\frac{\partial}{\partial t}$ is the partial derivative with respect to time. The balance of linear momentum is

$$-div\mathbf{P} + \rho \mathbf{b} = \rho \frac{d\mathbf{v}}{dt}, \tag{7}$$

where $\frac{d}{dt}$ is the material time derivative and $\mathbf{b}$ is the body force. The pseudo energy equation in its general form is

$$-tr(\mathbf{P}\,\mathbf{D}) - div\mathbf{Q} - \gamma = \frac{3}{2}\rho \frac{dT}{dt}, \tag{8}$$

where $\mathbf{Q}$ is the flux of fluctuation energy, γ is the collisional rate per unit volume of energy dissipation. The derivation of these equations for the dissipative flows was first given by Jenkins & Savage (1983). The basic flow governing the flow of granular materials down an inclined plane has been solved approximately by Richman and Marciniec (1990) and numerically by Rajagopal and Gudhe (1991).

STABILITY ANALYSIS

Consider solutions which consist of the basic flow plus an infinitesimal disturbance

$$v = v_0 + \varepsilon v_1 \tag{9}$$
$$u = u_0 + \varepsilon u_1 \tag{10}$$
$$V = \varepsilon u_2 \tag{11}$$
$$T = T_0 + \varepsilon T_1 \tag{12}$$

where v_0, u_0 and T_0 correspond to the basic solution of the governing equations and v_1, u_1, u_2 T_1 represent the disturbance. It is assumed that for infinitesimal disturbances, the equations may be linearized *i.e.* the terms of order ε^2 and higher order can be neglected. In general, in addition to perturbing the volume fraction, velocity field and granular temperature, it is necessary to perturb the free surface. Ofcourse, the base solution will not hold in all of the perturbed domain. Here, we do not allow for the perturbation of the free surface. Such a stability study is incomplete in that it addresses only the disturbances corresponding to a special class. Ofcourse, a small disturbance without such a constraint

may prove to be unstable, nullifying the instability predictions. The basic flow is assumed to have the form

$$\begin{aligned} v_0 &= v_0(y) \\ u_0 &= u_0(y)i \\ T_0 &= T_0(y) \end{aligned} \tag{13}$$

Now substituting equations (9) through (12) into conservation of mass, balance of linear momentum and balance of energy, the appropriate non-dimensional equations corresponding to the basic flow *i.e.* of order one are given by:

$$S_1 \overline{W_0} \frac{d^2\overline{u_0}}{d\bar{y}^2} + \left\{ S_1 \frac{d\overline{W_0}}{d\bar{y}} + S_6 \overline{W_0} \frac{dv_0}{d\bar{y}} \right\} \frac{d\overline{u_0}}{d\bar{y}} = -20\sqrt{\pi}\, v_0 \sin\alpha, \tag{14}$$

$$S_3 \overline{W_0^2} \frac{dv_0}{d\bar{y}} + 2 S_2 \overline{W_0} \frac{d\overline{W_0}}{d\bar{y}} = -v_0 \cos\alpha \tag{15}$$

$$S_7 \overline{W_0} \frac{d^2\overline{W_0}}{d\bar{y}^2} + 2 S_7 \left\{ \frac{d\overline{W_0}}{d\bar{y}} \right\}^2 + S_8 \overline{W_0} \frac{d\overline{W_0}}{d\bar{y}} \frac{dv_0}{d\bar{y}} + \frac{S_1}{40} \left\{ \frac{d\overline{u_0}}{d\bar{y}} \right\}^2 - 6 S_9 \overline{W_0^2} = 0, \tag{16}$$

We need to solve the equations (14), (15) and (16) subject to the appropriate boundary conditions.

$$\bar{u} = \sqrt{\frac{\pi}{2}} \tan\alpha f \overline{W_0}$$

$$\frac{1}{\overline{W}} \frac{d\overline{W_0}}{d\bar{y}} = b \qquad \text{at } \bar{y} = \beta \text{ (on the inclined plane)} \tag{17}$$

$$Q = \frac{1}{\beta} \int_0^{\beta} v \, d\bar{y} \tag{18}$$

and,

$$\frac{d\bar{u}_0}{d\bar{y}} = 0$$

$$\overline{W_0^2}\frac{d\overline{W_0}}{d\bar{y}} = 0 \qquad \text{at } \bar{y} = 0 \text{ (at the free surface)} \tag{19}$$

$$\overline{W_0^2} = W_{01} \text{ (Specified)}$$

where g denotes the acceleration due to gravity and α is the angle of inclination of the plane.

$$With,\ S_1 = \frac{16\,\nu_0^2\,(2-\nu_0)}{(1-\nu_0)^3} + \frac{\pi}{12}\frac{(-5\nu_0^3+11\nu_0^2-7\nu_0+5)^2}{(2-\nu_0)\,(1-\nu_0)^3}$$

$$S_2 = \nu_0\left\{\frac{2\,\nu\,(2-\nu)}{(1-\nu_0)^3} + 1\right\}$$

$$S_3 = \frac{(7\nu_0^4-4\nu_0^3+4\nu_0^2+4\nu_0+1)}{(1-\nu_0)^4}$$

$$S_4 = \frac{16\,\nu_0\,(4-\nu_0)}{(1-\nu_0)^4}$$

$$S_5 = \frac{\pi}{12}\left\{\frac{50\,\nu_0^9-375\,\nu_0^8+2000\,\nu_0^7-4706\,\nu_0^6+6500\,\nu_0^5-5942\,\nu_0^4+3584\,\nu_0^3-1332\,\nu_0^2+186\,\nu_0+35}{(2-\nu_0)^2\,(1-\nu_0)^6}\right\}$$

$$S_6 = S_4 + S_5$$

$$S_7 = \frac{2\,\nu_0^2\,(2-\nu_0)}{(1-\nu_0)^3} + \frac{\pi}{64}\frac{(-5\nu_0^3+9\nu_0^2-3\nu_0+5)^2}{(2-\nu_0)\,(1-\nu_0)^3}$$

$$S_8 = \frac{dS_7}{d\nu}$$

$$S_9 = \frac{\nu_0^2\,(2-\nu_0)}{(1-\nu_0)^3}\,(1-e)$$

Equation $(17)_1$ indicates the slip condition on the inclined plane. Condition (18) gives the amount of material that is fed in and which remains the same at all locations of x.

In the above equations,

$$b = \frac{F}{M\sqrt{2}}\left\{\pi\left(tan\alpha\right)^2\frac{f}{2} - 2\,(1-e_w)(1-cos\theta)\,csc^2\theta\right\} \tag{20}$$

where, $$f = \frac{\left(1 - \frac{5F\bar{a}}{2^{3/2}E}\right)\left\{1 + \frac{B}{\bar{a}}\right\} sin^2\theta}{(2/3)\,[2\,csc^2\theta\,(1 - cos\theta) - cos\theta]} + \frac{5\bar{a}F}{\sqrt{2}E}$$

$$B(\nu) = \pi\frac{(1+5/8G)}{12\sqrt{2}}$$

$$M(\nu) = 1 + 9\pi\frac{(1+5/12G)^2}{32}$$

$$\bar{a} = \frac{1}{2}\left\{1 + \frac{1}{r}\right\}$$

$$r = \frac{\sigma}{d}$$

$$\bar{r} = \frac{s}{d}$$

$$\theta = sin^{-1}\left\{\frac{(1+\bar{r})}{(1+r)}\right\}$$

Here, $\bar{\sigma}$ is the diameter of the particle, d is the diameter of the hemispherical particles attached to the flat wall, and s is the average distance between the hemispherical particles. e_w is the coefficient of restitution that characterizes the energy dissipated in particle-wall collisions.

The appropriate non-dimensional equations corresponding to order of ε are:

$$\frac{\partial\nu_1}{\partial\bar{t}} - \nu_0\left\{\frac{\partial\bar{u}_1}{\partial\bar{x}} + \frac{\partial\bar{u}_2}{\partial\bar{y}}\right\} - \bar{u}_0\left\{\frac{\partial\nu_1}{\partial\bar{x}}\right\} - \frac{d\nu_0}{d\bar{y}}\bar{u}_2 = 0 \qquad (21)$$

$$P_1\left\{\frac{\partial^2\bar{u}_1}{\partial\bar{y}^2} + \frac{4}{3}\frac{\partial^2\bar{u}_1}{\partial\bar{x}^2}\right\} + \frac{4}{3}P_1\frac{\partial^2\bar{u}_2}{\partial\bar{x}\partial\bar{y}} + P_2\frac{\partial\bar{u}_1}{\partial\bar{y}} + 20\sqrt{\pi}\,\nu_0\,\bar{u}_0\frac{\partial\bar{u}_1}{\partial\bar{x}}$$

$$+ 2\,\overline{W}_1\,P_3\frac{\partial\overline{W}_1}{\partial\bar{y}} + 40\sqrt{\pi}\,S_2\,\overline{W}_1\frac{\partial\overline{W}_1}{\partial\bar{x}} + p_5\frac{\partial\bar{\nu}_1}{\partial\bar{y}} + 20\sqrt{\pi}\,S_{14}\,\overline{W}_0^2\frac{\partial\bar{\nu}_1}{\partial\bar{x}}$$

$$+ P_4 \overline{W}_1^2 + P_6 \nu_1 + 20 \sqrt{\pi}\, \nu_0 \frac{\partial \bar{u}_0}{\partial \bar{y}} \bar{u}_2 = 20 \sqrt{\pi}\, \nu_0 \frac{\partial \bar{u}_1}{\partial \bar{t}} \tag{22}$$

$$\frac{P_1}{20\sqrt{\pi}} \frac{\partial^2 \bar{u}_2}{\partial \bar{x}^2} - \frac{P_1}{15\sqrt{\pi}} \frac{\partial^2 \bar{u}_2}{\partial \bar{y}^2} + \frac{P_1}{15\sqrt{\pi}} \frac{\partial^2 \bar{u}_1}{\partial \bar{x} \partial \bar{y}} - P_8 \frac{\partial \bar{u}_2}{\partial \bar{y}} + \nu \bar{u}_0 \frac{\partial \bar{u}_2}{\partial \bar{x}}$$

$$- 2 S_2 \overline{W}_1 \frac{\partial \overline{W}_1}{\partial \bar{y}} + 2 P_7 \overline{W}_1 \frac{\partial \overline{W}_1}{\partial \bar{x}} - P_{10} \frac{\partial \bar{\nu}_1}{\partial \bar{y}} - P_{11} \overline{W}_1^2 + P_9 \nu_1 = \nu_0 \frac{\partial \bar{u}_2}{\partial \bar{t}} \tag{23}$$

$$P_{21} \overline{W}_1 \left\{ \frac{\partial^2 \overline{W}_1}{\partial \bar{x}^2} + 2 \frac{\partial^2 \overline{W}_1}{\partial \bar{x} \partial \bar{y}} + \frac{\partial^2 \overline{W}_1}{\partial \bar{y}^2} \right\} + P_{21} \left\{ \left\{ \frac{\partial \overline{W}_1}{\partial \bar{x}} \right\}^2 + 2 \frac{\partial \overline{W}_1}{\partial \bar{x}} \frac{\partial \overline{W}_1}{\partial \bar{y}} + \left\{ \frac{\partial \overline{W}_1}{\partial \bar{y}} \right\}^2 \right\}$$

$$+ H_3 \overline{W}_1 \left\{ \frac{\partial \overline{W}_1}{\partial \bar{y}} + \frac{\partial \overline{W}_1}{\partial \bar{x}} \right\} + P_{19} \left\{ \frac{\partial \bar{\nu}_1}{\partial \bar{x}} + \frac{\partial \bar{\nu}_1}{\partial \bar{y}} \right\} + 2 P_{23} \frac{\partial \bar{u}_1}{\partial \bar{y}} + P_{28} \frac{\partial \bar{u}_1}{\partial \bar{x}} + P_{23} \frac{\partial \bar{u}_2}{\partial \bar{x}} + P_{28} \frac{\partial \bar{u}_2}{\partial \bar{y}}$$

$$+ H_1 \overline{W}_1^2 + H_2 \nu_1 = 3 \nu_0 \overline{W}_1 \frac{\partial \overline{W}_1}{\partial \bar{t}} \tag{24}$$

and the boundary conditions become

$$\bar{u}_1 = \sqrt{\frac{\pi}{2}} \tan\alpha\, \overline{W}_0 \left\{ f_p \nu_1 + f \frac{1}{2 \overline{W}_0^2} \overline{W}_1^2 \right\}$$

$$\bar{u}_2 = 0 \tag{25}$$

$$\int_0^{\beta} \nu_1 \, d\bar{y} = 0 \tag{26}$$

$$S_1 \frac{\partial \bar{u}_1}{\partial \bar{y}} + S_1 \frac{\partial \bar{u}_2}{\partial \bar{x}} + A_1 \frac{d \bar{u}_0}{d \bar{y}} \nu_1 + \frac{S_1}{2 \overline{W}_0^2} \frac{d \bar{u}_0}{d \bar{y}} T_1 = 0 \tag{27}$$

$$2 \overline{W}_0 \overline{W}_1 \frac{\partial \overline{W}_1}{\partial \bar{y}} + \frac{d \overline{W}_0}{d \bar{y}} \overline{W}_0^2 = 0 \tag{28}$$

$$\overline{W}_1^2 = 0 \tag{29}$$

where, $\bar{y} = \dfrac{L-y}{\bar{\sigma}}$; $\overline{u_0} = \dfrac{u}{\sqrt{\bar{\sigma} g}}$; $\overline{W_0} = \left\{ \dfrac{T_0}{\bar{\sigma} g} \right\}^{1/2}$; $\bar{x} = \dfrac{L-x}{\bar{\sigma}}$,

$$\overline{u_1} = \frac{u_1}{\sqrt{\bar{\sigma} g}}; \quad \overline{u_2} = \frac{u_2}{\sqrt{\bar{\sigma} g}}; \quad \overline{W_1} = \left\{ \frac{T_1}{\bar{\sigma} g} \right\}^{1/2}; \quad \bar{t} = t \sqrt{\frac{g}{\bar{\sigma}}} \tag{30}$$

where L is the characteristic length. Equations $(25)_{1,2}$ are the boundary conditions at $\bar{y} = \beta$ on the inclined plane and equations (27), (28) and (29) are the boundary conditions at $\bar{y} = 0$ at the free surface. We shall assume the disturbances to be spatially periodic. That is the perturbed quantities have the form

$$\nu_1 = \nu_p(\bar{y})\, e^{s\bar{t}}\, e^{i\sigma\bar{x}} \tag{31}$$

$$\bar{u}_1 = U_{px}(\bar{y})\, e^{s\bar{t}}\, e^{i\sigma\bar{x}} \tag{32}$$

$$\bar{u}_2 = U_{py}(\bar{y})\, e^{s\bar{t}}\, e^{i\sigma\bar{x}} \tag{33}$$

$$\overline{W_1^2} = W_p(\bar{y})\, e^{s\bar{t}}\, e^{i\sigma\bar{x}} \tag{34}$$

Where, ν_p is the amplitude of the volume distribution function,
U_{px} and U_{py} are the amplitudes of the perturbed velocity,
W_p is the amplitude of the granular temperature,
i is the imaginary number such that $i^2 = -1$,
σ is the wave number (real) and
$s = \zeta + i\,\omega$.

It would be appropriate at this juncture to observe that there is no equivalent of Squire's theorem for parallel flows of granular materials and thus we should in general study three dimensional disturbances. However, the equations, even for the class of disturbances (31) through (34), are so complicated that at this stage we wish to restrict ourselves to this case. Substituting (31) through (34) into the equations (21), (22), (23) and (24), and the corresponding boundary conditions (25) through (29) we end up with

$$\nu_0 \frac{dU_{py}}{d\bar{y}} + \frac{d\nu_0}{d\bar{y}} U_{py} + i\,\sigma\,\nu_0\, U_{px} + (i\,\sigma\,\bar{u}_0 - s)\,\nu_p = 0 \tag{35}$$

$$P_1 \frac{d^2U_{px}}{d\bar{y}^2} + i\frac{4\,\sigma}{3} P_1 \frac{dU_{py}}{d\bar{y}} + P_2 \frac{dU_{px}}{d\bar{y}} + P_3 \frac{dW_p}{d\bar{y}} + P_5 \frac{d\nu_p}{d\bar{y}}$$

$$- \left\{ \frac{4}{3}\sigma^2 P_1 - i\,20\sqrt{\pi}\,\sigma\,\nu_0\,\bar{u}_0 + 20\sqrt{\pi}\,\nu_0\, s \right\} U_{px} + 20\sqrt{\pi}\,\nu_0 \frac{d\bar{u}_0}{d\bar{y}} U_{py}$$

$$+ \left\{ P_6 + i\,20\sqrt{\pi}\, S_{14}\,\sigma\,\overline{W_0^2} \right\} \nu_p + \left\{ P_4 + i\,20\sqrt{\pi}\, S_2 \right\} W_p = 0 \tag{36}$$

$$-\frac{P_1}{15\sqrt{\pi}}\frac{d^2U_{py}}{d\bar{y}^2}+i\frac{P_1\sigma}{15\sqrt{\pi}}\frac{dU_{px}}{d\bar{y}}-P_8\frac{dU_{py}}{d\bar{y}}-P_{10}\frac{dv_p}{d\bar{y}}-S_2\frac{dW_p}{d\bar{y}}$$

$$+\left\{i\sigma v_0\bar{u}_0-\frac{P_1\sigma^2}{20\sqrt{\pi}}-v_0 s\right\}U_{py}+P_9 v_p+\left\{i\sigma P_7-P_{11}\right\}W_p=0 \tag{37}$$

$$\frac{P_{21}}{2}\frac{d^2W_p}{d\bar{y}^2}+\left\{i\sigma P_{21}+H_3\right\}\frac{dW_p}{d\bar{y}}+2P_{23}\frac{dU_{px}}{d\bar{y}}+P_{28}\frac{dU_{py}}{d\bar{y}}+P_{19}\frac{dv_p}{d\bar{y}}+\left\{H_2+i\sigma P_{19}\right\}v_p$$

$$+i\sigma P_{28}U_{px}+i\sigma P_{23}U_{py}+\left\{i\sigma H_3+H_1-\frac{\sigma^2 P_1}{2}-\frac{3}{2}v_0 s\right\}W_p=0 \tag{38}$$

and the boundary conditions become

$$U_{px}=\sqrt{\frac{\pi}{2}}\tan\alpha\,\overline{W}_0\left\{f_p v_p+f\frac{1}{2\overline{W}_0^2}W_p\right\}$$

$$U_{py}=0 \tag{39}$$

$$\int_0^{\beta} v_p\,d\bar{y}=0 \tag{40}$$

$$S_1\frac{dU_{px}}{d\bar{y}}+i\sigma S_1 U_{py}+A_1\frac{d\bar{u}_0}{d\bar{y}}v_p+\frac{S_1}{2\overline{W}_0^2}\frac{d\bar{u}_0}{d\bar{y}}W_p=0 \tag{41}$$

$$2\overline{W}_0\frac{dW_p}{d\bar{y}}+\frac{d\overline{W}_0}{d\bar{y}}\overline{W}_p=0 \tag{42}$$

$$W_p=0 \tag{43}$$

In the above equations P_1 through P_{28}, H_1 through H_3, G_1 through G_{39}, S_{10} through S_{18} and A_1 through A_3 are quantities that depend on the basic solution and we shall leave out their specific forms for brevity. Equation (35) is used in equations (36) through (38) so that v_p is eliminated from the three equations and the boundary conditions. In the above equations we set $s = 0$ as we are interested in the marginal stability curve and we end up with three second order ordinary differential equations. The final equations are

$$P_1\frac{d^2U_{px}}{d\bar{y}^2}+iG_7\frac{d^2U_{py}}{d\bar{y}^2}+G_8\frac{dU_{px}}{d\bar{y}}+(G_{10}+iG_9)\frac{dU_{py}}{d\bar{y}}+P_3\frac{dW_p}{d\bar{y}}$$

$$+(G_{11}+iG_{12})U_{px}+(G_{13}+iG_{14})U_{py}+(P_4+iG_{15})W_p=0 \tag{44}$$

$$(G_{16}+i\,G_{17})\frac{d^2U_{py}}{d\bar{y}^2}+(G_{18}+i\,G_{19})\frac{dU_{py}}{d\bar{y}}+(G_{20}+i\,G_{21})\frac{dU_{px}}{d\bar{y}}$$

$$-S_2\frac{dW_p}{d\bar{y}}+(G_{22}+i\,G_{23})\,U_{py}+G_{24}\,U_{px}+(G_{25}+i\,G_{26})\,W_p=0 \tag{45}$$

$$G_{27}\frac{d^2W_p}{d\bar{y}^2}+i\,G_{30}\frac{d^2U_{py}}{d\bar{y}^2}+(G_{31}+i\,G_{32})\frac{dU_{py}}{d\bar{y}}+G_{33}\frac{dU_{px}}{d\bar{y}}+(G_{28}+i\,G_{29})\frac{dW_p}{d\bar{y}}$$

$$+(G_{34}+i\,G_{35})\,W_p+(G_{36}+i\,G_{37})\,U_{py}+(G_{38}+i\,G_{39})\,U_{px}=0 \tag{46}$$

and the boundary conditions become

$$U_{px}=\sqrt{\frac{\pi}{2}}\,tan\alpha\,\overline{W_0}\left\{f_p\,\nu_p+f\frac{1}{2\,\overline{W_0}^2}\,W_p\right\}$$

$$U_{py}=0 \tag{47}$$

$$\int_0^{\beta}\left\{i\,\nu_0\frac{dU_{py}}{d\bar{y}}+i\frac{d\nu_0}{d\bar{y}}\,U_{py}-\sigma\,\nu_0\,U_{px}\right\}d\bar{y}=0 \tag{48}$$

$$S_1\frac{dU_{px}}{d\bar{y}}+i\frac{A_1\,\nu_0}{\sigma\,\overline{u_0}}\frac{d\bar{u}_0}{d\bar{y}}\frac{dU_{py}}{d\bar{y}}+i\left\{\sigma\,S_1+\frac{A_1}{\sigma\,\overline{u_0}}\frac{d\bar{u}_0}{d\bar{y}}\frac{d\nu_0}{d\bar{y}}\right\}U_{py}$$

$$-\frac{A_1\,\nu_0}{\overline{u_0}}\frac{d\bar{u}_0}{d\bar{y}}\,U_{px}+\frac{S_1}{2\,\overline{W_0}^2}\frac{d\bar{u}_0}{d\bar{y}}\,W_p=0 \tag{49}$$

$$2\,\overline{W_0}\frac{dW_p}{d\bar{y}}+\frac{d\overline{W_0}}{d\bar{y}}\,W_p=0 \tag{50}$$

$$W_p=0 \tag{51}$$

where,

$$\beta=\frac{L}{\sigma}$$

$$\phi_1=\frac{\pi}{192}\,\frac{(5-7\nu_0+11\nu_0^2-5\nu_0^3)^2}{(2-\nu_0)^2\,\nu_0^2}$$

$$\phi_2 = \frac{4}{\nu_0 (2-\nu_0)} - \frac{2 (7-22\nu_0+15\nu_0^2)}{(5-7\nu_0+11\nu_0^2-5\nu_0^3)}$$

$$\phi_3 = \frac{(1-\nu_0)^3}{2 \nu_0 (2-\nu_0)}$$

$$\phi_4 = \frac{3}{(1-\nu_0)} + \frac{2 (1-\nu_0)}{\nu_0 (2-\nu_0)}$$

$$\phi_5 = \frac{\phi_3 \phi_4}{1+\phi_3} + \frac{\phi_1 \phi_2}{1+\phi_1}$$

$$\phi_6 = \frac{5 (1-\nu_0)^3}{2 \nu_0 (2-\nu_0)}$$

$$\zeta = \frac{2}{3} \{ 2 \, csc^2\theta \, (1-cos\theta) - cos\theta \}$$

$$\phi_7 = \frac{5 \bar{a}}{2^{3/2}} \frac{(1+\phi_3)}{(1+\phi_1)} \left\{ \frac{\pi \phi_4 \phi_6}{12 \sqrt{2} \bar{a}} + \phi_5 + \frac{\pi (1+\phi_6) \phi_5}{12 \sqrt{2} \bar{a}} \right\}$$

$$f_p = \frac{\phi_7 \, sin^2\theta}{\zeta} - \frac{5 \bar{a} \phi_5}{\sqrt{2}} \frac{(1+\phi_3)}{(1+\phi_1)}$$

RESULTS AND DISCUSSION

The system of equations (45), (46) and (47) with the boundary conditions (47) through (51) are solved numerically to obtain marginal stablity curves. For the base solution we use Richman and Marciniec (1990) approximate solution in the stablity analysis. In Figure 1, Q *Vs* σ (marginal stability curve) is plotted for different values of angle of inclination (α). Ofcourse, there are so many paramters involved in the problem, α, e_w, e, Q etc. that a systematic parametric study needs to be carried out. However, Figure 1 shows clearly that increasing the angle α by a small amount from 12.2 to 12.9 destablizes the flow, a result that is in keeping with our physical expectation. How the coefficient of restitution between the particles e and the coefficient of restitution between the particles and the wall will be studied.

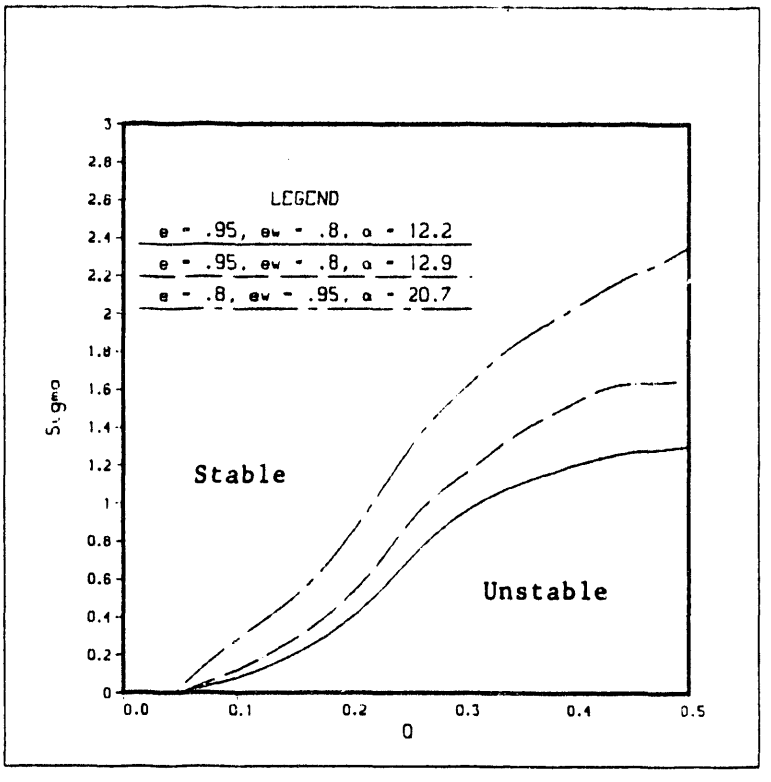

Figure 1. Marginal Stability Curve [Q vs σ]

REFERENCES

1. **Ahmadi, G. and D.N. Ma 1986**, *Int. J. Bulk Solid Storage in Silos*, 2: 8.

2. **Ahmadi, G. and M. Shahinpoor 1983a** "Towards a Turbulent Modeling of Rapid Flow of Granular Materials", *Powder Tech.*, 35: 241-248.>

3. **Ahmadi, G. and M. Shahinpoor, 1984** "A Kinetic Model for Rapid Flows of Granular Materials", *Int. J. of Non-Linear Mech.*, 19: 177-186.

4. **Boyle, E.J. and M. Massoudi, 1989** "Kinetic Theories of Granular Materials with Applications to Fluidized Beds", Technical Note, DOE/METC-89/4088.

5. **Hui. K., P.K. Haff, J.E. Unger and R. Jackson, 1984** "Boundary Condition's for High-Shear Grain Flows",*J. of Fluid Mechanics*, 145: 223-233.

6. **Hutter, K., F. Szidarovszky, and S. Yakowitz, 1986a** "Plane Steady Shear Flow of a Cohesionless Granular Material Down an Inclined Plane: A Model for Flow Avalanches Part-I: Theory," *Acta Mechanica*, 63: 87-112.

7. **Hutter, K., F. Szidarovszky, and S. Yakowitz, 1986b** "Plane Steady Shear Flow of a Cohesionless Granular Material Down an Inclined Plane: A Model for Flow Avalanches Part-II: Numerical Results," *Acta Mechanica*, 65: 239-261.

8. **Jenkins, J.T. and S.B. Savage, 1983** "A Theory for the Rapid Flow of Identical, Smooth, Nearly Elastic, Spherical Particles", *J. Fluid Mech.*, 130: 187-202.

9. **Jenkins, J.T. and M.W. Richman, 1985** "Grad's-13 Moment System for a Dense Gas of Inelastic Spheres", *Arch. Rat. Mech. & Anal.*, 87: 355-377.

10. **Jenkins, J.T. and M.W. Richman, 1986** "Boundary Conditions for Plane Flows of Smooth, nearly Elastic, Circular Disks", *J. of Fluid Mechanics*, 771: 53-69.

11. **Johnson, P.C. and R. Jackson, 1987** "Frictional-Collisional Constitutive Relations for Granular Materials, with Application to Plane Shear", *J. of Fluid Mechanics*, 176: 67-93.

12. **Johnson, P.C., P. Nott and R. Jackson, 1990** "Frictional-Collisional Equations of Motion for Particular Flows and their Application to Chutes", *J. of Fluid Mechanics*, 210: 501-535.

13. **Lun, C.K.K., S.B. Savage, D.J. Jeffrey, and N. Chepurnity, 1984**, "Kinetic Theories for Granular Flow: Inelastic Particles in Couette Flow and Slightly Inelastic Particles in a General Flow Feild", *J. Fluid Mech.*, 140: 223-256.

14. **Ma, D. and G. Ahmadi, 1985** "A Turbulent Model for Rapid Flows of Granular Materials, Part II. Simple Shear Flows", *Powder Tech.*, 44: 269-279.

15. **Ma, D. and G. Ahmadi, 1988** "A Kinetic Model for Rapid Granular Flows of Nearly Elastic Particles including Interstitial Fluid Effects", *Powder Tech.*, 56: 191.

16. **Ogawa, S., A. Umemura, and N. Oshima, 1980** "On the Equations of Fully Fluidized Granular Materials), *ZAMP*, 31: 483-493.

17. **Rajagopal, K.R., and R. Gudhe, 1991** "A Theoretical and Numerical Study of the Flow of Granular Materials", *Proceedings of the Joint DOE/NSF Workshop on Flow of Particulates and Fluids*, **Eds.** S.I. Plasynski, W.C. Peters, and M.C. Roco, pp. 299-309.

18. **Richman, M.W., and R.P. Marciniec, 1990** "Gravity-Driven Granular Flows of Smooth, Inelastic Spheres Down Bumpy Inclines", *J. of Applied Mechanics*, 57: 1036-1043.

19. **Savage, S.B., 1979** "Gravity Flow of Cohesionless Granular Materials in Chutes and Channels", *J. Fluid Mech.*, 92: 53-96.

20. **Shen, H., 1981** "Constitutive Relationships for Fluid-Solid Mixtures", Ph.D. Diss., Clarkson College of Technology, Potsdam, Germany.

Statistical Mechanics of Colloidal Suspension Rheology

Norman J. Wagner

Department of Chemical Engineering

University of Delaware

Newark, DE 19716

wagner@che.udel.edu

(September 29, 1993)

Paper presented at:

Joint DOE/NSF

Workshop On

Flow of Particulates and Fluids

Ithaca, New York

September 29- October 1, 1993

Statistical Mechanics of Colloidal Suspension Rheology

Norman J. Wagner
Department of Chemical Engineering
University of Delaware, Newark DE 19716 USA
(September 29, 1993)

A self-consistent, statistical mechanical theory for the dynamics and rheology of suspensions of Brownian colloids completely in terms of physicochemical suspension properties is presented. The theory uses the Rogers-Young closure of the Ornstein-Zernike (Phys. Rev. A, 1984) equation for the equilibrium structure and the generalized hydrodynamics theory developed by Hess and Klein (Adv. Phys., 1983) for the dynamic properties. Direct hydrodynamic interactions are neglected. Mode-mode coupling is used to close the generalized hydrodynamics equations and provide a self-consistent set of equations for the dynamics. All accessible linear viscoelastic properties of the suspension are then calculated from the the dynamics of the intermediate scattering function. Numerical solutions are obtained for Yukawa particles through the viscoelastic approximation. Comparison with rheological data from the literature on model systems demonstrates the accuracy of the theory for predicting both qualitative trends and quantitative behavior. The results are interpreted in terms of the cage melting model for colloid dynamics.

I. OVERVIEW OF NSF-PYI SPONSORED RESEARCH

The focus of this research sponsored by the National Science Foundation's Presidential Young Investigator Award is the physics and chemistry of complex fluids under flow. Specifically, we are determining the complex interplay between viscometric flows and molecular architecture in liquid crystalline polymers (both lyotropic and thermotropic), lcp containing blends, colloidal suspensions, and microemulsions. Understanding and controlling the microstructure of complex fluids and the products derived from them requires the development of theories and experiments capable of analyzing the *molecular level* detail of a fluid under flow. Thus, we are developing new in situ scattering techniques (both polarized light and small-angle neutron scattering) capable of resolving molecular architecture under flow [1–4]; new theoretical approaches capable of treating polydisperse and multicomponent systems [5–8] and new simulation algorithms that use massively parallel computers to study the shear flow of $\geq 10^6$ particles [9]. This comprehensive program of experimentation on model systems, statistical mechanical theory, and simulation promises predictive capabilities in the design of new materials and materials processing strategies. The following is a listing of the current thesis projects in my research group (both Ph.D. and undergraduate) along with an indication of any the source of funding for the PYI grant and any other collaborations:

Liquid Crystalline Polymer Science:

- Rheology and microstructure of lyotropic LCPs at low shear stresses (Leuven-Belgium)
- Rheology, structure, and processing of thermotropic LCP containing blends (du Pont)
- Thermodynamics and microstructure of rod-like macromolecules (NIST)
- Prediction of coupled diffusion and morphological change in polymers (Dow)

Colloidal Suspensions and Self-Assemblying Surfactant Solutions:

- Rheology and rheo-optics of colloidal spheres, rods, and disks (Kodak)
- Viscosity and structure of inverse microemulsions and lamellar phases
- The structure and rheology of the square-well colloidal fluid (CRS4-Italy)
- Massively parallel simulations of suspensions (LANL)
- Novel ferrofluid systems and magnetorheology
- Generalized Hydrodynamics of dense colloidal suspensions (Konstanz-Germany)

The following report describes recent progress in the last of these topics.

II. INTRODUCTION

One important aim of applying statistical mechanics to describe the dynamics of Brownian suspensions has been to predict the measurable dynamic and rheological properties, such as the dynamic relaxation of density fluctuations and the frequency dependent shear viscosity, solely in terms of the fundamental interparticle interactions. Understanding the macroscopic ramifications of changing the nature of the microscopic forces acting on the colloidal level is a challenging problem with a rich history and is of obvious technological importance. As with molecular fluids, it is the collective, many-body interactions that provides the wealth of interesting behavior one hopes to explain in terms of the microscopic forces between the individual Brownian particles. The advent of larger computers and the application of methods designed to tackle many-body interactions in statistical mechanics make a direct comparison of predicted and measured dynamics now feasible. Because of the long time and length scales involved in probing macromolecular fluids (versus molecular fluids), there is relatively easy experimental access to both macroscopic and colloidal level properties for comparison with theory. Further, from an engineering, modeling standpoint it is important to have a fundamental theoretical foundation to judge the applicability of more phenomenological approaches. It is the goal of this paper to describe a self-consistent statistical mechanical description of dense fluid dynamics and rheology valid for colloidal suspensions that connects the colloidal level interactions to the macroscopic properties and to test the validity of this theory directly against experiments on a model colloidal suspension.

The method for describing the dynamics of Brownian suspensions is based on the mode-coupling closure of a system of generalized hydrodynamic equations [10–19]. It should be noted that a similar approach has had marked success in elucidating the dynamics of *molecular* fluids, in contrast to the *macromolecular* fluids considered here, for over a decade [20–25]. The theory yields a set of self-consistent equations for the collective dynamics of a fluid composed of Brownian particles completely in terms of the static structure of the suspension. Since there are now accurate solutions for the structure of charged, Brownian particles in terms of the intercolloidal potentials [26–28], a direct link between the underlying microscopic forces and the dynamics of Brownian suspensions is possible. In this paper, these two developments are combined and a method for numerically calculating a self-consistent solution for the dynamics, starting only from the basic physicochemical properties of the Brownian particles and the solvent, is derived. Further, the linear viscoelastic rheological properties

are derived in terms of the collective dynamics of density relaxations. Thus, the viscosity of the suspension in the limit of linear response is also calculated directly from the the physicochemical colloidal properties.

Significant comparisons have been made between predictions of the generalized hydrodynamics approach for dilute, weakly interacting polystyrene colloid suspensions [10,19,29], concentrated suspension self-diffusion [30,31] and for hard-sphere colloidal glasses [25,32-35]. Although mechanical measurements of collective dynamics are quite prevalent in the literature, actual quantitative comparison of theories based on generalized hydrodynamics against rheological measurements on concentrated, fluid systems are absent.

This theory can be contrasted with an alternative, but complementary, approach based on solving a nonequilibrium Smoluchowski equation for an applied shear field [36-39,5,40-44]. The necessary inputs include the equilibrium microstructure, the microscopic interaction forces, and closure relations for many-body distribution functions. By ensemble averaging the microscopic stresses resulting from the interactions between the Brownian particles over this nonequilibrium microstructure, the theory predicts the bulk stresses in the deforming suspension (principally the low shear limiting viscosity). Again, rheological measurements of the low shear limiting viscosity provide quantitative tests. Further, static light and neutron scattering measurements of the nonequilibrium microstructure provide quantitative tests of the predictions for the steady nonequilibrium microstructure [39,45-50]. In comparison, one advantage of using the generalized hydrodynamics approach employed here is the formulation of a self-consistent set of equations for the full dynamics of the suspension through the mode-mode coupling ansatz. Further, generalized hydrodynamics yields the full time dependence of all measurable quantities, such as densities and fluxes, as part of the self-consistent solution.

In what follows, the theoretical approach is reviewed and solutions for a model system of charged, Brownian particles are presented. Much of the background for the technical derivation can be found in the review article by Hess and Klein [10] and the derivations specific to this work are to appear in a companion article [7]. The effect of polydispersity on suspension properties is included in the cumulant and equilibrium structure calculations. The generalized hydrodynamics equations are defined and the mode-mode coupling closure invoked. A tractable numerical solution of the self-consistent equations is obtained through the use of the viscoelastic approximation. This also enables asymptotic examination ong coupling limit and the glass transition. Numerical calculation of the self-consistent eq d comparison to rheological experiments on a well-characterized model system are made t validity of the theory. Finally, a physical picture of the generalized hydrodynamic theory with mode-mode coupling is presented through the cage melting model and a possible criterion for the ideal glass transition discussed.

III. EQUILIBRIUM SUSPENSION PROPERTIES

A. microstructure

To define the model systems of interest in this study and to connect the physicochemical properties of the suspension to the equilibrium structure, an integral equation approach is employed [51,52]. The equilibrium microstructure of a suspension is characterized by the radial distribution function $g(r)$, which is proportional to the probability of finding a particle at the relative distance r from the origin given that a particle is centered at this origin. This function can be calculated from the Ornstein-Ze.nike equation (OZ) [26]

$$h(r_{12}) = g(r_{12}) - 1 = c_d(r_{12}) + C \int c_d(r_{13}) h(r_{23}) d\mathbf{x}_3, \tag{1}$$

where $c_d(r)$ is the direct correlation function and C is the number density of the colloidal particles. A closure relation is needed to connect $h(r)$ and $c_d(r)$ with the interaction potential. The Rogers-Young scheme (RY) [27], which mixes the well known Percus-Yevick (PY) and hypernetted chain (HNC) closures, is appropriate for the colloids considered in this work. Defining $\nu(r) = h(r) - c_d(r)$ the RY closure can be written as,

$$g(r) = exp(\Phi(r))(1 + \frac{exp(\nu(r)\lambda(r)) - 1}{\lambda(r)}), \tag{2}$$

with $\Phi(r)$ the dimensionless pair interaction potential and $\lambda(r) = 1 - exp(-\xi r)$, with ξ the RY mixing parameter. When $\xi = 0$ the closure reduces to the PY closure and when $\xi = \infty$ it reduces to the HNC closure. This parameter is determined by requiring thermodynamic consistency in matching the bulk modulus predicted by the compressibility equation and the pressure equation. As the HNC and PY equations bracket the compressibility and microstructure for repulsive and hard-sphere potentials, [26,27] mixing these two integral equations generates an equilibrium structure yielding equal compressibilities from both of the above equations. The accuracy of this scheme has been demonstrated previously by comparison with Monte Carlo simulations and structure measurements [27,28] .

Given the pair distribution function, the static structure factor is the Fourier transform as (with r dimensionless with particle radius a):

$$S(k) = 1 + 3\phi \int \frac{\sin kr}{kr}(g(r) - 1)r^2 dr. \tag{3}$$

where $\phi = 4\pi C a^3/3$ is the volume fraction.

B. Interaction Potential

The model systems treated here are suspensions of charged Brownian particles, typically realized as suspensions of polystyrene latex particles in water. The potential depends on the screening length κ, which is related to the concentration of all small ions n_k with charge z_k, including both added salt ions and the counterions from the colloids themselves, as

$$\kappa^2 = \frac{4\pi e^2}{\epsilon k_b T} \sum_k n_k (z_k)^2. \tag{4}$$

The interaction potential is of Yukawa form [53] (with r and κ made dimensionless with the particle radius a and the potential scaled on $k_b T$)

$$\Phi(r) = \frac{(Qe)^2}{k_b T \epsilon (1 + \kappa a)^2 r} e^{-\kappa(r-2)} \tag{5}$$

with colloid charge Q, and the dielectric constant of the material ϵ.

(6)

In this and previous work, the other colloidal forces, such as van der Waals attractions, have been neglected based on simple calculations of their relative magnitude [5]. It is straightforward to include other pairwise additive potentials within the formalism. For the systems under consideration, the simple Yukawa interaction will dominate the other thermodynamic and hydrodynamic interactions between the particles. A more complete discussion of the role of colloidal forces in suspension rheology can be found in [54].

C. polydispersity

Significant work has been done to investigate the effects of polydispersity on the equilibrium properties of Yukawa suspensions through the OZ-RY formalism, with comparable investigations of the self-diffusion dynamics [19,28,51,55,56,52]. Comparing the results to DLS and monte carlo simulations demonstrates the validity of the treatment. For the work considered here, polydispersity will

be explicitly accounted for in the calculation of the inputs to the generalized hydrodynamics theory, i.e. the structure factor, the cumulants and the elastic constants. These inputs will then *define* the effective fluid properties necessary for the calculation of the dynamics. No explicit treatment of the dynamics of multicomponent mixtures will be considered; however, as the Generalized Hydrodynamic description is derived in terms of a hydrodynamic level description of an effective OCF model, this approximation should be correct to first order.

The central quantity that must be considered is the equilibrium structure factor S(k). Previous work [28,51] has derived the correct form of the structure factor within the OZ-RY scheme using the Schulz distribution as a model for the polydispersity [57], and demonstrated its accuracy [56] against scattering measurements and monte carlo simulation. The structure factor that corresponds to the generalized compressibility $S^T(k)$ is to be used in the calculation of the generalized hydrodynamics equations for polydisperse suspensions in place of S(k).

For input into the generalized hydrodynamics equations, thermodynamic cumulants are defined as

$$< \mu_1^c(k) >^T = k^2 \frac{\sum_\alpha \sum_\beta D^o_{\alpha\beta}}{S^T(k)}$$

$$D^o_{\alpha\beta} = \frac{k_b T}{3\pi\mu_o}\left(\frac{1}{a_\alpha} + \frac{1}{a_\alpha}\right) \tag{7}$$

$$< \mu_2^c(k) >^T = - < \mu_1^c(k) >^T \frac{k^2}{C\zeta_o}\left(< E'_\infty(k) > - \frac{Ck_bT}{S^T(k)}\right). \tag{8}$$

where ζ_o is the hydrodynamic friction coefficient for a bare particle. A decoupling approximation is used for the second cumulant [7].

The high frequency elastic constants are generalized from the Zwanzig-Mountain formulation [58] as

$$\frac{G'_\infty < a >^3}{k_B T} = \frac{3}{4\pi}\bar{\phi} + \frac{3}{8\pi}\sum_{ij}\frac{\phi_i\phi_j}{(\alpha_i\alpha_j)^3}\int \frac{d^2\Phi_{ij}(s)}{ds_z^2} g_{ij}(s)\frac{1-cos(ks_z)}{k^2}ds, \tag{9}$$

$$\frac{E'_\infty < a >^3}{k_B T} = \frac{9}{4\pi}\bar{\phi} + \frac{9}{8\pi}\sum_{ij}\frac{\phi_i\phi_j}{(\alpha_i\alpha_j)^3}\int \frac{d^2\Phi_{ij}(s)}{ds_z^2} g_{ij}(s)\frac{1-cos(ks_z)}{k^2}ds, \tag{10}$$

where $\alpha_i = \frac{a_i}{<a>}$, $\bar{\phi} = \frac{4\pi C <a>^3}{3}$, Φ_{ij} is the Yukawa potential between particles of type i and j, g_{ij} is the partial radial distribution function, and $s = \frac{2r}{a_\alpha + a_\beta}$. In the above equation, all hydrodynamic interactions have been neglected but can be readily included in the pairwise additive approximation (see [39,6]).

IV. GENERALIZED HYDRODYNAMICS AND THE MODE-MODE COUPLING CLOSURE

On the hydrodynamic level, the motion of a linearly viscoelastic fluid subject to a weak flow is governed by the Navier-Stokes equation of motion. The primary assumption of the generalized hydrodynamics theory is that the transport properties appearing in the Navier-Stokes equation are generalized to become a function of length and time. This *non-local* description of the fluid enables the study of the fluctuations in density, mass currents, and stress underlying the dynamics of the material, including the linear viscoelastic rheology. As this generalization can be directly derived from the Fokker-Planck equation, the generalized transport properties themselves can be represented entirely in terms of the physicochemical properties of the colloidal particles and the solvent. For suspensions, the *fluid* under consideration is the hydrodynamic description of the Brownian particles.

The solvent enters the description through Brownian motion and hydrodynamic interaction. For now, this theory is limited to the linear regime, or weak-flow limit.

Generalized hydrodynamics naturally arises when considering non-local relationships for the fundamental properties of molecular and complex fluids [22,10,19]. Here it is desired to obtain transport coefficients expressed entirely in terms of equilibrium suspension properties, i.e. physicochemical parameters and the structure factor. Significant development in this regard has evolved a self-consistent set of equations that express suspension dynamics entirely in terms of equilibrium properties. Coupled with the above theory for predicting the equilibrium structure in terms of fundamental parameters of the system, this program leads to a complete and consistent treatment of complex fluids in equilibrium and in the linear response regime. In what follows, the basic relations are presented and some approximate solutions discussed.

The correlation function of interest is the dynamic structure factor

$$S(k,t) = \frac{1}{N}\sum_{i,j=1}^{N} < exp[i\mathbf{k}\cdot(\mathbf{r}_i(0) - \mathbf{r}_j(t))] > \tag{11}$$

This can be expressed in terms of the Fourier components of the macroparticle density

$$C(\mathbf{r},t) = \sum_{i=1}^{N} \delta(\mathbf{r} - \mathbf{r}_i(t)) \tag{12}$$

as

$$S(k,t) = \frac{1}{N} < C(\mathbf{k},t)C(-\mathbf{k},0) >= \frac{1}{N} < \hat{c}(\mathbf{k},t)\hat{c}(-\mathbf{k},0) >,$$
$$\hat{c}(\mathbf{k},t) = C(\mathbf{k},t) - < C > \tag{13}$$

The particle density must satisfy a continuity equation, written in terms of the particle current density $\mathbf{j}(\mathbf{r},t)$ as

$$\frac{\partial C(\mathbf{r},t)}{\partial t} = -\nabla\cdot\mathbf{j}(\mathbf{r},t). \tag{14}$$

This current density satisfies a non-local, (in both space and time), generalization of Fick's law:

$$\mathbf{j}(\mathbf{r},t) = \int_0^t dt' \int d\mathbf{r}'\mathbf{D}(\mathbf{r}-\mathbf{r}',t-t')\nabla_{r'}C(\mathbf{r}',t') \tag{15}$$

Using equations (13) and (15) to calculate the dynamic structure factor and Laplace transforming yields the generalized diffusion equation (GDE)

$$\tilde{S}(k,z) = \frac{S(k)}{z + \tilde{D}(k,z)k^2},$$
$$\tilde{D}(k,z) = \frac{\mathbf{k}\cdot\tilde{\mathbf{D}}(\mathbf{k},z)\cdot\mathbf{k}}{k^2} \tag{16}$$

where $\tilde{D}(k,z)$ plays the role of the memory function for the dynamic structure factor. Setting $\tilde{D}(k,z) = D_c$, the collective diffusion coefficient, recovers the local, decoupled solution of the ordinary Fick's law. In the time domain, equation (16) above has the form of a memory equation,

$$\frac{\partial S(\mathbf{k},t)}{\partial t} = -k^2\int_0^t dt' D(\mathbf{k},t-t')S(\mathbf{k},t'), \tag{17}$$

with the collective diffusion coefficient as the memory function.

The mass diffusion coefficient is directly related to the wave vector dependent, longitudinal friction coefficient via the generalized hydrodynamic relation [10]

$$\tilde{D}(k,z) = \frac{kT/(mS(k))}{z + \tilde{\zeta}_{\parallel}(k,z)/m}. \tag{18}$$

This equation represents the generalized Stokes-Einstein relation (GSE), with $\tilde{\zeta}_{\parallel}(k,z)$ playing the role of the memory function (to be called the second memory function). The longitudinal friction coefficient is defined as

$$\tilde{\zeta}_{\parallel}(k,z) = \frac{\mathbf{k}\cdot\tilde{\zeta}(\mathbf{k},z)\cdot\mathbf{k}}{k^2} = \zeta_o(k) + \frac{k^2}{C}\tilde{\eta}_{\parallel}(k,z), \tag{19}$$

The hydrodynamic contribution ζ_o is taken to be time independent on the time scales of interest here. Again if the longitudinal friction coefficient is assumed to be constant (i.e. $\tilde{\zeta}_{\parallel}(k,z) = \zeta_o$) and in the noninteracting limit ($S(k) \rightarrow 1$) the Stokes-Einstein relation is recovered as

$$D_o = \frac{k_b T}{\zeta_o}. \tag{20}$$

In the hydrodynamic limit ($k \rightarrow 0, \quad z \rightarrow 0$) the GSE relation reduces to

$$D_c = \frac{k_b T}{S(0)\tilde{\zeta}_{\parallel}(0,0)} = \mu_o \frac{\partial \pi}{\partial C}\Big|_T. \tag{21}$$

Here π represents the osmotic pressure.

For systems without hydrodynamic interactions, the longitudinal dynamic viscosity is entirely due to potential interactions. Projection operator techniques lead to the following relation for the longitudinal viscosity in terms of the interparticle stress tensor [10]

$$\tilde{\eta}_{\parallel}(\mathbf{k},z) = \frac{\beta}{V} < \dot{\sigma}_{zz}(\mathbf{k})[z - \tilde{\Omega}\tilde{Q}]^{-1}\dot{\sigma}_{zz}(-\mathbf{k}) >, \tag{22}$$

with $\tilde{\Omega}$ the Fokker-Planck operator and $\tilde{Q}$ the orthogonal projection operator (orthogonal to the subspace spanned by current and concentration fluctuations). Closure of this set of relations requires a relationship between the interparticle contribution to the stress and the density fluctuations in the suspension.

A. overdamped limit

For times large relative to the momentum relaxation time for the Brownian particle $\frac{m}{\zeta_o}$, the fluid of Brownian particles is overdamped. For such times, the generalized Stokes-Einstein relation can be reduced to:

$$\tilde{D}(k,z) = \frac{kT/(mS(k))}{\tilde{\zeta}_{\parallel}(k,z)/m}. \tag{23}$$

which can be conveniently expressed in the following form. Defining

$$\Delta D(\mathbf{k},t) = D(\mathbf{k},t) - D(\mathbf{k},0) \tag{24}$$

leads to the following memory equation in the time domain

$$\Delta D(\mathbf{k},t) = \frac{D_o \mathbf{k}^4 \eta_{\parallel}(\mathbf{k},t)}{S(\mathbf{k})C\zeta_o} - k^2 \int_0^t dt' \Delta D(\mathbf{k},t-t')\frac{\eta_{\parallel}(\mathbf{k},t)}{C\zeta_o} \tag{25}$$

Here $\eta_{\parallel}(\mathbf{k},t)$ plays the role of the memory function. Also, the generalized diffusion equation (16) becomes

$$\frac{\partial S(\mathbf{k},t)}{\partial t} = -\frac{D_o \mathbf{k}^2}{S(\mathbf{k})} S(\mathbf{k},t) + k^2 \int_0^t dt' \Delta D(\mathbf{k}, t-t') S(\mathbf{k},t') \tag{26}$$

Again, these equations are valid for times longer than the relaxation time of the Brownian particle's momentum. Alternately, one can start directly from the Smoluchowski dynamics and arrive at the same result [17,18].

B. Mode-Mode Coupling Approximation

The final step needed to close the system of equations is to express the longitudinal viscosity, in terms of the dynamic structure factor. A critical part of this work involves analyzing the approximations used in formulating the mode-mode coupling closure. The details of this analysis can be found in reference [7]. A projection operator technique is used to separate the slow and fast relaxing variables of the system. The mechanistic approximations required follow the usual paradigm [59,10,24], with the exception of the detailed treatment of three-body terms arising in the final expression. As has been shown, the two versions of the resultant expressions for the vertex, or coupling functions found in the literature arise from different approximations used in simplifying the three-body terms.

1. Convolution Approximation

In the molecular theory of simple fluids and the study of colloidal glass transitions, the three-point correlation function above is approximated wholely in terms of two-point correlation functions through the convolution approximation (denoted by ^{CA}), which is analogous to the Kirkwood superposition approximation but in Fourier space [60]. This approximation results in an expression for the longitudinal friction coefficient:

$$\eta_{\parallel}(\mathbf{k},t)^{CA} = \frac{2C^2\beta}{(2\pi)^3} \int d\mathbf{k}' g_{zz}^{CA}(\mathbf{k},\mathbf{k}') g_{zz}^{CA}(-\mathbf{k},-\mathbf{k}') S(\mathbf{k}_1,t), S(\mathbf{k}_2,t)$$

$$g_{zz}^{CA}(\mathbf{k},\mathbf{k}') = \frac{i}{2\beta k^2} \left(\mathbf{k}\cdot\mathbf{k}_1' c_d(k_1') + \mathbf{k}\cdot\mathbf{k}_2' c_d(k_2')\right)$$

$$\mathbf{k}_{1,2}' = \mathbf{k}/2 \mp \mathbf{k}' \tag{27}$$

The vertex function g_{zz}^{CA} has strong coupling to low k values through the direct correlation function $c_d(\mathbf{k}) = (1 - S(\mathbf{k}))/CS(\mathbf{k})$. Note that in the convolution approximation the three-body terms are completely reduced to two-body terms. The shear component of the longitudinal stress, by a similar derivation yields

$$\eta_s(\mathbf{k},t)^{CA} = \frac{2C^2\beta}{(2\pi)^3} \int d\mathbf{k}' g_{xx}^{CA}(\mathbf{k},\mathbf{k}') g_{xx}^{CA}(-\mathbf{k},-\mathbf{k}') S(\mathbf{k}_1,t), S(\mathbf{k}_2,t)$$

$$g_{xx}^{CA}(\mathbf{k},\mathbf{k}') = \frac{i}{2\beta k} \left(k_{1,x}' c_d(k_1') + k_{2,x}' c_d(k_2')\right) \tag{28}$$

This completes the closure of the generalized hydrodynamics equations by relating the second memory function, the longitudinal friction, to the dynamic structure factor and vertex functions that depend only on equilibrium, static quantities.

2. Two-body Treatment

Hess and Klein [10] employed a rigorous factorization of the vertex function instead of the convolution approximation employed above, which will be referred to throughout this paper as the two-body treatment As three-body correlations are difficult to calculate and require additional approximation, Hess and Klein argued in favor of neglecting the entire three-body term, thus leaving a tractable result containing only two-body correlation functions. Using this form for the 3-point correlation function results in the following for the longitudinal and shear viscosity functions

$$\eta_{\parallel}(\mathbf{k},t)^{TB} = \frac{2C^2\beta}{(2\pi)^3}\int d\mathbf{k}' g_{zz}^{TB}(\mathbf{k},\mathbf{k}')g_{zz}^{TB}(-\mathbf{k},-\mathbf{k}')S(\mathbf{k}_1,t),S(\mathbf{k}_2,t)$$

$$g_{zz}^{TB}(\mathbf{k},\mathbf{k}') = \frac{i}{2\beta k^2 S(\mathbf{k}_1')S(\mathbf{k}_2')}\left(\mathbf{k}\cdot\mathbf{k}_1' h(k_1') + \mathbf{k}\cdot\mathbf{k}_2' h(k_2')\right)$$

$$\eta_s(\mathbf{k},t)^{TB} = \frac{2C^2\beta}{(2\pi)^3}\int d\mathbf{k}' g_{xx}^{TB}(\mathbf{k},\mathbf{k}')g_{xx}^{TB}(-\mathbf{k},-\mathbf{k}')S(\mathbf{k}_1,t),S(\mathbf{k}_2,t)$$

$$g_{xx}^{TB}(\mathbf{k},\mathbf{k}') = \frac{i}{2\beta k S(\mathbf{k}_1')S(\mathbf{k}_2')}\left(\mathbf{k}_{1,x}' h(k_1') + \mathbf{k}_{2,x}' h(k_2')\right) \tag{29}$$

This form, in contrast to the convolution approximation, results in a slightly more complex coupling for the vertex function. The two wave vectors are mixed to a greater degree than in the former case. Notice also that both forms reduce, in the limit of weak coupling to the exact weak coupling limit [7]. This comparison is reminiscent of the various methods of closing three-body correlation functions in equations for the equilibrium structure. As there does not seem to be any fundamental reason to choose one form over the other, the results of using both forms in a numerical calculation will be performed to determine their performance.

C. Corrections for the Zero Time Limit

It is known that the MMC approximation is more accurate in describing the time evolution of the dynamic friction function than the initial, zero time value, which is an equilibrium property of the suspension calculable from mechanical [38,5,6] and fluctuation dissipation [58,22,6] derivations. Thus, it is preferable to use the MMC approximation to calculate only the relaxation or time dependence of the dynamic friction functions and rely on the exact calculations for the initial prefactor. The relaxation functions are defined as:

$$\tau_{\parallel}(\mathbf{k},t) = \frac{\eta_{\parallel}(\mathbf{k},t)}{\eta_{\parallel}(\mathbf{k},0)}$$

$$\tau_s(\mathbf{k},t) = \frac{\eta_s(\mathbf{k},t)}{\eta_s(\mathbf{k},0)} \tag{30}$$

The correct longitudinal and shear friction functions are written in terms of the high frequency elastic constants [22]

$$\eta_{\parallel}(\mathbf{k},0) = E_{\infty}'(\mathbf{k})$$

$$\eta_s(\mathbf{k},0) = G_{\infty}'(\mathbf{k}) \tag{31}$$

This leads to the following relations based on the above definitions,

$$\eta_{\parallel}(\mathbf{k},t) = E_{\infty}'(\mathbf{k})\tau_{\parallel}(\mathbf{k},t)$$

$$\eta_s(\mathbf{k},0) = G_{\infty}'(\mathbf{k})\tau_s(\mathbf{k},t) \tag{32}$$

Note that this scheme takes advantage of the known, exact initial values without compromising the integrity of the MMC approximation for the dynamics.

The macroscopic dynamic properties of the suspension, such as the rheology, can then be directly calculated in terms of these dynamic friction coefficients. For example, as shown in the appendix, the definition of the Newtonian shear viscosity yields,

$$\eta_s = \int_0^\infty \eta_s(0,t)dt = \int_0^\infty G(t)dt$$
$$\eta_\parallel = \int_0^\infty \eta_\parallel(0,t)dt = \int_0^\infty G_\parallel(t)dt, \tag{33}$$

where G(t) is the shear viscosity relaxation function discussed in the appendix. Thus, measurement of the frequency dependent viscosity or modulus can be directly compared to the time dependent viscosity function determined from generalized hydrodynamics via Fourier transforming the dynamic friction function with respect to time. All the rest of the linear viscoelastic functions can be determined directly in this way, as demonstrated in the appendix.

V. RESULTS AND DISCUSSION

A. Short-time Approximation

The simpliest method of solving the GH-MMC hierarchy has been to approximate the time and wave vector dependent structure factor by a short-time (ST) expression [15,10]. This essentially decouples the hierarchy and permits calculation of the rheological properties in terms of the static structure factor and the single particle diffusion coefficient. Lindsay et al. [29] predicted the Maxwell relaxation time, relating the steady shear viscosity to the high frequency modulus as $\tau_s^M = \eta_s/G'_\infty$, to have a form similar to a Lindemann melting criterion. Here a similar approach is used to predict the frequency dependent complex shear viscosity and comparison is made with a common model for the relaxation spectrum.

In the short-time approximation the memory function for the GDE relation is neglected and the original Fick's law is maintained. The dynamic structure factc is of single exponential form with a wave vector dependent relaxation time as given by the collective diffusion coefficient:

$$S(\mathbf{k},t)^{ST} = S(\mathbf{k})exp\left(-D_c(\mathbf{k})k^2t\right). \tag{34}$$

The generalized mass or collective diffusion coefficient is written as

$$D_c(\mathbf{k}) = D^0H(\mathbf{k})/S(\mathbf{k}). \tag{35}$$

For the strongly charged system considered here hydrodynamic interactions will be neglected in these calculations and so the generalized sedimentation coefficient $H(\mathbf{k})$ appearing above reduces to unity. Recent calculations by Genz and Klein [61] have demonstrated the importance of including hydrodynamic interactions, treated via the renormalization of Beenakker [62], for weakly charged suspensions. Mathematically, this form for $S(\mathbf{k},t)^{ST}$ follows from replacing the fully time and wave vector dependent diffusion coefficient in the generalized diffusion equation (26) with its time integral, the collective diffusion coefficient. The physical argument is that collective concentration relaxation would occur on a time long enough that it would sample this net mass diffusion rate. In essence, this neglects memory effects and would be the result from neglecting coupling between stress and concentration fluctuations in the formalism.

With the above approximation the viscosity functions are readily calculated from knowledge only of the static structure factor. Lindsay et al. [29] give typical solutions for the time dependence of the shear and longitudinal viscosities for very dilute, charged systems of spherical particles within the two-body treatment. These were then integrated, yielding the steady shear viscosity from equation (33). Over a dilute range of concentrations it was determined that

$$\eta_s = G'_\infty \frac{(0.1\bar{d})^2}{D_0} \tag{36}$$

where $\bar{d}$ is the average spacing between particles. The proportionality between the shear viscosity and the high-frequency modulus defines the Maxwell relaxation time for the system, the mean relaxation time for the stress fluctuations. The above relation is interpreted within a cage melting picture to express an idea similar to the well known Lindemann melting criterion. Namely, the viscosity is proportional the force acting on a test particle, surrounded by an instantaneous configuration of neighbors times a relaxation time. The characteristic time required for this force to relax is given by the time necessary for the test particle to travel about one-tenth the average neighbor separation distance. This is the time necessary for the surrounding cage to "melt", hence the analogy.

B. Viscoelastic Approximation

A more sophisticated approximation to the GE-MMC equations that maintains the self-consistency is the viscoelastic approximation (VEA). This is physically motivated by trying to approximate the time behavior of the system by an interpolation between short time elasticity and long time fluid behavior. For "short" times (on the diffusion time scale) the suspension behaves like an elastic solid while for "long" times the suspension will flow like a fluid. Thus, the approximation defines generalized Maxwell relaxation times for the shear and longitudinal viscosities and approximates the time dependence of the generalized mass diffusivity as a simple exponential decay [10]. Alternately, one can consider this as a model for the second memory function, the memory function for the GSE relation [10,17,18]. The VEA replaces the full wave vector and time dependent memory function with a single exponential containing a time constant that is wave vector-dependent. However, unlike the previous models for the memory function, this approximation does not specify the wave vector dependence explicitly; it is to be determined by the self-consistent solution of the generalized hydrodynamic equations.

Mathematically, the above assumption translates into the statement

$$\Delta\dot{\zeta}_{\parallel}(\mathbf{k},z) \approx \frac{\Delta\zeta_{\parallel}(\mathbf{k},0)}{z+(\tau_{\parallel}^{M}(\mathbf{k}))^{-1}} \tag{37}$$

defining the Maxwell relaxation time for longitudinal friction. This can also be calculated, in the absence of hydrodynamic interaction, from the contribution of interparticle interaction to the longitudinal viscosity

$$\tau_{\parallel}^{M}(\mathbf{k}) = \frac{1}{\eta_{\parallel}(\mathbf{k},0)}\int_{0}^{\infty} dt\eta_{\parallel}(\mathbf{k},t) = \frac{\dot{\eta}_{\parallel}(\mathbf{k},z=0)}{\eta_{\parallel}(\mathbf{k},0)} \tag{38}$$

where $\Delta\zeta_{\parallel}(\mathbf{k},z) = k^2\Delta\dot{\eta}_{\parallel}(\mathbf{k},z)/(C\zeta_o)$. Substitution into the GSE (23) leads to a single exponential for the time dependent part of the generalized mass diffusivity in the overdamped limit,

$$\Delta\dot{D}(\mathbf{k},z) = D^{\infty}(\mathbf{k})\frac{\Delta\dot{\zeta}_{\parallel}(\mathbf{k},z)}{\zeta_{\parallel}^{\infty}(\mathbf{k})+\Delta\dot{\zeta}_{\parallel}(\mathbf{k},z)} \approx \frac{-\mu_2(\mathbf{k})/k^2}{z+(\tau_{\parallel}^{M}(\mathbf{k}))^{-1}} \tag{39}$$

This single exponential ansatz defines the Maxwell relaxation time for diffusion as

$$(\tau_{D}^{M}(\mathbf{k}))^{-1} = (\tau_{\parallel}^{M}(\mathbf{k}))^{-1} - \frac{\mu_2(\mathbf{k})}{\mu_1(\mathbf{k})}$$

$$\Delta D(\mathbf{k},t) = D^{\infty}(\mathbf{k}) - D(\mathbf{k},t) = -\frac{\mu_2(\mathbf{k})}{k^2}e^{-t/\tau_{D}^{M}(\mathbf{k})}\theta(t) \tag{40}$$

Direct substitution into the overdamped GDE, equation (26), leads to two poles resulting in a double exponential form for the dynamic structure factor:

$$\frac{S(\mathbf{k},t)}{S(\mathbf{k})} = a(\mathbf{k})e^{-t/\tau_1(\mathbf{k})} + (1-a(\mathbf{k}))e^{-t/\tau_2(\mathbf{k})}$$

$$(\tau_{1,2}(\mathbf{k}))^{-1} = \frac{1}{2}\left(\mu_1(\mathbf{k}) + (\tau_D^M(\mathbf{k}))^{-1}\right) \pm \left[\frac{1}{4}\left(\mu_1(\mathbf{k}) - (\tau_D^M(\mathbf{k}))^{-1}\right)^2 - \mu_2(\mathbf{k})\right]^{1/2}$$

$$a(\mathbf{k}) = \frac{1}{2} + \frac{\mu_1(\mathbf{k}) - \tau_D^M(\mathbf{k})^{-1}}{2\left[\left(\mu_1(\mathbf{k}) - (\tau_D^M(\mathbf{k}))^{-1}\right)^2 - 4\mu_2(\mathbf{k})\right]^{1/2}}. \tag{41}$$

The mean structural relaxation time is given by

$$\tau^m_{S(k)}(k) = a(k)\tau_1(k) + (1-a(k))\tau_2(k). \tag{42}$$

The three parameters $a(k)$ $\tau_{1,2}(k)$ are then algebraically related to the mean diffusion and longitudinal viscosity relaxation times as

$$\tau_D^M(\mathbf{k}) = \frac{\tau_1(\mathbf{k})\tau_2(\mathbf{k})}{a(\mathbf{k})\tau_1(\mathbf{k}) + (1-a(\mathbf{k}))\tau_2(\mathbf{k})}$$

$$\tau_{\|}^M(\mathbf{k}) = a(\mathbf{k})\tau_2(\mathbf{k}) + (1-a(\mathbf{k}))\tau_1(\mathbf{k}) \tag{43}$$

The result is a closed set of nonlinear equations that are simplier than the more general set but still formidable. Because of the viscoelastic approximation, one might expect to predict the correct overall behavior but not capture all of the details of the relaxation processes from this approach.

C. Glass Transition

As discussed in detail in the literature [25,32,33,35,63-66], the dynamics of a similar molecular model show a slowing down and eventual transition to a "glass" state, as characterized by the existence of an infinite relaxation time in S(k,t). For the OCF model in the overdamped limit, the existence of such an infinite relaxation time can be determined from an asymptotic solution of the GDE. In Laplace transform notation, the GDE in the overdamped limit within the viscoelastic ansatz becomes

$$\left(\frac{\tilde{S}(\mathbf{k},z)}{S(k)}\right)^{-1} = \tilde{F}(\mathbf{k},z)^{-1} = z + \mu_1^c + \frac{\mu_2^c}{z + (\tau_{\|}^M)^{-1} - \frac{\mu_2^c}{\mu_1^c}} \tag{44}$$

As discussed, this equation is closed via the mode-mode coupling scheme for the Maxwell relaxation time. Now, if an infinite relaxation time exists for the density fluctuation correlation function, then in the limit as $z \to 0$

$$\frac{\tilde{S}(\mathbf{k},z)}{S(k)} = \tilde{F}(\mathbf{k},z) \approx \frac{f(\mathbf{k})}{z}. \tag{45}$$

Substitution of this relation into equation (44) and rearrangement results in the following closed equation for the function $f(\mathbf{k})$

$$f(\mathbf{k}) = \frac{-z\tau_{\|}^M \frac{\mu_2^c}{(\mu_1^c)^2}}{1 + \frac{(\mu_1^c)^2 - \mu_2^c}{(\mu_1^c)^2} z\tau_{\|}^M}, \tag{46}$$

where the Maxwell time for longitudinal viscosity is given by the appropriate mode-mode coupling approximation, equation (28) or (29). Note that these equations differ from those derived in the abovementioned reference due to the viscoelastic ansatz employed here. Otherwise, as the slowing

of the density fluctuations are presumed responsible for the glass transition in simple fluids, the two theories converge.

The limit of $z\tau_{\|}^{M} \rightarrow 1$ provides an upper bound for the values of $f(k)$, yielding

$$f(k) = \frac{-\mu_2^c}{2(\mu_1^c)^2 - \mu_2^c}. \tag{47}$$

This is always positive and will approach 1 in the limit of infinite elasticity, as expected. This limiting value provides a useful initial condition for iterative solutions. Numerical iterations converging to a stable, non-zero value of $f(k)$ distinguish the existence of an ideal glass [35,63] or non-relaxing structure, whereas convergence to the trivial solution indicates the presence of liquid-like dynamics.

An asymptotic analysis can be performed in a manner similar to that by Bengtzelius [64] by using the additional approximation for the structure factor of

$$S(k) \approx 1 + A_o\delta(k_o), \tag{48}$$

where A_o is an undetermined constant characterizing the height of the maximum peak in the structure factor $S(k)$ and k_o is the value of k corresponding to this maximum. Substitution into the expression for the longitudinal Maxwell relaxation time results in

$$\begin{aligned} -\beta f(k_o)^2 + \gamma f(k_o) - 1 &= 0 \\ \beta &= \frac{(\mu_1^c)^2}{(\mu_1^c)^2 - \mu_2^c} \\ \gamma &= \frac{-\mu_2^c}{(\mu_1^c)^2 - \mu_2^c}, \end{aligned} \tag{49}$$

Note that the viscoelastic ansatz makes the resulting characteristic equation for $f(k_o)$ independent of the value of A_o, but still dependent upon the elasticity of the suspension. Further, in this limit, the results are the same for both choices of the vertex function.

The roots of this equation can be found simply by noting that $\gamma = \beta - 1$, resulting in

$$\begin{aligned} f(k_o) &= \frac{1 - \beta \pm C}{-2\beta} \\ c &= \sqrt{\beta^2 - 6\beta + 1}. \end{aligned} \tag{50}$$

Real positive roots for $f(k_o)$ exist only if C is real, requiring $\beta \geq 3 + 3\sqrt{2}$. (note that the negative root yields a negative beta, which is unphysical.

The coefficient β has a simple physical meaning as directly proportional to the longitudinal elasticity

$$\beta = \frac{4\pi}{3\phi} S(k_o) \frac{E'_\infty(k_o)a^3}{k_bT}. \tag{51}$$

In the dilute limit $\phi \rightarrow 0$, $\frac{E'_\infty(k_o)a^3}{k_bT} \rightarrow \frac{9\phi}{4\pi}$ plus terms proportional to higher orders in volume fraction. Then, $\beta \approx (1 + A_o) * 3$, requiring $A_o \geq \frac{2\sqrt{2}}{3}$ for divergence. This simple model solution is promising in its ability to predict the existence of a nonrelaxing structure that will depend primarily on the strength of the longitudinal elasticity and the height of the structure factor peak (correlation in nearest neighbor position). A simple method for estimating rheological properties near the glass transition is sketched in what follows.

D. Comparison with Experiment

The rheology and structure of suspensions of charged, polystyrene spheres have been measured via small angle neutron scattering (SANS), static and dynamic light scattering (SLS,DLS) and mechanical spectrometry over a wide range of particle and added salt concentrations [55,67]. This

experimental data base provides a check of the above theoretical predictions by direct comparison of the microstructure, density fluctuations, and rheological predictions for systems where the equilibrium structure and the colloidal interaction parameters are well characterized.

In two recent publications [6,7] a detailed test of the theoretical predictions against this model colloidal system was performed. Briefly, the major conclusions of that work are:

- the OZ-RY equation yields excellent predictions for the light scattering from polydisperse charged suspensions
- the high-frequency elastic constants from the predicted structures are in excellent agreement with wave-rigidity measurements
- quasi-elastic light scattering results on strongly correlated but dilute (in a volume fraction sense) suspensions demonstrate that the double exponential behavior predicted by the viscoelastic ansatz is a good representation of the decay of the dynamic structure factor
- the short-time solution yields results in agreement with the Lindemann law
- for these dilute samples the primary relaxation time predicted from the the two-body closure is in good agreement with the measured values while the convolution approximation overestimates the primary relaxation time
- for concentrated suspensions the convolution approximation correctly predicts the onset of a kinetic glass transition
- the rheology predicted from the convolution approximation demonstrates the strong divergence as the glass transition is approached
- the two-body approximation was found not to yield a divergence in the mechanical properties in the region of the glass transition.

E. Shear Melted Colloidal Crystals

Recently, measurements of the capillary viscosity of dilute suspensions of charged particles in deionized water have been reported as a function of particle size and ionic strength [68–70]. The viscosity was found to increase almost linearly with volume fraction with a slope that greatly exceeded the Einstein prediction for spheres as the ionic strength was decreased. Further, it was found that the viscosity reduced to a master curve for a given type of particle when plotted against number density; that is, the master curve reduced viscosity data on all particle sizes for deionized suspensions. The former result is intriguing in that one would expect interparticle interactions to enter as a concentration squared term. However, as will become apparent, the change in the electrostatic screening length with particle density is responsible for this apparent linear behavior.

Calculations were performed for particles of size 33.5nm and charge 980e at both 1.e-5 and 5.e-5 Molar added 1:1 electrolyte (see table I). The solutions of the RY-OZ equation are shown in figure 1. Using the criteria proposed by Hansen and later verified by Robbins et al. [71] that at the crystallization point the peak in S(k) goes through 2.85, it is apparent that the systems should be crystalline at the higher volume fractions. Of course, the integral equation theory does not contain information about this first-order phase transition so it yields a metastable fluid structure. One is tempted to postulate that this metastable fluid structure should, to some reasonable approximation, resemble the shear melted structure seen in the experiments.

TABLE I
Experimental System Characteristics

system	Radius (nm)	Charge (e)	Salt Conc. (Molar)
A	33.5	980	1.e-5
B	33.5	980	5.e-5
C	35	390	1.e-3

The mechanical properties are shown in figure 2. Both high frequency moduli exhibit power law scaling that is less than squared, which is characteristic of charged suspensions at low ionic strength [5,6]. Further, the longitudinal elasticity is relatively weak even for the most concentrated sample; therefore, the systems should not be kinetically trapped into a glass phase.

Calculations for the Maxwell relaxation times are shown in figure 3. Predictions are made for the short-time closure and the two-body viscoelastic treatment, as the two-body closure has been determined to be more accurate for these volume fractions and elasticities. The maxwell relaxation times for the short-time solution follow the Lindemann law, while the self-consistent calculation predicts a significant increase in the cage lifetime. The total relative viscosity is given as:

$$\mu_s/\mu_o = 1 + 2.5\phi + G'_\infty \tau_s^M \tag{52}$$

In figure 4 it is seen that the viscosity scales sublinearly with concentration for both closures, again a consequence of the increased screening length due to the increasing counterion concentration accompanying the increasing macroion concentration. The self-consistent coupling results in an order of magnitude increase in the reduced viscosity above the Lindemann result. The experimental data, indicated by the best fit curve to the data reported by Mallamace et al. [70], falls on the results from the short-time solution and is below the predictions of the viscoelastic ansatz. The quantitative agreement of the short-time solution with the data is excellent. The theory could be fine tuned to provide a surface charge that would also make the predictions of the viscoelastic solution quantitatively consistent with the experiments. Indeed, the titration results for the surface charge on the particle usually overestimate the effective surface charge needed for the Yukawa model of the potential [55]. Therefore, in the absence of structural information, such as structure factor measurements, other mechanical measurements, such as high frequency elasticity measurements, or self-diffusion measurements, the consistency of the fit cannot be unambiguously determined. This points to the necessity for measuring one or more additional transport or structural suspension property to completely characterize a colloidal suspension.

In the original paper, Mallamace et al. [70] apply an approximate analysis based on earler work that did not benefit from a rigorous statistical mechanical treatment of the suspension mechanics. The authors fit their viscosity data to the lattice model proposed by Buscall et al. [72] and concluded that the maxwell relaxation time must be a constant for a given particle size and electrolyte concentration; i.e. it does not depend upon concentration, in seeming violation of the Lindemann analogy. However, this analysis demonstrates that the observed behavior is in complete agreement with the cage melting analogy. The discrepancy is in the use of the lattice model for the high-frequency elasticity. As has been demonstrated, approximation of the liquid structure by a lattice and the neglect of the first derivative term makes the lattice model suspect when applied to colloidal suspensions [6].

F. Viscosity Divergence near the Glass Transition

Due to the direct correspondence between the equations for colloids and simple fluids at the glass transition, it is possible to use previous results calculated for molecular fluids to predict colloid rheology near the glass transition. Again, this correspondence is exact only when hydrodynamic interactions are neglected. Bengtzelius et al. [64] have studied the convolution closure version of the generalized hydrodynamic equations without the viscoelastic ansatz for a Lennard-Jones fluid approaching the glass transition. This transition is from metastable liquid to glass, which is preempted by the crystalline transition in monodisperse samples in equilibrium. They showed the development of a long-time tail in $S(k,t)$ that resulted in a divergence in the self-diffusion coefficient as the glass transition is approached. Through the use of hard-sphere structure factors, they determined that

$$D_s/D_o = \left(1 - \frac{\phi}{\phi_c}\right)^{1.76}, \tag{53}$$

where $\phi_c = 0.516$ is the expected transition concentration for molecular hard-spheres.

As a first order estimate for the rheology, this result is combined with the Lindemann melting criterion above, equation (36), to yield an equation for the mean viscous relaxation time

$$\tau_s^M \approx \frac{(0.1\bar{d})^2}{D_o}\left(1-\frac{\phi}{\phi_c}\right)^{-1.76} \tag{54}$$

where the self-diffusion coefficient has replaced the bare diffusion coefficient in the expression. The proportionality between shear viscosity and long-time self diffusion has been noted experimentally in the colloid literature [73] and some modeling has argued for this [44], however exact dilute limiting expressions demonstrate they are indeed different [74,75]. This approximation is consistent with the cage model as the diffusion of a particle at high volume fractions must feel the hindering effects of particle interactions as the phase transition is approached. As previously noted [5], the result yields an equation similar in form to the Krieger-Dougherty relation, which has wide application in fitting the viscosity of suspensions. The exponent of -1.76 is between the values of $-2.5 * \phi_c$ to -2 that are typically reported for hard-sphere suspensions [44,76,77], however the experimental critical concentration is close to the random close packing limit ($\phi = 0.63$) not the concentration at the onset of the phase transition. The similarity suggests that a full numerical analysis of the hard-sphere collective dynamics near the glass transition would be fruitful.

This estimate can also be directly applied to charged systems by using a thermodynamic mapping onto an effective hard-sphere system through the relationship

$$\phi_{hs} = \phi\left(1+\frac{\alpha}{\kappa a}\right)^3. \tag{55}$$

This is essentially a statement that the effective hard-sphere radius is the true particle radius increased by some proportion of the Debye screening length in a charged system. Typically, α has been reported to be about 1.6 [78,55], as determined by fitting the phase transition ϕ_c to that of hard spheres. Figure 5 demonstrates that this approach can estimate the divergence of the shear viscosity of system C reasonably accurately, where $\phi_c = 0.63$ has been used. The self-consistent calculation using the convolution approximation, which is also shown in figure 5 for comparison, shows an almost exponential rise in viscosity with concentration [7] that anticipates the experimental data. The convolution approximation also yields a glass transition at a volume fraction of 24 %, in good agreement with experiment.

G. physical interpretation in terms of cage melting

A popular method of envisioning the dynamics in simple and colloidal fluids is the cage melting model [79]. In this model, the particles are temporarily localized, or "trapped" in a cage of their nearest neighbors. Diffusion for short times is confined to the cage, while for longer times, the cage "melts" and particles diffuse distances beyond the nearest neighbors. Colloidal transport is achieved by this process of cage melting, freeing the test particle to diffuse until the next cage is encountered. The general expression for the interparticle viscosity, $\eta_s = G'_\infty \tau_s^M$ is to be interpreted as G'_∞ representing the strength of the force localizing the particle in the cage (relative to shear deformations) and τ_s^M representing the melting time of the cage. The latter is modeled through extension of the Lindemann melting criterion for suspensions (see also [80]). This interpretation of the Lindemann law works as long as the melting time is simply controlled by free diffusion [29], as would be the case for the isolated cage. As has been shown here, this result is also recovered from the short time approximation, which neglects coupling of density fluctuations to the suspension viscoelasticity.

The mode-mode coupling solution can be interpreted as the consideration of the caging of these neighboring particles within a cage of their nearest neighbors, a "multiple cage" phenomena. Thus, for the nearest neighbor to diffuse so as to free the test particle, they themselves must escape their cages of nearest neighbors, and so on. Put another way, correlated motion of a collection of particles is required to dissipate the cage surrounding the test particle. This intuitive picture helps

to put in perspective the dependence of the transport coefficient upon collective dynamics of density fluctuations.

The glass transition can also be interpreted with regards to the longitudinal fluctuations that control the collective diffusion. The large increase in $\tau_{\parallel}^{M}$ is controlled by the force localizing the neighbors forming the cage, or rather, the stiffness of the nearest neighbor forces with respect to longitudinal fluctuations, E'_{∞}. Thus, once E'_{∞} on a per particle basis becomes significantly larger than the Brownian energy available to create local density fluctuations, the particle cages become permanent and the system is kinetically trapped as a glass. The ratio of this energy per particle to the Brownian thermal energy is, to a first estimate, just $E'_{\infty}a^3/kT$. This physical picture is consistent with the rheological predictions and measurements, and the asymptotic treatment of the glass transition.

VI. SUMMARY AND CONCLUSIONS

A method to calculate all of the collective dynamics and linear viscoelastic rheology for Brownian colloidal suspensions simply in terms of the fundamental physicochemical properties has been demonstrated. A self-consistent solution of the generalized hydrodynamics equations and for the rheology of strongly interacting colloidal spheres has been obtained numerically through the viscoelastic approximation. The predicted rheology for charged colloids interacting via a Yukawa potential is in good agreement with experiments for the rheology of charged latex suspensions. It is shown how to explicitly account for polydispersity effects for the structure, cumulants, and elastic constants. Calculations are performed to demonstrate the viscoelastic predictions for hydrodynamically dilute suspensions yield a linear scaling with volume fraction, but of much steeper slope than the single particle Einstein correction. The theory can also predict the onset of the glass transition and the commensurate divergence in the viscosity.

Further work comparing this self-consistent solution against the details of Brownian dynamics simulations for model systems are currently under study to firm some of the interpretations and conclusions suggested by the comparisons with actual measurements. This work complements current research using the generalized hydrodynamics formalism to describe both dilute suspensions and glass systems by providing a self-consistent solution valid for colloidal suspensions in the fluid phase. Future work includes the study of other Brownian systems relevant to the colloid community.

VII. ACKNOWLEDGEMENTS

This research was supported through the NSF (CTS 9158164),and NATO Collaborative Research Grant # CRG 910465. Many helpful discussions with R. Klein and G. Nägele of Konstanz, Germany are gratefully acknowledged. The author is also indebted to Bruno D'Aguanno of CRS4, Italy for help with the equilibrium structures.

APPENDIX A: RHEOLOGICAL PROPERTIES STUDIED

As a starting point we take the generalized Maxwell model for the relaxation spectrum of a complex fluid [81], consisting of an infinite superposition of Maxwell elements each with a characteristic relaxation time λ. The relaxation modulus is defined as

$$G(t) = \frac{\tau^{xy}(t)}{\epsilon_o{}^{xy}} \tag{A1}$$

where the experiment is a shear stress relaxation $\tau^{xy}(t)$ at infinitesimal shear strain levels ϵ_o^{xy}.

The steady shear viscosity is defined as a time integral over the relaxation modulus

$$\eta_s = \int_o^\infty G(s)ds \tag{A2}$$

and by frame invariance [82], the primary normal stress difference,

$$N_1 = \Psi_{1,0}\dot{\gamma}^2 = 2\dot{\gamma}^2 \int_o^\infty sG(s)ds. \tag{A3}$$

Although not itself a linear property, the primary normal stress coefficient is related simply to the first term in an expansion for the shear modulus in frequency and, as such, can be obtained from the dynamic viscosity. Through linear viscoelasticity, the primary normal stress coefficient gives the recoverable strain upon flow cessation γ_∞^r as

$$\frac{\gamma_\infty^r}{\dot{\gamma}_o} = \frac{\frac{1}{2}\Psi_{1,0}}{\eta_s} \tag{A4}$$

showing this is zero in the limit of zero shear rate. The other relevant rheological function, the secondary normal stress coefficient, cannot be determined solely from linear viscoelasticity, as it depends on the choice of constitutive equation [82].

The steady elongational viscosity in the linear limit can also be expressed (for an incompressible fluid) as

$$\bar{\eta} = 3\eta_s, \tag{A5}$$

leading to the Trouton ratio of 3. For a general, compressible fluid, this can be written as

$$\bar{\eta} = \frac{3\eta_s(\eta_{||} - \frac{4}{3}\eta_s)}{\eta_{||} - \eta_s}, \tag{A6}$$

where $\eta_{||}$ is the longitudinal viscosity, which is calculated in a manner analogous to equation A2 with $G_{||}(t)$ replacing $G(t)$. In the model to be considered here, the OCF, the solvent is taken to be an incompressible, Newtonian fluid. The stresses from the solvent and the fluid of Brownian particles are taken to be additive. Thus, the Trouton ratio must be 3 as the longitudinal viscosity for the suspension as a whole is essentially infinite. However, it is still instructive to examine the contribution of the Brownian fluid to the longitudinal viscosity and the resultant elongational "pseudo-viscosity" as the former property can be determined through optical techniques [83].

Defining the frequency dependent modulus

$$G(\omega) = G'(\omega) + iG''(\omega), \tag{A7}$$

yields

$$G'(\omega) = \omega \int_0^\infty G(t)sin\omega t dt \tag{A8}$$

$$G''(\omega) = \omega \int_0^\infty G(t)cos\omega t dt. \tag{A9}$$

This function is also directly related to the frequency dependent shear viscosity:

$$\eta_s^*(\omega) = \eta_s'(\omega) - i\eta_s''(\omega) = \frac{G^*(\omega)}{i\omega}. \tag{A10}$$

Further, the primary normal stress coefficient is related to the dynamic viscosity by

$$\Psi_{1,0} = lim_{\omega \to 0} \frac{2\eta_s''}{\omega}. \tag{A11}$$

Therefore, predictions of the time and wave vector dependent shear and longitudinal viscosity functions yields the full linear viscoelastic behavior for the suspension.

[1] N.J. Wagner and B.J. Ackerson. *Journal of Chemical Physics*, 97:1473, 1992.
[2] L.M. Walker and N.J. Wagner. In P. Moldenaers and R. Keunings, editors, *Proc. XIth International Congress on Rheology*. Elsevier Science Publishers, B.V., 1992.
[3] L.M. Walker and N.J. Wagner. *Journal of Rheology*, to be submitted, 1993.
[4] N.J. Wagner, L.M. Walker, and B. Hammouda. *Macromolecules*, to be submitted, 1993.
[5] N.J. Wagner and R. Klein. *Coll. and Poly. Sci.*, 269:295, 1991.
[6] N.J. Wagner. *Journal of Colloid and Interface Science*, accepted for publication, 1993.
[7] N.J. Wagner. *Physical Review E*, accepted for publication, 1993.
[8] N.J. Wagner and A.T.J.M. Woutersen. *Journal of Fluid Mechanics*, to be submitted, 1993.
[9] N.J. Wagner, B.L. Holian, and A.F. Voter. *Physical Review A*, 45:8457, 1992.
[10] W. Hess and R. Klein. *Adv. Phys.*, 33:173, 1983.
[11] B.J. Ackerson. *J. Chem. Phys.*, 64:242, 1976.
[12] B.J. Ackerson. *J. Chem. Phys.*, 69:684, 1978.
[13] W. Hess. *Physica*, 107A:190, 1981.
[14] W. Hess. *J. Phys. A: Math Gen*, 14:L145, 1981.
[15] R. Klein and W. Hess. *Faraday Discuss. Chem. Soc.*, 76:137, 1983.
[16] W. Hess and R. Klein. *Progress in Colloid and Polymer Science*, 69:174, 1984.
[17] B. Cichocki and W. Hess. *Physica A*, 141:475, 1987.
[18] B. Cichocki and B.U. Felderhof. *J. Chem. Phys.*, 96:9055, 1992.
[19] R. Klein. In S.-H. Chen et al., editor, *Structure and Dynamics of Strongly Interacting Colloids and Supramolecular Aggregates in Solution*, page 39. Kluwer Academic, Netherlands, 1992.
[20] B. J. Berne, editor. *Statistical Mechanics: Part B: Time-Dependent Processes*. Plenum, New York, 1977.
[21] M.H. March and M.P. Tosi. *Atomic Dynamics in Liquids*. Dover, New York, 1976.
[22] J.P. Boon and S. Yip. *Molecular Hydrodynamics*. McGraw-Hill, New York, 1980.
[23] J.-P. Hansen and I.R. McDonald. *Theory of Simple Liquids*. Academic Press, London, 1986.
[24] W. Goetze. In J.-P. Hansen, D. Levesque, and J. Zinn-Justin, editors, *Liquids, Freezing and Glass Transition*, pages 288–503. North-Holland, Amsterdam, 1989.
[25] M. Fuchs, I. Hofacker, and A. Latz. *Physical Review A*, 45:898, 1992.
[26] D.A. McQuarrie. *Statistical Mechanics*. Harper and Row, New York, 1976.
[27] F.J. Rogers and D.A. Young. *Phys. Rev. A.*, 30:999, 1984.
[28] B. D'Aguanno, R. Klein, and N.J. Wagner. In *Mat. Res. Soc. Symp. Proc.*, volume 177, page 219. Materials Research Society, 1990.
[29] H.M. Lindsay, W.D. Dozier, P.M. Chaiken, R. Klein, and W. Hess. *J. Phys. A: Math Gen.*, 19:2583, 1986.
[30] G. Naegele, M. Medina-Noyola, R. Klein, and J.L. Arauz-Lara. *Physica*, 149 A:123, 1988.
[31] R. Klein, W. Hess, and G. Naegele. In S. A. Safran and N.A. Clark, editors, *Physics of Complex and Supermolecular Fluids*, page 673. John Wiley and Sons, New York, 1987.
[32] J.-L. Barrat, W. Goetze, and A. Latz. *J. Physics; Condens. Matter*, 1:7163, 1989.
[33] J.-L. Barrat, J.-P. Hansen, and G. Pastore. *Physical Review Letters*, 58:2075, 1987.
[34] I. Snook, W. van Megen, and P. Pusey. *Physical Review A*, 43:6900, 1991.
[35] H. Loewen, J.-P. Hansen, and J.-N. Roux. *Physical Review A*, 44:1169, 1991.
[36] G.K. Batchelor and J.T Green. *J. Fluid. Mech.*, 56:375;401, 1972.
[37] B.U. Felderhof. *Physica A*, 147:203;533, 1987.
[38] W.B. Russel and A.P. Gast. *J. Chem. Phys.*, 89:1580, 1988.
[39] N.J. Wagner and W.B. Russel. *Physica*, 155 A:475, 1989.
[40] J.K.G. Dhont. *Physica A*, 146:541, 1987.
[41] J.K.G. Dhont. *Journal of Fluid Mechanics*, 204:421, 1989.
[42] D. Ronis. *Phys. Rev. A.*, 34:1472, 1986.
[43] I.M. de Schepper, H.E. Smorenburg, and E.G.D. Cohen. *Physical Review Letters*, 70:2178, 1993.
[44] J.F. Brady. *J. Chem. Phys.*, to appear, 1993.
[45] B.J. Ackerson and N.A. Clark. *Phys. Rev A*, 30:906, 1984.
[46] B.J. Ackerson, J. van der Werff, and C.G. de Kruif. *Phys. Rev. A.*, 37:4819, 1988.
[47] N.J. Wagner and W.B. Russel. *Physics of Fluids*, 2:491, 1990.
[48] S. Ashdown, I. Markovic, R.H. Ottewill, P. Lindner, R.C. Oberthur, and A.R. Rennie. *Langmuir*, 6:303, 1990.
[49] C.G. deKruif, W.J. Briels, R.P. May, and A. Vrij. *Langmuir.*, 4:668, 1988.

[50] J.C. van der Werff, B.J. Ackerson, R.P. May, and C.G. de Kruif. *Physica A*, 165:375, 1990.
[51] B. D'Aguanno and R. Klein. *J. Chem. Soc. Faraday Trans.*, 87:379, 1991.
[52] B. D'Aguanno, R. Klein, I M. Méndez-Alcaraz, and G. Naegele. *to appear in Phys. Rev. A.*
[53] S. Bell, G.M. Levine and L.N. McCartney. *J. Coll. Int. Sci.*, 33:335, 1970.
[54] W.B. Russel, D.A. Saville, and Schowalter W.R. *Colloidal Dispersions*. Cambridge Univ. Press, Cambridge, 1989.
[55] N.J. Wagner, R. Krause, A.R. Rennie, B. D'Aguanno, and J. Goodwin. *J. Chem. Phys.*, 95:494, 1991.
[56] R. Krause, J.L. Aruaz-Lara, G. Naegle, H. Ruiz-Estrada, M. Medina-Noyola, R. Weber, and R. Klein. *Physica*, A178:241, 1991.
[57] J.B. Hayter. In V. Degiorgio and M. Corti, editors, *Physics of Amphiphiles: Micelles, Vesicles and Microemulsions*, page 59. 1985.
[58] R. Zwanzig and Mountain R.D. *J. Chem. Phys.*, 43:4464, 1965.
[59] T. Keyes. In B. J. Berne, editor, *Statistical Mechanics: Part B: Time-Dependent Processes*, page 259. Plenum, New York, 1977.
[60] H.J.M. Hanley, J.C. Rainwater, and S. Hess. *Phys. Rev. A.*, 36:1795, 1987.
[61] U. Genz and Klein R. *Physica A*, 171:26, 1991.
[62] C.J.W. Beenakker and Mazur P. *Phys. Lett.*, 98 A:22, 1983.
[63] G. Szamel and H. Loewen. *Physical Review A*, 44:8215, 1991.
[64] U. Bengtzelius, W. Goetze, and A. Sjoelander. *J. Phys. C.: Solid State Phys.*, 17:5915, 1984.
[65] U. Bengtzelius. *Phys. Rev. A*, 34:5059, 1986.
[66] M. Fuchs, W. Goetze, S. Hildebrand, and A. Latz. *Zeitschrift fuer Physik B*, 87:43, 1992.
[67] S. Keeping. PhD thesis, University of Bristol, 1989.
[68] T. Okubo. *J. Chem. Phys.*, 87:3022, 1987.
[69] T. Okubo. *J. Chem. Phys.*, 87:6733, 1987.
[70] N. Mallamace, F. Micali and Vasi C. *Physical Review A*, 42:7304, 1990.
[71] M.O. Robbins, K. Kremer, and G. Grest. *J. Chem. Phys.*, 88:3286, 1988.
[72] R. Buscall, J.W. Goodwin, and R.H. Hawkins, M.W. Ottewill. *J. Chem. Soc. Faraday Trans. 1*, 78:2889, 1982.
[73] A. van Blaaderen, J. Peetermans, G. Maret, and J.K.G. Dhont. *J. Chemical Physics*, 960:4591, 1992.
[74] G.K. Batchelor. *J. Fluid Mech.*, 74:1, 1976.
[75] G.K. Batchelor. *J. Fluid. Mech.*, 83:97, 1977.
[76] C.G. van der Werff, J.C. de Kruif and J.K.G. Dhont. *Physica A*, 160:205, 1990.
[77] J.F. Brady. *J. Chem. Phys.*, 98:3335, 1993.
[78] S. Mitaku, T. Ohtsuki, A. Kishimoto, and Okano K. *Biophys. Chem.*, 11:411, 1980.
[79] P.N. Pusey. *J. Phys. A.*, 11:119, 1978.
[80] H. Loewen, T. Palberg, and R. Simon. *Physical Review Letters*, 70:1557, 1993.
[81] W.R. Schowalter. *Mechanics of Non-Newtonian Fluids*. Pergamon, Oxford, 1978.
[82] R. Larson. *Constitutive Equations for Polymer Melts and Solutions*. Butterworths, New York, 1988.
[83] F. Gruener and W. Lehmann. *J. Phys. A*, 12:303, 1979.

APPENDIX B: FIGURE CAPTIONS

1. Equilibrium microstructures S(k) versus ka, systems A and B.

2. Normalized high-frequency elasticities (- - -) $\frac{G'_\infty a^3}{kT}$ (——) $\frac{E'_\infty a^3}{kT}$: (O) System A (□) System B.

3. Dimensionless Maxwell relaxation times for: (O) System A, (□) System B, (——) Lindemann Law, (- - - -) two-body self-consistent solution.

4. Total viscosity (in cp) for the short-time (—-) and two-body (- - -) solutions, (O) System A (□) System B. The thick lines represent data taken by Mallamace et al. [70]

5. Reduced interparticle viscosity (η/μ_o) for system C (b) 1.0 millimolar salt concentration. Symbols: measured (◇), short time (- - -), convolution approximation (○), equation 54 (——-).

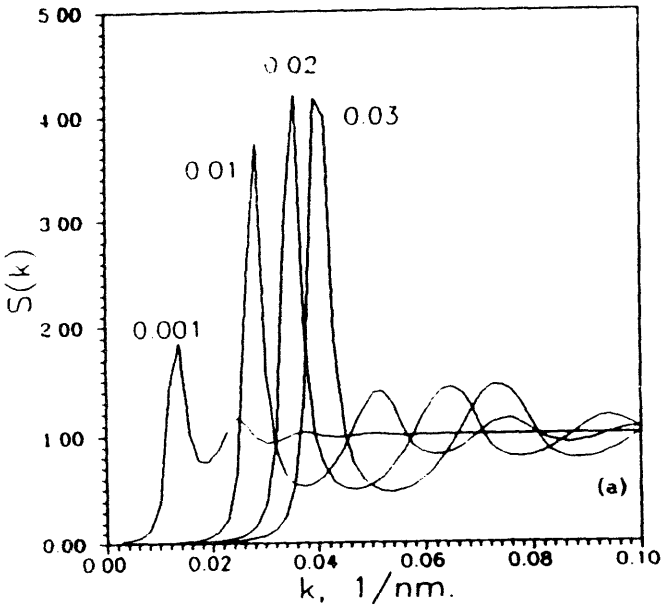
5.00
4.00
3.00
2.00
1.00
0.00
S(k)
0.02
0.03
0.01
0.001
(a)
0.00
0.02
0.04
0.06
0.08
0.10
k, 1/nm.

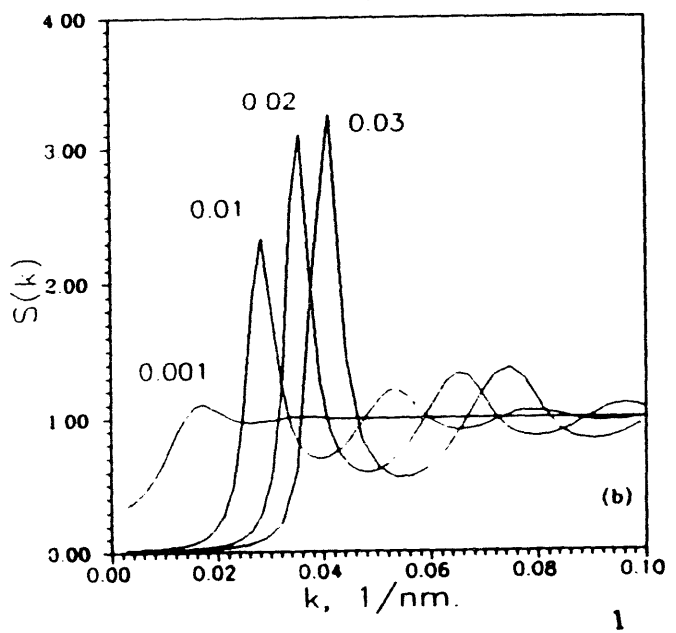
4.00
3.00
2.00
1.00
0.00
S(k)
0.02
0.03
0.01
0.001
(b)
0.00
0.02
0.04
0.06
0.08
0.10
k, 1/nm.

1

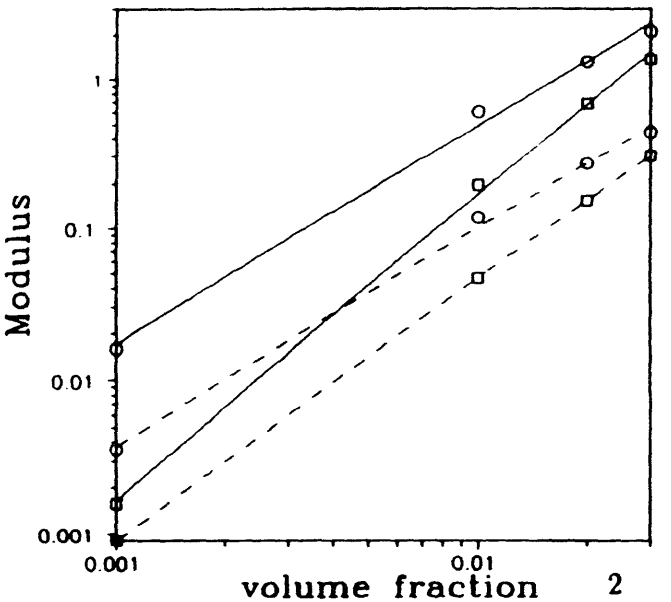
Modulus
1
0.1
0.01
0.001
0.001
0.01
volume fraction

2

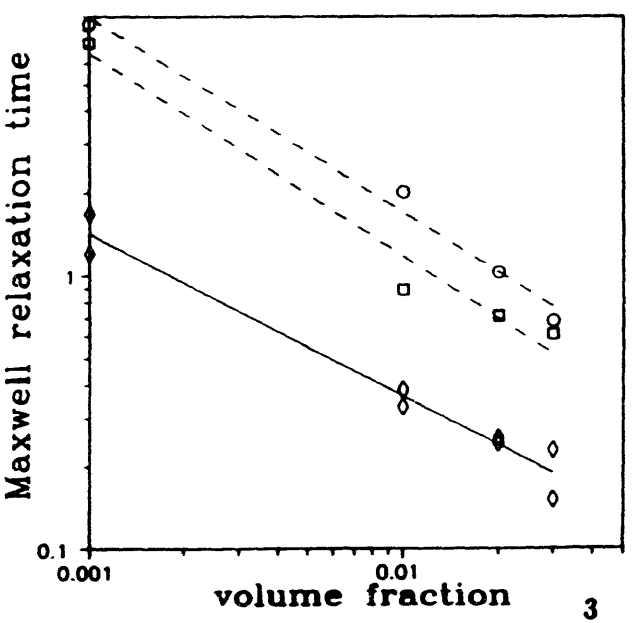
Maxwell relaxation time
1
0.1
0.001
0.01
volume fraction

3

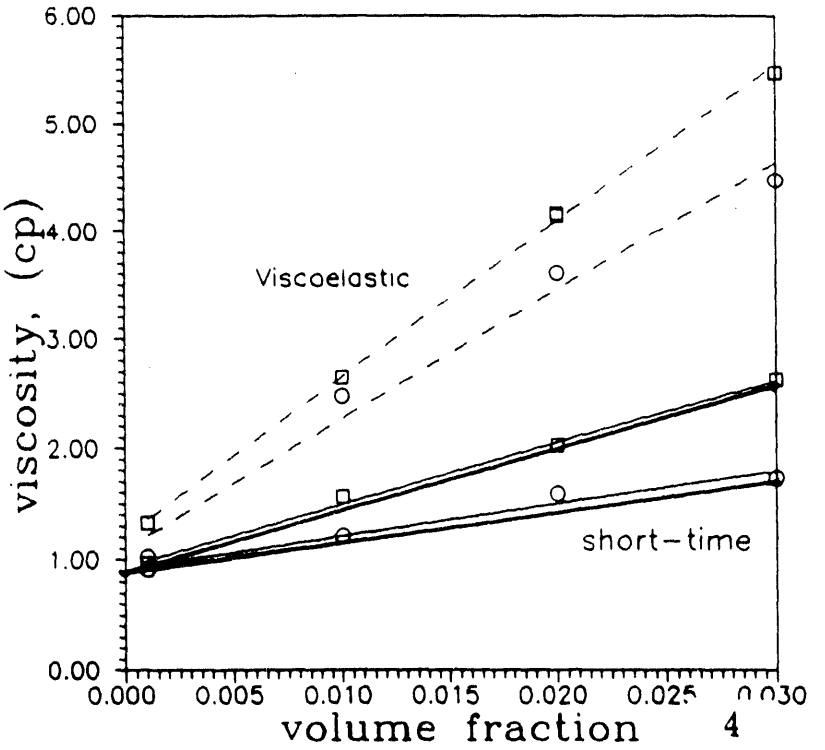
6.00
5.00
4.00
3.00
2.00
1.00
0.00
viscosity, (cp)
Viscoelastic
short-time
0.000
0.005
0.010
0.015
0.020
0.025
0.030
volume fraction

4

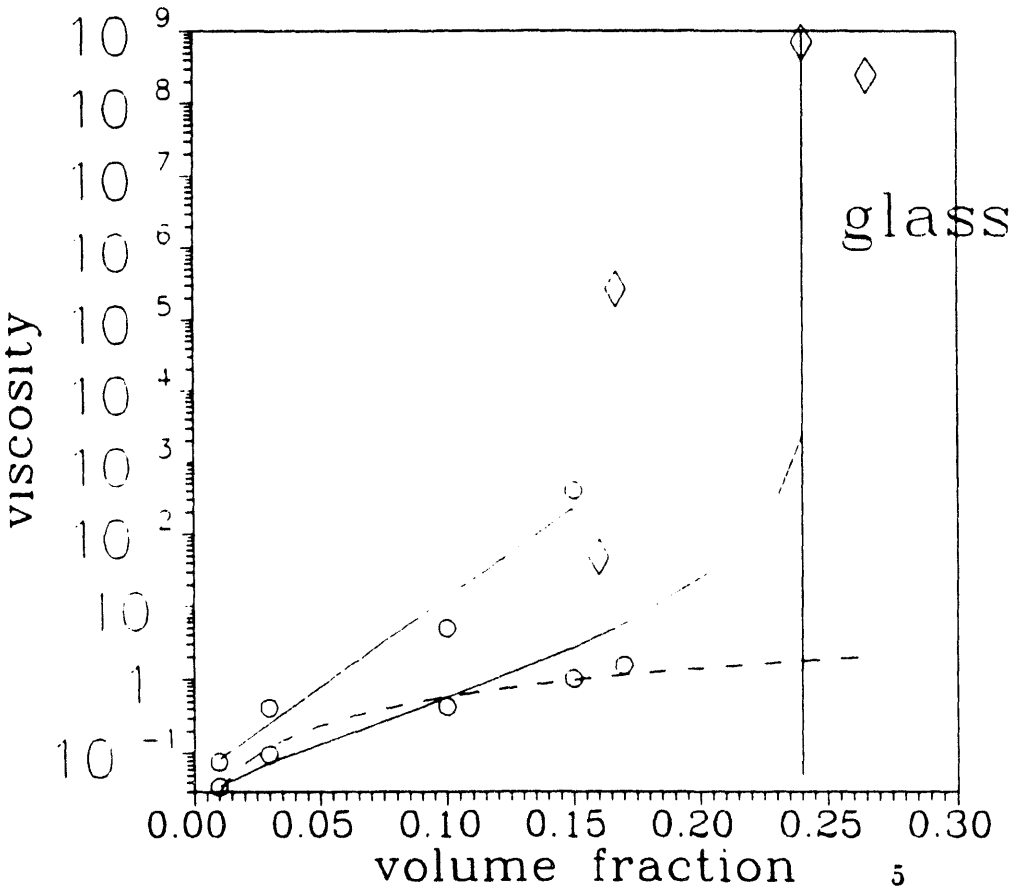
viscosity
glass
0.00
0.05
0.10
0.15
0.20
0.25
0.30
volume fraction

5

NUMERICAL SESSION

Simulations of Particle Transport in Plasma Processing Discharges

Seung J. Choi, Peter L. G. Ventzek, Robert J. Hoekstra, and Mark J. Kushner[a]
University of Illinois
Department of Electrical and Computer Engineering
1406 W. Green St., Urbana, IL 61801

Abstract

The transport of particles ("dust") in low pressure electrical glow discharges is of interest with respect to contamination of semiconductor wafers during plasma etching and deposition. The distribution of dust particles in these reactors is determined by a variety of forces; the most important being electrostatic, viscous ion drag, gravitational, thermophoretic and neutral fluid drag. In this paper, we present results from a series of computer models to predict the spatial distribution of dust particles in capacitively coupled electrical glow discharges considering these forces. The results are parameterized over power deposition, gas flow, and particle size. We find that the spatial distribution of dust depends on the spatial dependence of the sheaths and potential in the bulk plasma which in turn depend upon the electrical topography of the surfaces. Experimentally observed "dome" and "ring" distributions of dust particles are computationally reproduced for specific combinations of discharge power, particle size and substrate topography.

[a]Author to whom correspondence should be addressed.

I. Introduction

Particulates ("dust" particles) are common contaminants in low pressure (< 100s mTorr), partially ionized (electron density 10^9 - 10^{11} cm^{-3}) plasma processing electrical glow discharges for semiconductor etching and deposition.[1-10] The dust particles negatively charge, and particles of a few microns in size have 100s to 1000s of elementary charges.[15,16] Dust particles generally accumulate in specific regions of the radio frequency (rf) discharges which are commonly used in plasma processing. Roth and Spears first used laser light scattering to observe that particles accumulate near the bulk plasma-sheath boundary in these discharges,[1] as later confirmed by Selwyn et al.,[2-4] Jellum et al.,[5-7] and Watanabe et al.[8,9] Large particles (> 0.1 μm) accumulate near the sheath edge, while small particles accumulate in the center of the discharge at

the location of the maximum in the plasma potential. (See Fig. 1.) Selwyn et al.[3] and Carlisle et al.[10] also observed that particles accumulated in rings around and domes above the semiconductor wafers in reactive-ion-etching (RIE) discharges.

Sommerer et al.[11] and Barnes et al.[12] have proposed that the transport of small particles (when gravity is not important) is dominated by two forces; electrostatic and viscous ion drag. The former force accelerates negatively charged particles towards the center of electropositive plasmas or towards local maxima in the plasma potential. The latter force accelerates particles in the direction of net ion flux, which is generally towards the boundaries of the plasma. (The ion drag force results from open orbits of positive ions around the dust particle which transfer momentum to the particle in the direction of the net ion flux.[15,16]) These forces have also been theoretically addressed by Graves et al.[13,14] and computationally addressed by Choi and Kushner.[15,16]

The details of the geometry of the reactor are important in determining the location at which particles accumulate in rf discharges. For example, for large particles, the electrostatic and ion drag forces balance near the edge of the sheath. The electrical topography of the substrate, which determines the shape of the sheath, is therefore important in determining the distribution of dust particles. Viscous fluid forces accelerate particles in the direction of the gas flow. The flow field through nozzles and around obstacles is therefore important with respect to dust distributions. The geometry of the reactor can also determine the temperature field, which generates thermophoretic forces.[24]

The importance of the electrical topography of the substrates in determining the distribution of dust has been noted by the experimental observations that dust often accumulates in rings and domes above semiconductor wafers.[17] Selwyn et al. also observed that particles accumulate in the center of metallic washers placed on the electrode and in grooves surrounding the wafer in rf discharges.[3] These observations are presumabely explained by the perturbing effects of these topographies on the potential profile and ion fluxes. Further evidence for the importance of the electrical topography in determining dust distributions can be found with recent electric probe measurements of the plasma potential in rf discharges. These measurements showed that particles

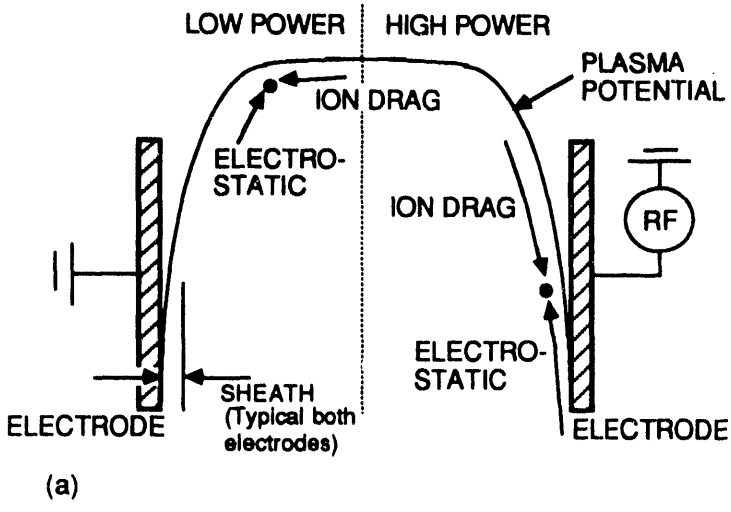

Fig. 1. Schematic of locations of particle trapping in a plasma processing discharge. a) At low power deposition and small particles, the particles are commonly found in the body of the plasma. At high power deposition and large particles, trapping occurs at the edge of the sheath. b) Particles are often trapped in domes above and rings around wafers. These trapping locations correspond to discontinuities in the wafer topography.

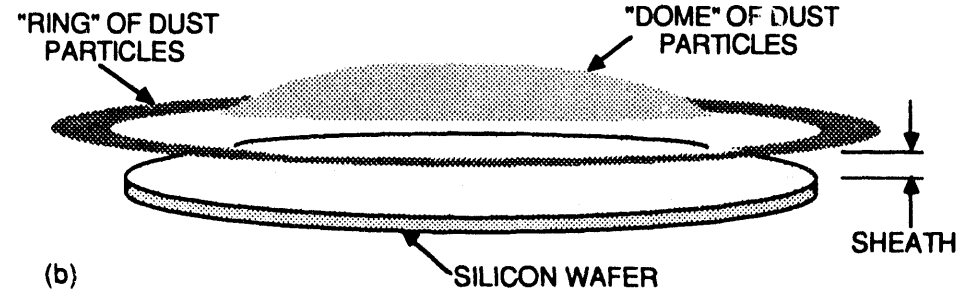

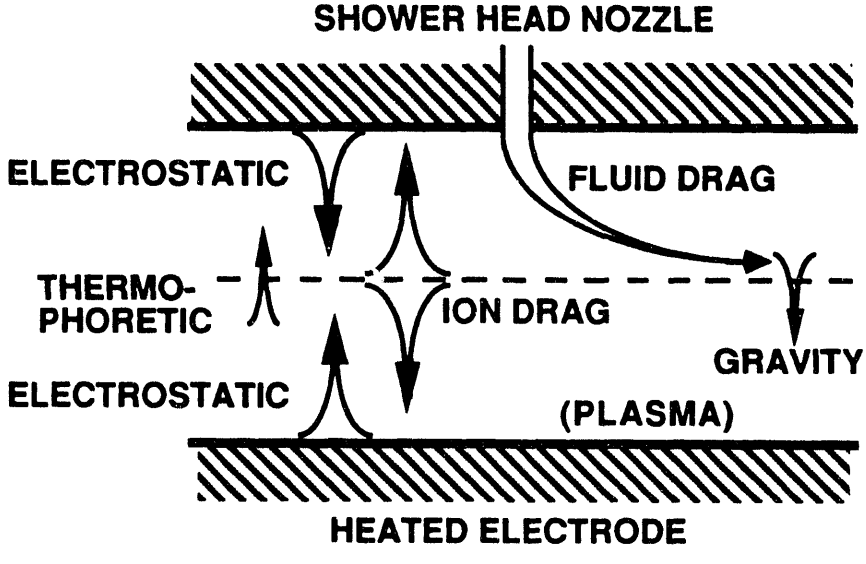

Fig. 2. Forces which act on particles in a plasma processing discharge.

are commonly found in the vicinity of positive potential traps (perhaps as large as 7 V) at the edges of wafers.[10,17]

A schematic of the forces acting on a dust particle in a plasma processing reactor having a showerhead nozzle is shown in Fig. 2. In this geometry, electrostatic forces accelerate the particle away from the electrode towards the center of the plasma or towards local maxima in the plasma potential. Ion drag forces accelerate particles towards the edges of the plasma or away from local maxima in the plasma potential. Thermophoretic forces accelerate particles away from the heated substrate towards the colder showerhead. The fluid drag forces accelerate particles in the direction of net advective motion away from the top electrode and radially towards the pump port. To predict the accumulation of particles in these rf discharges, one must therefore self-consistently account for the shielding and charging of particles in the plasma, the ion flux which provides the ion drag forces, the electric field which generates the electrostatic force, the fluid flow field which provides the viscous drag force and the temperature field which generates thermophoretic forces. A series of computer models has been developed to predict the dynamics of the motion of dust particles in capacitively coupled rf discharges considering these forces. The models are described in Section II followed by a discussion of our results in Section III. Our concluding remarks are in Section IV.

II. Description of the Model

The model we have used in this study is a series of five linked simulations, schematically shown in Fig. 3. The first model is a pseudoparticle-in-cell simulation (PICs) which provides the electrical charges on the dust particle and ion-dust momentum transfer cross sections.[15,16] The second is a 2-dimensional Monte Carlo-fluid hybrid (MCFH) model for plasma properties of rf discharges.[18] The third is a 2-dimensional plasma chemistry Monte Carlo simulation (PCMCS) which provides ion velocity distributions.[18] The fourth is an advective flow field model. The fifth is the dust particle transport (DPT) model which is the module in which the dust particle trajectories are actually computed. (To avoid confusion, computational particles in a PICs or Monte

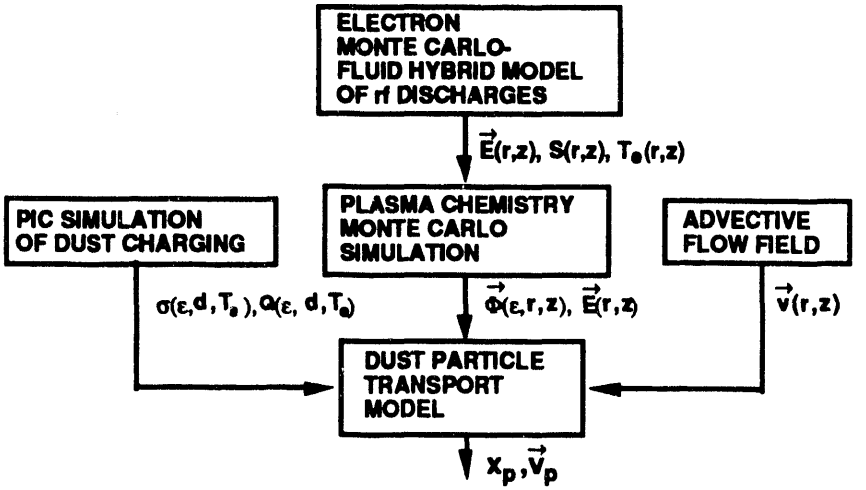

Fig. 3. Schematic of the model for particle trapping. Results from a Monte Carlo-fluid hybrid model for rf discharges provide ion sources, electron temperature and electric potential. A PIC simulation provides ion-dust momentum transfer cross sections and charges on the dust. A plasma chemistry Monte Carlo simulation provides ion fluxes. A separate model provides the fluid flow field. These results are combined in the dust transport model.

Carlo simulation will be called pseudoparticles; contaminating particulates in the plasma will be called dust particles.)

The modeling process begins by computing the electrical charges on the dust and the ion-dust momentum transfer cross sections to be used for ion drag forces as a function of ion energy and plasma parameters (such as electron density and temperature). These cross sections are obtained from the PICs which follows electron and ion trajectories in the vicinity of a dust particle while solving Poisson's equation for the electric field. Before executing the PICs, Monte Carlo simulations (MCs) of both the electron and ion swarms are performed using a specified and spatially uniform E/N (electric field/gas number density). The purpose of performing the MCs is to obtain the quasi-steady state electron energy distribution and ion energy distribution for use as initial conditions in the PICs. The details of the MCs are described in Ref. 19. All pertinent elastic and inelastic collisions of electrons with the neutral gas and ions are included in the MCs.

After the electron and ion energy distributions are obtained, a spherical dust particle is introduced into the center of the computational volume having a specified charge, Q. The PICs is then performed while including all the collision processes. This portion of the model differs from the MCs in that now the self-consistent electric field in the vicinity of the dust particle is obtained by solving Poisson's equation while the equations of motion of the pseudoparticles are advanced. When solving Poisson's equation, the net charge density in the plasma and on the surface of the dust particle are accounted for. The surface charge density provides a boundary condition in the form of the electric field at the surface. Pseudoparticles striking the dust particle are assumed to be collected with unity efficiency. The collected charge density was averaged over the surface of the dust particle. The PICs is executed to obtain dQ/dt. Based on the sign of dQ/dt, the PICs is repeated with different values of Q to search for the value of Q which yields dQ/dt = 0 which signals an equilibrium of electron and ion fluxes to the dust particle. An example of the results from this model are shown in Fig. 4 where the charge and electrical potential on dust particles as a function of position are plotted. The particles charge to a few times the electron temperature. The amount of charge on the dust particle scales approximately with its radius.

At the end of the PICs, cross sections for electron and ion momentum transfer to the dust particle, and for collection by the dust particle are calculated using molecular dynamics techniques. Given the electric field around the dust particle obtained from the PICs, electron and ion pseudoparticles are launched into the computational volume with varying impact parameters. By gathering statistics on the change in momentum and number of pseudoparticles as they leave the volume, one can calculate the momentum transfer and capture cross sections.

A 2-dimensional MCFH model of rf discharges is then used to obtain electric fields as a function of position and source functions for ions and radicals.[18] The 2-dimensional (r,z) model is a hybrid simulation consisting of an electron Monte Carlo Simulation (EMCS), a fluid-chemical kinetics simulation (FKS), and an off-line plasma chemistry Monte Carlo simulation. The model is conceptually a 2-dimensional analogue of the 1-dimensional MCFH model for rf discharges described in Ref. 20. The hybrid model begins by estimating electric fields in the plasma as a

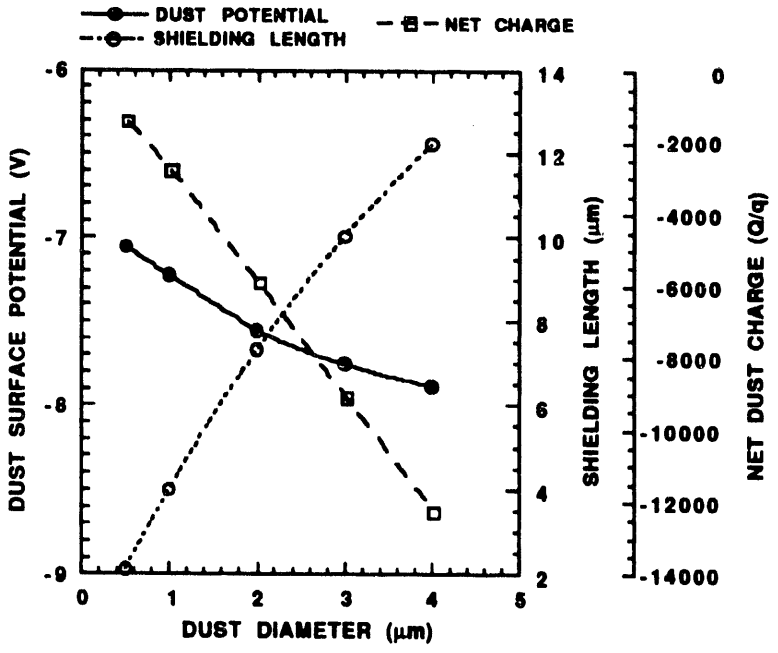

Fig. 4. Charge and potential on a dust particle, and shielding distance of the plasma around the dust particle as a function of radius of the dust particle. The bulk plasma density far from the dust particle is 3 x 10^{10} cm^{-3}.

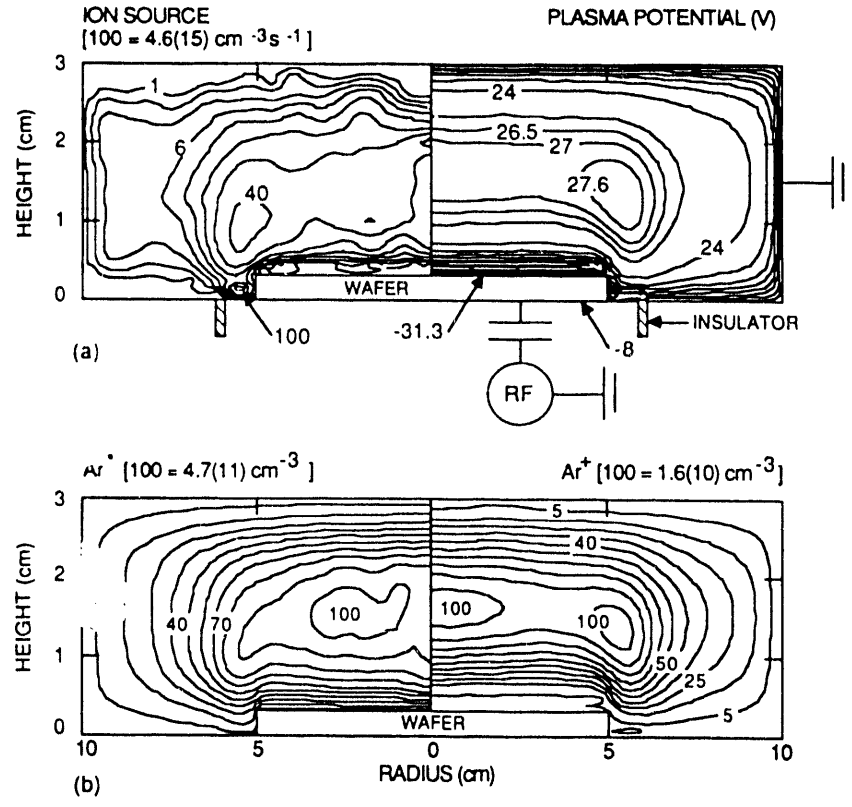

Fig. 5. Plasma parameters from the MCFH model for a capacitively coupled rf discharge (13.56 MHz) in 100 mTorr Ar. a) ion source and plasma potential; and b) Ar(4s) and Ar^+ densities. The contour labels for ion source and densities are a percentage of the maximum value, noted at the top of the figure. A 3 mm thick wafer (10 cm diameter) is on the lower powered electrode. The electrode topography produces a local maximum in the plasma potential and the ion source.

function of position and phase, $E(r,z,\phi)$. These fields are used in the EMCS to advance electron trajectories to calculate the time averaged electron energy distribution, $f(\varepsilon,r,z)$. This is obtained by averaging electron trajectories over 50 rf cycles while including all pertinent elastic, inelastic, and coulomb collisions.[20] $f(\varepsilon,r,z)$ is then used to calculate source functions for electron impact processes, transport coefficients, and average electron energies as a function of (r,z). These quantities are then passed to the FKS. The FKS integrates the continuity equations for the densities of all charged and neutral species and solves Poisson's equation for the electrostatic plasma potential using the method of successive-over-relaxation. A semi-implicit solution of Poisson's equation allow us to take time steps 10s-100s times larger than the dielectric relaxation time if necessary. An acceleration technique is used to speed the convergence of the FKS by predicting future species densities based on recent time histories of those densities.[21]

We account for the different effective areas of the electrodes by using a simple circuit having a blocking capacitor, and calculate the dc bias generated on the substrate. The surfaces of the chamber are specified as being either metal or dielectric. We can also include topography on the substrate such as wafers, disks and grooves of specified dielectric constant. After the FKS, $E(r,z,\phi)$ and species densities are cycled back to the EMCS to iterate through the model until the plasma density converges.

In the MCFH model, electrons are treated kinetically while ions are treated as a fluid. We therefore do not generate the information on the ion energy distributions that is required to compute the ion drag forces on the dust particles. To obtain these ion energy distributions the electric field and source functions from the MCFH model are imported into the PCMCS. In the PCMCS, source functions and electric fields from the MCFH are used to launch and follow trajectories of pseudoparticles representing ions and radicals. All pertinant elastic and inelastic collisions for both ions and radicals are included. An iterative particle-mesh algorithm incorporating a modified null cross section technique is used to account for ion-ion (such as negative ion-positive ion neutralization) and radical-radical collisions.[22] Statistics are collected on the velocity and spatially resolved ion momentum flux distribution, $\phi_I(r,z,\vec{v}_I)$ $[g/(cm^2\ s^{-1})/(cm/s)]$.

The fluid flow field in the reactor is obtained by solving the perturbative pressure form of the continuity and momentum equations.

$$\frac{\partial \vec{u}}{\partial t} = - \nabla \cdot \vec{u}\,\vec{u} - \frac{\nabla \rho'}{\rho_o} - D \nabla^2 \vec{u} \qquad (1a)$$

$$\frac{\partial \rho'}{\partial t} = - \rho_o c_o^2 \nabla \cdot \vec{u} \qquad (1b)$$

In Eq. 1, $\vec{u}$ is the advective fluid velocity, ρ' is the perturbative pressure, ρ_o is the gas density, c_o is the sound speed and D is the velocity diffusion coefficient. This flow field is also used in the PCMCS to account for momentum transfer between the pseudoparticles and buffer gases during elastic collisions.

The motions of the dust particles are calculated in the DPT model where we compute the spatially dependent [$\vec{r}$ =(r,z)] forces on the dust particles. To obtain these forces we import the ion-momentum transfer cross sections for ion drag forces and dust charges (from the PICs), electric fields (from the MCFH model), ion momentum distributions (from the PCMCS model) and the fluid flow field. For this work we have simply specified a temperature gradient. The force on a dust particle i having a specified radius (r_i) and mass (M_i) is

$$\vec{F}_i(\vec{r}) = M_i \vec{g} + q_i \vec{E} + \int \sigma(|\vec{v}_I|)\, \phi_I(\vec{r}, \vec{v}_I)\, |\vec{v}_I|\, d\vec{v}_I$$

$$- \frac{6\pi\mu r_i}{C(Kn)} (\vec{v}_i - \vec{u}) \cdot C_D(Re_p) \frac{Re_p}{24} - 6\pi\mu r_i \nu K_T \cdot \frac{\nabla T}{T} \qquad (2)$$

The terms on the right-hand-side of Eq. 2 are for gravitational, electrostatic forces, ion drag, viscous fluid drag and thermophoretic forces. $\vec{E}$ is the electric field (obtained from the MCFH model), q_i is the charge on the dust particle (obtained from the PICs), σ is the ion-momentum transfer cross section (obtained from the PICs) and ϕ is the ion momentum flux

distribution (obtained from the PCMCS model). The last two terms, viscous fluid drag and thermophoretic forces, are derived from classical thermodynamics based on the hard sphere particle assumption.[23,24] The constants are

$$C(Kn) = 1 + Kn(\alpha + \beta) \cdot \exp(-\frac{\gamma}{Kn}) , \tag{3a}$$

$$C_D(Re_p)\frac{Re_p}{24} = 1 + 0.173 \cdot Re_p^{0.657} + \frac{0.01721 \cdot Re_p}{1 + 16{,}300 \cdot Re_p^{-1.09}} , \tag{3b}$$

$$Re_p = \frac{2\rho r_i |\vec{v}_i - \vec{u}|}{\mu} , \tag{3c}$$

$$K_T = \frac{2C_s(\frac{k_g}{k_p} + C_t Kn)}{(1 + 3C_m Kn)(1 + 2 \cdot \frac{k_g}{k_p} + 2C_t Kn)} . \tag{3d}$$

$\vec{v}_i$ is the velocity of the dust particle, Kn is the Knudsen number (λ/r_i), Re_p is the Reynolds number, μ is the fluid viscosity, $\nu = \mu/\rho$ (ρ is the gas density), and T is the mean gas temperature. In Eq. 3, α, β and γ are experimental constants which depend on the nature of the gas-particle interaction at the particle surface and so are affected by both gas composition and particle surface roughness. k_g and k_p are the gas and particle thermal conductivities, and C_t, C_s, and C_m are the thermal creep coefficient, temperature jump coefficient, and velocity jump coefficient, respectively. All values of the constants in Eq. 3 are listed in Table I.

To begin the DPT model, we specify a volumetric rate of generation of dust particles of a given radius. We then launch pseudoparticles representing the dust particles from those locations, and simply integrate the equations of motion of those pseudoparticles while continuously launching additional pseudoparticles until the dust distribution achieves a steady state.

Table 1

Values of Constants Used in Force Calculations

Constants	Value	Ref.
α	1.227	23
β	0.42	23
γ	0.85	23
k_g	0.1799 mW/cm-K	27
k_p	1240 mW/cm-K	27
C_t	2.2	23
C_s	1.147	23
C_m	1.146	23

III. Distribution of Dust Particles

In this work, we investigated dust particle distributions in a capactively coupled radio frequency (13.56 MHz) discharge sustained in 100 mTorr of argon with a nominal power deposition of ≈ 20-200 W. (See Fig. 5.) The electrodes are separated by 3 cm and the plasma zone is 10 cm in diameter. The gas flows through a showerhead nozzle and out radially to a pump port. (See Fig. 6.) A wafer (dielectric constant $\varepsilon/\varepsilon_0 = 11.8$, thickness 3 mm) sits on the lower powered electrode. The top electrode is grounded. The radial boundary condition is approximated as a ground plane (at r = 10 cm) which allows the advective flow to pass. For these results we have assumed a constant thermal gradient of 15°K/cm as might occur when actively cooling the wafer. We observe that the calculated thermophoretic force is 1-2 orders of magnitude smaller than the electrostatic or ion drag forces, and therefore is not a major consideration under our operating conditions.

Typical results from the MCFH models are in Fig. 5 where the time averaged plasma potential, ion source, ion density, and argon metastable density are shown. A 10 cm diameter

wafer is placed on the powered electrode. The powered diameter of the lower surface is ≈ 12 cm and is separated from the annular ground plane by a dielectric spacer. The metal surface of the powered electrode generates a dc bias of -8 V, while the surface of the wafer acquires a dc bias of -31 V. Note that there are local maxima in the plasma potential, electron sources and ion density in the form of a toroidal ring 1-1.5 cm from the edge of the wafer.

The positive potential well has a depth of ≈ 1-1.5 V. These local maxima, perhaps similar to those observed by Geha et al.[17] result from a discontinuity in the electrical topography produced by the sharp edge of the wafer, and by the transition between the dielectric wafer and the metal. In this regard, the discontinuity in electrode topography resembles the metal-gas-dielectric triple point at which electric field enhancement occurs in high voltage switches.[28] The ion density shows a small maximum in this toroidal region as well as at the center of the plasma. The Ar(4s) density also shows a weak off axis peak. Note that although the ion source has a local maximum near the edge of the wafer, its absolute maximum value is near the exposed powered electrode. This results from the fact that the full capacitve voltage drop is across the sheath as opposed to sharing the voltage between the wafer and the sheath.

The ion flux (obtained from the PCMCS) and fluid flow fields for these conditions are shown in Fig. 6. The ion flux typically flows from maxima in the plasma potential and ion sources to the peripheries of the reactor. The local maxima in the plasma potential and ion source at the edge of the wafer produces a vertex in the ion flux with ions flowing from that location. The fluid flows starts from the showerhead and gains speed in the radial direction as the edge of the showerhead is approached.

Predictions of dust particle locations for dust diameters of 0.5 to 4 μm are shown in Fig. 7 for the geometry just discussed. These results are an instantaneous "snapshot" of the dust particle locations 0.15 s after beginning to generate particles. The dust particles are generated at a constant rate of 2.6×10^4 s^{-1} in the plasma region of the reactor weighted by a cosine (maximum in the center) in both the axial and radial directions. The power is 80 W and the gas flow is turned off. The smaller sized particles are trapped near the center plane of the reactor at the maximum in the

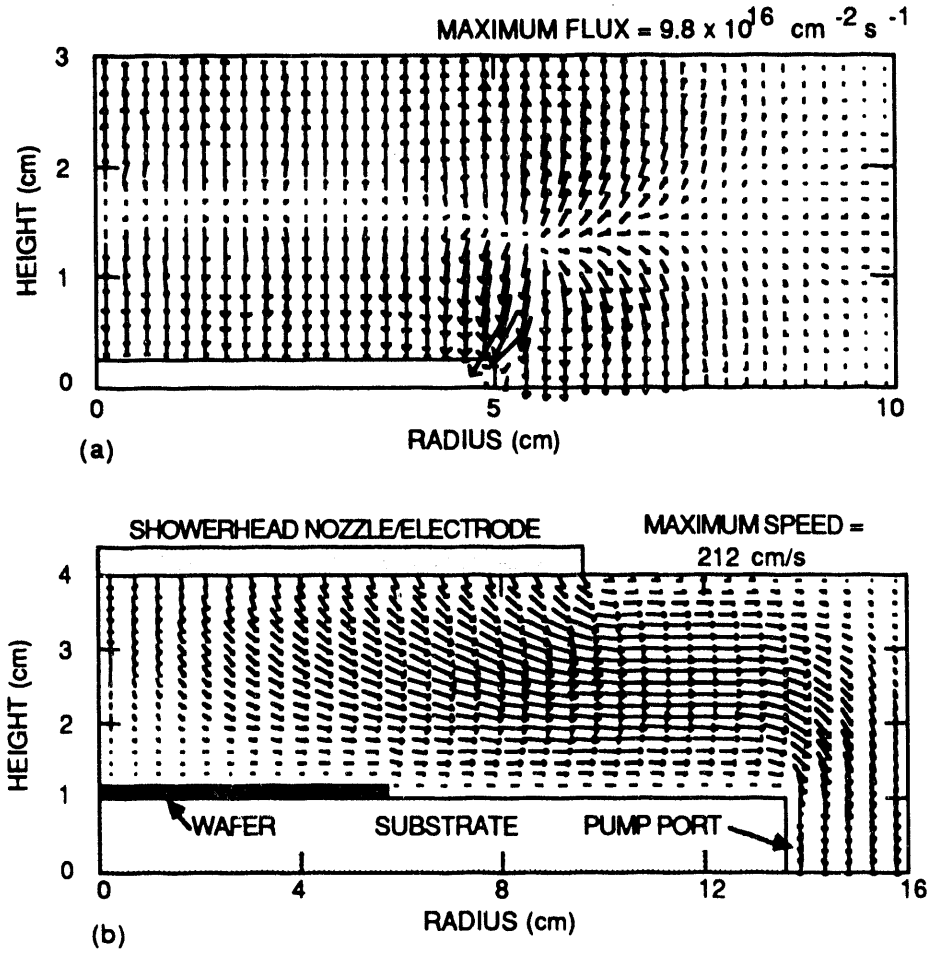

Fig. 6. Flow fields for the conditions of Fig. 2. a) ion flux and b) advective fluid velocity. The size of the arrow denotes the magnitude of the ion flux or fluid velocity. The maximum value is shown at top. The ion flux moves away from the local maxima in ion source and plasma potential to the boundaries. The fluid velocity is most negative at the showerhead nozzle and is almost totally radial near the edge of the wafer.

plasma potential. The dust particles are also trapped around, but not in, the positive potential well. Ion flux flowing out of the well is fairly efficient at removing particles from that region and holding them at the periphery. We also observe that the plasma optical emission and particle locations do not necessarily coincide. Trapped particles follow a contour on which ion drag and electrostatic forces balance. This contour moves down towards the edge of the wafer around both sides of the local maximum in potential on both sides. These loci of points forming the trapping locations give the appearance of a "dome" above the wafer and "ring" around the wafer as experimentally observed by Selwyn et al.[2,25,26] at similar power deposition (240 mW-cm^{-2}).

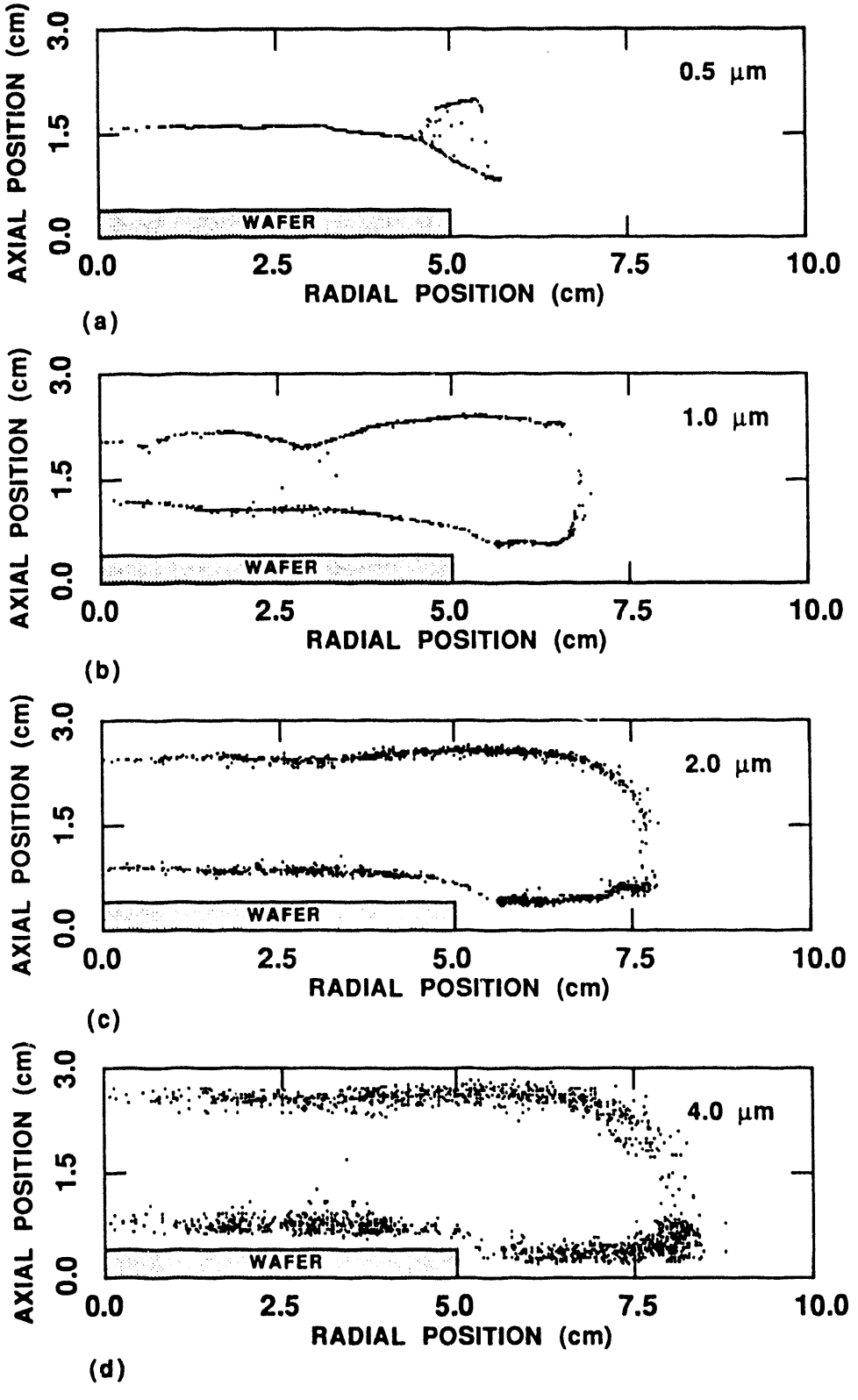

Fig. 7. Dust particle locations with a 10 cm diameter wafer on the powered electrode. Locations are shown for a) 0.5, b) 1.0, c) 2.0 and d) 4.0 μm particles. Small particles are more sensitive to the electric potential and may form domes and rings around local maxima in the potential by ion drag away from those locations. Large particles have larger ion drag forces, which push them towards the boundaries. Inertial effects cause oscillation about the equilibrium locations.

As the particle size increases, the trapping location moves toward the electrodes and a flatter dome and a wider ring form. The ion drag force increases at a faster rate with increasing particle size than does the electrostatic force; and so the large particles are pushed by the ions towards the periphery. The ion drag forces are sufficently large for particles ≈ 2-4 μm that inertial effects are important. That is, the dust particles are accelerated to high velocities which overshoot the equilibrium location at which ion drag and electrostatic forces are balanced. The particles therefore oscillate about those locations as their velocities are slowly damped by fluid drag forces. The oscillation is shown by the "blurring" of the particle locations in the snapshot of Fig. 7d. Although we collect all particles striking the electrodes, many of the larger particles strike the electrodes and could conceivably bounce off the surface.

Particle locations are shown in Fig. 8 (1 μm diameter) for similar conditions to Fig. 7 except having a 15 cm diameter wafer on the powered electrode and power deposition of 20-240 W. The largest difference which occurs with increasing power deposition is an increase in the ion flux while the potential profile does not appreciably change. As with the smaller wafer, there is a local maximum in the plasma potential and ion flux near the edge of the wafer as shown in Fig. 9. But now with the larger wafer, there is also a maxima in the plasma potential at the center of the wafer. At low power deposition, the electrostatic forces dominate, and the particles accumulate at the ridge of the maxima in the plasma potential. As the power increases and ion drag forces increase, the particles are pushed away from the maxima in the plasma potential, and form disk- and dome-like structures. These locations are on opposite sides of the maxima in plasma potential where the ion drag caused by ions flowing away from the maxima is balanced by electrostatic forces. As the power continues to increase, the ion drag forces dominate and push the particles to the sheaths at the edge of the wafer. At high powers, the ion drag forces accelerate the dust particles to sufficiently high velocities that they overshoot the equilibrium location. Evidence of oscillation in the location of the particles can be seen by the "blurred" line of particles. These predictions agree with the experimental observations of Selwyn et al. who noted that particle traps

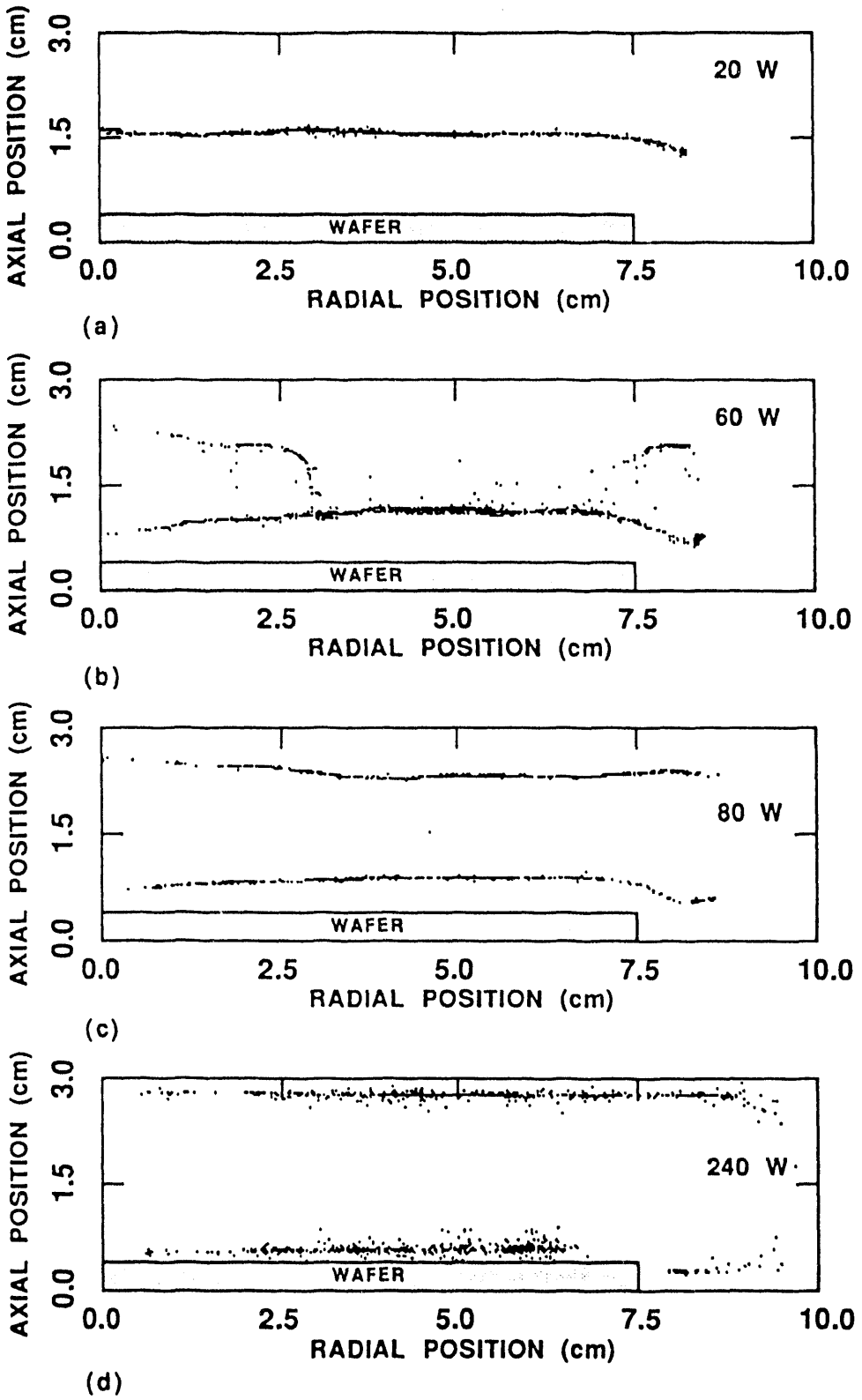

Fig. 8. Dust particle (1 μm) locations with a 15 cm diameter wafer on the powered electrode. Locations are shown for power depositions of a) 20, b) 60, c) 80 and d) 240 W. Increasing power increases the ion drag force, pushing particles towards the electrodes. The dome and ring structures result from local maxima in the plasma potential.

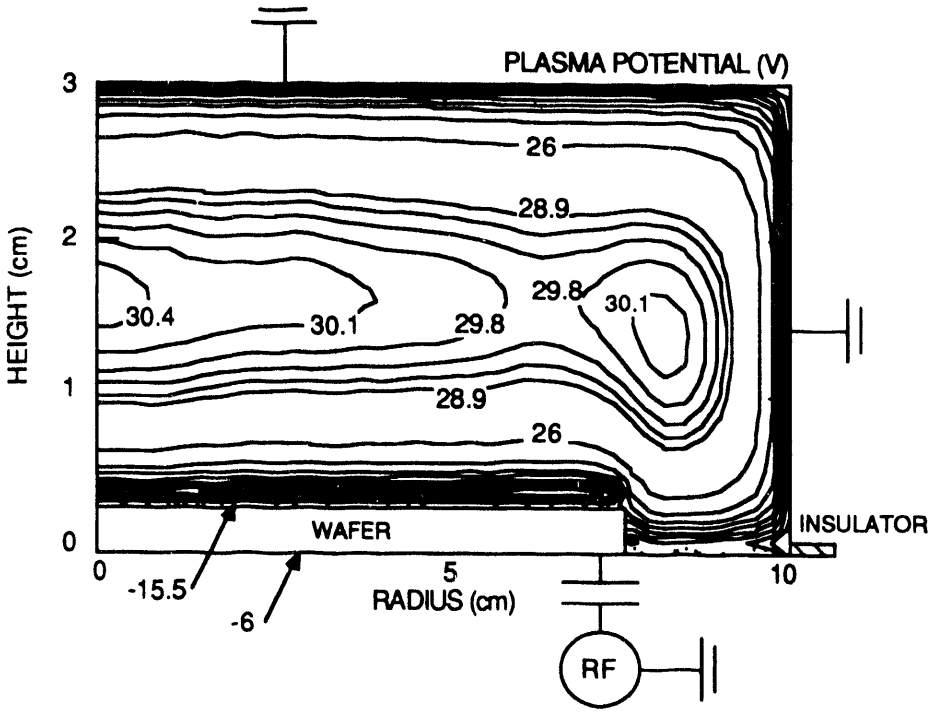

Fig. 9. Plasma potential for the conditions of Fig. 5 (20 W). The dots denote regions of negative potential. Maxima in plasma potential occur near the edge of the wafer and in the center of the reactor.

can be emptied by increasing power deposition, an effect we attribute to an increased component of ion drag.[25]

The effects of gas flow on trapping are shown in Fig. 10. for 1 μm particles and a power deposition of 80 W. Note that no wafer is used in this sequence where we varied the gas flow from zero to 500 sccm. Without gas flow, the particles are trapped at the sheath edges where electrostatic and ion drag forces balance. As the gas flow increases the particle trap near the top grounded electrode is eliminated by the fluid forces. At this location the fluid drag force is negative (towards the lower electrode) and opposes the ion drag which forces the particles towards the upper electrode. (See Fig. 6). With increasing gas flow particles are swept in the radial direction where they are both lost out the gas outlet and accumulate to some degree at the radial sheath. This accumulation may be exaggerated by our electrical radial boundary condition. At very high gas

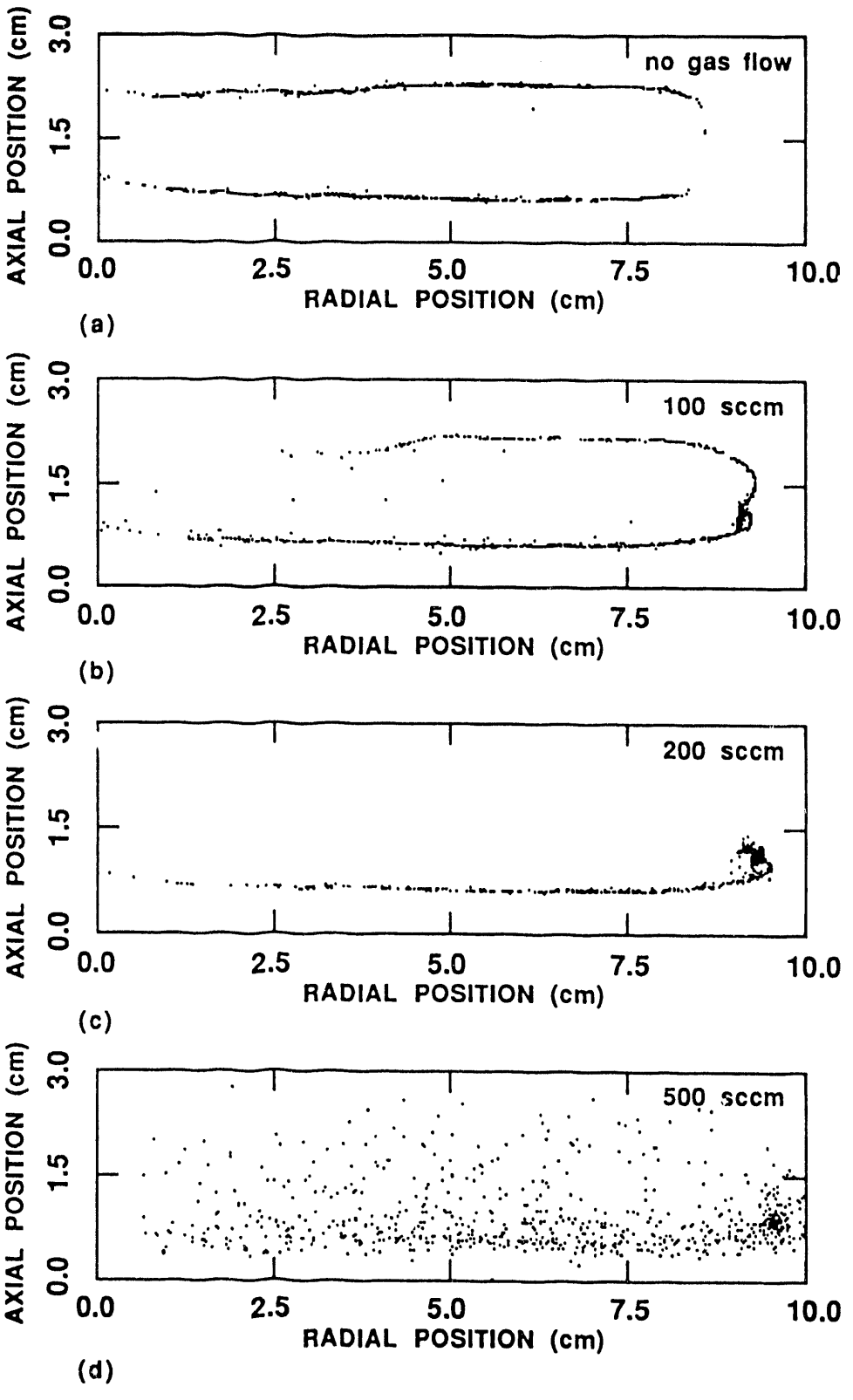

Fig. 10. Dust particle locations with a bare powered electrode. Locations are shown for a) 0, b) 100, c) 200 and d) 500 sccm of gas flow. The gas flow detraps particles at the upper boundary where the fluid velocity is negative and opposes the ion drag forces. Particles are lost out the radial pump port at high gas flow.

flow, the inertia imparted to the particles by the high axial gas flow near the showerhead causes particles to oscillate about equilibrium trapping points.

The disposition of 1 μm particles are shown in Fig. 11 where the normalized rates of loss of particles to traps, the top electrode, the bottom electrode (but not the wafer), the wafer and to the side wall (or out the pump port) are shown. Results are presented as a function of power deposition (without gas flow) and gas flow (at 80 W). In the low power regime and without gas flow, most particles are trapped in the plasma. As the power increases the trapping rate decreases and the particle loss to the reactor boundaries increases. This results from ion drag forcing particles over the potential hill at the boundaries. At 300 W (without gas flow), only 10% of the particles are trapped. Note that the rate of loss of particles to the wafer is smaller than to the top electrode because of its more negative sheath (and smaller size). The particle dispositions as a funciton of gas flow show that at sufficiently high gas flows, the particles can be blown out the pump port. Larger particles are more easily blown out of the reactor because both the fluid drag and ion drag forces increase with radius of the dust particle.

The interplay between electrostatic, ion drag and fluid forces ultimately determine the disposition of the particles. This interplay is illustrated in Fig. 12 where particle locations are shown when a metal washer is placed on the lower electrode. The gas flow is 200 sccm and results are shown for 20 and 80 W power deposition. The sheath follows the contours of the washer, thereby creating a potential well with respect to axial location in the center of the washer. At the lower power 1 μm particles are trapped in a flat dome above wafer, and are blown towards the radial boundary. When the power is increased to 80 W, the particles are pushed by ion drag to the electrodes. Some particles, which are generated in the center of the reactor, are trapped inside the washer. The particles inside the washer do not have enough energy to climb the electrostatic potential barrier over the washer and exit through the gas outlet. The gas flow inside the washer has no appreciable radial component to push the particles out of the center of the ring.

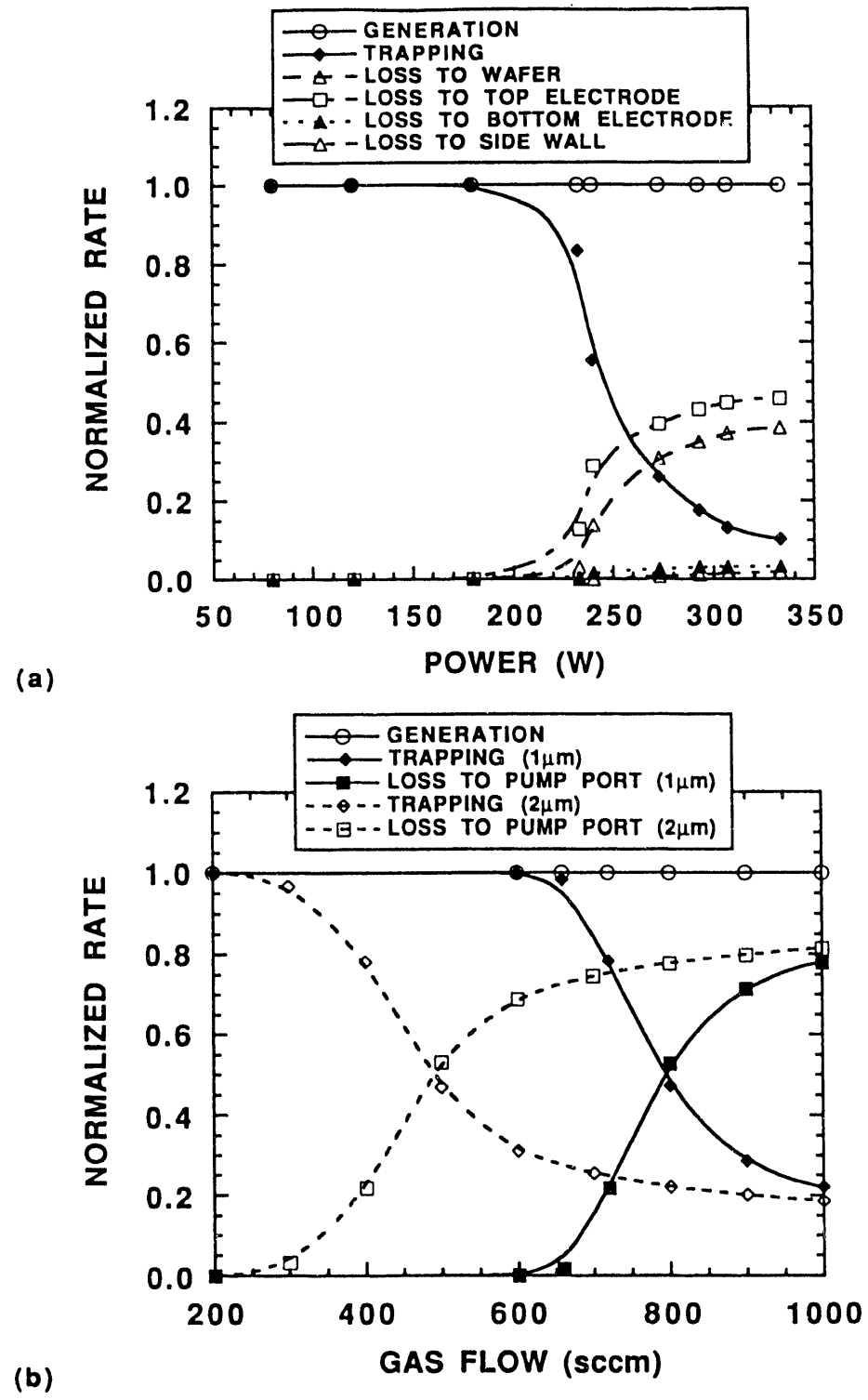

Fig. 11. Disposition of particles as a function of a) power deposition (1 μm diameter) and b) gas flow (1 and 2 μm diameter). Rates of trapping and loss to the wafer, bottom electrode (but not the wafer), top electrode and to the side wall or gas outlet are shown.

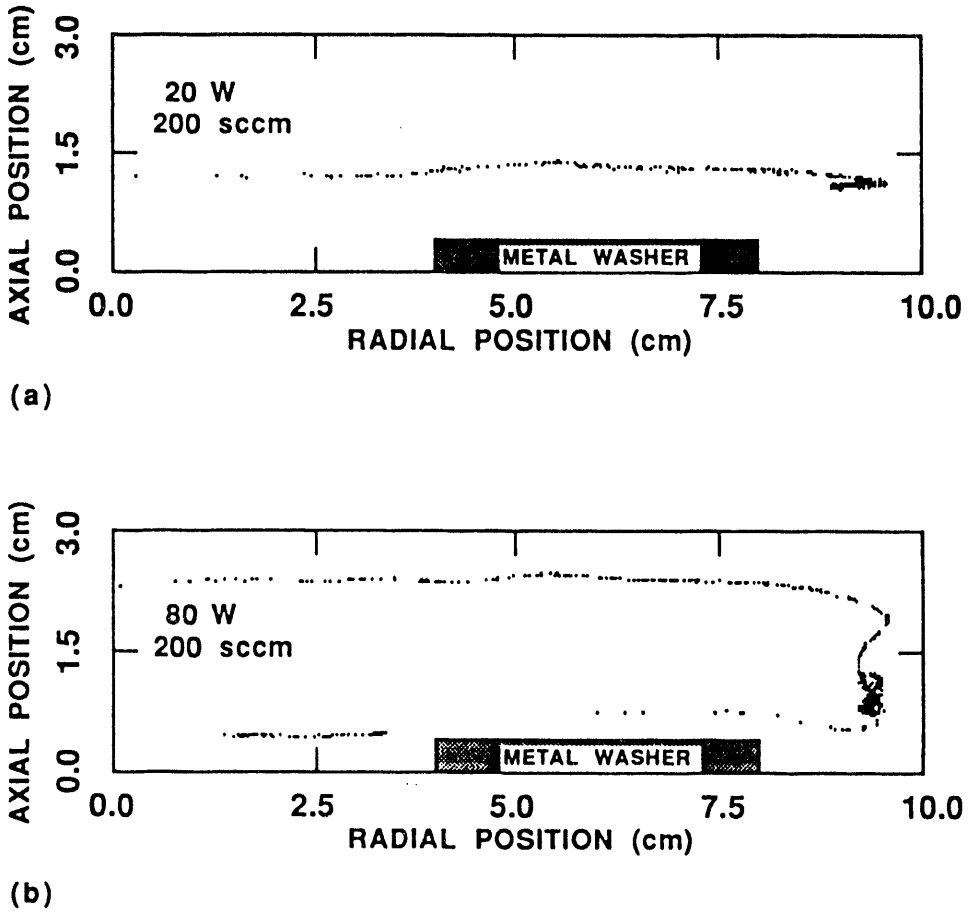

Fig. 12. Particle traps are shown when a metal washer is placed on the powered electrode for a gas flow of 200 sccm with a) 20 W and b) 80 W of power deposition. With the higher power particles are trapped on the inside of the wafer where an axial potential well exists.

IV. Concluding Remarks

A series of linked computer models have been developed and used to investigate the trapping of dust particles in capacitively coupled rf discharges with various electrode topographies. Lower rates of wafer contamination are obtained at low power deposition where particles are allowed to trap in the gas phase; and high gas flow where the particles are blown towards the pump ports. At higher power deposition, ion drag forces dominate; and particles are pushed through the sheaths to the boundaries. Various shapes of particle trapping locations are formed at different operating conditions. At low powers, we observed both dome and ring types of particle traps as

seen experimentally [3,25,26] which result from a balance of ion drag and electrostatic forces generated by perturbations in these quantities caused by local extrema in the ion generation and potential; ultimately caused by electrode topography. At high power or high gas flow, the dust particles can gain sufficient inertia that they will oscillate about the equilibrium trapping locations, or climb potential hills of 10's volts to reach the substrate.

V. Acknowledgments

The authors would like to thank D. Rader, A. Geller, M. Barnes, G. Selwyn, J. Goree, J. Keller and D. Graves for their advice and discussions on dusty plasmas. This work was supported by the National Science Foundation (CTS 91-13215 and ECS 91-09326), Sandia National Laboratory, and the Semiconductor Research Corporation.

References

1. R. M. Roth, K. G. Spears, G. D. Stein, and G. Wong, Appl. Phys. Lett. **46**, 235 (1985).
2. G. S. Selwyn, J. E. Heidenreich, and K. L. Haller, Appl. Phys. Lett. **57**, 1876 (1990).
3. G. S. Selwyn, J. Singh, and R. S. Bennett, J. Vac. Sci. Technol. A **7**, 2758 (1989).
4. G. S. Selwyn, J. S. Mckillop, K. L. Haller, and J. J. Wu, J. Vac. Sci. Technol. A **8**, 1726 (1990).
5. G. M. Jellum and D. B. Graves, Appl. Phys. Lett. **57**, 2077 (1990).
6. G. M. Jellum and D. B. Graves, J. Appl. Phys. **67**, 6490 (1990).
7. G. M. Jellum, J. E. Daugherty, and D. B. Graves, J. Appl. Phys. **69**, 6923 (1991).
8. Y. Watanabe, M. Shiratani, and H. Makino, Appl. Phys. Lett. **57**, 1616 (1990).
9. Y. Watanabe, M. Shiratani, M. Yamashita, Appl. Phys. Lett. **61**, 1510 (1992).
10. R. N. Carlile, S. G. Geha, J. O'Hanlon, and J. Stewart, Appl. Phys. Lett. **59**, 1167 (1991).
11. T. J. Sommerer, M. S. Barnes, J. H. Keller, M. J. McCaughey, and M. J. Kushner, Appl. Phys. Lett. **59**, 638 (1991).
12. M. S. Barnes, J. H. Keller, J. C. Forster, J. A. O'Neill, and D. K. Coultas, Phys. Rev. Lett. **68**, 313 (1992).
13. J. E. Daugherty, R. K. Porteous, and D. B. Graves, J. Appl. Phys. **73**, 1617 (1993).

14. M. D. Kilgore, J. E. Daugherty, R. K. Porteous, and D. B. Graves, J. Appl. Phys. **73**, 7195 (1993).
15. S. J. Choi and M. J. Kushner, Appl. Phys. Lett. **62**, 2197 (1993).
16. S. J. Choi and M. J. Kushner, submitted to IEEE Trans. Plasma Sci. Special Issue on Charged Dust in Plasmas.
17. S. G. Geha, R. N. Carlile, J. F. O'Hanlon, and G. S. Selwyn, J. Appl. Phys. **72**, 374 (1992).
18. P. L. G. Ventzek, T. J. Sommerer, R. J. Hoekstra, and M. J. Kushner, Appl. Phys. Lett. **63**, 605 (1993).
19. Y. Weng and M. J. Kushner, Phys. Rev. A **42**, 6192 (1992).
20. T. J. Sommerer and M. J. Kushner, J. Appl. Phys. **71**, 1654 (1992).
21. H. Pak and M. Riley, Proceeding of the 45th Gaseous Electronics Conference, Boston MA, 1992 (unpublished), paper BB-5.
22. M. J. Hartig and M. J. Kushner, Appl. Phys. Lett. **62**, 1594 (1993)
23. D. J. Rader, submitted to Plasma Sources Science and Technology.
24. L. Talbot, R. K. Cheng, R. W. Schefer, and D. R. Willis, J. Fluid Mech. **101**, 737 (1980).
25. G. S. Selwyn, J. E. Heidenreich, and K. L. Haller, J. Vac. Sci. Technol. A **9**, 2817 (1991).
26. G. S. Selwyn, J. Vac. Sci. Technol. B **9**, 3487 (1991).
27. R. C. Weast, D. R. Lide, M. J. Astle, and W. H. Beyer, eds., CRC Handbook of Chemistry and Physics, (CRC Press, Boca Raton, 1989).
28. G. Gradinaru and T. S. Sudarshan, J. Appl. Phys. **73**, 7643 (1993)

Inertial effects in suspensions

H.-K. Tsao and D. L. Koch
School of Chemical Engineering
Cornell University, Ithaca, NY 14853

G.-B. Mo and A. S. Sangani
Department of Chemical Engineering and Materials Science
Syracuse University, Syracuse, NY 13244

1 Introduction

Our current research efforts are aimed at understanding the behavior of suspensions in which both the viscous and inertial effects are significant. The two types of suspension which are particularly amenable to a detailed many-particle interaction calculation are (i) gas-solid suspensions at small Reynolds number, Re, and finite Stokes number, St, and (ii) bubbly liquids at large Re. The uniform states of these suspensions are known to be generally unstable under the action of a gravitational force. For example, gas-solid fluidized beds exhibit a bubbling phenomenon in which macroscopic regions (of linear dimensions much greater than the particle size) devoid of particles form, and bubbly liquids form slugs. While there is still some debate on the exact form of the equations that describe the macroscopic behavior of these suspensions[1-4], it is generally recognized that the particle-phase pressure plays an important role in stabilizing the uniform state of these suspensions. For example, the stability criterion for the gas-solid suspension is[4]

$$\frac{dP}{d\phi} > \rho_p U^2 \phi^2 (1-\phi)^2 \left[\frac{1}{C_d}\frac{dC_d}{d\phi}\right]^2, \tag{1}$$

where P is the particle-phase pressure, ρ_p the density of particles, U the velocity of particles relative to the mixture, ϕ the volume fraction of particles, and C_d the viscous drag coefficient. In general, the particle-phase pressure is a tensor of rank two, and for the disturbances travelling in the direction of the gravity, taken to be aligned along the x-axis, P must be replaced by the component P_{xx}.

The particle-phase pressure for solid particles sedimenting through gas under conditions of small Re and ϕ and finite St has been evaluated by Koch[5]. His calculations suggest that the magnitude of P is generally not large enough to satisfy the above criterion. Similarly, Sangani and Didwania[6] have recently determined the bubble-phase pressure for bubbly liquids at large Re and found it to be negative for the flow induced due to gravity. This negative pressure has a destabilizing influence on the dynamics of bubbly liquids as shown through the dynamic simulations in Ref.7.

Understanding the mechanisms by which the particle-phase pressure is increased can lead to the imporved design of fluidized beds and bubble columns. For example, in magnetically

fluidized beds, the application of the magnetic field oriented in the direction of gravity is used to increase the pressure. In the present study, we are interested in investigating the effect of nonuniformity in the flow field on the particle phase pressure. Such nonuniformities may exist, for example, due to unevenly distributed gas at the bottom of the bed or in the flows of suspensions through converging-diverging nozzles. The nonuniformity in the flow will induce greater fluctuations in the particle motion and thereby increase the particle phase pressure. Thus, we shall examine the dependence of the variance in the particle-phase motion on the gradient in mean flow. We began our study with dynamic simulations of bubbly liquids under simple shear using the numerical simulations method described in Sangani and Didwania[4] but quickly found the behavior of bubbly liquids to be sensitive to the initial conditions, Re, and ϕ. Since these calculations were very time consuming, we found it desirable to first study the phenomena for a simple model in which the hydrodynamic interactions between particles or bubbles are neglected.

2 Dusty gas under simple shear

Let us consider a monodisperse suspension of solid particles of radii a in a gas undergoing a simple shear with the shear rate γ. Non-dimensionalizing the velocity with γa, time with γ^{-1}, distance with a, and forces with $ma\gamma^2$, m being the mass of the particle, and neglecting the hydrodynamic interactions and the gravitational force, we obtain for the trajectory of a particle at $\mathbf{x}$

$$\dot{\mathbf{v}} = -St^{-1}[\mathbf{v} - \mathbf{u}^{\infty}(\mathbf{x})] + \mathbf{f}^{col} \tag{2}$$

where $St = \gamma\tau_v$ is the Stokes number with $\tau_v = m/(6\pi a\mu)$ the viscous relaxation time, μ being the viscosity of the gas. The force on the particle due to collision and the other interparticle forces is denoted by $\mathbf{f}^{col}$. We shall assume that the particles undergo perfectly elastic collisions and that the interaction is that corresponding to a hard core repulsion. Finally, the undisturbed flow is the simple shear

$$\mathbf{u}^{\infty}(\mathbf{x}) = y\mathbf{e}_x, \tag{3}$$

where $\mathbf{e}_x$ is the unit vector along the x-axis and y is measured along the gradient of the flow.

The above model of gas-solid suspension will be referred to as the dusty gas model. Dynamic simulations of a dusty gas are relatively easy to carry out. We used 100 particles in a box with the usual periodic boundary conditions. The particle trajectories were determined through an exact solution of (2) neglecting the collisional force $\mathbf{f}^{col}$ and the particles moved accordingly for a specified time step. The particles were checked for overlap at the end of time step and, if necessary, the corrections were made for the collison. Various averages were computed by averaging over 10^5 time steps after discarding the first 10^5 time steps to allow for the system to attain steady state.

Figure 1 shows the velocity variance as a function of St for $\phi = 0.01$. Here $\mathbf{U}$ is the non-dimensional fluctuation velocity, i.e. $\mathbf{U} = \mathbf{v} - \mathbf{u}^{\infty}$. The simulation results are indicated by squares whereas the solid line corresponds to the theory to be described in the next section.

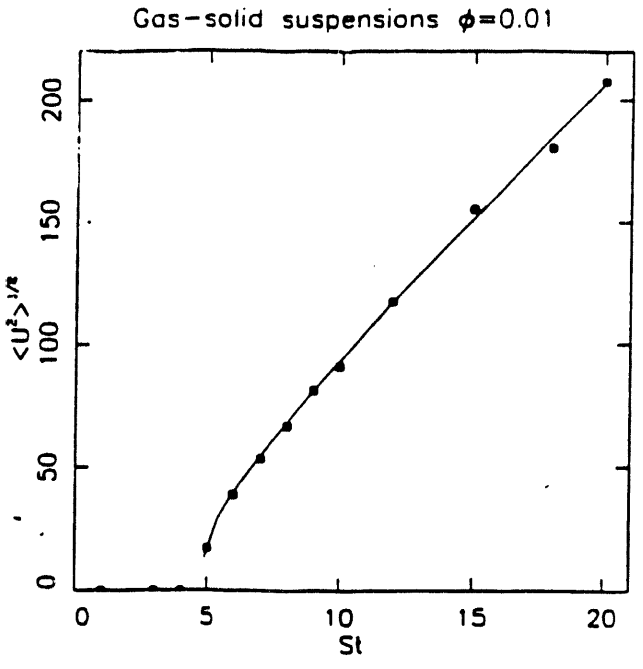

Figure 1

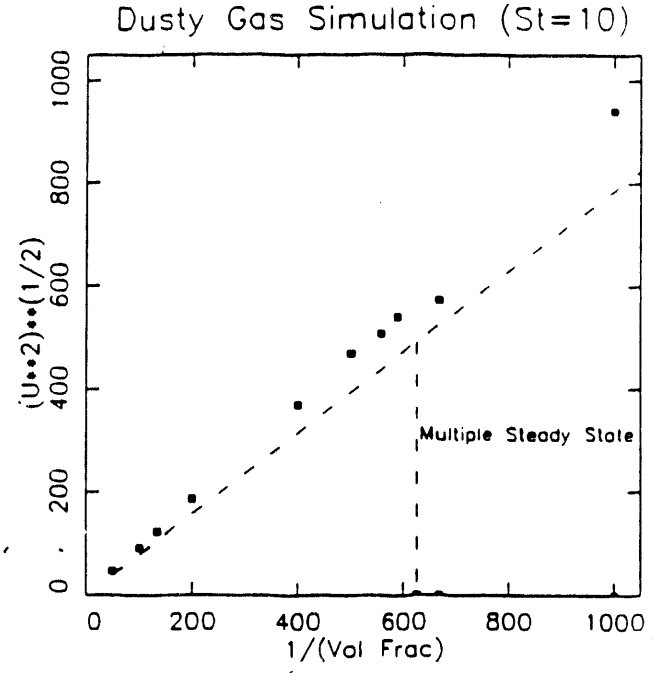

Figure 2

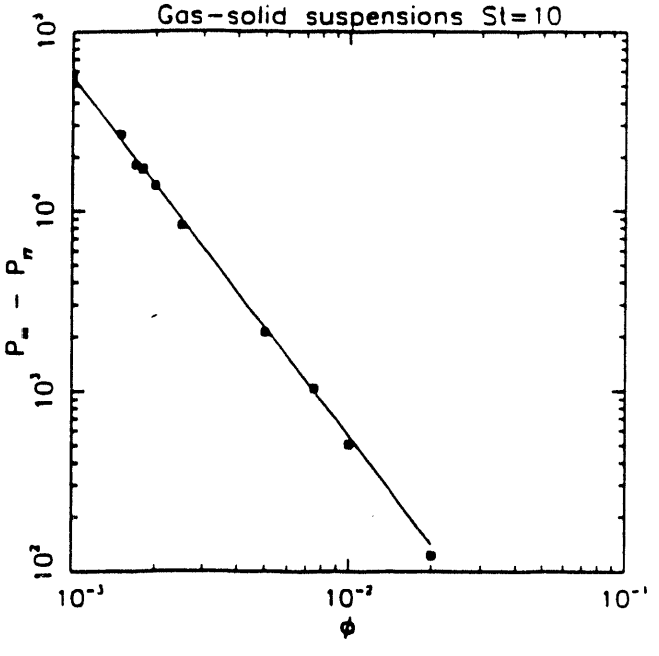

Figure 3

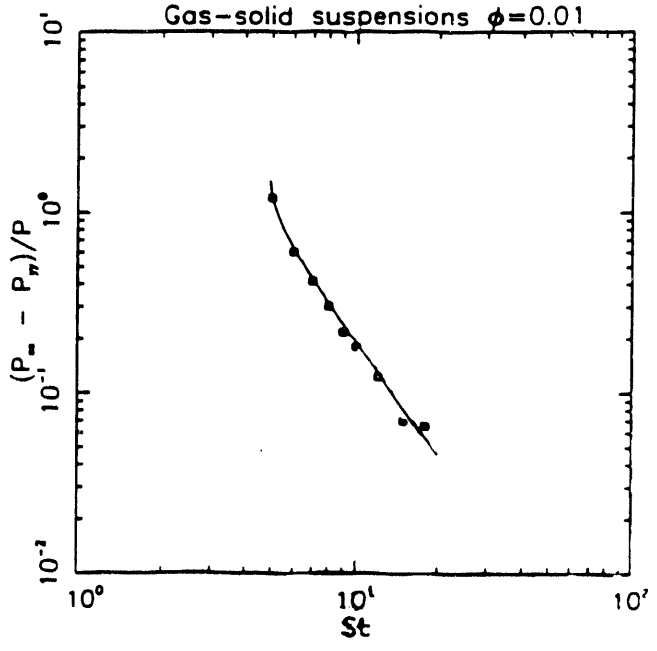

Figure 4

The root mean squared fluctuation $< U^2 >^{1/2}$ is seen to increase linearly with St at large Stokes numbers indicating that a large variance and hence a large particle-phase pressure are attained at large St. At $St \simeq 5$, the quantity $< U^2 >^{1/2}$ is seen to abruptly change from about 10 to zero. For smaller St with finite number N of particles in simulations, the particles take up positions such that the collisions are entirely avoided, and, since the particle interactions are neglected in the calculations, the variance becomes zero at small Stokes numbers. It may be noted that the final state with zero variance is actually an artifact of the periodic boundary conditions with finite N. We are in the process of using the direct-simulation Monte-Carlo technique to determine more precisely the variance at smaller Stokes numbers. In this method, the positions of two colliding particles before collision are chosen at random.

Figure 2 shows $< U^2 >^{1/2}$ as a function of $1/\phi$ for $St = 10$. Note that two steady states are observed for $\phi < 1/600$. In this range the final steady state depends on the initial conditions. If the initial variance is large enough, then the resulting steady state has a large variance; we shall refer to this as the ignited state. On the other hand, for small initial variance the final steady state corresponds to a zero variance, or a quenched state. For larger ϕ only one steady state, the ignited state, is obtained regardless of the initial velocity distribution. The abrupt drop in the variance at $St \simeq 5$ in Figure 1 thus corresponds to the truncation of the ignited steady state branch of solution.

In analogy with the kinetic theory of dilute gases, let us define the pressure tensor non-dimensionalized by $\rho_p \phi \gamma^2 a^2$ as

$$\mathbf{P} = < \mathbf{UU} > . \tag{4}$$

If the dispersed phase obeys a Newtonian rheology, then the diagonal elements of this tensor must be equal for a simple shear flow. As shown in Figures 3 and 4, however, this is not the case. We see that the normal stress difference increases like $1/\phi^2$ as $\phi \to 0$ for fixed St and decreases as $1/St^2$ for a fixed ϕ as $St \to \infty$.

3 A kinetic theory for dusty gas under shear

The simulations presented in the previous section show that multiple steady states exist and that the dispersed phase rheology is non-Newtonian. In this section, we present a simple kinetic theory to explain these findings. Since the particle interactions are neglected except for the collisions, and since the number density of particles is assumed to be constant throughout the space, the probability density distribution $f(U)$ satisfies[8]

$$\frac{\partial f}{\partial t} - \nabla_{\mathbf{U}} \cdot [\mathbf{e}_x U_y f + St^{-1} \mathbf{U} f] = J[f, f], \tag{5}$$

where $J[f, f]$ is the usual collision integral

$$J[f, g] = \int d\mathbf{v}_1 \int d\Omega B(w, \theta)[f(\mathbf{v}')g(\mathbf{v}_1') - f(\mathbf{v})g(\mathbf{v}_1)], \tag{6}$$

in which $\mathbf{v}$ and $\mathbf{v}_1$ are the velocities of particles before the collision, $\mathbf{v}'$ and $\mathbf{v}_1'$ the velocities after the collision, $w = |\mathbf{v}_1 - \mathbf{v}|$ the initial relative velocity, and $B(w, \theta)$ the probability

density for a relative deflection by an angle $\pi - 2\theta$ of the particle at $\mathbf{x}$ as a result of an encounter with the particle labeled 1. In particular, if the interparticle potential force is repulsive and given by a power law $F = \kappa r^{-n}$, then, as shown in Chapman and Cowling (Sec. 10.3, Ref. 8),

$$B(w,\theta) \propto \kappa^{2/1-n} w^{(n-5)/(n-1)}. \tag{7}$$

Note that B becomes independent of the relative velocity when $n = 5$. Because of this simplification, we shall assume in the development of the approximate kinetic theory below that the particles have the interparticle repulsive force with $n = 5$. In the kinetic theory of gases, molecules with such a repulsive force are termed as Maxwell molecules.

To make further progress in the analytical development, we shall replace the actual velocities $\mathbf{v}$ and $\mathbf{v}_1$ in the collision integral by the relative velocities $\mathbf{U}$ and $\mathbf{U}_1$. In other words, we ignore the mean shear flow in evaluating the collison integral. The pressure tensor can now be determined by multiplying (5) with $\mathbf{UU}$, integrating in the velocity space, and using the result

$$\int \mathbf{UU} J[f,f] d\mathbf{U} = 2\lambda\phi(p\mathbf{I} - \mathbf{P}), \tag{8}$$

where $\mathbf{I}$ is the identity tensor of rank 2, p the scalar pressure equal to one-third the trace of $\mathbf{P}$, and

$$\lambda = 0.3465\sqrt{\kappa}. \tag{9}$$

The dynamic simulations described in Section 2 were for the hard-sphere model. In order to make the collision frequency and the transport coefficients of the Maxwell particle model have the same temperature dependence, we need to make the force law constant κ to be temperature dependent as given by

$$\kappa = 32T/[A_2(5)\Gamma(7/2)]^2, \tag{10}$$

where $A_2(5) = 0.436$ (Ref. 9) and T is the temperature defined by

$$T = \frac{1}{3}\int fU^2 dU. \tag{11}$$

Note that $T = p$. Combining (5) and (8), we obtain four simultaneous equations governing P_{xx}, P_{yy}, P_{zz} and P_{xy}. Solving these equations for the steady state yields

$$P_{zz} = P_{yy} = -\frac{2P_{xy}}{St} = \frac{\lambda St\phi T}{1 + \lambda St\phi} \tag{12}$$

$$P_{xx} = P_{yy} + \frac{\lambda St^3\phi T}{2(1 + \lambda St\phi)^3}. \tag{13}$$

Now using $T = (P_{xx} + P_{yy} + P_{zz})/3$, noting that λ is a function of T via (9)-(10), and solving the energy balance equation

$$\frac{T}{St} + \frac{P_{xy}}{3} = 0, \tag{14}$$

we obtain three steady state solutions with the corresponding steady temperatures given by

$$T_1 = 0, \quad T_2^{1/2} = \frac{\alpha - \sqrt{\alpha^2 - 1}}{2.7055 St\phi}, \quad T_3^{1/2} = \frac{\alpha + \sqrt{\alpha^2 - 1}}{2.7055 St\phi}, \tag{15}$$

where $\alpha = St^2/12 - 1$.

Thus we note that while three steady states are possible for $St \geq \sqrt{24}$, only one steady state exists for $St < \sqrt{24}$. The state labeled 2 is unstable, while those labeled 1 and 3 are respectively the quenched and ignited states observed in dynamic simulations described in Section 2. The variance of state 2 is $O(St^3/\phi)^2$. Thus, the simple kinetic theory presented here shows that when the initial velocity distribution has a variance greater than this value, the final state will be the ignited state for $St \geq \sqrt{24}$. A smaller initial variance or smaller St will lead to the quenched state. Actually, this is not a precise criterion since our calculations neglected the mean shear flow effect in evaluating the collision integral. It can be shown that the shear flow induces an additional variance of $O(St^3\phi)$. If this shear-induced variance is greater than T_2, then, regardless of the initial velocity distribution, the final state is the ignited state for $St \geq \sqrt{24}$.

To recapitulate, the final steady state for $St < \sqrt{24}$ is a quenched state regardless of the initial velocity distribution. For $St \geq \sqrt{24}$, only the ignited state is possible when $St^3\phi > O(1)$. For very dilute suspensions for which $St^3\phi < O(1)$, the final state depends on the initial conditions. This is in agreement with the results of dynamic simulations with the $O(1)$ constant being about 1.5. For $St \gg 1$, the ignited state with the Maxwell particle model corresponds to

$$T_3^{1/2} = \frac{\sqrt{\pi}}{16.61} \frac{St}{\phi} \tag{16}$$

and

$$\frac{P_{xx} - P_{yy}}{p} = \frac{18}{St^2} \tag{17}$$

which agree well with the results for hard spheres for which the constants 16.61 and 18 in the above expressions are replaced by 16.63 and 117/7, respectively.

4 Large St, finite ϕ, simulations

When the Stokes number is large and ϕ is finite, the steady state variance in the ignited state can be determined with the help of Monte-Carlo simulations. Since the viscous relaxation time is much greater than the collision time in this limit, the leading order velocity distribution is the isotropic Maxwellian. The steady state variance is determined from the energy balance according to which the energy input in shearing the suspension is lost via the viscous energy dissipation. The calculations are similar to those in the theory of rapid granular flows developed by Jenkins[10] except that in his calculations the energy input by shear was dissipated through inelastic collisions.

To estimate the viscous energy dissipation we carry out Monte-Carlo simulations in which the velocity of each particle is randomly chosen from a set of numbers with a Guassian

(Maxwellian) statistics. The position of the particles are generated from the usual hard-sphere dynamic simulation code. The force on each particle is then determined using a Stokes flow interaction code[11,12] which accounts for the full hydrodynamic interactions among many particles. The energy dissipated per particle is then expressed in terms of an energy dissipation coefficient C_d^* defined via

$$E_{dis} = - < \mathbf{F} \cdot \mathbf{U} >= 6\pi\mu a C_d^* < U^2 > . \tag{18}$$

In these calculations, the rotational velocity of each particle is taken to be unity as the energy dissipated will be dominated by the random fluctuations in the translational velocity in the limit of large St.

Results for C_d^* are presented in Figure 5. In our calculations we assumed that the usual continuum approximation breaks down when a pair of particles is sufficiently close to each other so that the forces on a pair of particles with a separation distance between their surfaces less than $2\epsilon_m a$ can be approximated to be the same as the force on particles separated by $2\epsilon_m a$. The lubrication breakdown parameter ϵ_m can be determined for a given gas-solid suspension and Stokes number from the detailed calculation of the forces between pair of particles with an appropriate non-continuum analysis[13,14]. It may be noted that since the force on two particles approaching each other with an $O(1)$ relative velocity increases like $1/\epsilon$ as $\epsilon \to 0$ according to the usual continuum analysis, C_d^* will diverge logarithmically with ϵ_m as $\epsilon_m \to 0$. (At large St, the velocity distribution of particles is independent of the spatial configuration of the particles.)

For the purpose of comparison, we have also shown in Figure 5 the average drag coefficient for the uniform flow through fixed beds of spherical particles and the hinderance factor in sedimenting suspensions. These quantities, which were also determined by our numerical code described in Refs. 11,12, are in very good agreement with the results reported earlier by Ladd[15]. The curve for C_d^* is based on $\epsilon_m = 0.02$. The results with other values of ϵ_m at $\phi = 0.4$ are indicated by asterisks. For very small ϕ, the behavior of C_d^* should resemble that of the average drag force in a fixed bed of particles since both problems correspond to specifying the velocity of the particles. Thus, for example, the velocity disturbance due to a particle is hydrodynamically screened, and for small ϕ, C_d^* behaves as $1 + 3\sqrt{\phi/2} + O(\log \phi)$ as in the case of drag in fixed beds[16]. The two quantites start differing at $O(\phi)$ because the velocity distributions in the two problems are different. The numerical calculations shown in Fig. 5 suggest that C_d^* is much lower than the corresponding values in fixed beds and sedimenting suspensions provided that ϵ_m is greater than 0.01.

We would like to note that in the limit of large St, various energy dissipative mechanisms are addititive so that, for example, if the collisions between particles are inelastic, we can add the extra energy lost in collisions to the total energy balance for the dispersed phase. In this sense our calculations of the viscous energy dissipation complements the theory of rapidly sheared granular flows due to Jenkins[10].

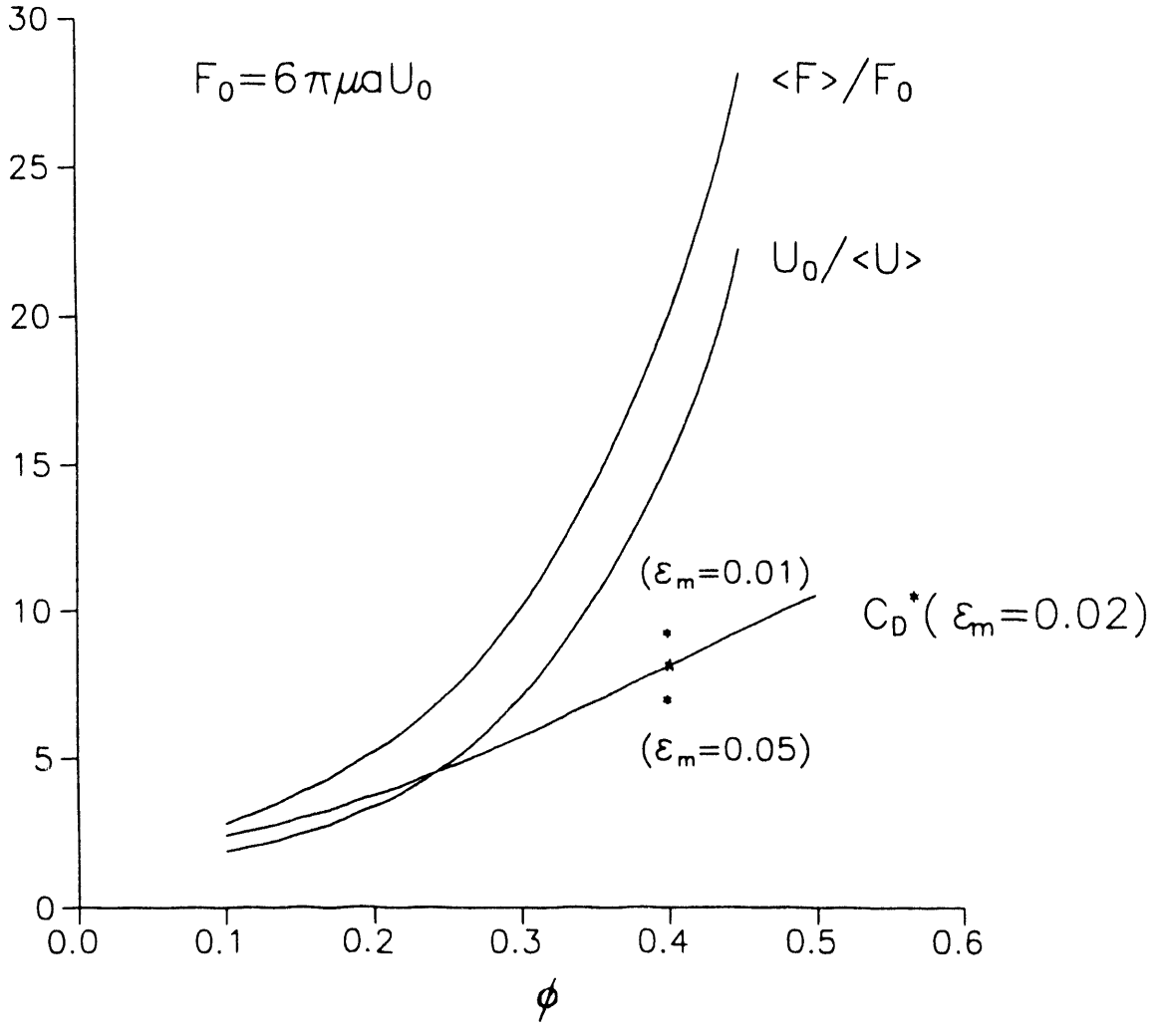
30
25
20
15
10
5
0
0.0
0.1
0.2
0.3
0.4
0.5
0.6
ϕ
$F_0 = 6\pi\mu a U_0$
$\langle F \rangle / F_0$
$U_0 / \langle U \rangle$
$(\varepsilon_m = 0.01)$
$C_D^*(\varepsilon_m = 0.02)$
$(\varepsilon_m = 0.05)$

Figure 5

5 Concluding remarks

We have shown that multiple steady states exist in the flows of gas-solid suspensions. Similar simulations for bubbly liquids at large Reynolds numbers Re have been carried out by Tsao and Koch[17]. The major conclusions of the present study, i.e. multiple steady states and a non-Newtonian dispersed phase rheology, also apply to the bubbly liquids in which $Re/18$ plays the same role as the Stokes number, although some important differences in the sign and magnitude of the the normal stress differences occur between the two suspension systems owing to the presence of the lift forces on bubbles in the presence of a mean vorticity.

Currently we are in the process of carrying out dynamic simulations accounting for the multiparticle interactions to obtain more accurate estimates of the variance and hence the particle phase pressure at intermediate Stokes numbers and to study the transition between the quenched and ignited states.

Acknowledgements

The work described here is supported by grants from the National Science Foundation. The computing support was provided by the Theory Center at Cornell University.

6 References

1. Anderson T. B. and Jackson R. A fluid mechanical description of fluidized beds - stability of the state of unifrom fluidization. *Ind. Eng. Chem. Fund.*, **7**, 12 (1968).

2. Wallis G. B. *One-dimensional Two-phase Flow*, McGraw-Hill (1969).

3. Homsy G. M., El-Kaissy M. M. and Didwania A. K. Instability waves and the origin of bubbles in fluidized beds. II. Comparison with theory. *Int. J. Multiphase Flow*, **16**, 171 (1980).

4. Batchelor G. K. A new theory of the instability of a uniform fluidized bed. *J. Fluid Mech.*, **193**, 75 (1988).

5. Koch D. L. 1990 Kinetic theory for a monodispersed gas-solid suspension. *Phys. Fluids A*, **2**, 1711 (1990).

6. Sangani A. S. and Didwania A. K. Dispersed-phase stress tensor in flows of bubbly liquids at large Reynolds numbers. *J. Fluid Mech.*, **248**, 27 (1993).

7. Sangani A. S. and Didwania A. K. Dynamic simulations of flows of bubbly liquids at large Reynolds numbers. *J. Fluid Mech.*, **250**, 307 (1993).

8. Chapman S. and Cowling T. G. *The Mathematical Theory of Non-Uniform Gases*, Cambridge University Press (1939).

9. Goldman E. and Sirovich L. Equations for gas mixtures. *Phys. Fluids*, **10**, 1928 (1967).

10. Jenkins J. T. Rapid flows of granular materials, pp. 213-225 in *Non-Classical Continuum Mechanics: Abstract Techniques and Applications*, (ed. R. Knops and A. Lacey) Cambridge University Press (1987).

11. Mo G.-B. and Sangani A. S. A method for computing Stokes flow interactions among spherical objects and its application to suspensions of drops and porous particles. *Phys. Fluids A* (submitted).

12. Sangani A. S. and Mo G.-B. Inclusion of lubrication forces in dynamic simulations. *Phys Fluids A* (submitted).

13. Hocking L. M. The effect of slip on the motion of a sphere close to a wall and of two adjacent spheres. *J. Engng Math.*, **7**, 207 (1973).

14. Sundararajakumar R. R. and Koch D. L. Lubrication flows between particles colliding in a gas (in preparation for *J. Fluid Mech.*).

15. Ladd A. J. C. Hydrodynamic transport coefficients of random dispersions of hard spheres. *J. Chem. Phys.*, **93**, 3484 (1990)

16. Hinch E. J. An averaged-equation approach to particle interactions in a fluid suspension. *J. Fluid Mech.*, **83**, 695.

17. Tsao H.-K. and Koch D. L. Bubbly liquids in shear (to be submitted for publication).

Simulation of Rotary-Drum and Repose Tests for Frictional Spheres and Rigid Sphere Clusters *

O. R. Walton and R. L. Braun
Lawrence Livermore National Laboratory, Livermore, CA 94550

ABSTRACT

The effects of rotation rate and interparticle friction on the bulk flow behavior in rotating horizontal cylinders are studied via particle-dynamic simulations. Assemblies of inelastic, frictional spheres and rigid sphere clusters are utilized, and rotation rates from quasistatic to centrifuging are examined. Flow phenomena explored include size segregation, avalanching, slumping and centrifuging. Simulated drum flows with two sizes of frictional spheres showed very rapid segregation of species perpendicular to the drum axis; however, simulations of up to 10 revolutions, utilizing periodic-boundary *ends*, did not exhibit the experimentally observed axial segregation into *stripes*. Angles of repose for uniform-sized spheres in slowly rotating cylinders varied from 13 to 31 degrees as the friction coefficient varied from 0.02 to 1.0. For simulated rotation rates higher than the threshold to obtain uniform flow conditions, the apparent angle of repose increases as the rotation rate increases, consistent with experiments. Also, simulations with rigid clusters of 4 spheres in a tetrahedral shape or 8 spheres in a cubical arrangement, demonstrate that particle shape strongly influences the repose angle. Simulations of cubical 8-sphere clusters, with a surface coefficient of friction of 0.1, produced apparent angles of repose exceeding 35 degrees, compared to 23 degrees for assemblies of single spheres interacting with the same force model parameters.

Centrifuging flows at very high rotation rates exist as stationary beds moving exactly as the outer rotating wall. At somewhat slower speeds the granular bed remains in contact with the wall but exhibits surface sliding down the rising inner bed surface, moving a short distance on each revolution. At still slower speeds particles *rain* from the surface of the upper half of the rotating bed. The boundary between stationary and sliding flow is given by $\Omega^2 = 1/\sin\phi_r$, and the boundary between sliding and raining flow is approximately fit by the empirical relation $\Omega^2 = 1/\sin[\tan^{-1}(0.16 + \tan\phi_r)]$, where the non-dimensional rotation rate, Ω, is determined by $\Omega^2 = \omega_d^2 R_i/g$, and ω_d is the drum rotation rate, R_i is the radius of the inner surface of the centrifuging bed, g is the acceleration of gravity, and ϕ_r is the angle of repose for the material.

INTRODUCTION

This paper describes numerical simulations of flows of inelastic, frictional particles in rotating drums. Many industrial applications utilize rotating cylinders in processes involving granular solids and a variety of intriguing qualitative phenomena have been observed in such devices. When a slowly rotating drum is partially filled with a granular material it will usually exhibit one of two modes of motion. For very small loads (or with a very smooth interior wall) the material will initially ride up on the rising wall, then, when sufficient tangential load develops to overcome friction, the material will *slump* back down the wall, moving almost as a rigid block, with inertia usually carrying it beyond its equilibrium position. After coming to rest with respect to the outer wall, it will rise again, and repeat the cycle. For drums half or more filled (or with a rough interior wall) the material will more likely exhibit periodic surface *avalanches* down the inclined top surface. The highest attained surface angle and the lowest *slumped* surface angle often differ by as much as 10 degrees [De Jaeger, 1993]. As the rotation rate is increased,

* Work performed under the auspices of the U.S. Department of Energy by the Lawrence Livermore National Laboratory under Contract W-7405-Eng-48.

the frequency of these avalanches increases, and, when the average period between avalanches becomes less than the average duration of an individual avalanche (a time that depends on the absolute size of the drum involved and on the characteristics of the material), the material often exhibits a continuously moving top surface that has a nearly constant angle of inclination. This angle, lying somewhere between the maximum and minimum angle observed quasistatically, is often referred to as the *dynamic* or *instantaneous* angle of repose [Brown & Richards, 1970].

As the rotation rate is increased beyond the threshold *dynamic angle-of-repose* rate, inertial effects cause the flow to change character, with the upper half of the flow increasing its apparent surface angle, and the lower half decreasing its apparent surface angle. Initially the surface simply appears curved, but, at higher rotation rates, some flows appear to almost form two distinct linear surfaces [Altobelli *et al.*, 1993].

If the rotation rate is increased even further, the centrifuging limit is approached. At a rotation rate high enough to produce centrifugal force on the outer wall nearly equal to gravity, many particles appear to follow parabolic ballistic trajectories, coming off of the upper half of the rising side of the drum and falling down to a *splash* bed at the foot. True centrifuging flow, with particles remaining in continuous contact with the outer wall, requires significantly higher rotation rates than the minimum that just cancels gravity at the top of the drum. Such flows are discussed in detail later in this paper.

The qualitative flow phenomena described above are not only observed in laboratory experiments [Brown & Richards, 1970; Altobelli, *et al.* 1993], but can also be reproduced in numerical simulations of assemblies of frictional, inelastic spheres and non-spherical particles [in addition to this paper, see also: Tsuji, 1993; Ting & Corkum, 1988; Nakagawa *et al.*, 1993; Hashimoto & Watanabe, 1993]. By utilizing numerical simulation models it is possible to test sensitivity of a variety of flow phenomena to individual particle-interaction parameters such as interparticle friction or degree of inelasticity in collisions. This ability to isolate the effects of individual particle or interaction parameters can facilitate development of theories and empirical relations that focus on the most important particle characteristics. For example, simulations with a fixed coefficient of friction, independent of sliding velocity, exhibit the slumping and avalanching behaviors described above. Such simulations demonstrate that avalanching flow and periodic slumping are inherent characteristics of slowly rotating drum flows, and do not depend on *stick-slip* friction or a velocity dependent friction coefficient acting between particles or at particle-wall interfaces.

METHOD

Molecular-dynamics algorithms and methods are widely utilized and are described in several texts [Allen & Tildesley, 1987; Hockney & Eastwood, 1988; Hoover, 1991] and these same methods have been applied to macroscopic granular systems for a variety of deformation and flow conditions (see, for example Cundall & Strack [1979] and Walton [1982]). We utilize a simple, explicit, leap-frog integration algorithm (algebraically equivalent to the popular Verlet scheme) wherein positions and forces are known at the ends of each timestep and the velocities are known at the mid-point of each time-step. Newton's equations of motion are expressed as two first order differential equations in each space dimension for each particle:

$$\dot{v}_\alpha = g_\alpha + F_\alpha/m \ , \quad \alpha = x, y, z \ ; \tag{1}$$

$$\dot{r}_\alpha = v_\alpha \ , \qquad \alpha = x, y, z \ . \tag{2}$$

These are differenced in time-centered form as:

$$v_\alpha^{n+\frac{1}{2}} = v_\alpha^{n-\frac{1}{2}} + \Delta t \left(g_\alpha + \frac{F_\alpha^n}{m} \right) \ , \quad \alpha = x, y, z \ ; \tag{3}$$

$$r_\alpha^{n+1} = r_\alpha^n + \Delta t \ v_\alpha^{n+\frac{1}{2}} \ , \qquad \alpha = x, y, z \ . \tag{4}$$

Where the superscript refers to the timestep, r is the position, v is velocity, F is the force from contacts or applied loads, m is mass, and g is the acceleration of gravity.

A radial *skin* search is employed to establish near-neighbor lists that are stored in a set of $n_p + 1$ intertwined linked lists (one list for each of the n_p particles, and a list of previously *released* memory locations that can be used for new or re-established neighbors). Individual list entries are deleted and the released memory locations are added to the *empty* list whenever a neighboring pair move further than the search distance. The entire set of neighbor lists is updated at irregular intervals, triggered by particle displacements exceeding the search radius.

Contact forces (and torques) are calculated for any near-neighbor pairs that are actually *overlapping*. The force-displacement model includes position dependent hysteresis in both the normal and tangential-friction forces. The normal-direction contact force is modeled with a linear loading (with a slope K_1) coupled with a somewhat stiffer linear unloading (with slope K_2) so that isolated, frictionless, two-body collisions will exhibit a constant coefficient of restitution, $e = \sqrt{K_1/K_2}$. The tangential force builds up (non-linearly) with finite tangential displacements after physical contact occurs. The initial slope of the tangential force displacement curve, K_{t0}, is a fixed fraction of the normal stiffness. The tangential force has a maximum value limited by the friction coefficient, μ, times the normal force. The resulting behavior is very similar to Mindlin's [1949] analysis of elastic frictional contacts between spheres. The justification for, and the details of, these force models are presented elsewhere† [Walton, 1993a,b].

The time derivatives of the angular velocities in the *principal* frame are given by Euler's equations of motion,

$$\dot{\omega}_x = \left[N_{px} + \omega_y \omega_z (I_{py} - I_{pz}) \right] / I_{px} \tag{5a}$$

$$\dot{\omega}_y = \left[N_{py} + \omega_z \omega_x (I_{pz} - I_{px}) \right] / I_{py} \tag{5b}$$

$$\dot{\omega}_z = \left[N_{pz} + \omega_x \omega_y (I_{px} - I_{py}) \right] / I_{pz} \tag{5c}$$

where $\mathbf{I}_p$ is the (diagonal) moment of inertia tensor in the principal body frame, and $\mathbf{N}_p$ is the torque vector in the principal body frame.

Because of the angular velocity products appearing on the right hand side in Equations (5a, b, c) a predictor-corrector algorithm is utilized for integrating the angular velocity derivatives.

---

† Position dependent hysteretic models were employed in these *dynamic* flows to demonstrate that the effects observed do not depend on any *viscous* or *rate-dependent* parameters in the models. The simulations could have used damped harmonic oscillator (*i.e.*, spring-dashpot) models in both the normal and tangential directions with the tangential force magnitude limited by Amonton's friction rule (Friction force < μ Normal force). If such models had been utilized instead of the position-dependent hysteretic models of these simulations, the results would have been substantially equivalent to the results presented here.

The torques are known *on* the time step and the angular velocities are known at the midpoints. First, angular velocities are estimated at the current time step by assuming constant angular acceleration for an additional one-half time step,

$$\omega_\alpha'^n = \omega_\alpha^{n-\frac{1}{2}} + \Delta\omega_\alpha^{n-1}/2 \ , \qquad \alpha = x,\ y,\ z \ . \tag{6}$$

These *extrapolated* angular velocities are used, along with the current torques, to make a first *prediction* of the angular accelerations at the current time step,

$$\Delta\omega_x'^n = \left[N_{px}^n + \omega_y'^n\omega_z'^n(I_{py} - I_{pz})\right]\Delta t/I_{px} \tag{7a}$$

$$\Delta\omega_y'^n = \left[N_{py}^n + \omega_z'^n\omega_x'^n(I_{pz} - I_{px})\right]\Delta t/I_{py} \tag{7b}$$

$$\Delta\omega_z'^n = \left[N_{pz}^n + \omega_x'^n\omega_y'^n(I_{px} - I_{py})\right]\Delta t/I_{pz} \tag{7c}$$

These predicted angular accelerations are then used to more accurately predict the angular velocities at the current time step,

$$\omega_\alpha^n = \omega_\alpha^{n-\frac{1}{2}} + \Delta\omega_\alpha'^n/2 \ , \qquad \alpha = x,\ y,\ z. \tag{8}$$

The corrected values for the derivatives are then,

$$\Delta\omega_x^n = \left[N_{px}^n + \omega_y^n\omega_z^n(I_{py} - I_{pz})\right]\Delta t/I_{px} \tag{9a}$$

$$\Delta\omega_y^n = \left[N_{py}^n + \omega_z^n\omega_x^n(I_{pz} - I_{px})\right]\Delta t/I_{py} \tag{9b}$$

$$\Delta\omega_z^n = \left[N_{pz}^n + \omega_x^n\omega_y^n(I_{px} - I_{py})\right]\Delta t/I_{pz}. \tag{9c}$$

At this point these *corrected* values can be used directly to update angular velocities to the midpoint of the next timestep,

$$\omega_\alpha^{n+\frac{1}{2}} = \omega_\alpha^{n-\frac{1}{2}} + \Delta\omega_\alpha^n \ , \qquad \alpha = x,\ y,\ z, \tag{10}$$

or, additional iterations through the last six equations (e.g. going back to Eqn 8) can be repeated until a convergence criteria based on changes in the quantities $\Delta\omega_x^n$, $\Delta\omega_y^n$, and $\Delta\omega_z^n$ between successive iterations is satisfied, or a predetermined number of iterations is completed.

Orientaions (*i.e.*, angles) for each particle are updated using an adaptation of Evans' singularity free quaternion approach [Evans & Murad, 1977]. For Euler's equations of motion and the integration of the quaternions, the torques are specified in the *body* or *principal* frame for each non-spherical body. The contact detection and force calculations are performed in a *space* or *global* reference frame. The rotation matrix transforming from *space* to *body* frame is given by:

$$\mathbf{A} = \begin{pmatrix} -q_1^2 + q_2^2 - q_3^2 + q_4^2 & -2(q_1q_2 - q_3q_4) & 2(q_2q_3 + q_1q_4) \\ -2(q_1q_2 + q_3q_4) & q_1^2 - q_2^2 - q_3^2 + q_4^2 & -2(q_1q_3 - q_2q_4) \\ 2(q_2q_3 - q_1q_4) & -2(q_1q_3 + q_2q_4) & -q_1^2 - q_2^2 + q_3^2 + q_4^2 \end{pmatrix} \tag{11}$$

Where the q's are the quaternions of Evans and Murad [1977].

$$q_1 = \sin\tfrac{\theta}{2}\sin(\tfrac{\psi-\phi}{2}) \ , \qquad q_2 = \sin\tfrac{\theta}{2}\cos(\tfrac{\psi-\phi}{2}) \tag{12a,b}$$

$$q_3 = \cos\tfrac{\theta}{2}\sin(\tfrac{\psi+\phi}{2}) \ , \qquad q_4 = \cos\tfrac{\theta}{2}\cos(\tfrac{\psi+\phi}{2}) \tag{12c,d}$$

and ϕ, θ, ψ are Euler's angles representing successive rotations about the z, x', and z' axes (see Goldstein [1950]).

The time derivatives of the orientation parameters (*i.e.*, the quaternions, q_1, q_2, q_3, q_4) can be expressed in terms of the quaternions themselves and the angular velocities [Evans & Murad, 1977],

$$\dot{q}_1 = \tfrac{1}{2}(-q_3\omega_x - q_4\omega_y + q_2\omega_z) \tag{13a}$$
$$\dot{q}_2 = \tfrac{1}{2}(q_4\omega_x - q_3\omega_y - q_1\omega_z) \tag{13b}$$
$$\dot{q}_3 = \tfrac{1}{2}(q_1\omega_x + q_2\omega_y + q_4\omega_z) \tag{13c}$$
$$\dot{q}_4 = \tfrac{1}{2}(-q_2\omega_x + q_1\omega_y - q_3\omega_z) \tag{13d}$$

Only three of the quaternions are independent and closure of this system of equations is obtained by the normalization relation,

$$\sum_{i=1}^{4} q_i^2 = 1. \tag{14}$$

Time centered finite difference versions of Eqns (13) can be solved explicitly for the quaternion values at the new time step in terms of the old values and the angular velocities at the midpoint of the timestep. The finite difference form of Eqns (13$a-d$) is,

$$q_1^{n+1} = q_1^n + \tfrac{\Delta t}{4}\left[-(q_3^{n+1}+q_3^n)\omega_x^{n+\frac{1}{2}} - (q_4^{n+1}+q_4^n)\omega_y^{n+\frac{1}{2}} + (q_2^{n+1}+q_2^n)\omega_z^{n+\frac{1}{2}}\right] \tag{15a}$$
$$q_2^{n+1} = q_2^n + \tfrac{\Delta t}{4}\left[(q_4^{n+1}+q_4^n)\omega_x^{n+\frac{1}{2}} - (q_3^{n+1}+q_3^n)\omega_y^{n+\frac{1}{2}} - (q_1^{n+1}+q_1^n)\omega_z^{n+\frac{1}{2}}\right] \tag{15b}$$
$$q_3^{n+1} = q_3^n + \tfrac{\Delta t}{4}\left[(q_1^{n+1}+q_1^n)\omega_x^{n+\frac{1}{2}} + (q_2^{n+1}+q_2^n)\omega_y^{n+\frac{1}{2}} + (q_4^{n+1}+q_4^n)\omega_z^{n+\frac{1}{2}}\right] \tag{15c}$$
$$q_4^{n+1} = q_4^n + \tfrac{\Delta t}{4}\left[-(q_2^{n+1}+q_2^n)\omega_x^{n+\frac{1}{2}} + (q_1^{n+1}+q_1^n)\omega_y^{n+\frac{1}{2}} - (q_3^{n+1}+q_3^n)\omega_z^{n+\frac{1}{2}}\right]. \tag{15d}$$

These equations can be solved for q_1^{n+1}, q_2^{n+1}, q_3^{n+1}, and q_4^{n+1}. Rearranging Eqns (15) we have,

$$q_1^{n+1} - \beta_z q_2^{n+1} + \beta_x q_3^{n+1} + \beta_y q_4^{n+1} = q_1^n + \beta_z q_2^n - \beta_x q_3^n - \beta_y q_4^n \tag{16a}$$
$$\beta_z q_1^{n+1} + q_2^{n+1} + \beta_y q_3^{n+1} - \beta_x q_4^{n+1} = -\beta_z q_1^n + q_2^n - \beta_y q_3^n + \beta_x q_4^n \tag{16b}$$
$$-\beta_x q_1^{n+1} - \beta_y q_2^{n+1} + q_3^{n+1} - \beta_z q_4^{n+1} = \beta_x q_1^n + \beta_y q_2^n + q_3^n + \beta_z q_4^n \tag{16c}$$
$$-\beta_y q_1^{n+1} + \beta_x q_2^{n+1} + \beta_z q_3^{n+1} + q_4^{n+1} = \beta_y q_1^n - \beta_x q_2^n - \beta_z q_3^n + q_4^n \tag{16d}$$

where,

$$\beta_x = \tfrac{\Delta t}{4}\omega_x^{n+\frac{1}{2}} \ , \qquad \beta_y = \tfrac{\Delta t}{4}\omega_y^{n+\frac{1}{2}} \ , \qquad \beta_z = \tfrac{\Delta t}{4}\omega_z^{n+\frac{1}{2}} \ . \tag{17a,b,c}$$

Now, let $\mathbf{B}$ be the matrix of coefficients from the left-hand side of Eqns (16) and C_i , $i = 1,2,3,4$ be the right hand sides of the four equations:

$$\mathbf{B} = \begin{pmatrix} 1 & -\beta_z & \beta_x & \beta_y \\ \beta_z & 1 & \beta_y & -\beta_x \\ -\beta_x & -\beta_y & 1 & -\beta_z \\ -\beta_y & \beta_x & \beta_z & 1 \end{pmatrix} \tag{18}$$

$$C_1 = q_1^n + \beta_x q_2^n - \beta_x q_3^n - \beta_y q_4^n \tag{19a}$$
$$C_2 = -\beta_x q_1^n + q_2^n - \beta_y q_3^n + \beta_x q_4^n \tag{19b}$$
$$C_3 = \beta_x q_1^n + \beta_y q_2^n + q_3^n + \beta_x q_4^n \tag{19c}$$
$$C_4 = \beta_y q_1^n - \beta_x q_2^n - \beta_x q_3^n + q_4^n \tag{19d}$$

Then

$$\det B = 1 + 2\beta_x^2 + 2\beta_y^2 + 2\beta_z^2 + 2\beta_x^2\beta_y^2 + 2\beta_y^2\beta_z^2 + 2\beta_x^2\beta_z^2 + \beta_x^4 + \beta_y^4 + \beta_z^4 \tag{20}$$

and

$$q_1^{n+1} = (C_1 + C_2\beta_z - C_3\beta_x - C_4\beta_y)(1 + \beta_x^2 + \beta_y^2 + \beta_z^2)/\det B \tag{21a}$$
$$q_2^{n+1} = (-C_1\beta_z + C_2 - C_3\beta_y + C_4\beta_x)(1 + \beta_x^2 + \beta_y^2 + \beta_z^2)/\det B \tag{21b}$$
$$q_3^{n+1} = (C_1\beta_x + C_2\beta_y + C_3 + C_4\beta_z)(1 + \beta_x^2 + \beta_y^2 + \beta_z^2)/\det B \tag{21c}$$
$$q_4^{n+1} = (C_1\beta_y - C_2\beta_x - C_3\beta_z + C_4)(1 + \beta_x^2 + \beta_y^2 + \beta_z^2)/\det B \tag{21d}$$

These explicit expressions for the updated q_i's are time centered (e.g., Eqns 15) and, thus avoid the additional predictor-corrector steps required by Allen and Tildesley [1987].

By their definition, Eqn (12), the quaternions satisfy the normalization relation, Eqn (14) and Evans [1977] demonstrated that Eqn (13) maintains that relation; however, to ensure that round-off error does not eventually cause normalization to fail, the resulting new quaternion values are scaled to conform with the normalization condition. A scale factor,

$$f = \left[\sum_{i=1}^{4} \left(q_i^{n+1}\right)^2\right]^{-\frac{1}{2}}, \tag{22}$$

is utilized to satisfy normalization for each particle, after each integration step,

$$q_i'^{n+1} = f q_i^{n+1}, \qquad i = 1,\ 2,\ 3,\ 4. \tag{23}$$

SIMULATIONS

Filling a vertical cylinder

Several qualitative differences in flow behavior between spheres and non-spherical particles are evidenced in simulations of particles dropping into an initially empty, vertical, right circular cylinder. In these generic simulations the ratio of loading to unloading stiffness in the normal force model (*i.e.*, K_1/K_2) is set to 0.64, corresponding to a coefficient of restitution of $e = 0.8$ for isolated collisions between spheres. For non-spherical particles the contact normal forces produce moments as well as rigid-body translational forces, so that the concept of a coefficient of restitution is somewhat less well defined. Nevertheless, the same force model parameters were used for individual contacts involving sphere clusters as for those involving single spheres. The coefficient of interparticle friction, μ, was 0.2, and the magnitude of the normal direction

stiffness was set so that the maximum *overlap* that would occur in a simulated impact would be less than one percent of a sphere diameter.

When a stream of particles falling from a height of one meter (*i.e.*, with an impact velocity of approximately $4.5m/s$) was used to fill a cylinder that was approximately 20 particle diameters across, the top of the resulting granular bed was nearly flat, as shown in Figure 1. Essentially the same surface condition was obtained whether the particles were spheres, tetrahedral clusters, cubic clusters or a mixture of the three as shown in Fig. 1. The kinetic energy imparted to the bed by each impacting particle was sufficient to vibrationally fluidize the upper surface, producing the fluid-like flat surface which remained after the vibrations attenuated. Laboratory tests of uniform sized spheres dropping into graduated cylinders can also result in flat top surfaces and, depending on both the drop height and flux, can result in a range of solid packings up to as high as 0.69 [Macrae and Gray, 1961] due to rearrangements caused, or allowed, by the energy of the impacting particles.

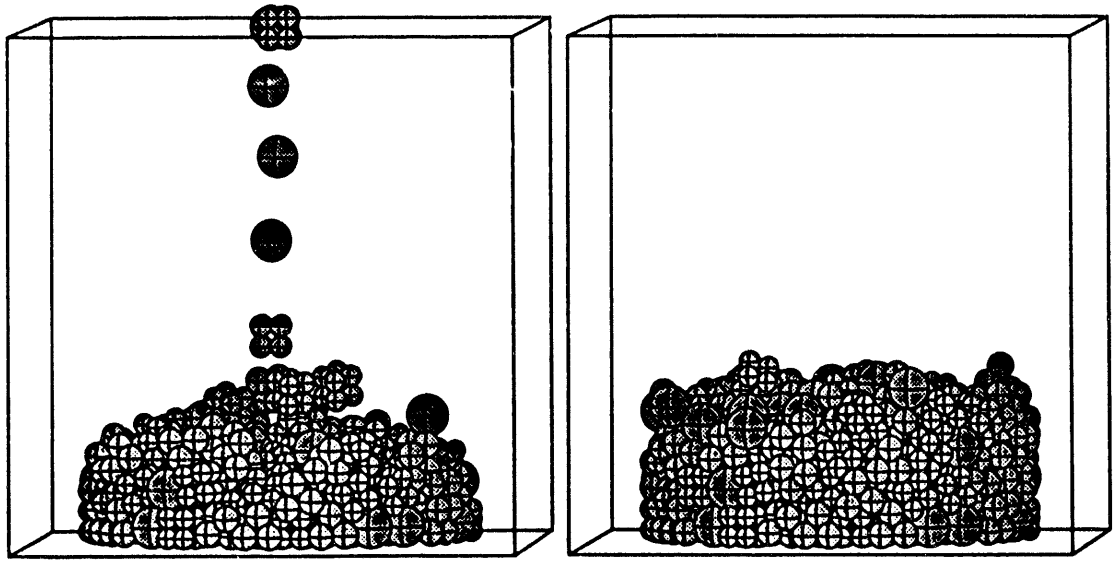

Figure 1.
Filling a right circular cylinder (not shown) with particles impacting at a velocity of $v_f \approx 4.5m/s$, $\mu = 0.2$, $e = 0.8$.

When simulated particles are dropped in a stream with a lower impact velocity (e.g., $v_f \approx 1.0m/s$) we obtain a mound under the fill stream as shown in Figures 2a and 2b. The slopes of the mounds in these two figures are significantly different, with the tetrahedral clusters forming a steeper surface than the spheres. These instantaneous snapshots of the mounds during filling are not altogether indicative of the final shape that is obtained after the fill stream is terminated. In these simulations there is sufficient kinetic energy and inertia existing near the mound peak

to allow it to flatten considerably after the fill stream is stopped. Similar inertial effects have been observed in simulations of spheres and sphere clusters by others [Hofstetter, 1993]. In experimental tests to determine angles of repose such inertial effects are usually minimized by allowing incoming particles to be quasistatically deposited from the end of a slowly raised small diameter tube (or straw) filled with the material being tested. Simulations of such angle-of-repose tests are planned.

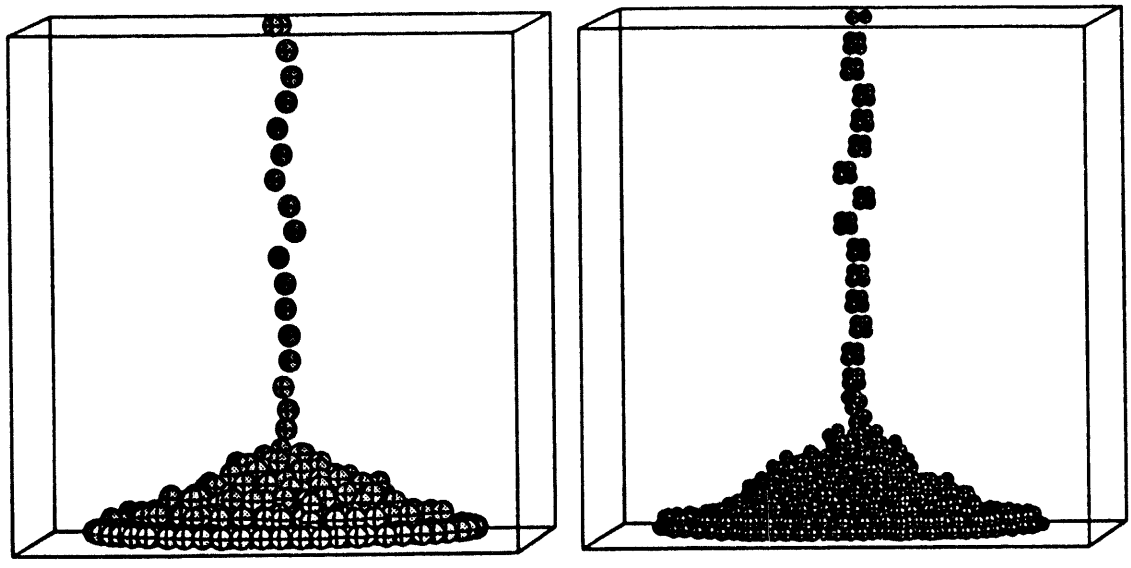

Figure 2.
Filling right circular cylinders with particles impacting at $v_f \approx 1.0m/s$, $\mu = 0.2$, $e = 0.8$, (a) spheres, and (b) sphere-clusters composed of 4 spheres in a tetrahedral arrangement.

Slowly Rotating Drums

Slumping and avalanching flows, as discussed in the introduction, are observed in simulations of very slowly rotating drums with both spheres and sphere-clusters. For the majority of the simulations discussed here the spheres were either $3mm$ (or $3.78mm$) in diameter, and the drum diameter was 42 (or 33) sphere diameters (*i.e.*, $12.6cm$). The simulation region was bounded by the rotating cylinder in the x and y directions and periodic boundaries were employed in the direction of the drum axis. The length of the cylinder section simulated was approximately 5 particle diameters (5 spheres for the single-sphere simulations, and 10 spheres for the *cubic* sphere cluster simulations).

The threshold rotation rate that produced nearly steady flows with relatively uniform inclination angles was approximately $\frac{\pi}{2}\ rad/s$. (At this rotation rate the centrifugal acceleration acting on a particle near the wall was approximately 1.5% of the gravitational acceleration, and

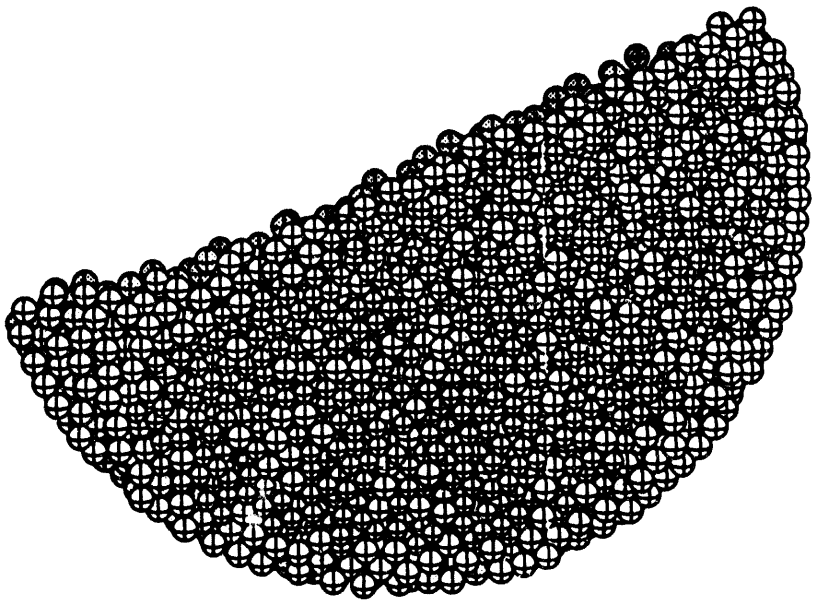

Figure 3.
Size segregation after slow partial rotation of drum containing an initially mixed assembly of 3*mm* and 3.78*mm* diameter spheres.

corresponds to a non-dimensional rotation rate, Ω_o, of 0.125, where $\Omega_o^2 = \omega_d^2 R_o/g$, ω_d is the rotation rate of the drum, R_o is the drum radius, and g is the acceleration of gravity). A variety of simulation calculations were performed at this rotation rate. Randomly mixed assemblies of two sizes of spheres, with diameters of 3*mm* and 3.78*mm* (*i.e.*, differing by a factor of 2 in volume) showed very rapid segregation in the radial drum direction. Figure 3 shows an instantaneous picture of the configuration after a rotation of just one complete revolution. The accumulation of large spheres at the toe of the incline and along the outer wall is quite evident. Similar behavior has been seen in 2-dimensional simulations of assemblies of discs [Ting & Corkum, 1988]. We obtained similar results in simulations with drums that were factors of 2 larger and smaller than the one shown in Fig. 3. These results are also consistent with the laboratory measurements of Altobelli *et al.* [1993] wherein radial direction segregation was observed to occur very rapidly in rotating drums containing binary distributions of mustard seed and also with sand.

In addition to radial segregation Nakagawa [1993] also observed segregation along the axis of the drum with alternating *stripes* of the different species appearing after several revolutions of the drum. One calculation was made to see if such *stripes* would occur in these simulated flows. The length of the simulated section was increased to approximately 50 sphere diameters, and the drum radius reduced to keep the total number of spheres at approximately 3000. After 10 simulated revolutions of the drum no axial segregation was evident. Nakagawa indicates that the segregation in his tests appears most often to originate at the ends of the drum, and he invariably obtains an odd number of stripes. The present simulations used periodic end conditions, and

thus, would not model any effects of real end walls rotating with the drum. Our very tentative conclusion is that it may be necessary to include rotating end walls in order to simulate axial segregation of binary distributions in slowly rotating drums.

Dynamic Angles of Repose

The coefficient of friction acting between particles was varied from 0.01 to 1.0 in a series of simulations examining the dynamic angle of repose of uniform sized spheres in a drum rotating at $\frac{\pi}{2}$ rad/s. Assemblies of spheres with very low coefficients of friction (*i.e.*, $\mu = 0.01$) exhibited slumping flows, wherein the entire granular load moves almost as a block back down the rising cylinder wall, even when the drum was 2/3 filled with spheres. Increasing the friction between the wall and the spheres (while leaving the interparticle interaction parameters fixed) still resulted in periodic slumping as a rigid body. The maximum static surface angle exhibited before slumping was approximately 10 degrees. Increasing the interparticle friction coefficient resulted in nearly steady circulating flows. Table 1 summarizes the angle-of-repose simulation results.

Table 1.
Simulated angle of repose, ϕ_r, obtained in 12.6cm diameter rotating drum simulations with interparticle friction coefficient, μ_p, and drum rotation rate, ω_d (rad/s), for uniform 3.78mm diameter spheres, ○, tetrahedral sphere clusters, △, and cubic sphere clusters, □.

μ_p	ϕ_r	ω_d	Shape
0.01	10°*	$\pi/2$	○
0.02	13°	$\pi/2$	○
0.1	23°	$\pi/2$	○
0.1	25°	π	○
0.2	25°	$\pi/2$	○
1.0	31°	$\pi/2$	○
1.0	35°	π	○
0.1	28°	$\pi/2$	△
0.1	35-39°	$\pi/2$	□

*(Maximum angle before rigid body slumping)

The exact role of friction on strength of granular assemblies and on the angle of repose has been the subject of much debate in the last 100 years (see discussion in Rowe, [1962 & 1969], and Horne, [1965]). The simulation results to date do not specifically confirm any of the existing theories. This is partially because most of the theoretical treatments have been concerned with shear strength of assemblies and have ignored rolling, a mode of motion that can play a key role in the stability of the free surface of an assembly of spheres. As we explore a wider range of material properties and flow conditions we expect to be able to make comparisons to both strength and repose measurements and theories and more clearly define the role of friction on both the shear strength and the angle of repose of assemblies of particles. A significant number of additional simulation calculations will be needed before the effects of shape can be adequately

quantified. The angle of repose for the cubic sphere-clusters of the last entry in Table 1 was somewhat uncertain because of the irregular nature of the inclined top surface an example of which is shown in Figure 4.

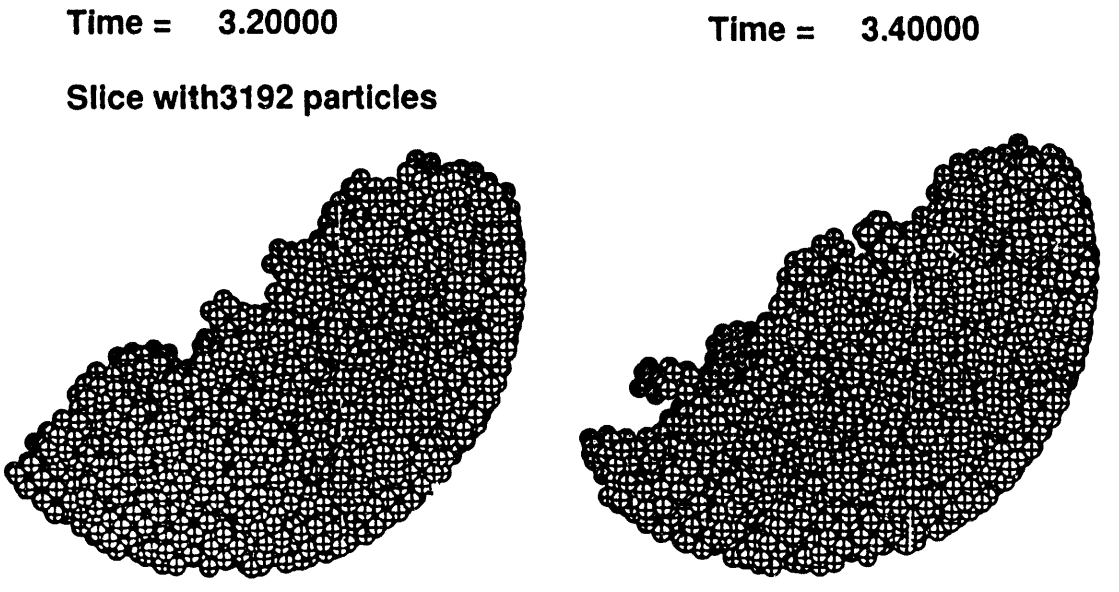

Figure 4.
Simulation with rigid 8-sphere clusters in cubical arrangement. Irregular surface makes estimate of angle of repose uncertain.

CENTRIFUGING DRUMS

When the rotation rate of a horizontal drum is fast enough for the centrifugal forces to be comparable to gravity, the character of the flow is changed considerably from the quasistatic flows discussed above. Figure 5 shows an instantaneous picture of the configuration in a simulation with a non-dimensional rotation rate, Ω_i, equal to 1.0, where $\Omega_i^2 = \omega_d^2 R_i/g$, ω_d and g are rotation rate and gavity, as before, and R_i is the radius of an imagined inner surface that would exist if all of the granular material were uniformly distributed around the circumference of the drum. At a rotation rate with $\Omega_i = 1.0$ the centrifugal force at the top of the drum just cancels gravity on a particle moving along with the outer wall, yet, as seen in Fig. 5, at this rotation rate the particles do not stay on the outer wall. Instead, they slide down the rising drum surface and also cascade in ballistic free-fall to a splash zone at the bottom of the drum. Such behavior is familiar to anyone who has run laboratory tests with granular materials in rapidly rotating drums (see, for example, Pitts [1983]). Rotation rates considerably higher than $\Omega_i = 1.0$ are required to keep a bed of granular material in continuous contact with the outer cylinder wall.

Single Frictional Particle Analysis

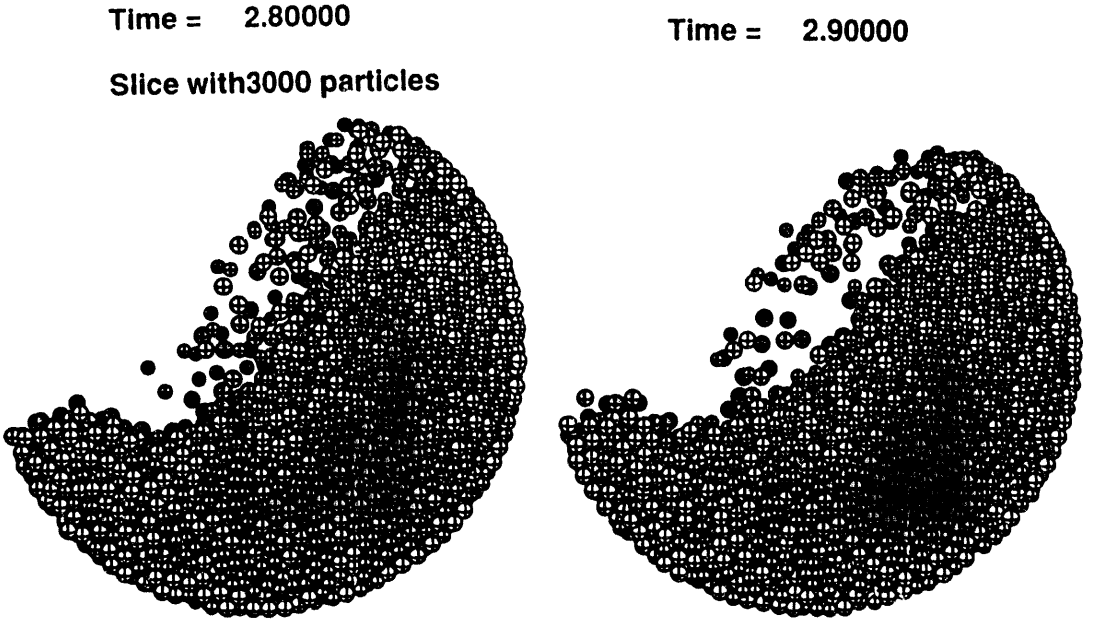

Figure 5.
Simulation of flow in a drum rotating at a rate that would cancel gravity if no slippage occurred, $\Omega_i = 1.0$. Particles interact with interparticle friction, $\mu = 0.2$, particle-wall friction, $\mu_w = 0.5$.

A simple two-body frictional contact analysis can be very useful in understanding the motion of particles on the inner surface of a centrifuging drum. Walton [1984] previously analyzed the motion of a single frictional particle on the interior frictional wall of a rotating horizontal cylinder. The numerical simulations in that previous work are essentially correct; however, the analytic form for the no-slip condition was flawed. We correct that analysis below.

The stability of particles located on the top surface of an inclined granular bed can be considered analogous to the stability of a single frictional block on an inclined plane. Whether the frictional block will remain stationary or will accelerate down the incline depends on whether the tangent of the angle of inclination of the plane is less than or greater than the coefficient of sliding friction between the block and the plane. Similarly, if the angle of inclination of a tipped granular bed exceeds the angle of repose, the top surface will flow down the incline. This is equivalent to noting that the flow is stable as long as, $\tan\alpha < \tan\phi_r$, where α is the inclination angle, ϕ_r is the angle of repose, and $\tan\alpha$ corresponds to the ratio of tangential to normal body forces due to gravity acting

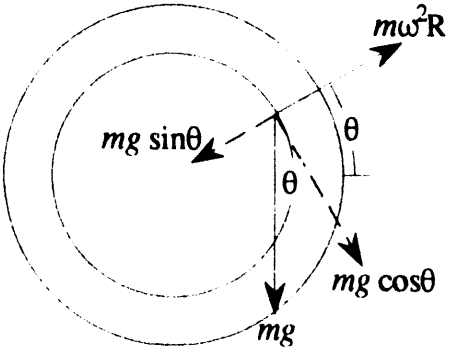

Figure 6.

on a particle on a plane inclined at the angle, α.

Extending this analogy to centrifuging flow in a horizontal rotating cylinder, we can determine the stability of a particle on the inner surface by examining the ratio of tangential to normal forces acting on it. Consider a two-dimensional view of a particle on the interior surface of a centrifuging granular bed in a rapidly rotating horizontal cylinder as shown in Figure 6, with the origin at the center of the cylinder and the polar angle, θ, measured from the horizontal. The force acting on the particle in the tangential direction, F_T, is given by

$$F_T = mg\cos\theta. \tag{24}$$

The force in the radial (*i.e.*, normal) direction, F_R, is given by

$$F_R = m\omega_d^2 R_i - mg\sin\theta, \tag{25}$$

where m is the mass of the particle, and all other variables are as previously defined. The ratio of tangential to normal force is,

$$\frac{F_T}{F_R} = \frac{\cos\theta}{\Omega_i^2 - \sin\theta} \tag{26}$$

where,

$$\Omega_i^2 = \frac{\omega_d^2 R_i}{g}, \quad \Omega_i > 1$$

We can differentiate Eqn. (26) with respect to θ to find the location of the extrema in the force ratio,

$$\frac{d}{d\theta}\left(\frac{F_T}{F_R}\right) = \frac{(\Omega_i^2 - \sin\theta)\sin\theta - \cos^2\theta}{(\Omega_i^2 - \sin\theta)^2} = \frac{\Omega_i^2\sin\theta - 1}{(\Omega_i^2 - \sin\theta)^2}\,. \tag{27}$$

Setting this derivative to zero, we find the circumferential location, θ_{max}, where the force ratio, (F_T/F_R), is a maximum,

$$\sin\theta_{max} = \frac{1}{\Omega_i^2}\,. \tag{28}$$

Substituting this into Eqn. (26) and rearranging we obtain an expression for the maximum value of the force ratio,

$$\left.\frac{F_T}{F_R}\right|_{\theta=\theta_{max}} = \tan\theta_{max}\,. \tag{29}$$

Based on the analogy with a single frictional particle, we would expect to have a *stationary* centrifuging bed with no movement of the surface particles with respect to the rotating drum (*i.e.*, no circumferential sliding) as long as

$$\frac{F_T}{F_R} < \tan\phi_r\,, \tag{30}$$

where ϕ_r is the angle of repose for the material. The maximum value reached by the ratio F_T/F_R during each revolution of the drum is given by Eqn. (29). Thus, we will have a stationary bed if

$$\tan\theta_{max} < \tan\phi_r\,. \tag{31}$$

From which it follows that no slip will occur as long as

$$\theta_{max} < \phi_r \ , \qquad 0 < \theta_{max} < \tfrac{\pi}{2} \ , \tag{32}$$

or, combining with Eqn. (28) and rearranging, we obtain an expression for the rotation rate necessary to ensure that *no slip* occurs on the inner surface of the centrifuging granular bed,

$$\Omega_i^2 > \frac{1}{\sin \phi_r} \ . \tag{33}$$

Equation (33) defines the boundary, for cohesionless granular materials in horizontal rotating cylinders, between a stationary centrifuging bed and a granular bed exhibiting small surface slippage on each revolution. Just because surface slippage occurs, however, does not mean that particles will lose contact with the bed or *rain* down into the open central region. Numerical simulations show that surface particles can experience slippage of as much as 1/8 radian on each revolution before their tangential surface velocity becomes so low that centrifugal forces are insufficient to maintain contact with the underlying granular bed.

Walton [1984] employed a numerical integration of the motion of a single frictional block on the inside of a rotating horizontal cylinder to determine the minimum rotation rate required to keep the block in continuous contact with the cylinder. He determined the dependence of that rotation rate on the coefficient of sliding friction acting between the block and the cylinder wall. The results were fit by an empirical relation,

$$\Omega_{min}^2 = \frac{\sqrt{2}}{2}\left(1 + \frac{1}{\mu + 0.125}\right) \ . \tag{34}$$

Identifying the friction coefficient, μ, in these single particle simulations with the tangent of the angle of repose for a granular bed, $\tan \phi_r$, it was hypothesized that this same relation would represent the boundary between *sliding* and *raining* flow for a granular bed in a rotating drum,

$$\Omega_{s/r}^2 = \frac{\sqrt{2}}{2}\left(1 + \frac{1}{\tan \phi_r + 0.125}\right) \ . \tag{35}$$

This hypothesis was partially corroborated by noting a laboratory test with sand in a drum rotating at a rate just below the minimum given by Eqn. (35) exhibited particles raining from the surface [Pitts, 1983; Walton, 1984]. Here we provide another piece of corroborating evidence by simulating a drum rotating at a rate just slightly faster than the minimum given by Eqn. (35) and obtaining slipping flow with no particles raining from the surface. Figure 7 shows two instantaneous configurations from this simulation; one after 5.5 complete revolutions of the drum and the other after 14 revolutions. Particles on the inner surface in this counterclockwise rotating drum slip a short distance down the rising bed each time they pass through the *2:00o'clock* to *11:00o'clock* zone. It took nearly 10 revolutions of the drum to accelerate an initially stationary bed to the point where all *loose* particles disappeared from the central region in this simulation.

Figure 8 summarizes the results of the centrifuging and single frictional particle flow analysis and simulations. The vertical axis is the square of the non-dimensional rotation rate, Ω_i^2, and the horizontal axis is the inverse of the sine of the angle of repose, ϕ_r, (or the inverse of the

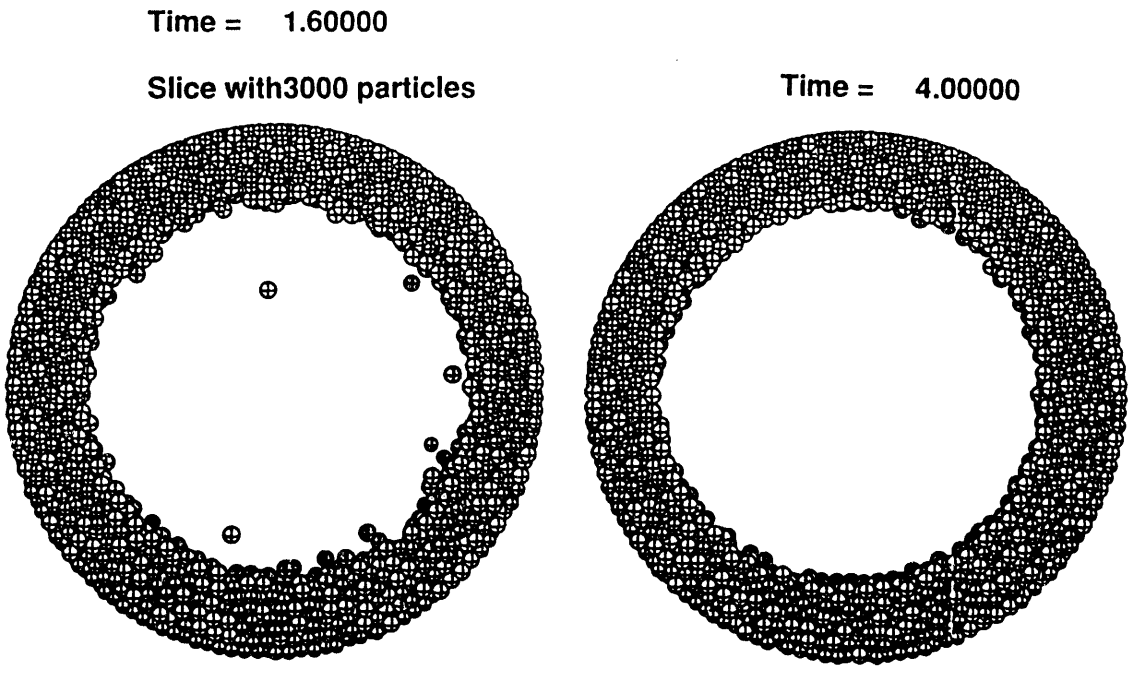

Figure 7.
Slipping flow, $\Omega_i^2 = 2.2$, $\mu = 0.2$, (a) after 5.5 revolutions of the drum and (b) after 14 complete revolutions, starting with the material stationary and the drum rotating.

sine of the friction angle for the single particle simulations). With this choice of axes, Eqn. (33) becomes a straight line demarking the boundary between stationary and sliding flows. The single particle simulations of Walton [1984], defining the boundary where particles lose contact with the wall, are plotted as open squares and triangles. The empirical curve, Eqn. (35), is shown as a dashed line. The raining sand experiment of Pitts is a filled circle and the slipping flow simulation of Fig. (7) is shown as an open circle. Also shown is the graph of an alternative empirical relationship for the bound between slipping and raining flow,

$$\Omega_{s/r}^2 = \frac{1}{\sin \phi_r'} , \tag{36}$$

where, ϕ_r' is an angle related to the angle of repose, ϕ_r, by the relation,

$$\tan \phi_r' = 0.16 + \tan \phi_r . \tag{37}$$

This empirical curve fits the majority of the single particle simulation results about as well as Eqn. (35); however, it appears to miss the last point on the right somewhat. Additional centrifuging assembly simulations are planned to test the validity of using the single particle simulation results, and thus, Eqn. (35) or (36) as the boundary between the raining and slipping flow conditions.

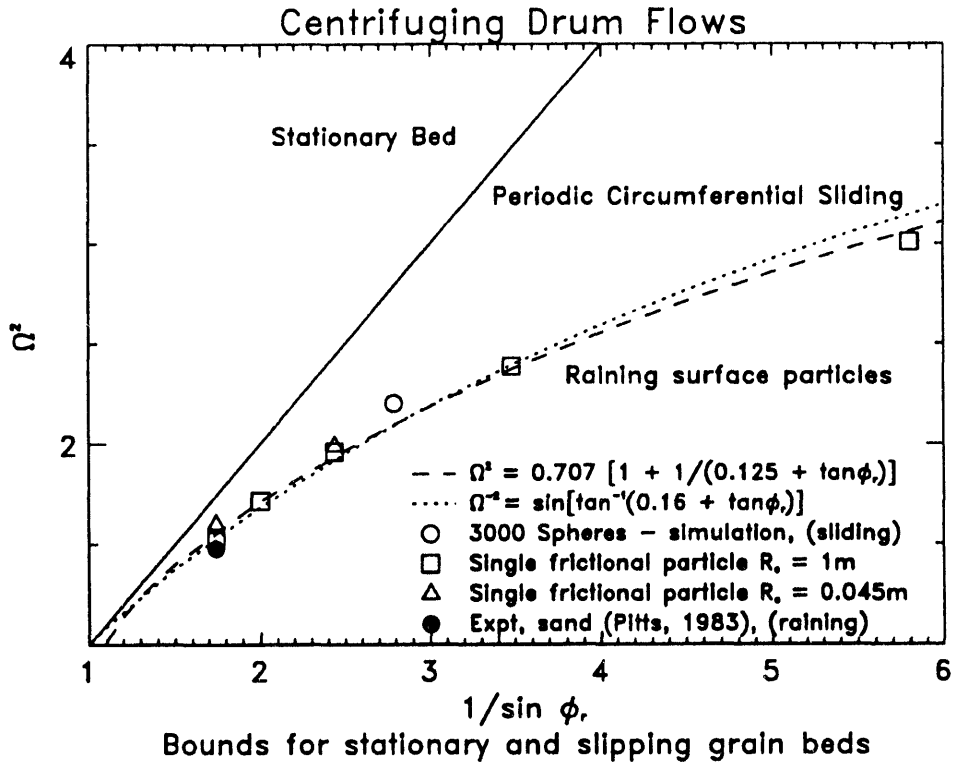

Figure 8.

CONCLUDING REMARKS

We have applied inelastic, frictional sphere models to the study of angles of repose and flows in rotating cylinders, demonstrating the significance of interparticle friction on both the angle of repose and on the slipping flow behavior in rapidly rotating drums. Analytic and empirical expressions demarking the boundaries between flow regimes in centrifuging drums are derived and/or hypothesized. These relations are consistent with experiments and simulations performed to date. We have applied the *rigid-polyatomic* approach of Evans & Murad to macroscopic granular systems and have confirmed that shape effects are as important as interparticle friction and, in some cases, are crucial to simulate in order to model observed behavior of real granular materials.

This paper is a status report of work in progress. The cylindrical outer boundary and the non-spherical particles are recent additions to our well established particle-dynamics capability. The simulations in this paper are the first exercises of those new capabilities. Some of the problems addressed here will require many additional simulation calculations in order to establish the form of expressions relating microscopic interparticle interaction parameters and measures of bulk flow behavior.

ACKNOWLEDGEMENT

This work was supported by the US Department of Energy, Office of Fossil Energy, Advanced Research and Technology Development under the Solids Transport Program administered by the Pittsburg Energy Technology Center. That support is gratefully acknowledged.

REFERENCES

Allen, M.P., and D.J. Tildesley (1987) *Computer Simulation of Liquids*, Clarendon Press, Oxford.

Altobelli, S.A., A. Caprihan, H. Cheng, E. Fukushima, M. Nakagawa, and L.Z. Wang (1993) "Progress Report: Granular Flow Studies by NMR," *DOE/NSF Workshop On Flow of Particulates and Fluids*, Plasynski, Peters, and Roco eds., Ithaca, NY.

Brown, R.L., and J.C. Richards (1970) *Principles of Powder Mechanics*, Pergamon Press, Oxford.

Cundall, P.A., and O.D.L. Strack (1979) "A Discrete Numerical Model for Granular Assemblies," *Geotechnique* **29**, 47-65.

De Jaeger, J. (1993) "Grain Shape and Size Influence on Low Stress Behavior Observing Discrete Avalanches in a Rotating Cylinder," *Powders and Grains 93*, Thornton (ed.), Balkema, rotterdam, ISBN 90 5410 323 X, p321-326.

Evans, D.J., and S. Murad (1977) "Singularity Free Algorithm for Molecular Dynamics Simulation of Rigid Polyatomics," *Mol. Phys.* **34**, p.327.

Goldstein, H. (1950) *Classical Mechanics*, Addison-Wesley.

Hashimoto, H., and R. Watanabe (1993) "Model Simulation of Impacting action of Milling Balls in Several Types of Ball Mills from Viewpoint of Mechanical Alloying," proceedings NEPTIS-1, Osaka, Japan, January 1993, Nisshin Engineering Co., Y.Tsuji, ed., p8-11.

Hockney, R.W., and J.W. Eastwood (1981) *Computer Simulation Using Particles*, McGraw-Hill, New York.

Hofstetter, K. (1993) personal communication, Caterpiller Inc., Peoria, IL.

Hoover, Wm.G. (1991) *Computational Statistical Mechanics*, Elsevier Sci. Pub., Amsterdam.

Horne, M.R. (1965) "The Behavior of an Assembly of Rotund, Rigid, Cohesionless Particles. I and II." *Proc. Roy. Soc.* **A 286**, 62 (Parts I and II); and Part III. *Proc. Roy. Soc.* **A 310**, 21-34 (1969).

Nakagawa, N., M. Hopkins, S. Altobelli, A. Caprihan, E. Fukushima, E.K. Jeong (1993) "Granular Flows in a Kiln: Non-Invasive MRI Measurements and Simulation," proceedings NEPTIS-1, Osaka, Japan, January 1993, Nisshin Engineering Co., Y.Tsuji, ed., p12-16.

Nakagawa, N. (1993) "Axial Segregation of Granular Flows in a Horizontal Rotating Cylinder," *Chem. Eng. Sci.* (Submitted).

Macrae, J.C., and W.A. Gray (1961) "Significance of the Properties of Materials in the Packing of Real Spherical particles," *Brt. J. Appl. Phys.* **12**, 164-172.

Mindlin, R.D. (1949) "Compliance of Elastic Bodies in Contact," *Trans. ASME, Series E, Journal of Appl. Mech.* **16**, 259.

Pitts, J. H., (1983) "Cascade Reactor," *Laser Program Annual Report 83*, Lawrence Livermore National Lab. Rept. UCRL-50021-83, p7-3.

Rowe, P.W. (1962) "The Stress Dilatancy Relation for Static Equilibrium of an Assembly of Particles in Contact," *Proc. Roy. Soc.*, **A 269**, 500-527.

Rowe, P.W. (1969) "Osborne Reynolds and Dilatancy," *Geotechnique* **19**, No. 1, 1-5.

Ting, J.M., and B.T. Corkum (1988) "Discrete Element Models in Geotechnical Engineering," in *Proceedings 3rd International Conference on Computing in Civil Engineering*, Vancouver, Canada, August 1988.

Tsuji, Y. (1993) private communication, Osaka, Japan.

Walton, O.R. (1982) "Explicit Particle Dynamics Model for Granular Materials," *Numerical Methods in Geomechanics*

Edmonton 1982, Z. Eisenstein, ed, A.A. Balkema, Rotterdam, Vol. 3, 1261-1268,

Walton, O.R. (1984) "Motion of Single Frictional Granules on Rotating Cylinders and Cones," *Laser Program Annual Report*, Lawrence Livermore National Laboratory Rept. UCRL-50021-84, p7.12 - 7.17.

Walton, O.R. (1993a) "Numerical Simulation of Inelastic Frictional Particle-Particle Interactions," *Particulate Two-Phase Flow* M. Roco, ed., Chap. 25, Butterworth-Heinemann, Boston.

Walton, O.R. (1993b) "Numerical Simulation of Inclined Chute Flows of Monodisperse, Inelastic, Frictional Spheres," *Mech. of Mat'ls* **16**, 239-247.

DIRECT NUMERICAL SIMULATION OF PARTICLE-TURBULENCE INTERACTION IN CHANNEL FLOW

Y. Pan, G. Hetsroni and S. Banerjee

Department of Chemical and Nuclear Engineering

University of California at Santa Barbara

ABSTRACT

This is a study of the interaction of dispersed solid particles with the turbulence in turbulent wall layer in a flume. The focus of the work is on horizontal channel flows (i.e. inhomogeneous in the wall-normal direction) because some puzzling and important phenomena have been recently discovered in the near-wall region. By using direct numerical solution of the incompressible Navier-Stokes equations for the continuous phase, with the effects of particles accounted for, a general methodology is developed to study the particle/turbulence interactions. This methodology is then applied to study: i) the effects of turbulent motion on particles with particle Reynolds number $Re_p << 1$ (Re_p is based on the particle's relative velocity in the fluid flow and the diameter of the particle), ii) the modification of turbulence by particles. The simulation is conducted for the cases of various particle sizes and particle loading, with gravity and without gravity. Based on the data obtained from numerical computations, Lagrangian and Eulerian statistics for both the fluid and the particles will be developed to study the macroscopic properties of two-phase dispersed flows and elucidate various existing modeling approaches. Also the data base will be used for visualization and animation. We are able to directly look into the details of particle-fluid motion and thus better understand the mechanisms involved in particle-turbulence interactions.

1. Introduction

The interaction between particles and turbulent flows provides a research topic of both fundamental importance and practical interest. Examples of applications are deposition of pollutants, fouling of surface, sedimentation and, the behavior of electrostatic precipitators. This topic consists of two problems: the first one is particle dispersion in turbulent flows with unmodified properties, called the "one-way" coupling problem. Physically, this situation is realized in very dilute flows with small particles e.g. flue gasses with fly ash. The problem has been investigated in a number of studies, but the experiments are difficult because particle trajectories must be followed, i.e. ideally it requires measurement in a Lagrangian reference frame. The second problem is to include the effects of particles on the turbulence structure itself, requiring measurements of how the turbulence gains (or loses) momentum in relation to the particles and how this in turn affects their trajectories. This interaction is referred to as "two-way" coupling.

Traditionally, the effects of particles are thought to act as an additional sources of dissipation and sometimes of turbulent kinetic energy. This view of turbulence modification by particles does not take into account the possible effects of turbulence structure on the resulting concentration field of particles. It was observed (Kaftori et. al 1993) that particles selectively are concentrated in certain regions by the turbulence structures such as quasi-streamwise vortices, and may cause rapid attenuation of the turbulence in those regions or trigger a new instability mechanism. Therefore, a related problem to that of turbulence modification by particles is the effect of the turbulence on the characteristics of the particle concentration field. All these effects are involved in the so called the two-way coupling problem.

The conventional modeling approach is usually to deal with some form of averaged conservation equations--ensemble or volume, or volume/ensemble double averages may be chosen depending on the problem. However, averaging removes information regarding local gradients, leading to closure requirements. Such closure relationships are usually semi-empirical and are meant to give mass, heat, and momentum transfer between phases, and correlations between fluctuations in these quantities (Reynolds-stress like terms). The averaged equations may be phrased in a manner such that the flow is viewed as interpenetrating continua or, for dispersed flow, the continuous phase calculated in a Eulerian frame with the particles being moved in Lagrangian coordinates. Whatever the mathematical structure of the model, one needs to know how the particles follow turbulent fluctuations and, in many cases, how the particles affect turbulence properties.

The present research is meant to elucidate these issues by studying turbulent flows containing particles by direct numerical simulation. Such simulations, if they are well verified in their main features by comparison with experiment, can provide information that is difficult to obtain experimentally. For example, direct numerical simulations of channel flows have been verified in a number of studies by comparison with experimental data on turbulence intensities, Reynolds stresses, streak spacing, burst frequencies, etc., and may be used to obtain Lagrangian correlation functions--quantities that give rise to formidable measurement problems but which are fundamental to an understanding of diffusion.

For the purposes of this investigation, we study particle-turbulence interactions near boundaries in a channel flow. There are two major objectives of this numerical study. One is to clarify the

mechanism of interaction between particles and turbulence structures in the wall region. Another is to contribute information base on which the simplified models may be developed. Both of these goals are very difficult, if not impossible, to achieve by either experimental or theoretical approaches alone.

There is a few number of experimental studies on particle motion in flow involving the studying particle effects on fluid. Rashidi et al. (1990), indicated that fairly large polystyrene particles, which are slightly heavier than fluid, about 5 to 10 wall units in diameter (non-dimensionalized with shear velocity and kinematic viscosity) increase the frequency of ejections, giving rise to corresponding increases in turbulence intensities and Reynolds stresses (understandable, since ejections and in-sweeps account for 60-80% of the Reynolds stresses). The particle loading can be very low (10^{-4}) for these effects to show, probably because the particles seem to concentrate in the low-speed streaks. Conversely, particles of 1 wall unit or less in diameter reduce ejection frequency and damp turbulence--again the effect shows at low loadings with increases in loading increasing the effect. The particles also tend to accumulate in the low-speed streaks, though the effect of particle size is not completely clear from the experiments. If the particle velocity and the fluid velocity at any point away from the wall is averaged, then differences in the average fluid velocity and particle velocity are found. However, this is not due to the instantaneous relative velocity between the particles and the fluid, but because the particles accumulate in the low-speed streaks and are ejected with low momentum fluid, i.e. they are associated usually with low streamwise momentum region of the flow since they are flung upwards with the ejections.

The questions related to why the particles go preferentially to the low-speed streaks and how this phenomenon depends on particle time constant, and then why the relatively large particles trigger ejections whereas the small particles damp ejections, remain unanswered.

Similarly, in homogeneous flows it has been found that large particles tend to enhance turbulence, whereas small particles suppress turbulence (see Hetsroni 1989, 1991 and Tsuji 1991 for reviews of experimental data). The conventional explanation has been that vortex shedding accounts for the the increase by large particles, whereas the small particles increase effective viscosity and hence increase the dissipation. However, it is known from several studies that heavier-than-fluid particles tend to accumulate preferentially in the vorticity/high strain rate regions-the tendency being influenced by the relative density between the fluid and particle, and the relative time constants for particle response to drag compared to that for the turbulence. Whether such heterogeneities in the particle concentration field are an important mechanism for the modification in turbulence intensities seen in experiments remains an open question. Thus a somewhat similar issue to the one discussed in the preceding paragraph exists even for homogeneous turbulence.

Yeh and Lei (1991a and 1991b) numerically simulated the small particle motion in homogeneous isotropic and homogeneous turbulent shear flow. They used the large eddy model to solve the turbulent flow field. They considered only one-way coupling problem. It focused on the effect of particle's inertia and particle free-falling velocity in still fluid on particle dispersion and settling velocities. Papanicolaou and Zhu (1991) investigated the two-dimensional, dilute fluid-particle system. A vortex method was used to calculate the fluid phase. The particle-fluid interaction was handled by adding a body force term into the Navier-Stokes equation. This body force term was calculated by the averaged particle relative velocity and the averaged particle concentration function. The Stokes solution was used in particle motion calculation, and the flow was laminar. McLaughlin (1989) studied small particle deposition in channel flow by direct numerical simulation. He studied only a one-way

coupling problem. Squires and Eaton studied (1990a, 1990b) the particle-fluid interaction in a homogeneous turbulent flow. They also added a body force term to account for the modification of particles on the fluid. Elghobashi and Truesdell (1992, 1993) studied the particle dispersion and particle-fluid interaction in the homogeneous turbulence. Again, they handled the particle-fluid interaction by acting the forces, due to the particles in the unit volume, on the fluid, as an additional body force. Some changes in the turbulence energy and turbulence dissipation have been observed.

In these studies, the particle-fluid interaction is either not considered (i.e. one-way coupling) or handled by an averaged way. The modified Navier-Stokes equation, used in these studies, is in a form like

$$\frac{\partial \vec{u}}{\partial t} + \vec{u} \cdot \nabla \vec{u} = -\frac{\nabla p}{\rho} + \nu \nabla^2 \vec{u} - \frac{\alpha C}{\rho}(\vec{u} - \vec{V}) \tag{1}$$

Here $\vec{V}$ is the averaged particle velocity vector in unit volume of fluid, C is the particle concentration α is a drag coefficient due to Stokes solution of a single particle motion in creeping flow. In the above equation the last term is the so called "particle-source" term. It appears like an additional body force acting on fluid. Then C and $\vec{V}$ are calculated either by Lagrangian method (following the particles) or by the macroscopic conservation of mass and momentum of particle phase,

$$\frac{\partial C}{\partial t} + \nabla \cdot (C\vec{V}) = 0 \tag{2}$$

$$\frac{\partial \vec{V}}{\partial t} + \vec{V} \cdot \nabla \vec{V} = \beta(\vec{u} - \vec{V}) \tag{3}$$

in which β is a constant involving the drag coefficient and the particle concentration. Obviously, by doing this, particles, which are discretely distributed in the fluid, are smeared into fluid, i.e. they are treated as a continuous media. This is equivalent to solving a two-fluid problem, and is the weakness of this approach, since the forces acting on the fluid by the particles have a distribution and can not be treated as a point-force. The smallest length scale of the turbulence, the Kolmogorov scale, which is inversely proportional to the flow Reynolds number, may be comparable to the particle size, at high Reynolds number. When this scale does not contain enough particles for averaging, the above model breaks down. Therefore, this model, though it can give significant results of particle distribution, is not capable to capture the mechanism of particle-fluid interaction, particularly in the case of dilute mixture, large particles and in the wall region where the coherent structure of turbulence exist.

In this study, the effect of each particle on the fluid is individually back to the fluid field. By assuming that the relative motion between each particle and the fluid motion in the particle's vicinity is within the Stokes regime, the disturbance velocity field due this relative motion is linear added on the fluid velocity field around the particle. The motion of each particle is traced by the Lagrangian method. This approach and the numerical scheme are discussed in the following sections.

2. Methodology

2.1 Direct simulation of turbulent flow in open channel

We solve time-dependent, three-dimensional, incompressible, continuity and Navier-Stokes equations. The computational domain for the simulation is shown in Fig. 1. The streamwise direction is denoted by x_1 (or x), the spanwise by x_2(or y), and the wall-normal direction by x_3 (or z), and the velocity components u_1 (or u), u_2 (or v), u_3 (or w), correspondingly. The flow is driven by a constant streamwise pressure gradient. Periodic boundary conditions are imposed in x_1 and x_2 directions, and no-slip boundary condition is applied at the wall, while at the free surface, the free-shear boundary condition is imposed. All the quantities are normalized with the effective velocity and the half-depth of the channel. The effective velocity is defined by the pressure gradient as, $u^{*2} = |dp/dx|h/\rho$, where dp/dx is the mean pressure gradient, ρ is fluid mass density, h is the half-depth of the channel. The effective Reynolds number is then defined as, $Re = (u^* h)/\nu$, where ν is the fluid viscosity. The velocity, length and time are scaled by u^*, h and h/u^*, respectively. The non-dimensional continuity and Navier-Stoke equations for incompressible fluid are:

$$\frac{\partial u_i}{\partial x_i} = 0 \tag{4}$$

$$\frac{\partial u_i}{\partial t} = S_i + \frac{1}{Re}\nabla^2 u_i - \frac{\partial p}{\partial x_i} \tag{5}$$

$$S_i \equiv -\frac{\partial (u_i u_j)}{\partial x_j} + \delta_{i1} \tag{6}$$

The pressure term is eliminated by taking the curl of the momentum equation

$$\frac{\partial \omega_k}{\partial t} = \varepsilon_{ijk}\frac{\partial S_j}{\partial x_i} + \frac{1}{Re}\nabla^2 \omega_k \tag{7}$$

A fourth-order equation can be obtained by taking the curl of above equation again,

$$\frac{\partial}{\partial t}(\nabla^2 u_i) = \nabla^2 S_i + \frac{\partial}{\partial x_i}(\frac{\partial S_j}{\partial x_j}) + \frac{1}{Re}\nabla^4 u_i \tag{8}$$

The procedure we followed is to solve the normal velocity u_3 and vorticity ω_3 first, through the following two equations,

$$\frac{\partial \omega_3}{\partial t} = \frac{\partial S_2}{\partial x_1} - \frac{\partial S_1}{\partial x_2} + \frac{1}{Re}\nabla^2 \omega_3 \tag{9}$$

$$\frac{\partial}{\partial t}(\nabla^2 u_3) = \nabla^2 S_3 - \frac{\partial}{\partial x_3}(\frac{\partial S_j}{\partial x_j}) + \frac{1}{Re}\nabla^4 u_3 \tag{10}$$

Later, the continuity equation and the definition of vorticity are used to solved the streamwise and spanwise velocity u_1, and u_2,

$$\frac{\partial u_1}{\partial x_1} + \frac{\partial u_2}{\partial x_2} = -\frac{\partial u_3}{\partial x_3} \tag{11}$$

$$\frac{\partial u_2}{\partial x_1} - \frac{\partial u_1}{\partial x_2} = \omega_3 \tag{12}$$

Then the pressure can be obtained by solving the following Poisson equation,

$$\nabla^2 p = \frac{\partial S_i}{\partial x_i} \tag{13}$$

A pseudo-spectral method is employed to solve the problem. In the homogeneous directions (x_1, x_2), all the quantities are expressed in a Fourier expansion. In the normal direction x_3, which is non-homogeneous, they are represented by Chebyshev polynomials, i.e.

$$f(x_1, x_2, x_3, t) = \sum_{k_1}\sum_{k_2}\sum_{n} \hat{f}(k_1, k_2, n, t) e^{i(k_1 x_1 + k_2 x_2)} T_n(x_3) \tag{14}$$

Time advancement of the equations is done by the two-level explicit Adams-Bashforth scheme for the convective terms and by the implicit Crank-Nicolson method for the diffusion terms. All the calculations are carried out in wave space except that the evaluation of the non-linear terms $\hat{S}_i$ which is done in real space and then transformed back to wave space in order to avoid the convolution sum which reduces the efficiency of the method. This method has become a standard method for directly simulating the turbulent flows in domains of simple geometry such as rectangular channels. A full description of the numerical scheme can be found in Lam & Banerjee (1988, 1992) and Lam (1989).

2.2 Equation of particle motion

No prediction of the dispersion characteristics of solid particles in turbulent flows can be accurately made without a valid description of the equation of motion for a single particle. This is especially important for particles in unsteady and non-uniform turbulent flow fields.

Assuming the particle Reynolds number, which is based on the particle diameter and relative velocity of particle to the fluid, is smaller than one, the most general form of the equation of motion is

$$m_p \frac{d\vec{V}}{dt} = 6\pi a\mu(\vec{U} - \vec{V})f(H) + m_f \frac{D\vec{U}}{Dt} + \frac{1}{2} m_f \frac{d}{dt}(\vec{U} - \vec{V})$$

$$+ 6\pi a^2 \mu \int_{t_0}^{t} d\tau \frac{\frac{d}{d\tau}(\vec{U} - \vec{V})}{[\pi\nu(t-\tau)]^{0.5}} + (m_p - m_f)\vec{g} \tag{15}$$

in which, m_p is the mass of the particle, a is its radius, μ is the fluid viscosity, $\vec{U}$ is the undisturbed fluid velocity at the particle position, $\vec{V}$ is the particle velocity, f(H) is the coefficient of wall effect to the Stokes drag, H is the distance from the center of particle to the wall, m_f is mass of fluid displaced by the particle, $\vec{g}$ is gravitational constant with direction pointing towards the wall, d/dt is the time rate of change following the particle, D/Dt is the total acceleration of the fluid as seen by the particle, $Du_i/Dt = (\partial u_i/\partial t) + u_j(\partial u_i/\partial x_j)$, evaluated at the particle position $\vec{x}_p$. The physical meaning of each term on the right hand side of above equation are, Stokes viscous drag, pressure gradient and viscous stresses of the undisturbed fluid, added mass force, the Basset history term and gravitational force respectively.

As a particle moves close to a solid wall, the well known Stokes drag formula, which is for a spherical particle going through a uniform flow in an unbounded medium, should be modified to include the wall effect. Within an accuracy to the order of $O([a/H]^5)$, the coefficient of wall effect is given as (Kim & Karrila 1991)

$$f(H) = \frac{1}{1 - (9/16)(a/H) + (1/8)(a/H)^3} \tag{16a}$$

and

$$f(H) = \frac{1}{1 - (9/8)(a/H) + (1/2)(a/H)^3} \tag{16b}$$

(16a) is for for a particle moving parallel to the wall, and (16b) is for a particle moving perpendicular to the wall.

For particle motion in turbulent flow in an open horizontal channel, the wall unit is commonly used to normalize the equations. The characteristic length scale, time scale and velocity scale are, $u_\tau = (\tau_w/\rho_f)^{1/2}$, $l_\tau = \nu/u_\tau$, and $l_\tau = \nu/u_\tau$. τ_w denotes the time-averaged wall shear stress. The characteristic length of the channel flow is the order of magnitude of the Kolmogorov scale. The system of units based on u_τ and ν/u_τ will be referred to as "wall units", with a + as the superscript.

By normalizing the quantities in wall unit, the equation of motion of a particle becomes,

$$\frac{d\vec{V}}{dt} = \frac{1}{\tau^+_p}(\vec{U} - \vec{V})f(H) + \frac{1}{2}\frac{\rho_f}{\rho_p}\frac{d}{dt}(\vec{U} - \vec{V}) + (1 - \frac{\rho_f}{\rho_p})\frac{1}{Fr^2}\hat{g}$$

$$+ \frac{\rho_f}{\rho_p}\frac{D}{Dt}\vec{U} + \frac{a}{\tau_p \pi^{0.5}}\int_{t_0}^{t}\frac{\frac{d}{d\tau}(\vec{U} - \vec{V})d\tau}{(t-\tau)^{1/2}} \tag{17}$$

Here τ^+_p is the particle time constant (in wall unit) defined as,

$$\tau^+_p = \frac{2}{9}(\frac{\rho_p}{\rho_f})(a^+)^2 \tag{18}$$

Fr is the Froude number defined as,

$$F_r = \frac{u_\tau}{(g\frac{\nu}{u_\tau})^{1/2}} \tag{19}$$

It is well known that (17) has no exact solution, except for a trivial case, even in its simplest form in which all but the first term on the right-hand side vanish. This is due to the nonlinearity originating from the need to evaluate the fluid velocity, $\vec{U}$, at the yet unknown particle position. The trivial case that has an exact solution is that of an invariant and uniform fluid velocity, i.e the flow can not be turbulent. Therefore, in order to get correct and accurate information of particle dispersion in turbulent flow, each term in (17) has to be examined for various cases. A number of investigations have been made for particle dispersion in isotropic and homogeneous turbulent flows. In most of these studies, the particles are much heavier than the fluid, like copper in air. So it is reasonable to neglect

the added mass, pressure gradient and Basset terms which are proportional to the ratio of fluid density to particle density. Since here we investigate the particle dispersion and suspension in turbulent flow in a horizontal open channel, the density of the particles needs to be equal to or only slightly greater than that of the fluid. Under this circumstance, the relative importance of each term in the equation of motion is still unclear. However, to have proper statistics of particle motion, one needs to follow thousands to hundreds of thousands of particles, and if all the terms are included, a huge amount of computer memory and time may be required. From the computational point of view, the most difficult term is the Basset term.

The majority of the Lagrangian computations have been made for situations where the Basset term is small in comparison with other terms. Therefore, this term is usually neglected, which is very convenient, reducing the order of the differential equation and making it explicit in the velocity, and diminishing the memory requirements of the computations by not retaining information on the history of the acceleration of the particle. Only a few studies (Thomas 1992) investigated the effect of Basset force on particle dispersion. It seems that the Basset term makes only a small contribution to the particle long-time dispersion due to the fact that Basset term decays as $(t-\tau)^{-1/2}$ at long times. A study (Mei et al. 1991) found that the functional form of the Basset term is incorrect since it implies that a difference in the initial condition of the particle gives a finite effect on the dispersion at long times, which is clearly unphysical. It was proven that the Basset term should have a form which decays much faster than $(t-\tau)^{-1/2}$ at long times. Based on these arguments, it may be acceptable to neglect the Basset term. At present, we include the Stokes drag, the added-mass force, the pressure-gradient force and the gravitational force in the numerical simulation. The final expression for the equation of motion of particles is,

$$\frac{d\vec{V}}{dt} = \frac{1}{\tau^{+}_{p}}(\vec{U}-\vec{V})f(H) + \frac{1}{2}\frac{\rho_f}{\rho_p}\frac{d}{dt}(\vec{U}-\vec{V}) + \frac{\rho_f}{\rho_p}\frac{D\vec{U}}{Dt} + (1-\frac{\rho_f}{\rho_p})\frac{1}{Fr^2}\hat{g} \qquad (20)$$

However, the relative importance of each force and their effect on particle dispersion and suspension under different particle size is still an unclear issue, particularly in turbulent channel flow. Therefore, as a part of this research, an investigation of this issue will be carried out.

2.3 Computation of particle trajectories

The integration of (20), via a second-order Adams-Bashforth scheme provides the new velocity, $V_i(t)$, in the x_i-direction for each particle as a function of time. In order to keep consistency with the computation of fluid field, we use u_*, h and h/u_* to rescale (20), and rearrange it into a form as,

$$(1+\frac{1}{2}C_p)\frac{d\vec{V}}{dt} = \frac{9C_p}{2a^2\,Re_*}f(H)(\vec{U}-\vec{V}) + C_p\frac{D\vec{U}}{Dt} + \frac{1}{2}C_p\frac{d\vec{U}}{dt} + \frac{1-C_p}{Fr^2}\vec{e_g} \qquad (21)$$

in which, $C_p = \rho_f/\rho_p$, a is the nondimensional radius of the particle (scaled by half depth of the channel h), $\vec{e_g}$ is the unit vector in the direction of gravity. The Froude number Fr is defined as,

$$Fr \equiv \frac{u_*}{(gh)^{1/2}} \qquad (22)$$

Particle velocity at time step (n+1) is evaluated through an explicit scheme by knowing the values of $\vec{V}$ and $\vec{U}$ at step (n) and (n-1). It is necessary to evaluate the instantaneous fluid velocity $\vec{U}$ at the location of the particle accurately. We compute this velocity via a three-dimensional cubic spline

interpolation scheme between the adjacent Eulerian fluid velocity values. This scheme is applied in the three coordinate directions at the particle location. Once the particle velocity at new time step (n+1) has been calculated, The new position of the particle, $x_{p,i}(t)$ is calculated as,

$$x_{p,i}(t_{n+1}) = x_{p,i}(t_n) + \frac{1}{2}\Delta t[V_i(t_{n+1}) + V_i(t_n)] \tag{23}$$

where t_n is the time at the previous time step, and $\Delta t = t_{n+1} - t_n$.

The fluid velocity $U_i[x_{p,i}(t)]$ at the particle location (initially, the velocities of the coincident fluid and particle are assumed equal), which is needed to integrate (24) is obtained by a fourth-order accurate , three-dimensional cubic spline interpolation scheme between the adjacent Eulerian fluid velocity values. This scheme is applied in the three coordinate directions at the particle position.

We start the computation of particle trajectories by uniformly distributing a number of particle within the computational domain. The initial velocity of each particle is assumed to be equal to the fluid velocity at the same location. We then integrate (21) in the three coordinate directions to obtain the subsequent particle velocity, and calculate the new position from (23). The magnitude of the time step Δt is bounded by the resolution needed to compute accurate trajectories. This accuracy requires Δt to be much smaller than the particle time constant τ_p, and consequently the three-dimensional velocity field of the fluid needs to be stored at intervals equal to Δt.

2.4 Particle effect on fluid flow

As a solid particle translates through a flow field, it changes the undisturbed velocity field. In order to feed the particle effect back to the fluid, we proposed a method, called the method of disturbing velocity, described as follows. At some time instant, $t = t_n$, the fluid velocity field $\vec{u}(t_n)$ has been generated by solving equations (4) and (5). Knowing the particle velocity and particle position from (21) and (23) at the same time step, we calculate the disturbing velocity field due to each particle $\vec{V}_{dis}$. Then we superimpose the disturbance velocity, due to the presence of each particle, onto the background of undisturbed velocity field. So that the modified fluid velocity is obtained by,

$$\vec{u}(t_n)_{modi} = \vec{u}(t_n) + \sum_n \vec{V}_{dis,n}(t_n) \tag{24}$$

This modified fluid velocity field is then put back into the Navier-Stokes equation solver to generate the field for next time step. The disturbance velocity from each particle is calculated as a local Stokes flow by assuming the relative motion of particle and surrounding flow is in the Stokes regime. It is also assumed that the particulate phase is dilute, and the particle-particle interactions are neglected, and linear superposition is adopted. Since the particles are really moving in a non-uniform flow, this method is an approximation only. In the following paragraph, we validate our assumption and give the conditions under which this assumption is valid.

The well-known Stokes theory of the velocity field around a sphere is based on the assumption that the incoming flow is uniform, which is not the case in turbulent flows. Therefore, the problem now is to solve the velocity field around a solid sphere moving through a nonuniform, known flow field. The equations, scaled by d_p, the diameter of the sphere and U_0, a typical incoming velocity, are expressed as,

$$\nabla \cdot \vec{u} = 0 \tag{25}$$

$$\vec{u} \cdot \nabla \vec{u} = -\nabla p + \frac{1}{Re_p} \nabla^2 \vec{u} \tag{26}$$

$$\vec{u} = 0 \quad \text{at the surface of the sphere}$$

$$\vec{u} = \vec{u}_0(\vec{x}) \quad \vec{x} \text{ at } \infty$$

Here Re_p is the particle Reynolds number,

$$Re_p \equiv \frac{U_0 d_p}{\nu} \tag{27}$$

According to the theory of asymptotic expansion, in the limit of Re_p approaching zero, the solution of (26) can be approximated as,

$$\vec{u} = \vec{u}^{(0)} + O(Re_p) \tag{28}$$

$\vec{u}^0$ is the first order approximation of $\vec{u}$. It is simply the solution of the Stokes problem,

$$\nabla \cdot \vec{u}^{(0)} = 0 \tag{29}$$

$$\nabla p^{(0)} = \mu \nabla^2 \vec{u}^{(0)} \tag{30}$$

The solution of the above equations is just the well-known Stokes solution. If this solution is to be used as the disturbance velocity, one needs to validate it as being the first approximation to non-uniform incoming flow.

The next order of approximation takes the nonuniformity of the incoming flow into account. Since the particle is small compared with the length scale variation in the undisturbed flow, the incoming flow can be approximated as a linear shear flow,

$$u_0 = U_0 + Gx \tag{31}$$

Here G is the shear rate. Now the second order problem for the disturbance velocity becomes,

$$(U_0 + Gx) \frac{\partial \vec{u}}{\partial z} + G u_1 \vec{e}_3 = -\frac{1}{\rho} \nabla p + \nu \nabla^2 \vec{u} \tag{32}$$

$$\nabla \cdot \vec{u} = 0 \tag{33}$$

It has been shown that the solution to this problem is (McLaughlin 1991),

$$\vec{u} = \vec{u}^{(0)} + Re_G^{1/2} \vec{u}^{(1)} \tag{34}$$

where Re_G is the particle shear Reynolds number defined as,

$$Re_G \equiv \frac{G d_p^2}{\nu} \tag{35}$$

Therefore, the disturbance velocity due to the particle can be expressed in an asymptotic expansion,

$$\vec{u} = \vec{u}^{(0)} + Re_G^{1/2} \vec{u}^{(1)} + O(Re_p, Re_G) \tag{36}$$

If the following conditions

$$Re_p < 1 \tag{37}$$

$$Re_G < 1 \tag{38}$$

are satisfied, $\vec{u}^0$ is a good approximation of $\vec{u}$. In other words, if the conditions (37) and (38) are met, the Stokes solution is the first approximation of the velocity field around a sphere in a nonuniform incoming flow. Condition (37) is satisfied if particle size is small enough. The particle shear Reynolds number, Re_G, can be rewritten as,

$$Re_G \equiv \frac{G d_p^2}{\nu} \equiv U_0 \frac{d_p^2}{\nu \eta} \equiv Re_p \frac{d_p}{\eta} \tag{39}$$

where η is the smallest length scale in turbulent flow. If the particle size d is smaller or comparable to η, the condition (38) is also satisfied.

Therefore we use $\vec{u}^0$ as the disturbance velocity and superimpose it on the undisturbed velocity field. This implies capturing the leading order of changes in the flow due to the presence of the particles. It is similar to the procedure of asymptotic expansion in which, the zeroth order solution is obtained first, and then substituted into the original equations to get the next order solution by gathering the terms of the same order. In our numerical simulation, the zero order solution to the disturbance field is introduced into the flow, and the numerical scheme handles the higher order terms. It should be emphasised that the inaccuracy introduced by using this method is of the higher order of $O(Re_p)$ and $O(Re_G)$.

2.5 Particle disturbing velocity

As validated in the last section, we adopted a local Stoke solution for the disturbing velocity field generated by each particle. The particle is treated as a point in the fluid field, which generates a disturbance velocity due to the motion relative to the surrounding fluid. This disturbance velocity is the solution of the creeping flow problem,

$$\nabla \cdot \vec{v} = 0 \tag{40}$$

$$\mu \nabla^2 \vec{v} = \nabla p \tag{41}$$

The disturbance velocity, which depends on the particle's relative velocity and particle's location, is calculated at each time step and then is used to perturb the fluid velocity around particle. This is the way we handle the coupling between small particle and fluid.

The theory of creeping flow around a particle and particle-wall interaction had been well established in microhydrodynamics (Kim & Karrila 1991). The disturbance velocity due to a particle moving in an infinite space is

$$\vec{v} = \frac{3}{4} a\vec{U} \cdot (1 + \frac{a^2}{6} \nabla^2)\bar{G}(\vec{x} - \vec{x}_p) \tag{42}$$

in which, $\vec{U}$ is the particle's relative velocity, a is the particle's radius, and $\vec{x}_p$ is the particle position, $\vec{x}$ is the position of the point of interest, as shown in Fig.2. $\bar{G}$, the Oseen tensor, is given by,

$$G_{ij} = \frac{1}{r} \delta_{ij} + \frac{1}{r^3} x_i x_j$$

$$\nabla^2 \cdot \bar{G} = \frac{2}{r^3} \delta_{ij} - \frac{6}{r^5} x_i x_j$$

$$r^2 = \sum_{i=1}^{3} (x_i - x_{pi})^2$$

When a particle moves close the wall, an additional term should be added to (42) to include the wall effects (Kim & Karrila 1991). A method of reflection is adopted here. As shown in Fig. 3, a mirror image of the particle is added at the other side of the wall to cancel the velocities on the wall. At the first reflection on the wall, the disturbing velocity from the mirror image is simply the image system for the Stokeslet and the degenerate quadrupole,

$$\vec{v}_* = \vec{F} \cdot \bar{G}(\vec{x} - \vec{x}_*) + 2H[(\vec{F}_1 - \vec{F}_2) \cdot \nabla]\vec{n} \cdot \bar{G}(\vec{x} - \vec{x}_*)$$

$$- H^2(\vec{F}_1 - \vec{F}_2) \cdot \nabla^2 \bar{G}(\vec{x} - \vec{x}_*) + 4(\vec{n} \cdot \nabla)^2(\vec{Q}_1 + \vec{Q}_2) \cdot \bar{G}(\vec{x} - \vec{x}_*)$$

$$- 2H(\vec{n} \cdot \nabla)(\vec{Q}_1 - \vec{Q}_2)\nabla^2 \cdot \bar{G}(\vec{x} - \vec{x}_*) - (3\vec{Q}_1 - \vec{Q}_2) \cdot \nabla^2 \bar{G}(\vec{x} - \vec{x}_*)$$

$$-8 (\vec{n} \cdot \nabla) (\vec{Q}_2 \times \vec{n}) \times \nabla \frac{1}{|\vec{x} - \vec{x}_*|} \tag{43}$$

in which, $\vec{x}_*$ is the mirror point of $\vec{x}_p$, $\vec{n}$ is the normal unit vector of wall, pointing into the fluid. $\vec{F}_1$ and $\vec{F}_2$ are the the vectors parallel and perpendicular to the wall, respectively, $\vec{Q}_1$ and $\vec{Q}_2$ are defined

as

$$\vec{F}_1 + \vec{F}_2 = \frac{3}{4} a\vec{U} \tag{44}$$

$$\vec{Q}_1 + \vec{Q}_2 = \frac{a^2}{6} (\vec{F}_1 + \vec{F}_2) \tag{45}$$

Now we are able to use the total disturbance velocity,

$$\vec{v} = \frac{3}{4} a\vec{U} \cdot (1 + \frac{a^2}{6} \nabla^2)\vec{G}(\vec{x} - \vec{x}_p) + \vec{v}_* \tag{46}$$

to modify the fluid velocity at each collocation point by superimposing $\vec{v}$ on the undisturbed fluid velocity $\vec{u}$.

3. Validation of numerical scheme

The validation of the numerical implementation consists of three part, force acting on the particles, the disturbance velocity and the particle's trajectory.

3.1 Stokes Drag Force With Wall Correction

In order to validate the drag force acting on the particle, a numerical study had been carried out for a sphere at various distance from a wall under a linear shear incoming flow, by using a finite difference code FLOW-3D. The problem is shown in Fig.4. The cases with different distances from the wall H were solved. The particle shear Reynolds number used in these simulations is $Re_G = 4.63$. Fig.5 compares the drag coefficients from numerical solution, Stokes drag with wall correction, which is used in (21) and a curve-fit formula, as functions of the distance from the wall. This curve-fit formula is modified with wall effect

$$C_d = \frac{24}{Re_p} f(H) + \frac{6}{1 + Re_p^{1/2}} + 0.4 \qquad 0 \le Re_p \le 2X10^5 \tag{47}$$

Here the coefficient of wall effect f(H) is given by (16a) and (16b). Figure 6 compares these three set of data as functions of particle Reynolds number. The Stokes drag is calculated assuming a uniform incoming flow with a value at the center of the sphere. It is seen that the shear gives higher value of drag. As stated before, the local Stokes flow assumption is valid only when condition (37), (38) are satisfied. One thing to note is that the curve-fit formula predicts the drag coefficient very well even in the case of shear flow.

3.2 Disturbance velocity

In Fig.7, the velocity profiles, for the problem shown in Fig.4, across the center of the sphere are shown. It compares the FLOW-3D result and our approach which is a Stokes disturbance flow with wall correction, as given by (43) and (46), superimposed on the incoming flow.

3.3 Particle trajectory

The validation of particle trajectory is made in following way. A sphere is released at the center of the channel, as shown in Fig.8. The nondimensional parabolic velocity profile, scaled by u^*, is given by,

$$u = Re\ (2z - \frac{1}{2}z^2) \tag{48}$$

Here u^* and Re are called effective velocity and effective channel Reynolds number as defined in section 2.1. The flow is made laminar by reducing the the effective channel Reynolds number Re to one. In this case analytical solutions of particle velocities and particle trajectory are easily obtained. The numerical results are obtained by tracing the particle using (21). The result is shown in Fig.(9). It can be seen that the numerical values agree with the exact values perfectly. In order to check the accuracy of our method for evaluating the fluid velocity at arbitrary point in the flow field, a single particle is released into a realization of a turbulent flow. The fluid velocity at the particle's position is calculated by three-dimensional cubic spline interpolation and compared with the value calculated from the fourier triple summation,

$$\vec{u}(\vec{x}_p, t) = \sum_{k_1}\sum_{k_2}\sum_{n} \hat{u}(k_1, k_2, n, t) e^{i(k_1 x_{p1} + k_2 x_{p2})} T_n(x_{p3}) \tag{49}$$

which can be considered as the exact value. Figure 10 shows the relative errors of the three components of the velocity.

3.4 Forces acting on the particle

The forces acting on the particle are the drag force, the hydrostatic force and the added-mass force. In the other studies (Squires & Eaton 1990a, 1990b, Elghobashi & Truesdell 1992, 1993), the particles are much heavier than the fluid. Therefore, the hydrostatic force and the added-mass force were neglected. In our study, the particles are slightly heavier than the fluid. The hydrostatic force and the added-mass force are not negligible. In order to compare the relative importance of the different forces, a particle is released into the flow. The forces acting on this particle is recorded as a function of time. The ratio of particle's mass density to that of fluid is 1.03. Figure 11 shows the nondimensional forces, in each direction, versus the time. It can be seen that the hydrostatic forces have the same magnitude as that of the drag forces. The small values of the added-mass force means that the particle follows the fluid closely.

4. Results

The computer code for small particles have been completed and tested with a case of 1700 particles in a channel with dimension which 4 π (1000 in wall unit) in the streamwise direction, 2 π (500 in wall unit) in the spanwise direction and 2 (170 in wall unit) in the normal direction of the channel, normalized by the half depth of the channel. The flow Reynolds number, defined by the friction velocity at the wall and the half depth of the channel, is 85.5. The diameter of particle is about 4.0 wall unit. The corresponding particle volume loading is about 3.5×10^{-3}. The Froude number is 0.02, which gives a settling velocity $V_{pt} = 0.6$, of the particles. The ratio of particle mass density to that of fluid is $\rho_p/\rho_f = 1.03$. The resolution of computational domain is 32x64x65.

We start from a uniform distribution of particles. One-way coupling case is simulated until the particles reach an equilibrium distribution. The stable particle distribution is shown in Fig.12. Due to the relatively large gravitational constant, most particles are in the region very close to the wall. Figure 13 shows the particle distribution and the contours of the streamwise fluctuation velocity u' ($u = \bar{u} + u'$) at a horizontal (x-y plane) plane with a distance of 5 wall units from the wall. In this figure, the green and blue color represent the negative value of u', which means the streamwise velocity in these region are lower than the mean value. The yellow and red regions represent the positive u', which correspond to the high velocities. It can be observed that the particles segregated in the low-speed streaks. This phenomena is supported by the experimental results (Kaftori 1993) and other numerical simulations (Pedinotti et al 1992). This is mainly due to the large inertia of the particles. In this simulation, the size of the particles is fairly large. For the smaller particles, the distribution will be more uniform. Fig.14 gives a three dimensional view of an instantaneous particle distribution in the channel. We see that most of the particles are in the region very close to the wall.

Once the particles reach the equilibrium state, the two-way coupling is simulated. The effects of particles on turbulence can be seen by looking at intensities of turbulence in each component, which are represented by the rms of the fluctuation velocities. From the simulation, we generate the instantaneous velocity field $\vec{u}(t)$ at a large number of times. These data base are used to carry out the statistics of the turbulent flow. Fig.15, 16, 17 show the rms velocities in streamwise, spanwise and normal direction respectively. The values of clean flow and flow containing particles are compared. The presence of the particles does not change the turbulence intensity in the spanwise component, as shown in Fig.16. In the streamwise and normal direction, some changes are observed. These changes are mainly in the wall region, which is obvious since most of the particles are settled in the wall region, which covers a distance of about 10 wall units from the wall. Outside of this region, the properties of the flow are the same as that of the clean flow. Fig.18 gives the Reynolds stress $\overline{u'w'}$ for two-phase flow and clean flow. A very significant increase occurs in the region about 10 wall units from the wall. The peak value changes about 20%. These results tell us that the particles do modify the turbulence. It should be pointed out that the results presented here are just for one typical case, where the particle size is large and gravity is high. To see the effect of particle size and gravity, more cases of various particle diameter and Froude number have to be simulated.

Fig.19 gives the averaged particle Reynolds numbers corresponding to three components of velocity. Re_{px} and Re_{py} are much smaller than unit. The large Re_{pz} is due the relative high gravity.

Acknowledgement : This research was supported by NSF Grant No. CTS-91-23297, Prof. M. Roco, Director.

REFERENCE

Elghobashi S. and Truesdell, G. C. 1992,"Direct Simulation of Particle Dispersion in a Decaying Isotropic Turbulence", J. Fluid Mech. Vol. 242, pp.655- 700.

Elghobashi S. and Truesdell, G. C. 1993 "On the Two-way Interaction Between Homogeneous Turbulence and Dispersed Solid Particles. I: Turbulence Modification ", Phys. Fluids A, Vol 5, No. 7.

Hetsroni, G. 1989 "Particles-Turbulence Interaction", Int. J. of Multiphase Flow , Vol. 15, No. 5.

Hetsroni, G. 1991 "The Effect of partilces on the Turbulence in a Boundary Layer ", (Ch.8; Roco, M., Editor), Butterworth.

Kaftori, D. 1993 "Structures in the Turbulent Boundary Layer and Their Interaction with Particles",Ph.D. dissertation, University of California, Santa Barbara.

Kim, S. and Karrila, S., 1991,"Microhydrodynamics", Butterworth-Heinemann.

Lam, K. and Banerjee, S., 1988 "Investigation of Turbulent Flow Bounded by a Wal l and a Free Surface", Invited Paper, ASME Winter Annual Meeting International Symposium on Fundamentals of Gas-Liquid Flows, Chicago.

Lam, K. 1989 "Numerical Investigation of Turbulent Flow Boundary by a Wall and a Free-Slip Surface", Ph.D. dissertation, University of california, Santa Barbara

Lam, K. and Banerjee, S., 1991 "On the Conditions of Streak Formation in Bounded Flows", Phys. Fluids A,

McLaughlin, J.B. 1989 "Aerosol Particle Deposition in Numerically Simulated Channel Flow", Phys. of Fluids A, Vol. 1.

McLaughlin, J.B. 1991 "Inertial Migration of a Small Sphere in Linear Shear Flow", J. Fluid Mech. 224, pp. 261-271.

Mei, R., Lawrence, C. J. and Adrian, R.J., 1991, "Unsteady Drag on a Sphere at Finite Reynolds Number with Small Fluctuations in the Free-stream Velocity",J. Fluid Mech., Vol.233, pp.613-631.

Papanicolaou, G. and Zhu, J., 1991, "A Vortex Method for Fluid-Particle System", CPAM Vol. 44, p.101-120.

Pedinotti, S., Mariotti, G. and Banerjee, S., 1992,"Direct Numerical Simulation of Partilce Behaviour in the Wall region of Turbulent Flows in horizontal Channe ls", Int. J. Multiphase Flow Vol. 18, No.6. pp.927-941.

Rashidi, M., Hetsroni, G. and Banerjee, S., 1990 "Particle-Turbulence Interaction in a Boundary Layer", Int. J. of Multiphase Flow, Vol. 16.

Squires, K.D. and Eaton, J.K., 1990b "The Interaction of Particles with Homogenous Turbulence", NASA/Stanford Center for Turbulence Research, Report No. MD-55.

Thomas, P. J., 1992,"On the Influence of the Basset History Force on the Motion of a Particle through a Fluid", Phys. Fluid A 4 (9), pp.2090-2093.

Tsuji, Y., 1991 "Review: Turbulence Modification in Fluid-Solid Flow", 1st Joint Conf. ASME-JSME.

Yeh, F. and Lei, U. 1991a "On the Motion of Small Particles in a Homogenous Turbulent Shear Flow", Phys. Fluids.

A3(11). pp.2758-2776.

Yeh, F. and Lei, U. 1991b "On the Motion of Small Particles in Homogenous Isotropic Turbulent Flow", Phys. Fluids A3(11), pp.2571-2586.

The caption of the figures

Figure 1. The computational coordinate system.

Figure 2. Coordinate system of particle position in fluid.

Figure 3. The mirror reflection operation for the Stokeslet field.

Figure 4. Single sphere close to a wall with a linear shear incoming flow.

Figure 5. Drag coefficient versus the particle's distance from the wall, for the problem shown in Fig.4, using different methods.

Figure 6. Drag coefficient versus particle Reynolds number, for the problem shown in Fig.4, using different methods.

Figure 7. The profile of the streamwise velocity, through the center of the sphere, for the problem shown in Fig.4., by different methods.

Figure 8. A testing case for the computer code.

Figure 9. Particle velocity versus time for the case shown in Fig.8.

Figure 10. The relative errors of fluid velocities evaluated by the cubic spline interpolation, $|(u_i - u_{i(exact)})/u_{i(exact)}|$. The time is scaled by h/u_*.

Figure 11. The forces acting on a particle moving through a turbulent flow. The diameter of the particle is 4.0 in wall unit. The forces, which are the forces acting the unit mass of the partilce, are scaled by u_*^2/h. The time is scaled by h/u_*.

Figure 12. The stable particle vertical distribution in the channel.

Figure 13. Particle distribution in the region close to the wall. The color contours show the streamwise fluctuating velocity at a x-y plane 5 wall unit from the wall.

Figure 14. A three-dimensional view of the distribution of all the particle in the channel. The color contours show the streamwise fluctuating velocity at a x-y plane 5 wall unit from the wall.

Figure 15. Streamwise turbulence intensity, $(\overline{u'^2})^{1/2}/u_*$, for flows with and without particles.

Figure 16. Spanwise turbulence intensity, $(\overline{v'^2})^{1/2}/u_*$, for flows with and without particles.

Figure 17. Turbulence intensity of velocity normal to the wall, $(\overline{w'^2})^{1/2}/u_*$, for flows with and without particles.

Figure 18. Reynolds stress, $\overline{(u'w')}/u_*^2$, for flows with and without particles.

FIgure 19. The averaged particle Reynolds number Re_p.

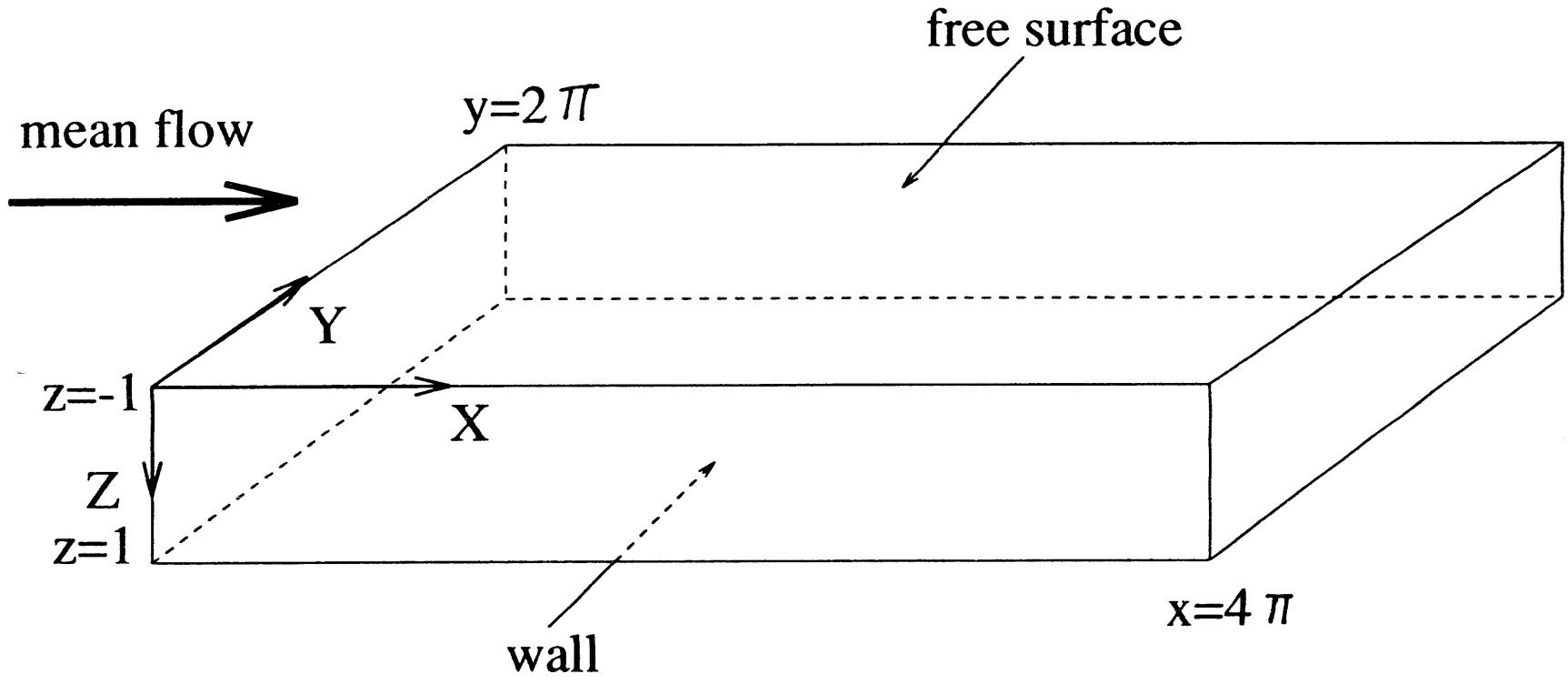

Fig 1

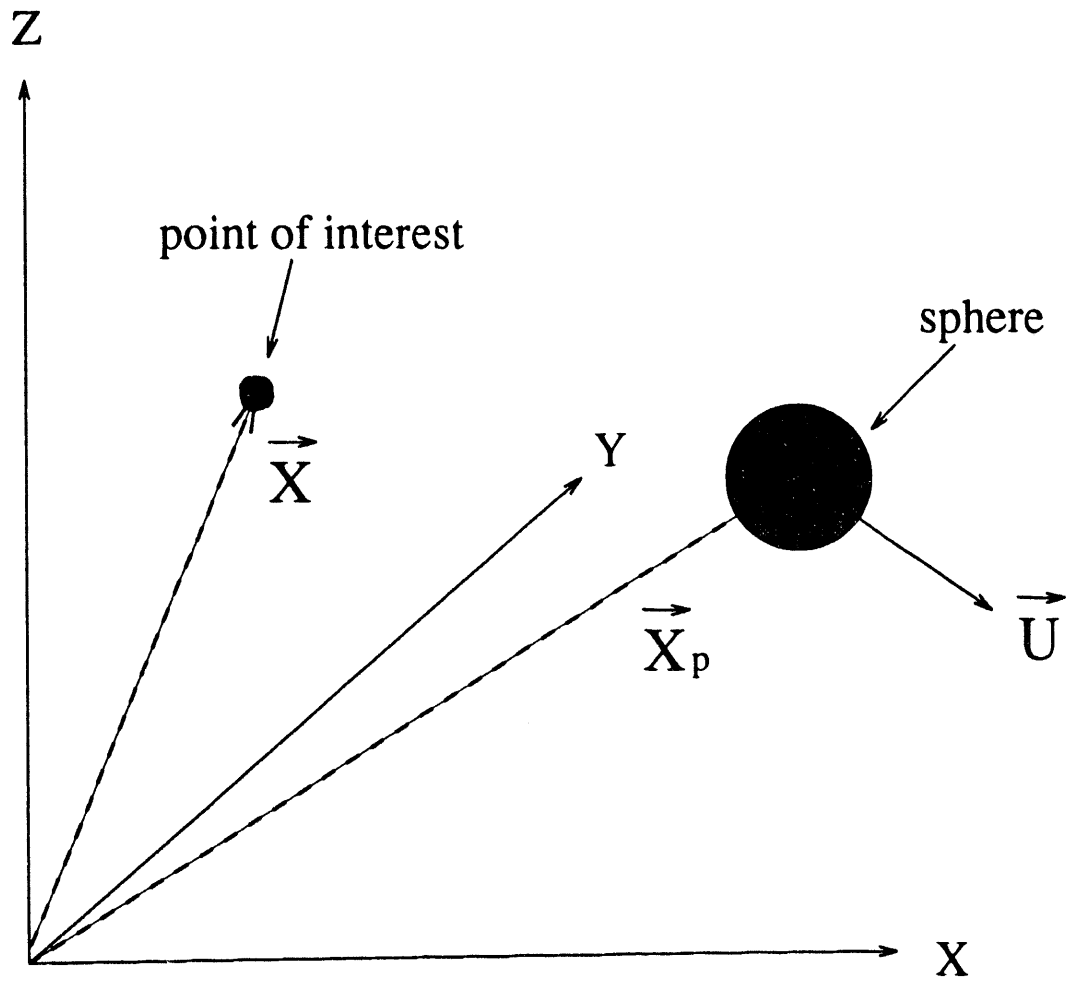

Fig. 2

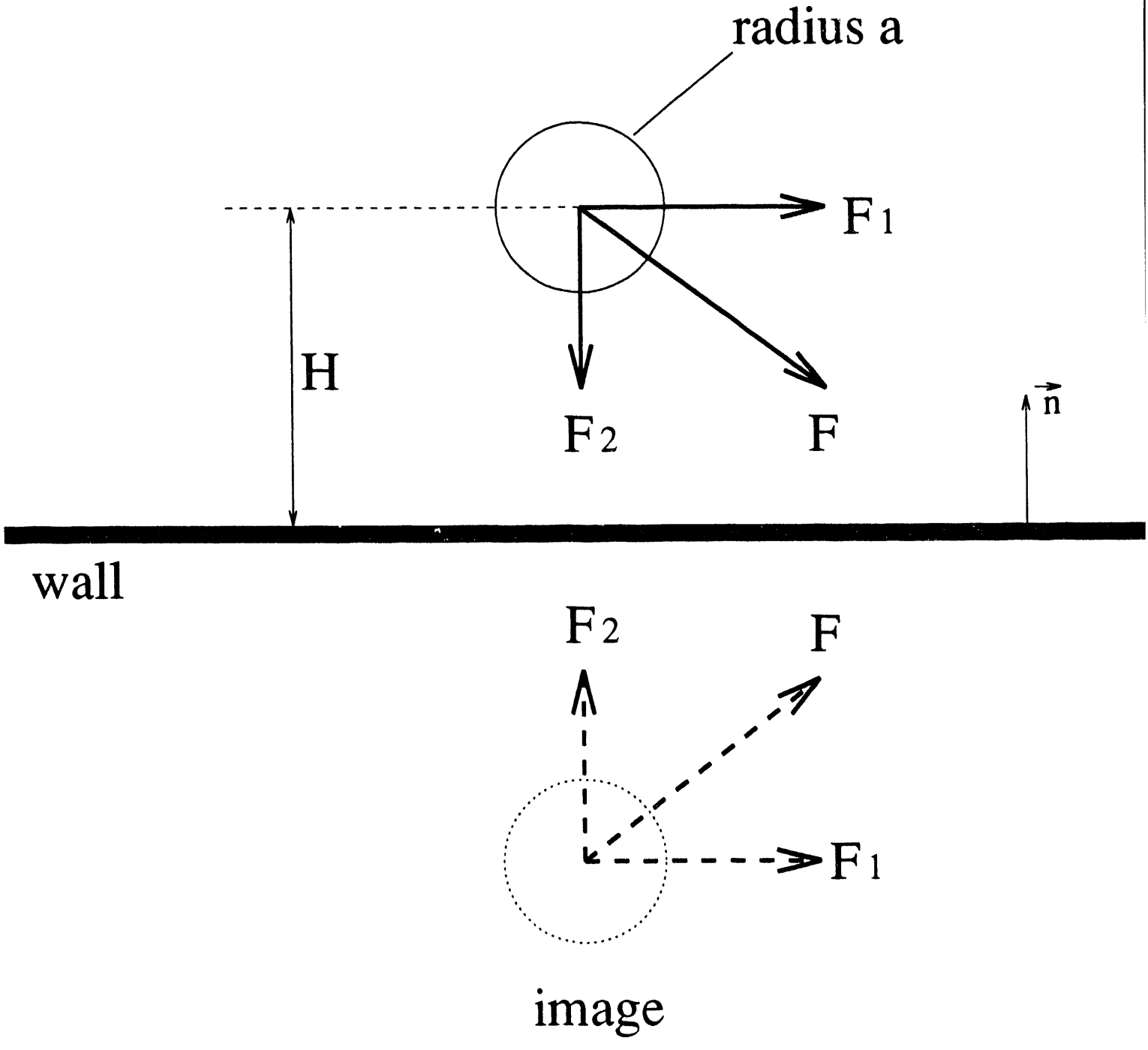

Fig. 3

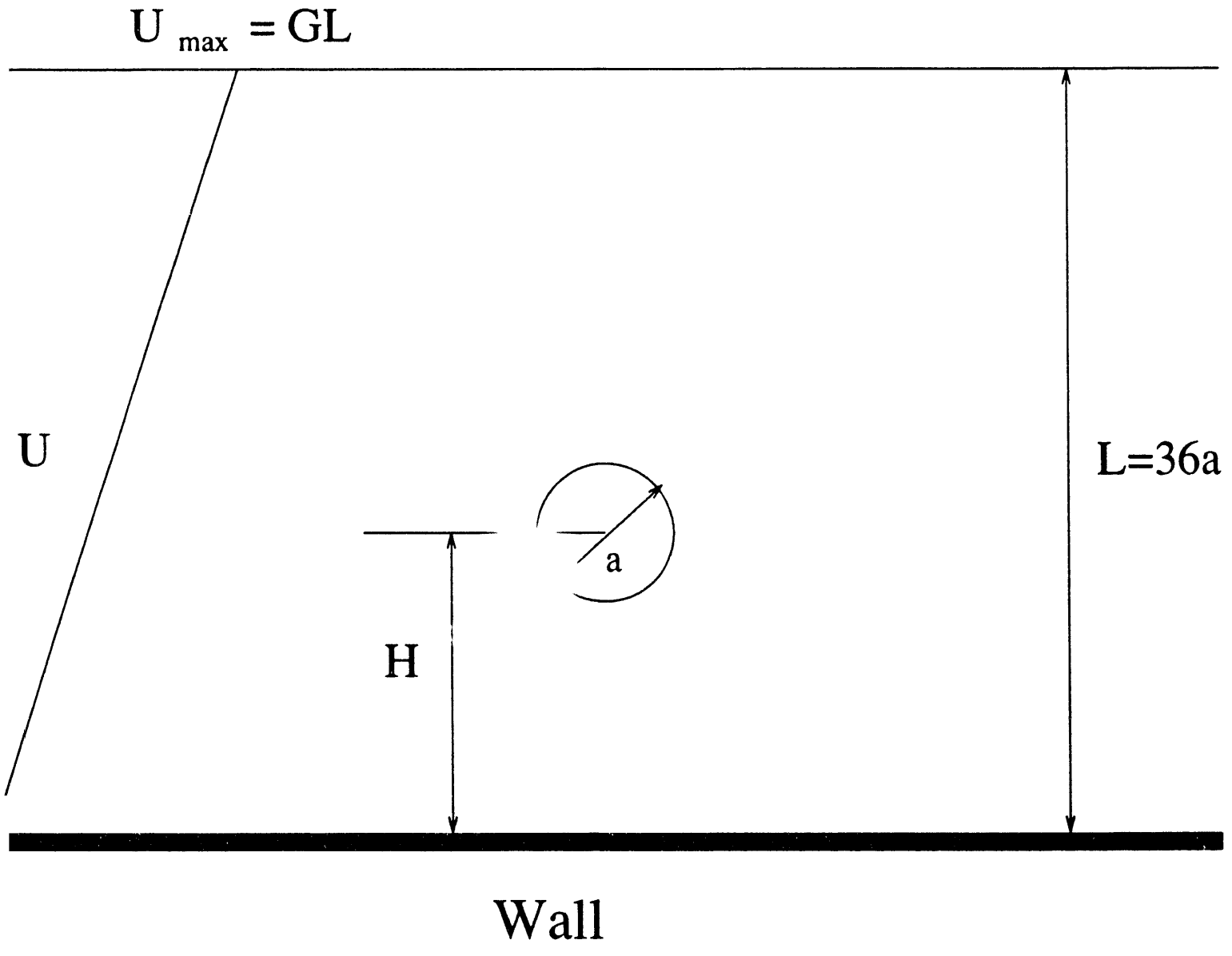

Fig. 4

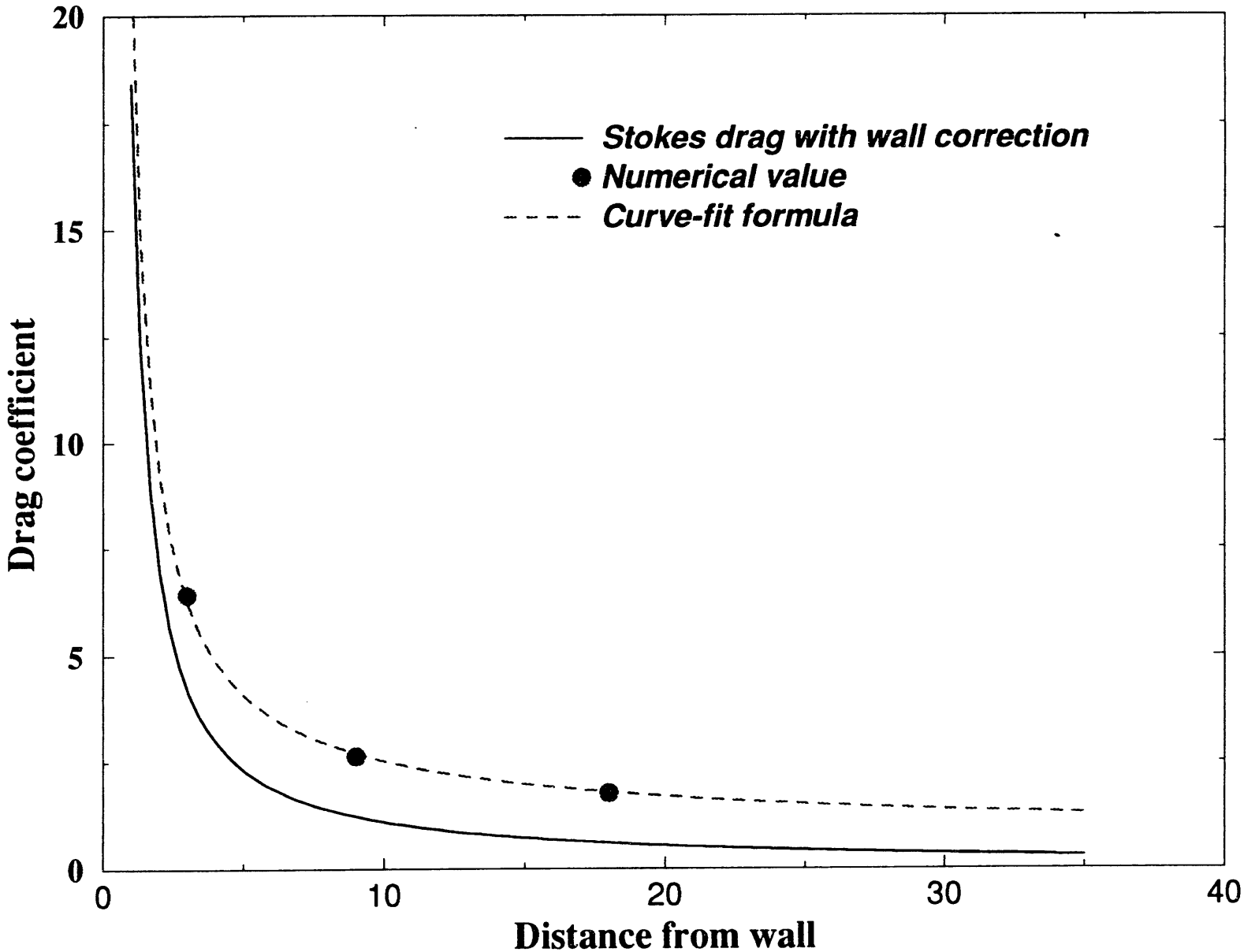
Stokes drag with wall correction
Numerical value
Curve-fit formula
Drag coefficient
Distance from wall
0
5
10
15
20
0
10
20
30
40

Fig. 4

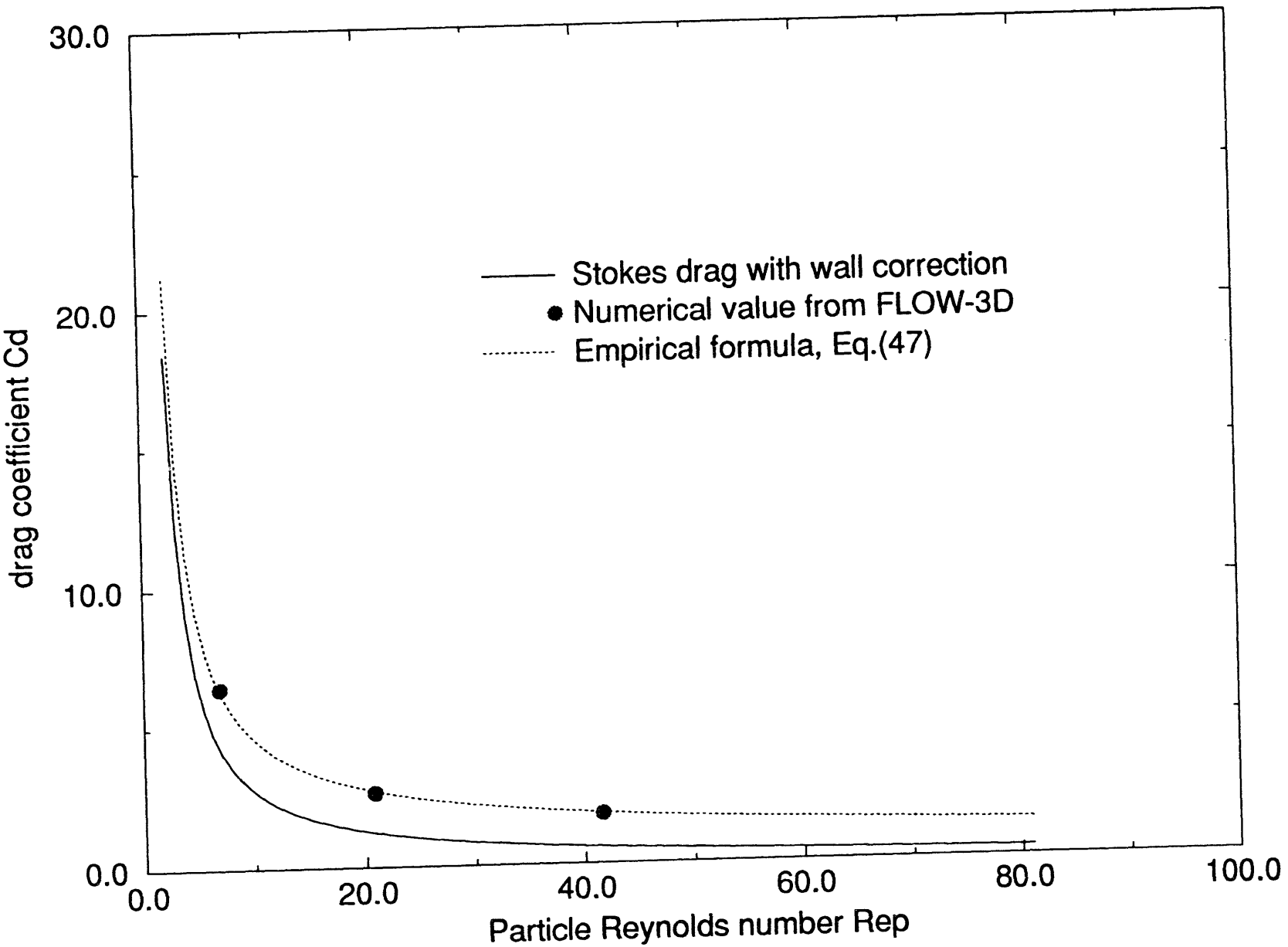
30.0
20.0
10.0
0.0
0.0
20.0
40.0
60.0
80.0
100.0
drag coefficient Cd
Particle Reynolds number Rep
Stokes drag with wall correction
Numerical value from FLOW-3D
Empirical formula, Eq.(47)

Fig 6

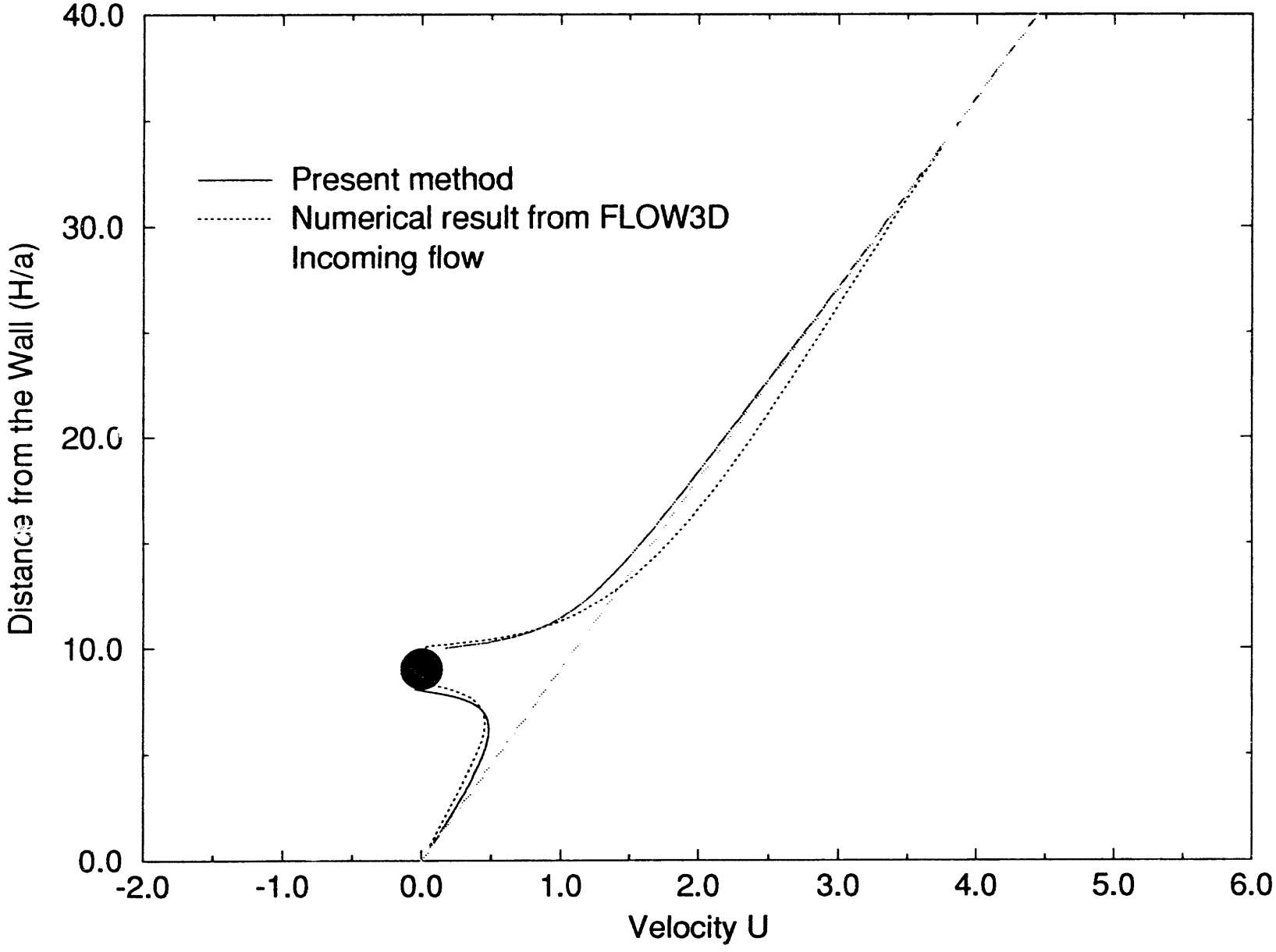
Present method
Numerical result from FLOW3D
Incoming flow
Distance from the Wall (H/a)
Velocity U
40.0
30.0
20.0
10.0
0.0
-2.0
-1.0
0.0
1.0
2.0
3.0
4.0
5.0
6.0

Fig 7

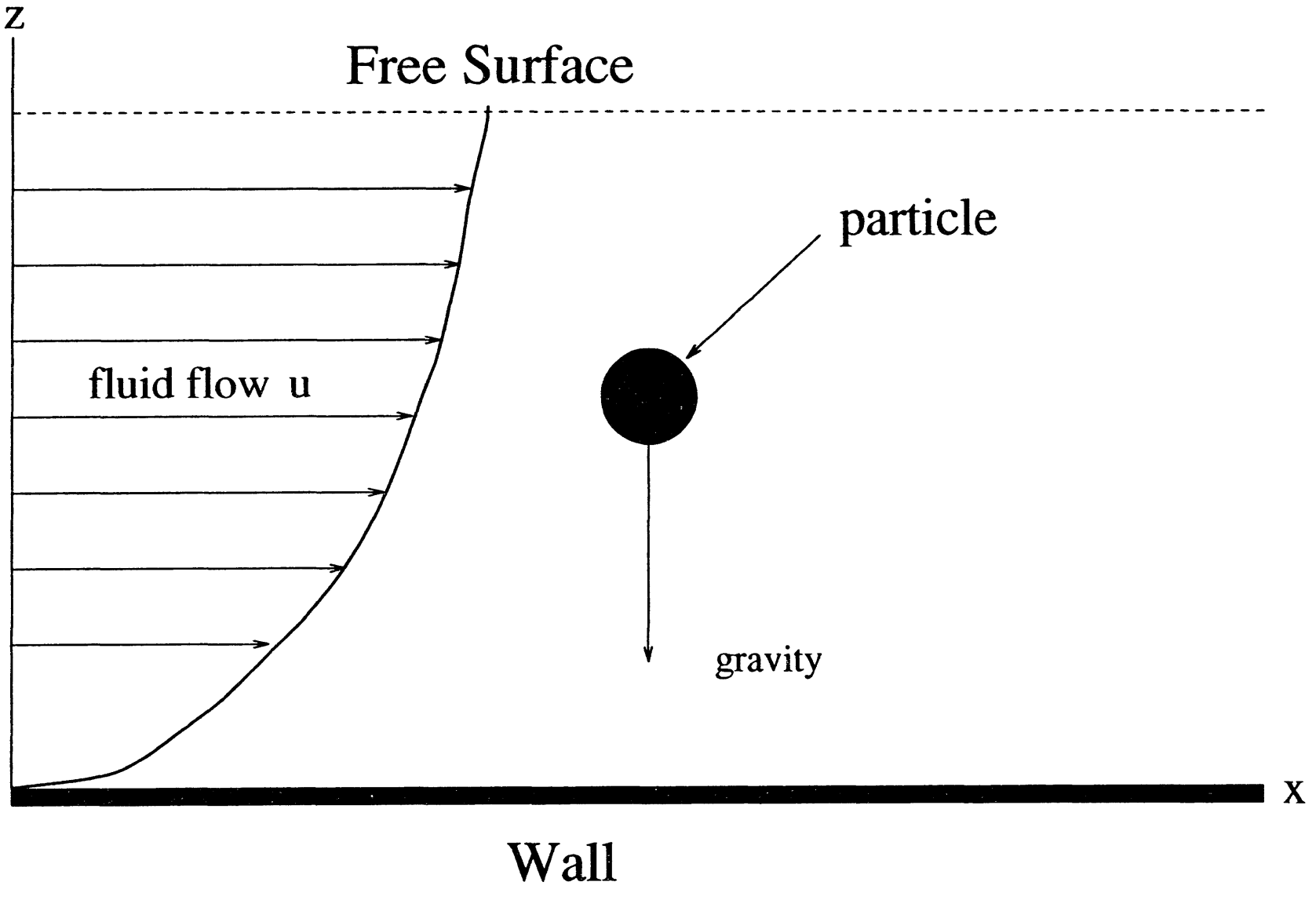

$$u = Re\,(2z - z^2)$$

Fig 8

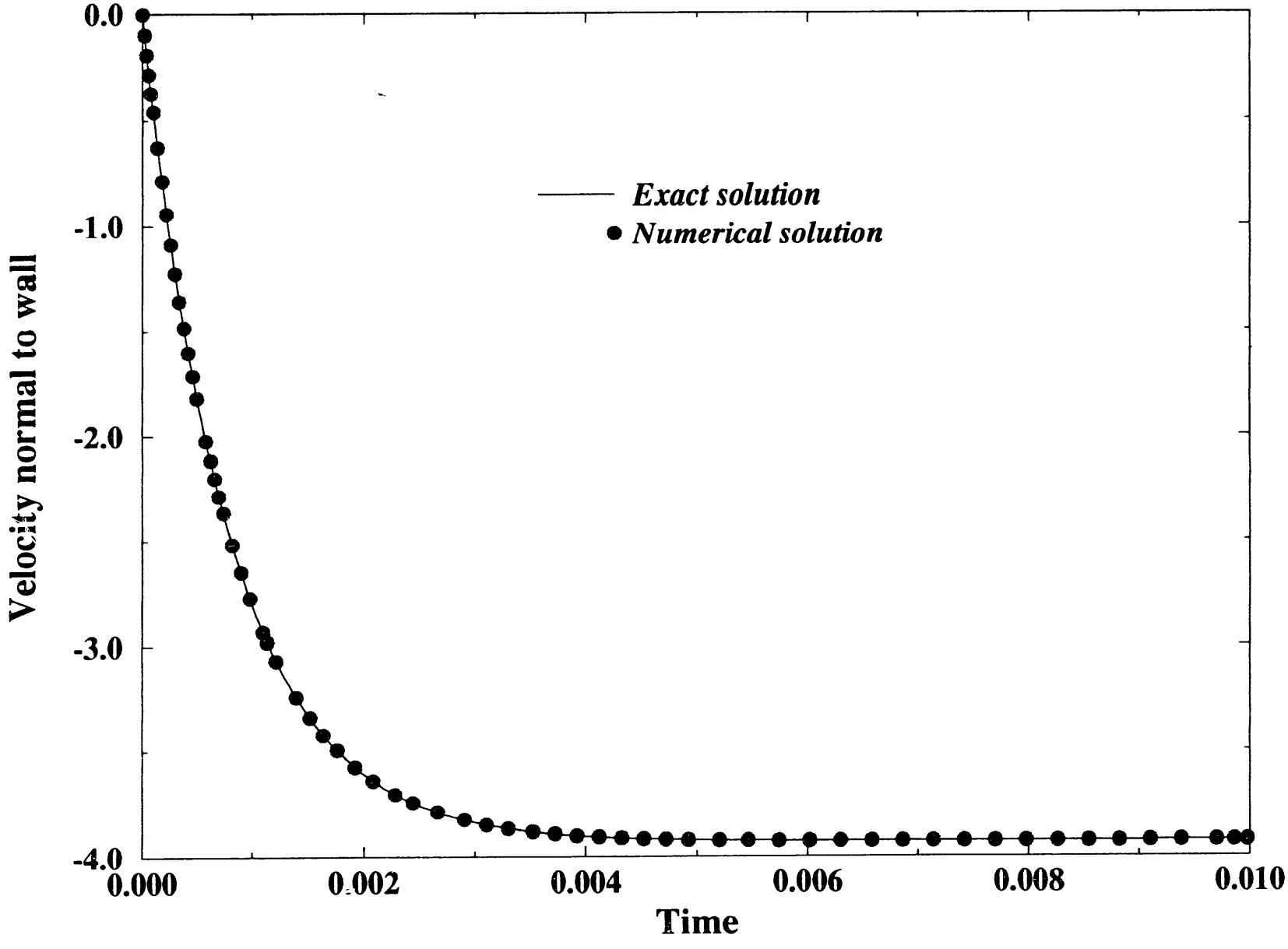
0.0
-1.0
-2.0
-3.0
-4.0
Velocity normal to wall
0.000
0.002
0.004
0.006
0.008
0.010
Time
Exact solution
Numerical solution

Fig 9

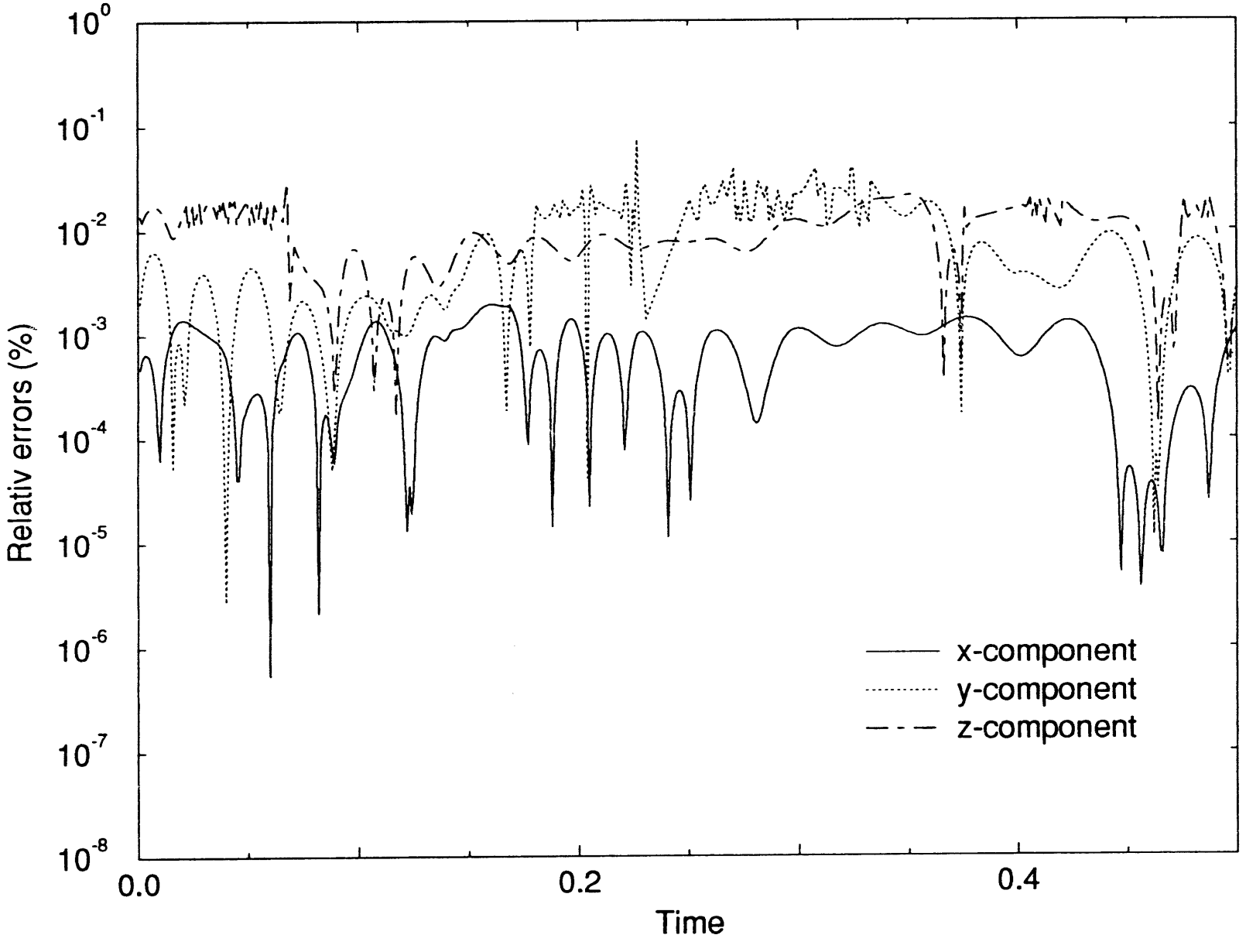
Relativ errors (%)
10^{0}
10^{-1}
10^{-2}
10^{-3}
10^{-4}
10^{-5}
10^{-6}
10^{-7}
10^{-8}
0.0
0.2
0.4
Time
x-component
y-component
z-component

Fig 10

Particle Reynolds number
Time
Rep(x)
Rep(y)
Rep(z)
0.00
0.10
0.20
0.30
0.40
0.50

Fz
Time
drag force
hydrostatic force
added-mass force
gravitational force
20.0
0.0
-20.0
-40.0
-60.0
0.00
0.10
0.20
0.30
0.40
0.50

Fy
Time
drag force
hydrostatic force
added-mass force
20.0
0.0
-20.0
-40.0
0.00
0.10
0.20
0.30
0.40
0.50

Fx
Time
drag force
hydrostatic force
added-mass force
20.0
0.0
-20.0
-40.0
-60.0
0.00
0.10
0.20
0.30
0.40
0.50

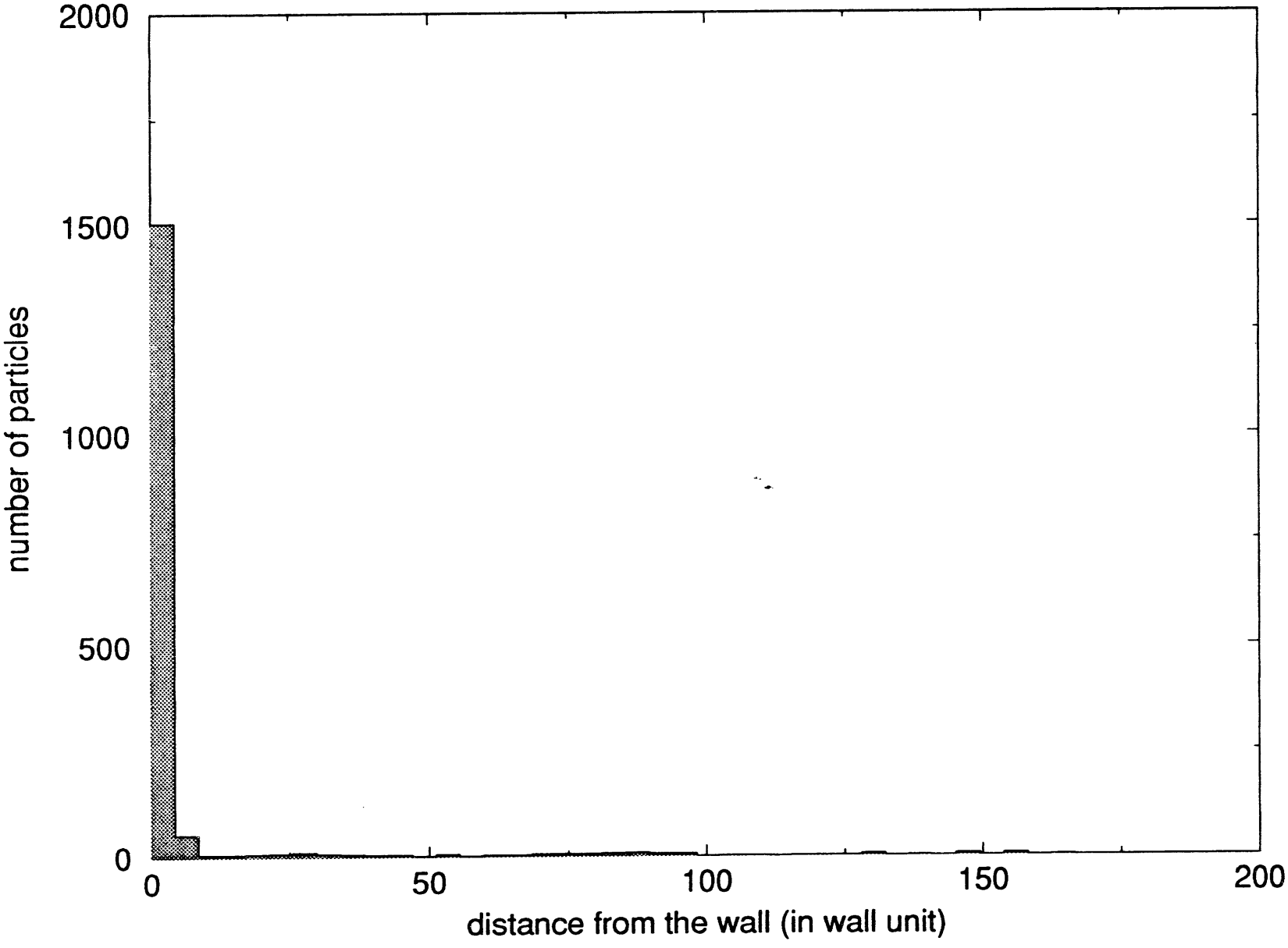
2000
1500
1000
500
0
number of particles
0
50
100
150
200
distance from the wall (in wall unit)

Fig 12

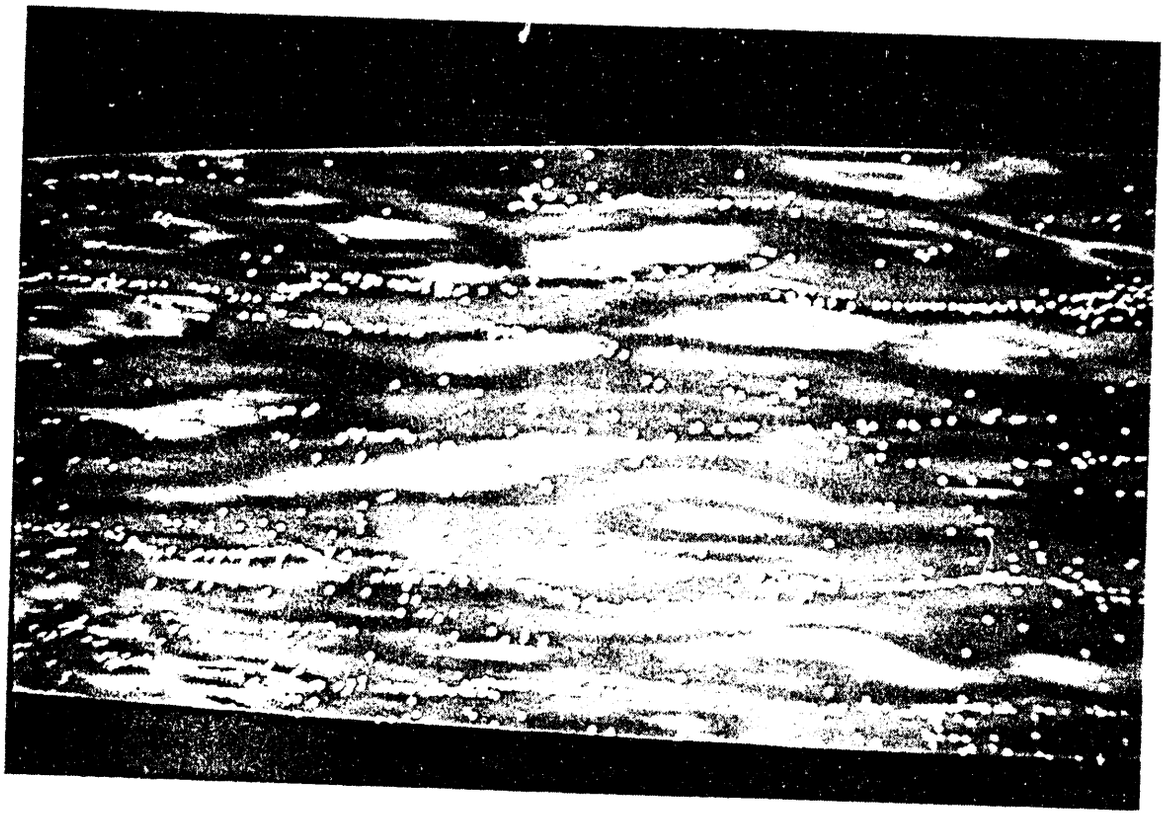

Fig 13

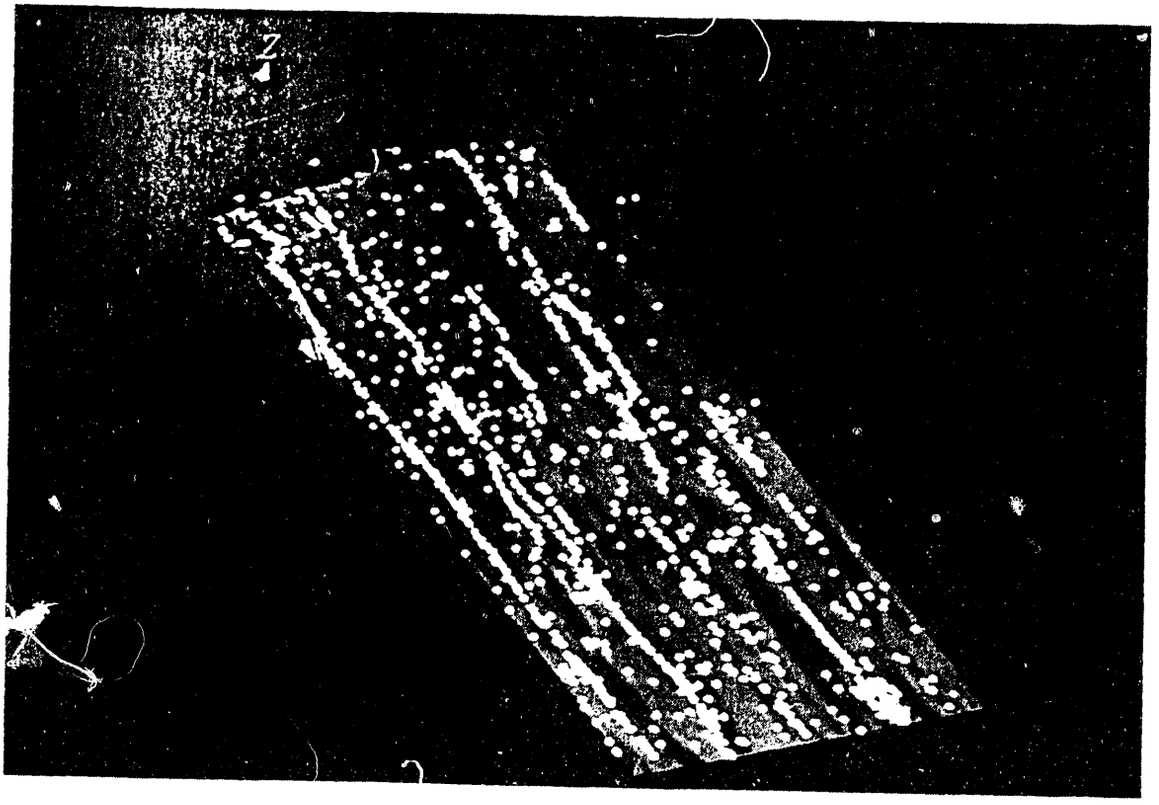

Fig 14

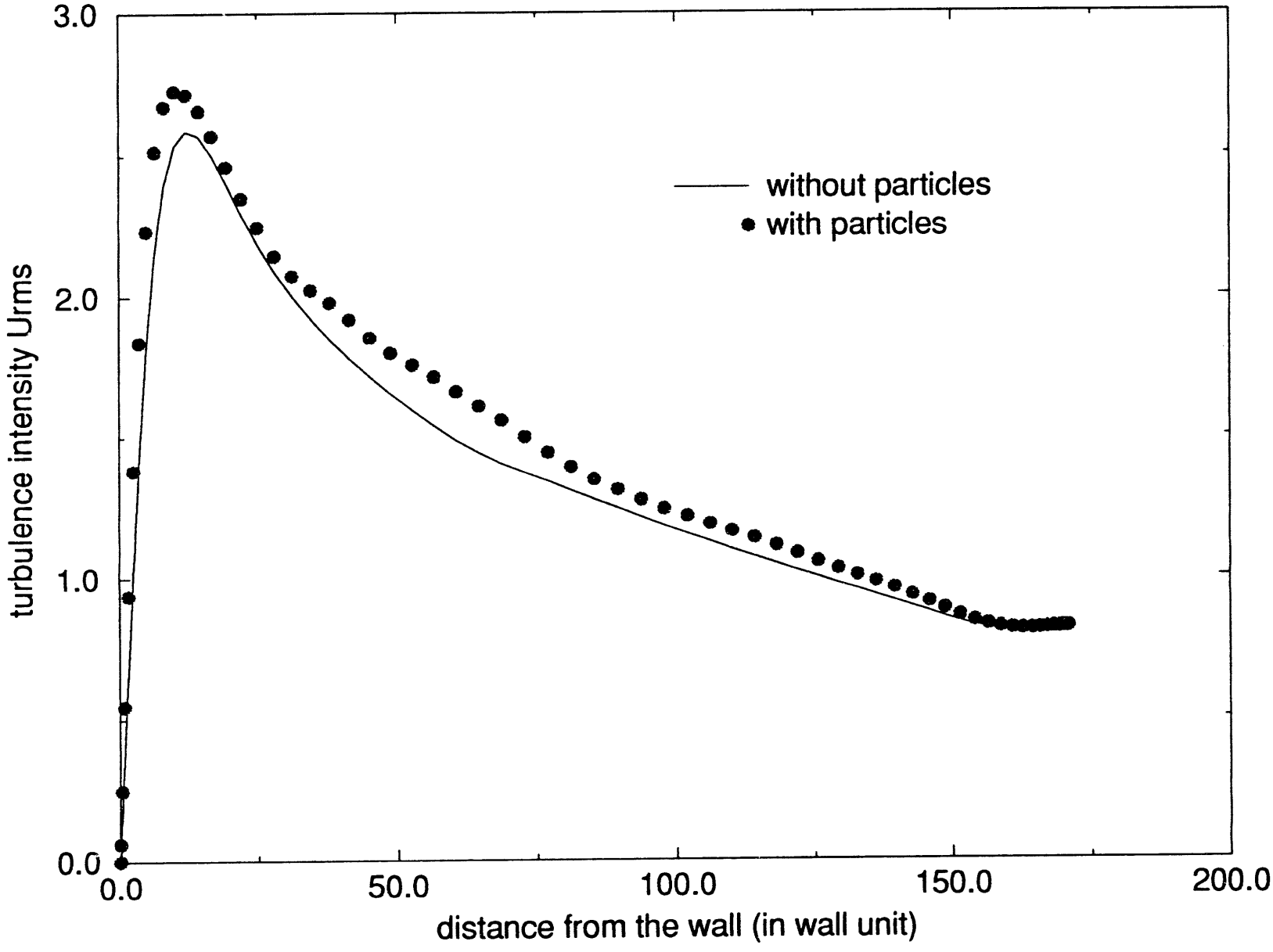
3.0
2.0
1.0
0.0
turbulence intensity Urms
without particles
with particles
0.0
50.0
100.0
150.0
200.0
distance from the wall (in wall unit)

Fig 15

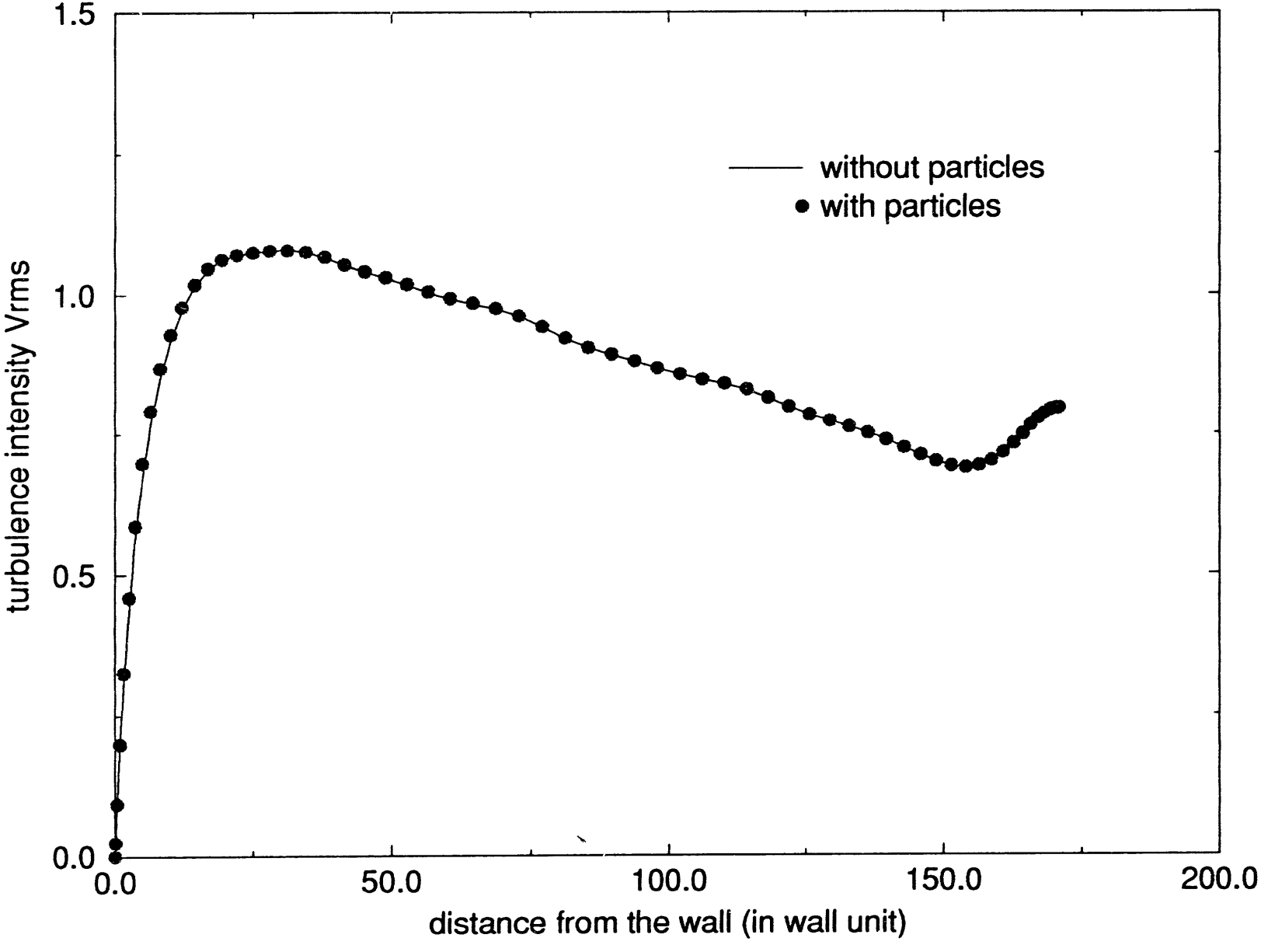
1.5
1.0
0.5
0.0
turbulence intensity Vrms
without particles
with particles
0.0
50.0
100.0
150.0
200.0
distance from the wall (in wall unit)

Fig 16

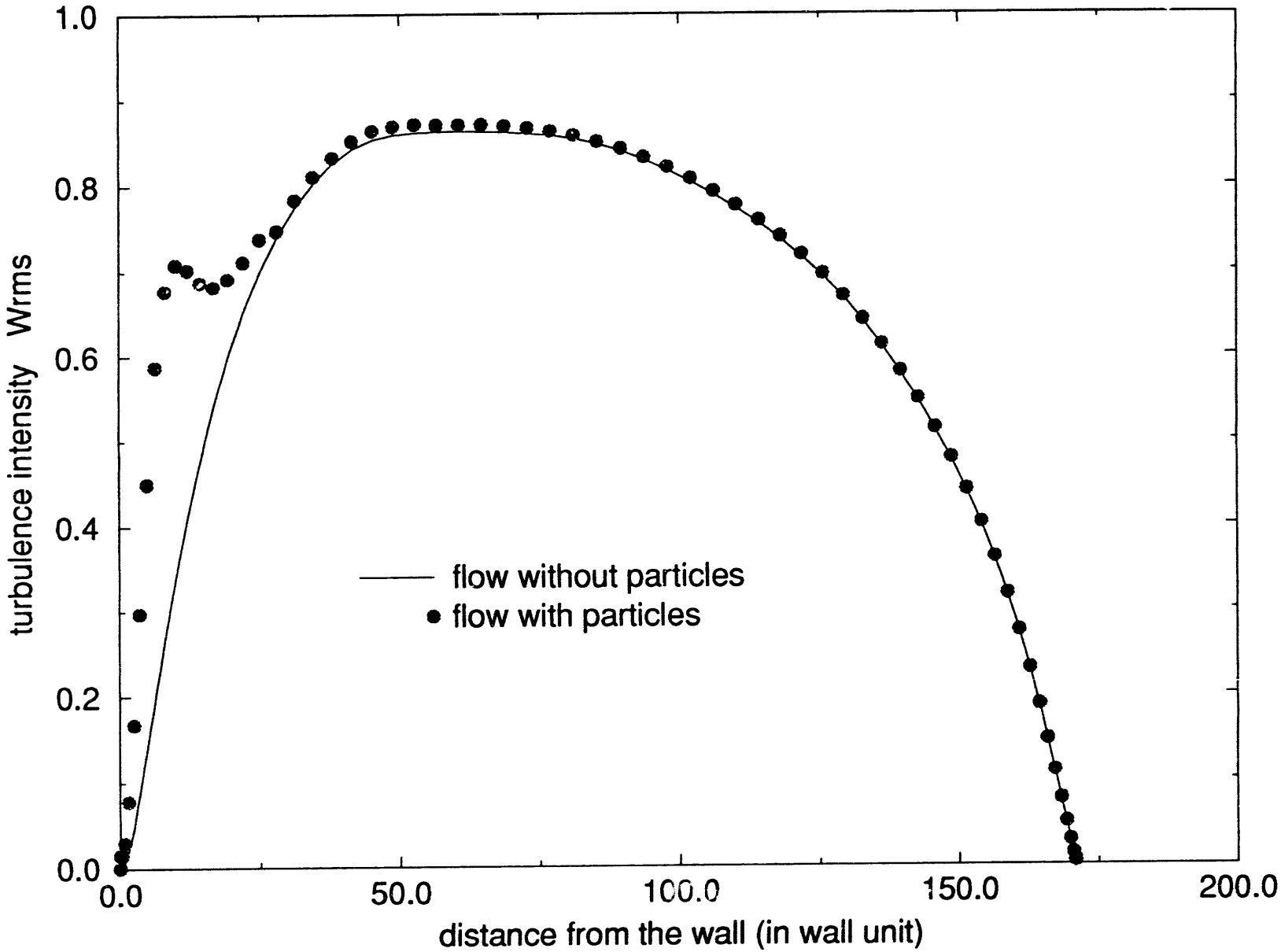
1.0
0.8
0.6
0.4
0.2
0.0
turbulence intensity Wrms
0.0
50.0
100.0
150.0
200.0
distance from the wall (in wall unit)
flow without particles
flow with particles

Fig 17

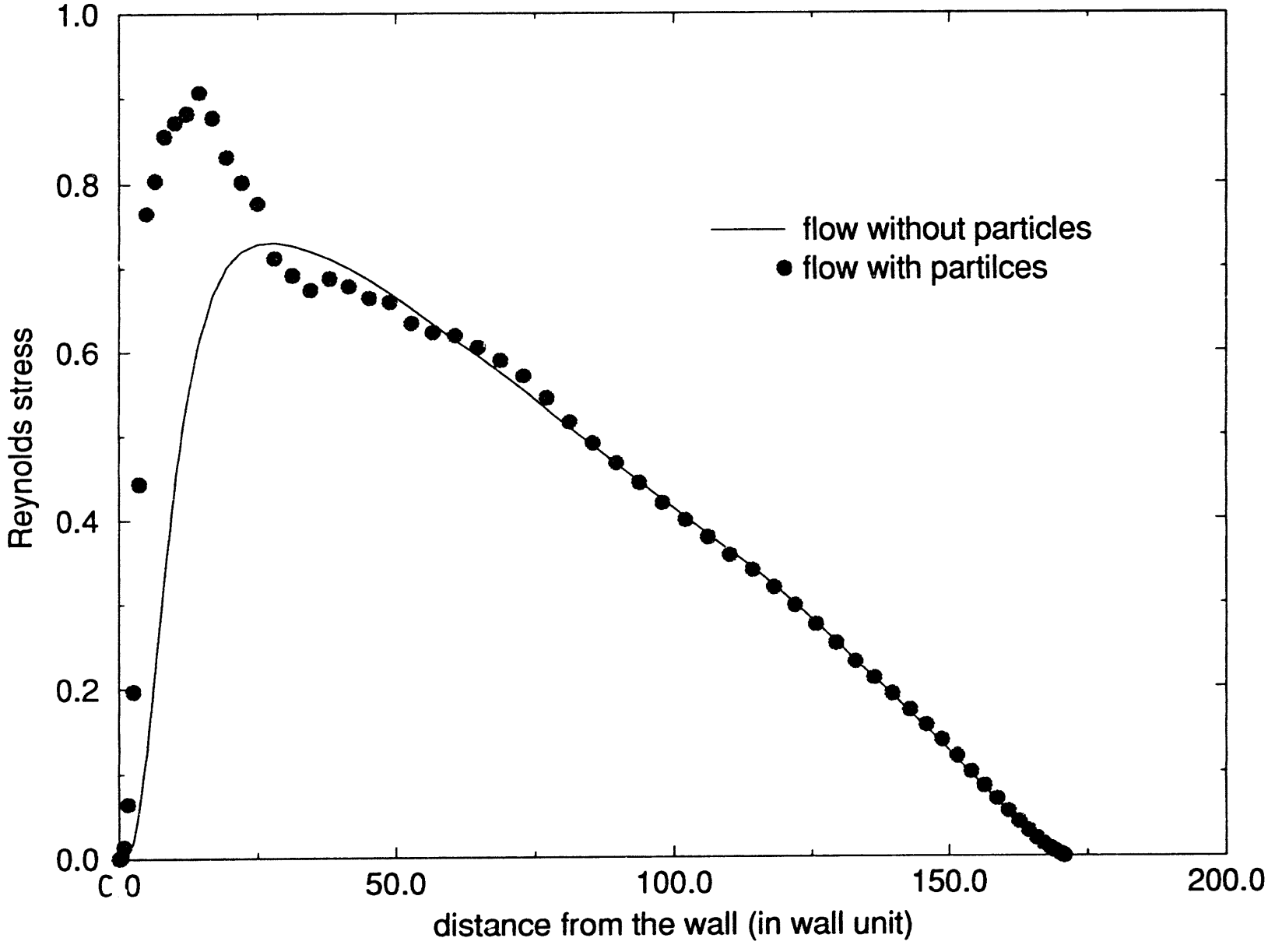
1.0
0.8
0.6
0.4
0.2
0.0
Reynolds stress
flow without particles
flow with partilces
C 0
50.0
100.0
150.0
200.0
distance from the wall (in wall unit)

Fig 19

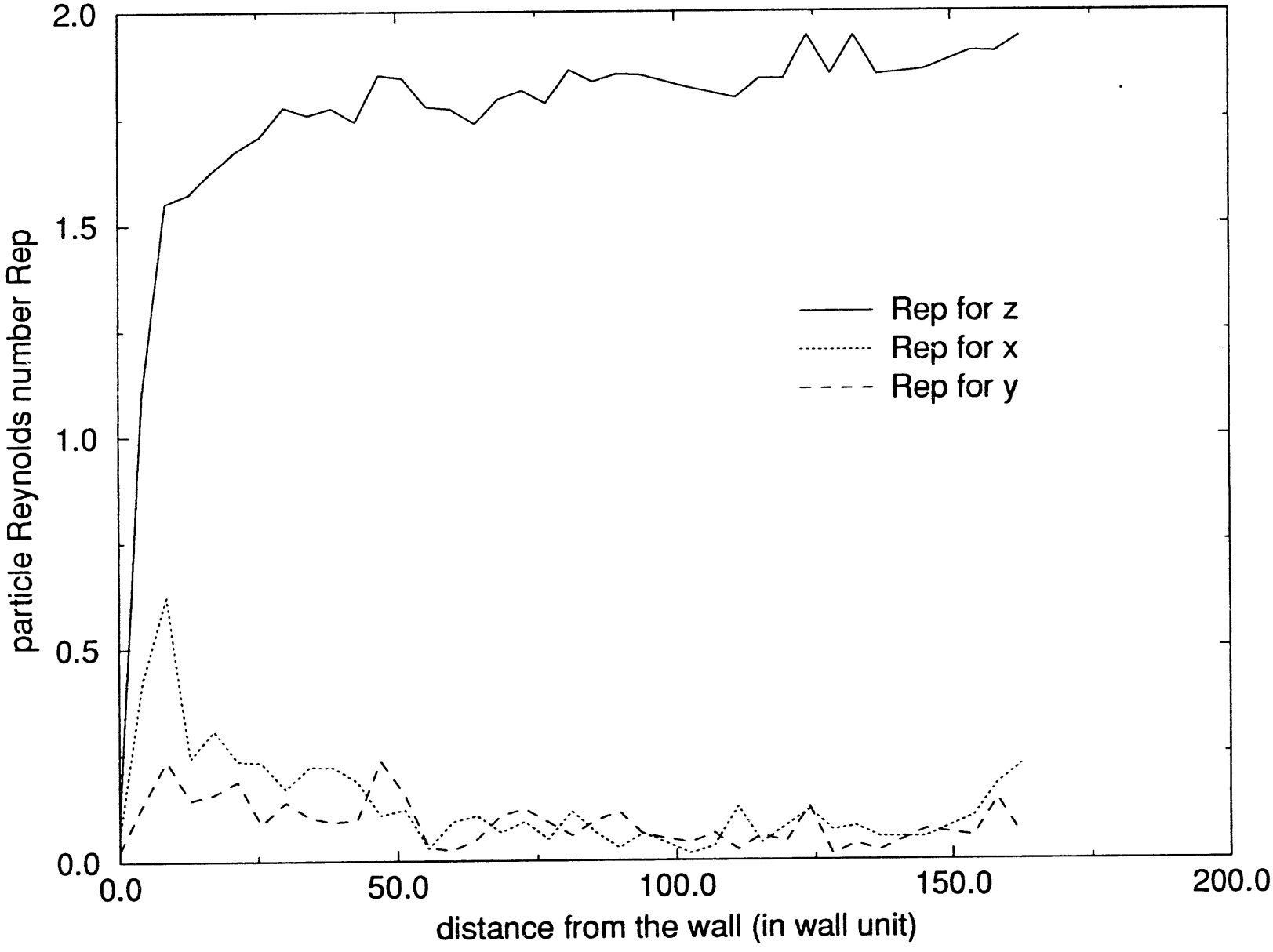
2.0
1.5
1.0
0.5
0.0
0.0
50.0
100.0
150.0
200.0
particle Reynolds number Rep
distance from the wall (in wall unit)
Rep for z
Rep for x
Rep for y

Fig 19

Bridging Microstructural and Continuum Theories of Dispersed Systems with Parallel Computer Architectures

Sangtae Kim
Department of Chemical Engineering
University of Wisconsin
Madison, WI 53706

Abstract

The project objective is to develop a foundation for the large-scale simulation of the behavior of suspensions ranging from dilute to concentrated systems. The suspended particles and container walls in the simulation can be of arbitrary and quite complex shape; detailed information at the microscopic level, such as the role of surface roughness, and nonsphericity (rod-like to disk-like) can be addressed. The solution methodology features fast iterative algorithms based on integral representations for the Stokes velocity field (and related equations in potential theory for the electrostatic effects) developed by our group. The overall computational design philosophy is consistent with the goal of optimal performance on new advanced computer architectures (parallel computers) capable of performing 10^9 (today) and 10^{12} (near future) floating point operations per second.

To achieve these objectives, we have initiated scalability studies to predict performance on massively parallel computers, using NSF/ARPA sponsored architecture prototyping environments developed by computer scientists at UW-Madison. Results are now coming out for such interesting constructs like massively parallel shared memory environments and other architecture designs of the next generation of parallel supercomputers.

As part of the testbed of benchmark suites to evaluate performance of various architectures, we are developing a large scale computational simulation of the kinetics of protein folding. The separation between time scales is too large for a direct Brownian dynamics simulation. Instead, we solve an equivalent set of Fokker-Planck equations over an optimal pathway in configuration space. Preliminary results for both parallelism and model fidelity are presented.

Introduction

In recent years, parallel computing has become a dominant issue in computational science and engineering, including computation and simulation of multiphase systems. We can now look back and analyze the trends of the past ten years. The shared memory parallel computers

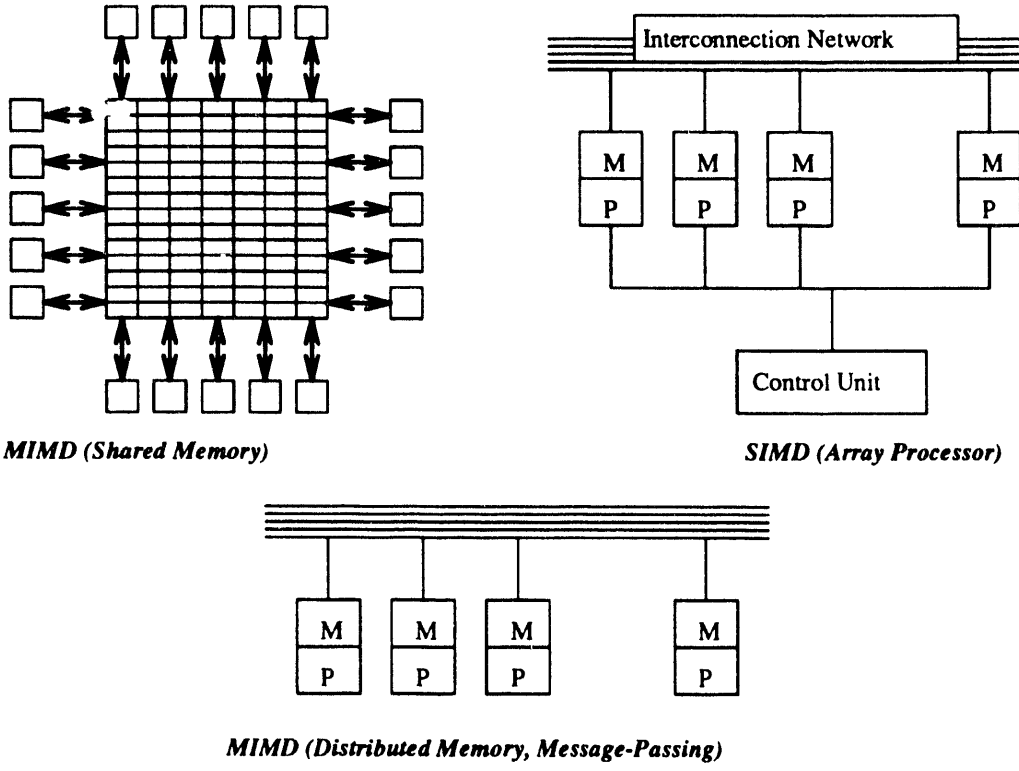

Figure 1: Conceptual view of the Sequent Symmetry, CM2 and newer MIMD machines (CM5, Intel Paragon).

of the mid 80's, such as the Sequent Symmetry, with bus-based architectures connecting on the order of 20 microprocessor chips have given way to message-passing distributed memory computers such as the CM5 and Intel Paragon, that combine many (up to 1000) powerful, workstation-like RISC processors.

This development has been dictated in part by the concept of scalability of architecture (the ability to increase the number of processors without impeding performance). The shared memory programming model assumes the idealized concept of uniform access to a common or shared memory. Processors communicate with each other by writing and reading from a uniform memory address space in a coordinated fashion determined by the programmer. Such architectures have fallen out of favor because of the difficulties in scaling uniform memory access to large numbers of processors.

At the present time, coarse-grain MIMD machines such as the Thinking Machine Corporation's CM5 and the Intel Paragon, consisting of smaller numbers (a thousand or less) of very powerful processors, distributed memory and message-passing on interconnects, dominate the market. Such machines can scale up to large numbers of processor and solve very large problems, as long as the users take responsibility for removing interprocessor communication bottlenecks, as in [1]. However, the gains in scalability comes at a price: programming such machines is relatively difficult in comparison with the shared memory machines.

At this point, a historical analogy analogy may be illuminating. In the early days of the digital electronic computers, computational scientists were willing to program in non-

portable machine code to squeeze the last ounce of performance from their machines. As the technology matured, the ease of portability to newer and faster machines became the paramount concern and gave rise to high level languages such as Fortran. Ultimately, the same phenomena must occur with high performance parallel computers. The challenge for those who wish to design the new high level languages is to identifying the common features of modern computationally extensive algorithms.

These ideas are tested in concrete form in an architecture prototyping environment that has been developed in the computer sciences department at UW-Madison [2]. This brings up a second point: the cost of implementing new ideas in hardware is becoming increasingly expensive. A prototyping environment, essentially an event simulation of a hypothetical machine, allows algorithm designers to test the the cross-performance of algorithms and architectures, without the prohibitive cost of building the real thing. The example described in the following section is a test of the CDL-BIEM algorithm [1,3] with the cooperative shared memory programming model, as implemented on the Wisconsin Wind Tunnel (the prototyping environment).

The Cooperative Shared Memory Model

The essential ideas behind the Fuentes & Kim [1] iterative algorithm for boundary integral equations can be summarized as follows. The suspension region is divided into regional subdomains (which can be as small as one particle per domain) and assigned to processors. Communication bottlenecks are removed by scheduling inter-processor communications as a function of distance. Distant regions (processors) communicate less frequently. This idea is readily implemented in the *Cooperative Shared Memory* programming model.

The cooperative shared memory model *is* a shared memory model in that the idea of a global memory accessible to all processors is preserved. But uniform access to memory (which does not scale) is dropped. The programming model allows processors to "check out" data to indicate immediate and/or frequent use, and "check in" data when such usage is terminated. In fact, CSM at Wisconsin actually resides on message-passing hardware (CM5) but messages are automatically generated by CSM in response to higher level directions of the programmer. If the programmer works properly with the programming interface, all variables are read in from local memory thereby giving the impression of a massively parallel shared memory machine.

The transition from the message-passing model to CSM was implemented by exploiting the idea that access to (physically) remote memory must correspond to messages. In practice, this means scheduling the prefetch and checkout directives of CSM. In Figure 2 we show typical results from the simulations on a 32-processor partition of a CM5. This plot, a boundary element calculation of the Laplace equation, shows good scale up to large numbers of processors.

Protein Folding Kinetics

Proteins can be viewed as biological polymers comprised of a specific sequence of amino acids (the so called primary structure). Most proteins of significant form secondary structures (alpha helices, beta sheets, etc.) which in turn combine to form a specific three-dimensional

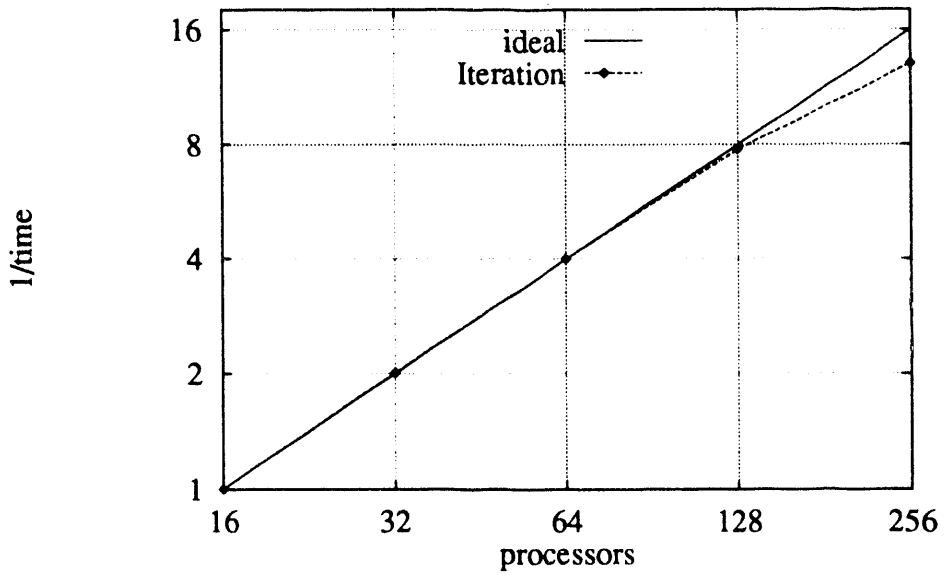

Figure 2: Boundary element solution of the Laplace equation, using CSM on the Wisconsin Wind Tunnel.

(tertiary) structure. One of the grand challenges of modern science is the prediction of protein folding given its amino acid sequence (predicting both the 3-D structure as well as the kinetic rate of the folding). Since folding to the correct tertiary structure has been observed to take seconds (even minutes in some cases) a direct molecular dynamics simulation of protein foldiong is infeasible.

Fortunately, some separation of time scales exits. It is known that proteins fold very quickly into their secondary structures. There is some hope that, given the energetics of interactions between these secondary structures, we will be able to construct the optimal pathway and thus compute tertiary structure. But even for this simplified situation, a direct molecular dynamics (or even Brownian dynamics) simulation is inherently difficult. Direct implementation of an integrator for the governing stochastic differential wastes most of the computational resources in following the rattling motion in local energy minima.

However, some progress has been achieved by working with the associated Fokker-Planck equation. To obtain the parameters for this associated equation, we perform many (parallel) short simulations along the pathway. Having obtained the necessary 'geometric' information about the pathway connecting local minima, we use a stiff PDE solver (PDESAC, [4]) to integrate along the path. The essential idea is that whereas a direct attack on the SDE would fail as the free energy barrier height increases at the the saddle point, the computational time for the PDE integration would be a much weaker function of the barrier height.

These ideas are illustrated using Figure 3, a two-dimensional potential energy surface that is still small enough to solve by direct integration of the SDE. The 'rate constant' for formation of products from the reactants is computed by direct simulation, as well as by the approximate method (running smaller simulations, obtaining the local curvature, then integrating with the PDE solver). The approximate and exact methods are compared for a range of anisotropic diffusivity (ratio of diffusion coefficients transverse to the path and along the path) and width of the gap. As can be seen in Figure 3, the agreement between

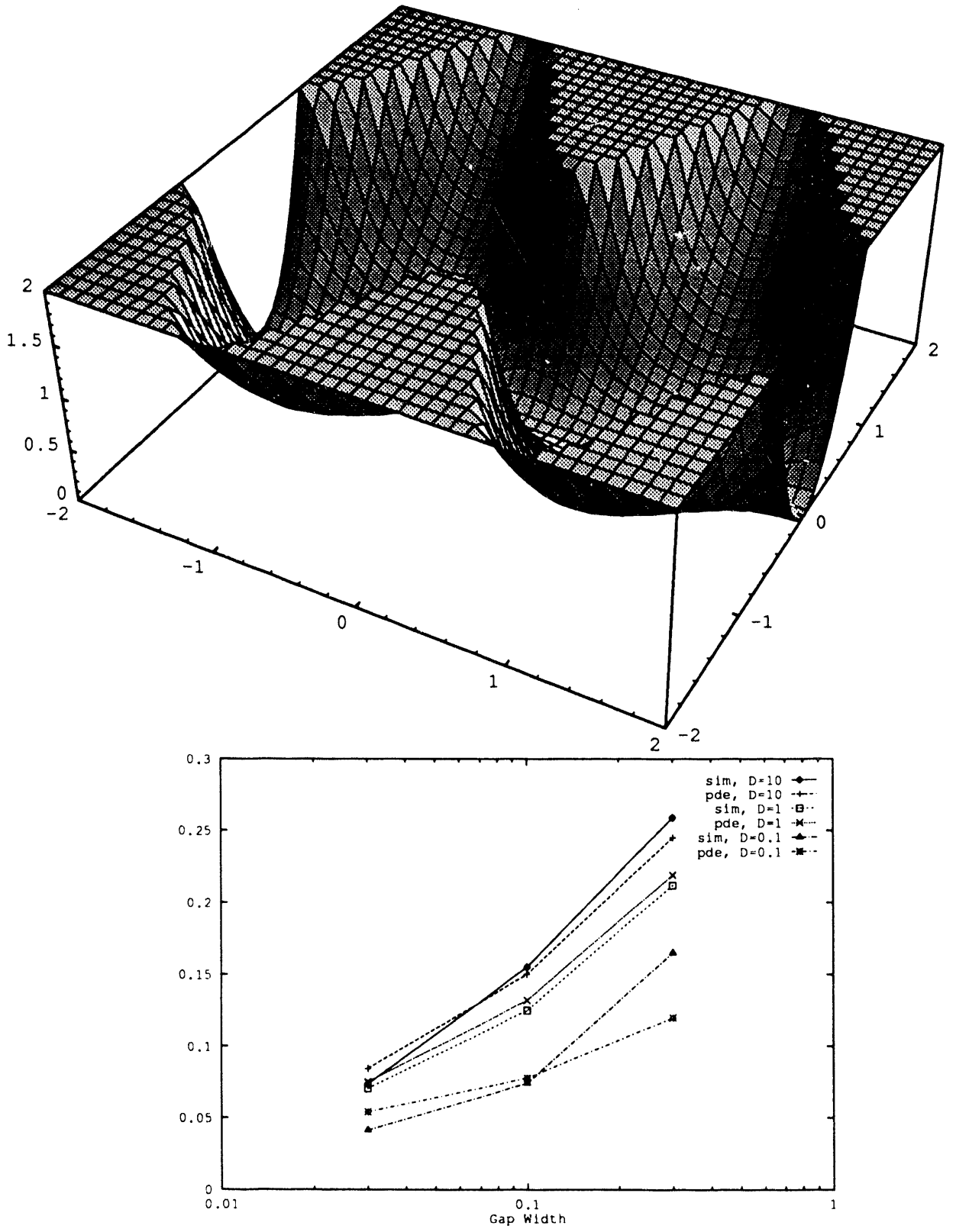

Figure 3: A model two-dimensional energy surface and reaction rates as predicted by the exact simulation (sim) and PDE method (pde).

the approximate method works well, except where it is expected to fail in the pathological case of wide gap (the free energy barrier is low) and transverse diffusion is extremely low.

Summary and Conclusions

There exists a large class of important computational problems that require computers that are a factor of at least 10^3 beyond the fastest machines of today. *Strategic research* areas such as computer-aided drug design fall into this category. Parallel computer architectures can and must evolve in a number of directions to attain these performance levels. On the other hand, it is prohibitively expensive to actually build real prototypes to test all these possibilities. Event simulations of these future machines allow us to test our algorithms on present day machines. Our experience with large scale computations suggest that the interaction between algorithm and architecture is important and point out the useful role of prototyping environments.

Acknowledgments

This work is based on research supported by NSF grant CTS-9218668. The CM5 at Wisconsin was obtained with funds from NSF grant CDA-9024618, for PRISM — Parallel Research in SIMD/MIMD respectively. Prof. Mark Hill of the Computer Sciences Department provided helpful discussions on CSM and access to the Wisconsin Wind Tunnel.

References

1. Fuentes, Y.O. and Kim, S., Parallel Computational Microhydrodynamics: Communication Scheduling Strategies, *A.I.Ch.E. J.*, vol.38, pp. 1059-1078, 1992.

2. Hill, M., Larus, J., Reinhardt, S. and Wood, D., Cooperative Shared Memory: Software and Hardware for Scalable Multiprocessors, *Proc. of Fifth Intl. Conf. on Architectural Support for Programming Languages and Operating Systems*, October 1992.

3. Kim, S. and Karrila, S.J., *Microhydrodynamics: Principles and Selected Applications*, Butterworth-Heinemann, Boston, MA, 1991.

4. Caracotsios, M. and Stewart, W.E.., Sensitivity Analysis of Initial Boundary Value Problems with Mixed PDEs and Algebraic Equations, *Computers and Chem. Engineering*, (in press).

EXPERIMENTAL SESSION

Paper presented at Joint DOE/NSF Workshop on
Flow of Particulates and Fluids, Ithaca, N.Y., October 1, 1993

Multiphase Flow Problems In Coal Log Pipeline

Henry Liu, Professor and Director
Capsule Pipeline Research Center
University of Missouri-Columbia

ABSTRACT

The emerging technology of coal log pipeline (CLP) for transporting coal has generated a host of new multiphase flow problems that require research and attention from researchers in the multiphase-flow field. These include the hydrodynamics of capsule flow (both steady and unsteady), dynamic modeling of the CLP system, drag reduction in CLP, coal log jamming and abrasion (wear), water absorption of coal logs, granular flow in extrusion/compaction, and coal log transport in coal slurry. This paper describes the state of the knowledge in each of these areas, and the remaining unknowns that must be researched.

INTRODUCTION

Coal log pipeline (CLP) is a special type of hydraulic capsule pipeline (HCP) that transports extruded or compacted coal logs (circular cylinders) through the pipe. As compared to the conventional coal slurry pipeline, the CLP new technology has distinct advantages including less headloss (energy consumption) at the same velocity, more coal and less water transported, and easy to dewater and to restart. When fully developed, the CLP technology is expected to be able to penetrate a large market of coal transportation that the coal slurry pipeline has been unable to penetrate. At present, the National Science Foundation, the U.S. Department of Energy, the State of Missouri, and a consortium of private companies are jointly funding an intensive R & D program in CLP, aimed at early completion of the development of this emerging technology.

The R & D program in CLP conducted at the Capsule Pipeline Research Center, University of Missouri-Columbia, is broad based. It includes hydrodynamics, coal log manufacturing, automatic control of CLP systems, CLP economics, CLP effluent

treatment, and legal studies including eminent domain issues, water rights, rights to cross railroads, etc. This paper is focused on the multiphase flow problems (areas) encountered in CLP, including the following:

1. Hydrodynamics of coal log flow.
2. Unsteady flow and water hammer in CLP.
3. Dynamic modeling of CLP system.
4. Drag reduction in CLP.
5. Prevention of coal log jamming in pipe.
6. Abrasion (wear) of coal logs.
7. Water absorption into coal logs—two-phase flow (air/water) through porous medium.
8. Granular flow in coal log extrusion and compaction.
9. Coal slurry suspension of coal logs.

Note that the first five of the above nine areas in CLP are common to both CLP and HCP. Therefore, when discussing them the terms CLP and HCP are used interchangeably. In contrast, areas 6 through 9 are unique to coal logs; the term HCP will not be mentioned there.

In what follows, each of the nine areas will be briefly described, and their state of development and remaining research will be pointed out. The intent is to encourage more researchers to become aware of and interested in the multiphase flow problems of CLP and HCP, especially areas that are still poorly understood and that require greatest research efforts.

HYDRODYNAMICS OF CAPSULE FLOW

The hydrodynamics of capsule flow in pipe is the most extensively explored area of HCP and CLP. Most of the early studies were conducted in Canada at the Alberta Research Council between 1958 and 1978. Results were mostly published in the CANADIAN JOURNAL OF CHEMICAL ENGINEERING, in several HYROTRANSPORT Conference proceedings, in numerous reports of the Alberta Research Council, and in the book THE FLOW OF COMPLEX MIXTURES IN PIPES by Govier and Aziz. They are exemplified or described by the first ten references listed at the end of this paper [1-10]. Since 1978, the hydrodynamics of capsule flow has been

studied in other nations including U.S.A. [11-13], Japan [14,15], the Netherlands [16,17], South Africa [18,19] and Australia [20]. Major progress has been made since 1990 in classifying capsule flow into four distinctly different regimes, and in deriving the equations in these regimes for predicting the headloss, incipient velocity, capsule velocity, and capsule drag coefficient [21,22].

A major unresolved problem in capsule hydrodynamics is the prediction of the lift force on capsules and the vertical position and the orientation of any capsule moving in the pipe, before and after lift-off. Such predictions are not possible unless and until the pressure variation around a capsule moving in a pipe can be predicted. Although several attempts have been made in the past to predict the velocity and pressure fields around a moving capsule, they all suffer from two unrealistic assumptions: (1) the flow in laminar, and (2) the capsule is parallel to the pipe (i.e., no angle of attack). In reality, all capsule pipeline applications involve turbulent flow, and capsules tilt slightly in the pipe which increases the lift

Therefore, there is a strong need for a good turbulent flow model to predict the flow field around a capsule in pipe. For such a model to be realistic, it must be three-dimensional, having the capsule at any vertical location in the pipe with an arbitrary angle of attack. The model also must include flow separation at capsule entrance, boundary layers along both the capsule and the pipe, and a three-dimensional wake behind the capsule. Once the flow field around the capsule is determined, the pressure around the capsule can be integrated to yield the drag, the lift, and their lines of action. The information can then be used to determine the moment on the capsule about a given point such as the capsule tail end. If the assumed position and orientation of the capsule in the pipe is correct, the overturning moment generated by pressure will be exactly balanced by the stabilizing moment generated by the weight of the capsule. On the other hand, if the two moments are not balanced, then the assumed position and orientation of the capsule are incorrect, and a new position/orientation must be assumed. This means many trials are

required before one can balance the two moments, and find the final flow field. Although the task of developing such a turbulent flow model appears formidable, it is within the reach of modern computational fluid dynamics.

UNSTEADY FLOW AND WATER HAMMER IN HCP

A practical means to inject coal logs and other capsules into a pipe is to use a set of parallel injection tubes (locks) at the pipeline intake. Trains of capsules (logs) are alternately drawn into the locks and pumped into the main pipeline by alternately switching valves; no capsules (logs) need to pass through the water pump. Likewise, at downstream booster stations, capsules (logs) are alternately let into two parallel branches (locks), and alternately pumped out to the downstream pipe by switching valves. Such valve switching generates unsteady flow and water hammer (pressure surges) that must be investigated and understood clearly before HCP or CLP can be used successfully. This subject has been explored at the Capsule Pipeline Research Center since 1988, using the method of characteristics. At first, they were analyzed without capsules or logs in the system [23-25]. Then, the problem was solved with capsules in the pipe [26-28]. Currently, experiments are underway to check the correctness and accuracy of the theory, and to improve the theory based on experimental evidence.

DYNAMIC MODELING OF HCP SYSTEM

The unsteady flow model (dynamic model) developed can be used to analyze the behavior of an entire HCP or CLP system during start-up, shut-down, regular operation involving periodic flow and water hammer generated by periodic valve switching, emergency valve closure, and capsule jamming. Work is near completion in developing such a dynamic model [29].

DRAG REDUCTION IN CLP

It is well known that when a small amount of polymer such as polyethylene oxide is added to the liquid flowing through a pipe, the headloss (pressure drop) becomes significantly less than that without the polymer [30-33]. This phenomenon, known since World War II and widely used nowadays by pipeline companies in long-distance crude oil and product pipelines, is usually referred to as "drag reduction." In addition to polymers, fibers such as wood pulp, and combinations of fiber and polymers, also have been found to be effective in drag reduction [34,35].

The reason for drag reduction to occur is that long-chain polymers and fibers inhibit turbulence which in turn is responsible for the large headloss and pressure drop in turbulent flow. Consequently, for any type of hydraulic capsule pipeline (HCP) including coal log pipeline (CLP), drag reduction is not expected at low velocities at which the capsules are sliding on the pipe bottom and contact friction between the capsules and the pipe dominates the headloss or pressure drop. However, at high velocities, the capsules are lifted off or totally suspended by the flow, and headloss is mainly due to turbulence. Under this condition it is expected that drag reduction will occur and become effective. Whether this is true or not is being tested at the Capsule Pipeline Research Center. By the end of 1993 we should know from the test result whether drag reduction by adding polymers is effective at velocities above capsule lift-off. The effectiveness of drag reduction in capsule flow by using fiber (pulp) at low concentration (0.5%) has been demonstrated in a previous study [36,37].

CAPSULE JAMMING IN PIPE

To prevent capsule jamming in pipe, the causes of jamming must be clearly understood, and ways to prevent jamming must be developed. This research involves a combination of experiments and theoretical analysis. It is currently being pursued at the

Capsule Pipeline Research Center. No previous study of capsule jamming has been found in the literature.

ABRASION OF COAL LOGS

To minimize coal log abrasion (wear) in pipe, the various causes of such abrasion must be clearly understood. This includes erosion of coal logs by the fluid (water), abrasion of coal logs by rough joints, impact of coal logs with pipe, valves and with each other, and possible damage of coal logs by water hammer. A systematic investigation of these causes is currently underway [38].

WATER ABSORPTION OF COAL LOGS

Dry or relatively dry coal logs, upon immersion in the water in a pipeline, absorbs water quickly in the high pressure region immediate downstream of any pump. As the logs travel downstream, the pressure in the pipe drops and the logs decompress and release water. This goes in cycles as the logs travel between pumping stations. How fast does a coal log absorb and release water and how much water is absorbed/released during such cycles affect the strength and the integrity of the coal log. It is a phenomenon that has been explored experimentally in a recent study [39].

A preliminary model to predict the water absorption of coal logs has been developed by the writer [40]. The model assumes that the water entering a coal log causes air to be entrapped in the center of the log, forming an air core. As the water enters the log, the air core compresses. The rate of shrinkage of the air core and the ultimate size of the core can be predicted by using the Darcy's law in the water-saturated outer region of the log, and using the polytropic equation for the air core. Due to surface tension, the capillary flow equation is also needed at the air/water interface. The resultant equations can be solved to determine the size of the air core as a function of time. This in turn allows the determination of the coal log water absorption rate as the log encounters a

high ambient pressure, and the rate of water released as the ambient pressure decreases. The validity of the model is being checked in the laboratory through a set of tests. It is likely that improvement of this preliminary theoretical model will be needed to yield accurate predictions. More research will be needed before accurate prediction of the water absorption of coal logs can be accomplished. This is a complex phenomenon that involves the motion of water and air through a porous cylinder (the log). A good understanding of this problem will also help to understand the absorption of water by other porous solids immersed in water or underwater--a rather general field with wide-spread potential applications.

GRANULAR FLOW IN COAL LOG EXTRUSION/COMPACTION

As a coal log is being formed in an extruder or a compactor, the material (coal-water-air mixture) undergoes intensive compression, shear deformation, dewatering, and deaeration. Existing models for predicting the extrusion of food products, plastic materials, ceramics and metals are all based on the assumption that the material is incompressible [41-43]. They also often assume that the materials behave as a certain non-Newtonian fluid, such as the power-law fluid used for food products [44]. It is believed that a more realistic model for coal log extrusion/compaction should be based on granular flow and should take into account the compressibility of the material. This is an area that has not yet been studied. It presents a challenge to researchers in the granular flow area. Success in developing such a model has far-reaching implications since it is applicable not only to coal log fabrication but also to other fields such as extrusion of food products.

COAL SLURRY SUSPENSION OF COAL LOGS

Strong coal logs made by compaction [45,46] have high density--specific gravity approaching 1.35. Such dense logs, when transported by water in a large-diameter pipe,

require a high water velocity before the logs can be lifted off (totally suspended). For instance, for a 20-inch diameter pipe (the largest expected for coal log transport), the lift-off velocity can approach 20 ft/sec. This is too high a velocity for it causes excessive headloss, abrasion and other operational problems.

A way to solve the problem is to use coal slurry instead of water to transport the logs through the pipe. The coal slurry, having a density higher than water, develops a stronger buoyancy than water can develop. Consequently, heavy logs can be suspended (lifted off) by slurry at a velocity much below that required for water.

This concept was tested recently in a 2-inch-diameter pipe [47,48], using a slurry that contains 50% coal by weight--the same slurry used in the Black Mesa Coal Slurry Pipeline. The test results showed that logs suspended in the slurry were lifted off at a much lower velocity than that required for water suspension of coal logs. The headloss for coal logs in slurry was found to be identical to that for slurry flow alone. This is promising because it means much more coal can be transported at the same energy consumed by a coal slurry pipeline. More experiments are needed to test the concept in a larger pipe, and to develop a theory (or semi-empirical approach) for predicting the lift-off velocity and the headloss for coal logs in slurry. This opens up a new frontier of opportunities for researchers working in the field of coal slurry transport.

CONCLUSION

Many multiphase flow phenomena have been discovered in the development of the coal log pipeline (CLP) technology. The rapid advancement of the CLP technology has far outstripped current ability to understand fully the basic phenomena involved. A strong need exists to explore the basics of these phenomena so that they can be better understood and more accurately predicted. Such basic research will cause further advancement in the CLP technology. The field is fertile and promising; it provides important new topics of multiphase low that will both frustrate and delight researchers for many years.

REFERENCES

1. Brown, R.A.S. (1987). "Capsule Pipeline Research at the Alberta Research Council,1958-1978", Journal of Pipeline, Vol. 6, pp. 75-82.
2. Govier, G.W. and Aziz, K. (1972). The Flow of Complex Mixtures in Pipe, Van Nostrand Reinhold, New York, 792 pages.
3. Liddle, R.T. (1968). A Photographic Study of Capsule Behavior in a Pipeline, M.S. Thesis, University of Alberta, Edmonton, Canada, 126 pages.
4. Charles, M.E., Govier, G.W. and Hodgson, G.W. (1961). "The Horizontal Pipeline Flow of Equal Density Oil-Water Mixtures", Canadian Journal of Chemical Engineering, Vol. 39, No. 1, pp. 27-36.
5. Ellis, H.S., Redberger, P.J. and Bolt, L.H. (1963). "Transporting Solids by Pipeline, Part 2: Capsules and Slugs", Industrial Engineering Chemistry, Vol. 55, No. 9, pp. 29-34.
6. Hodgson, G.W. and Charles, M.E. (1963). "The Pipeline Flow of Capsules - Part 1: The Concept of Capsule Pipelining", Canadian Journal of Chemical Engineering, Vol. 41, No. 2, pp. 43-45.
7. Ellis, H.S. and Kruyer, J. (1970). "The Pipeline Flow of Capsules, Part 10: Empirical Pressure and Velocity Correlations for Cylindrical Capsules Conveyed in Pipelines up to 4 Inches in Diameter", Hydrotransport 1, Paper C2, Coventry, England.
8. Kruyer, J. and Ellis, H.S. (1974). "Predicting the Required Liquid Throughput from the Capsule Velocity and Capsule Pressure Gradient in Capsule Pipelines, " The Canadian Journal of Chemical Engineering, Vol. 52, pp. 215.221.
9. Jensen, E.J. et al (1975). TDA-RCA Capsule Pipeline Project, Phase 3 Report, Part 1, Alberta Research Information Series, No. 63, 267 pages.
10. Ellis, H.S. (1976). "An Analysis of the Lift-Off of Pipeline Capsules", Hydrotransport 4, Paper C1.

11. Liu, H. (1982). "A Theory on Capsule Lift-Off in Pipeline", Journal of Pipelines, Vol. 2, pp. 23-33.

12. Liu, H. and Graze, H.R. (1983). "Lift and Drag on Stationary Capsule in Pipeline," Journal of Hydraulic Engineering, Vol. 109, No. 1 pp. 28-47.

13. Liu, H. and Mohandas, S. (1987). "Experimental Study of Capsule Lift-Off in a 190 mm Pipe," Journal of Pipeline, Vol. 6, pp. 253-262.

14. Yanaida, K., Ohashi, A., Kudo, M., and Matsuike, T. (1980). "Flow Characteristics of Solid Capsules in Pipes," Hydrotransport 7, Sendai, Japan, pp. 397-422.

15. Yanaida, K. (1982). "Capsule Pipeline Research in Japan", Journal of Pipelines, Vol. 2., Nos. 2-4, pp. 117-131.

16. Van den Kroonenberg, H.H. (1978). "A Mathematical Model for Concentric Horizontal Capsule Transport", Canadian Journal of Chemical Engineering, Vol. 56, No. 5, pp. 538-543.

17. Van den Kroonenberg, H.H. (1979). "A Novel Vertical Underwater Lifting System for Manganese Nodules Using a Capsule Pipeline", Proc., Offshore Technology Conference, Houston, Texas.

18. Lazarus, J.H. and Kilner, F.A. (1974). "Incipient Motion of Solid Capsules in Pipelines", Hydrotransport 3, Golden, Colorado, Paper G4, pp. 43-63.

19. Lazarus, J.H. (1974). "Power Optimization of Hydraulic Transportation of Solid Capsules", Hydrotransport 3, Golden, Colorado, Paper G4, pp. 43-63.

20. Graze, H.R., and Brasington, J.A. (1987). "The Influence of Collar on an HCP Capsule," Journal of Pipelines, Vol. 6, No. 2. pp. 181-191.

21. Liu, H., (1992). "Hydraulic Behaviors of Coal Log Flow in Pipe," Proc. of the 7th International Symposium on Freight Pipelines, Wollongong, Australia, pp. 201-205.

22. Liu, H. and Richards, J.L. (1993). "Hydraulics of a Stationary Capsule in Pipe," Journal of Hydraulic Engineering, American Society of Civil Engineers (In Print).

23. Woodson, R.J. (1988). Transient Control of Hydraulic Capsule Pipeline Bypass, M. S. Thesis, Department of Civil Engineering, University of Missouri-Columbia 112 pages.

24. Woodson, R.J., Lenau, C.W. and Liu, H. (1989). "Analysis of Pressure Surges in a Pump Bypass System for Hydraulic Capsule Transport," Freight Pipelines: Proceedings of the 6th International Symposium on Freight Pipelines, Hemisphere Publishing Corporation, New York.

25. Phimjarchon, R. (1992). Prediction of Water Hammer in HCP Pump Bypass System, M. S. Thesis, Department of Civil Engineering, University of Missouri-Columbia, 80 pages.

26. El-Bayya, M.M. (1991). Transient Flow in Hydraulic Capsule Pipeline, M. S. Thesis, Department of Vicil Engineering, University of Missouri-Columbia, 113 pages.

27. Lenau, C.W. and El-Bayya, M.M. (1992). "Treatment of Unsteady Flow through Capsule Pipeline: Capsule-Water Interaction," Proceedings of the 7th International Symposium on Freight Pipelines, Wollongong, Australia, pp. 215-219.

28. El-Bayya, M.M. (1994). Unsteady Flow of Capsules in a Hydraulic Pipeline: Theory and Experiment.Ph.D Dissertation, Department of Civil Engineering, University of Missouri-Columbia. (Expected to complete in May 1994).

29. Wu, J.P. (1994). Dynamic Modeling of an HCP System and Its Control, Ph.D Dissertation, Department of Civil Engineering, University of Missouri-Columbia. (Expected to complete in January 1994).

30. Lumley, J.L. (1969). "Drag Reduction by Additives," Annual Review of Fluid Mechanics, pp. 367-384.

31. Hoyt, J.W. (1972). "The Effect of Additives on Fluid Friction, A Freeman Scholar Lecture," Journal of Basic Engineering, American Society of Mechanical Engineers, pp. 258-285.

32. Virk, P.S. (1975). "Drag Reduction Fundamentals," AIChE Journal, Vol. 21, No. 4, pp. 625-656.

33. Sellin, R.H.J. (1989). "Drag Reducing Polymer Use in Hydrotransport," Proc. Institution of Engineers, Part 1, Vol. 86, pp. 381-394.

34. Kale, D.D. and Metzner, A.B. (1976). "Turbulent Drag Reduction in Dilute Fiber Suspension: Mechanistic Consideration," AIChE Journal, Vol. 22, No. 4, pp. 669-674.

35. Lee, P.F.W. and Duffy, G.G. (1976). "Relationships between Velocity Profiles and Drag Reduction in Turbulent Fiber Suspension Flow," AIChE Journal, Vol. 22, No. 4, pp. 750-753.

36. Rhee, K.H. (1989). Behavior of Cylindrical Capsules in Fiber-Water Flow in Pipe, Ph.D. Dissertation, Department of Civil Engineering, University of Missouri-Columbia, 258 pages.

37. Rhee, K.H. and Liu, H. (1990). "Preliminary Experiments on Capsule Suspension in Fiber-Water Flow," Freight Pipelines: Proceedings of the 6th International Symposium on Freight Pipelines, Hemisphere Publishing Corporation, New York, pp. 343-350.

38. Cheng, C.C. (1994). Wear and Damage of Coal Logs in Pipeline, Ph.D Dissertation, Department of Civil Engineering, University of Missouri-Columbia. (Expected to complete in Summer 1994).

39. Chen, S.H. (1993). Effects of Particle Size, Binder Concentration and Compaction Pressure on Selected Properties of Coal Logs, M.S. Thesis, Department of Chemical Engineering, University of Missouri-Columbia, 102 pages.

40. Liu, H. (1993). A Preliminary Theory to Predict Water Absorption Rate of Coal Logs, CPRC Report, 20 pages.

41. Griffith, R.M. (1962). "Fully Developed Flow in Screw Extruders," Industrial and Engineering Chemistry Fundamentals, Vol. 1, pp. 180-187.

42. Hami, M.L., and Pittman, J.F.T. (1980). "Finite Element Solutions for Flow in a Single-Screw Extruder, Including Curvature Effects," Polymer Engineering and Science, Vol. 20, pp. 339-347.

43. Gopalakrishna, S. and Jaluria, Y. (1992). "Modeling of Starch Gelatinization in a Single-Screw Extruder," Food Extrusion Science Technology, Editor: Koteini et al., Marcel Dekker, Inc., New York.

44. Lai-Fook, R.A., Li, Y. and Smith, A.C. (1991). "A 2-D Numerical Study of Intermeshing Self-Wiping Screws in Biopolymer Extrusion," Polymer Engineering and Science, Vol. 31, No. 15, pp. 1157-1163.

45. Liang, Z. (1993). Compaction of Binderless Coal for Coal Log Pipelines. M.S. Thesis, Department of Civil Engineering, University of Missouri-Columbia, 127 pages.

46. Gunnink, B.W. and Liang, Z. (1993). "Compaction of Binderless Coal for Coal Log Pipelines. Fuel Processing Technology, Elsevier Science Publisher (In Print).

47. Xu, G. (1993). Behavior of Capsules in Slurry Medium in a Pipe, M.S. Thesis, Department of Mechanical and Aerospace Engineering, University of Missouri-Columbia, 106 pages.

48. Seaba, J.P. and Xu, G. (1993). "Slurry Suspension of Coal Logs--An Exploratory Study," presented at the 18th International Technical Conference on Coal Utilization and Fuel Systems, Clearwater, Florida.

Measurement of the Shear-Induced Coefficient of Self-Diffusion in Dilute Suspensions

Sean Biemfohr
Thomas Looby
Shannon Biemfohr
David T. Leighton, Jr.

Department of Chemical Engineering
University of Notre Dame

Abstract:

The shear induced coefficient of self-diffusion is measured for dilute suspensions of non-colloidal particles at low Reynolds numbers in a simple shear flow. Previous models predicted that the diffusivity for dilute suspensions of smooth spheres should scale as the square of the concentration ϕ in the dilute limit since at least three particle interactions are required for any permanent displacement across streamlines (Leighton and Acrivos, 1987). In this study the diffusivity is shown to be linear in the concentration in this limit, with a value of approximately $0.024\ \phi\ \dot{\gamma}a^2$. Further investigation showed that the surface roughness of the particles was insufficient to account for this behavior (Da Cunha and Hinch, 1993), however the particles were also shown to be eccentric with an average aspect ratio of 1.19. The observed diffusivity may be due to the breaking of the symmetry of two particle interactions by this eccentricity.

1. Introduction:

When non-colloidal particles interact in the presence of a shear flow under creeping flow conditions, they will experience some displacement away from their original streamlines. Such displacements lead to a random walk which can be characterized by a shear-induced coefficient of self-diffusion. Since the rate at which such interactions occur is proportional to the shear rate $\dot{\gamma}$, and the length scale of each displacement is the particle radius a, the diffusion coefficient has the dimensional scaling $\dot{\gamma}a^2$ (Eckstein, *et al.*, 1977). In a dilute suspension of smooth spheres undergoing purely hydrodynamic interactions it takes at least three interacting particles to produce a net displacement, thus since the rate at which a tracer sphere interacts with two other particles is

proportional to the square of the concentration ϕ, the diffusion coefficient should also scale with ϕ^2 in the dilute limit (Leighton and Acrivos, 1987). In contrast, if there is some source of irreversibility in two particle interactions which breaks the symmetry of the interaction, such as is produced by surface roughness (Rampall, *et al.*, 1993), or if there is any anisotropy in the particles which also breaks the symmetry, then two particle interactions can lead to a net displacement and the coefficient of self-diffusion will be proportional to ϕ in the dilute limit.

In this paper we present the results of experiments designed to distinguish between these two possible limiting behaviors. In the next section we describe the materials and procedure used in the experimentation. The third section describes the statistical analysis necessary to determine the diffusivity from observations of the random walk of particles in a Couette flow, and the fourth section presents the results of our experimentation. The final section presents our conclusions and offers possible explanations for the observations.

2. Experimental Approach:

The method for measuring the diffusivity employed in this study is the same as that developed by Leighton and Acrivos (1987). The diffusivity was measured in the Couette viscometer depicted in figure 1. The device had an inner radius of 9.73cm and an outer radius of 11.74cm, resulting in a gap width of 2.01 cm. The aluminum inner cylinder was aligned with the rotation axis to within $\pm 50\mu m$ and the outer PMMA cylinder to within $\pm 200\mu m$, thus the variability in the gap width was on the order of 1%. To test the effect of this small non-uniformity of the gap on the measured diffusivity, a new PMMA outer ring was machined which was aligned to $\pm 70\mu m$ and the diffusivity of a dilute suspension was remeasured. No statistically significant difference was found.

A stress free lower boundary was provided by a 1cm thick layer of mercury, and the upper surface was open to the atmosphere. The radial diffusivity was determined by measuring the variation in the length of time a marked particle took to complete a series of rotational transits of the device. Since particles on different streamlines move with different velocities, the variation in the transit time can be used to measure the radial diffusion coefficient.

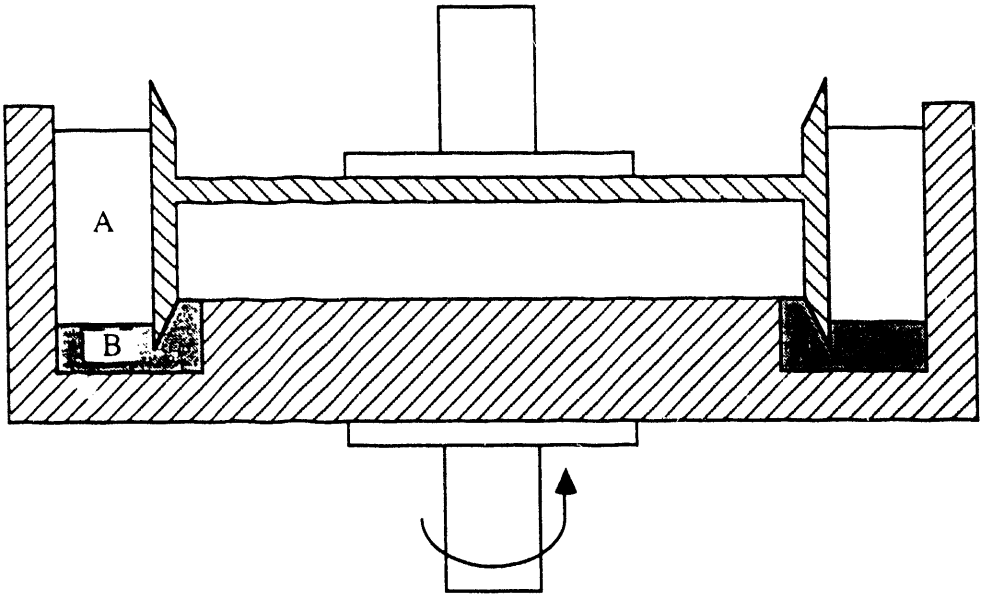

Figure 1. Measurement apparatus. The device consisted of a 9.73cm radius aluminum inner cylinder and a 11.74cm radius PMMA outer cylinder. The suspension A was floated on a layer of mercury B between the inner and outer cylinders. Transit times were determined by recording the times at which a marked particle would pass in front of a vertical line drawn on the inner cylinder.

The particles used in the experiments were PMMA particles sieved from a polydisperse sample of MG102 particles obtained from ICI, Inc. They were observed to be slightly eccentric, ranging from a prolate spheroidal shape to (in the case of two fused spheres) a cylindrical shape with hemispherical end caps. It was found that in air the particles would tend to stick to a plane surface, and would not always lie with the major axis parallel to a plane. Thus to characterize the shape it was necessary to drop a sample of the particles one at a time through a fluid onto a plane inclined at an angle of about 70° to the horizontal. The particles were aligned by travelling down the plane, and observed using a video microscope to determine the size and shape. A sample of 75 particles was used. The average ratio of major axis to minor axis was determined in this way to be 1.19, characterized by a population standard deviation of 0.07. The average diameter was 771μm and the population standard deviation was ±54μm. Many of the particles were observed to contain air bubbles in their interiors, and on some spheres these inclusions led to a visible bump on the exterior of the sphere.

In addition to size and shape characterization, it was also necessary to determine the characteristic surface roughness of the particles. The hydrodynamic technique of Smart and Leighton (1989) was employed, in which the surface roughness was determined by measuring the time taken for a particle initially in contact with a plane surface to fall away. It is simple to show that, for spherical particles, this time is related to the largest scale of surface roughness which is of sufficient surface coverage to support the particle. The relationship is approximately given by:

$$\varepsilon_s \approx 2 \exp\{2 - [t_d / (t_d - t_a)] [1 + \ln(2)]\} \qquad 2.1$$

where ε_s is the surface roughness rendered dimensionless with the particle radius a, t_a is the time for the sphere to fall from contact to one radius from the plane, and t_d is the time to fall from contact to one diameter.

A sample of 12 particles were tested in this way in an 8ml sealed cube containing an 80wt% Triton X-100 and 20wt% water solution. The plane surface was a freshly cleaved mica sheet. The

Table 1. Tracer particle major and minor diameters. The diameter measured for the largest particle is within 0.5% of that expected for a 1/8 inch ground asrylic sphere.

major diameter (μm)	minor diameter (μm)	aspect ratio
317	310	1.02
420	401	1.05
656	602	1.09
770	659	1.17
770	663	1.16
802	651	1.23
1157	667	1.73
1434	1402	1.02
3190	-	1.00

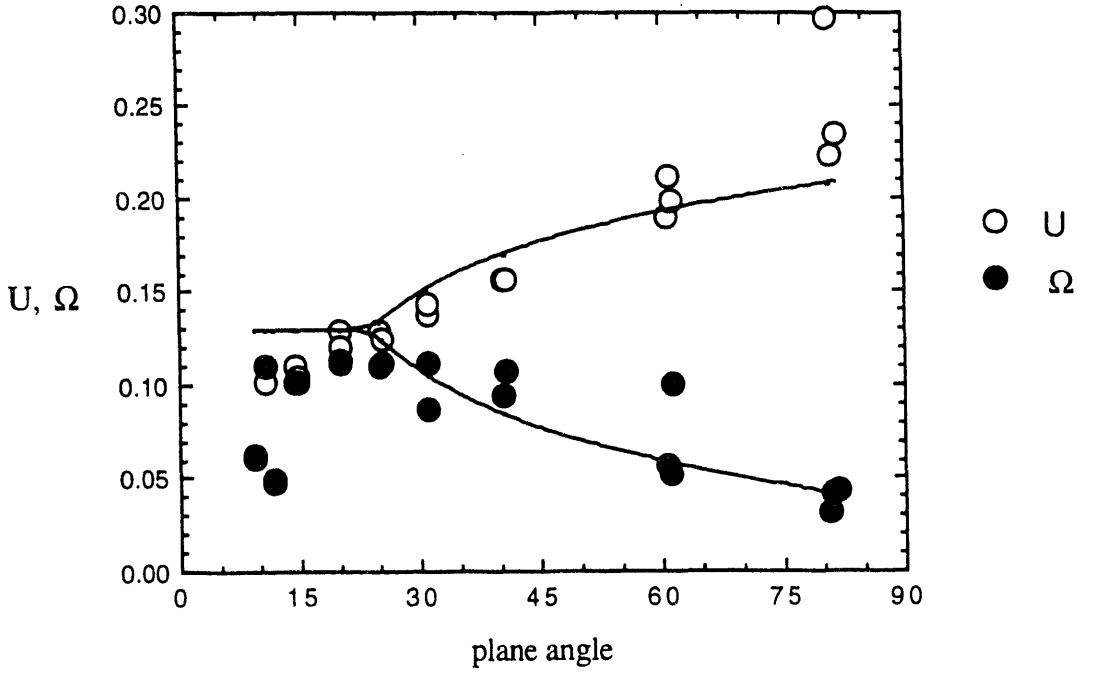

Figure 2. Translational and angular velocities of a sphere along an inclined plane. The dimensionless translational and rotational velocities of the 1418μm sphere along an inclined acrylic plane are presented as a function of inclination angle. The curves are fitted by a dimensionless roughness of 7.5×10^{-4} and a coefficient of sliding friction of 0.22.

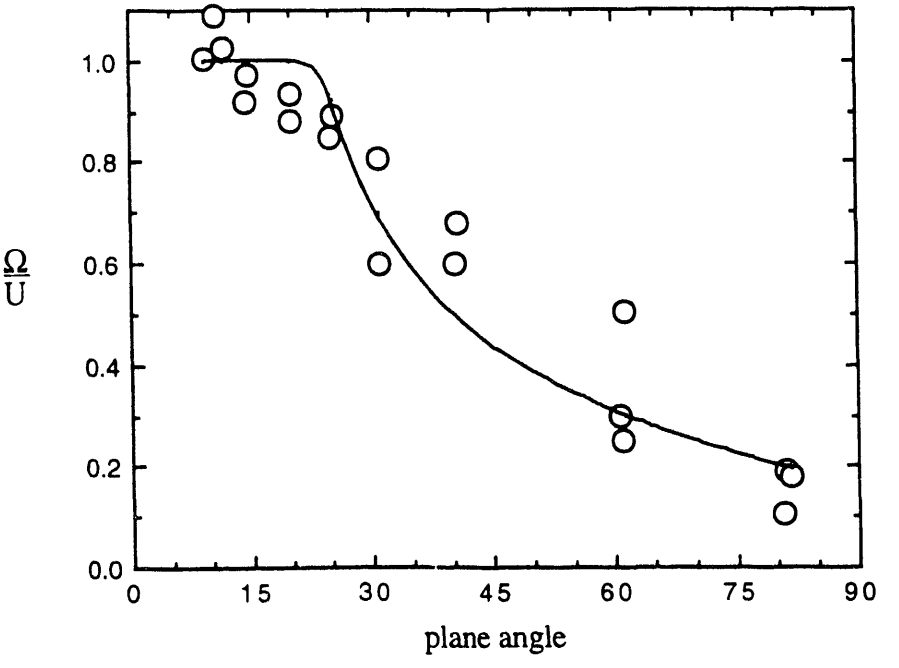

Figure 3. The ratio of rotational to translational velocities along an inclined plane. Data are for the same experiments as in figure 4, with solid body rotation being achieved at about a 15° plane angle of inclination.

data exhibited a large amount of scatter, likely due to the use of an equation derived for spheres to describe the behavior of ellipsoidal particles. The average dimensionless surface roughness over all orientations examined was approximately 1×10^{-3}.

A number of the acrylic particles were marked by boiling them in a concentrated solution of black RIT fabric dye. Several particles were selected from this batch as tracer particles. Both the shape and sizes of these particles were determined by examining their motion down an inclined plane. The sizes and aspect ratios of these particles are given in table 1. The largest particle was a ground acrylic sphere obtained from Engineering Laboratories, Inc.

To determine the influence of the dying process on the surface roughness, the 1418μm particle was more completely characterized. This particle was chosen because it was the most nearly spherical of the larger ICI acrylic particles, and thus the roughness models developed by Smart (Smart and Leighton, 1989; Smart *et al.*, 1991) would better apply. We were unable to find a dyed acrylic particle of the same size as those in the suspension which was also spherical.

The 1418μm particle was characterized by determining its time to fall away from an acrylic plane, and by measuring its rotational and translational velocities along an inclined plane. The latter portion of the experiment allows us to determine both the surface roughness and the coefficient of friction between the dyed acrylic particle and the acrylic plane. The details of this experiment are identical to those described by Smart, *et al.* (1991). The measured velocities as a function of angle are given in figure 2, rendered dimensionless with the Stokes settling velocity and the component of gravity tangential to the plane. The ratio of these velocities, a sensitive function of the coefficient of friction, is given in figure 3. The data are best fit by a dimensionless surface roughness of 7.5×10^{-4} and by a coefficient of sliding friction of 0.22. Thus, it appears that the dying process does not significantly add to the surface roughness.

The fluid used in the diffusion experiments was a solution of 77.93wt% Triton X-100 (a non-ionic surfactant manufactured by Rohm and Haas), 13.06% anhydrous zinc chloride, and 9.07% water. In addition, 0.2wt% concentrated hydrochloric acid was added to the final solution to prevent the formation of zinc hypochlorite precipitate. This was the same solution employed by

Phan and Leighton (1993) in their study of tracer diffusion at high concentrations. The fluid had a viscosity of 32p at the operating temperature of 24.5°C and a density of $1.17g/cm^3$. Both the index of refraction and the density of the fluid closely matched those of the acrylic particles.

In operation, the Couette device was brushed with a thin coating of the suspending fluid to protect aluminum surfaces from the mercury, and then the mercury and the pure fluid were added. The height of the pure fluid layer in the gap was approximately 3.3cm. Particles were added in the desired quantity at a shear rate of $4s^{-1}$. Shearing was continued at this shear rate until the particles were fully wetted, and then the shear rate was increased to $40s^{-1}$. At this higher shear rate secondary currents produced either by inertial flow in the mercury or by shear waves visible at the mercury / solution interface caused rapid vertical mixing of the particles. After 3 minutes of shearing it was found that the particles were well dispersed in the vertical direction, however at lower concentrations (1% - 5%) there appeared to be a band of particle free fluid near the inner wall. The cause of this band was not investigated, however it decreased in width as the concentration increased and disappeared altogether at a concentration of 7.5%.

Before taking data the suspension was well mixed. The mixing procedure consisted of shearing at $4s^{-1}$ and simultaneously scraping the fluid upward along the inner and outer cylinders around the entire circumference. This procedure was repeated twice, and then the marked particle was positioned near the center of the Couette gap. The suspension was sheared for a further 5min to 13min at $4s^{-1}$ before data taking was commenced. No inertial currents or interfacial instabilities were observed at this lower shear rate.

The position of the particle vertically in the gap was recorded before and after each series of transits to guage the significance of any secondary currents. These currents, apparently thermally driven, were of small magnitude (on the order of 3μm/sec), and typically varied in strength over a time scale of about 1 hour. Because the diffusivity for a dilute suspension is very small, however, this magnitude drift velocity could have a significant impact on the calculated value of the diffusion coefficient. As will be described in the next section, reduction techniques were employed to eliminate any constant drift velocities from the calculated diffusivity. Measurements were taken over

a period of approximately 20min to ensure that the drift velocity did not appreciably change during the measurements. Particle transit times were measured by determining successive times for a marked particle to pass a line drawn on the inner cylinder. Typically 100 transits would be observed, the suspension would be remixed according to the procedure described above, and the process would be repeated.

The experiments were done in two parts. First, the behavior of the 1.23 aspect ratio particle was investigated as a function of concentration. The number of measurements varied with concentration, with 500 to 700 transits observed at concentrations from 1% to 5%, and 300 transits observed at concentrations from 7.5% to 15%, the highest concentration used in this study. These measurements were done in two series, the first a sequence of 2.5%, 5%, 7.5%, 10% and 15% concentrations, and the second a sequence of 1%, 2.5%, and 5% concentrations. The migration behavior in the pure fluid was observed for both series. In addition, this particle was also examined at a 1% concentration using the newly machined outer ring which reduced the variability in the gap. The diffusivity measured in the two experimental runs differed by only 18%, which was well within the expected random error.

In the second part of the study, the behavior of the other tracer particles was examined at a 1% concentration alone. Typically 600 transits were observed for each particle. Difficulties were encountered for both the 314μm and 3190μm spheres (the smallest and largest particles used in the study). For the smallest sphere additional lights were required to sufficiently illuminate the particle to make it readily detectable, and these lights apparently induced significant thermal secondary currents in the gap. The large acrylic sphere, obtained from a different source than the 771μm particles, did not quite match the density of the fluid and displayed a tendency to settle. Diffusivities were calculated for this particle only from data taken when the particle was in the middle third vertically in the gap.

3. Statistical Analysis:

As is described in more detail by Leighton and Acrivos (1987), it is possible to use the

variation in the observed transit time of a marked particle as it travels around a Couette viscometer to determine the diffusion coefficient in the radial direction. For a device with finite curvature such as is employed here we may define a variable α_i such that:

$$(\alpha_{eff})_i = \frac{t' - t}{\left(\frac{1}{3} a_s^2 \dot{\gamma}_{eff} t^2 t'^2 (t + t') \left(\dot{\gamma}/x_0\right)^2_{eff}\right)^{1/2}} \qquad 3.1$$

where γ_{eff} and $(x_0)_{eff}$ are defined as:

$$(x_0)_{eff} = 2\pi n R \left(1 - \frac{n\varepsilon}{vt}\right)^{\frac{1}{2}} \qquad 3.2$$

and

$$\dot{\gamma}_{eff} = \frac{4\pi v}{\varepsilon}\left(1 - \frac{n\varepsilon}{vt}\right) \qquad 3.3$$

where v is the rotational frequency of the outer cylinder, t is the average of the transits t and t', and n is the number of successive transits summed together in calculating both t and t'. The device aspect ratio ε is defined as

$$\varepsilon = \frac{\frac{W}{R}\left(2 + \frac{W}{R}\right)}{\left(1 + \frac{W}{R}\right)^2} \qquad 3.4$$

where R is the radius of the inner cylinder and W is the gap width.

This expression, derived for a Newtonian velocity profile, explicitly accounts for the variation in both the path length that the sphere travels and the shear rate as a function of radial position in the gap. The calculated diffusivity is given by:

$$\hat{D} = \frac{D}{\dot{\gamma} a^2} \approx \frac{1}{2N} \sum_{i=1}^{N} (\alpha^2_{eff})_i \qquad 3.5$$

in which it is assumed that there are no measurement errors, or periodic displacements of particles such as would occur due to the rotation of doublets or clusters of particles. As was demonstrated by Leighton and Acrivos (1987), however, the contribution of errors to the calculated diffusion coefficient can be greatly reduced by summing successive transits together. Thus, instead of using the time for a particle to complete one transit in calculating α_i, we can use n successive transits and increase x_0 accordingly. It was demonstrated that the contribution of either observational errors or periodic displacements with variance σ_{obs}^2 to the calculated diffusivity would scale as $1/n^3$:

$$\hat{D}_{obs} \approx \hat{D} + \left[\frac{9}{512\,\pi}\frac{\dot{\gamma}^2 W^5}{R^3 a^2}\right]\frac{\sigma_{obs}^2}{n^3} \qquad 3.6$$

The actual diffusivity can thus be obtained by plotting the calculated diffusivity vs $1/n^3$ and extrapolating to zero. This is particularly important for small concentrations, since the contribution of observation error to the calculated diffusion coefficient may be larger than the actual diffusivity for single transits.

The extrapolation procedure suggested above only applies in the case where wall limitations of the random walk of the particle are not significant. In order to prevent wall limitations from becoming significant we limit $n \leq 6$ and we use only those migrations which begin in the central region of the Couette gap. We choose an observation window whose edges are the same multiple of diffusion lengths from the nearest wall. Because transits are much longer nearer the inner wall (and thus the elapsed strain between observations and diffusion length are longer), the window is displaced toward the outer wall. For our experiments we have chosen the window $0.308 < y^* < .808$ where $y^* = (r - R)/W$ is the dimensionless position in the gap.

The maximum information can be obtained from a series of transits if we make use of all of the observed transit times even for values of $n \neq 1$. For example, in the n=2 case we can calculate a value of α_i by using the total time to complete the first and second transits and then the third and fourth as t and t'. We can also determine a n=2 α_i by using the total time to complete the second and third transits and then the fourth and fifth. By interleaving the data in this way we take maximum

advantage of the transit observations and somewhat reduce the greater statistical error produced by calculating diffusivities using larger values of n.

In addition to the above treatment, it is also necessary to remove any contributions due to secondary currents. At a concentration of 1% the magnitude of the dimensionless diffusivity is only about 2.3×10^{-4}. For this diffusivity the expected rms radial displacement after 20 minutes of shearing at $4 s^{-1}$ is only about 1 particle diameter, thus it can be easily masked by drift motion arising from secondary currents. For a Newtonian velocity profile, the time to complete a transit of the device is related to the radial position r by:

$$t = \frac{\varepsilon}{v}\left(1 - \frac{R^2}{r^2}\right)^{-1} \qquad 3.7$$

The variation in the transit time due to some constant radial velocity U is thus given by:

$$\Delta t \approx \frac{dt}{dr}\Delta r \approx \frac{dt}{dr} U t \qquad 3.8$$

Taking the derivative of equation 3.7 and rearranging yields an estimate for the scaled drift velocity from the observed data:

$$U \sim \frac{1}{N}\sum_{i=1}^{N} \frac{(\alpha_{eff})_i}{(v \bar{t}_i)^{1/2}\left(1 - \frac{\varepsilon}{v \bar{t}_i}\right)^{1/2}} \qquad 3.9$$

where the mean is taken over all of the observed transits in a particular series. The diffusion coefficient can then be calculated by removing this bias:

$$\hat{D}_{obs} \approx \frac{1}{2(N - 1.5\,n)}\sum_{i=1}^{N}\left\{(\alpha_{eff})_i - U(v \bar{t}_i)^{1/2}\left(1 - \frac{\varepsilon}{v \bar{t}_i}\right)^{1/2}\right\}^2 \qquad 3.10$$

where n is the number of transits summed together in evaluating the data as described above. Note that the diffusivity is no longer simply the variance of the unbiased α_i's, but rather is different from this by a factor of N/(N-1.5n). This factor arises because of the reduction in the number of degrees of freedom by using the measured α_i's to determine the drift velocity. The factor of 1.5 is greater than unity (which would be expected for independent α_i's) since the successive transits are not independent, but depend in a complex way on the time history of the radial position of the particle during the migration. The factor of 1.5 was determined by examining the results of a numerical simulation of the migration process involving 160,000 transits. Since the value of N for the experimental data was kept at about 100, however, and n was less than or equal to 6 in the data reduction, this degree of freedom correction was only a few percent.

The magnitude of the drift velocity was small in our experiments, however it was sufficient to affect the calculated diffusion coefficient at the lowest concentrations studied. In figure 4 we plot the diffusion coefficient calculated for 0% concentration both with and without the drift correction. As can be seen, without the drift correction the calculated diffusivity is close to that measured for the 1% concentration suspension. The drift correction reduces the magnitude of the calculated diffusivity by more than an order of magnitude.

In order to determine if the period of 20 minutes was sufficiently short that the drift velocity could be regarded as constant, the five 1.0% concentration 20 minute time series observations were divided into ten 10min segments and reanalyzed using the same procedure. The results of this analysis are depicted in figure 5. As may be seen, the diffusivities calculated in this way differ by only 4%, which is much less than the random statistical error in the diffusivity. A somewhat different result was obtained for the 314μm and 3190μm acrylic spheres. In the former case, the illumination lights required for the small particle induced a secondary current much larger than that found for the other tracer particles. Thus, during the observation time the particle actually moved radially far enough for the magnitude of the drift velocity to change significantly. The calculated diffusivity for this particle decreased by 15% when the intervals used were divided in half. We have reported the lower value.

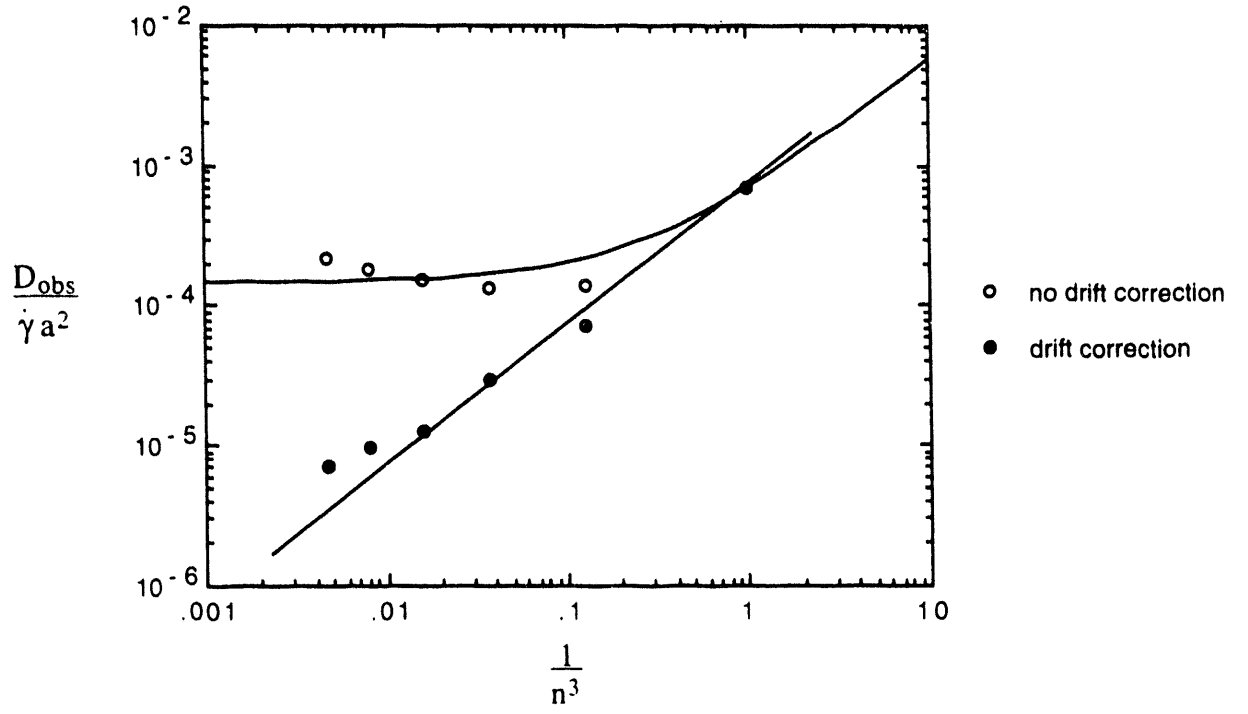

Figure 4. Diffusivities measured for the 1.23 aspect ratio particle at zero concentration. Open symbols are calculated diffusivities using equation 3.5, filled symbols are for the same data with the drift correction given by equation 3.10. The straight line is what would be expected for zero diffusivity from equation 3.6. Note that the calculated diffusivity is reduced by more than an order of magnitude.

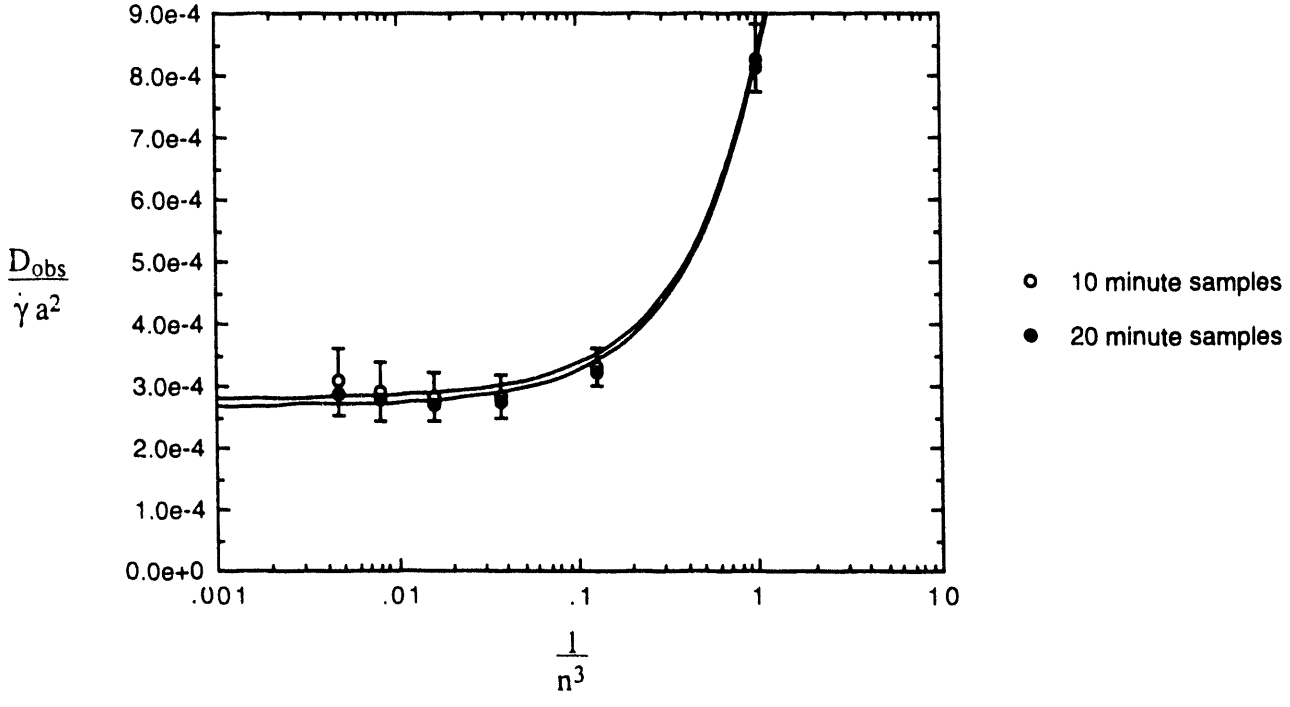

Figure 5. The effect of observation time on the calculated diffusivity for the 1.23 aspect ratio particle at 1% concentration. Open symbols are calculated diffusivities using 10 minute samples, filled symbols are the same data using 20 minute samples. The two results are similar, thus indicating that the drift velocity was approximately constant over this period.

With the 3190μm sphere, a different difficulty was encountered. Since this particle both had a very low diffusivity (about a factor of 4 less than that of a 771μm particle) and settled through the suspension vertically, the drift (while small) tended to be outwards for half of the observation series and inwards for the other half. The drift correction described above treats the drift velocity as a constant. When the observation series for this particle were divided in half, the diffusivity decreased by 35%. Again, we have reported the lower value, but the calculated diffusivity for this tracer particle must be regarded as only approximate.

Another consideration is whether sufficient strain elapses between observations for the diffusivity to approach its steady long-time value. This is particularly true for dilute suspensions in which interparticle interactions are more infrequent than at higher concentration. The elapsed strain between particle observations is a function of the position of the tracer particle in the gap, however for this geometry it was typically about 50. During this time a tracer sphere in a 1% suspension can be expected to undergo a close encounter (impact parameter at infinite separation of less than one diameter) with, on average, 1.3 spheres. The number of such encounters can be increased by increasing the number of successive transits summed together in calculating the diffusivity. In figure 6 we have plotted the calculated diffusivity for the 1.23 aspect ratio particle in a 1% concentration suspension as a function of $1/n^3$ up to n=20, together with a linear fit to the data. As can be seen, the data clearly approach an asymptotic value for $n \geq 4$, thus suggesting that the diffusivity approaches its steady value for $\dot{\gamma}t \leq 200$. Note that we cannot set a lower limit on this value since it is impossible to separate the experimental error from the strain necessary to approach steady state.

In addition to calculating the diffusion coefficient, it is also necessary to determine its accuracy. The variance of a set of independent measurements x_i has an error which is characterized by the chi square probability distribution. In the limit that the number of observations N becomes large, this distribution reduces to a Gaussian form with a standard deviation given by:

$$\sigma_D \approx D\left(\frac{2}{N}\right)^{1/2} \qquad 3.11$$

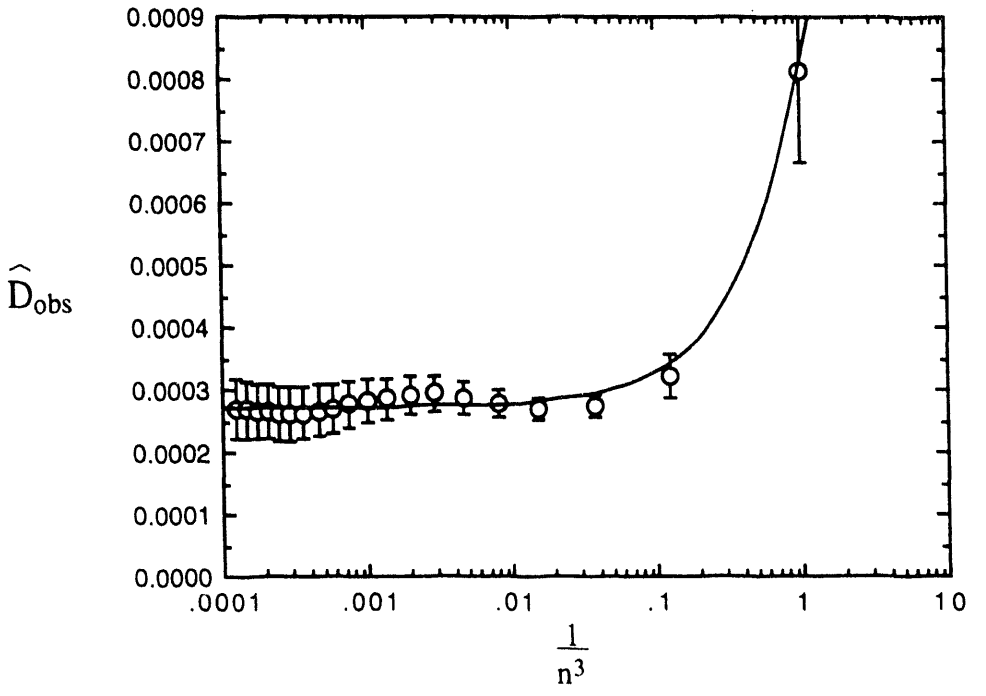

Figure 6. Effect of elapsed strain on the calculated diffusivity. Data are for the 1.23 aspect ratio particle at 1% concentration. The calculated diffusivity did not change significantly for n > 4, suggesting that steady-state had been achieved by this point. The curve is the fit suggested by equation 3.6.

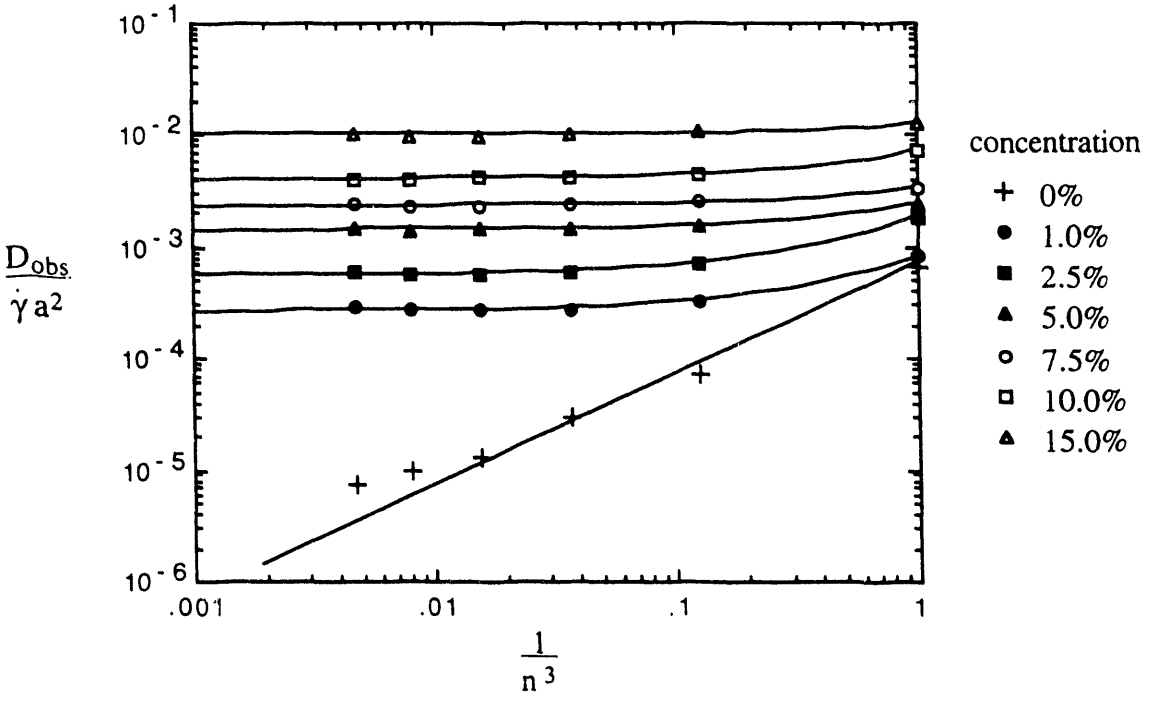

Figure 7. Calculated diffusivities for the 1.23 aspect ratio particle as a function of the number of transits summed together. Note that the measured diffusivity at 0% concentration is more than an order of magnitude below that measured at 1% concentration.

Unfortunately, the problem examined here is more complex, since the individual α_i's are *not* statistically independent, and we are also subjecting the data to an extrapolation to $1/n^3 = 0$. In order to more accurately determine the error in the calculated diffusivity we used two approaches. First, the statistics of the diffusivity calculated via the numerical simulation was examined. This showed that the error of the diffusivity calculated using the extrapolation procedure described above was roughly twice what would be expected from a random sample of N elements as given by equation 3.11. Second, the scatter in the diffusivity measured in the actual experiments for each 20 minute sample was also determined and used to estimate the error. This had the added advantage of also including any error due to incomplete mixing before each experimental run. The error in the diffusivity calculated both ways was quite similar, suggesting that the contribution to the error produced by the mixing was small in comparison to the statistical source of error.

4. Results:

The diffusivities measured using the procedure described above for the 1.23 aspect ratio particle are presented in figure 7 as a function of $1/n^3$, and the extrapolated values are given with one σ error in table 2. The curves in the figure are linear fits to each data set. Note that the diffusion coefficient calculated for the pure fluid case is more than an order of magnitude below the extrapolated value for the 1% concentration case. This large degree of separation demonstrates that this technique can be used to accurately measure the diffusivity even at these low concentrations.

In order to determine the asymptotic behavior of the diffusivity in the dilute limit, it is useful to examine the ratio D/ϕ. This is done in figure 8. As can be seen, the ratio approaches a constant value as the concentration goes to zero, showing that the diffusivity is proportional to the concentration in the dilute limit, with a coefficient of $0.024 \pm .003$. The earlier work of Leighton and Acrivos suggested that the diffusivity scaled with ϕ^2 in the dilute limit. Their data was correlated by the expression:

$$\hat{D} = 0.5\,\phi^2\left(1 + 0.09\,e^{7\phi}\right) \qquad 4.1$$

Table 2. Measured dimensionless coefficient of self-diffusion as a function of concentration for the 1.23 aspect ratio tracer particle. The diffusivities are rendered dimensionless by the shear rate and the average radius of the particles in the suspension.

ϕ	$\hat{D} \times 10^4$	$\sigma_{\hat{D}} \times 10^4$
0	0.008	0.02
0.01	2.42	0.23
0.025	5.76	0.67
0.05	14.5	1.6
0.075	23.2	4.1
0.10	41.6	7.8
0.15	102	18

Table 3. Virial expansions for the diffusivity of the 1.23 aspect ratio tracer particle. The errors given are those calculated by assuming the form of the virial expansion is correct, and accounting for the statistical error in the measured diffusivities. These one standard deviation errors thus do not reflect any systematic error in the measurement procedure, or error due to the assumed form of the virial expansion. Note that the $O(\phi^2)$ coefficient is within one standard deviation of zero, and that the constant term is also zero to within error.

ϕ^0	ϕ^1	ϕ^2	ϕ^3	range
8.5×10^{-7} $\pm 2.1 \times 10^{-6}$	0.0242 $\pm$0.0031	-0.05 $\pm$0.14	2.28 $\pm$1.19	$0 \le \phi \le 0.15$
-	0.0232 $\pm$0.0016	-	1.86 $\pm$0.43	$0 \le \phi \le 0.15$
8.3×10^{-7} $\pm 2.1 \times 10^{-6}$	0.0222 $\pm$0.0028	0.11 $\pm$0.10	-	$0 \le \phi \le 0.05$

Some of the data from this earlier study, together with their proposed correlation, is also reproduced in figure 8. As may be seen, the data in the present study agrees very well with the earlier measurements, with the correlation drawn through the new data passing through the old as well. The difference is, of course, that it is necessary to make measurements at concentrations much below the lowest value (4.6%) used in the Leighton and Acrivos study to measure the very small $O(\phi)$ coefficient.

It is interesting to try to determine the next coefficient in the virial expansion for the diffusivity in this suspension from the data. We have tried three different expansions, with the results given in table 3. The coefficients are obtained using a weighted linear regression scheme, and the errors in the coefficients are determined from the error in the measured diffusivities rather than the degree of fit to the data. As can be seen, the $O(\phi^2)$ coefficient is always within one standard deviation of zero. Indeed, the data is adequately fit by the correlation:

$$\hat{D} \approx 0.023\,\phi + 1.86\,\phi^3 \qquad 4.2$$

where the $O(\phi^2)$ term is absent entirely. The cause for this behavior is unclear, however it may be that the region in concentration over which solely three particle interactions can contribute significantly to the particle migration is very small. At a concentration of 10% the average interparticle separation distance is only 3.5 radii, and thus multiple particle interactions may already be becoming significant. Also, the work of Graham (Graham and Bird, 1984; Graham and Steele, 1984) has demonstrated that particles tend to cluster at relatively low concentrations, making multiple particle interactions more likely.

The measured diffusivities for the other tracer particles at 1% concentration are presented in table 4. As may be seen, the diffusivities of the three tracer particles larger than those in the suspension are lower. These data are presented graphically in figure 9, where we have plotted the measured diffusivity vs. the ratio of the tracer major axis to the average major axis of the suspending particles. While the observations for the 3190μm sphere are somewhat uncertain for the reasons

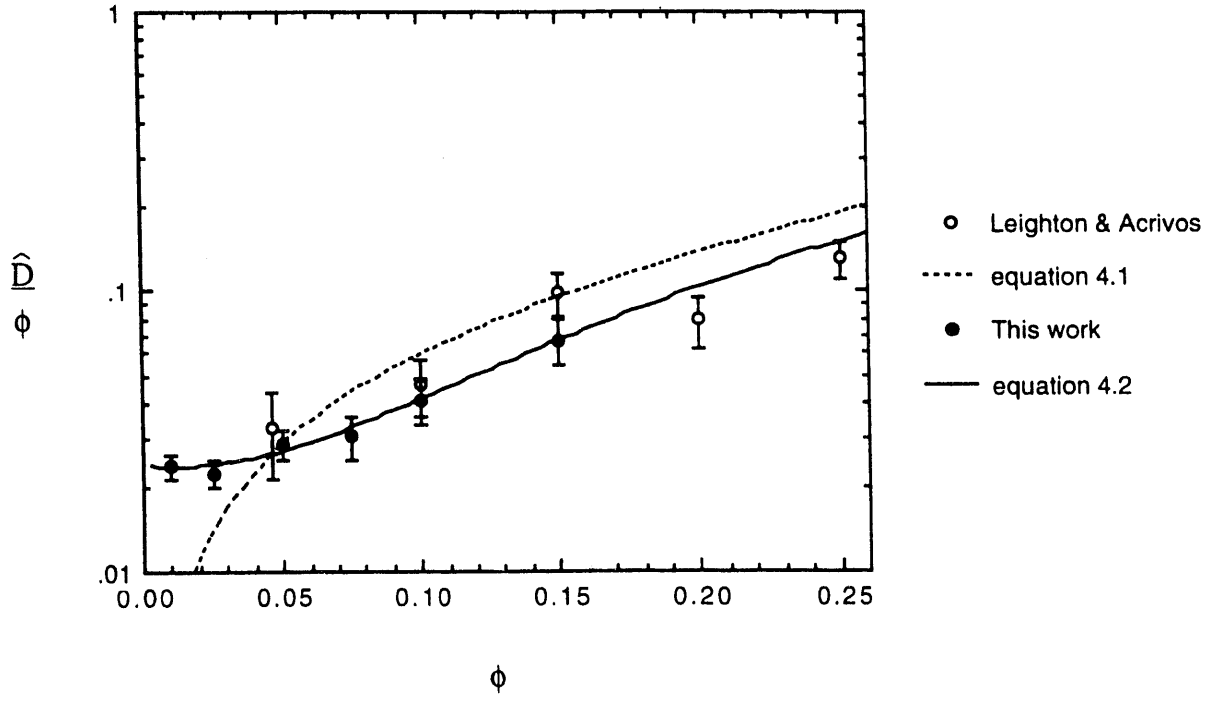

Figure 8. Measured diffusivity as a function of concentration for the 1.23 aspect ratio particle. Note that the diffusivities are in close agreement with the earlier 670μm sphere data of Leighton and Acrivos (1987). The low concentration data clearly show that the diffusivity approaches zero as $O(\phi)$ rather than as $O(\phi^2)$ as had been suggested by the correlation of Leighton and Acrivos.

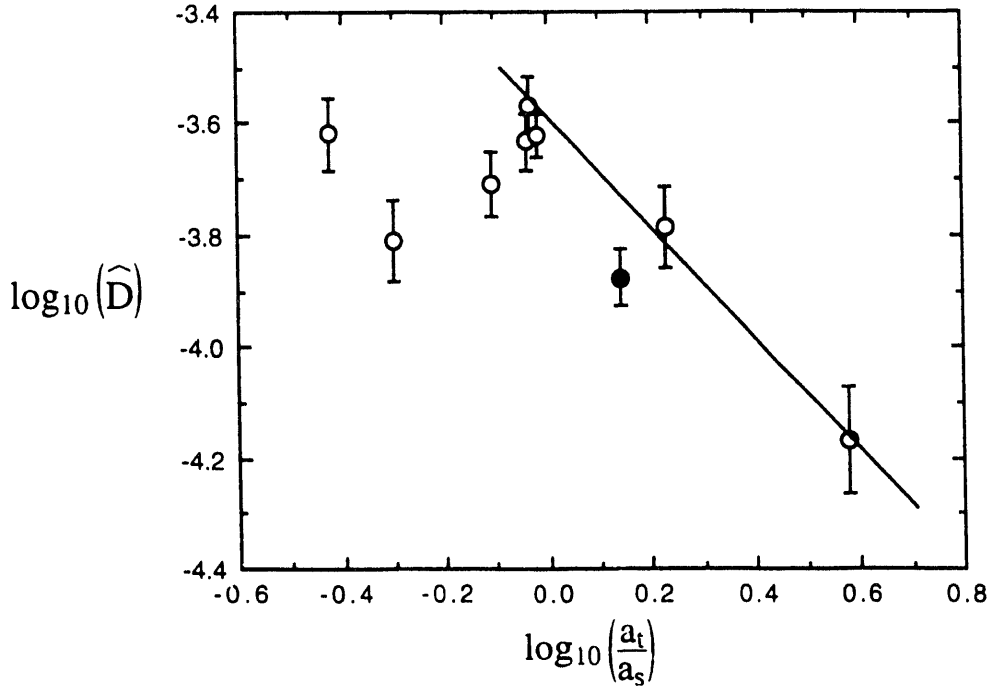

Figure 9. Measured diffusivity as a function of particle size and shape at 1% concentration. The diffusivity is plotted against the ratio of the tracer major axis to the average suspending particle major axis. Note that the diffusivitis of the larger tracer particles is much less than those of tracer particles closer in size to those of the suspension. The data is consistent with an inverse dependence on tracer particle size for large tracers. The filled symbol is the highly eccentric 1.73 aspect ratio particle.

Table 4. Dimensionless tracer diffusivities measured at 1% concentration for all tracer particles. The diffusivities are rendered dimensionless with respect to the shear rate and the square of the average suspending particle radius.

average diameter (μm)	aspect ratio	$\hat{D} \times 10^4$	$\sigma_{\hat{D}} \times 10^4$
314	1.02	2.17	0.38
411	1.05	1.58	0.29
630	1.09	2.01	0.29
714	1.17	2.77	0.34
717	1.16	2.38	0.30
726	1.23	2.43	0.23
912	1.73	1.36	0.17
1418	1.02	1.68	0.31
3190	1.00	0.70	0.17

described in the last section, the data are at least consistent with the inverse size ratio dependence observed by Phan and Leighton (1993) for concentrated suspensions. Much more precise measurements at larger aspect ratios would be required to confirm this relationship, however.

The dependence on tracer particle size for small tracers is much less clear, particularly due to the uncertainty in the 314μm tracer measurements. The data appear to be consistent with the interpretation that the $O(\phi)$ contribution to the diffusivity does not vanish for small tracer size. This is also similar to the behavior observed in concentrated suspensions. Again, it would be useful to explore a larger range in tracer particle sizes, but the 314μm particle was the smallest which could be detected in this experiment.

An effort was made to determine the effect of particle shape on the tracer diffusivity. A 1.73 aspect ratio particle was examined. This particle was capsule in shape and had a minor axis comparable to the minor axis of the particles making up the suspension. Its major axis, however, was significantly larger. As may be seen from figure 9, its diffusivity was less than that which would be expected for a more spherical particle with a characteristic radius of either the major axis or minor axis. This suggests that a high degree of anisotropy retards the diffusivity in a suspension of moderately anisotropic spheroids.

5. Conclusions:

In this work we have demonstrated that there exists a finite $O(\phi)$ contribution to the shear-induced tracer diffusivity. In order for such a contribution to exist something must break the symmetry of two-particle interactions to yield a net displacement. One possible explanation for this interaction assymetry is the presence of surface roughness on the particle. As has been demonstrated (Arp and Mason, 1977; Rampall, *et al.*, 1993) surface roughness acts to keep particles at distances greater than some minimum separation distance. Since particles are driven very close together in simple shear flows, surface roughness can significantly modify the particle trajectories. Such a displacement reveals itself in the assymetry of the pair particle distribution function. In figure 10 we

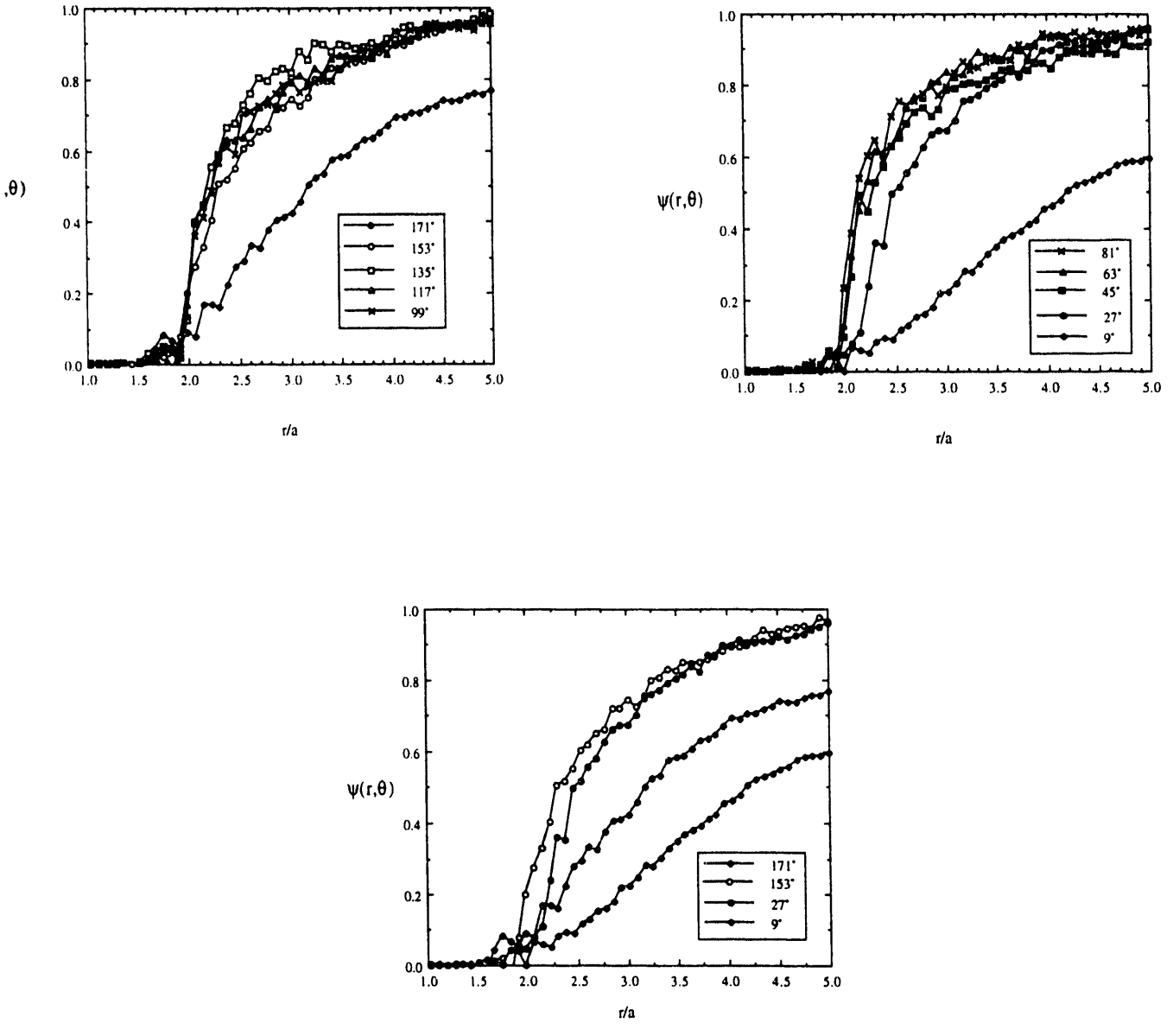

Figure 10. Area average pair distribution function for a 5% concentration suspension of 3175μm spheres in a simple shear flow: a. compression quadrant, b. extensional quadrant, c. comparison of compression and extension quadrants at low angles. The data were taken for ground acrylic particles similar to the large tracer sphere employed in our work. The measured surface roughness for these spheres was 2 x 10^{-3} radii. From Rampall, *et al.* (1993).

reproduce the area average pair distribution function observed by Rampall, *et al.* (1993) for a 5% suspension of 3175μm acrylic spheres undergoing simple shear flow. This average is defined as:

$$\psi(r,\theta) = \frac{\int_{\theta - \Delta\theta/2}^{\theta + \Delta\theta/2} \int_{0}^{r} q(r,\theta)\, r\, dr\, d\theta}{\frac{1}{2} r^2 \Delta\theta} \qquad 5.1$$

where $q(r,\theta)$ is the pair distribution function normalized by its value at infinity. The range $0°<\theta<90°$ corresponds to the recession side of an interaction while $90°<\theta<180°$ corresponds to the approach side. Note that the lack of fore and aft symetry in the pair distribution function, with a depletion of particles on the recession side, provides clear evidence of the displacement of particles during particle interactions. Such displacements can lead to a random walk.

Recently Da Cunha and Hinch (1993) have calculated the shear-induced self-diffusion for equal sized particles in a simple shear flow arising from surface roughness. From their calculations, a dimensionless surface roughness of 1.0×10^{-3} would result in an $O(\phi)$ coefficient for the random walk diffusivity of 9.75×10^{-4}, more than a factor of 20 less than the value measured in this study. In order for the surface roughness to account for the observed diffusivity, it would have to have a value of 0.07, a factor of 70 greater than is observed, leading us to conclude that while the surface roughness can significantly modify the structure of a dilute suspension of spheres, it plays no direct role in the random walk for the suspension studied here.

A second possibility is that the assymetry in interactions is induced by the anisotropy of the particles in the suspension. While it is possible to numerically simulate the interaction of two ellipsoidal particles in a shear flow, and a few such calculations have been carried out (Kim and Karilla, 1991), these simulations have not yet been used to calculate the displacement upon interaction or the resulting $O(\phi)$ contribution to the coefficient of self-diffusion. Our observations of the effect of tracer particle size are at least qualitatively consistent with this explanation, however. In addition to causing an $O(\phi)$ contribution to the self-diffusion, the anisotropy of a dilute suspension of

spheroids would also contribute an $O(\phi)$ term to the shear-enhanced fluid diffusivity. Thus, one would expect to find a non-zero limit to the tracer diffusivity as the tracer particle becomes small in such suspensions. In contrast, a suspension of rough spheres would have little or no $O(\phi)$ contribution to the fluid diffusivity, since for isolated spheres the limiting closed orbit streamline for the fluid lies approximately 0.3 sphere radii away from the surface. Roughness elements would have to project outside this layer to significantly contribute to the fluid diffusivity, and thus the tracer diffusivity would vanish as the tracer particle size became small.

It is important to note that the diffusivity measured in the experiments described here is that due to the random walk of the particle, and not the gradient or effective diffusivity which is determined from the actual flux of particles arising from a concentration gradient. This latter quantity, which has only been measured for concentrated suspensions (Leighton and Acrivos, 1987b; Chapman and Leighton, 1991; Phillips, *et al.*, 1991), is of necessity greater than or equal to the random walk diffusivity. Cunha and Hinch (1993) have calculated this quantity as well for the interaction of rough spheres in dilute suspensions, and have shown that the gradient diffusivity is greater than the random walk diffusivity by about a factor of 4, at least for irreversibilities arising from surface roughness. Thus, if we are permitted the analogy between interacting ellipsoidal particles and interacting rough spheres, this suggests that the asymptotic limit of the gradient diffusivity should be about $0.1\ \phi\ \gamma a^2$ in the dilute limit for the suspension examined in this srudy. The actual value for other suspensions, however, will be strongly dependent on the geometry and surface morphology of the particles and will likely vary significantly.

Acknowledgements:

The authors gratefully acknowledge helpful conversations with Dr. E. J. Hinch during the early phases of this work. This work was supported by a grant from Lockheed Missiles and Space, Inc.

References:

Arp, P. A. & Mason, S. G. 1977 Kinetics of flowing dispersions. 9. Doublets of rigid spheres (experimental). *J. Colloid Interface Sci.* **61**, 44.

Da Cunha, F. R. & Hinch, E. J. 1993 Shear-induced dispersion in a dilute suspension of rough spheres. manuscript in preparation.

Eckstein, E. C., Bailey, D. G. & Shapiro, A. H., 1977 Self-diffusion of particles in shear flow of a suspension. *J. Fluid Mech.* **79**, 191.

Graham, A. L. & Bird, R. B. 1984 Particle clusters in concentrated suspensions. Part I: Experimental observations of particle clusters. *Ind. Eng. Chem. Fundam.* **23**, 406.

Graham, A. L. & Steele, R. D. 1984 Particle clusters in concentrated suspensions. Part II: Information theory and particle clusters. *Ind. Eng. Chem. Fundam.* **23**, 411.

Kim, S. & Karrila, S J. 1991 *Microhydrodynamics: Priciples and Selected Applications.* Boston: Butterworth-Heinemann.

Leighton, D. T. & Acrivos, A. 1987 Measurement of shear-induced self-diffusion in concentrated suspensions of spheres. *J. Fluid Mech.* **177**, 109.

Phan, S. E. & Leighton, D. T. 1993 Measurement of the shear-induced tracer diffusivity in concentrated suspensions. *J. Fluid Mech.* (submitted).

Rampall, I., Smart, J. R. & Leighton, D. T. 1993 The influence of surface roughness on the pair-particle distribution function of dilute suspensions of noncolloidal spheres in simple shear flow. *J. Fluid Mech.* (submitted).

Smart, J. R., Beimfohr, S. & Leighton, D. T. 1993 Measurement of the translational and rotational velocities of a noncolloidal sphere rolling down a smooth inclined plane at low Reynolds number. *Phys. Fluids A* **5**, 13.

Smart, J. R. & Leighton, D. T. 1989 Measurement of the hydrodynamic surface roughness of noncolloidal spheres. *Phys. Fluids A* **1**, 52.

Granular Flow Studies by NMR

S. A. Altobelli, A. Caprihan, H. A. Cheng, E. Fukushima,
M. Nakagawa, and L. Z. Wang

The Lovelace Institutes,
2425 Ridgecrest Dr. SE, Albuquerque, NM 87108

Abstract

In recent years, Nuclear Magnetic Resonance (NMR) has been applied to a few non-medical problems including flows of pure fluids, immiscible fluids, concentrated suspensions, and grains. In this report, we provide examples of applications to granular flows. In particular, flows of granular materials in a partially filled, horizontal, rotating cylinder (such as a rotating drum or kiln), have been studied by NMR to yield not only the velocity and concentration field, but also 'diffusion' coefficient components which are related to the fluctuations of velocity. The velocity is measured from phase images wherein the phase is correlated with the velocity. The concentration is measured by a flow compensated imaging sequence corrected for intensity attenuation caused by diffusion. The diffusion coefficient components are often anisotropic, for example, flat particles have significantly anisotropic diffusion along the direction of flow as opposed to perpendicular to the flow. We have used NMR measurements of concentration and velocity to calculate energy dissipation from all sources including the collisional losses, from velocity and acceleration fields, and compared the results with a macroscopic measurement of the total dissipation. Preliminary numerical experiments from a 2D direct simulation are being used to assess the performance of the NMR experiments. Experiments with two solid phases yielding different NMR signals can be used to study mixing/demixing phenomena such as segregation; we have imaged radial segregation of a mixture of mustard seeds and glass beads of identical sizes but different density.

Introduction

Experimental investigation of the interior of granular flows is difficult. Since such experimental data could be useful in applications which require efficient solids handling , and since NMR imaging can provide information on structure and motion of protons inside optically opaque samples without

mechanical intrusion, we have endeavored to develop, evaluate and use NMR techniques appropriate to studies of granular dynamics. In this report, we will:

- describe the physical bases of velocity and diffusion imaging;
- describe the flow being used to evaluate our NMR techniques (partially filled, horizontal, rotating cylinder);
- present examples of NMR concentration, velocity, and diffusion measurements;
- present dissipation images calculated from NMR data and direct observation;
- briefly describe visual and NMR observation of segregation phenomena, and mention simulations which help evaluate NMR results;
- and summarize recent progress in NMR technology and in understanding granular flow in rotating cylinders.

NMR Measurements

NMR measurements were performed in the horizontal bore (31 cm diameter) of a super conducting magnet (1.89 T from Oxford Instruments). A "bird-cage" radio frequency (rf) probe, tuned to 80.3 MHz, and actively shielded gradient coils (Magnex Scientific) were controlled by a versatile VAX-based (Digital Equipment Corp.) imager/spectrometer (Quest 4400 from Nalorac Cryogenics Corp.). Data collected by the NMR imager was transferred via ethernet to a workstation (Sun Microsystems) for analysis using customized data-reduction software. Figure 1 shows the main elements of the imager/spectrometer.

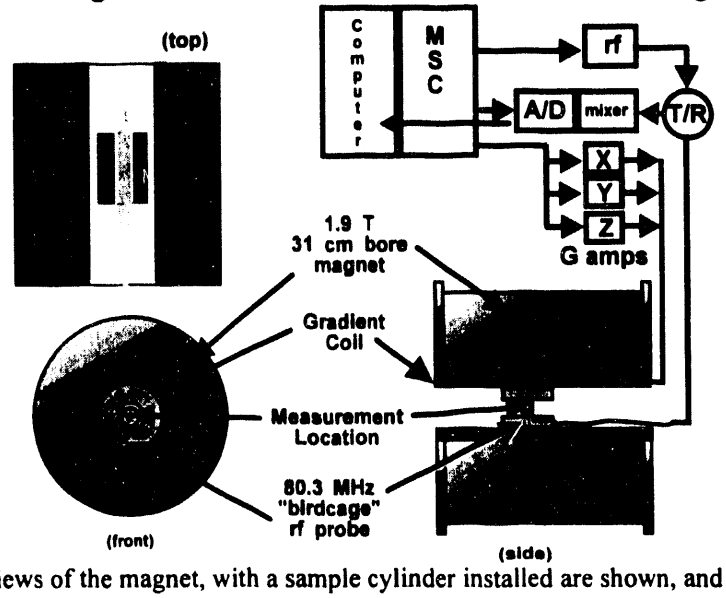

Figure 1. Three views of the magnet, with a sample cylinder installed are shown, and the associated electronics are a summarized schematically. The experiment is controlled by a micro-state controller (MSC) which controls the radio frequency (rf) and gradient (X, Y, Z) outputs and sampling (A/D).

velocity imaging and diffusion imaging . The images presented here are of the type termed phase-warp, Fourier images. Velocity or diffusion information is obtained by first performing a set of experiments with varying sensitivity to the desired parameter, and then mathematically fitting the NMR data on a pixel-by-pixel basis. NMR imaging experiments make use of the proportionality between NMR frequency ω and magnetic field B expressed in the Larmor equation $\frac{\omega}{2\pi} = \gamma B$ where γ has the value 42.5 MHz/T for protons. Gradient coils were used to generate spatially linear variation of B of the form $(B_0 + G_x x + G_y y + G_z z)$, with concomitant changes in ω. The gradients were small compared to the static field: the peak values for the gradients used in these experiments were 1-10 mT/m. NMR signals were induced by the small, transient, magnetization resulting from the precession of a large number of nuclear spins. This magnetization was initially excited by an rf pulse, modified by gradient pulses, and then observed in the presence of a "readout" gradient. The process encoded one spatial coordinate in the frequency of the signal and additional spatial (and velocity) information in the phase of the signal. Diffusion / fluctuation information is derived from pixel-by-pixel variations in a series of images, as described below. In Fourier imaging, data is taken in a domain conjugate to the image domain termed **k**-space. We acquire 128 by 128 samples on a rectangular grid in **k**-space, one "row" per sub-experiment. After each of the sub-observations, the magnetization is allowed time to re-equilibrate. In fluctuating systems like the granular flows considered here, 4 complete acquisitions are summed and Fourier transformed to produce an image.

In order to measure, for example, the x-component of flow or diffusion (more precisely, one of the diagonal components of the self-diffusion tensor, e.g., D_{xx}), a gradient with the profile shown in Figure 2 may be used.

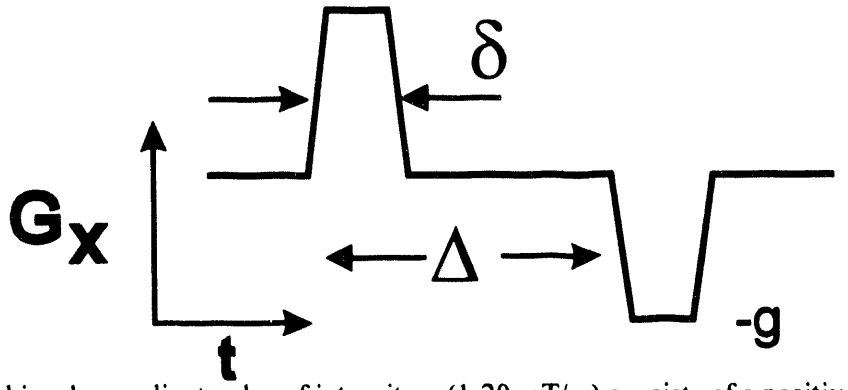

Figure 2 A bi-polar gradient pulse of intensity g (1-20 mT/m) consists of a positive and a negative pulse of duration δ (e.g., 1 ms) separated by an interval Δ (1-100 ms).

The NMR signal S(g), in the presence of such a pulse, compared to the signal observed without the gradient pulse is given by (according to Stejskal and Tanner)

$$\frac{S(g)}{S(0)} = e^{i\gamma\delta\vec{g}\cdot\vec{v}\Delta-\gamma^2\delta^2g^2D\left(\Delta-\delta_3\right)} \qquad [1]$$

The effect of the bulk flow is a phase shift, and the effect of the random motion due to self-diffusion is an attenuation of the signal. By performing a series of NMR imaging experiments with increasing values of g and fitting the model equation for each pixel, images of velocity components and D are calculated.

Four aspects of the imaging process may be discerned from these comments. First, information from all parts of the sample was received simultaneously in the NMR signal, which could only be observed when most of the magnetization was nearly in phase. Second, in order to decode the information present in the phase of the signal, repeated measurements with systematic variation of the phase encoding gradients were made. Third, since the velocity and one spatial coordinate were both encoded in the phase of the signal, velocity was extracted from the difference between two images. Fourth, velocity fluctuation information is derived by curve fitting image attenuation.

Direct Observations and Numerical Experiments

The basic flow we are using to evaluate the NMR techniques is generated by a partially filled, horizontal, rotating cylinder. Mustard seeds, sesame seeds, sunflower seeds, sand, and glass spheres are used singly and in combination as flowing substances. NMR signals are not obtained from the sand or the glass spheres. The dimensions of the cylinder are shown in Figure 3. When installed inside the rf coil, inside the magnet, the cylinder was supported by two sets of plastic rollers. NMR measurements were obtained from a tomographic slice transverse to the cylinder. All NMR measurements reported here were taken from slices within 2 cm of the (lengthwise) center of the cylinder.

The cylinder was also used outside the magnet to perform direct observation of segregation phenomena. Many two component mixtures and some sand samples with a broad size distribution were studied.

Global dissipation in flowing mustard seeds and sesame seeds was estimated by observing half filled cylinders rolling down an inclined plane. For a range of inclinations a period of nearly constant velocity was observed. Total dissipation was estimated from the constant velocity observations.

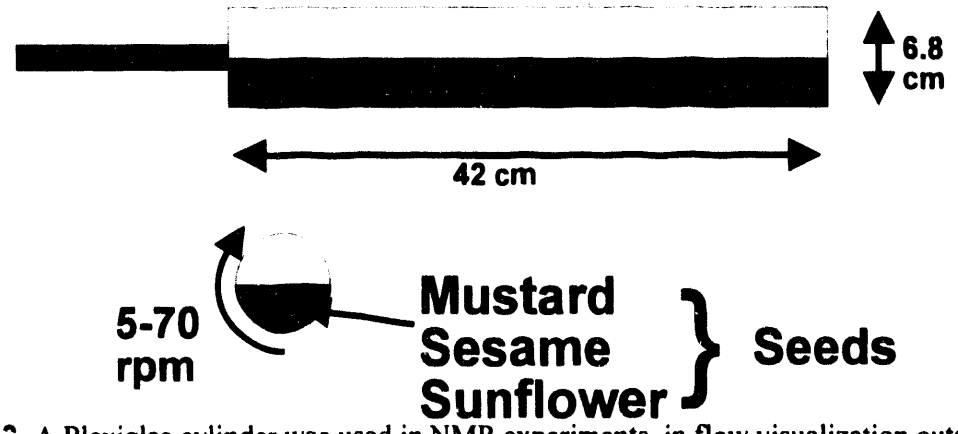

Figure 3 A Plexiglas cylinder was used in NMR experiments, in flow visualization outside the magnet, and in experiments which estimate global dissipation in flowing granular materials. The ID and length of the cylinder are shown.

A 2-dimensional, direct numerical simulation developed by Hopkins and Louge is being matched to mustard seed studies. Parameters such as the mean rotation of the flowing seeds and the mean time between collisions are difficult to measure directly, and the simulation is used to estimate them. The output of the simulation is also used as input to numerical simulation of the NMR experiments.

Results

An example of NMR measurements of V_x, and V_y in mustard seeds is shown in Figure 4. The cylinder was rotated clockwise at 24 rpm. The x- and y-components of mustard seed velocity are shown as gray scale images. The flow

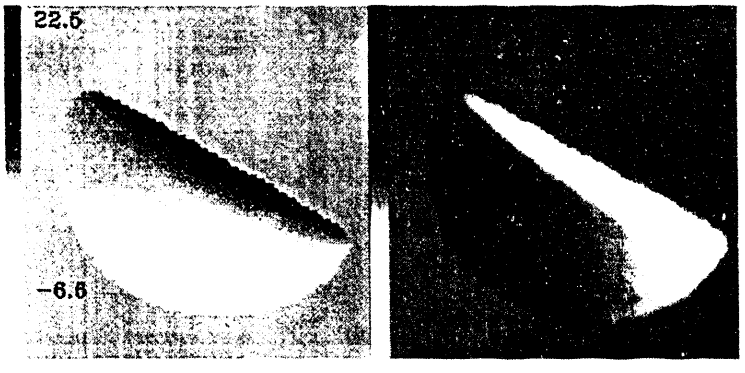

Figure 4. Left image shows the horizontal component of velocity in a half-filled cylinder of mustard seeds. The right hand image shows the vertical component of velocity for the same flow.

consists of two regions: a region of seeds in rigid body rotation in contact with the cylinder and a flowing shear layer which arises from the top of the rigid rotation

region and returns the granular material to the bottom of the incline. At low rotation rates, such as this example, the upper surface of flowing mustard seeds is planar. X-velocity is positive to the right as indicated by darker grey values, the positive direction for y-velocity is taken to be upward. Alternate presentations of the velocity information are possible, as shown in Figure 5.

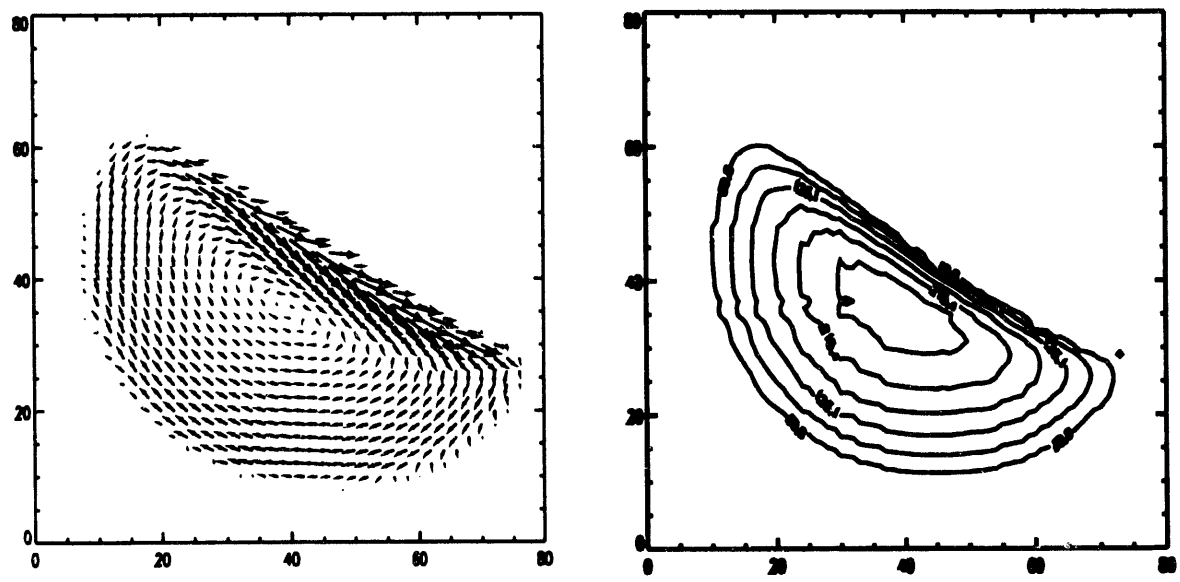

Figure 5. Velocity data is presented as a vector plot, on the left, and as iso-lines of the computed stream function on the right.

NMR measurements of D_{xx}, D_{yy}, and D_{zz} of mustard seeds rotated at 24 rpm are shown in Figure 6.

Figure 6. Diagonal components of the self-diffusion tensor for flowing mustard seeds, imaged by NMR, are shown. D_{xx} is on the left, D_{yy} in the center and D_{zz} is on the right. See Figure 7 for a comparison in a similar flow of sesame seeds.

For comparison, NMR measurements of D_{xx}, D_{yy}, and D_{zz} of sesame seeds rotated at 24 rpm are shown in Figure 7. Note the distinctly different distribution and the anisotropy of the diffusion components.

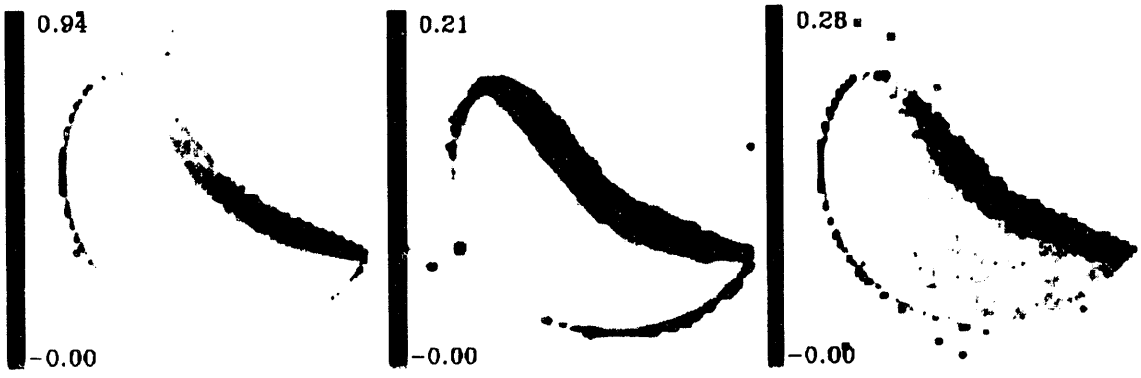

Figure 7. Diagonal components of the self-diffusion tensor for flowing sesame seeds, imaged by NMR, are shown. D_{xx} is on the left, D_{yy} in the center and D_{zz} is on the right. See Figure 6 for a comparison in a similar flow of mustard seeds.

One final result, a photograph showing the axial segregation which was observed in a sand sample is in Figure 8. The sand had a broad size distribution and the smallest particles were darker in color than the larger particle. The sand was initially well-mixed, and the configuration shown in the figure evolved within one hour of rotation at approximately 30 rpm. All mixtures studied have demonstrated either radial or axial segregation based on particle size, density and surface characteristics.

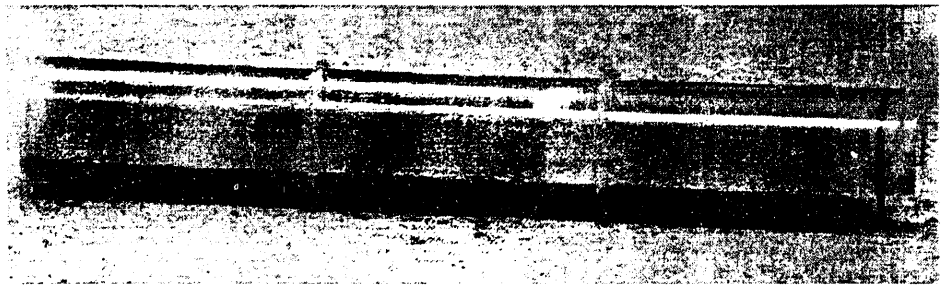

Figure 8. Photograph shows the alternating dark and light bands of sand resulting from rotation of a mixed sand sample. This is an example of 'axial' segregation observed in many flowing granular mixtures.

Summary

NMR concentration images have been improved by accounting for signal loss due to velocity fluctuations. Velocity measurement resolution and S/N have similarly been improved. Fluctuation/diffusion imaging techniques applicable to granular flows have been developed, and are currently being evaluated and used.

The concentration and velocity data already obtained accounts for most observable energy dissipation. Fluctuation/diffusion images show anisotropy apparently related to particle shape. Radial and axial segregation occur by virtue of density, size and surface property differences in granular flows with two or more components.

We are currently working on understanding what aspects of the motion spectrum of granular materials can be extracted from NMR experiments, how the image acquisition process affects averaging, how to adapt new imaging strategies to granular dynamics.

References

Watkins, J. C. and Fukushima, E. 1988 "High-pass, birdcage coil for nuclear magnetic resonance", *Rev. Sci. Instrum.* **59**, 926-929.

Morris, P. G. 1986 *Nuclear Magnetic Resonance Imaging in Medicine and Biology* Oxford, Clarendon.

Caprihan, A. and Fukushima, E. 1990 "Flow Measurements by NMR", *Phys. Rep.* **198**, 195-235.

Callaghan, P. T. 1991 *Principles of Nuclear Magnetic Resonance Microscopy*, Oxford Press.

Caprihan, A., Altobelli, S., Benitez-Read, E. 1990 "Flow-Velocity Imaging from Linear Regression of Phase Images with Techniques for Reducing Eddy-Current Effects" *J. Magn. Reson.* **90**, 71-89.

Hopkins, M. A. and Louge, M. 1991 "Inelastic microstructure in rapid granular flows of smooth disks" *Phys. Fluids A* **31**(1) 47-57.

Nakagawa, M. Altobelli, S. Caprihan, A., Fukushima, E. and Jeong, E.-K. 1993 "Non-invasive Measurements of Granular Flows by Magnetic Resonance Imaging", *Exp. in Fluids* In print.

Stejskal, E. O. and Tanner, J. E. (1965) *J. Chem Phys*. **42**, 288.

Flow of Colloidal Crystals

M.K. Chow, M. E. Fagan and C.F. Zukoski
Department of Chemical Engineering and Beckman Institute
University of Illinois
Urbana, IL 61801

Abstract

The microstructure and flow properties of crystals consisting of charge stabilized, uniform spheres is explored as a function of particle packing fraction and shear rate. An order parameter characterizing the degree of hexagonal close packing in the velocity-vorticity plane for the crystals under shear is developed to explore the effect of shear on microstructure. For volume fractions above the equilibrium ordering transition as shear rate is increased, long range orientational order is lost, regained and then lost again. While these transitions are broad, often spanning an order of magnitude in shear rate, rheological transitions accompanying changes in microstructure can be quite abrupt.

The mechanisms of deformation and flow in crystalline solids have seen extensive investigation in a stress range on the order of a few percent of the material's shear modulus[1]. Experimental and modelling studies have resulted in a detailed understanding of the roles of defect and dislocation nucleation and movement in yielding, and creep phenomena. More recent studies focusing on the microstructural and mechanical properties at elevated pressures and stresses have demonstrated that crystalline solids can be stressed into an X-ray amorphous state and that some materials sustain plastic deformation over strain ranges far in excess of what would be expected under normal processing conditions[2,3]. The origins of high stress microstructures and flow properties are poorly understood. In this paper we report recent work on model crystalline solids where microstructures and mechanical properties have been probed over a wide of crystal densities with stresses up to $0.5\text{-}1G_0$ where G_0 is the crystal's equilibrium elastic shear modulus. A non-equilibrium phase diagram is developed where mechanical properties and microstructures are correlated over a crystal density range up to $1.7\phi_f$ where ϕ_f is the freezing density.

Our model system consists of uniform spherical charge stabilized particles suspended in an aqueous electrolyte[4]. As a result, the scaling relationships we derive are most obviously

applicable to overdamped systems and thus have immediate applications in the field of dense suspension rheology. However, the similarity of the microstructures and scaling relationships we see with those predicted or measured for atomic or molecular crystals suggests a common underlying physics dominated by the role of particle packing in the transfer of stress in crystalline solids. Our results show that the key parameter linking molecular and colloidal crystals is a characteristic structural relaxation time, t_r[5]. For molecular solids t_r will depend on particle mass, size and interaction potential while for the colloidal solid the structural relaxation time will depend on continuous phase viscosity, particle size and interaction potential. However, we expect that when deformed at rates comparable to t_r^{-1}, molecular and colloidal crystals undergo similar structural and flow transitions.

The aqueous suspensions studied consisted of uniform polystyrene latex particles 238 and 255 nm in diameter dialyzed to equilibrium against 10^{-3} M KCl. Rheological studies were made with a Bohlin Constant Stress Rheometer with a cup and bob geometry. Both constant rate of strain and constant stress experiments could be carried out using this instrument. SANS patterns were gathered on samples in a Couette shear cell as a function of shear rate. A two dimensional scattering pattern was gathered where $k_y = k_e$ and $k_x = k_v\underline{e}_v + k_\nabla\underline{e}_\nabla$. Here $\underline{e}_e$, $\underline{e}_v$ and $\underline{e}_\nabla$ are unit vectors in the vorticity, velocity and shear gradient directions. x and y denote horizontal and vertical directions on the SANS detector and the k_i are magnitudes of the wave vectors along the i^{th} direction. When the beam passed through the axis of rotation, $k_\nabla = 0$. When the beam was off-axis, k_x contains components from both k_v and k_∇. Examination of the modulation of intensity maxima at fixed k_e and k_v with varying k_∇ was used to explore the stacking correlations for hexagonally closed packed layers[6-8].

Samples were loaded into the rheometer or SANS shear cell and presheared at 10-20 s^{-1} for 5 min prior to allowing the sample to sit for an additional 30 min before determining equilibrium elastic modulus and SANS patterns. For ϕ<freezing volume fraction, ϕ_f, the suspensions were opaque white, had well defined zero shear rate viscosities and showed no shear induced ordering for $\phi/\phi_f<0.97$. When $\phi/\phi_f>1$, preshearing established long range orientational order, LROO, corresponding to hexagonally close packed planes oriented with the close packed direction along $\underline{e}_v$. The stacking sequence of these layers was explored by following the intensity along $\underline{q}_l(k_\nabla) = ((2\pi/d)\underline{e}_e, (2\pi/(d\sqrt{3}))\underline{e}_v, k_\nabla\underline{e}_\nabla)$ where d is the crystal lattice parameter. Stacking

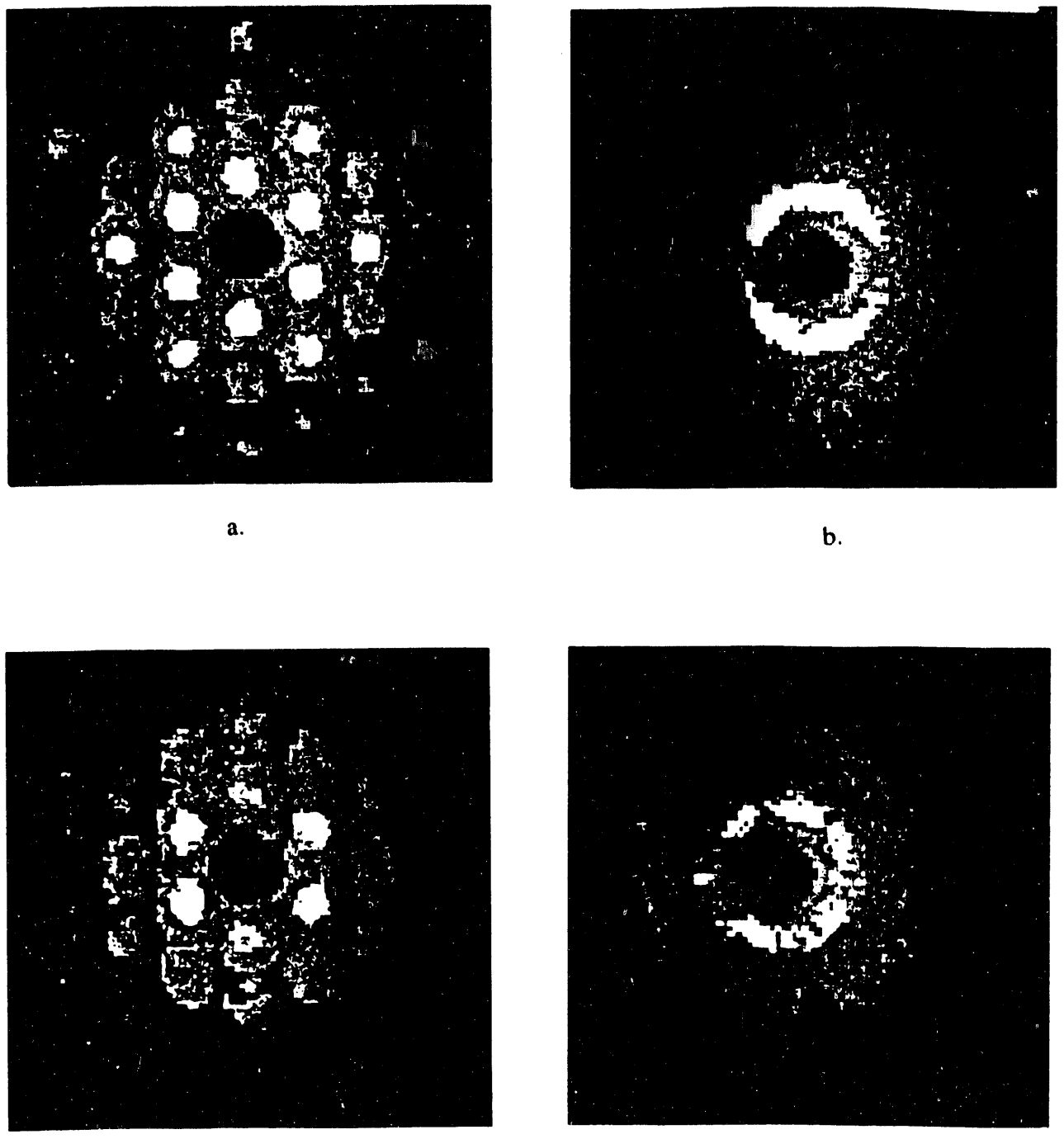

a. b.

c. d.

Fig. 1. Small angle neutron scattering patterns typical of colloidal crystals. Patterns taken on 255 nm particles at a volume fraction of 0.505: a) at rest, b) $\dot{\gamma}$ = 1 s^{-1}, c) $\dot{\gamma}$ = 70 s^{-1}, d) $\dot{\gamma}$ = 5,000 s^{-1} corresponding to LROO at rest, polycrystals, shear layers and amorphous microstructures.

correlations of hexagonally close packed layers in the e_∇ direction show up as modulations in $\underline{q}_1(k_\nabla)$. For all samples investigated where $\phi>\phi_f$, a broad maximum in $\underline{q}_1(k_\nabla)$ occurred near $k_\nabla = 0.6(2\pi/d)$ indicating a weak registration between layers consistent with the random registered stacking. Visually, these samples showed a smooth iridescence due to Bragg scattering of white light. The elastic modulus of the crystals, G_0, was determined when a small strain was applied along the (110) direction of the (111) planes of the crystalline phase (i.e., along $\underline{e}_v$) producing an elastic modulus which varied exponentially with volume fraction ranging from 4 Pa at $\phi=0.395$ to 2031 Pa at $\phi=0.61$. The solids were linear up to strains of 0.012. The static yield stress (i.e., the stress above which plastic deformation occurred) τ_y^s, was found to equal $(0.012\pm0.003)G_0$. For $\tau>\tau_y^s$, the suspensions deformed in a plastic, work hardening manner never reaching a steady state rate of strain. Visually, the sample showed signs of becoming polycrystalline in this stress region.

When a stress larger than the dynamic yield stress, τ_y^d, a steady state rate of strain was established and all remnants of the smooth iridescence were replaced by a polycrystalline optical appearance[9,10]. The intensity maxima seen at rest in SANS were replaced by broad rings with regions of greater intensity forming crescents concave up and down in the primary scattering ring. However, $\underline{q}_1(k_\nabla)$ retained a maximum near (0.6) $2\pi/d$ indicating the continued presence of stacked layers. At higher shear rates ($\tau/G_0>0.04$), visually the samples showed a coexistence of zones of uniform iridescence and regions displaying polycrystals. These two phases coexisted over a range of shear rates with the fraction of observed surface covered by regions of smooth iridescence increasing with shear rate. Over the same shear rate region, distinct intensity maxima grew out of the polycrystalline SANS pattern and all signs of polycrystals were lost. In the high shear rate region showing LROO, the samples showed a uniform iridescence optically and a SANS pattern characteristic of hexagonally close packed planes lying parallel to the rheometer walls. In the first scattering ring, the intensity of the top and bottom maxima was less than that of the four side maxima indicating a shift of layers in the $\underline{e}_\nabla$ direction. In this shear rate region and for all $\phi/\phi_f>1$, $\underline{q}_1(k_\nabla)$ displayed a broad maximum for $0.4< k_\nabla d/2\pi<0.8$ indicating that the hexagonally close packed layers retain correlations in the k_∇ direction. These results suggest the suspension deforms with a microstructure consisting of freely slipping layers interspersed with zones of strained crystal.

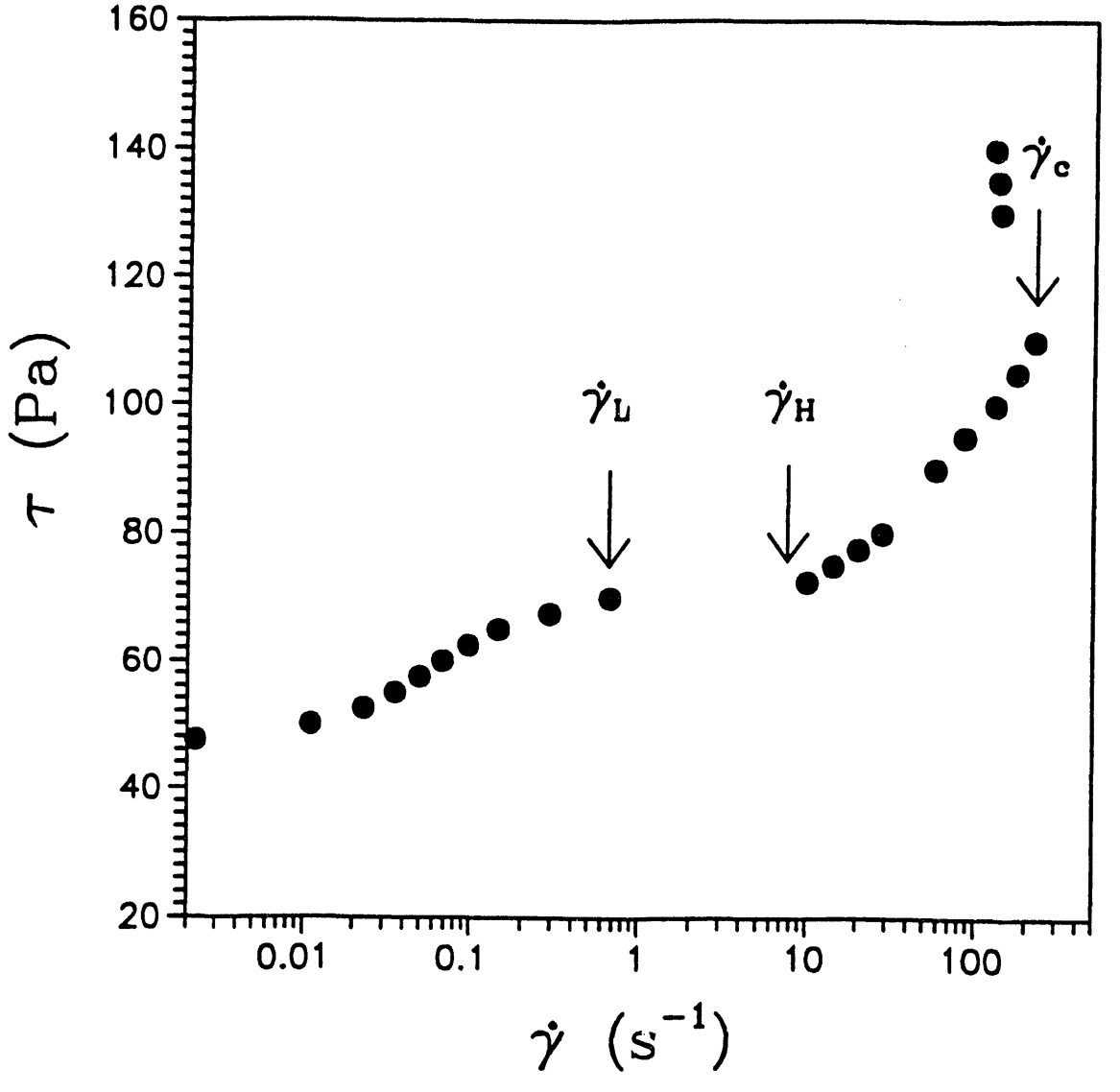

Fig. 2. Stress as a function of steady state shear rate for a suspension of 255 nm diameter particles at $\phi = 0.395$.

Further increases in shear rate produced a broadening of intensity maxima until the sample was amorphous by SANS and white under optical observation. Over a range of shear rates near that where the samples became fully amorphous, the SANS patterns fluctuated in time between patterns showing greater and lesser degrees of LROO[4,10].

Changes in microstructure were quantified through an order parameter, OP_{60}, defined to characterize the degree of hexagonal close packing seen in the vorticity, velocity plane (i.e., when $k_\nabla = 0$):

$$OP_{60} = \sum_{i=1}^{N} \left((I(\theta_i)\, I(\theta_i + \pi/3) - \langle I \rangle^2) / I_{max}^2 \right)$$

where $\langle I \rangle = \frac{1}{N} \sum_{i=1}^{N} I(\theta_i)$. Here the intensity of the neutrons in the first Debye ring, $I(\theta_i)$, are evaluated at angles θ_i measured from $\underline{e}_v$. I_{max} is the maximum intensity in the angles sampled. The sum is over 12 angles where the intensities are determined every 30 degrees starting from the vorticity axis at $k\ (= (k_e^2 + k_v^2)^{1/2}) = 2\pi/d$ (the parameter of the primary intensity ring). Due to the symmetry of the scattering patterns, intensities were only measured for $\theta_i = 0, \pi/6, \pi/3, \pi/2$ and symmetry applied for all other angles. For amorphous samples $OP_{60} = 0.0 \pm 0.1$. Increases in OP_{60} indicate an increase in the strength of hexagonal close packing in the $\underline{e}_e$, $\underline{e}_v$ plane.

A characteristic plot of OP_{60} as a function as shear rate is shown in Fig. 3 where a decrease to a minimum at $\dot{\gamma}_1$ is followed by an increase to a maximum at $\dot{\gamma}_{max}$. OP_{60} decays for $\dot{\gamma} > \dot{\gamma}_{max}$ to a value near zero at $\dot{\gamma}_{melt}$. Similar changes in OP_{60} with shear rate were reproduced for all samples where $\phi > \phi_f$. A summary phase diagram of $\dot{\gamma}_i$ is shown in Fig. 4.

Near ϕ_f, the viscosity decreased smoothly over the shear rate range which could be probed. However, for $\phi/\phi_f > 1.12$, at a critical stress, τ^*, the viscosity decreased discontinuously one order of magnitude. This abrupt change in rheological behavior coincided with the first

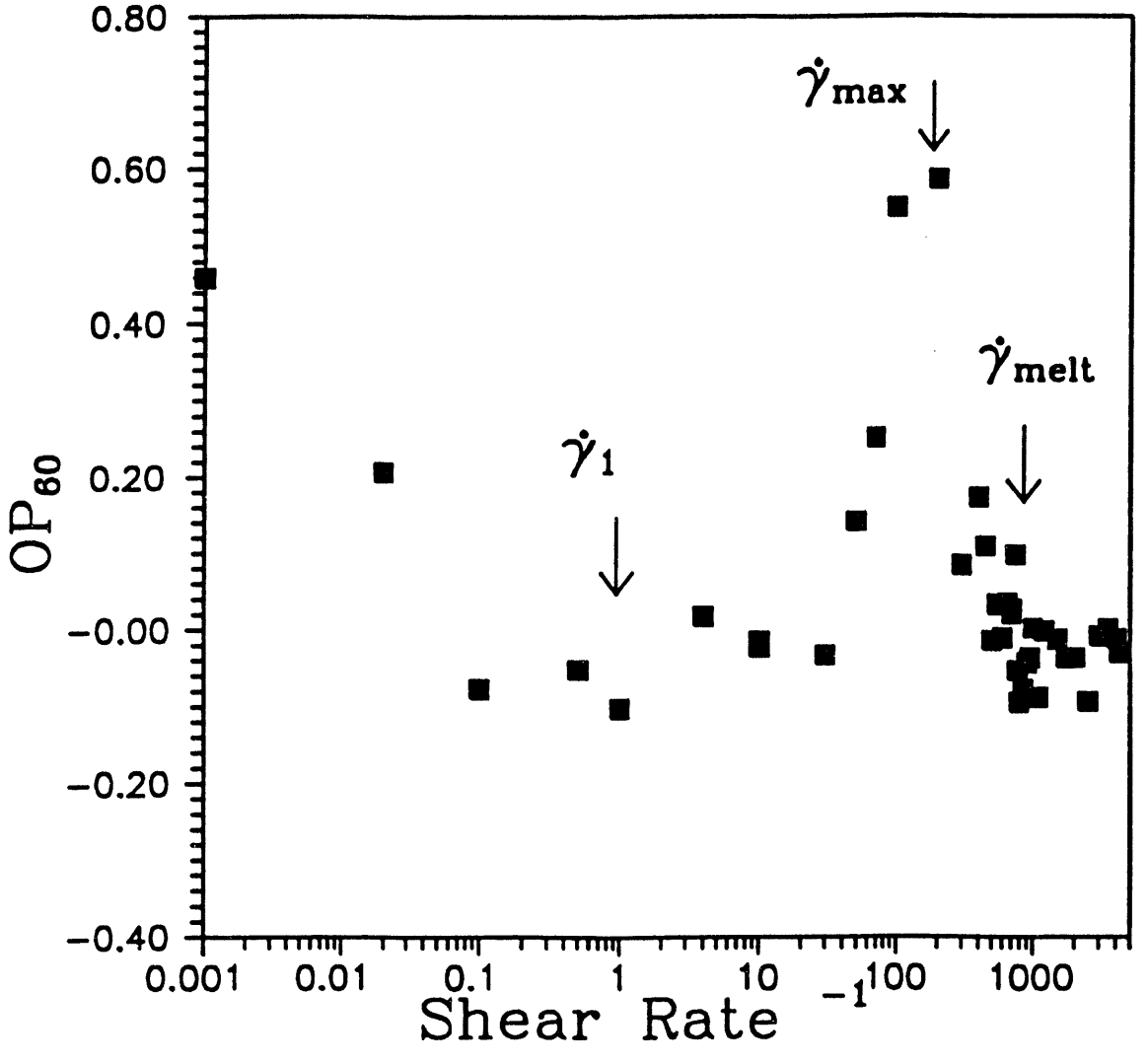

Fig. 3. OP_{60} as a function of shear rate for 255 nm particles at a volume fraction of 0.543. The at rest value is plotted at a nominal shear rate value of 0.001 s^{-1}.

observation of regions of smooth iridescence amongst polycrystals when the samples were observed visually. We define $\dot{\gamma}_L$ and $\dot{\gamma}_H$ to correspond to the lower and higher shear rates observed at τ^* and these values are given in the phase diagram in Fig. 4. Note that $\dot{\gamma}_H < \dot{\gamma}_l$ indicating that the rheology is more sensitive to the nucleation of shearing layers than is the scattering from the suspension.

For $\phi<\phi_c \approx 0.5$, the viscosity decreased monotonically to an apparent high shear rate plateau value through the shear melting transition (i.e., no rheological anomalies were observed as $\dot{\gamma}$ approached and surpassed $\dot{\gamma}_{melt}$). However, for $\phi>\phi_c$, shear thickening was observed as $\dot{\gamma}$ increased. Near ϕ_c, the shear thickening transition could be traversed reversibly. However, as volume fraction increased towards 0.6, shear thickening accompanied irreversible aggregation of the sample. The shear rate marking the onset of shear thickening, $\dot{\gamma}_c$, depended on the sample's previous shear history. Here $\dot{\gamma}_c$ is defined as the first shear rate where the stress became an erratic function of time.

As indicated in Fig. 4, the stable low shear rate microstructure for $\phi/\phi_f>1$ is that of polycrystals. This polycrystalline phase persists over a wide range of shear rates and volume fractions. If the suspension is sheared such that it has a polycrystalline microstructure and the shear rate is set to zero, LROO is not reestablished in a reasonable period of time (i.e., several days). However, low strain amplitude oscillations will produce LROO suggesting an energetic barrier to the large degree of cooperative movement required to produce single crystals from polycrystals[9]. As the shear rate is increased, the nucleation of shearing layer structures (as observed visually by the appearance of large regions of uniform color) is associated with τ^*. However, as ϕ_f is approached from above, the nucleation of sliding layers occurs with sufficient ease that $\dot{\gamma}_H$ and $\dot{\gamma}_L$ merge. At volume fractions where discontinuous shear thinning occurs, metastable viscosities can be measured by setting the structure in the polycrystalline region and stepping to stresses above τ_c. The length of time required to nucleate the lower viscosity phase decreases with increasing τ[4,13].

As shown in Figs. 3 and 4, microstructural transitions (i.e., the increase in order for

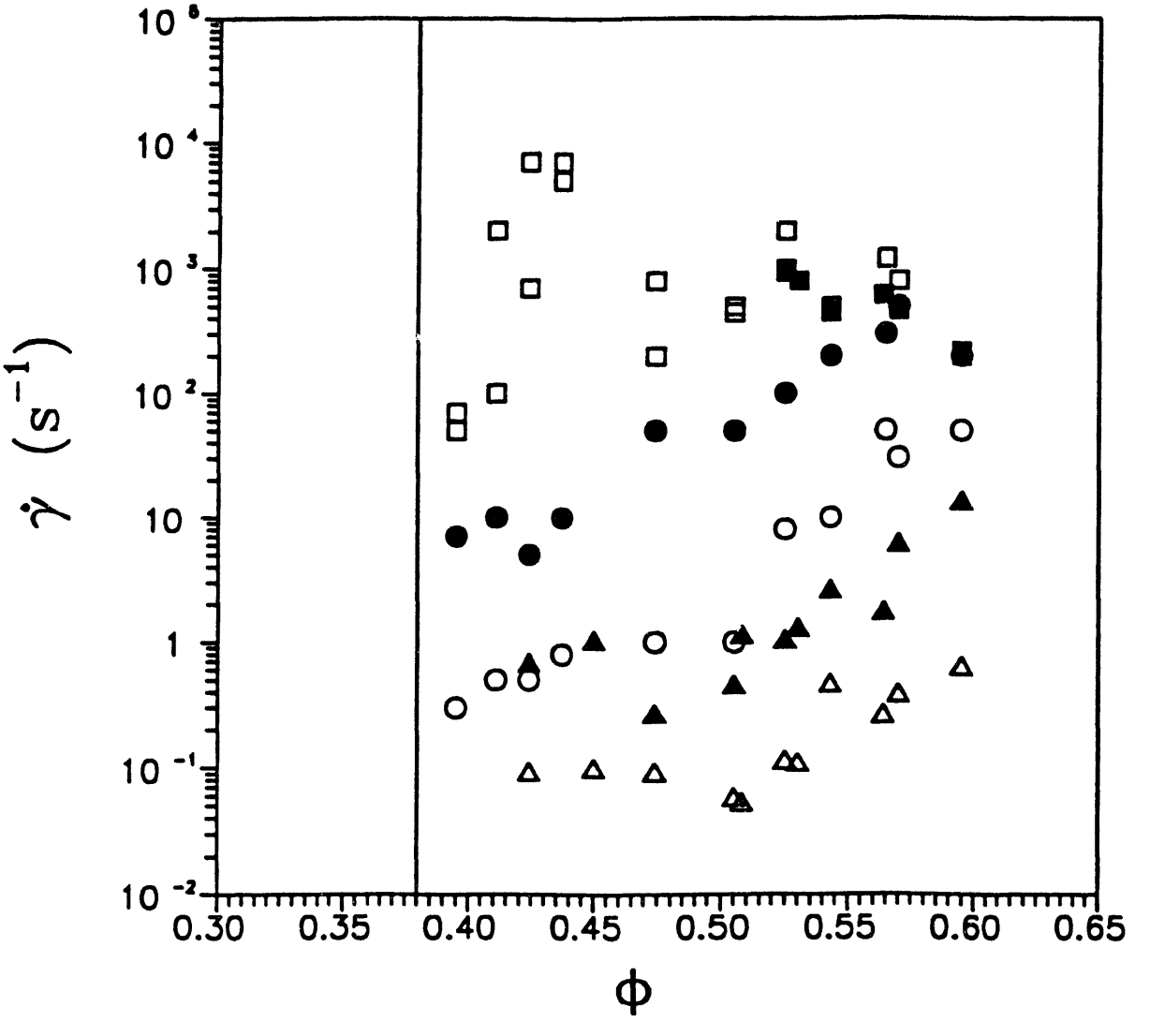

Fig. 4. Nonequilibrium phase diagram for 238 and 255 nm particles as a function of $\dot{\gamma}$ and ϕ. The vertical line marks ϕ_f. For $\phi<\phi_f$, no shear induced order was observed up to $\dot{\gamma} = 2\text{x}10^4\ s^{-1}$. Microstructurally determined shear rates: (○), $\dot{\gamma}_l$, (●) $\dot{\gamma}_{max}$, (□) $\dot{\gamma}_{melt}$. Rheologically determined shear rates: (△) $\dot{\gamma}_L$, (▲) $\dot{\gamma}_H$, (■) $\dot{\gamma}_c$.

$\dot{\gamma}_1<\dot{\gamma}<\dot{\gamma}_{max}$ and the loss of order for $\dot{\gamma}_{max}<\dot{\gamma}<\dot{\gamma}_{melt}$ occur over a broad shear rate range. As with particles experiencing a soft interaction investigated here, hard spheres display microstructural transitions over a range of shear rates suggesting that abrupt microstructural transitions are not common in systems containing particles suspended in a dissipative medium[11]. Despite the broad nature of microstructural transitions, rheological transitions are abrupt.

As reported on similar samples[12,13], τ_y^s/G_0 (=0.014±0.003), τ_y^d/G_0 (=0.029±0.008) and τ^*/G_0 (=0.039±0.008) are weakly dependent on ϕ. We also find that the stresses at $\dot{\gamma}_{max}$, $\dot{\gamma}_{melt}$, and $\dot{\gamma}_c$, scale on G_0 (i.e., τ_{max}/G_0 = 0.09±0.02, τ_{melt}/G_0 = 0.4±0.2, and τ_c/G_0 = 0.12±0.05). The constancy of these ratios suggests a scaling of the crystal constitutive response given in Fig. 5 where relative viscosity is presented as a function of τ/G_0. Given the two order of magnitude range of G_0 values covered by the samples in Fig. 5, we feel the resulting correlation is remarkable. τ/G_0 may be interpreted as a Debora number (i.e., the ratio of t_r to the characteristic deformation time, $\dot{\gamma}^{-1}$) yielding $t_r=\eta/G_0$ where η is the suspension viscosity at the shear rate and viscosity of interest. The superposition of viscosities for crystals with such a wide volume fraction range when plotted as a function of De (= $t_r\dot{\gamma} = \eta\dot{\gamma}/G_0 = \tau/G_0$) suggests that transitions in flow behavior and microstructure occur when the crystal is deformed at a rate comparable to the suspension's structural relaxation time, a concept in agreement with recent simulations[5].

The correlation shown in Fig. 5 suggests a useful definition of t_r in colloidal crystals is η/G_0 indicating that the suspension relaxation time decreases with increasing $\dot{\gamma}$. Fig. 5 demonstrates that when De is 0(1), microstructural and rheological transitions occur. In passing we note that the data in Fig. 5 can be replotted as τ/G_0 vs $\eta_c\dot{\gamma}/G_0$ to show equally good super position. Here η_c is the continuous phase viscosity. In this manner, a Debora number is naturally defined with $t_r = \eta_c/G_0$ such that transitions in rheology and microstructure occur when De<<1 (i.e., $\eta_c\dot{\gamma}_H/G_0 = 7\pm2\times10^{-6}$ and $\eta_c\dot{\gamma}_{melt}/G_0 = 9\pm5\times10^{-4}$). Either definition of De provides a master curve defining rheological and microstructural properties which are independent of ϕ for $\phi/\phi_f > 1$.

Previous studies of shear thickening and shear melting [14-20] in colloidal suspensions

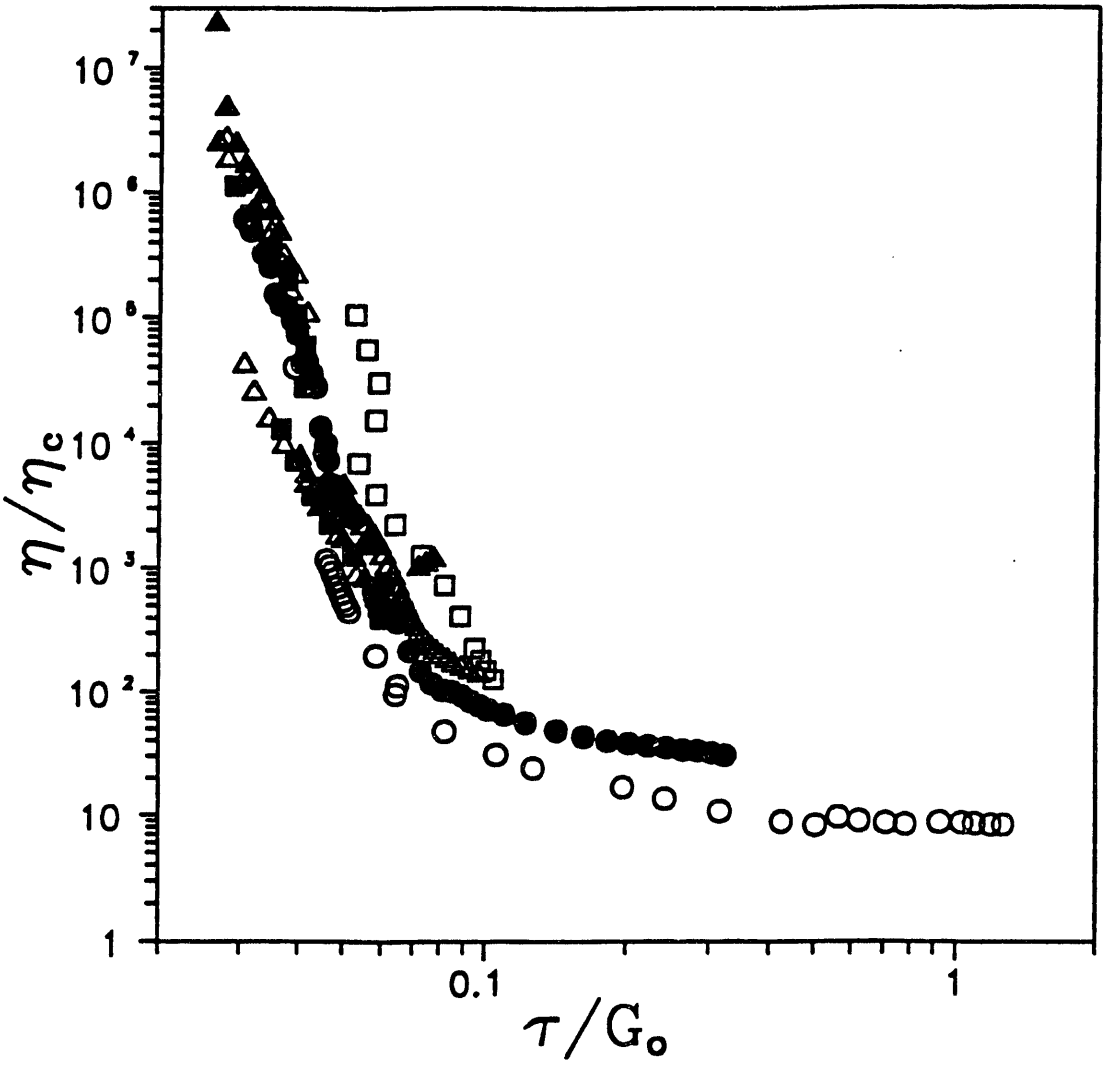

Fig. 5. Relative viscosity as a function of τ/G_0 for suspensions of 255 nm particles at various volume fractions: (○) $\phi = 0.395$, $G_0 = 3.97$ Pa; (●) $\phi = 0.412$, $G_0 = 5.39$ Pa; (□) $\phi = 0.437$, $G_0 = 13.3$; (■) $\phi = 0.507$, $G_0 = 31$ Pa; (△) $\phi = 0.525$, $G_0 = 178$ Pa; (▲) $\phi = 0.564$, $G_0 = 238$ Pa.

suggest both phenomena are due to a transition from interparticle force control of microstructure to one where viscous forces dominate. Investigations at low volume fraction with charge stabilized particles show that shear melting occurs at a shear rate which is an increasing function of volume fraction[15] while separate studies at high volume fractions suggest melting and $\dot{\gamma}_c$ are decreasing functions of shear rate[14,15,17-20]. Here we report the both branches of the melting shear rate (either $\dot{\gamma}_{max}$ or $\dot{\gamma}_{melt}$) for a single system. The general features of the transition can be understood if the structural instability is taken as occurring when there is a balance between viscous and electrostatic repulsive forces. Following Boersma[17,18], we account for lubrication forces by writing the viscous force acting on a particle as $6\pi\eta_c a^2\dot{\gamma}[a/(r-2a)]$ where η_c is the continuous phase viscosity, a is the particle radius and r is the average particle separation. Instability will occur when the shear forces acting to destabilize layers balance the interparticle forces holding particles in planes given as $\{4\pi\varepsilon_0\varepsilon_c\psi_0^2 a\}\exp(a\kappa(r/a-2))/(r/a)$ where $\varepsilon_0\varepsilon_c$ is the product of the permittivity of free space and the dielectric constant of the continuous phase, ψ_o is the particle surface potential and κ is the Debye Huckel screening parameter and a is the particle radius. Balancing these forces yields a relationship for the shear rate at melting which shows a maximum near a volume fraction of 0.58. The predicted curve is sharper than observed for $\dot{\gamma}_{melt}$ due to inaccuracies in describing both viscous and interparticle forces acting on the particles. However, the predicted magnitudes of $\dot{\gamma}_{melt}$ and existence of a maximum are in keeping with the model.

Shear thickening is often associated with the formation of large particle clusters. Evidence that particles are jammed together with great force in our experiments is supported by the onset of irreversible flocculation accompanying shear thickening as ϕ approaches 0.6. The onset of shear thickening with increasing ϕ can be understood in terms of the sensitivity of viscosity to volume fraction at elevated ϕ and fluctuations in local density and shear rate. In constant stress experiments, the shear rate decreases with the onset of shear thickening while in constant shear rate experiments, stresses and microstructures are erratic for $\dot{\gamma} > \dot{\gamma}_{melt}$. In addition, shear thickening is associated with the complete loss of LROO suggesting that as $\dot{\gamma}_{melt}$

is approached, the sheared volume contains disordered regions which have a higher viscosity and thus are deforming at a lower than average shear rate. Regions which are still deforming through a shearing layer mechanism are thus subjected to a larger than the average shear rate. Due to the sensitivity of viscosity to volume fraction at high ϕ, small density or shear rate fluctuations will generate large viscous forces driving particles together and resulting in the development of large clusters. At low volume fractions, the viscous forces increase slowly with volume fraction such that local density fluctuations will not result in large clusters.

Our results suggest that for monodisperse particles, shear melting occurs when there is a balance of deformation and structural relaxation times. Due to the way these forces change with interparticle spacing, a maximum shear rate is observed above which the suspensions are not ordered at any volume fraction. This result is in keeping with recent predictions of shear melting in suspensions which are body centered cubic at rest[21]. The abrupt shear thickening observed as ϕ exceeds ϕ_c is associated with the inability of density fluctuations produced during melting to decay in a time frame comparable to the deformation time.

Acknowledgements: The authors would like to thank J. Barker, C. Glinka, H. Hanley, G. Straty and B. J. Ackerson for stimulating discussions. The SANS measurements were carried out at the Cold Neutron Facility at NIST. M. K. Chow acknowledges support of the US Department of Energy through the Materials Research Lab at the University of Illinois through grant number DEFG02-91ER45439. M. E. Fagan acknowledges support of the National Science Foundation through NSF CTS 92-00121.

References.

1) A. H. Cottrell, Theory of Crystal Dislocations, Gordon Breach, NY (1964).
2) O. Mishima, L. D. Calvert and E. Whalley, Nature 310, 393 (1984); R. R. Winters and W. S. Hammock, Phys. Rev. Lett. 68, 3311 (1992).
3) J. O. Chua and A. L. Rooff, J. Appl. Phys. 53, 5669 (1982).
4) M. K. Chow, Shear Thickening and Microstructures of Concentrated Charge Stabilized Suspensions, Ph.D. Dissertation, University of Illinois, 1993.
5) These ideas build on the concepts developed for simulations of molecular crystals under shear reported by M. J. Stevens, M. O. Robbins and J. F. Belak, Phys. Rev. Lett. 66, 3004 (1991).
6) W. Loose and B. J. Ackerson, to appear 1993.

7) P. N. Pusey, W. van Megen, B. J. Ackerson, P. Bartlett and S. M. Underwood, Phys. Rev. Lett. 63, 2753 (1989).
8) L. B. Chen, B. J. Ackerson and C. F. Zukoski, to appear in J. Rheol. 1994.
9) L. B. Chen, C. F. Zukoski, B. J. Ackerson, H. J. M. Hanley, G. Straty, C. Barber and C. Glinka, Phys. Rev. Lett. 688 (1992).
10) L. B. Chen, M. K. Chow, B. J. Ackerson and C. F. Zukoski, to appear 1994.
11) B. J. Ackerson, J. Rheol. 34, 533 (1990).
12) L. B. Chen, Ph.D. Dissertation, University of Illinois, 1991.
13) L. B. Chen and C. F. Zukoski, J. Chem. Soc. Faraday Trans. 86, 2629 (1990); Phys. Rev. Lett. 65, 44 (1990).
14) R. L. Hoffman, J. Colloid Interface Sci. 46, 491 (1974).
15) H. A. Barnes, J. Rheol. 33, 329 (1989).
16) B. J. Ackerson and N. A. Clark, Phys. Rev. A 30, 906 (1984).
17) W. H. Boersma, J. Lavan and H. N. Stein, J. Colloid Interface Sci. 149 (1992).
18) W. H. Boersma, P. H. M. Bates, H. N. Stein, J. Rheol. 35, 1096 (1991).
19) H. M. Laun, Progress and Trends in Rheology II, 287 (1988).
20) H. M. Laun, R. Bury, S. Hess, W. Loose, K. Hahn, E. Hadicke, R. Hingmann, F. Schmidt and P. Lindner, J. Rheol. 36, 743 (1992).
21) B. Bagchi and D. Thiromalai, Phys. Rev. A 37, 2530 (1988).

Observations of Granular Flow in an Inclined Chute

Daniel M. Hanes
University of Florida

Introduction

The dynamics of flowing granular material has been previously observed in inclined chutes (e.g. Savage, 1979; Johnson et. al, 1990; Ahn et. al, 1991). One of the questions arising from previous work regards the existence of fully developed, steady flows. Depending upon the friction or bumpiness of the chute base, experiments have indicated that under some conditions the flow appears to be steady and fully developed. While a truly fully developed flow can never be proven to exist in an experimental apparatus because of its finite length, apparent fully developed flows are observed to within reasonable experimental accuracy's. The present series of experiments focuses on the existence of steady, fully developed flows over a low friction, bumpy base.

Experimental Apparatus

The inclined chute is 4 meters long, with an adjustable width set to 15 cm. A belt conveyer provides material recirculation that allows for continuous operation. The granular material used in these experiments are medium quality glass spheres with diameters of approximately three millimeters. The angle of inclination is variable; for these experiments the angle is varied between 19 and 28 degrees. The base of the chute is removable and exchangeable; in these experiments the base consists of 3 mm glass spheres fixed in a closely spaced hexagonal pattern. For the data to be shown below, the separation between base grain centers is 4 mm.

A series of flow-trapping gates has been developed to measure the mass hold-up in six sections along the chute. These gates fall

under the influence of gravity when holding pins are simultaneously removed by a solenoid driven piston. The mass hold-up can be combined with flow thickness measurements and discharge measurements in order to calculate the average volume fraction and velocity in each of the six sections.

Results and Discussion

A variety of flow regimes are observed in the chute. The flows exhibit distinctive characteristics that relate to the inclination of the chute, the nature of the base of the chute, and the entrance/exit conditions. The flow is frequently observed to have constant mass flux and constant flow thickness along the chute. However, the volume fraction and velocity of these flows generally changes with position along the chute. It is found that fully developed flows exist only over a small range of inclinations (with all other variables constant).

An example of a steady, fully developed flow is shown in Figure 1. The angle of chute inclination for this flow was 23.4 degrees. The volume fraction, velocity, mass hold-up, and flow thickness are all nearly constant along the chute.

A technique to measure the structure of the velocity and concentration fields is under development. These quantities are estimated from high speed images transmitted through a 5 mm diameter boroscopic lens. The lens is inserted into the side wall to be flush with the wall, or the lens may be inserted thorough the side wall into the flow. In the latter case, some disturbance to the flow is likely, but not yet quantified. Preliminary analyses of some images indicate a nearly linear velocity profile with slip at the base and an abrupt concentration gradient (interface) at the top of the flow.

In conclusion, we have observed steady, fully developed flows of glass spheres in an inclined chute. These flows seem to exist over a range of inclination angles of a few degrees.

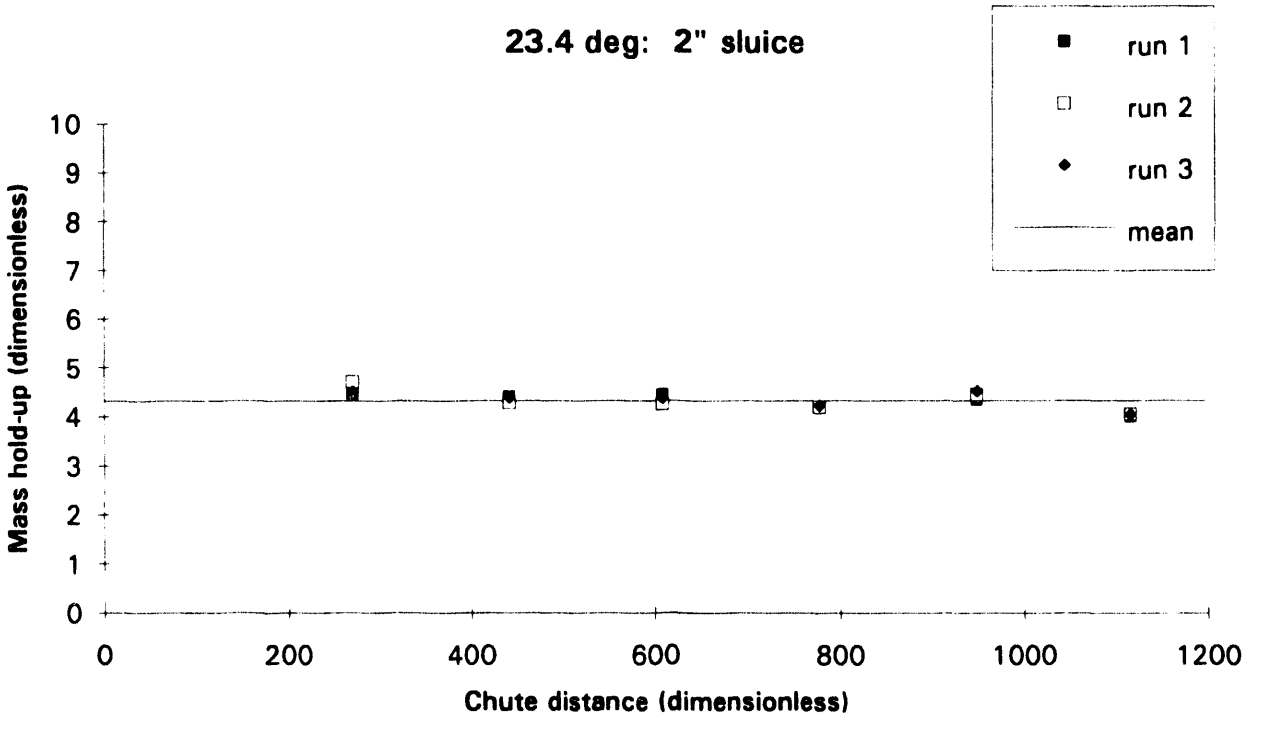
23.4 deg: 2" sluice
run 1
run 2
run 3
mean
Mass hold-up (dimensionless)
10
9
8
7
6
5
4
3
2
1
0
0
200
400
600
800
1000
1200
Chute distance (dimensionless)

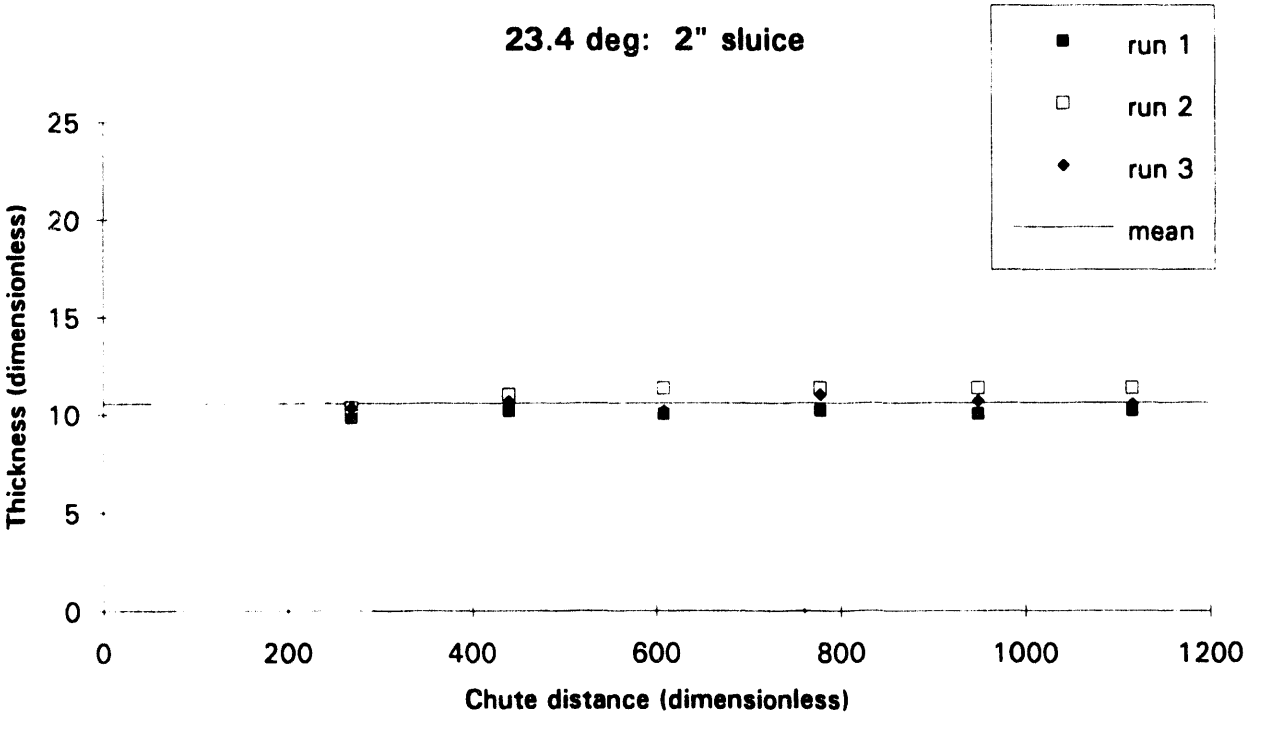
23.4 deg: 2" sluice
run 1
run 2
run 3
mean
Thickness (dimensionless)
25
20
15
10
5
0
0
200
400
600
800
1000
1200
Chute distance (dimensionless)

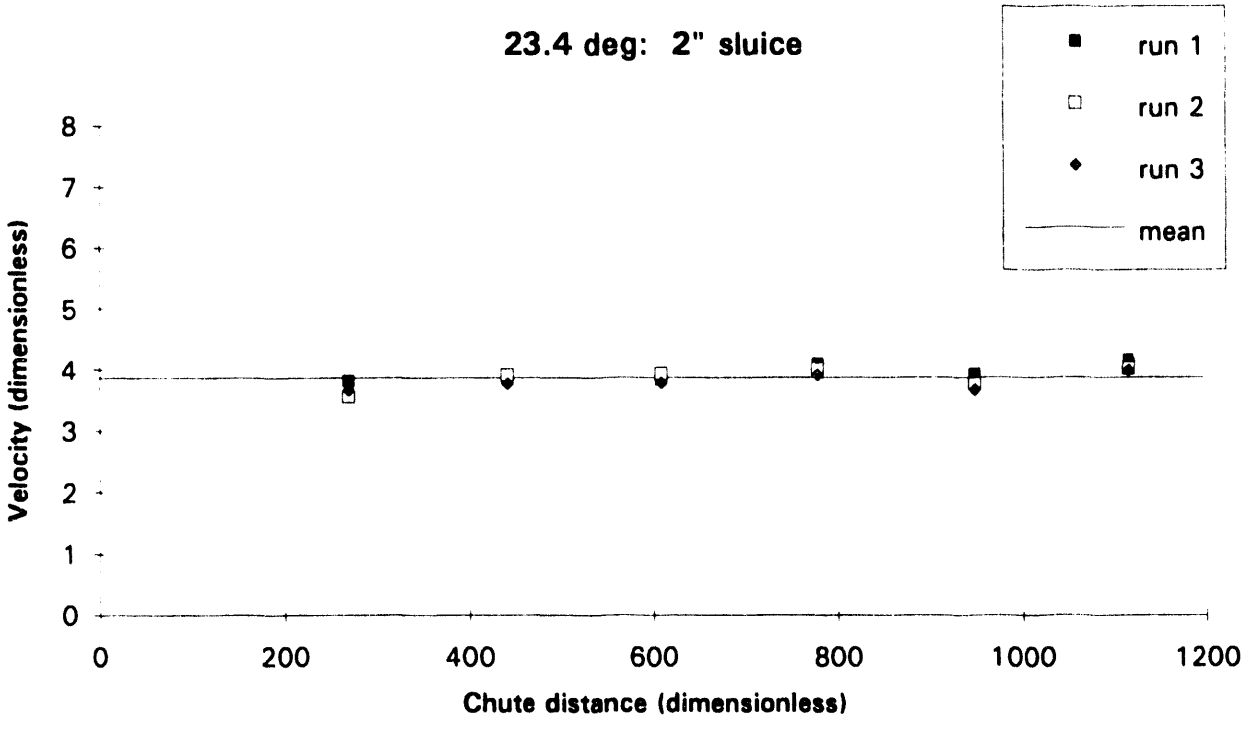
23.4 deg: 2" sluice
run 1
run 2
run 3
mean
Velocity (dimensionless)
8
7
6
5
4
3
2
1
0
0
200
400
600
800
1000
1200
Chute distance (dimensionless)

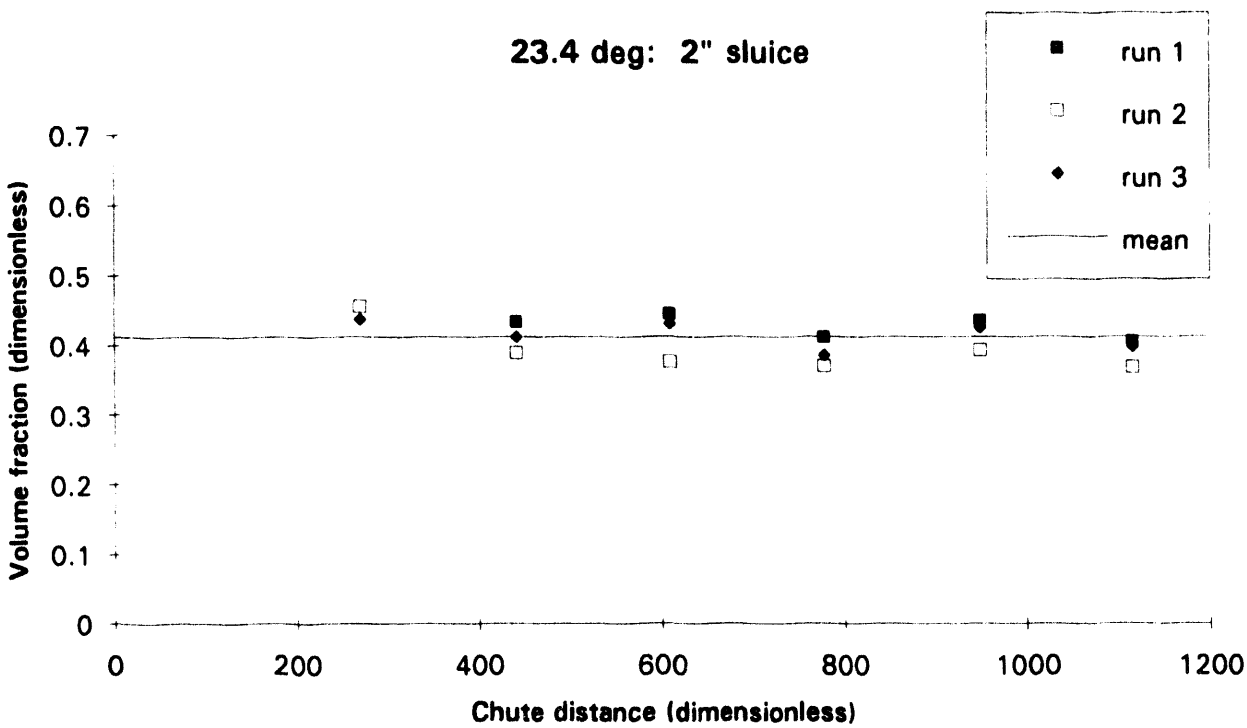
23.4 deg: 2" sluice
run 1
run 2
run 3
mean
Volume fraction (dimensionless)
0.7
0.6
0.5
0.4
0.3
0.2
0.1
0
0
200
400
600
800
1000
1200
Chute distance (dimensionless)

References

Ahn, Brennen, Sabersky, JAM, ASME, 1991.

Augenstein and Hogg, Powder Technology, 1978.

Drake, JFM, 1991.

Hungr and Morgenstern, Geotechnique, 1984.

Ishida and Shirai, J. Chem. Eng. Japan, 1978.

Johnson, Nott, and Jackson, JFM, 1990.

Patton, Brennen, Sabersky, JAM, ASME, 1987.

Ridgeway and Rupp, Chem. and Process Eng, 1970.

Roberts, J. Eng. Ind, ASME, 1969.

Savage, JFM, 1979.

Suzuki and Tanaka, Ind. Eng. Chem. Fund., 1971.

Acknowledgments

This work was supported by the U.S. Department of Energy as a part of the Granular Flow Advanced Research Objective (GFARO).

Measurements of Microstructure of Colloidal Dispersions: Rationale & Prospects

Raj Rajagopalan

Departments of Chemical Engineering & Physics
University of Houston
Houston, Texas 77204-4792

Paper presented at

JOINT DOE/NSF WORKSHOP
on
FLOW OF PARTICULATES AND FLUIDS
September 30 - October 1, 1993
Ithaca, New York

Measurements of Microstructure of Colloidal Dispersions: Rationale & Prospects

Raj Rajagopalan

Departments of Chemical Engineering & Physics
University of Houston
Houston, Texas 77204-4792

ABSTRACT

Model colloidal dispersions have become very popular in the last decade as ideal vehicles for studying phase transitions and structural transitions in atomic fluids and alloys and for understanding non-equilibrium structure and flow of suspensions. The issues of interest are numerous. Some questions that have motivated studies on the microstructure of dispersions are: How do the interparticle forces affect equilibrium (and non-equilibrium) structures? How does polydispersity (in size as well as interaction forces) influence the phenomena? Can one obtain reliable information on the properties of particles (size, charge, aggregation numbers in the case of associations, etc.) from measurements of the microstructure? Can one use colloidal model systems to study nucleation and crystallization phenomena, formation of alloys and composites, two-dimensional and three-dimensional order/disorder transitions, defect generation and propagation and the like? How do the experimental limitations such as measurement errors and inaccessibility of data over the relevant ranges of parameters restrict the information that can otherwise be obtained, and how can one circumvent such limitations? In this paper, we focus on obtaining information on interaction forces from static structure factors and discuss a new method for obtaining the details of interparticle interaction forces from the static structure factor is outlined. We then outline some of the potential experimental limitations of scattering experiments and suggest the use of video-enhanced microscopy for direct visualization and mapping of the microstructure and spatial correlations.

I. INTRODUCTION: COLLOIDS AS MODEL MANY-BODY SYSTEMS

There has been a long-standing and almost unending need to relate microscopic interaction forces to macroscopic structure and properties of dispersions (and suspensions) and atomic, molecular and supramolecular materials. One encounters at least two levels of mutually related goals in this respect, namely, (i) predicting equilibrium or non-equilibrium behavior and properties from 'given' microscopic forces, and (ii) ability to deduce interparticle interactions from macroscopically observed behavior and properties of materials. Over the last decade, colloidal dispersions have been found to be excellent model systems for studying a number of fundamental issues in simple (but nevertheless important) fluids. Dispersions of controlled sizes and surface properties have been used to study phase transitions in 'soft' systems, structural transitions in Coulombic fluids, ordering and melting in two-dimensional crystals, etc.; see, for example, Denkov *et al.* (1992), Dosho *et al.* (1993), Murray (1992) and Nagayama (1993). (Some of the advantages of using colloids as model systems are summarized later in this section.) The utility of colloids in this context has given rise to a need to develop reliable and accurate experimental techniques for observing and recording the microstructure of dispersions as a function of time and of the relevant physical and chemical parameters. Moreover, understanding the interactions in colloids has intrinsic merit in view of the numerous practical applications of materials in the colloidal state. The purpose of the present paper is to focus on one of the many questions of interest and relate it to the need for systematic microscopic studies of structure of dispersions.

We focus here on the determination of interaction forces from observed properties of materials. As well-known, the nature and the details of interaction forces in a number of practically important materials (ranging from liquid metals in the case of atomic fluids to sterically stabilized dispersions in non-aqueous fluids in the case of colloids) are not clearly understood, and systematic ways to study these are badly needed. In approaching this task, one often measures the static structure factor (a function related to the atomic or molecular pair correlation function of the material) of the material and employs a suitable statistical mechanical formalism to fit the observed structure factor data using assumed potentials. This procedure, a standard practice in statistical physics, is used extensively in colloid science, especially in the case of association colloids for determining the aggregation number, the effective charge, and the size of the micelles and microemulsion droplets. This approach, although standard, can lead to quite misleading results, as we have emphasized elsewhere (Rajagopalan 1992) since the techniques used to calculate the

structure factor from assumed potentials are usually insensitive to subtle details of the potentials. Further, a priori assumptions concerning the form of the potentials bias the outcome of the results and conclusions. To complicate the matters further, the results lack uniqueness since essentially similar structure factors may result from different forms or versions of the potentials. New techniques that avoid a priori assumptions concerning the nature and the form of the potentials are therefore needed. Use of model colloids to develop such techniques and to study interaction forces in steric systems is, therefore, highly attractive. This again leads to the issue of developing ways to map the microstructure of dispersions as a function of the relevant parameters.

Colloidal dispersions offer a number of advantages as model systems:

i. Particles of very narrow size distributions can be prepared, thereby assuring practically identical particles. Polystyrene latex particles and a few other types of polymer particles are readily available commercially.

ii. To a limited extent, non-spherical particles of specific shapes can also be prepared.

iii. The surface charge on the particles can be controlled adequately, and charges as high as one electronic charge per nm^2 are possible.

iv. Methods to adsorb or graft polymers and polyelectrolytes onto the surfaces are available. These allow one to tailor the interparticle forces according to specification (e.g., hard-sphere interactions, adhesive sphere interactions and interactions with 'soft' repulsive cores and attractive or repulsive tails). Methods have also been developed, using polymer-coated silica particles, to adjust both the interaction forces and the refractive indices of the surface layers. The latter allows one to vary the optical contrast of the particles by suitably choosing the suspending medium. In principle, particles can be made invisible selectively and differentially.

v. Model particles with fluorescent dyes of different colors can be prepared or can be obtained commercially.

vi. The use of colloidal particles in the appropriate ranges of sizes also allows one to use optical imaging experiments to observe and record the microstructure directly.

vii. The dynamics of colloidal particles has a strong Brownian component. Thus, the dynamics is described by Langevin equations and the dispersions has a true thermodynamic temperature. Further, the interparticle 'collision' times are large (relative to those in atomic

fluids) and the evolution of structure and other microstructural features such as defect dynamics can be monitored at convenient time scales. As a consequence, the evolution of phases occurs over large enough time scales (from hours to weeks) for convenient experimental design. As emphasized by Murray (1992), the ability to monitor the structure by direct observation is particularly important in studies of order/disorder transformation in which diffraction results are difficult to interpret (see also Section IV).

viii. If experiments can be designed to monitor and record the positions of the particles accurately, the results can be used as analog Brownian dynamics experiments that do not have some of the drawbacks of computer experiments. In particular, systems with a large number of particles can be studied without limitations imposed by periodic boundary conditions and insufficient equilibration times. Assumptions necessitated by uncertainties in pair interactions and the need for and the form of three-body and higher-order interactions can be avoided.

As mentioned earlier, this paper is restricted to describing a new method to extract information on interaction forces from structure factors. We use this as a vehicle for illustrating the need for developing good methods for mapping the microstructure of dispersions as functions of the physicochemical parameters and time. The paper begins with an outline of some outstanding issues in the interpretation of microstructure of charged dispersions (Section II). We then move on to the inversion problem, namely, the problem of inverting static structure factors for obtaining interaction forces (Section III). Section IV discusses the advantages of using direct measurements of the microstructure of dispersions to study interaction forces in colloids. This is followed by some concluding remarks.

II. Questions Concerning the Nature of Interparticle Forces in Charged Dispersions

As mentioned earlier, there is a need to examine the microstructure of charged dispersions systematically and to relate the observed structure to interparticle interaction forces. For instance, experiments based on highly charged latex particles seem to lead to some puzzling observations. Ise and coworkers have reported for some time that the results observed in their experiments on the structure of charged dispersions cannot be explained without a long-range attractive tail in the pair-potential [with a minimum in the potential at interparticle distances of the order of a few particle diameters; see Dosho *et al.* (1993) and references therein]. Their

experiments lead to a number of interesting observations which suggest the existence of long-range attraction in apparently purely charged dispersions. For eample:

i. The dispersions undergo an order/disorder transition, *but the ordered phase is not space-filling*, as would be the case if only large repulsion exists between the particles.

ii. The experimentally measured interparticle separations in the ordered phase (measurements based on a number of techniques such as scattering experiments, Kossel-line analyses or direct observations) are *smaller* than the average interparticle distances expected from the bulk density.

iii. Gas-like structures and large void structures seem to coexist with regions with liquid-like order.

Moreover, a recent experiment reported by Tata *et al.* (1992) using dilute aqueous polystyrene latex dispersions suggests the existence of a *'vapor/liquid'* phase transition below a critical particle concentration. The particles used in the experiments have an estimated charge of about 600e per particle, and the interparticle distances observed in the liquid-like phases are again of the order of a few particle diameters. The van der Waals attraction is practically zero at such large distances for the types of systems studied by both Ise's research group and Tata *et al.* These lead to questions such as: Is there an attraction in these Coulombic systems? If 'yes', what is the source of such attraction? What are the implications of such an attraction to the non-equilibrium structure and properties of the dispersions?

Issues such as the above can be examined systematically if (i) methods can be developed to obtain the microstructure and interparticle correlations (e.g., the structure factor) accurately and unambiguously, and (ii) analytical methods can be developed to extract interparticle forces from measured structure factors without any a priori assumptions concerning the nature or the functional form of the interparticle potentials. In what follows, we address item (ii) and use it as motivation for designing new experiments along the lines of item (i).

III. INVERSION OF STRUCTURE FACTORS

It is our purpose in this section to show that if sufficiently accurate static structure factor data are available over a broad enough range of wave vectors, one can invert such data for obtaining effective interaction potentials. This forms the motivation for designing experiments that can

provide accurate spatial correlation functions and structure factors. In this section, we present the essential details of a method based on perturbation theory for extracting effective interaction potentials from static structure factors of monodispersed colloids and simple fluids. The presentation here follows an earlier lecture given at a NATO Advanced Study Institute (Rajagopalan 1990); Additional details and recent results are presented in Sen and Rajagopalan (1991) and Rajagopalan (1992).

Although the past attempts on the development of solutions to the inverse problem have been largely unsuccessful, the inverse problem has attracted considerable attention in view of the potential benefits that can be derived from successful theories. Using a perturbation approach, which assumes that the large-scale structure is determined by the excluded-volume effect of the core of the potential and that the finer details are supplied by the rest of the potential, we have shown that the essential details of the effective pair-potential can be extracted from the static structure factor. The performance of this approach is examined for two model potentials for which the structure factors are first obtained using an independent theory and computer simulations.

III.1. Inversion of Structural Data: Background

As we have emphasized previously, statistical physics traditionally has concerned itself primarily with the description of the microscopic and macroscopic properties of the system under consideration from *given* interatomic or intermolecular pair potentials. In contrast, the inverse problem of extracting effective interaction potentials from observed structural data has received limited (and, to this day, incomplete) attention. The inverse problem is especially important in the case of interactions in dispersions with 'liquid-like' ordering since under such circumstances potentials (or forces) based on the dilute-limit may not be rigorously correct. [The term 'liquid-like ordering' alludes to the fact that the dispersed species can be treated, conceptually and analytically, as elementary constituents of a fluid-like collection of 'particles'. The host medium in which they are dispersed may be assumed to be structureless and treated as an effective dielectric. Correspondingly, the motion of the species is described by Brownian dynamics (with appropriate hydrodynamic contributions) rather than by molecular dynamics; see Castillo *et al.* 1984; Hirtzel and Rajagopalan 1990.] The interaction potentials in the dilute limit are based on the assumption that the interacting species are imbedded in an infinite reservoir of counterions and that they have surfaces in equilibrium with the bulk — conditions that do not always hold in strongly interacting dispersions. Even in the case of classical liquids, the effective potentials

contain a wealth of fundamental information on density dependence, possible long-range oscillatory behavior of the interaction forces and cooperative effects (March and Senatore 1984).

Past attempts to extract effective potentials from structural data can be traced to a method suggested by Johnson and March (1963), for rare-gas liquids and liquid metals, based on certain integral equation theories developed originally for predicting the equilibrium structure of liquids from known potentials [with the Percus-Yevick (PY) and the hypernetted chain (HNC) closure schemes (Friedman 1985)], and the limited efforts in the last twenty years have been largely unsuccessful. The PY and the HNC effective potentials can be obtained in a straightforward manner from the known static structure factor S(q), where q is the magnitude of the scattering vector **q**, through

$$\beta\, u_{PY}(r) = ln\,[1 - c(r)/g(r)] \tag{1}$$

and

$$\beta\, u_{HNC}(r) = g(r) - c(r) - 1 - ln\, g(r) \tag{2}$$

where g(r) and c(r) are, respectively, the radial distribution function and the direct correlation function, which are related to S(q) through Fourier transforms [see Eqns. (4) and (5)].

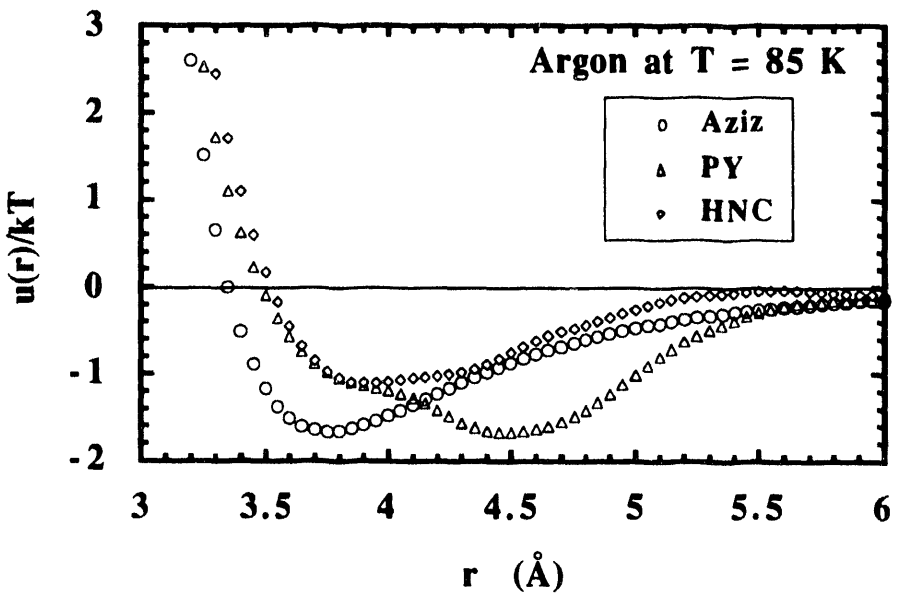

Figure 1. Inverted effective pair-potentials for argon based on the Percus-Yevick (PY) closure and the hypernetted chain (HNC) closure. The potential marked 'Aziz' is the AMS pair-potential mentioned in the text.

However, the integral equation approximations break down at high densities (or, in the case of supramolecular fluids, when liquid-like ordering develops). Consequently, the extracted potentials bear little resemblance to the ones obtained by fitting thermodynamic and transport properties to assumed forms of potentials. An example of such a case is illustrated in Figure 1, which shows the effective pair potential in liquid argon (at 85 K and at the reduced density, $\rho\sigma^3 = 0.84$) obtained through the PY and the HNC integral equation theories. This particular example of liquid argon has been chosen here as a model system since very good experimental scattering data are available in the literature (Yarnell *et al.* 1973) and since the interaction potentials in argon have been studied extensively by computer simulations in the past. Figure 1 also shows a three-parameter potential known as the Aziz-Maitland-Smith potential, parametrized for argon by Aziz, and the properties of argon derived from it match experimental data very well for argon at *low* densities (Fender and Halsey 1962; Maitland *et al.* 1981). The Aziz-Maitland-Smith (AMS) potential is shown primarily for comparison, and this potential is strictly valid only in the dilute-limit. (Three-body corrections are needed for predicting at least some of the properties of argon at liquid-densities.) It is clear from the figure that both the PY and the HNC pair-potentials [obtained from the data of Yarnell *et al.* using Eqs. (1) and (2)] deviate substantially, in both the location and the magnitude of the minimum in the potential. Equally important is the fact that the hard core of the potential as well as the attractive tail also differ significantly. The PY and HNC potentials shown are actually *effective* pair-potentials and one would expect them to deviate from *pair*-potentials such as the AMS potential. However, attempts to use these extracted potentials for predicting properties of argon have not been successful. Conclusions similar to the above can also be drawn from the results of Nieuwenhuis and Vrij (1979), who used the integral equations to extract pair-potentials for polymethylmethacrylate latex dispersions in benzene.

Results similar to the above have generated considerable skepticism in the literature about the success one might expect from attempts to obtain interaction potentials from macroscopic data (Croxton 1974).However, these negative results are in fact very instructive and are helpful in formulating a few key requirements concerning structural and thermodynamic consistency and sensitivity, which must be met by any prospective theory of inversion in order for the theory to provide meaningful and useable interaction data from macroscopic structural information. These are outlined elsewhere (Sen and Rajagopalan 1991; Rajagopalan 1992) and will be discussed briefly in the concluding section of this paper.

In the following we discuss briefly some results based on an inversion method that is derived from perturbation theories of liquid-state physics. The primary focus here will be on illustrating the promise of this method and on examining the quality of the results one can expect from it.

III.2. Effective Interaction Potentials from Static Structure Factors

The inversion of static structural data presented in this paper follows the conceptual framework used in perturbation theories of liquids; therefore, we present in this section the essential details of the forward formalism necessary to follow the logical structure of the inversion.

In the perturbation theories, the configurational integral is expanded in a series, relative to a convenient reference potential, in terms of a perturbation of the pair-potential (McQuarrie 1976). Since excellent descriptions of various forms of perturbation theories and approximations, including the optimized random-phase approximation that will be used here, are readily available in the literature, the present section will be restricted to a basic outline of the details necessary for understanding the approach used in the inversion method. Results of applications of Barker-Henderson and Chandler-Weeks-Andersen perturbation schemes to colloidal fluids are presented in Castillo *et al.* 1984; the high level of accuracy one can expect for dense systems from such perturbation schemes is demonstrated through Monte Carlo computer experiments in Hirtzel and Rajagopalan (1990).

Both in the forward perturbation theories and in the inversion scheme, it is assumed that the pair potential, u(r), can be written as

$$u(r) = u_0(r) + u_p(r) \tag{3}$$

where $u_0(r)$ is a suitable reference potential (usually an appropriate representation of the hard core) and $u_p(r)$ is the perturbation (the soft attractive tail). In the inversion scheme one begins with the static structure factor, S(q), at known intervals of the scattering vector, q. The radial distribution function, g(**r**), and the direct correlation function, c(**r**), are related to S(**q**) through

$$g(\mathbf{r}) = [\rho\,(2\pi)^3]^{-1} \int d\mathbf{q}\ [S(\mathbf{q})-1]\, exp\,(i\mathbf{q}\cdot\mathbf{r}) \tag{4}$$

and

$$c(\mathbf{r}) = [\rho\,(2\pi)^3]^{-1} \int d\mathbf{q}\ \{[S(\mathbf{q})-1]/S(\mathbf{q})\}\, exp\,(i\mathbf{q}\cdot\mathbf{r}) \tag{5}$$

Eqs. (4) and (5) can be used to obtain the radial distribution function and the direct correlation function for the fluid from the observed structure factor. In the case of isotropic systems, the above equations can be simplified and can be written in terms of the scalar variables q and r. Details may be found in Hansen and McDonald (1986) or in standard books on scattering theory or statistical mechanics.

The (forward) perturbation theories begin with the decomposition of the pair-potential as in Eqn. (1). One then usually chooses an effective hard-sphere diameter d, which defines a hard-sphere potential $u_d(r)$ that replaces $u_0(r)$ in Eqn. (1) and defines the trial potential, $u_T(r)$, i.e.,

$$u_T(r) = u_d(r) + u_p(r). \tag{6}$$

A number of options exists for the selection of d; the use of the following criterion due to Lado is known to lead to better predictions of the thermodynamic properties of the fluid (Lado 1984; Hansen and McDonald 1986):

$$\int [\partial y_d(r)/\partial d] \{\exp [-\beta u_0(r)] - \exp [-\beta u_d(r)]\} \, dr = 0, \tag{7}$$

where y_d is the well-known cavity function corresponding to u_d. Finally, the trial structure factor can be written as (Andersen *et al.* 1976):

$$S_T(q) = S_d(q) / [1 + S_d(q) \rho \beta u_p(q)], \tag{8}$$

where r is the number density, $u_p(q)$ is the Fourier transform of an optimized $u_p(r)$ which is redefined inside the hard core in terms of a polynomial obtained by a well-known optimization prescription (Andersen *et al.* 1976), and $S_d(q)$ is the structure factor of a hard-sphere fluid of diameter d. The radial distribution function in the so-called EXP-approximation can be written as

$$g_{EXP}(r) = y_d(r) \, exp \, [C_L(r) - u_0(r)], \tag{9}$$

where $C_L(r)$ is a renormalized potential (Andersen *et al.* 1976).

In the case of inversion, we will begin with an estimate of the effective hard-sphere diameter, d, from the compressibility limit of the structure factor, namely, S(0). This is then used in combination with Eqn. (8) and the given structure factor data to obtain the perturbative part of the effective potential and subsequently the renormalized potential. The core can now be 'softened' using Eqn. (9) under the assumption that the experimental radial

distribution function can be approximated by $g_{EXP}(r)$. The resulting effective potential is refined further through additional iterations by returning to the above scheme with a new hard-sphere diameter obtained from the extracted potential. The details of this inversion scheme and the implications of the assumptions involved in the procedure are presented elsewhere (Sen and Rajagopalan 1991; Rajagopalan 1992); here, we restrict ourselves to a brief discussion of some sample results.

III.3. Sample Results

We now present some results based on this *predictor-corrector* method. Two different classes of potentials, one a simple potential with a single minimum (a Lennard-Jones potential) and another with a more complex shape with two minima (a weakly charged model colloidal dispersion), have been chosen for examining the method. In order to avoid the complications arising from possible effects of three-body potentials on structure, we restrict our attention here to data generated from *known* pair-potentials using an *independent* theoretical method. For this purpose, we have chosen the reference hypernetted chain (RHNC) theory. We have independently verified, using computer simulations, that the structure factors computed using RHNC for the above Lennard-Jones potential and the colloid potential are sufficiently accurate for testing the inversion method.

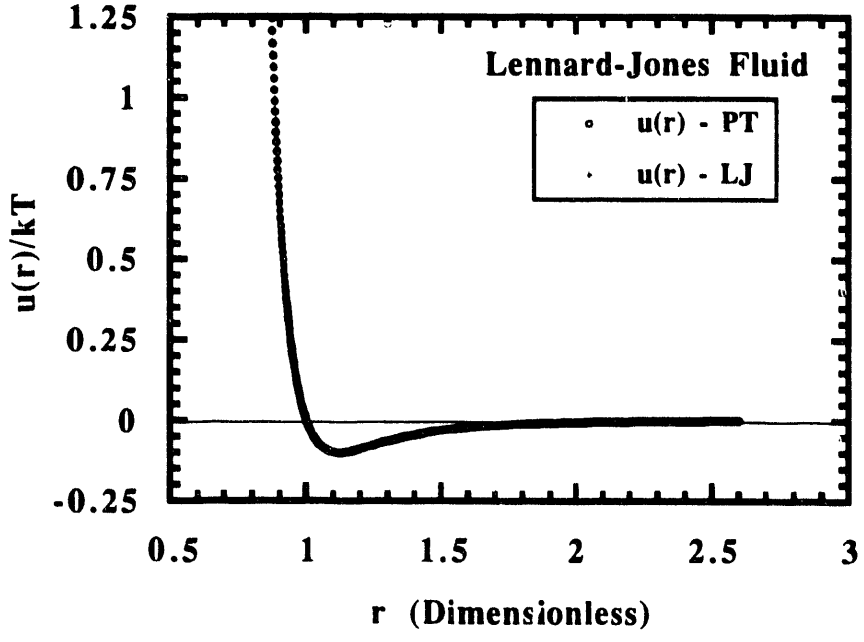

Figure 2. Inverted potential based on the perturbation method for an LJ fluid. Please see the text for details.

III.3.1 A LENNARD-JONES FLUID

The parameters of the Lennard-Jones potential considered are taken to be $\sigma = 1$ and $(\varepsilon/k_BT) = -0.1$, where σ is the so-called collision diameter and ε is the minimum in the pair-potential:

$$u(r) = 4\varepsilon [(\sigma/r)^{12} - (\sigma/r)^6] \quad (10)$$

The structure factor data for this potential were generated for a fluid at a reduced density, $\rho\sigma^3$, of 0.382 [corresponding to a 'volume fraction', $(\pi\rho\sigma^3/6)$, of 0.2] using RHNC. This moderately low value for the density was taken so that the structure factor generated was sufficiently accurate. Although computer simulations could have been used for this purpose, we chose to use the RHNC theory in order to avoid the need for smoothing the computer-generated data (to eliminate the statistical noise) and to avoid the need for extending the data sets further in both r and q spaces. However, the accuracy of the data generated from the RHNC theory has been verified using simulations [see Rajagopalan (1992) for sample results for related systems][1]. The resulting structure factor was used in the inversion scheme and the extracted potential is shown in Figure 2 along with the known potential. The excellent agreement between the two is evident from this figure. An enlargement of the results near the minimum further illustrates the accuracy of the results.

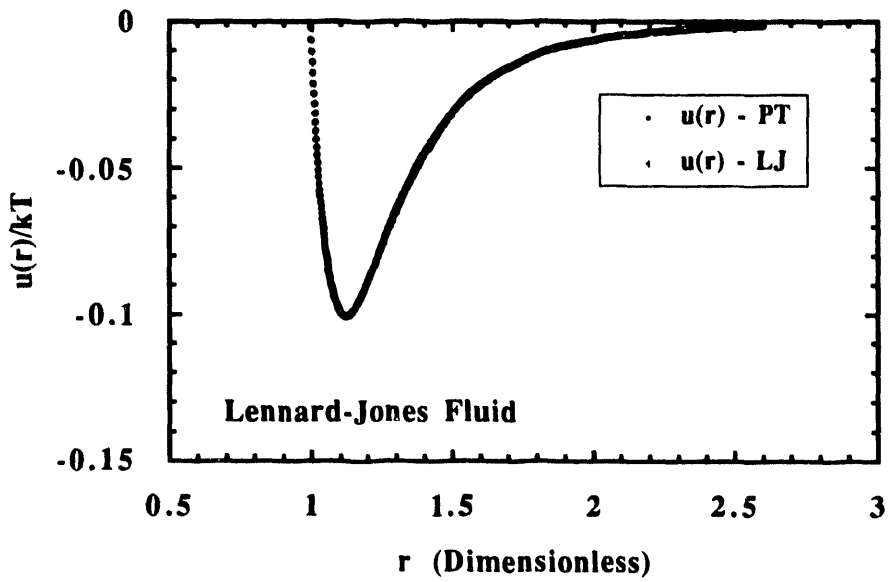

Figure 3. Enlargement of Figure 2 near the minimum in the extracted and the known potentials.

[1]The use of an analytical theory for generating structural data allows the choice of arbitrarily fine intervals in r and q, without any concern for statistical noises.

III.3.2 A MODEL COLLOIDAL FLUID

It is now instructive to examine a case corresponding to colloidal interactions. A model colloidal potential, which is described below in some detail, is chosen for this purpose. The structure factors and the radial distribution functions were generated for a colloidal fluid interacting through this potential for a number of densities using the RHNC theory. We have found that the RHNC results compare very well with the results of Monte Carlo simulations (for the model colloidal potential used here) for low densities (e.g., volume fractions of about 0.15 or lower). At larger volume fractions (especially around 0.4 or above), even though the radial distribution function appears to be quite accurate, the structure factor at low q [particularly the S(0) value, which is related to the isothermal compressibility] is in error by about 30% or more. Since the S(q) at low q's will have significant contributions to the extracted potential for large r, the larger density has been chosen here so that the resulting error in the extracted u(r) could be examined.

The hypothetical, but sufficiently realistic, model colloidal potential used here has a hard core (of unit diameter), a strong London-van der Waals attraction, u_A, a weak electrostatic repulsion, u_E, and a steep Born-type repulsion near the core, u_B:

$$u(r) = u_A(r) + u_E(r) + u_B(r) , \tag{11}$$

where r is the center-to-center distance of separation between the particles in units of particle diameter, and the pair-potentials are in units of k_BT. The expression for the London-van der Waals interaction u_A between two identical spheres is given by (Vold and Vold 1983; Castillo *et al.* 1984) :

$$u_A(r) = -N_{LO} \{1/(2r^2) + 1/[2(r^2-1)] + ln [(r^2-1)/r^2]\} , \tag{12}$$

where $N_{LO} = H/(6k_BT)$.

The Hamaker constant, H, in the above equation is a material property. The repulsive contribution, u_E, in Eqn. (11) arises from the electrostatic interaction between the diffuse portions of the electrical double layers surrounding each particle. The general expressions for electrostatic interaction energies are rather complicated and depend on whether the interacting surfaces keep their potentials constant or their charge densities constant. We have used an expression that reproduces the essential features well for systems with constant surface-charge densities and thick

electrical double layers, i.e., small inverse-screening lengths, $\kappa a \geq 2.5$ (Vold and Vold 1983; Verwey and Overbeek 1948):

$$u_E(r) = N_E \{ exp [- \kappa a (r-1)] \} / r, \quad (13)$$

where a is the radius of the particles (equal to 0.5 in our dimensionless units) and the premultiplying factor N_E is related to the contact potential.

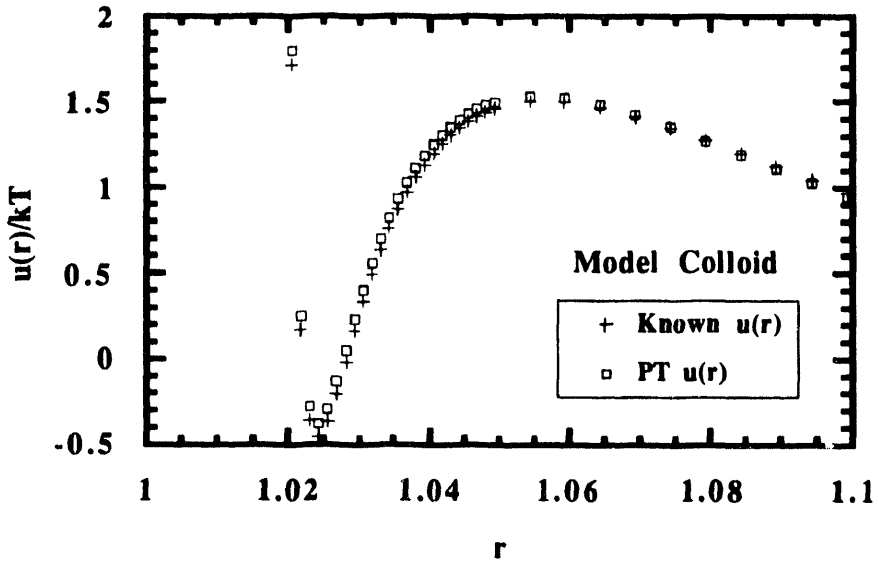

Figure 4. The inverted and the known potentials for the model colloid near the primary minimum in the potentials.

The other repulsive contribution, u_B, despite its very short range, has to be taken into consideration for dispersions with moderate or low electrostatic interactions, since the probability of finding two particles at very close separations can be far from negligible at sufficiently high particle concentrations. An expression of the following form was used for the Born repulsion u_B so that the appropriate shape of the pair-potential could be generated:

$$u_B(r) = N_B (r-1)^{-12} \quad (14)$$

with N_B is a scale factor that we call the Born parameter. The numerical values that were used for the dimensionless parameters are $N_{LO} = 1.025$, $N_E = 10.0$, $\kappa a = 3.75$, and $N_B = 2.275 \times 10^{-20}$. The resulting pair-potential has both a *primary* minimum and a *secondary* minimum, with a moderate energy barrier in between. Moreover, the attractive force immediately beyond the primary minimum is quite large.

Figures 4 and 5 show that the inverted pair-potential for volume fraction of 0.4 is in good agreement with the known potential. All the major features of the potential and the shape are reproduced well. As mentioned earlier, the structure factor generated by the RHNC theory for volume fraction equal to 0.4 is not very accurate in the compressibility limit; consequently, one should expect to see disgreements between the model potential and the extracted potential for large r's, and this is confirmed by the far-field results presented in Figure 5. Overall, the results for the colloidal fluid demonstrate that the method is capable of reproducing both the near-field and the far-field behavior of the potential well, *and* in a physically consistent manner, as long as sufficiently accurate structural data are available. The difference between the extracted potential and the exact potential in the far-field region can be reduced if the structure factor in the low-q region can be calculated with better accuracy. This is, in fact, evident from the results shown previously for the Lennard-Jones fluid (see Figures 2 and 3). This has also been verified by testing the inversion for a dispersion with the same potential but at a lower volume fraction (at which RHNC produces more accurate structure factors); these will be discussed in subsequent publications.

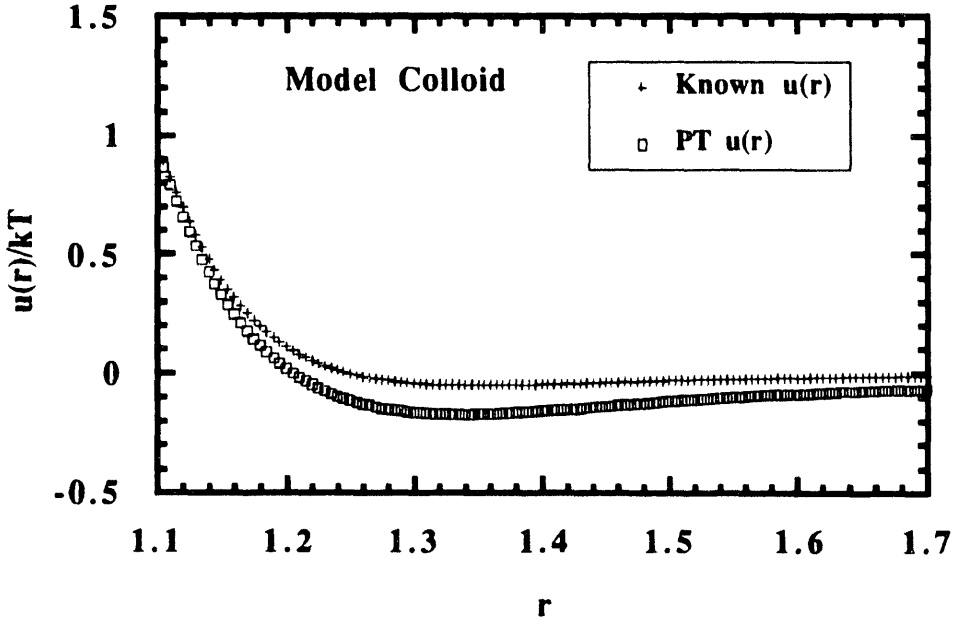

Figure 5. The inverted and the known potentials for the model colloid near the secondary minimum. The difference between the two is due to the large inaccuracy in the structure factor data near q = 0.

III.4. Caveats

The primary objectives of this section have been to demonstrate that static structure factors retain a considerable amount of information on the microscopic details of pair interaction potentials and that such details can be recovered to a large extent if the inversion method places proper emphasis on the crucial features of the interactions. The results shown above support these arguments. The method presented here is also the first successful analytical scheme that does not require any computer simulations in the inversion process. Nevertheless, a number of outstanding issues remain and require systematic examination. These issues include (i) the influence of errors in the structure factor (i.e., the sensitivity of the inverted potential to these errors), (ii) effects of cutoffs in the range of q,s over which the data are available, and (iii) the influence of smoothing and extension procedures that are used for refining and extending the range over which the data are available. It should also be emphasized here that the inverted potentials actually represent effective pair-potentials when three-body interactions and other non-additive interactions are present in the system. In view of this, additional constraints (such as consistency between experimentally measured thermodynamic or transport properties and the ones derived from the extracted potential) may need to be imposed. These and related issues will be addressed in future publications.

IV. Experiments for Direct Observation of Structure

What we have shown above is that interaction forces in colloids and atomic systems can be investigated using experimentally measured static structure factors and the inversion method outlined above. This approach is particularly useful to study steric and electrosteric interactions in relatively dense systems. As emphasized elsewhere (Rajagopalan 1992), techniques such as the one based on the surface force apparatus or total internal-reflection microscopy provide interactions between flat surfaces or between a sphere and a flat surface taken in isolation. In contrast, the method we have outlined here allows one to obtain interactions between spherical particles at arbitrary densities, thereby providing a systematic way to study interaction forces (including the onset of multibody interactions) as functions of density and other relevant parameters.

Given the above prospects, it is natural to ask what experimental limitations exist currently and how they might affect the results generated by the above method. At the outset, the following points deserve mention in this context:

1. Currently, the most common method of collecting structural information is through scattering experiments (especially neutron and light scattering). However, the scattering experiments typically provide structure factors over a restricted range of scattering vectors because of instrumental limitations and limitations due to q-values physically inaccessible. For the inversion method to lead to reliable results, data over a sufficiently large range of q's [low-q region (i.e., below the primary peak in S(q)) as well as large q's, for which S(q) reaches the asymptotic limit of unity] are necessary; otherwise, the problem becomes ill-posed. However, notice that this drawback also applies to 'fitting' methods[2] traditionally used in the analysis of scattering data. We have illustrated in Figure 5 that accuracy in the low-q range is essential for obtaining reliable results in the far-field region of the potential. We have also demonstrated elsewhere (Rajagopalan 1992) that the low-q results may also be important in the region of the core of the pair-potential. In particular, a combination of light scattering and neutron scattering experiments may be necessary to cover the relevant range of q's. Further, as well-known, the low-q region offers a particular challenge to the experimentalists.

2. Reduction of the scattered intensities to structure factor involves approximations, including the need to factor out the form factor. Methods to determine the structure factor directly will therefore be invaluable.

3. In the case of colloids, polydispersity (of size, charge, etc.) is a fact of life. Polydispersity affects the low-q values of the average structure factor when the standard deviation is more than about 10% of the mean value of the corresponding parameter [see Salgi and Rajagopalan (1993) for a review of the effects of polydispersity]. Therefore, experiments that are designed to probe interaction forces need to be restricted to highly monodisperse systems.

Experiments designed to provide direct visualization of the microstructure and to measure the correlation functions directly are very appealing since they can be designed to circumvent the difficulties mentioned in Items 1 & 2 above. In particular, correlation functions over 100 micrometers can be measured (corresponding to q's of the order of 10^{-5} $Å^{-1}$). In addition, since the spatial positions are measured directly, the structure factor can be computed directly (without the need for making

[2]By 'fiting methods', we mean 'forward' methods, in which one fits the observed structure factor data using assumed forms of pair-potentials and either computer simulations or theoretical methods for calculating structure factors. An extreme case of the uncertainties implicit in this approach is illustrated in Rajagopalan (1992).

approximations concerning form factors). Confocal microscopy can be used for layer-by-layer construction of positions as demonstrated by Dosho *et al.* (1993). We illustrate the use of such an approach through a video presentation of some sample results as part of this lecture.

V. CLOSING REMARKS

We have shown here that useful and quite accurate information about the interaction forces in dispersions (and atomic fluids) can be obtained from static structure factors. It is shown that use of colloids as model many-body systems, in combination with direct visualization and mapping of the microstructure of dispersions, can be profitable in studying systematically issues on the interaction forces that are otherwise inaccessible.

VI. ACKNOWLEDGMENTS

I would like to thank the National Science Foundation for partial support of the work reported here through grants CTS-9100139 and CTS-9218751, and the Petroleum Research Funds, administered by the American Chemical Society. I would also like to thank Dr. Norio Ise (Rengo Co., Fukui, Japan), Dr. Kenasaku Ito (Toyama University, Toyama, Japan), Prof. Ivan B. Ivanov (University of Sofia, Sofia, Bulgaria), Dr. A. K. Arora (Indhira Gandhi Centre for Atomic Research, Kalpakkam, India) and Dr. Cherry A. Murray (AT&T, Murray Hill, NJ) for sharing their data and experience with me.

VII. REFERENCES

Andersen, H. C. and Chandler, D., *J. Chem. Phys.* **53**, 547 (1970).

Andersen, H. C., Chandler, D. and Weeks, J. D., *J. Chem. Phys.* **56**, 3812 (1972).

Castillo, C. A., Rajagopalan, R. and Hirtzel, C. S., *Rev. in Chem. Eng.* **2**, 237 (1984).

Chen, S.-H. and Rajagopalan, R., Eds., *Micellar Solutions and Micro emulsions: Structure, Dynamics, and Statistical Thermodynamics*, Springer-Verlag, New York, 1990.

Croxton, C. A., *Liquid State Physics - A Statistical Mechanical Introduction*, Cambridge University Press, Cambridge, UK, 1974.

Degiorgio, V. and Corti, M., Eds., *Physics of Amphiphiles: Micelles, Vesicles and Microemulsions*, North-Holland, Amsterdam, 1985.

Denkov, N. D., Velev, O. D., Kralchevsky, P. A., Ivanov, I. B., Yoshimura, H., Nagayama, K., *Langmuir* **8**, 3183 (1992).

Dosho, S., Ise, N., Ito, K., Iwai, S., Kitano, H., Matsuoka, H., Nakamura, H., Okumura, H., Ono, T., Sogami, I. S., Ueno, Y., Yoshida, H., and Yoshiyama, T., *Langmuir* **9**, 394 (1993).

Fender, B. E. F., and Halsey, Jr., G. D. , *J. Chem. Phys.* **36**, 1881 (1962).

Friedman, H. L. , *A Course in Statistical Mechanics*, Prentice-Hall, Englewood Cliffs, NJ, 1985.

Hansen, J. P. and McDonald, I. R., *Theory of Simple Liquids*, 2nd. Edn., Academic Pr., New York, 1986.

Hirtzel, C. S. and Rajagopalan, R., *Colloidal Phenomena: Advanced Topics*, Noyes Publ., Park Ridge, NJ, 1985.

Hirtzel, C. S. and Rajagopalan, R. , "Computer Experiments for Structure and Thermodynamic and Transport Properties of Colloidal Fluids", in *Micellar Solutions and Microemulsions: Structure, Dynamics, and Statistical Thermodynamics*, Chen, S-H. and Rajagopalan , R., Eds., Springer-Verlag, New York, 1990.

Johnson, M. D. and March, N. H., *Phys. Lett.* **3**, 313 (1963).

Lado, F., *Mol. Phys.* **52**, 871 (1984).

Maitland, G. C., Rigby, M., Smith, E. B. and Wakeham, W. A., *Intermolecular Forces*, Clarendon Press, Oxford, 1981.

March, N. H. and Senatore, G., *Phys. Chem. Liq.* **13**, 285 (1984).

McQuarrie, D. A., *Statistical Mechanics*, Harper & Row, New York, 1976.

Murray, C. A., "Experimental Studies of Melting and Hexatic Order in Two-Dimensional Colloidal Suspensions", pp. 137 - 215 in *Bond-Orientational Order in Condensed Matter Systems*, Strandburg, K. J., Springer-Verlag, New York, 1992.

Nagayama, K., "Fabrication of Two-Dimensional Colloidal Arrays", *Phase Transitions*, 1993; in press.

Nieuwenhuis, E. A. and Vrij, A., *J. Colloid Interface Sci.* **72**, 321 (1979).

Rajagopalan, R., *Langmuir* **8**, 2898 (1992).

Rajagopalan, R., "Effective Interaction Potentials of Colloids from Structural Data: The Inverse Problem", pp. 695 - 706 in *The Structure, Dynamics and Equilibrium Properties of Colloidal Systems*, Bloor, D. M., and Wyn-Jones, E., Eds., Kluwer, Dordrecht, Amsterdam, 1990.

Salgi, P. and Rajagopalan, R., *Adv. Colloid Interface Sci.* **43**, 169 (1993).

Sen, A. K. and Rajagopalan, R., *Phys. Chem. Liq.* **22**, 195 (1991).

Tata, B. V. R., Rajalakshmi, M., and Arora, A. K., *Phys. Rev. Lett.* **69**, 3778 (1992).

Verwey, E. J. W. and Overbeek, J. Th. G., *Theory of the Stability of Lyophobic Colloids*, Elsevier, Amsterdam, 1948.

Vold, R. D. and Vold, M. J., *Colloid and Interface Chemistry*, Addison-Wesley, Reading, MA, 1983.

Yarnell, J. L., Katz, M. J., Wenzel, R. G. and Koenig, S. H., *Phys. Rev. A* **7**, 2130 (1973).

Non-Invasive Rigid Body Tracking

R. Dave*† B. Bukiet‡† A. Rosato*† I. Fischer* J. Volcy*

Abstract

We report on efforts to non-invasively track a sphere as it moves under gravity down an inclined chute. The sphere contains an electrical transmitter and its position and orientation are deduced using only the voltages received in a set of antennae mounted on the chute. The ultimate goal of this project is to detect the motion of a single particle flowing within a mass of particulates.

Model equations have been developed for the voltages induced in the receivers. These nonlinear equations predict the voltage induced in a given antenna as a function of the transmitter's orientation and position. In order to obtain the position and orientation of the transmitter from the voltage measurements, we apply the ideas of gradient search algorithms with those of Monte Carlo methods to obtain the best agreement between the model predictions and experimental measurements.

Results have been obtained using our model equations and inversion algorithm to find the position and orientation of the sphere being tracked as it proceeds along a known trajectory. Comparisons with simulated and experimental data are presented which establish the feasibility of our approach.

1 Introduction

The study of granular flows is of great importance because an improved understanding of such processes may lead to methods to reduce energy costs to industry by improving the efficiency of certain transport processes. Unlike fluids, which behave according to well-established equations, the flow of granular materials is not well-understood. and

*Department of Mechanical and Industrial Engineering, New Jersey Institute of Technology, Newark, New Jersey 07102

†Center for Applied Mathematics and Statistics

‡Department of Mathematics, New Jersey Institute of Technology, Newark, New Jersey 07102

scaling laws for these systems are not known. In order to understand the behavior of particulates subjected to various mechanical disturbances, it is necessary to perform non-invasive experiments. In this way, one can examine the kinematics of an individual particle without inserting a probe which would affect the flow. In this paper, we report on efforts to track a moving rigid body in a rectangular three-dimensional region in a non-invasive manner.

In the following section, the experimental apparatus for studying the flow of a spherical rigid body containing a transmitter is described. A radio-transparent chute has been built on which is mounted an array of antennae to receive the transmitter signals. The antennae voltage measurements are recorded and used to compute the positions and orientations of the sphere.

In section 3, we present the model equations for the voltages induced in the antennae. The voltages depend on the six orientation and position variables describing the location of the tracked body. We describe our method to solve the inverse problem, i.e., finding the position and orientation of the sphere given the measured voltages. This problem is complicated by the fact that the equations are nonlinear. Our solution technique combines the ideas of steepest descent, and trust regions (Levenberg-Marquardt method) with the ideas of stochastic (Monte Carlo) methods.

In section 4, we present the results of the numerical method with simulated data (using the model equations) and experimental data taken in our chute for known trajectories. Finally, in section 5, results are summarized and ideas are briefly discussed that may lead to improvements in the accuracy of the method.

2 The Physical Setup

Although, there are many different techniques available for particle flow measurements [10], few are suitable for the quantitative measurement of position and orientation of an individual particle. Fewer still can be considered non-invasive and most of these have significant problems associated with them. For example, X-rays methods can be dangerous. Photo-optical systems are reliable only if the body being tracked is near a clear wall. Reflections and refractions can degrade the results. Other bodies in the flow can interfere with ultrasound measurements.

We have constructed a rectangular radio-transparent chute 120" x 12" x 14" (see Fig. 1). The chute is surrounded by an array of rectangular antennae in which a voltage can be induced by an electrical transmitter. The details of the construction of the minia-

ture transmitter and the receiving equipment were reported in [2]. Because the chute is constructed entirely of non-metallic radio-transparent material, it does not interfere with the transmitted electromagnetic signals. Our apparatus allows measurements to be received from a rigid sphere (1" in diameter) containing an electrical transmitter from any location in the chute. There are no health risks associated with such a setup and other (non-metallic) bodies in the chute do not influence the results.

3 The Model Equations

The voltage induced in a receiving antenna is determined by the position and orientation of the sphere containing the transmitter and the positions of the corners of the (rectangular) receiving antenna.

A small loop of wire carrying a sinusoidal current $I = I_0 sin\omega t$ (where ω is the frequency) produces a magnetic field and induces a current in any small nearby loop of wire. The magnitude of the induced voltage depends on the relative position and orientation of the transmitting and receiving loops. with respect to one another. If both loops are small, the magnetically induced voltage, V, is found to be

$$V = \frac{(\mu_0 I_0 A_1 A_2 \omega)}{(4\pi r^3)}[2cos\theta_1 cos\theta_2 + sin\theta_1 sin\theta_2] \tag{1}$$

A_1 and A_2 are the areas of the transmitting and receiving antenna loops, μ_0 is the permeability of free space, I_0 is the magnitude of the current and r is the distance between the transmitter and the receiver. θ_1 and θ_2 are the angles made by the normals to the transmitter and receiver respectively with the line connecting the center of each. (Fig. 2).

From the above equation, it can be seen that the magnitude of the induced voltage is proportional to cross-sectional area of each loop of wire. In order to increase the magnitude of the signal produced in each receiving coil, receivers of much larger area are required. Rectangular shaped antennae are most practical, see Fig. 1. For this setup, equation (1.1) becomes

$$V = -\omega(B \cdot A) \tag{2}$$

where B is the magnetic-field density vector, and A is the vector normal to the plane of the transmitter. For each rectangular receiving coil, the magnetic field density is

$$B = \sum_{1}^{4} \frac{\mu_0 I_0}{(4\pi R_i)} (cos\phi_{i1} - cos\phi_{i2})\Theta_i \tag{3}$$

This sum contains one term for each side of the receiving rectangle. R_i is the distance from the transmitter to the center of the side. ϕ_{i1} and ϕ_{i2} are angles made by lines connecting the transmitter to the ends (vertex) of a side of the rectangular loop of wire with those sides of the rectangle. Θ_i is the unit normal to the triangle with the two ends of the side of the rectangle and the transmitter as vertices. (Fig. 3). This model was derived by Carr and Parasar [1] based on the principle of reciprocity in linear electrical networks [11].

With the receiving antennae fixed, one observes that the voltage depends on the position and orientation of the tracked sphere containing the transmitter. Since a voltage is induced in each receiver, there is one equation for each receiver and there are six unknown quantities, 3 for position (x,y,z) and three for orientation (α, β, γ - the angles made by the transmitter with the coordinate axes). Thus, at least six receiving antennae are required in order to resolve the six unknown values. In practice, some antennae may receive low voltages if they are far from the transmitter, or if the vector normal to the transmitting loops is almost parallel to the plane of the receiving antenna. In such cases, background noise becomes more significant, causing unacceptable errors. Thus, we have used ten antennae in our experiments.

The model equations, of course, do not exactly predict experimental values. However, the measured values are usually close to the voltages predicted by the model. Although the apparatus was built with special care using only radio-transparent materials, there are other sources for the differences between the model and experimental voltage values. These may include asymmetries in the transmitter, effects of background radiation, the coupling between antenna coils and nonlinearities in the signal amplifiers and other parts of the electronics used.

From a set of measured voltage readings, we need to determine the position and orientation of the transmitter. That is, we want to find the values of position (x,y,z) and orientation angles made with the coordinate axes (α, β, γ) satisfying as closely as possible the model equation for each receiver. To do this, we need to minimize the residual between the model voltages predicted and the measured voltages. The algorithm we have developed to solve this inverse problem is described in the following section.

4 Algorithm for finding position and orientation

In our experimental setup described above, there are ten antennae recording voltage signals from a moving transmitter. This leads to an overdetermined system of ten nonlinear equations in six unknowns $(x, y, z, \alpha, \beta, \gamma)$.

Methods of solution for such nonlinear optimization problems (see [3]) involve making initial guesses for the values of all the unknowns and updating the guesses in order to minimize error, the difference between measured and model values. By letting the measured voltages be denoted by v_k and the model values by $f_k(x)$, where the index k designates values from one to the number of receivers, we want to find X such that

$$r_k(X) = f_k(X) - v_k = 0 \text{ for } k = 1, 2, 3, ..., 10 \tag{4}$$

where X is the vector of unknowns $X = (x, y, z, \alpha, \beta, \gamma)^T$.

We let $R(X)$ be the vector whose entries are each of the $r_k(X)$. In general, no value of X exists such that R(X) is zero since the model equations do not exactly reflect the experimental results. We use the standard measure of error

$$Residual = .5 \sum_k r_k^2(X). \tag{5}$$

A first order Taylor expansion of $R(X)$ about the guess X_c yields

$$R(X) \approx R(X_c) + J(X_c)(X - X_c) \tag{6}$$

where $J(X)$ is the 10×6 Jacobian matrix J whose entries are

$$J_{ij}(X) = \partial r_k(X)/\partial x_j \tag{7}$$

where $x_1 = x, x_2 = y, x_3 = z, x_4 = \alpha, x_5 = \beta$ and $x_6 = \gamma$. We want to find the vector X such that $R(X) = 0$. Setting $R(x)$ to zero, one would like to solve

$$R(X_c) + J(X_c)(X - X_c) = 0 \tag{8}$$

for x. Since J is a 10×6 matrix, it cannot be inverted. To solve for X, we multiply this equation by $J^T(X_c)$ to obtain

$$J^T(X_c)R(X_c) + J^T(X_c)J(X_c)(X - X_c) = 0. \tag{9}$$

If the 6×6 matrix $J^T(X_c)J(X_c)$ is invertible, (all eigenvalues of such a "least squares matrix" are non-negative) we can multiply by $(J^TJ)^{-1}$ and solve for X in the least squares sense - i.e. we minimize the residual.

$$X = X_c - (J^TJ)^{-1}J^TR(X_c). \tag{10}$$

This Gauss-Newton method is simply the extension of Newton's Method to systems of nonlinear equations. This method may be problematic if J^TJ is not invertible or if any eigenvalue is small. This is because the amount that X_c is updated, $X - X_c$, is proportional to the reciprocal of the smallest eigenvalue of J^TJ. Hence, if any eigenvalue is small, the correction may be large, leading to instabilities and non-robustness of the method. To improve the stability of this algorithm, one may perform the following update,

$$X = X_c - (J^TJ + \mu I)^{-1}J^TR(X_c). \tag{11}$$

where the scalar μ is non-negative and I is the identity matrix. This increases each eigenvalue of the matrix to be inverted by μ. This method is called the Levenberg-Marquardt algorithm [5], [6]. Various complicated methods have been suggested for obtaining the value of μ. We have used More's implementation [8], in the publically available MINPACK [9] code. Here, μ is reset using an iterative method at each step. The Levenberg-Marquardt method combines the quadratic convergence of Newton's Method (when the current iterate, X_c, is close to the solution) with the trust region approach (which does not allow the next iterate be too far away from the current iterate). The algorithm also guarantees that the correction is in a descent direction, i.e. the residual decreases for small corrections in that direction.

We have found the Levenberg-Marquardt method to converge well to a local minimum of the residual for our problem. However, since there are multiple local minima, the Levenberg-Marquardt method alone may not find the optimal solution (the global minimum) especially if the initial iterate, X_0, is not close to the solution. In our computations, the initial iterate is based on the computed position of the tracked sphere at the previous time. Thus, if for some reason, the computed trajectory wanders away from the correct trajectory, it tends to remain off course for the remainder of the computation.

To handle this problem, we have combined the Levenberg-Marquardt method with the ideas of Monte Carlo methods [7], [4]. An initial iterate is chosen based on the computed position of the tracked sphere at the previous time and several steps of the Levenberg-Marquardt method are performed. Another starting iterate is chosen by perturbing the result of the Levenberg-Marquardt iterations randomly within a spherical volume several

inches in radius. We have found that by taking five to ten starting guesses in this manner and selecting as the computed solution, the iterate which yields the smallest residual, yields high quality results. Since this method does not always guarantee a physically realistic trajectory, a limit is placed on the distance that the sphere can move within the small time interval between the captured voltages. The effect is that we test for the minimum residual in several nearby valleys and choose the deepest one which satisfies reasonable physical constraints. As we show in the following section, this method is more robust than the straight Levenberg-Marquardt method in that if a computed trajectory strays off course, it may be able to recover and get back on course. This is especially important when the trajectory strays off course due to the transmitter orientation being almost parallel to some receivers. In rolling trajectories, there often will be points for which the transmitter axis is almost parallel to planes of some of the receiving antennae.

5 Comparison with Simulated and Experimental Data

In this section, results of several tests are presented in order to validate the computational method and establish the feasibility of the approach. First, in order to test only the numerical method without having to deal with the inexactnesses in the model equations, tests were performed with simulated data. That is, the input voltages were produced by the model equations. Figs. 4 and 5 present plots of simulated experiments, both a straight line trajectory and a sinusoidal one. Figs. 6 and 7 show plots of the same experiment in which random noise was introduced into the simulated voltage readings.

Experiments were performed using the chute and transmitting sphere. The number of counts received through each antenna are measured and scaled with the model to compute a voltage. This data is then inverted to calculate the position and orientation of the transmitting sphere. Since the model equations do not exactly represent reality, there are additional sources of error. In Figs. 8a-c, experimental results are shown in which the transmitter was hooked to a motor-driven ski-lift type device and pulled through the chute in a straight line at constant velocity. The orientation of the transmitter was more or less constant during the experiment. Experimental readings were taken during the approximately twenty second run. The initial iterates were chosen using linear extrapolation on the two previous computed positions and orientations.

Difficulties may arise when the orientation of the transmitter is close to being parallel to the planes of some of the antennae loops. This is because the voltage readings will be small and consequently the effects of background noise and other causes of error will be magnified. This issue is important for the study of realistic trajectories of a particle traversing a path through the chute. Large changes in the orientation variables (α, β, γ)

could be expected during such an experiment. A relatively small fraction of these orientations would be almost parallel to some antennae. However, we have found that if this occurs, the simple algorithms used (Gauss-Newton and Levenberg-Marquardt) can miscalculate the position and orientation of the particle. Because calculating the location of the particle at any time critically depends on the intial guess (previous computed location), an error incurred at some instant can cascade thereafter. This problem is circumvented via the combined Levenberg-Marquardt-Monte Carlo algorithm. The improvement using the combination algorithm for such a case (Figs. 10a-f) is demonstrated by comparing it to the result using the Levenberg-Marquardt method alone (Figs. 9a-f). Readings were taken in which both the orientation and position of the transmitting sphere were varied. Although the algorithm yields larger errors when the transmitter is almost parallel to some antennae, the method quickly corrects itself as the transmitter moves away from being parallel to some antennae.

6 Summary and Conclusions

We have constructed an experimental system in which particle flows can be studied non-invasively based on the principle of magnetic-induction coupling. This allows computation of the trajectory of an individual sphere containing a transmitter as it travels through a inclined chute. To do this, a model has been derived which expresses the position and orientation of the transmitting sphere as a function of the experimental voltage measurements. A numerical algorithm has been developed which combines the ideas of multidimensional descent methods with Monte Carlo methods to solve the inverse problem, i.e. compute the sphere's position and orientation based on the measured voltage data.

The thoeretical model has been shown to be a reasonable representation of reality. However, it is believed that heuristic modifications may prove useful in improving the accuracy of the method. Such work could include corrections for the influence of the receiving antennae on one another and incorporating higher order correction terms in the model equations based on experimental results. Our numerical method has been tested against both simulated and experimental data. The technique has been shown to improve the robustness of standard inversion techniques. This work provides the foundation for experimental studies for the behavior of an individual particle in an inclined chute flow. The system also has applicability to other dry granular and multiphase systems.

Acknowledgments

We would like to thank Anthoy Troiano, Avadhani Ashok, Kurra Bhaswan and Elliotte Harold for their contributions to this work. This work was supported in part by the United States Department of Energy under contract DE-AC22-91PC90181.

References

[1] Carr, W. N., and A. Parasar, *Private Communication*, New Jersey Institute of Technology, Newark, New Jersey, 1991.

[2] R. Dave, A. D. Rosato, I. S. Fischer, B. Bukiet, W. N. Carr, "Non-intrusive three-dimensional particle tracking system", in Proceedings of the Fourth NSF-DOE Workshop on Flow of Particulates and Fluids, Gaithersburg, Maryland, 1992.

[3] Dennis, J. E. and R. B. Schnabel, *Numerical Methods for Unconstrained Optimization and Nonlinear Equations*, Prentice-Hall, Englewood Cliffs, New Jersey, 1983.

[4] Kalos, M. and P. Whitlock, *Monte Carlo Methods*, J. Wiley & Sons, New York, 1986.

[5] Levenberg, K., "A Method for the Solution of Certain Problems in Least Squares", *Quart. Appl. Math.*, **vol. 2**, pp. 164-168, 1944.

[6] Marquardt, D., "An Algorithm for Least Squares Estimation of Nonlinear Parameters", *SIAM J. Appl. Math.*, **vol. 11**, pp. 431-441, 1963.

[7] Metropolis, N., A. W. Rosenbluth, M. N. Rosenbluth, A. H. Teller, and E. Teller, "Equation of state calculations by fast computing machines", *J. Chem. Phys.*, **vol. 21**, p 1087, 1953.

[8] Moré, J. J., "The Levenberg-Marquardt Algorithm: Implementation and Theory", in *Numerical Analysis*, G. A. Watson, ed., Lecture Notes in Math. 630, Springer-Verlag, Berlin, pp. 105-116, 1977.

[9] Moré, J. J., B. S. Garbow, and K. E. Hillstrom, "User Guide for MINPACK-1", Argonne National Lab Report ANL-80-74, 1980.

[10] Tuzun, U., G. T. Houlsby, R. M. Nedderman, and S. B. Savage, "The Flow of Granular Materials - II", *Chem. Eng. Sci.*, **vol. 37**, (12), pp. 1691-1709, 1982.

[11] Van Valkenberg, M. E., *Network Analysis*, p. 258, Prentice-Hall, Englewood Cliffs, New Jersey, 1974.

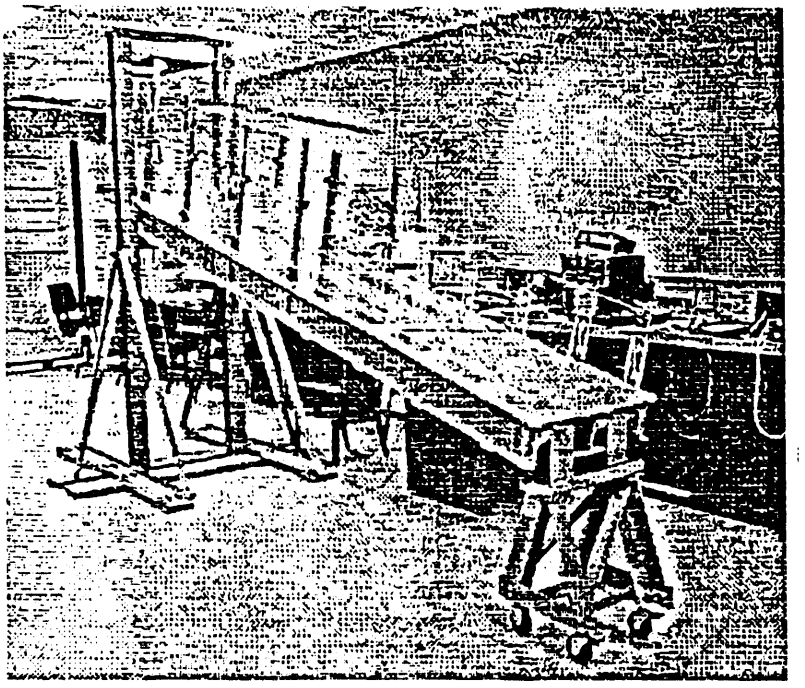

Fig. 1 A chute has been constructed for proof-testing of the radiosonde system and the conduct of particulate-flows experiment. It features all-plastic construction for radio-transparency.

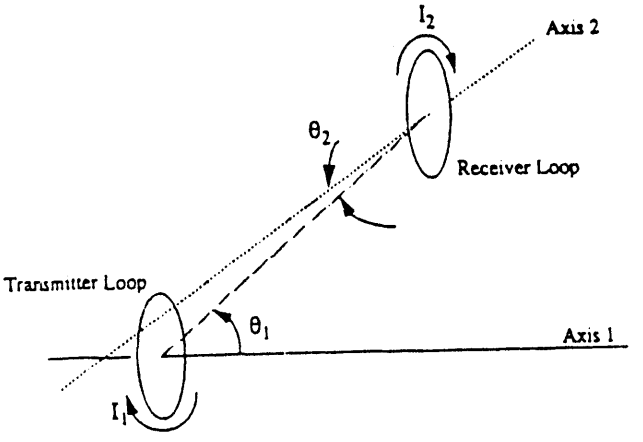

Fig. 2 Geometry for a small circular loop transmitter-receiver pair.

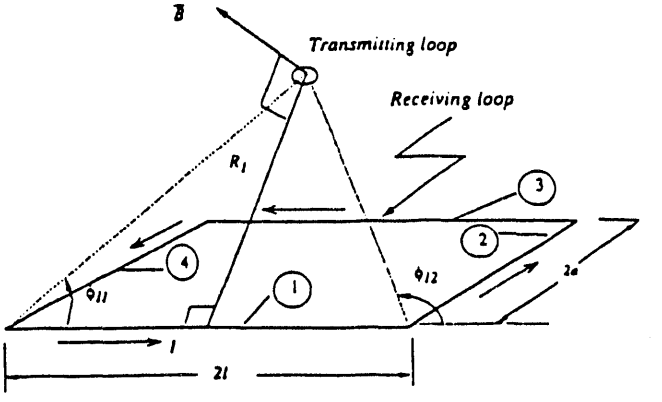

Fig. 3 Configuration for a small circular loop transmitter and a rectangular loop receiving antennae.

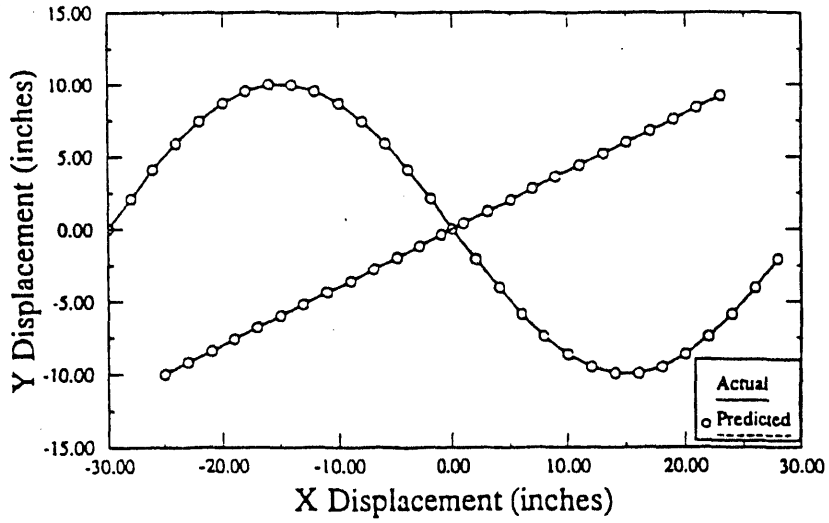

Fig. 4 Simulated experiment without noise, projection on xy plane. Curves are actual trajectories while the markers are the predicted trajectories.

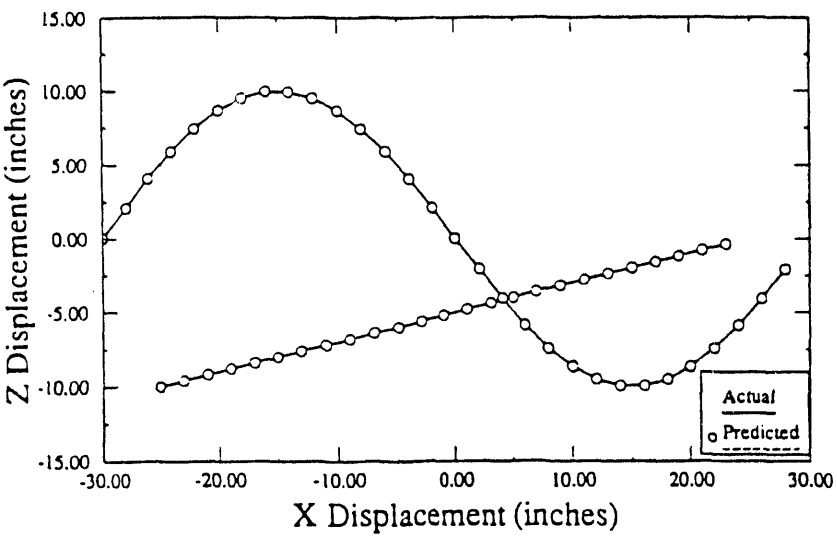

Fig. 5 Simulated experiment without noise, projection on xz plane. Curves are actual trajectories while the markers are the predicted trajectories.

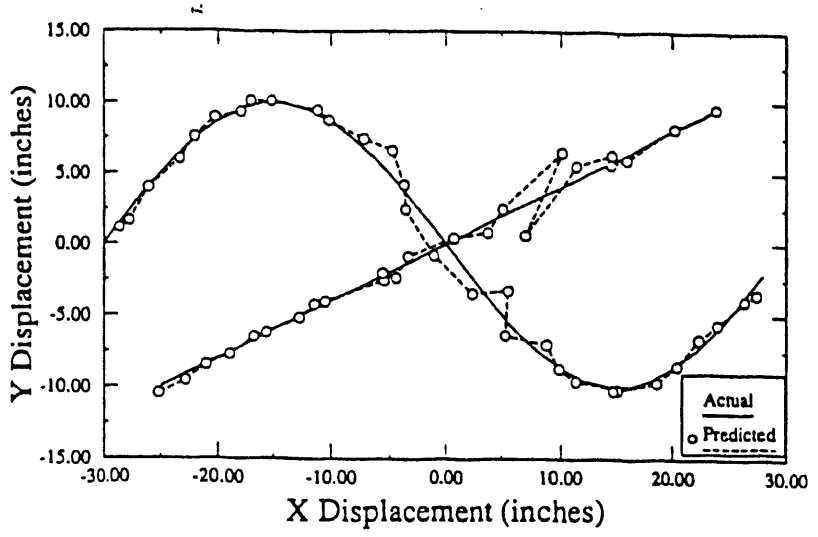

Fig. 6 Simulated experiment with added noise, projection onto the XY plane. Curves are actual trajectories, while the markers are predicted trajectories.

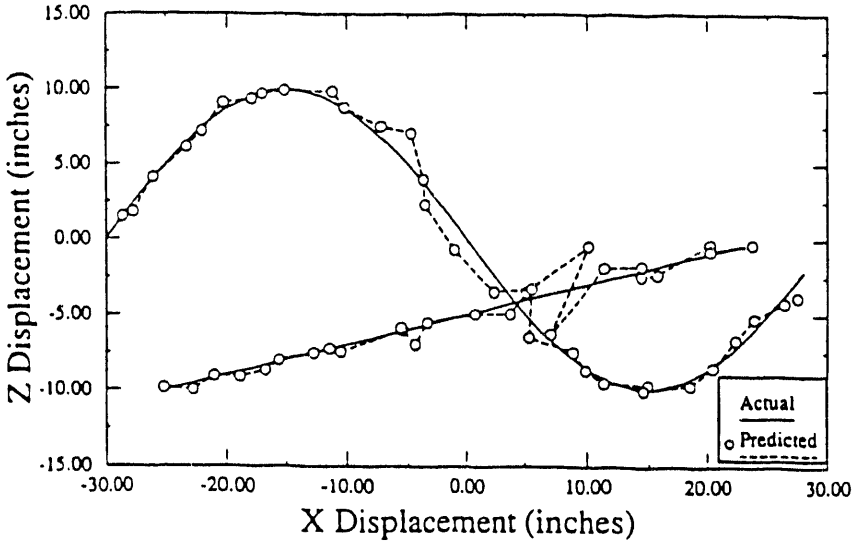

Fig. 7 Simulated experiment with added noise, projection onto the XZ plane. Curves are actual trajectories, while the markers are predicted trajectories.

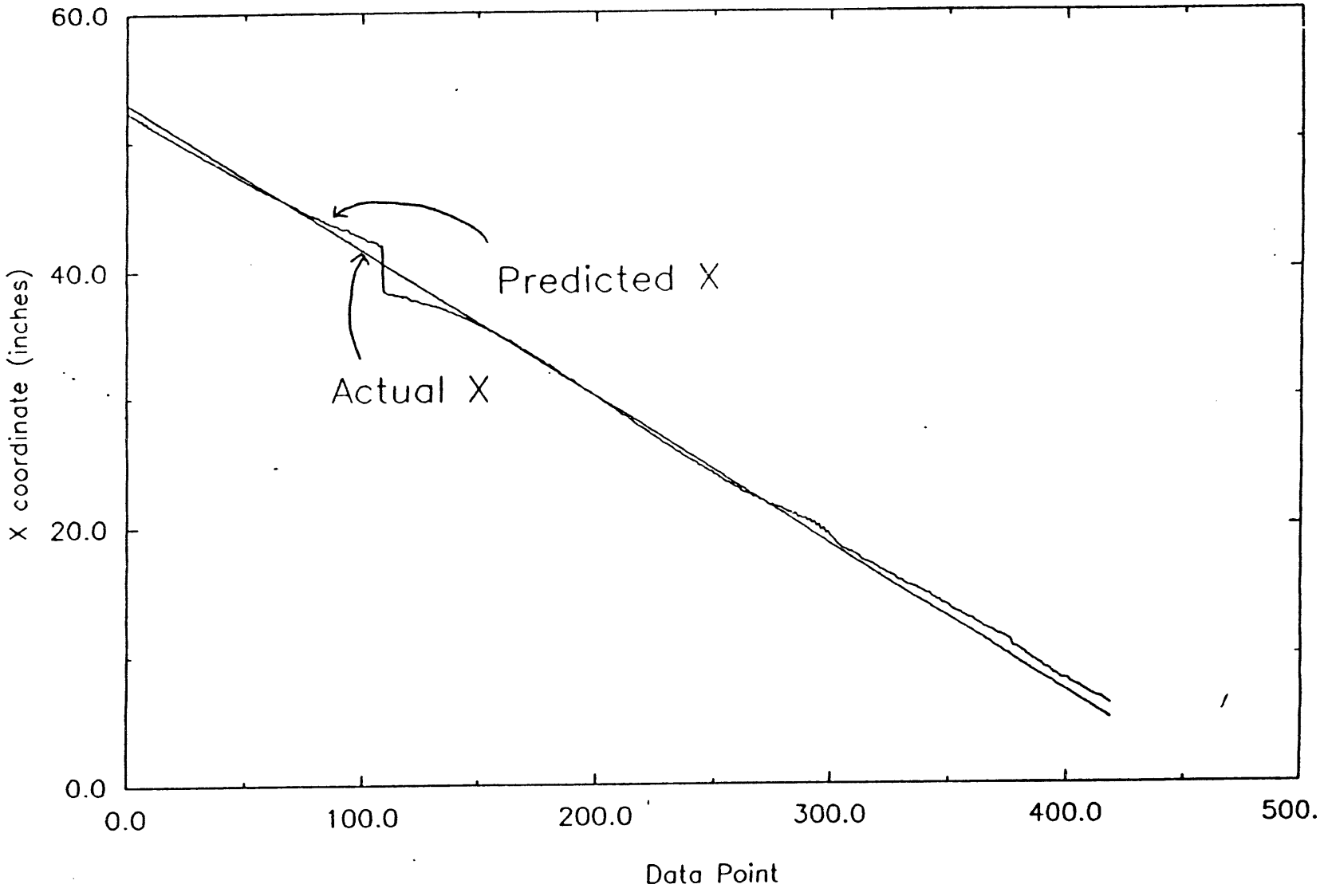
60.0
40.0
20.0
0.0
X coordinate (inches)
Predicted X
Actual X
0.0
100.0
200.0
300.0
400.0
500.
Data Point

Fig. 8a

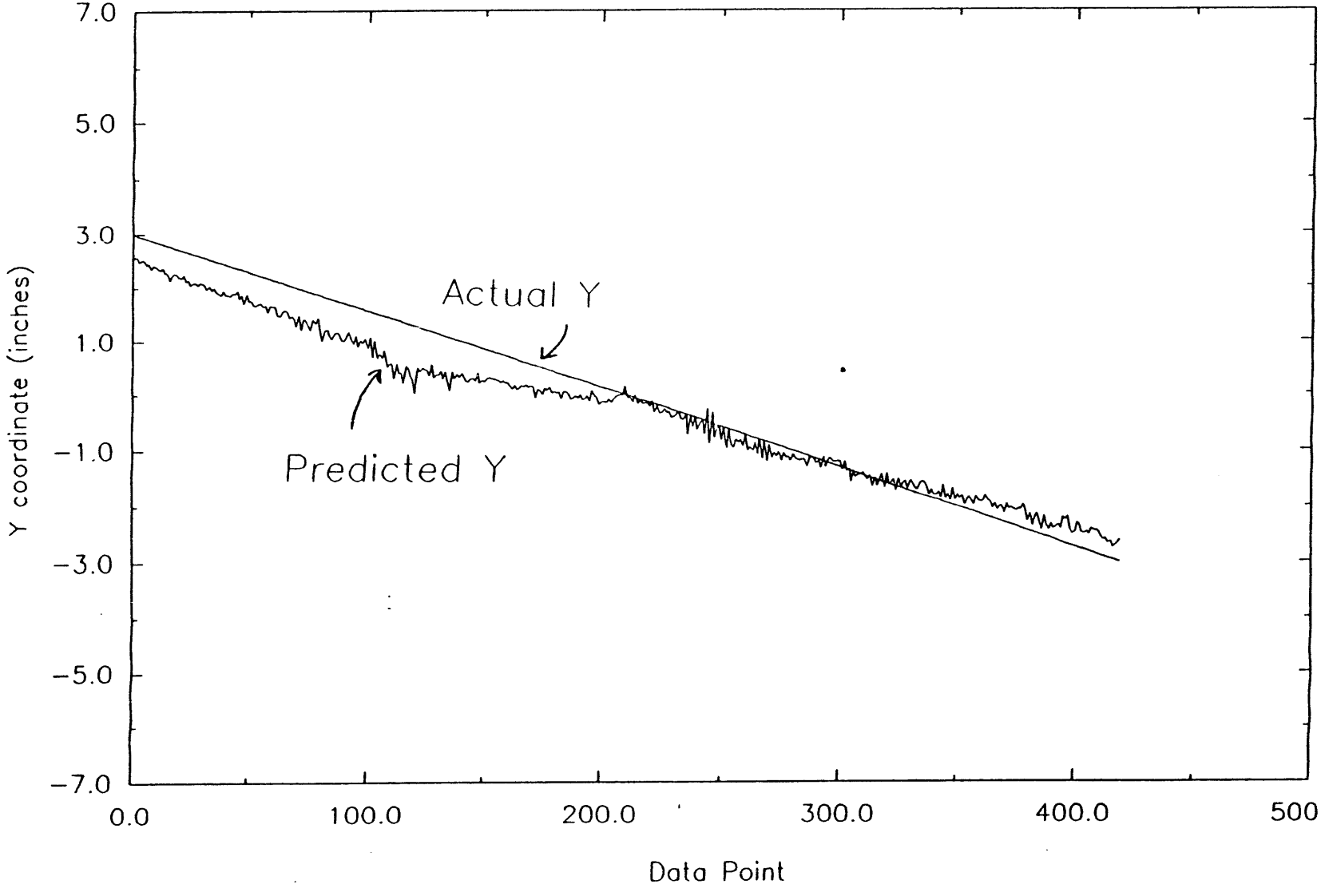
7.0
5.0
3.0
1.0
−1.0
−3.0
−5.0
−7.0
Y coordinate (inches)
Actual Y
Predicted Y
0.0
100.0
200.0
300.0
400.0
500
Data Point

Fig. 8b

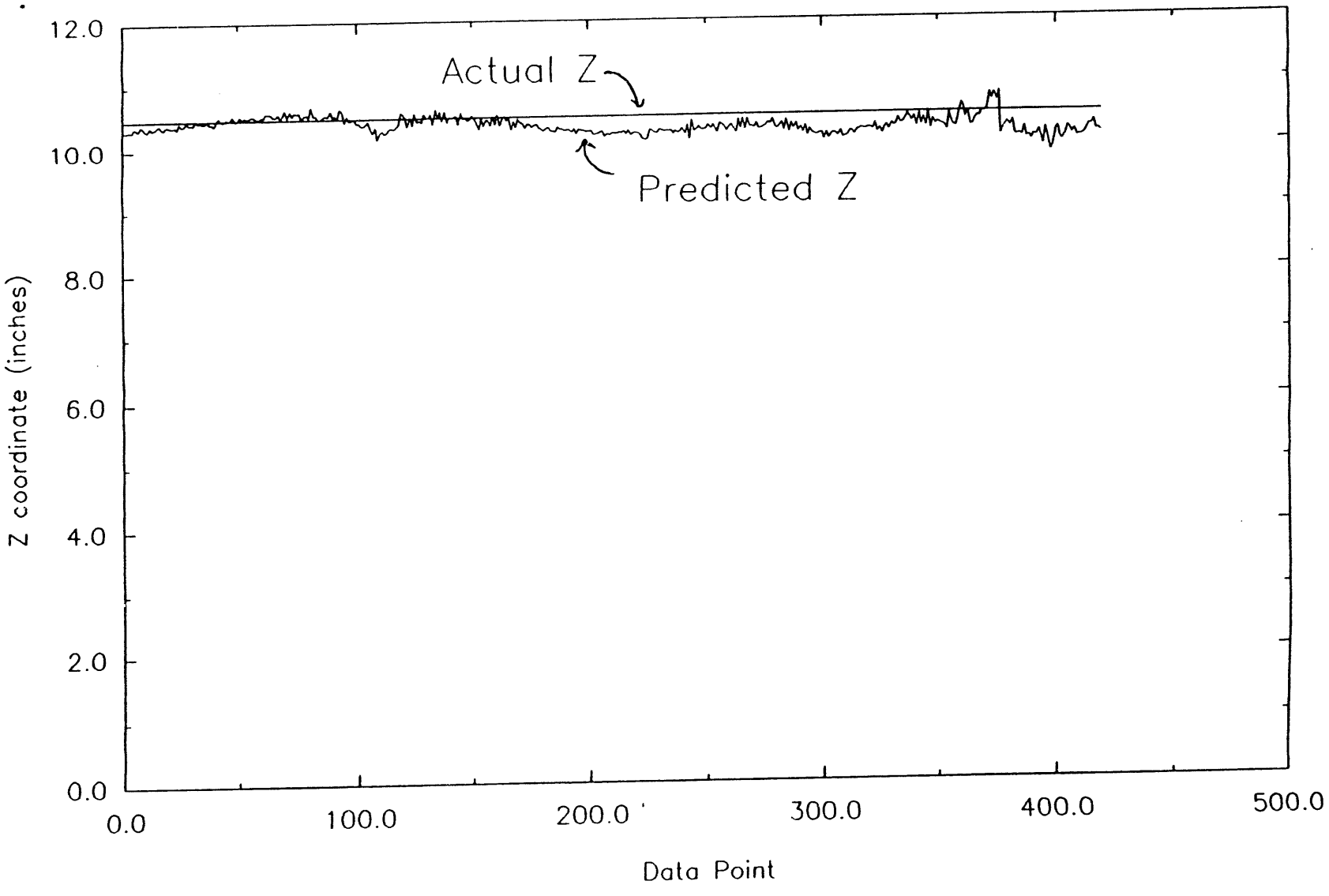
Actual Z
Predicted Z
Z coordinate (inches)
12.0
10.0
8.0
6.0
4.0
2.0
0.0
0.0
100.0
200.0
300.0
400.0
500.0
Data Point

Fig. 8c

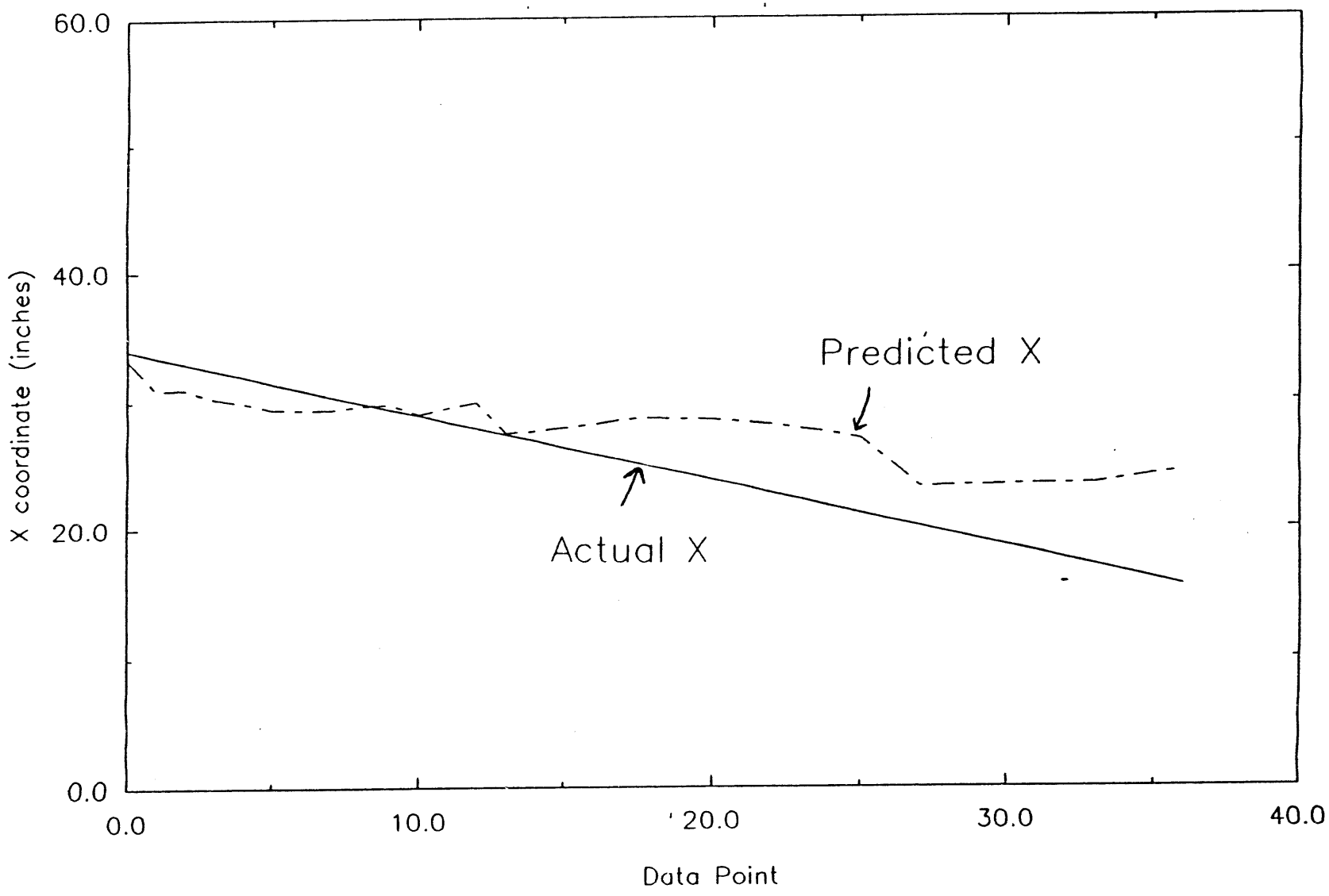
60.0
40.0
20.0
0.0
X coordinate (inches)
Predicted X
Actual X
0.0
10.0
20.0
30.0
40.0
Data Point

Fig. 9a

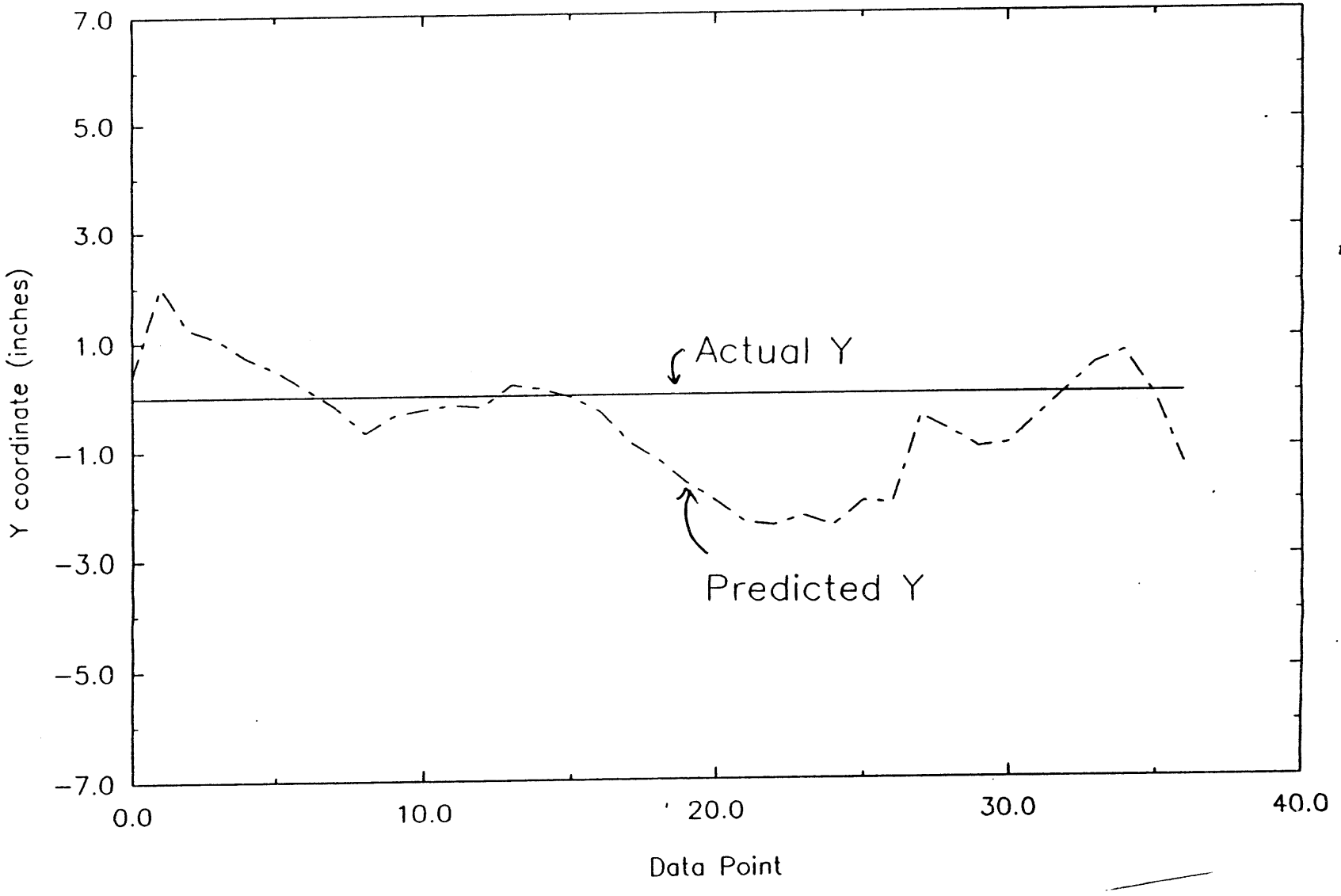
7.0
5.0
3.0
1.0
-1.0
-3.0
-5.0
-7.0
Y coordinate (inches)
Actual Y
Predicted Y
0.0
10.0
20.0
30.0
40.0
Data Point

Fig. 9b

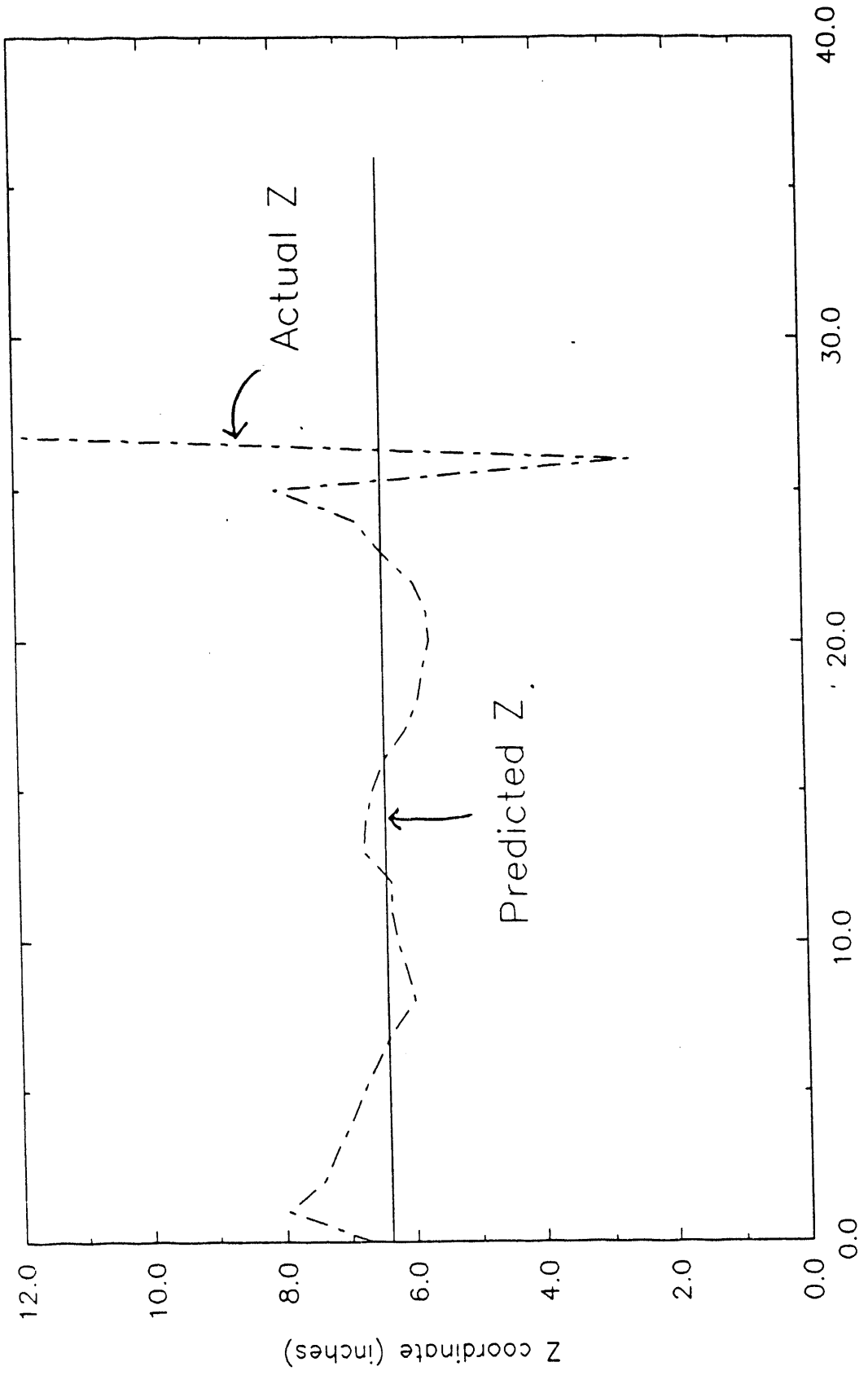
Actual Z
Predicted Z
Z coordinate (inches)
Data Point
12.0
10.0
8.0
6.0
4.0
2.0
0.0
0.0
10.0
20.0
30.0
40.0

Fig. 9c

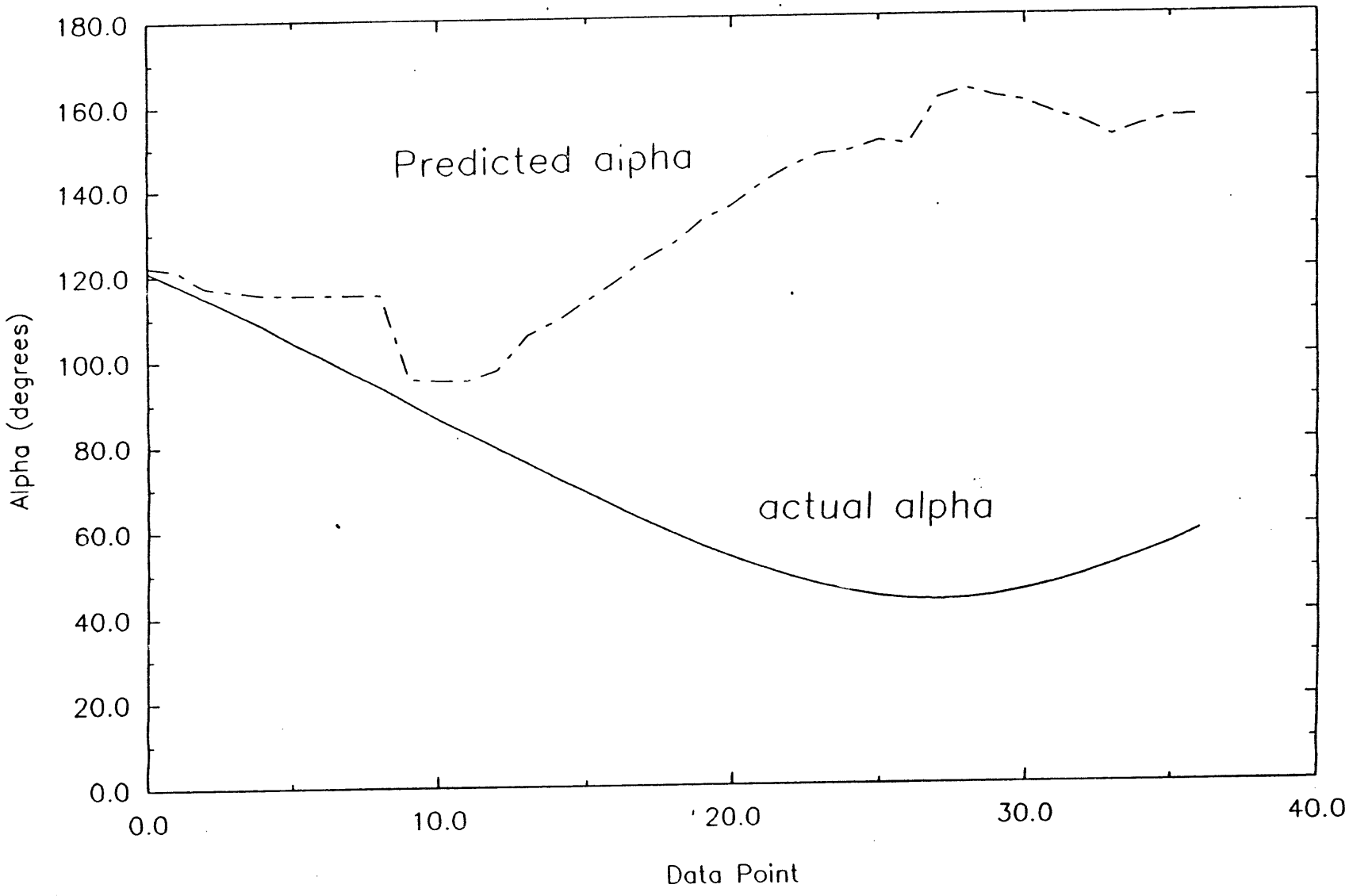
180.0
160.0
140.0
120.0
100.0
80.0
60.0
40.0
20.0
0.0
Alpha (degrees)
Predicted alpha
actual alpha
0.0
10.0
20.0
30.0
40.0
Data Point

Fig. 9d

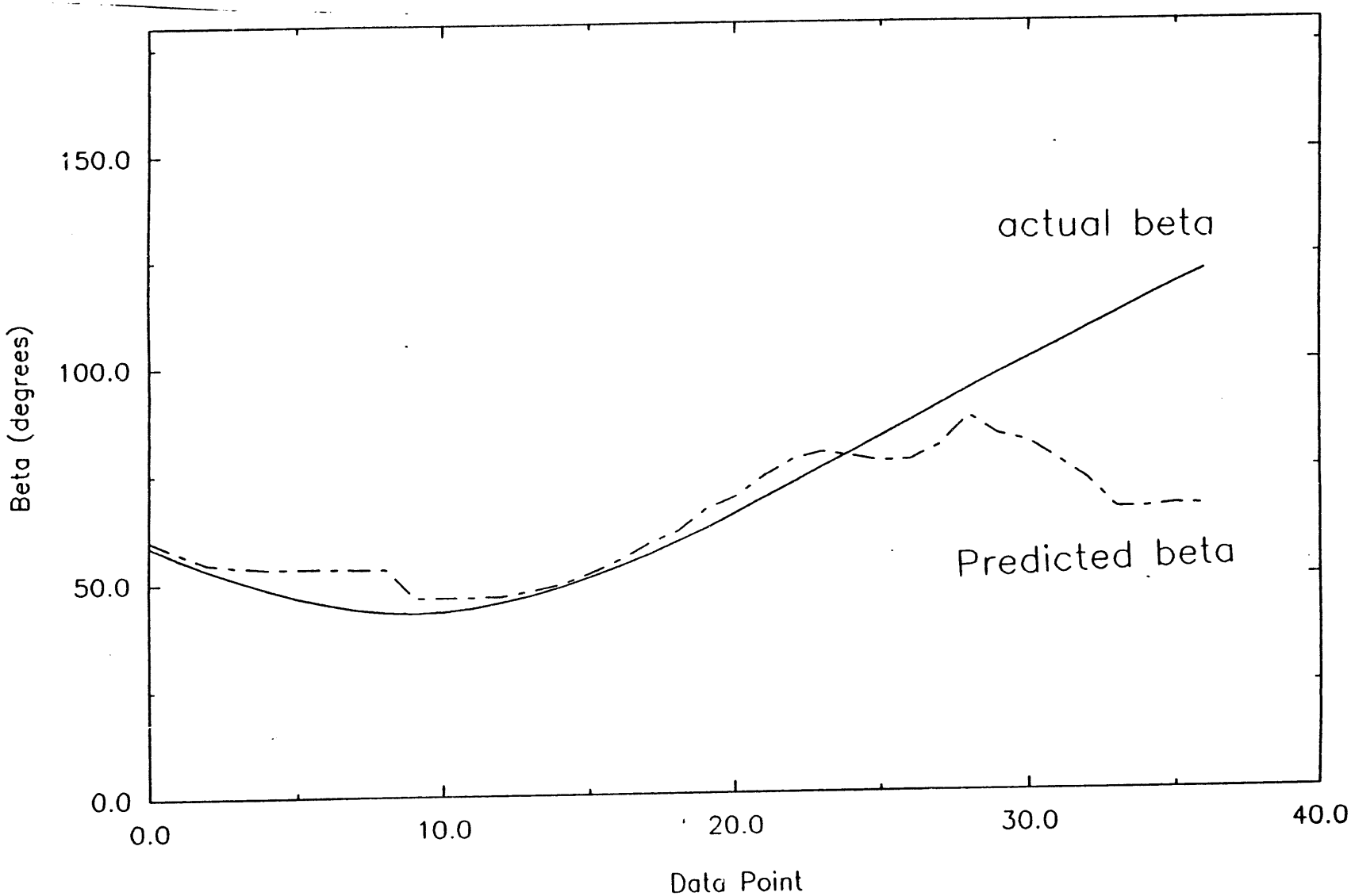
150.0
100.0
50.0
0.0
Beta (degrees)
actual beta
Predicted beta
0.0
10.0
20.0
30.0
40.0
Data Point

Fig. 9e

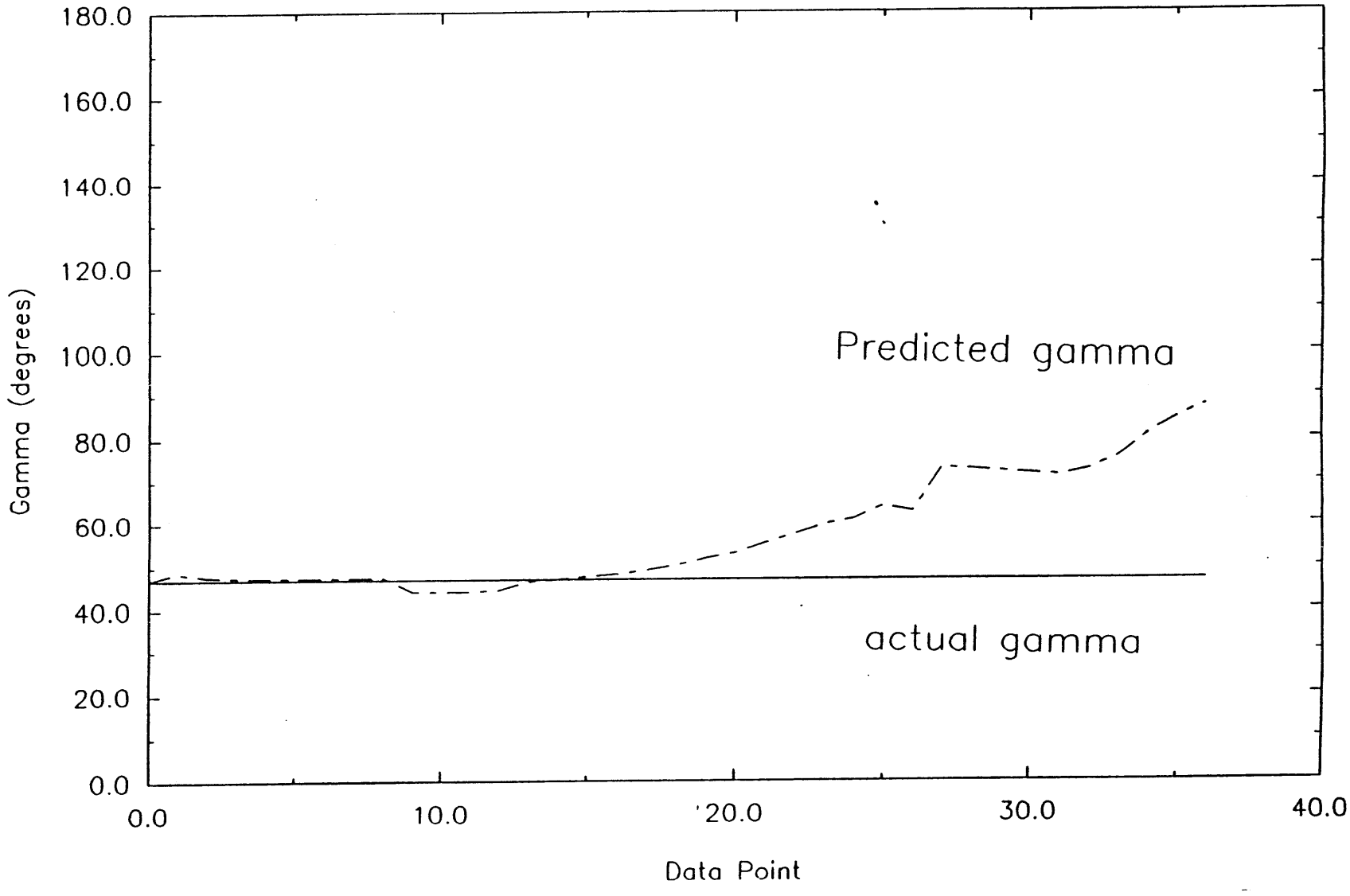
180.0
160.0
140.0
120.0
100.0
80.0
60.0
40.0
20.0
0.0
Gamma (degrees)
0.0
10.0
20.0
30.0
40.0
Data Point
Predicted gamma
actual gamma

Fig. 9f

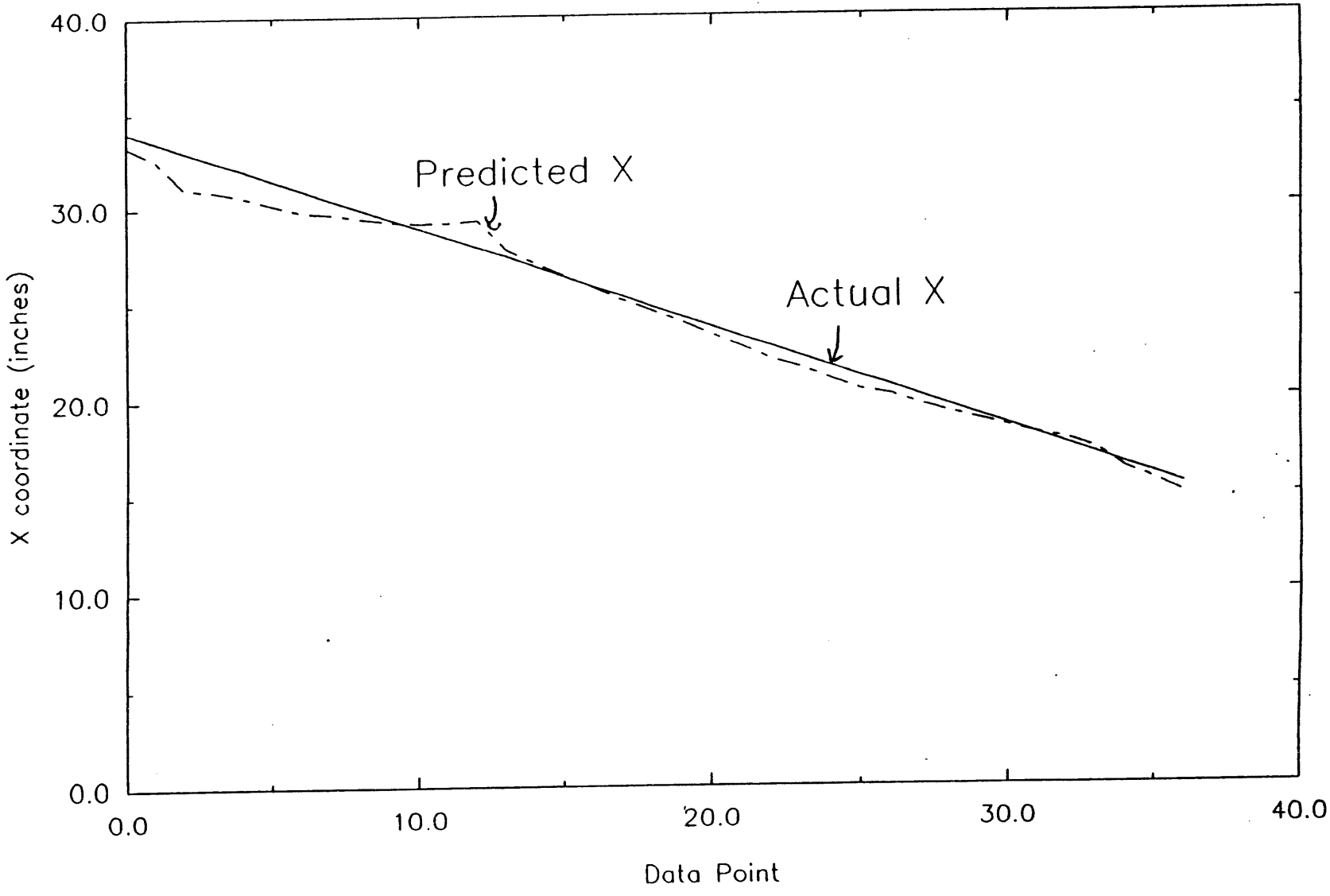
40.0
30.0
20.0
10.0
0.0
X coordinate (inches)
Predicted X
Actual X
0.0
10.0
20.0
30.0
40.0
Data Point

Fig. 10a

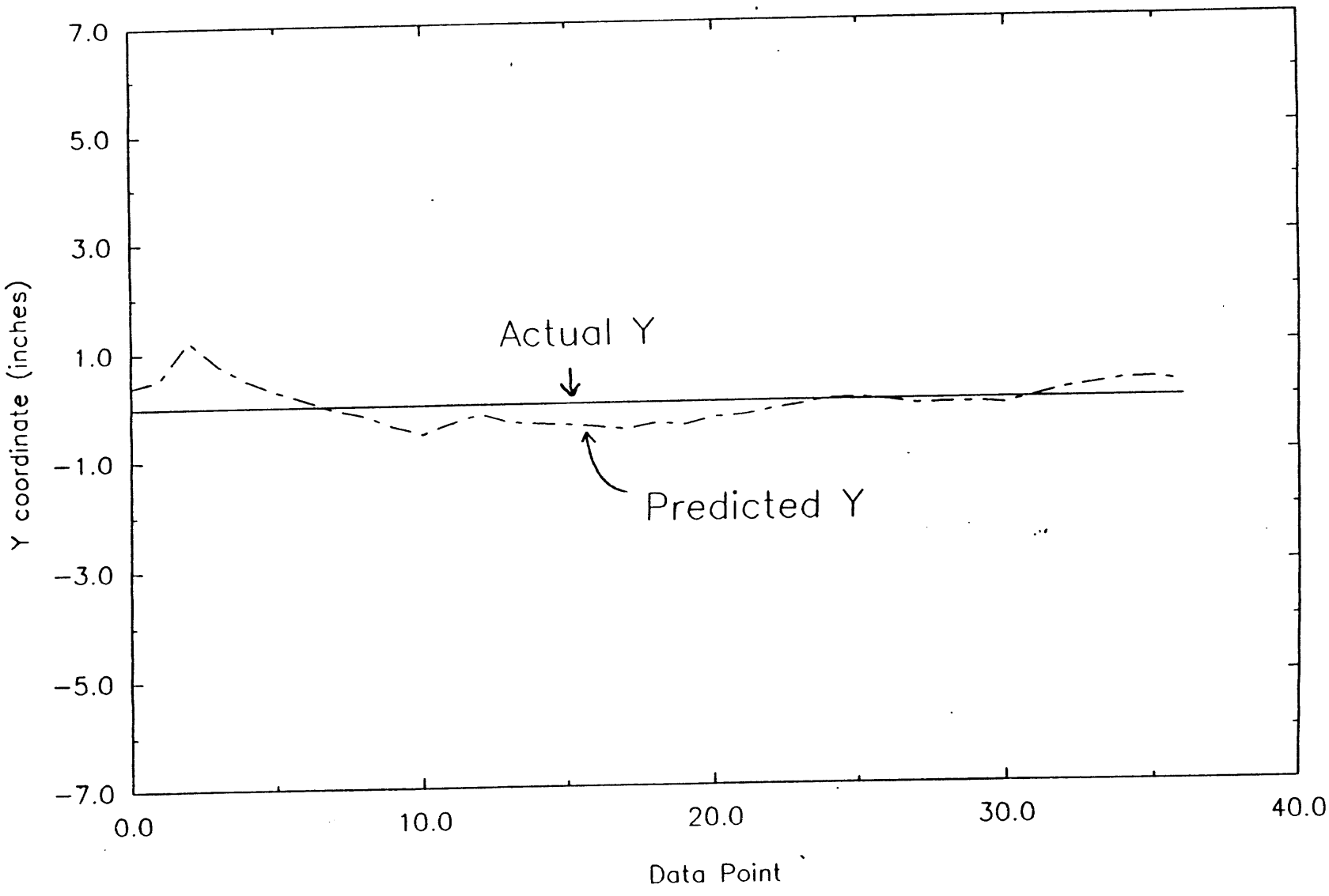
7.0
5.0
3.0
1.0
-1.0
-3.0
-5.0
-7.0
Y coordinate (inches)
Actual Y
Predicted Y
0.0
10.0
20.0
30.0
40.0
Data Point

Fig. 10b

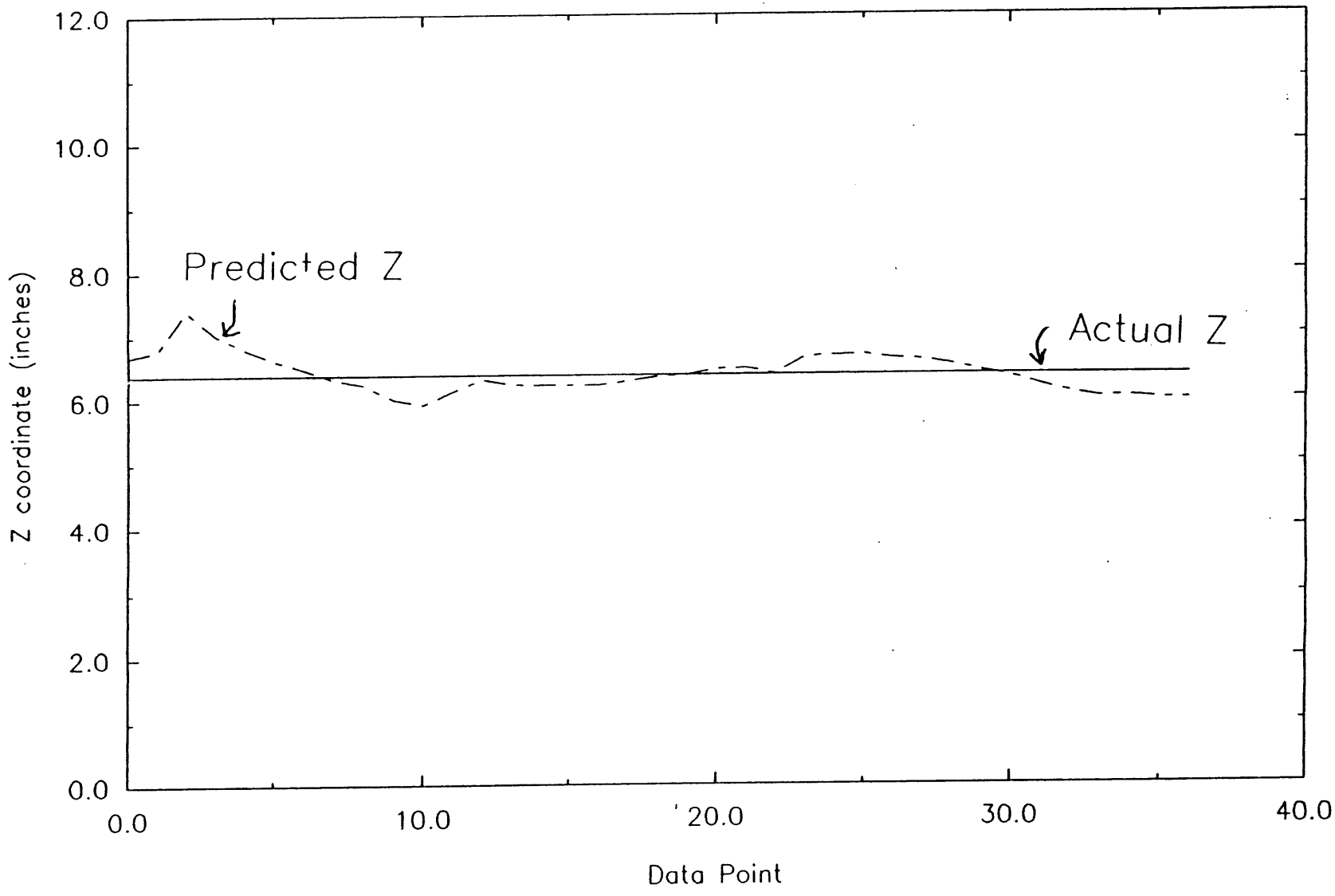
12.0
10.0
8.0
6.0
4.0
2.0
0.0
Z coordinate (inches)
Predicted Z
Actual Z
0.0
10.0
20.0
30.0
40.0
Data Point

Fig. 10c

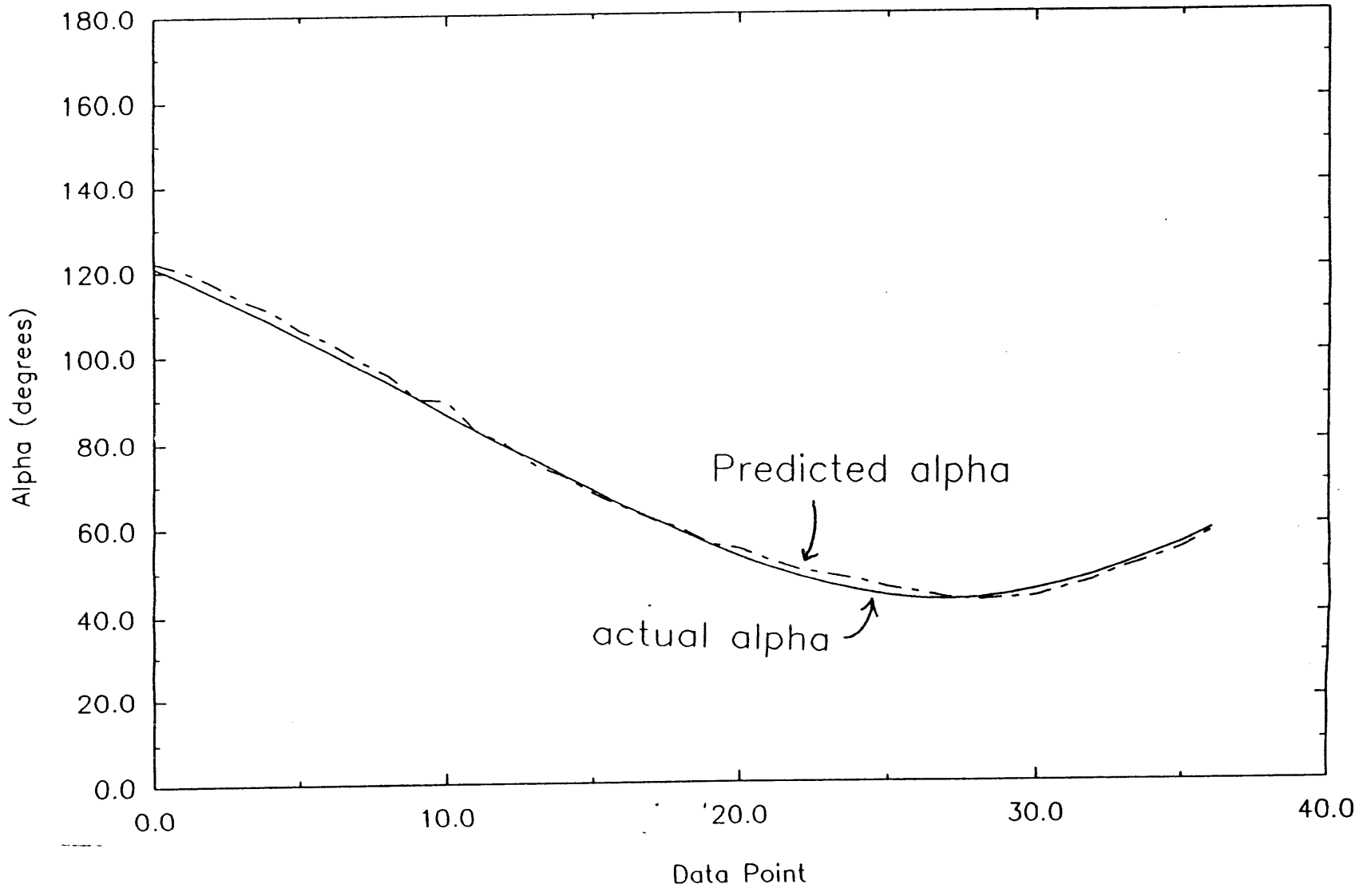
180.0
160.0
140.0
120.0
100.0
80.0
60.0
40.0
20.0
0.0
Alpha (degrees)
0.0
10.0
20.0
30.0
40.0
Data Point
Predicted alpha
actual alpha

Fig. 10d

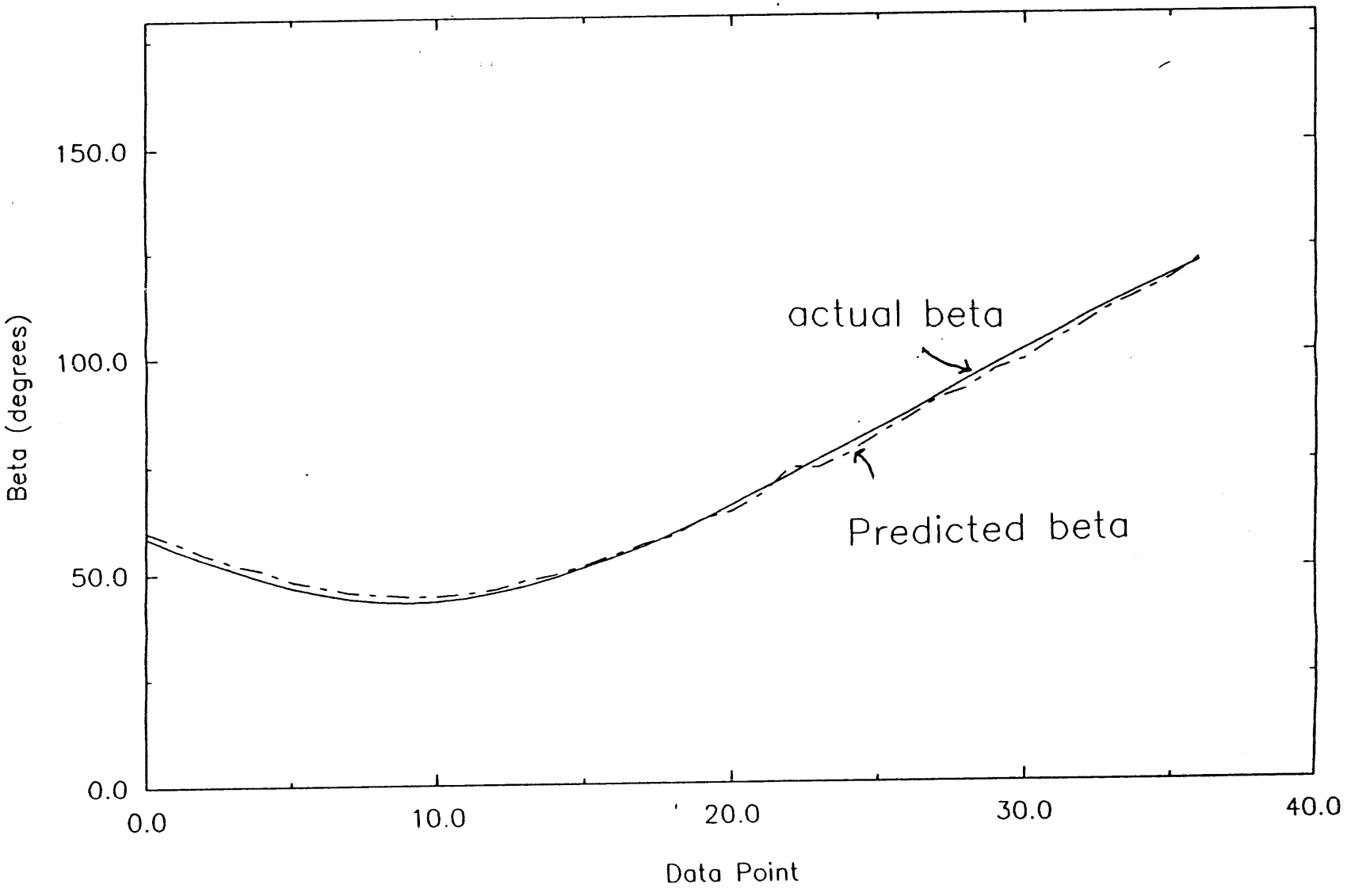
150.0
100.0
50.0
0.0
Beta (degrees)
actual beta
Predicted beta
0.0
10.0
20.0
30.0
40.0
Data Point

Fig. 10e

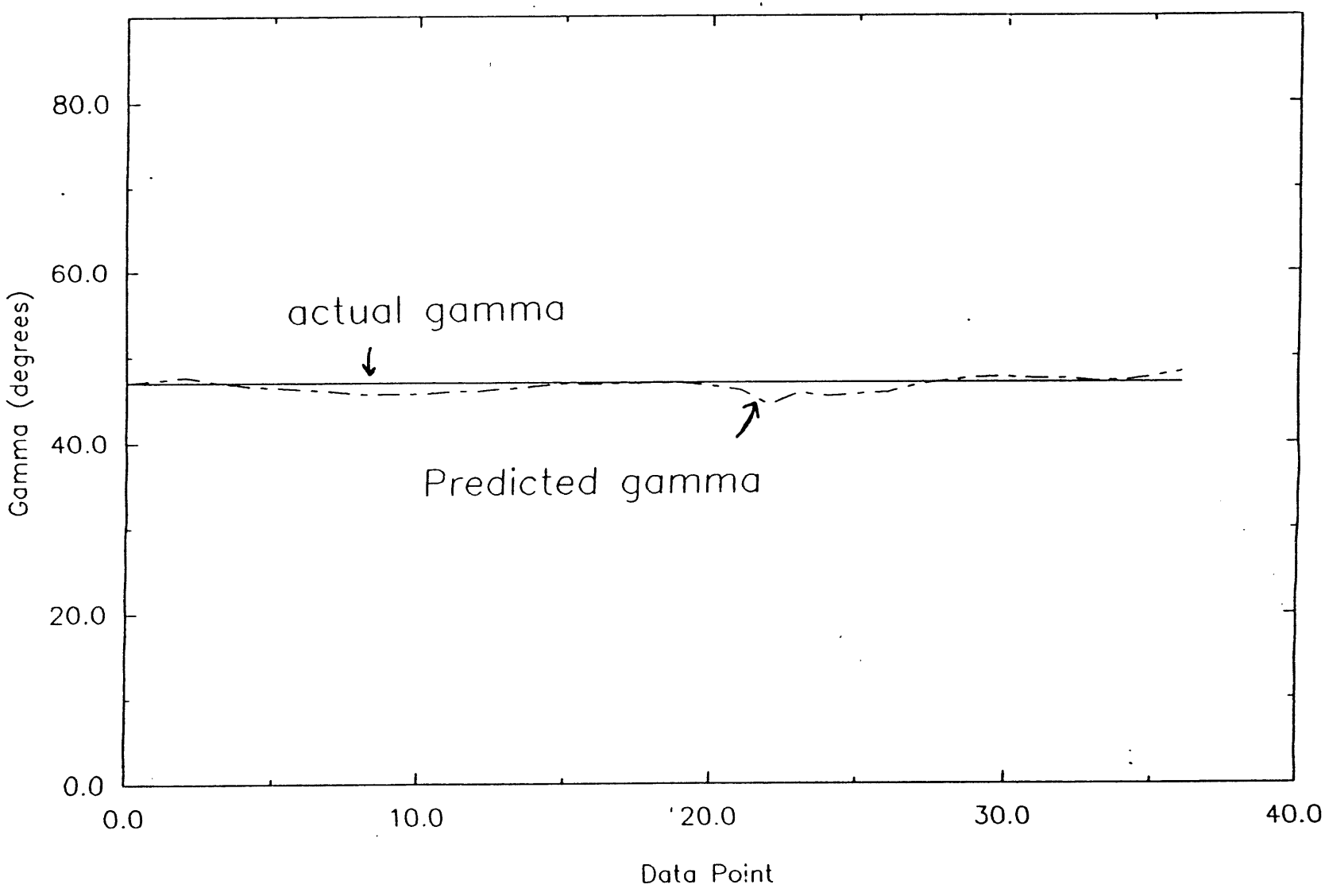
80.0
60.0
40.0
20.0
0.0
Gamma (degrees)
actual gamma
Predicted gamma
0.0
10.0
20.0
30.0
40.0
Data Point

Fig. 10f

Aggregation and Dispersion of Spheres Falling in Viscoelastic Liquids

D.D. Joseph, Y.J. Liu, M. Poletto and J. Feng

Department of Aerospace Engineering and Mechanics, University of Minnesota,
107 Akerman Hall, 110 Union Street, Minneapolis, MN 55455, USA

Abstract

This paper focuses on the settling of one sphere near another or near a wall. We find maximum differences between Newtonian and viscoelastic liquids, with repulsion between nearby bodies in the Newtonian case and attraction in the viscoelastic case. Side-by-side arrangements of sedimenting spheres are unstable in exactly the same way that broadside-on settling of long bodies is unstable at subcritical speeds in a viscoelastic fluid. The line of centers between the spheres rotates from across to along the stream as the spheres are sucked together. The resulting chain of two spheres is a long body which is stable when the line between centers is parallel to the fall, but this configuration breaks up at supercritical speeds in which inertia again dominates. To explain the orientation of particles in the subcritical case, we correlate the aggregative power of a viscoelastic fluid with the zero shear value of the coefficient of ratio of the first normal stress difference to the shear stress and for exceptional cases we introduce the idea of the memory of shear-thinning leading to corridors of reduced viscosity.

Keywords: aggregation of spheres; dispersion of spheres; elastic stress ratio; Newtonian liquids; numerical simulation; settling of spheres; sphere-sphere interaction; wall-sphere interaction; viscoelastic liquids

---

The material reported here will appear in a paper with the same title to be published in J. Non-Newtonian Fluid Mech.

CONTENTS

1. Introduction

Liu and Joseph [1] discussed the sedimentation of cylinders and flat plates in viscoelastic and Newtonian liquids, noting that the flow-induced anisotropy of sedimenting spherical particles is associated with the natural orientation of long bodies, longside parallel to the stream when viscoelasticity dominates and perpendicular to the stream when inertia dominates. They reviewed the literature on the sedimentation of long bodies. Joseph and Liu [2] did further experiments on the orientation of a cylinder settling in viscoelastic and pseudoplastic fluid and attempted to identify the main mechanisms controlling orientation. They stressed the fluid's ability to remember where it was thinned and introduced the notion of evanescent corridors of reduced viscosity. In this paper we highlight the importance of the elastic stress ratio N_1/τ, which turns out to be a subtle measure of fluid elasticity.

This paper focuses on the settling of one sphere near another or near a wall. Again we find maximum differences between Newtonian and viscoelastic liquids, with repulsion between nearby bodies in the Newtonian case and attraction in the viscoelastic case. This observation has applications for manipulative strategies addressing the problem of placements of particles by flowing liquids.

Christopherson and Dowson [3] took notice of a tendency for balls to rotate and fall off-center while settling in Newtonian liquids in a cylinderical container. Tanner [4] noticed that this tendency is enhanced in non-Newtonian liquids, stating that "if one carefully drops the balls axially in the fall tube, there appears to be a critical ball/tube radius after which the ball is seen to fall off-center and rotate." The critical radius ratio may possibly be associated either with a critical fall speed or with other critical values associated with instability. The effects of eccentricity on the precision of falling ball viscometry were discussed by Caswell [5].

Many papers treat problems of sedimentation of spheres in Stokes flow (Leal [6, 7] are convenient references). Goldman, Cox and Brenner [8] treat the problem of interaction between a

sphere and a wall. They also consider the problem of a sphere "rolling" down an inclined wall and find that the sphere cannot be in physical contact with the wall and that it slips, giving rise to anomalous rotation when forced into close approach. Bungay and Brenner [9] showed that the rotation of a tightly fitting ball falling down a vertical tube would change sign as the distance between the ball and the tube wall tends to zero. These Stokes flow predictions involve neither inertia nor elasticity. The phenomenon of anomalous rolling predicted by these authors appears in the experiments of Humphrey and Murato [10] who found that the rotation of a sphere gradually changes from positive (opposite to downhill rolling) to negative (in the sense of downhill rolling) as the tube inclination angle is increased and the sphere contacts the wall. They conclude that inertia induced lift keeps the rolling ball off the wall at the smaller angles of inclination.

Joseph, Nelson, Hu and Liu [11] found anomalous rolling of a sphere in viscoelastic liquids along an inclined plane. The angle between the wall and the direction of gravity is varied from zero to 45°. A sphere falling down these inclined walls rotates as if rolling down the wall in viscous liquids as it does in dry rolling, but rotates as if rolling up the wall against intuition in viscoelastic liquid. Liu, Nelson, Feng and Joseph [12] documented this phenomenon with measured data.

Sigli and Coutanceau [13, 14] studied the effects of the walls of a round tube on a sphere settling under gravity. Like Tanner [4], they noted that there are critical ball/tube radii for off-center positions. A small initial eccentricity is magnified by the effects of the fluid's elasticity. It is likely that the sense of rotation of a sphere falling off-center in a tube filled with viscoelastic liquid is anomalous.

Riddle, Narvaez and Bird [15] presented an experimental investigation in which the distance between two identical spheres falling along their line of centers in a viscoelastic fluid was determined as a function of time. They found that, for all five fluids used in the experiments, the spheres attract if they are initially close and separate if they are not close. There is a critical separation distance. We will show that there is also a critical separation for side-by-side attraction.

This suggests that the critical separation distance for end-to-end settling may not be associated with a negative wake as has been suggested by Bird, Armstrong and Hassager [16].

Lateral migration and chaining of spheres in a 0.5% aqueous polyacrylamide solution and in a solution of high molecular weight polyisobutelene in a low molecular weight polyisobutelene were observed by Michele, Pätzold and Donis [17] in experiments using very tiny spheres (60-70 μm). A droplet of the suspension was placed between two glass plates that were pushed together as close as possible (about 100 μm). Different kinds of aggregation were observed in rectilinear and rotary shear. They also showed chaining and lateral migration of these tiny spheres in an elongational flow by pulling a glass plate out of a droplet of the suspension. The aggregation of particles appears to be a generic feature of flows of viscoelastic fluids that occurs in many different types of fluids, for vastly different scales and types of motion.

Brunn [18] did a theoretical analysis of the interaction between spheres in a second order fluid with inertia neglected and although he found an attractive force drawing the spheres together he did not find a critical separation distance for attraction. Brunn's analysis cannot treat close approach because it has been assumed that the distance between sphere centers is large. His results, as far as they go, are consistent with our observations and suggest that the mechanism involved is associated with the normal stresses, which are in his analysis, and not with shear-thinning, which is neglected in his analysis. In fact, shear-thinning plus memory may play an important role, at least in the chaining of spheres, as we shall see.

Giesekus [19] tried to explain end-to-end and side-to-side attractions in terms of normal stresses using 2nd order theory with inertia neglected, like Brunn. These two authors could not explain the critical separation distance observed by Riddle et al. [15] and they did not investigate the possibility that this distance is determined by a competition of non-Newtonian and inertial effects.

As far as we know, ours is the first study of side-by-side sphere-sphere attraction. We find that the spheres attract when the initial separation distance is smaller than a critical value and they do not attract when the initial distance is larger than this critical distance. The side-by-side spheres

never attract in a Newtonian fluid; if they are initially separated by a small distance, they repel each other; just the opposite of their behavior in a viscoelastic fluid.

Side-by-side arrangements of sedimenting spheres are unstable in exactly the same way that broadside-on settling of long bodies is unstable at subcritical speeds in a viscoelastic fluid (Liu and Joseph [1], Joseph and Liu [2]). The line of centers between the spheres rotates from across to along the stream as the spheres are sucked together. The resulting chain of two spheres is a long body that is stable when the line between centers is parallel to the fall, but this configuration breaks up at supercritical speeds in which inertia again dominates. These authors last mentioned have presented evidence that the critical fall velocity is not too much greater than the measured value of the shear wave speed in nearly all cases.

Van der Brule and Gheissary [20] saw a videotape (shown at the International Congress of Rheology) of the experiments of Joseph and Liu on sedimenting spheres, which form long chains in all viscoelastic liquids at the slow fall speeds in which long bodies rotate their long side parallel to the fall. This stimulated them to undertake experiments of their own on sedimenting spheres. They attempted to isolate the effects of shear-thinning and normal stresses by using test fluids that have one and not the other of these properties. They dropped spheres in aqueous polyacrylamide, an ordinary viscoelastic fluid with large normal stresses and strong shear-thinning, and found results identical to ours. Then they did experiments in "shellflo", an aqueous Xanthan solution that has no measurable normal stresses in shear but is strongly shear-thinning. They found that the spheres chained in this fluid in much the same way that they did in the aqueous polyacrylamide. This suggests that shear-thinning is the important parameter. They then did experiments in a Boger fluid that they prepared with small amounts of polyacrylamide (100 ppm) in glycerin and water. This is a very viscous fluid with large but saturated normal stresses, which lead to constant values of the recoverable shear at high rates of shear. They did not observe chaining in this Boger fluid, and thus concluded that shear-thinning, not elasticity, is the mechanism controlling the chaining of spheres.

Joseph and Liu [2] did experiments on sedimenting cylinders in liquids like the ones used by Van der Brule and Gheissary [20]. They found that in 0.3% aqueous Xanthan (Kelco) and 0.4% Carbopol in 50/50 glycerin-water solutions (see Fig.s 11 and 12 in that paper) which are shear-thinning fluids without normal stresses, the cylinder puts its long side parallel to gravity when falling at speeds less than critical. The critical speed in the Xanthan solution was the shear wave speed measured on our meter, but the critical speed for Carbopol was 1/10 the value measured on the meter, the only exception so far. In other respects the Carbopol solution, we shall see, is nearer to Newtonian than to viscoelastic. Spherical particles dropped in the 0.4% Carbopol did not exhibit side-by-side attraction, they repelled each other when they were initially together as in Newtonian fluids. They were repelled by a vertical wall and exhibited only the feeblest form of anomalous rolling (Liu et al. [12]), and apparently no chaining.

These results are surprising because they appear to associate strange effects like tilting and chaining with shear-thinning rather than with normal stresses. In fact, theoretical results for second order fluids, without shear-thinning, give rise to all the observed effects, so we are confronted with a real mystery.

In the case of fluids without normal stress, which do not climb a rod, we may entertain the idea that 2nd order correlations to viscous behavior are negligible, so that we might learn something important at the next non-trivial third order.

Thinking more globally, Joseph and Liu [2] introduced the idea that a combination of memory with shear-thinning is required and may be enough to induce nose-down turning and the related chaining of spheres. They concluded that shear-thinning alone affects particle's orientation much less, because, like the Carbopol solution, although it shear-thins, the thinning is not persistent and decays very rapidly. The Xanthan solution remembers the place where the viscosity was reduced, so that the back part of a nose-down cylinder, or the spheres behind the lead sphere in a chain, experience a smaller viscosity than the leading end of the cylinder or leading sphere. We

might think that corridors of reduced viscosity are marked on the fluid by shear-thinning as a particle drops in the fluid and persist for a time before they relax.

These theories could be tested with standard test liquids provided that they shear-thin and have long memories, whether or not they exhibit normal stresses or climb rods.

The existence of relaxing corridors of reduced viscosity, marked on the fluid by the shear-thinning induced by a falling ball, is consistent with the observations of Cho and Hartnett [21] and Cho, Hartnett and Lee [22]. They studied falling ball rheometry, measuring the drag on balls that were dropped in the test liquid in specified and definite intervals of time. They found the same memory effects that we did, effects that were particularly evident in a 10^4 wppm solution of aqueous polyacrylamide (Separan, AP-273), a highly viscoelastic and highly shear-thinning liquid. The measured terminal velocity depended strongly on the time interval between the dropping of successive balls in the cylinder. Balls launched after only a short wait period would fall up to nearly twice as fast as the speed of the initial ball, and it took intervals of thirty minutes or more for the memory of the corridor of reduced viscosity to relax.

We can imagine the trailing spheres in a chain or the trailing end of a long particle setting itself in a corridor of reduced viscosity. For this behavior to occur, shear-thinning and the memory of shear-thinning is required. We should recall at this point that similar effects in weaker form occur in our constant viscosity fluid (STP) and in stronger form in S1 where the degree of shear-thinning is small. Thus shear-thinning plus memory cannot explain everything. The experiments with semi-dilute Xanthan are interesting because shear-thinning and memory are present, but many other mechanisms that could come into play are absent.

2. Material and dimensionless parameters

The material parameters that were measured in the liquids used in the experiments are the density ρ , viscosity $\eta = k\dot{\gamma}^{n-1}$, where $\dot{\gamma}$ is the shear rate in reciprocal seconds, the climbing constant $\hat{\beta}$ measured on a rotating rod viscometer (Beavers and Joseph [23]) and the wave speed c. To compute $\hat{\beta}$ from measured values of the climb we need the interfacial tension that we measured with a spinning drop tensiometer (Joseph, Arney, Gillberg et al. [24]). The value of $\hat{\beta}$ is insensitive to a small change of surface tension (chap.16 in Joseph [25]). Table 1 is the summary of material parameters.

Fluid	ρ (g/cm^3)	η_o (Pa.s)	k	n	$\hat{\beta}$ (g/cm)	ψ_{1o} (g/cm)	c (cm/s)	λ_o (s)	$\frac{\psi_{1o}}{\eta_o} = \frac{10\hat{\beta}}{3\eta_o}$ (s)
1.5% aqueous polyox	1	17.3	5.71	0.44	132	440	20.3	0.420	2.54
1.25% aqueous polyox	1	12.7	4.21	0.45	117	389	17.2	0.429	3.07
1.0% aqueous polyox	1	7.65	3.97	0.42	108	360	15.0	0.34	4.70
0.4% Carbopol in 50/50 glycerin/water	1.13	0.76	0.31	0.67	0	0	15.9	0.027	0
0.3% aqueous Xanthan	1	5.21	1.1	0.28	0	0	12.2	0.35	0
S1	0.875	8.06	7.14	0.62	11.8	39.3	72.4	0.018	0.49
STP	0.86	18.0	17.8	0.85	0.97	3.23	286	0.0026	0.02

Table 1. Summary of material parameters. Liu and Joseph [1] did some experiments with the 1.0% aqueous polyox listed in this Table, but not used in the experiments reported here. The stress ratio ψ_{1o}/η_o is a measure for which the more dilute polyox solutions are relatively more elastic.

The climbing constant $\hat{\beta}$ is related to the limiting (zero shear) value of the first and second normal stress differences

$$(\psi_{1o}, \psi_{2o}) = \lim_{\dot{\gamma}\to 0} (N_1(\dot{\gamma}), N_2(\dot{\gamma}))/\dot{\gamma}^2 \tag{2.1}$$

by

$$\hat{\beta} = \frac{1}{2}\psi_{1o} + \psi_{2o}. \tag{2.2}$$

The climbing constant

$$\hat{\beta} = 3\alpha_1 + 2\alpha_2 \tag{2.3}$$

may also be expressed in terms of quadratic constants

$$(\alpha_1, \alpha_2) = \left(-\frac{1}{2}\psi_{1o}, \psi_{1o} + \psi_{2o}\right) \tag{2.4}$$

of the second order fluid. $\alpha_2/|\alpha_1|$ is the ratio of quadratic constants and

$$[\alpha_1, \alpha_2] = [-m, 2m-2]\hat{\beta}/(m-4) \tag{2.5}$$

where $m = 2\alpha_1/(2\alpha_1 + \alpha_2) = -\psi_{1o}/\psi_{2o}$ is the ratio of the first to second normal stress difference. It can be argued (§17.11 in Joseph [25]) that $m = 10$ is a reasonable value for our polymer solutions. Then

$$\frac{\alpha_2}{|\alpha_1|} = \left|\frac{2(1-m)}{m}\right| = 1.8 \tag{2.6}$$

is a constant and α_1 and α_2 are determined by the measured values of the climbing constant $\hat{\beta}$. We are going to assume (2.6) in the calculations that follow. The value of ψ_{1o} that we get from measuring $\hat{\beta}$ is not sensitive to the value of the ratio ψ_{2o}/ψ_{1o} as long as ψ_{2o} is relatively small and negative (see §17.11 in Joseph [25]).

The measured value of the climbing constant, together with the assumption that the second normal stress difference is -1/10 as large as the first, allows us to evaluate Roscoe's [26] formula

$$T_{11} - T_{22} = 3\dot{s}\eta_o + 3(\alpha_1 + \alpha_2)\dot{s}^2 \tag{2.7}$$

for the extensional stress difference, where $\dot{s}$ is the rate of stretching in the direction x_1 and η_o is the zero shear viscosity. Using (2.6) and $\alpha_1 = -\psi_{1o}/2$ we get

$$T_{11} - T_{22} = 3\dot{s}\eta_o + 1.2\psi_{1o}\dot{s}^2. \tag{2.8}$$

The zero shear value of the first normal stress difference $\psi_{1o} = \frac{2m}{m-4}\hat{\beta} = \frac{10}{3}\hat{\beta}$ and the zero shear quadratic correction $4\dot{s}\hat{\beta}$ of Troutons viscosity, $3\eta_o$, increase with $\hat{\beta}$. An argument given by Liu and Joseph [1] shows how extensional stresses broadly speaking can control some of the properties of the aggregation of particles in viscoelastic liquids documented here.

Material parameters of the fluids used in our experiments are listed in Table 1. The percent of the polymers and the percent of the glycerin in water are by weight. Glycerin is a Newtonian liquid. Carbopol is basically a non elastic but shear-thinning fluid. STP is a weakly viscoelastic liquid with small normal stresses and basically constant viscosity (see Fig. 5 in Beavers and Joseph [23]). For shear rates below 100 sec $^{-1}$, STP could be called a Boger fluid. The polyacrylamide and polyox solutions are standard viscoelastic liquids.

An important measure of elasticity is the elastic stress ratio

$$\frac{N_1(\dot{\gamma})}{\tau(\dot{\gamma})} \stackrel{def}{=} \frac{\psi_1(\dot{\gamma})\dot{\gamma}}{\eta(\dot{\gamma})} \tag{2.9}$$

where ψ_1/η is the elastic stress ratio coefficient whose limiting $\dot{\gamma} \to 0$ value is ψ_{1o}/η_o. (The ratio N_1/τ is twice the recoverable shear; see Barnes, Hutton and Walters [27]). This ratio vanishes for Newtonian fluids and is very small for dilute solutions with Newtonian solvents, like Boger fluids. For small values of $\dot{\gamma}$, (2.9)

$$\lim_{\dot{\gamma}\to 0} \frac{N_1(\dot{\gamma})}{\tau(\dot{\gamma})} \to \frac{\psi_{1o}}{\eta_0}\dot{\gamma} \tag{2.10}$$

where

$$\frac{\psi_{10}}{\eta_0} \sim \frac{10\hat{\beta}}{3\eta_0} \tag{2.11}$$

is a material parameter. Values of $\frac{10\hat{\beta}}{3\eta_0}$ are listed in Table 1. The stress ratio coefficient could have a finite and even large value in mobile liquids with small values of η under circumstances in which N_1 and even $\hat{\beta}$ are too small to measure. In this sense, the stress ratio of mobile liquids is

indeterminate. We thought at first that this indeterminism might apply to the 0.3% Xanthan solution but the viscosity of Xanthan at the shear rates in our experiments is too large to support any conclusion other than $\hat{\beta}/\eta = 0$.

The stress ratio is not a monotonic function of concentration. Aggregation of particles occurs more readily in fluids with high stress ratios independent of concentration.

The dimensionless parameters used in this study are the Reynolds number

$$\mathbb{R}_0 = \frac{UD}{\eta_0} \tag{2.12}$$

where U is the terminal velocity of a sphere of radius D, the Weissemberg number

$$W_o = \frac{\lambda_0 U}{D} \tag{2.13}$$

where $\lambda_0 = \eta_0/\rho c^2$ is computed from measured values of η and the wave speed c, the Mach number $M^2 = U^2/c^2 = \mathbb{R}W$ and the elasticity $E = \eta\lambda/\rho D^2$. The flows in the experiments reported here are strongly subcritical with M<<1.

Two different solutions of aqueous polyox (WSR 301) at concentrations by weight of 1.5 and 1.25% were used as test liquids. Plots of viscosity vs shear rate for both solutions are given in Fig. 2.1. Values of dynamic moduli of these two solutions as a function of shear frequency are shown in Fig. 2.2.

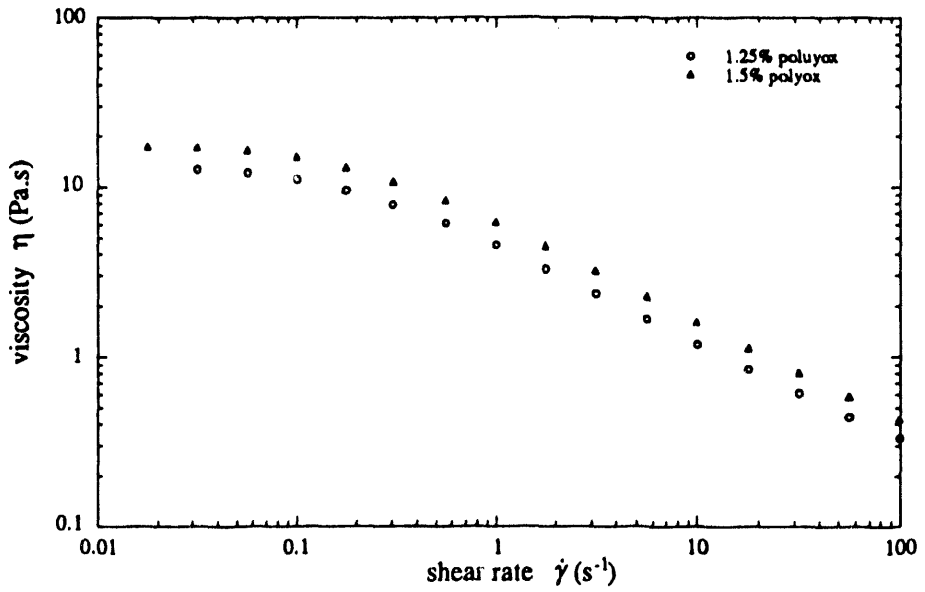

Fig. 2.1. The viscosities of Polyox solutions as a function of the shear rate were measured, at room temperature, on a RSF2 Rheometrics fluid rheometer with a couette apparatus.

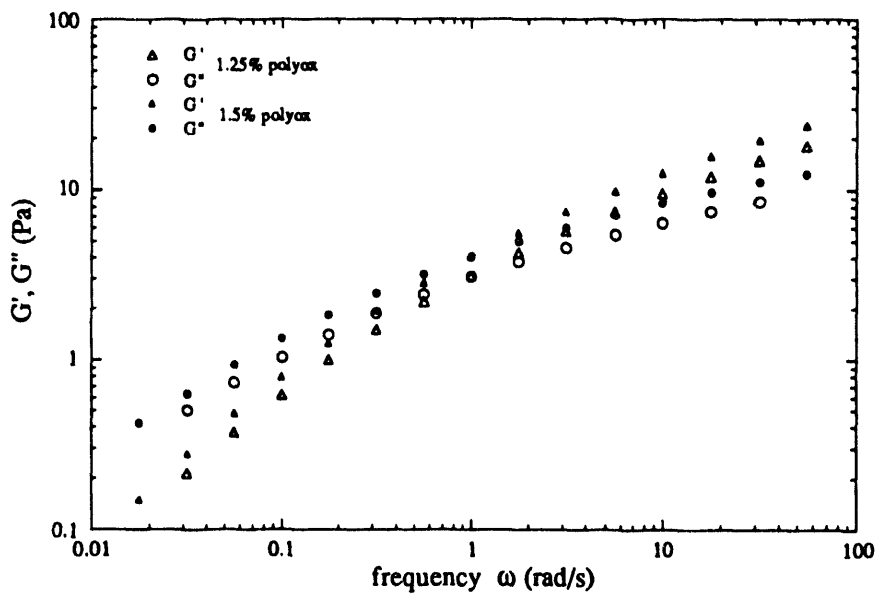

Fig. 2.2. The dynamic moduli of Polyox solutions as a function of the shear frequency were measured, at room temperature, on the same rheometer used for viscosity measurements.

STP is a solution of polyisobutylene (PIB) in petroleum oil that was used extensively in early studies of rod climbing (see Joseph [25]). S1 is a solution of 5% W/W of PIB in decalin plus 50% polybutene oil. The viscosity and the values for the dynamic moduli of these two polymer solutions

are shown in Fig.s 2.3 and 2.4 respectively. The viscosity of STP is nearly constant for shear rates less than 100. The viscosity of S1 decreases with increasing $\dot{\gamma}$, but the decrease is very slow for shear rates less than 10. The viscosity of S1 is an order of magnitude smaller than STP; it is a much more mobile liquid. Both solutions climb a rotating rod, but the STP is not a good climber; the climbing constant at a temperature of 26.7°C is 0.97 g/cm. We can say that STP is a Boger fluid with very weak normal stresses. The climbing constant of S1 at 25°C is 11.8 g/cm and S1 can be said to resemble STP with much larger normal stresses, especially at low rates of shear. The loss modulus for STP is an order of magnitude higher than S1. The storage modulus of S1 is larger than STP for shear rates less than about 10 s^{-1}, and the shear rate at which the loss modulus falls below the storage modulus is much lower in S1 than in STP. It is clear that S1 is a more mobile and much more elastic liquid than STP.

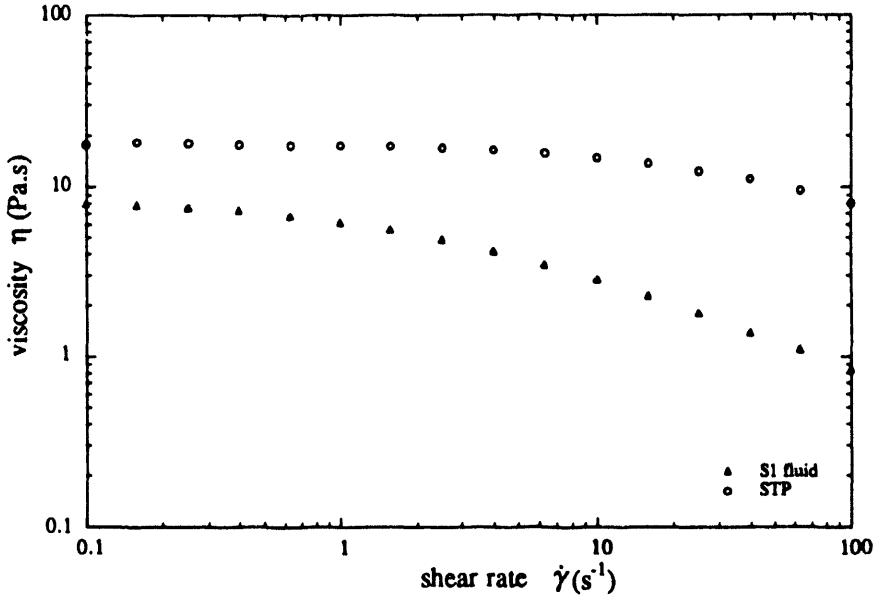

Fig. 2.3. The viscosities of STP and S1 fluid as a function of the shear rate at temperature of 24.5°C, on a RSF2 Rheometrics fluid rheometer with a cone - plate apparatus. The viscosity of S1 is an order of magnitude smaller than STP; it is a much more mobile liquid. S1 is weakly shear-thinning.

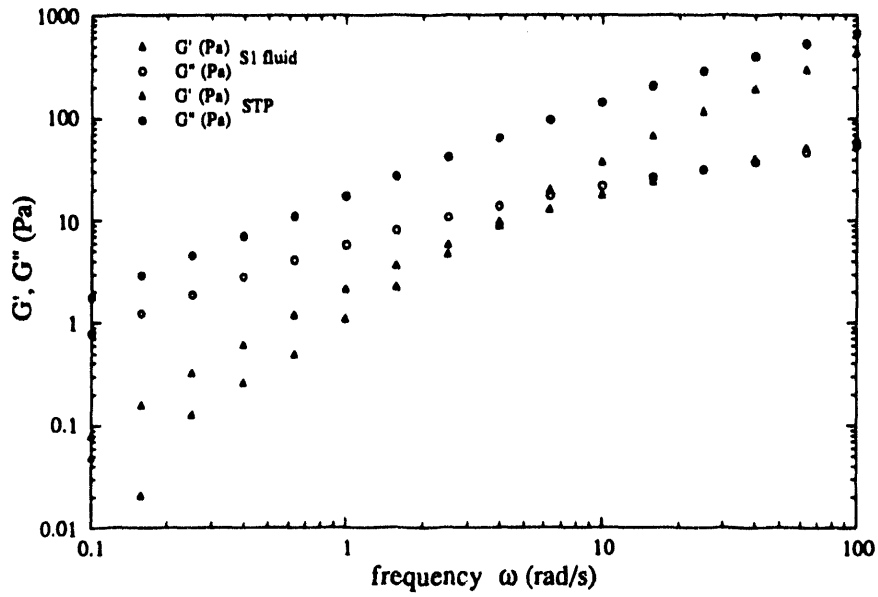

Fig. 2.4. Dynamic moduli of STP and S1. The loss modulus for STP is an order of magnitude higher than S1. The storage modulus of S1 is larger than STP for shear rates less than about 10. The shear rate at which the loss modulus falls below the storage modulus for S1 is much lower than that for STP.

We attempted to isolate the role of shear-thinning by suppressing both normal stresses and elasticity by using a solution of 0.4% Carbopol 690 (Goodrich) in a 50/50 glycerin/water mixture in our attraction experiments. The viscosity versus shear rate for this Carbopol solution is plotted in Fig. 2.5, and the dynamic moduli are plotted in Fig. 2.6. Carbopol is thought to be a pseudoplastic fluid without elasticity. Since our Carbopol solution has a non-zero storage modulus, it cannot be said to be without elasticity. The presence of small elasticity in Carbopol solutions has been noted before. There is no evidence that Carbopol 690 in 50/50 glycerin/water has a measurable value of the first normal stress difference, and it does not climb a rotating rod.

To determine the effects of shear-thinning in a fluid with a strong memory but no normal stresses, we used a solution of 0.3% Xanthan (Kelco) in water. The graph of viscosity versus shear rate is shown in Fig. 2.5, and the variation of the storage and loss moduli with frequency is shown in Fig. 2.6. This Xanthan solution is very shear-thinning and it has no measurable normal stresses. We could not register a first normal stress difference on the Rheometrics fluid rheometer and the 0.3%

Xanthan solution would not climb a rotating rod. On the other hand, this fluid has a high storage modulus and can be said to be linearly elastic.

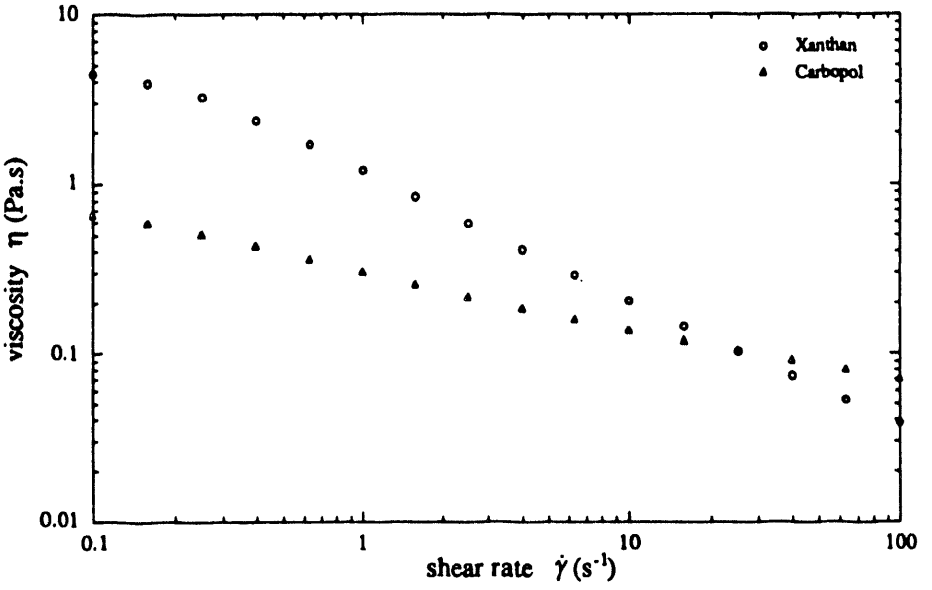

Fig. 2.5. The viscosities of 0.3% aqueous Xanthan and 0.4% Carbopol in 50/50 glycerin/water solution as a function of the shear rate at temperature of 24.5°C. The Xanthan solution has a higher but more shear-thinning viscosity than the Carbopol solution.

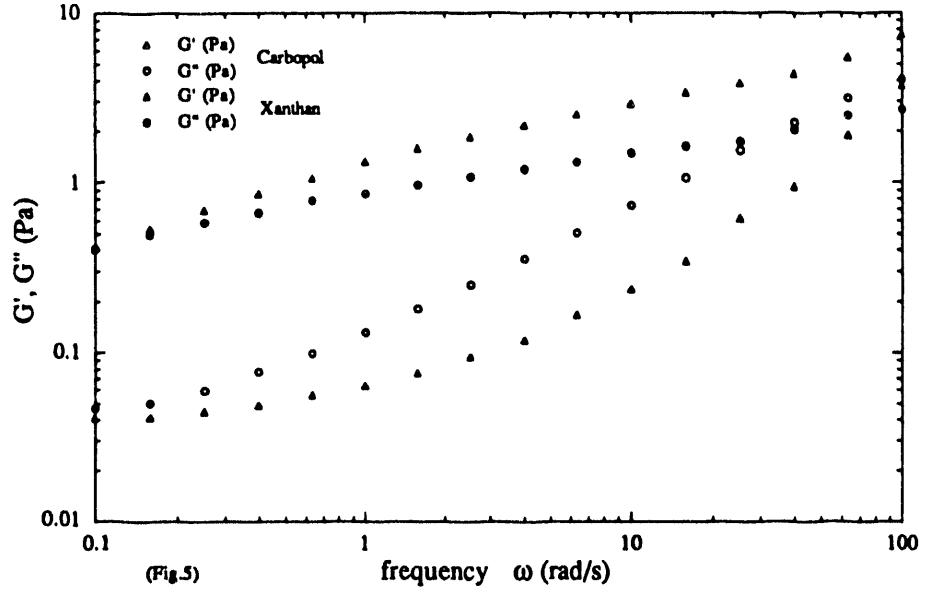

Fig. 2.6. Dynamic moduli of Xanthan and Carbopol solutions. For modest shear rates ranging from 0.1 to 100, both the storage modulus and loss modulus of the Xanthan solution are higher than those of the Carbopol solution. The storage modulus G' of Xanthan is greater than the loss modulus G"; in the Carbopol G" is greater than G'.

3. Description of the experiments

Spheres were dropped in liquid filled channels made of transparent plexi-glass to allow video recording of experiments. The first channel, which was used to test 1/4-in spheres, has a gap of 0.44-in, is 6.5-in wide and 25-in high. The second one, which was used to test spheres with different diameters from 1/8-in to 5/8-in, has a gap of 1-in, is 7-in wide and 30-in high. The motion of sedimenting spheres in these beds is basically two dimensional with spheres centering themselves between two close walls. This centering was described by Liu and Joseph [1]. We did some of our experiments in channels with distant side walls. The phenomena of attraction of nearby bodies in viscoelastic liquids, opposite effects in Newtonian liquids, and anomalous rolling are the same in channels with close and distant side walls. These effects do not depend strongly on the exact distance between the center sphere and the side wall. Velocities and position of spheres were measured with a video system and image processing software.

To facilitate the side-by-side and contemporary dropping of two spheres we used a small device which we call the "clothespin dropper", shown and described in Fig. 3.1. The same device was also used to release a single sphere at a distance from a straight prismatic rod. The rod was almost as deep as the channel and simulated the presence of a side wall. It was supported by an external support that could be tilted several degrees from the vertical upright position. A sketch of this device is given in Fig. 3.2. We also used another single sphere dropper to drop spheres with different diameters.

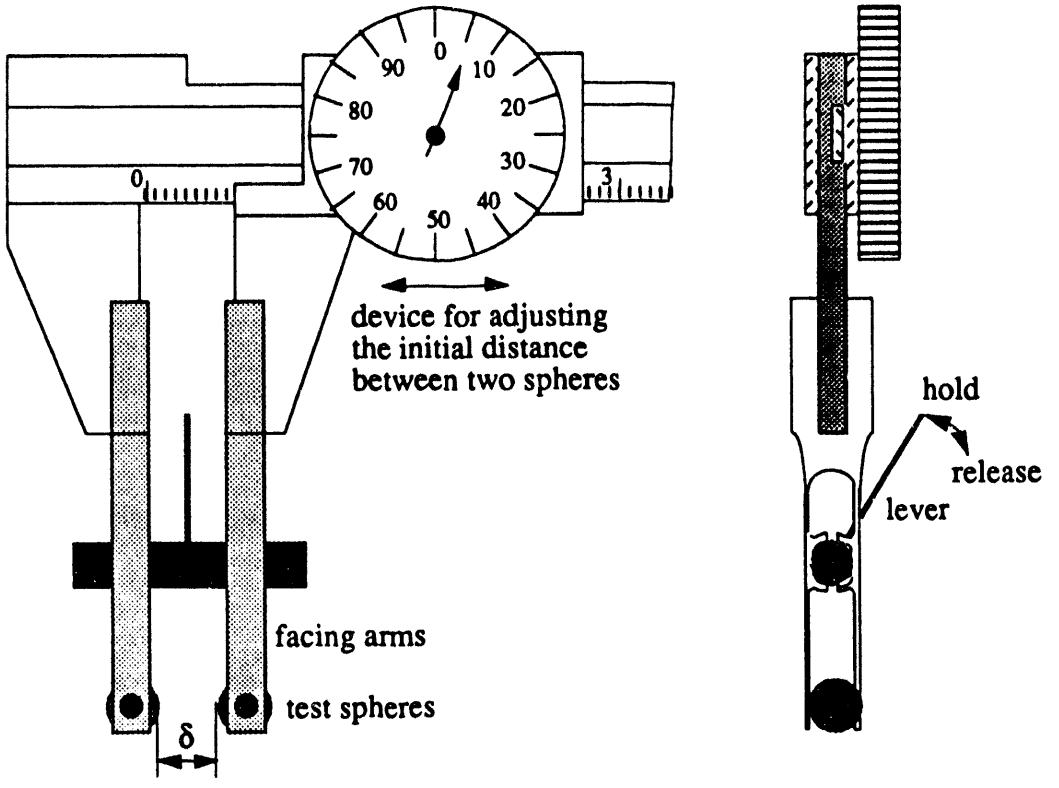

(a) front view (b) side view

Fig. 3.1 The "clothespin dropper". The two spheres are held at the ends of the facing arms. The circular holes on these keep the spheres at the same height. Pulling the lever on the facing arms shown in (b) opens the clothespin and releases the two spheres at the same instant.

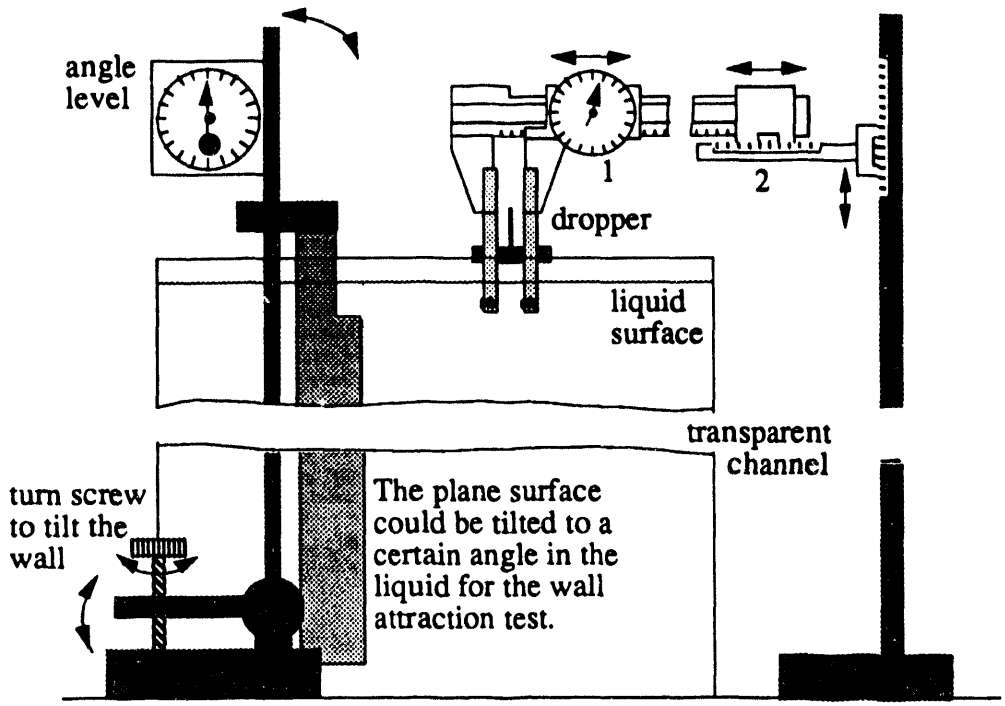

Fig. 3.2. The front view of the experimental apparatus (not including the video system and image processing system). For the side-by-side test, the initial distance between the two spheres can be adjusted and measured by moving ruler 1; for the wall-sphere test, the initial distance of the sphere from the wall is controlled by ruler 2. The solid plane surface can be inclined by turning the screw and the tilt angle can be measured by the angle level.

In order to test the effects of sphere diameter, we selected spheres having different diameters and weight, keeping the Reynolds number

$$\mathbf{R}(\dot{\gamma}) = \frac{2aU\rho_l}{\eta} = \text{constant}, \tag{3.1}$$

where a and U are the radius and the terminal velocity of sphere, and ρ_l and η are the density and viscosity of liquid, by the following approximate method. Assuming Stokes flow, we have

$$(\rho_s - \rho_l)g\frac{4}{3}\pi a^3 = 6\pi\eta aU \tag{3.2}$$

where ρ_s is the density of sphere. The terminal velocity can be determined from equation (3.2) as

$$U = \frac{2}{9}\frac{(\rho_s - \rho_l)ga^2}{\eta}. \tag{3.3}$$

The shear rate will be

$$\dot{\gamma} = \frac{U}{2a} = \frac{(\rho_s - \rho_l)ga}{9\eta}. \tag{3.4}$$

Substituting this into the power law equation

$$\eta = \kappa\dot{\gamma}^{n-1}, \tag{3.5}$$

we have

$$\eta = \kappa^{\frac{1}{n}}\left(\frac{(\rho_s - \rho_l)ga}{9}\right)^{\frac{n-1}{n}}. \tag{3.6}$$

From equations (3.1) and (3.6), the following condition for determining the diameter and material of spheres can be obtained:

$$(\rho_s - \rho_l)^{2-n} a^{2+n} = \text{constant}. \tag{3.7}$$

We chose 1.5% aqueous polyox as the test liquid; then spheres were picked according to equation (3.7) and availability in the market as listed in Table 2. The 1/8-in tungsten carbide, 1/4-in steel, 7/16-in ceramic and 5/8-in aluminum spheres were used to test size effects, and 1/4-in teflon, aluminum, steel and tungsten carbide spheres were used to test weight (or velocity) effects on attraction and dispersion.

Material	Diameter (in.)	Weight (g)	Density (g/cm^3)
tungsten carbide	1/8	0.26	15.8
steel	1/4	1.02	7.61
ceramic	7/16	2.74	3.81
aluminum	5/8	5.78	2.76
teflon	1/4	0.29	2.18
aluminum	1/4	0.37	2.76
tungsten carbide	1/4	2.12	15.8

Table 2. Spheres tested.

4. Interactions between spheres falling side-by-side

We dropped two spheres side-by-side in a channel filled with different liquids. In viscoelastic liquids, when the initial separation distance is small, the two spheres will attract; the line between centers will turn as they attract, until the spheres touch and chain with the line of centers vertical. Close side-by-side settling at slow speeds is unstable in viscoelastic fluids and the dynamics creates stable vertical chains. The tilting of the line of centers between falling spheres starts at the instant of release and the two spheres appear as a dumbbell pair sliding along the tilting line of centers as in Fig. 4.1(a).

If the initial distance is large enough, the two spheres appear not to interact and to fall straight down as in Fig. 4.1(c). Sphere-sphere interactions in this regime are not strong. We shall call this regime "non-interacting" though we recognize that some small interactions that could produce a large effect over long time periods are probably at work.

In Newtonian fluids, two spheres launched side-by-side, which are initially separated by a small gap or no gap, will separate as in Fig. 4.1(b). If the initial gap is large enough the two spheres enter into the non-interacting regime described in the preceding paragraph and in Fig. 4.1(c). Side-by-side sedimentation is relatively stable or only weakly unstable and spheres will never chain in Newtonian liquids.

Two heavy spheres falling faster than the wave speed for the fluid in a viscoelastic fluid will disperse as in a Newtonian fluid. This phenomenon is the same one that causes long bodies that fall straight down at slow speeds to turn 90° into broadside-across-the-stream fall at supercritical speeds when inertia dominates viscoelasticity (Liu and Joseph [1], Joseph and Liu [2]).

Returning now to the fall of spheres launched side-by-side in the strongly subcritical case, we look at a range of initial separation distances that are larger than those for which chaining occurs and smaller than those for which the falling spheres apparently do not interact. The dynamics of aggregation and dispersion here is more complicated. Two spheres will attract initially and the line

of centers between them turns toward the vertical. The spheres do not touch but instead, enter into a non-interacting regime, or else actually separate in a manner reminiscent of the settling behavior of distant spheres, with the line of centers vertical, that was studied by Riddle et al. [15]. The triangles in Fig. 4.3 (see section 4.1) exhibit the behavior just described. The two spheres attract initially, but they do not come into touching contact and eventually separate.

Now we are prepared to define two distinguished distances. The first distance δ_C is the largest side-by-side distance δ for which attraction can be observed, as shown in Fig. 4.1. This critical distance may not be a precisely defined value; it may depend on the level of resolution of the measurement of the mutual attraction that we can achieve in our experiment. If $\delta \leq \delta_C$ the spheres will attract initially. For small $\delta < \delta_C$ the line of centers between spheres will turn from the vertical and the spheres will attract, touch and then fall in a chain with line of centers vertical. For large values of $\delta < \delta_C$ the spheres attract initially and the line of centers between spheres will turn from the vertical but the spheres eventually separate, or stop interacting and never touch or chain. We did not try to measure δ_C. The set of small $\delta \leq \delta_T$ for which falling side-by-side spheres eventually touch is defined by a second distance $\delta_T < \delta_C$, called the critical touching distance. δ_T is determined by observations associated with measurements. We increased the initial separation distance by small steps and repeated experiments a few times under each condition. The vertical distance between release and the point of touching is called the vertical touching distance $\ell_T(\delta)$ (Fig. 4.1(a)).

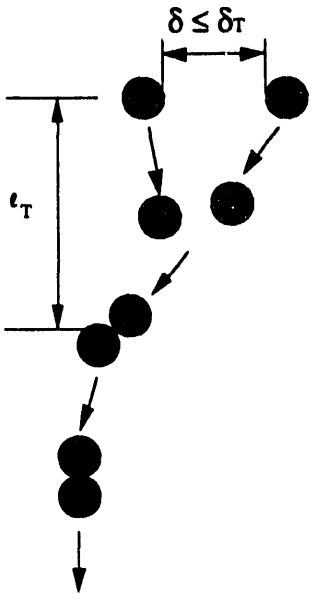

(a) Settling spheres in a viscoelastic liquid when $\delta(\leq \delta_T)$ is small

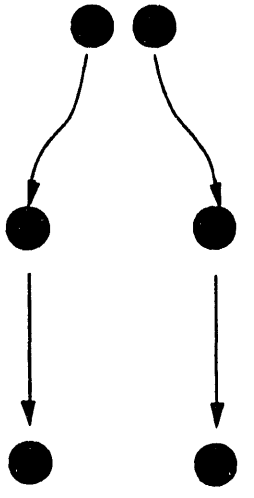

(b) Settling spheres in a Newtonian liquid when δ is small

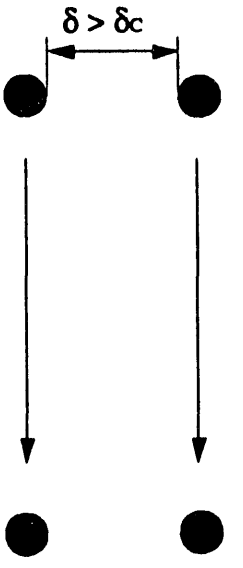

(c) Settling spheres in any liquid when δ is large

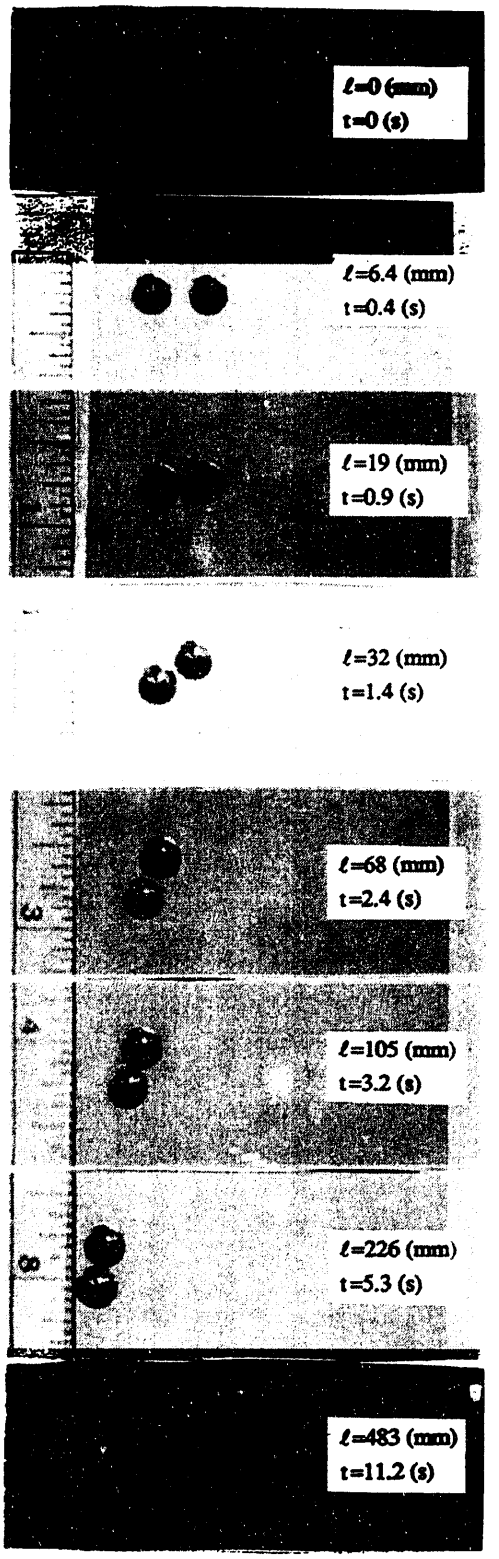

(d) 1/4-in steel spheres falling in 1.5% aqueous polyox, initial distance δ=3.8 mm.
ℓ is the vertical distance from the point of release to the mid-point on the line of centers

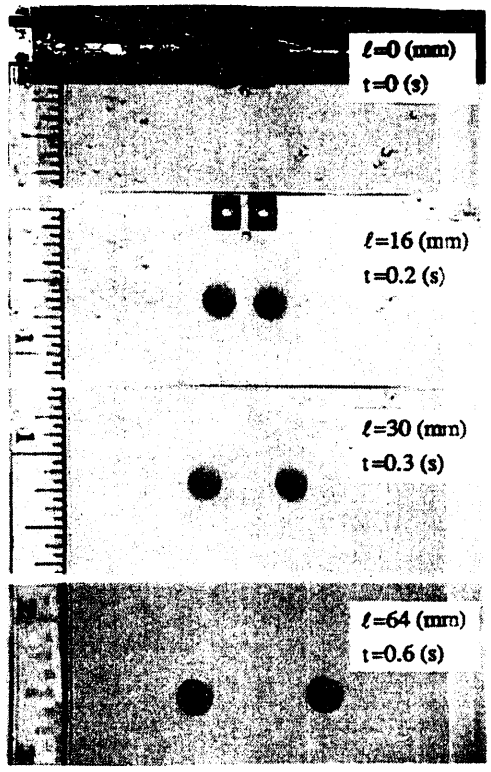

(e) 1/4-in teflon spheres falling in 50/50 glycerin/water solution

Fig. 4.1. Two spheres released side-by-side at the same time in a viscoelastic fluid with $\delta < \delta_T$ will attract each other while the line of centers between the spheres rotates toward the vertical (as in (d)). The final result is a vertical chain of two spheres (a). If $\delta > \delta_C$, then the spheres appear not to attract (c). If $\delta_T < \delta < \delta_C$, the spheres attract initially and the line of centers between spheres will turn from the vertical but the spheres eventually separate, or stop interacting and never touch or chain. In a Newtonian liquid, two spheres dropped side-by-side with a small gap or no gap will disperse rather than aggregate (b). If the initial distance between two spheres is large enough, then they apparently will fall without interaction. Some photographs from experiments are shown in (d) and (e).

Table 3 lists measured values of the fall velocity U and the shear rate $\dot{\gamma} = U/D$. The Reynolds number $\mathbb{R}_0$ and Weissemberg number W_o are zero shear values (2.12) and (2.13).

Table 4 lists the vertical distance $\ell_T(\delta)$ traveled by spheres before touching (Fig. 4.1) as a function of the initial distance δ between the spheres

The lateral migration of spheres depends on the fall velocity, which is determined by the weight of the sphere, as well as on the properties of the fluid in the settling bed. Effects of the weight of the particles can be assessed to a degree by normalizing all the lengths with the lateral touching distance δ_T which also depends on the weight. Fig. 4.2 shows that heavier particles achieve larger fall distance ratios ℓ_T/δ_T for a given initial distance fraction δ/δ_T. The effect of the weight of particles is weak. 1/4-in tungsten, steel and teflon spheres have very different weight (Table 2) and fall speeds in S1 (Table 3), but the ratio of the lateral drift distance to the vertical touching distance is not very great. The weak effects of weight are more easily seen in experiments, discussed in section 6 and section 7, in which spheres are attracted to vertical wall. We do not mean to imply that weight effects are generally not important, but only to note the tendency of the lateral drift velocity to increase in proportion to the fall velocity.

It is of interest to examine data for steel particles. The data for steel in Fig. 4.2 orders weakly with the elastic stress ratio coefficient $10\hat{\beta}/3\eta_o$ in Table 1, with strength of interaction for steel in different fluids in the order: STP, S1, 1.5% Polyox and 1.25% Polyox. The data for teflon is too sparse for us to draw a definite conclusion. Xanthan which is strongly shear-thinning and has a zero elastic stress coefficient, does not seem to be greatly different than S1, which does not shear-thin at the small shear rate of 0.17 of our experiments (see Table 3).

Liquid-solid	U (cm/s)	$\dot{\gamma}$ (s^{-1})	R_o	W_o
1.25% Polyox-1/4-in steel	6.34	9.98	0.032	4.29
1.5% Polyox-1/4-in steel	3.08	4.85	0.011	2.04
STP-1/4-in steel	0.37	0.58	0.001	0.001
S1-1/4-in steel	0.99	1.56	0.008	0.028
S1-1/4-in tungsten	2.11	3.32	0.017	0.058
S1-1/4-in teflon	0.11	0.17	0.001	0.003
Xanthan-1/4-in teflon	10.9	17.2	0.133	6.01
Carbopol-1/4-in teflon	4.99	7.86	0.417	0.209

Table 3. Measured values of the fall velocity and related quantities.

Liquid-solid	Initial distance δ (mm)	Vertical distance ℓ_T from releasing to touching (mm)	Critical touching distance δ_T (mm)
0.3% aqueous Xanthan --teflon	2.5	57	6
	5	79	
0.4% Carbopol in 50/50 glycerin/water--teflon			no attraction
STP--steel	1.3	60	11
	2.5	120	
	3.8	290	
	5.1	470	
	6.4	590	
S1--steel	2.5	23	17.5
	5.1	61	
	7.6	130	
	10.2	225	
	11.4	300	
S1--tungsten	3.8	100	15
	7.6	300	
S1--teflon	3.8	75	5
1.5% aqueous polyox --steel	1.3	9.5	5
	2.5	51	
	3.3	68	
	3.8	89	
	4.1	102	
1.25% aqueous polyox --steel	1	12	8
	2	21	
	3	74	
	4	90	
	5	108	
	5.8	114	
	7.1	150	

Table 4. Attraction between side-by-side spheres in different liquid-solid systems. The vertical distance $\ell_T(\delta)$ traveled before touching depends on the ratio of the fall velocity to the lateral migration velocity.

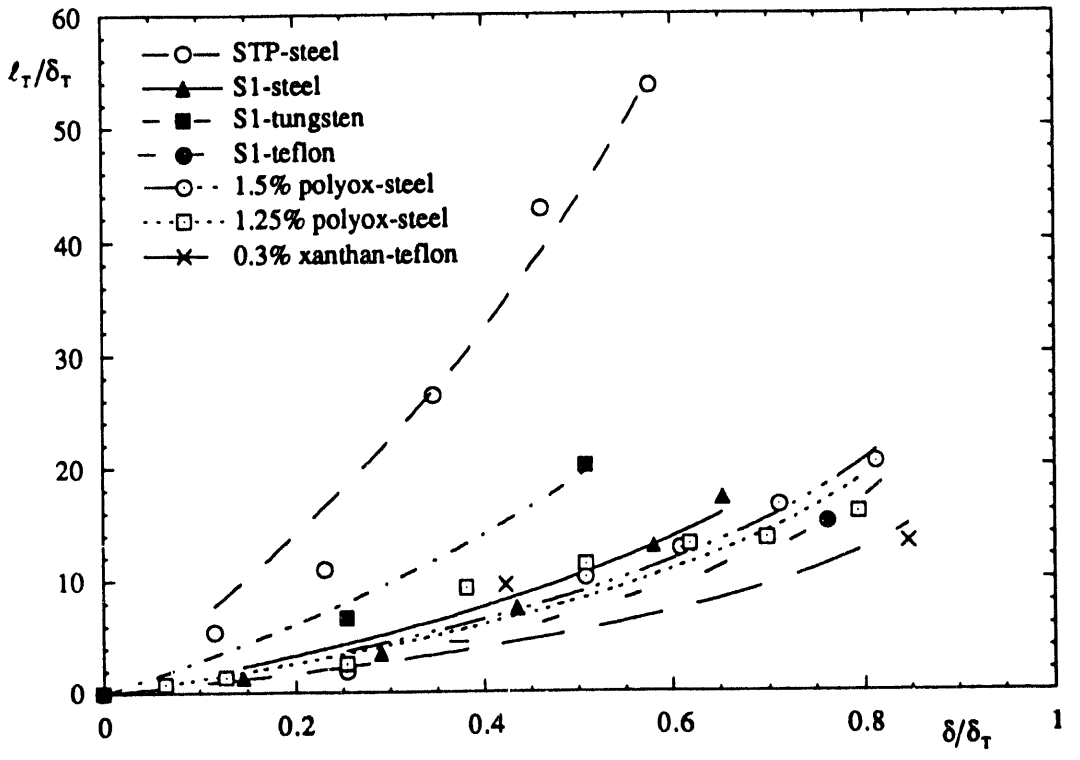

Fig. 4.2. Interaction between side-by-side sedimenting spheres in different fluids in terms of the ratio ℓ_T/δ_T of vertical distance traveled by the sphere before touching over the critical touching distance as a function of the ratio δ/δ_T. Full symbols refer to S1 and empty circles to STP.

4.1. Interaction in aqueous polyox solutions

In Fig. 4.3 the distances between two 1/4-in falling spheres dropped side-by-side are shown as a function of the vertical distance from the point of release. Four different values of δ are considered. Attraction between the particles is stronger and particles aggregate at a smaller distance from the point of release when the initial side-by-side distance δ is small. If δ is large, falling spheres will not touch.

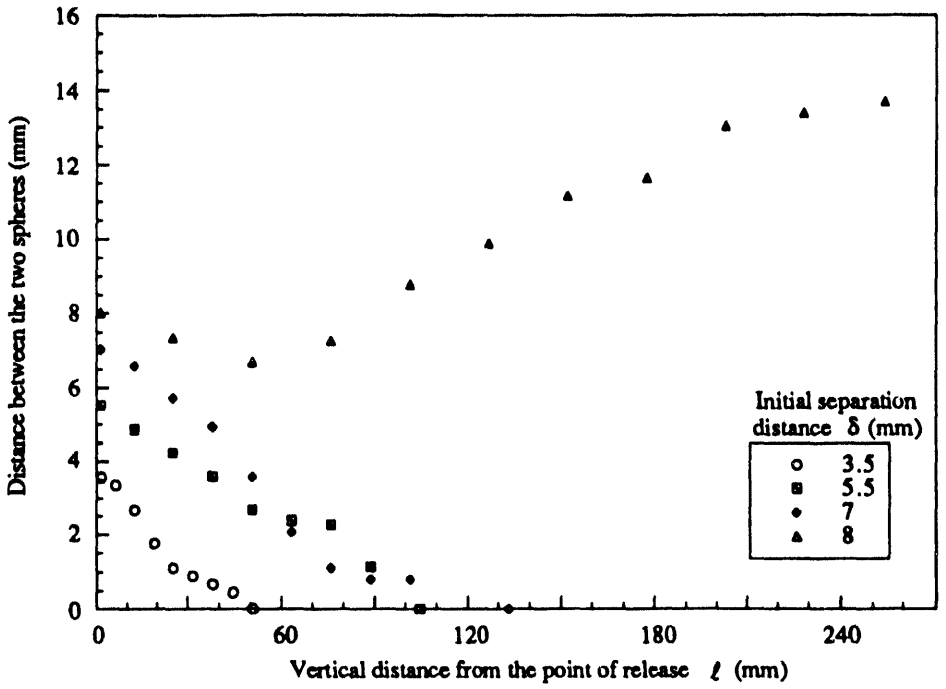

Fig. 4.3. Separation distance between spheres measured along the line of centers vs. the vertical distance ℓ to the mid-point between the spheres in 1.25% polyox solution.

The vertical distance $\ell_T(\delta)$ traveled by 1/4-in steel spheres before touching versus the initial distance δ between the spheres is plotted in Fig.s 4.4(a) and (b). Spheres falling in 1.25% aqueous polyox solution did not touch when $\delta > \delta_T \approx 8\,\text{mm}$ and $\delta_T \approx 5\,\text{mm}$ in 1.5% aqueous polyox solution. Values of flow parameters for the experiments shown in Fig. 4.4 are listed in Table 3.

We were at first surprised to find that the critical touching distance was greater in the 1.25% polyox solution than in the 1.5% solution. This unexpected result perhaps finds its explanation in the fact that the stress ratio N_1/τ (Table 1) is actually larger in the more dilute solutions, indicating a sense in which the dilute solution is actually more elastic. Consequently, we would predict even stronger interaction in the 1.0% than in the 1.25% solution.

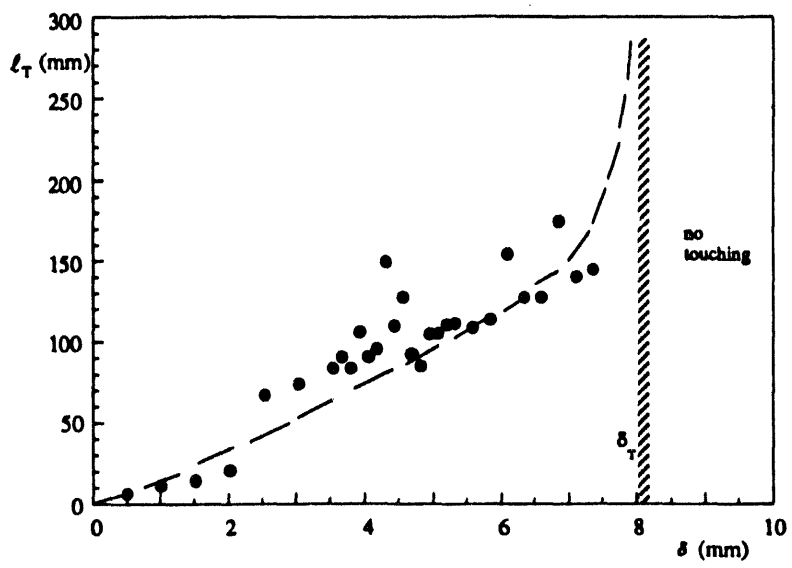

(a)

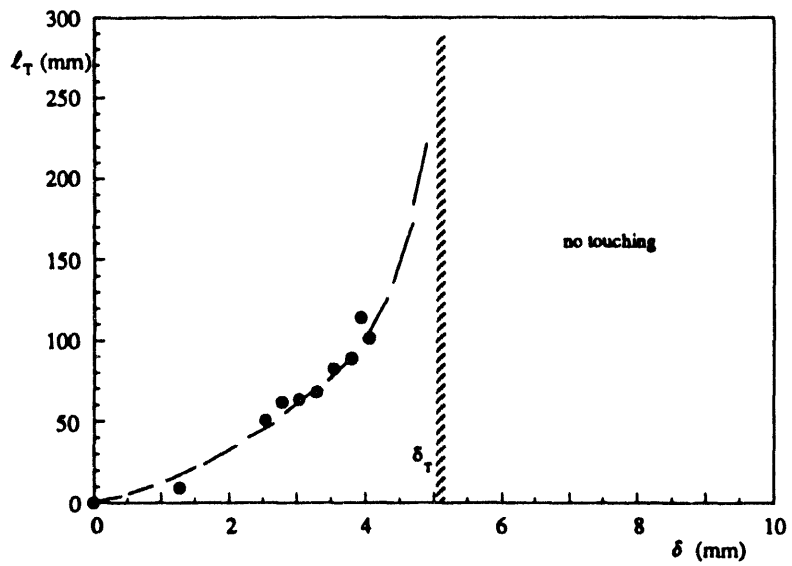

(b)

Fig. 4.4. $\ell_T(\delta)$ vs δ for 1/4-in steel spheres in (a) 1.25% aqueous polyox solution and (b) 1.5% aqueous polyox solution. The critical touching distance is larger in the 1.25% solution.

Clusters of spheres dropped together in the polyox solution will form streamline arrays (see Fig. 4.5). Chains of spheres, like long bodies, tilt their longside parallel to streamlines. Their falling speeds are less than the shear wave speeds in these cases.

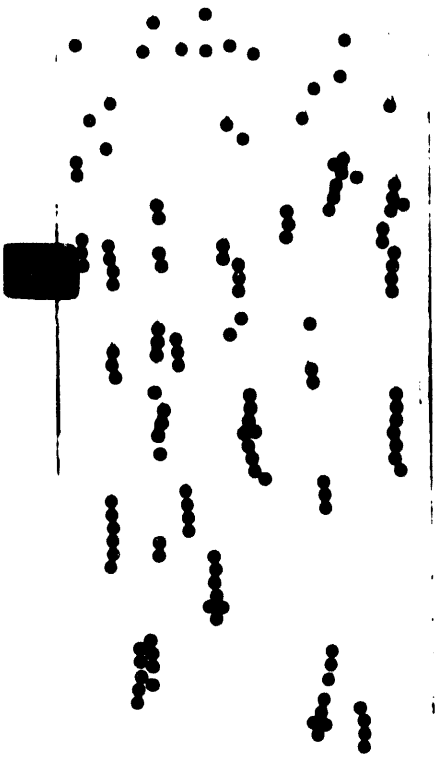

Fig. 4.5. Chains of 1/4-in steel spheres falling in 1.25% aqueous polyox solution. The same kind of chaining was observed in the 1.5% aqueous polyox solution.

4.2. Interaction in S1 and STP

Pairs of steel spheres were released in STP. Pairs of steel, tungsten and teflon spheres were released in S1. The behavior of attracting spheres in this experiment was qualitatively similar to that described in the previous section. The critical touching distance in STP is about 11 mm. This is smaller than the critical touching distance of 17.5 mm in S1. The elastic ratio of the first normal stress to the shear stress at small rates of shear is an order of magnitude larger in S1 than in STP (Table 1). The experimental results are presented in detail in Table 3, Table 4 and Fig. 4.2. Fig. 4.6 shows chains of spheres falling in S1 and STP.

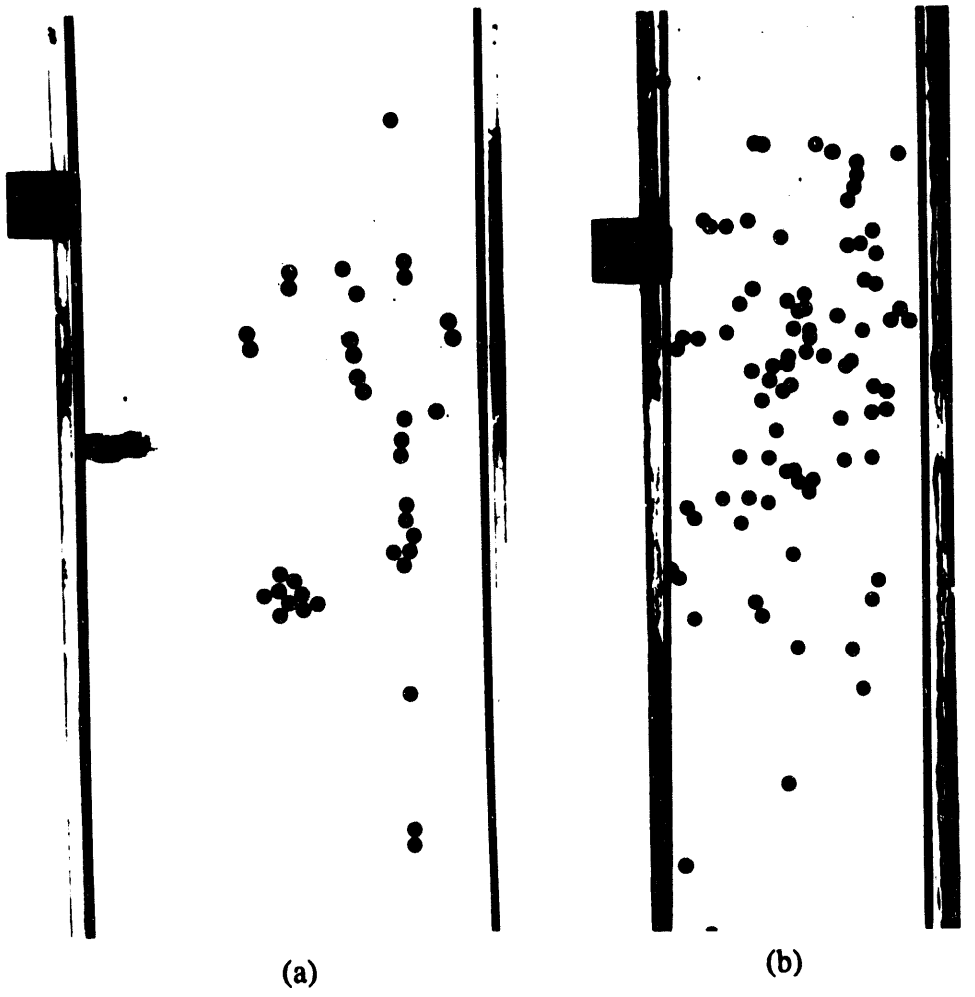

Fig. 4.6. Chains of 1/4-in steel spheres falling in (a) S1 and (b) STP.

4.3. Interaction in Xanthan and Carbopol

Experimental results for side-by-side attraction in all liquid-solid systems including Xanthan and Carbopol are given in Table 4. Two spheres dropped side-by-side do attract in 0.3% aqueous Xanthan solution, but the attraction is weak. The critical touching distance of teflon spheres is about 6 mm. There is no attraction in 0.4% Carbopol in 50/50 glycerin/water solution. Two spheres dropped closely side-by-side will separate as in a Newtonian liquid. The flow parameters are given in Table 3. The chains of spheres falling in these two liquids are shown in Fig. 4.7.

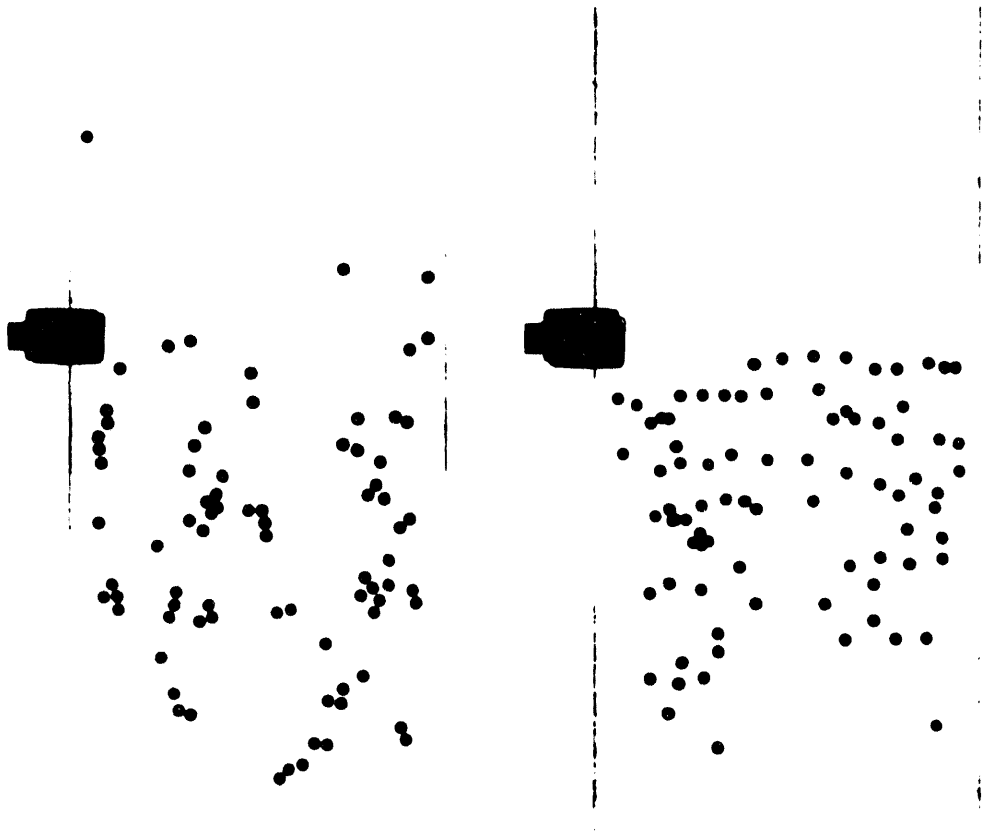

Fig. 4.7. Chains of 1/4-in teflon spheres falling in (a) 0.3% aqueous Xanthan and (b) 0.4% Carbopol in 50/50 glycerin/water solution. Horizontal arrays of spheres are relatively stable in the Carbopol solution and vertical arrays are relatively stable in the Xanthan solution.

In comparing the results we have obtained in our experiments with different liquids, we see a definite difference between side-by-side attraction and the chaining spheres. In this tentative and preliminary interpretation of our results we focus on the effects of normal stresses and shear-thinning with and without memory. STP and S1 are basically non-shear-thinning at the low rates of shear characteristic of our experiments. Side-by-side spheres attract in these fluids and they also chain, indicating that shear-thinning is not a necessary condition for these effects. S1 is a more mobile and elastic fluid than STP and it gives rise to stronger attraction and chaining. This suggests that fluids for which the elastic ratio of normal stress effects to viscous effects are large will give rise to strong interparticle forces, attraction and chaining. The Polyox solutions have large elastic normal stresses,

elastic stress ratios and times of relaxation as well, but they also shear-thin strongly at shear rates characteristic of our experiments. Although the presence of all the viscoelastic effects in Polyox solutions does not allow us to isolate the properties of a viscoelastic fluid that give rise to the strong particle interactions that we observed in our experiments, these interactions also appear to correlate well large values of the stress ratio. The correlation in Polyox is subtle because the less concentrated solutions have higher stress ratio and stronger interactions.

To isolate the effects of shear-thinning we looked at the Xhanthan and Carbopol solutions, which do not give measurable values of normal stresses at any rate of shear. The value of the elastic stress ratio may be large in Xanthan, but the ratio cannot be determined because the normal stresses are too small to measure. However, the 0.3% aqueous Xanthan has a much higher linear elasticity than Carbopol. We are assuming that this means that the memory of shear-thinning is much longer in Xanthan. In fact the Xanthan will exhibit side-by-side attraction weakly and chain strongly, but the 0.4% Carbopol does neither.

Our experiments show that different mechanisms promote aggregation in viscoelastic liquids; more than one property is involved. A possible generalization of our observations is that large values of the elastic stress ratio N_1/τ are sufficient but not necessary for strong interactions. Shear-thinning plus memory, which creates corridors of reduced viscosity, is also sufficient but not necessary for strong interactions. Aggregation seems not to occur in inelastic fluids with short memory or small values of N_1/τ, whether or not they shear-thin.

5. Direct two-dimensional simulation of the interactions between two particles falling side-by-side in Newtonian fluids

The hydrodynamic mechanisms that cause circular particles to rotate and drift away from each other in a Newtonian fluid can be understood by direct (two-dimensional) numerical simulation, using the Navier-Stokes equations to find the fluid motion and hydrodynamic forces which move the rigid particles according to Newton's equation of motion. A finite element package based on POLYFLOW with this capacity has been presented by Hu, Joseph and Crochet [28], and a video of

this simulation together with a short paper has been given by Hu, Joseph and Fortes [29]. Huang, Feng and Joseph [30] applied this code to study the forces and the turning couple on an elliptic particle settling in a vertical channel, and they showed that there is high pressure on the front side of the ellipse at the place where the shear stress vanishes, which corresponds to a stagnation point in potential flow. This pressure acts always to keep the long side of the body perpendicular to the fall. Feng, Hu and Joseph [31] used this code to solve initial value problems for circular particles settling in a channel and this section is an adaptation of their work to the problem at hand. An analysis like this one has been applied by Liu et al. [12] to the problem of interaction between a circular particle falling in a Newtonian fluid and a vertical wall.

We want to understand how two heavier-than-liquid circular particles dropped side-by-side from rest in a channel will rotate and move. Referring to Feng et al. [31] for details, we note here that in the regimes of moderately low Reynolds numbers in which there is no vortex shedding, the particles will commence to rotate as if turned by the shears from the fluid going around the outside of the particle and not from the fluid in the gap. As the particles acquire angular velocity, they separate and fall side-by-side for a time before they enter into a staggered arrangement. The side-walls of the channel are important, especially in the later stages of the motion.

In our experiments, spheres dropped side-by-side in Newtonian liquids would begin to rotate and drift rapidly away from each other and after a short time reach an apparently steady state with definite angular velocity and a fixed stand-away distance with no further drift. In this simulation, a fixed stand-away distance with the line of centers perpendicular to the flow is not achieved. The side-by-side configuration, however, is very persistent as Fig. 5.1 shows.

this simulation together with a short paper has been given by Hu, Joseph and Fortes [29]. Huang, Feng and Joseph [30] applied this code to study the forces and the turning couple on an elliptic particle settling in a vertical channel, and they showed that there is high pressure on the front side of the ellipse at the place where the shear stress vanishes, which corresponds to a stagnation point in potential flow. This pressure acts always to keep the long side of the body perpendicular to the fall. Feng, Hu and Joseph [31] used this code to solve initial value problems for circular particles settling in a channel and this section is an adaptation of their work to the problem at hand. An analysis like this one has been applied by Liu et al. [12] to the problem of interaction between a circular particle falling in a Newtonian fluid and a vertical wall.

We want to understand how two heavier-than-liquid circular particles dropped side-by-side from rest in a channel will rotate and move. Referring to Feng et al. [31] for details, we note here that in the regimes of moderately low Reynolds numbers in which there is no vortex shedding, the particles will commence to rotate as if turned by the shears from the fluid going around the outside of the particle and not from the fluid in the gap. As the particles acquire angular velocity, they separate and fall side-by-side for a time before they enter into a staggered arrangement. The side-walls of the channel are important, especially in the later stages of the motion.

In our experiments, spheres dropped side-by-side in Newtonian liquids would begin to rotate and drift rapidly away from each other and after a short time reach an apparently steady state with definite angular velocity and a fixed stand-away distance with no further drift. In this simulation, a fixed stand-away distance with the line of centers perpendicular to the flow is not achieved. The side-by-side configuration, however, is very persistent as Fig. 5.1 shows.

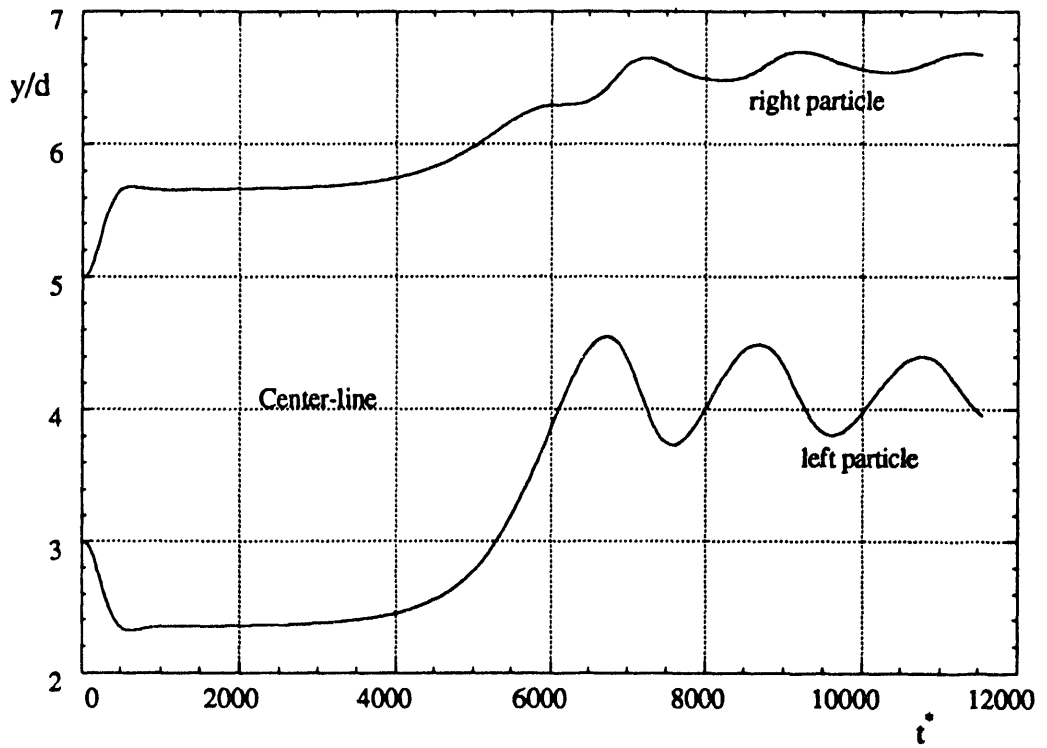

Fig. 5.1. Trajectories of two circular cylinders dropped from a side-by-side initial condition in a channel of 8 diameters width. The dimensionless time is defined by $t^* = t\sqrt{g/d}$. The oscillation seen in the trajectories is associated with a wall effect.

At first, when the side-by-side particles are close together, the passage of fluid between the particles is blocked, so that the flow passes over the outside of the particle, turning them as in Fig. 5.2. We are going to show that the pressure and the shear stress distributions on the surface of the particle give rise to a lateral force and a torque that define the drift and rotation of the particles.

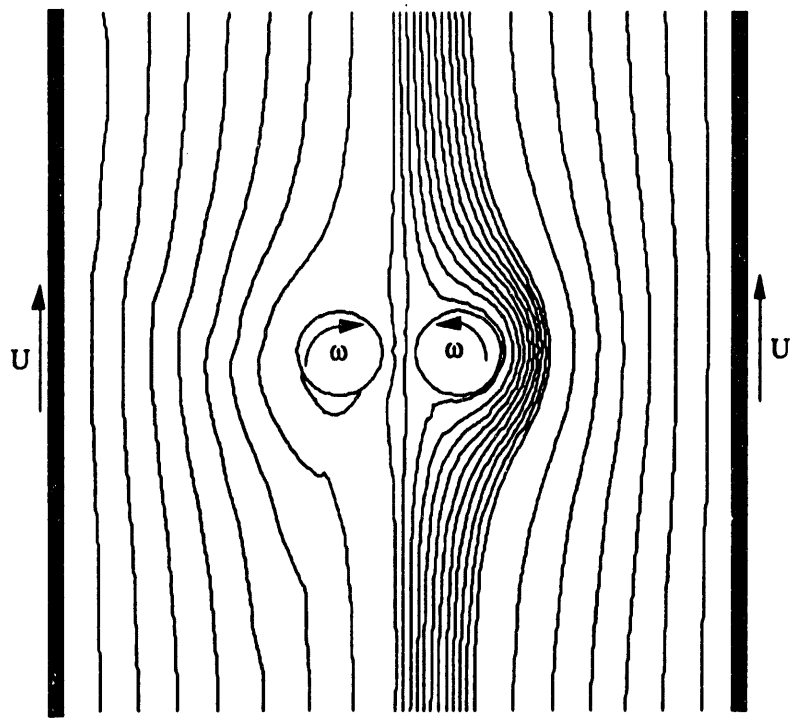

Fig. 5.2. Streamlines for side-by-side sedimentation of two circular particles dropped from rest in an 8d channel. The particles are at an early stage of sedimentation ($t^* = 31$ in Fig. 5.1). To visualize the streamlines, we use a coordinate system fixed at the center of the right particle, which is moving down and to the right side. In this system, the centerline between the particles is not a streamline.

Fig. 5.3 shows that the maximum pressure occurs near $\theta = 202.5^0$. This position is also where the dividing streamline seems to hit the surface of the body in Fig. 5.2. Because the circular particle is rotating, the no-slip condition implies that there are closed streamlines around the surface of the particle and a stagnation point cannot be strictly defined. But considering the outside streamlines, we will call the point with maximum pressure a viscous stagnation point. We have shown that the stagnation point usually corresponds to vanishing shear stress (Huang et al. [30], Liu et al. [12]). This is not the case here because of the strong rotation of the particle. If we modify the shear stress by taking out the contribution from rotation, we should still have the correspondence. This is done by considering a potential vortex at the center of the particle with velocity:

$$u_\theta^p = \omega a^2 / r \tag{5.1}$$

where ω is the angular velocity at this moment. The shear stress at $r = a$ for this is:

$$\tau_{r\theta}^{p} = -2\eta\omega \tag{5.2}$$

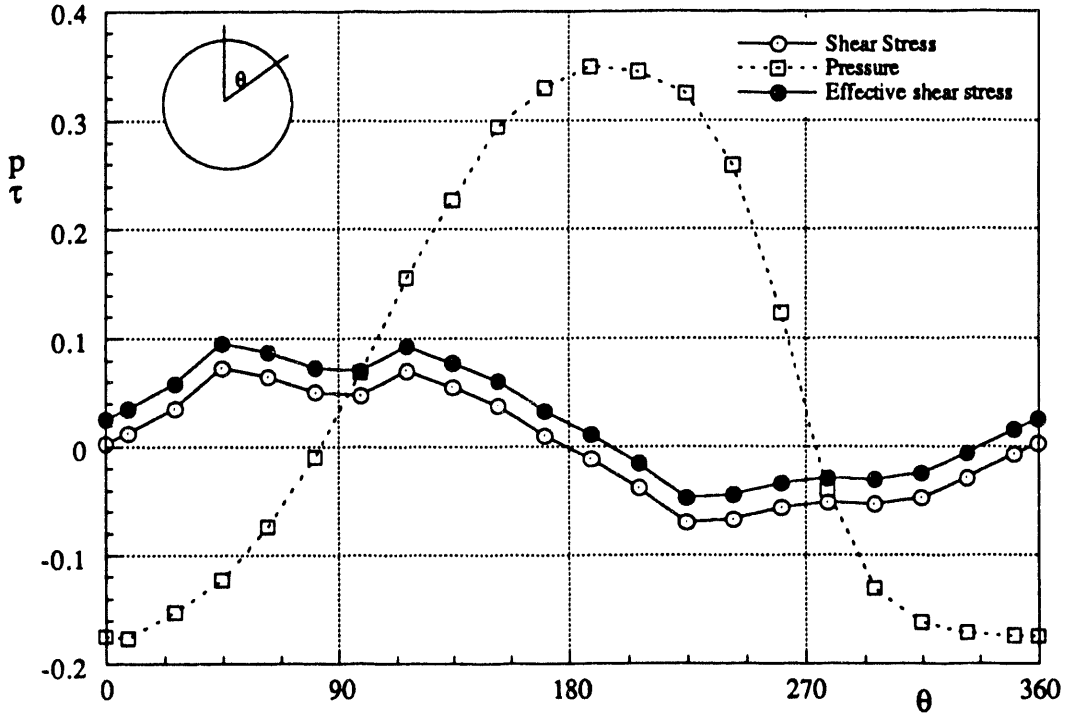

Fig. 5.3. The pressure and shear stress distribution on the surface of the right particle. Dimensionless time $t^* = 31$, and instantaneous Reynolds number $\mathbb{R} = 2.65$.

After removing the shear stress (5.2), we obtain the effective shear stress in Fig. 5.3. Thus, the maximum pressure occurs at the stagnation point where the effective shear stress vanishes. We also tested a particle prevented from rotation and settling at virtually the same Reynolds number. The distributions of pressure and viscous stresses are shown in Fig. 5.4. The shear stress distribution is very much like the modified shear stress in Fig. 5.3, and the zero of the shear stress is the viscous stagnation point that locates the pressure maximum.

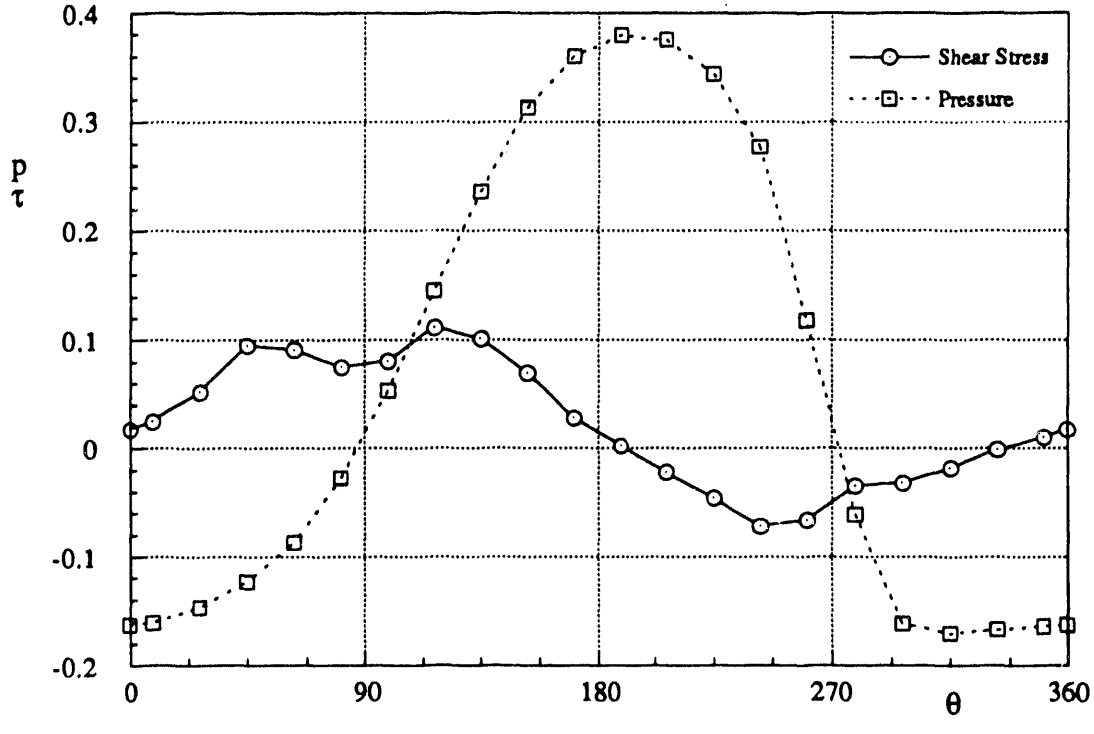

Fig. 5.4. The pressure and shear stress distributions on the right particle. The particles are prevented from rotation. Dimensionless time $t^* = 30$, instantaneous Reynolds number $\mathbb{R} = 2.76$.

Fig. 5.5 shows that the stagnation pressure controls the sidewise drift, increasing the distance between repelling particles. In this Fig. we have compared the side thrusts, $psin\theta$ of the pressure and $\tau cos\theta$ of the shear stress on the surface of the particle. The resultant forces are:

$$[F_p, F_\tau] = \int_0^{2\pi} [p\sin\theta, \tau\cos\theta] a d\theta = (1.602\text{x}10^{-3}, 8.034\text{x}10^{-4})\ \ dyn/cm \tag{5.3}$$

The pressure force is larger than the shear stress force, and the separation of the two particles is therefore determined mainly by the stagnation pressure.

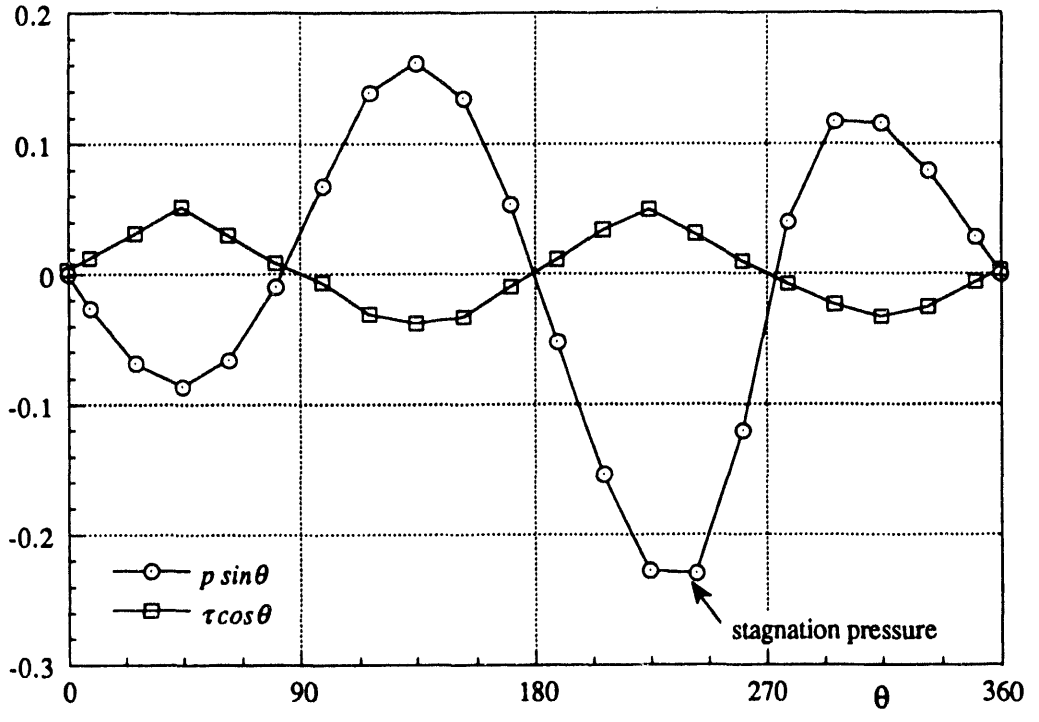

Fig. 5.5. The horizontal component of the pressure and shear stress shown in Fig. 5.3. Because of the definition of θ, negative lateral thrusts point to the right.

The rotation of the particle is associated with the fact that the positive shear stress on the right side is larger than the negative shear stress on the left. This is even clearer in the case of non-rotating particles shown in Fig. 5.4.

6. The interaction between a wall and a settling sphere

If a sphere is released at a small distance from a vertical wall in a viscoelastic fluid it will eventually approch the wall and fall while rolling up along the wall (anomalous rolling is discussed by Joseph et al. [11] and Liu et al. [12], see Fig. 6.1(a)). Even when the wall is slightly tilted away from gravity, the wall will attract a sedimenting sphere that is dropped near the wall. On the other hand if δ is large the sphere and wall do not appear to interact during the short fall time of our experiments (Fig. 6.1(b)).

Spheres dropped at or near a vertical wall in a Newtonian fluid will be repelled by the wall (Fig. 6.1(c)), just the opposite of what occurs in a viscoelastic fluid. Spheres that are sufficiently far from the wall initially do not appear to interact. The results of a direct two dimensional numerical simulation of a circular particle falling near a vertical wall in a Newtonian fluid was given by Liu et al [1993].

Returning to the case of viscoelastic fluids near a tilted wall, we may define two critical values δ_C and δ_T , the critical distance of interaction and the critical touching distance respectively, with $\delta_T \leq \delta_C$ as in the case of the interacting pairs of spheres. If $\delta < \delta_T$, then the sphere eventually migrates nearly all the way to the wall and never falls away. Usually, the gap between the sphere and the wall is too small to measure easily. If $\delta_T < \delta < \delta_C$, the sphere will move toward the wall, but it will eventually fall away (Fig. 6.1(b)). In our experiments, spheres were dropped at increasing distances from the top corner of the tilted rod, at different angles of inclination of the rod between 0 and 5°. There is a critical tilt angle θ_T such that when $\theta > \theta_T$, spheres are not attracted all the way to the wall.

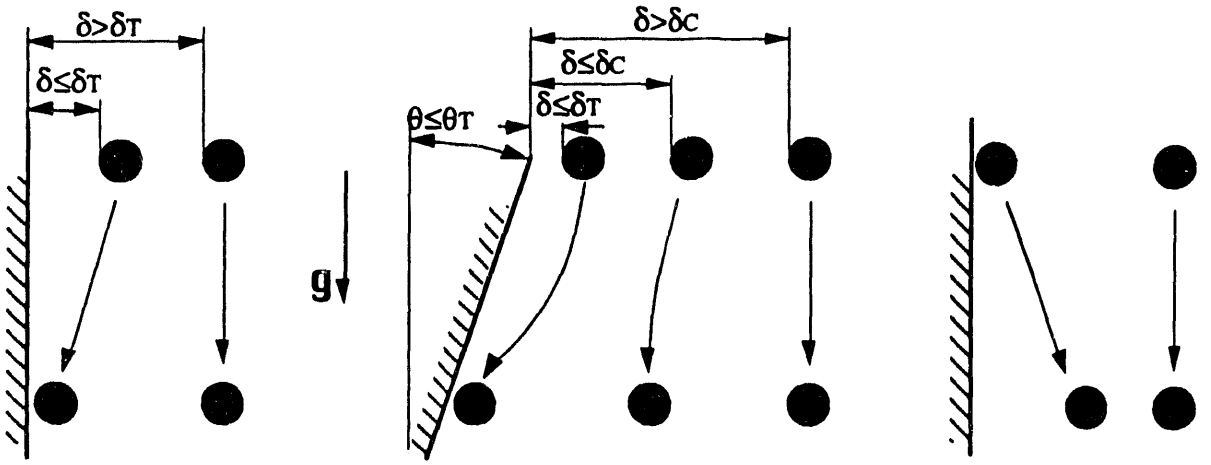

(a) Settling of spheres in viscoelastic liquid near a vertical wall

(b) Settling of spheres in viscoelastic liquid near a tilted wall

(c) Settling of spheres in Newtonian liquid near a vertical wall

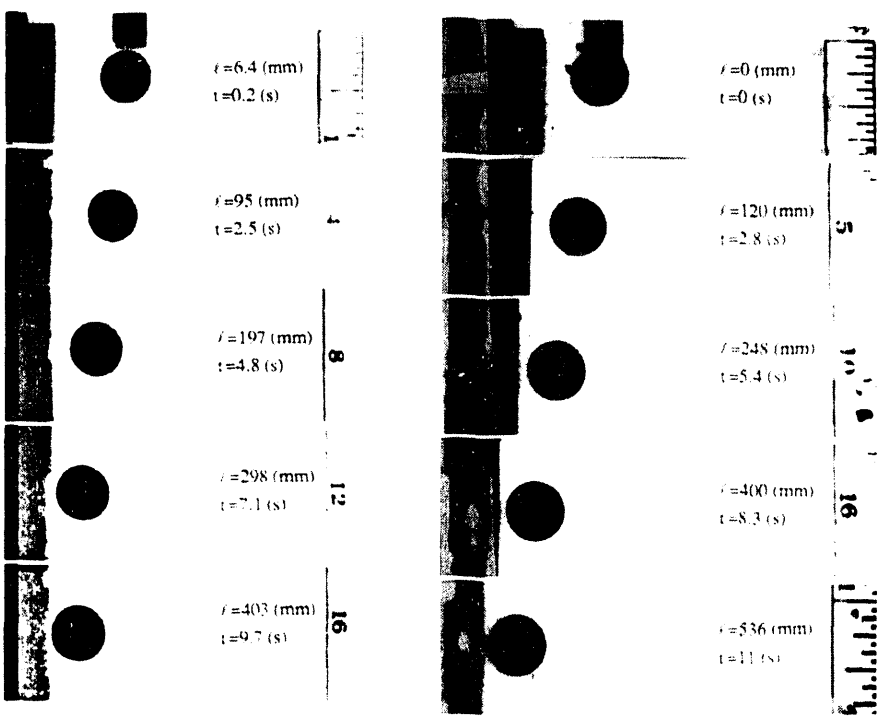

(d = 7.16-in ceramic sphere falling near a vertical wall (left, δ=10 mm) or a 15° tilted wall (right, δ=5 mm) in 1.5% aqueous polyox solution.

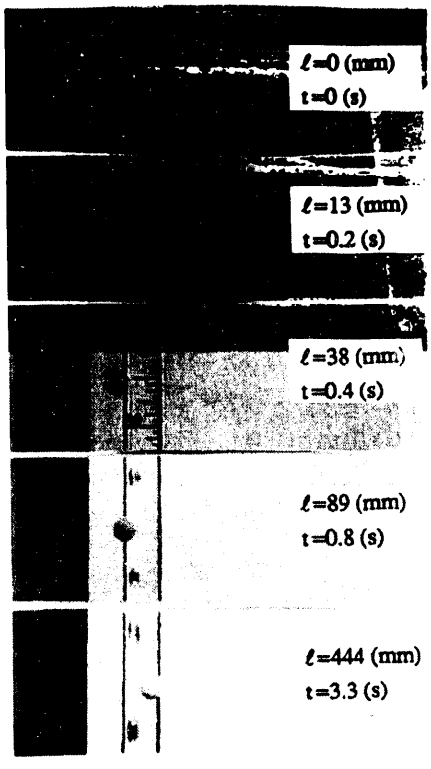

(e) a 1/4-in teflon sphere falling near a vertical wall in 50/50 glycerin/water solution

Fig. 6.1. A sphere released in a viscoelastic liquid will be attracted to the wall: (a) when the initial distance δ of the sphere from vertical wall is smaller than the critical touching distance δ_T; (b) when the wall is slightly tilted with $\theta \leq \theta_T$, a sphere will fall straight down if $\delta > \delta_T$ in case (a) or (b). In case (b), when $\delta_T < \delta < \delta_C$, a sphere will experience some wall attraction but will not migrate all the way to the wall and will eventually fall straight down. In Newtonian liquids, a sphere dropped at a small distance or no distance from the wall will migrate away from the wall (c). (d) Ceramic sphere falling in aqueous polyox solution. (e) Teflon sphere falling in aqueous glycerin.

6.1. Vertical wall

Sphere trajectories are shown in Fig. 6.2 for 1/4-in. steel spheres dropped in 1.5% polyox at different initial distances from a vertical wall ranging from 2 to 12 mm. These trajectories are approximately straight lines suggesting that the ratio of the fall velocity to the lateral migration velocity is constant. The free fall terminal velocity was reached at a distance of about 5 cm from the release point by those particles that had not touched the wall. Spheres starting at smaller initial distances δ migrate to the wall more rapidly. For larger initial distances, attraction between the falling sphere and the wall could not be observed in the time it takes for a particle to fall to the

bottom of the channel. $\delta = \delta_T$ is an effective critical distance such that when $\delta > \delta_T$ the sphere is apparently not attracted by the wall. Fig. 6.3(a) and (b) plots the vertical distance traveled by the sphere before touching the wall as a function of the initial distance between the sphere and the wall for 1.25% and 1.5% polyox solutions. The open circles in Fig. 6.3 are for values of ℓ_T longer than our channel which were extrapolated from particle trajectories. The 1.25% solution, which has a higher elastic stress ratio N_1/τ than the 1.5% solution (see Table 1), also has a larger δ_T.

It is of interest to compare the critical values of δ for a plane wall with a sphere and for two spheres launched side-by-side. The attracting or repelling power of a wall is larger than that between two spheres, because the wall can be visualized as a vertical array of touching spheres. Each sphere in the array attracts or repells the free test sphere, but with a different power of interaction depending on the variable distance between the spheres. So the interaction power of a wall is obtained by integration of the interaction of each small part of it. Reasoning in this way we would think that a wall could attract a free particle in a viscoelastic fluid at a much greater power than a single sphere could do. In fact, because the wall would not move by interaction with the free particle, we should actually define the critical touching distance $(\delta_T)_{ws}$, in the case of wall-sphere interaction, as twice of the distance between the sphere and the wall, i.e., the distance between the sphere and its image with respect to the wall. Comparing $(\delta_T)_{ws}$ with $(\delta_T)_{ss}$, which is the critical touching distance for falling spheres launched side-by-side, we see from Table 5 that $(\delta_T)_{ws}/(\delta_T)_{ss} = 1 \sim 4$ for all the liquids that show attraction except STP. The falling velocity is slowest in STP so the lateral migration velocity may also be too small to produce a noticable effect in channels as short as those used in our experiments. In a Newtonian fluid, the wall will force the test particle move out further than spheres settling side-by-side. In the experiments in which 1/4-in teflon spheres fall in a 50/50 glycerin/water solution, twice the distance between the sphere and the wall is ultimately 1.7 times greater than the distance between two spheres.

Liquid-solid	$(\delta_T)_{ss}$	$(\delta_T)_{ws}$
Polyox 1.25% -- steel	8	26
Polyox 1.5% -- steel	5	24
S1 -- steel	17.5	24
S1 -- tungsten	15	20
S1 -- teflon	5	6
STP -- steel	11	--
Xanthan -- teflon	6	6

Table 5. Comparison of critical values between wall-sphere and sphere-sphere interctions.

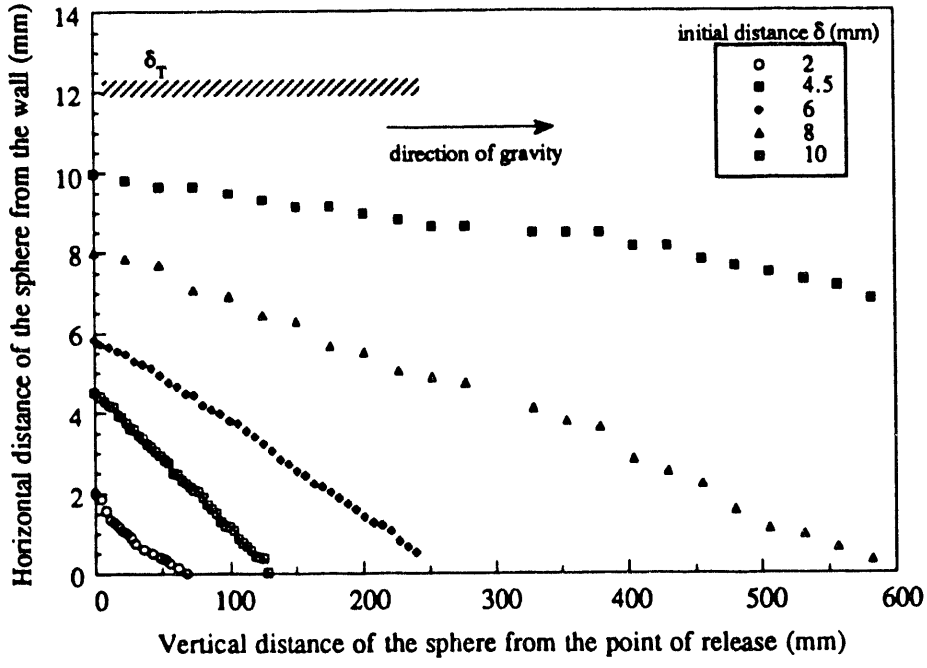

Fig. 6.2. Distance between a falling sphere and a vertical wall in 1.5% polyox as a function of the vertical distance of the spheres from the point of release.

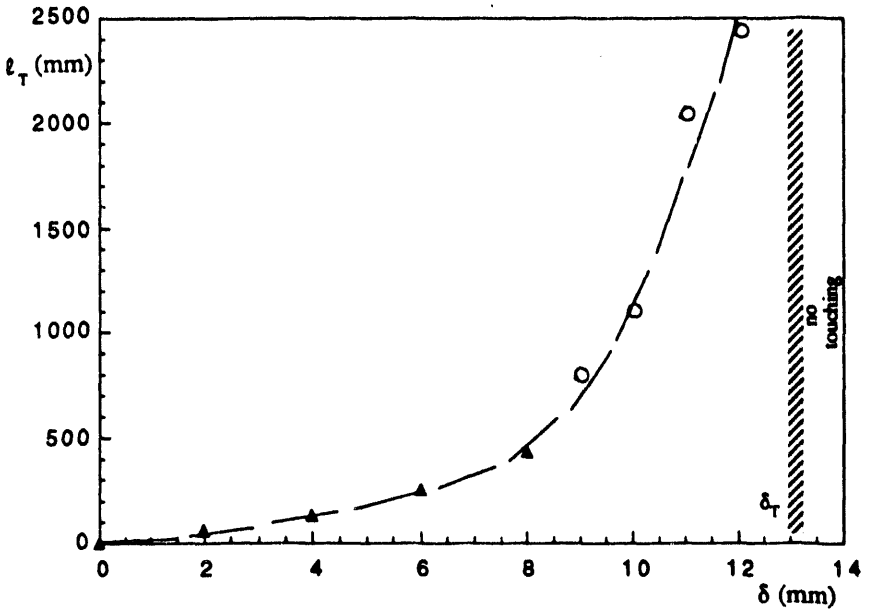

(a)

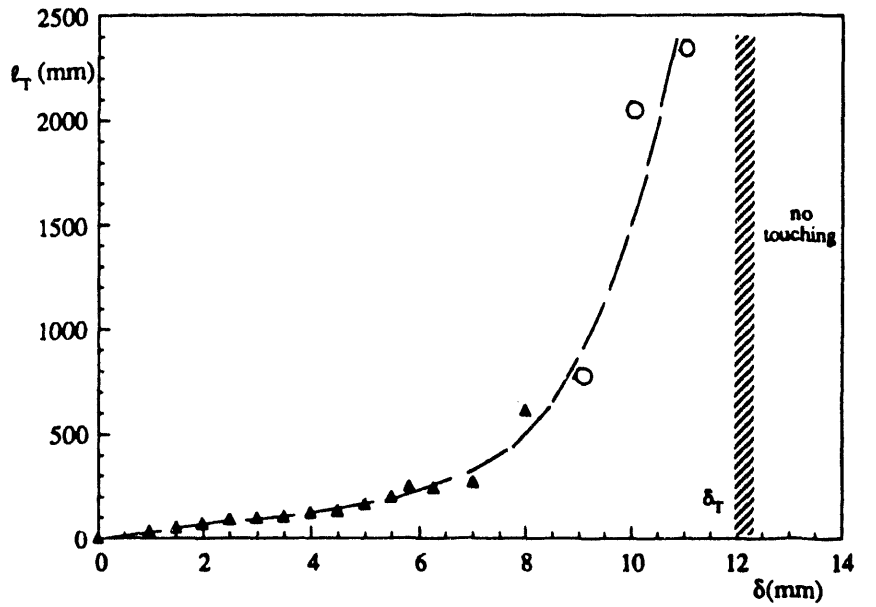

(b)

Fig. 6.3. Interaction between a falling sphere (steel, 1/4in. diameter) and a vertical wall in terms of the vertical distance ℓ_T traveled by the sphere before touching the wall as a function of the initial separation distance δ between the sphere and the wall: (a) 1.25% polyox solution, (b) 1.5% polyox solution.

6.2. Tilted wall

The case of inclined wall is more complex. The settling sphere can move toward the wall initially and then fall away. In Fig. 6.4, we have plotted trajectories of a 1/4-in steel sphere falling near a 1.5° tilted wall for different initial distances in a 1.5% aqueous polyox solution. We can identify a first critical distance, critical touching distance δ_T, that separates the initial distances for which spheres appear to eventually touch the wall from those for which they will not touch. As in the case of attracting spheres, we were able to identify a second critical distance δ_C. When $\delta < \delta_C$ the sphere will move toward the wall initially, but it may not reach the wall. When $\delta > \delta_C$ no attraction was observed. In Fig. 6.5, we have plotted δ_T and δ_C as a function of the tilt angle for 1.25% polyox solution (Fig. 6.5(a)) and for 1.5% polyox solution (Fig. 6.5(b)). From this figure we see that δ_T and δ_C decrease with increasing tilt angle.

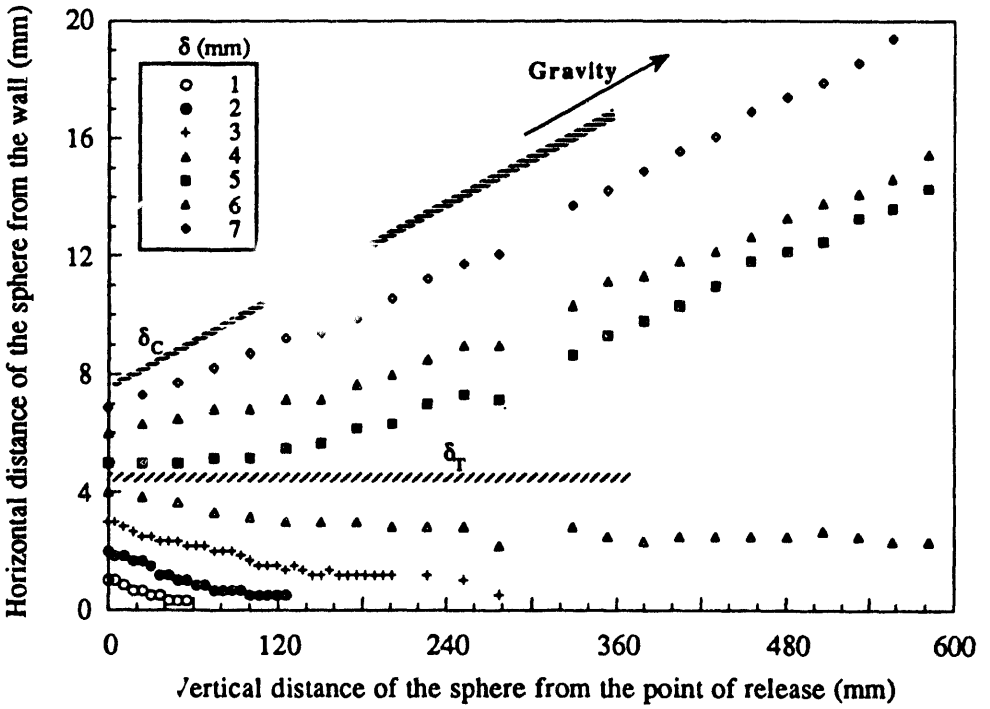

Fig. 6.4. Trajectories of a 1/4-in steel sphere falling near a wall tilted 1.5° from the vertical in a 1.5% aqueous polyox solution. The plane is divided into three regions $\delta < \delta_T$, $\delta_T < \delta < \delta_C$ and $\delta > \delta_C$. The arrow shows the slope of the trajectory a particle would have if it fell vertically.

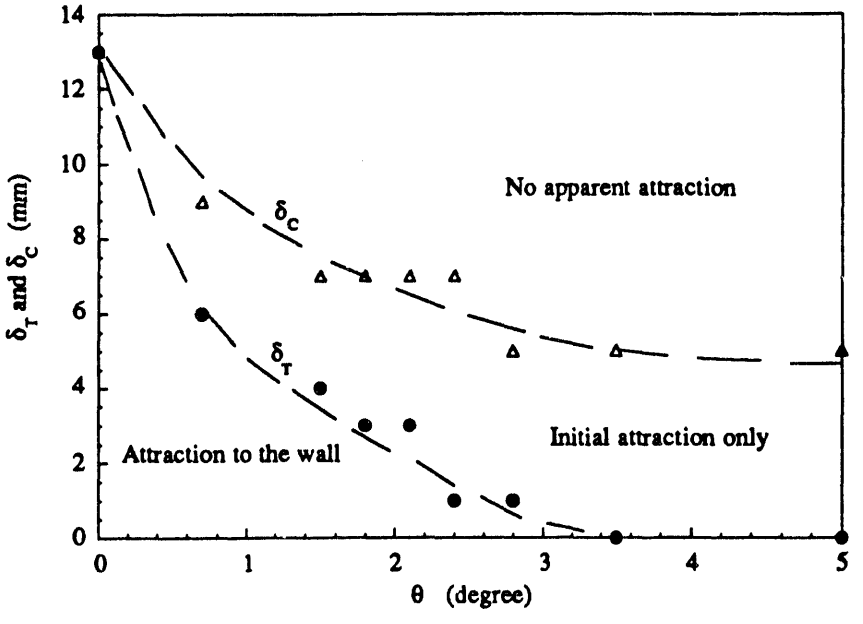

(a)

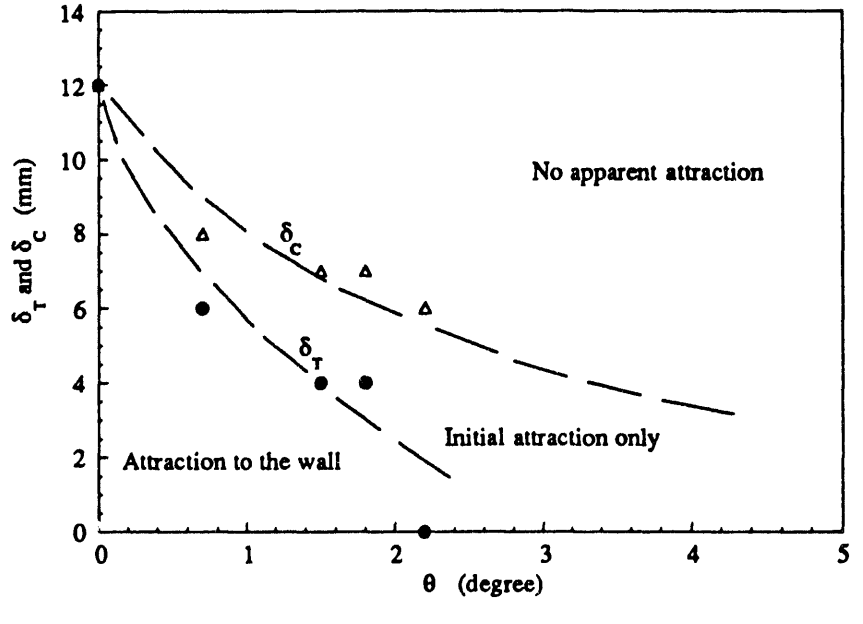

(b)

Fig. 6.5. Critical values of δ between a 1/4-in steel sphere and a tilted wall in terms of the critical distances as a function of the tilt angle: (a) 1.25% polyox solution, (b) 1.5% polyox solution.

Table 6 lists critical touching distances δ_T and critical interaction distances δ_C for 1/4-in spheres of different weights falling in various fluids. Spheres falling near vertical and tilted walls in STP or Carbopol are not attracted to the wall. STP has normal stresses but does not shear-thin. Carbopol shear-thins but has no measurable normal stress. On the other hand, the wall attracts spheres in the shear-thinning Xanthan, which also has no measurable normal stresses, but has much longer memory than Carbopol. Sphere-wall interactions are strong in S1 and polyox solutions. We do not yet understand the mechanisms that control lateral migration. Spheres with different weights (Table 2) were dropped in S1. The results show that the effect of particle weight on δ_T is the same as in the case of side-by-side settling of spheres (cf. Table 4).

Liquid-solid	θ (degree)	δT (mm)	δC (mm)
Polyox 1.25% - steel	0	13	13
	0.7	6	9
	1.5	4	7
	1.8	3	7
	2.1	3	7
	2.4	1	7
	2.8	1	5
	3.5	0	5
	5	0	5
Polyox 1.5% - steel	0	12	12
	0.7	6	8
	1.5	4	7
	1.8	4	7
	2.2	0	6
S1-steel	0	12	12
	1	2	5
	2	0	5
S1-tungsten	0	10	10
	1	0	5
	2	0	3
S1-teflon	0	3	3
STP-steel		no detectable attraction	
Xanthan-teflon	0	3	3
	1	2	3
	2	2	3
Carbopol-teflon		no attraction	

Table 6. Critical touching and interaction distances in different fluid-solid systems at different tilt angles.

6.3. Effects of sphere size and weight

These experiments were done later than the others and we used a fresh 1.5% aqueous polyox solution as a test liquid. The graphs of viscosity and the dynamic moduli of this solution as functions of shear rate or frequency are similar to those shown in Fig. 2.1 and Fig. 2.2. The parameters, listed in Table 1, for this solution are as follows: η_o = 10.6 Pa.s, κ = 4.67, n = 0.46, $\hat{\beta}$ = 144 gm/s, ψ_{1o} = 480 gm/s, c= 23.0 cm/s, λ_o = 0.20, $\frac{\psi_{1o}}{\eta_o} = \frac{10\hat{\beta}}{3\eta_o}$ = 4.52 s. The flow parameters of the experiments are listed in Table 7.

Spheres	U (cm/s)	$\dot{\gamma}$ (s^{-1})	$\mathbb{R}_0$	W_0
1/8-in tungsten	3.44	10.8	0.010	2.17
1/4-in steel	4.13	6.5	0.025	1.30
7/16-in ceramic	5.58	5.02	0.058	1.01
5/8-in aluminum	5.08	3.2	0.076	0.641
1/4-in teflon	0.17	0.27	0.001	0.054
1/4-in aluminum	0.39	0.61	0.002	0.123
1/4-in tungsten	14.6	23	0.087	4.61

Table 7. Measured values of the fall velocity and related quantities in the 1.5% aqueous polyox.

Fig. 6.6 shows the interactions between falling spheres and a vertical wall in terms of the vertical distance traveled by the sphere before touching the wall as a function of the initial distance between the sphere and the wall. It can be seen from Fig. 6.6(a) that the particle weight does not have an obvious effect on attraction between a sphere and a vertical wall. All the tested spheres of the same size but different weight have about same critical distances. For a given initial separation distance δ each of the four different spheres travels approximately the same distance in the vertical direction before touching the wall; $\ell_T(\delta)$ does not depend strongly on weight. However, the size of the sphere has an effect on the attraction. This effect is shown in Fig. 6.6(b). The larger the sphere, the shorter it travels in the vertical direction before touching the wall, and the greater the critical distance. Fig. 6.7 plots all data together in the normalized form.

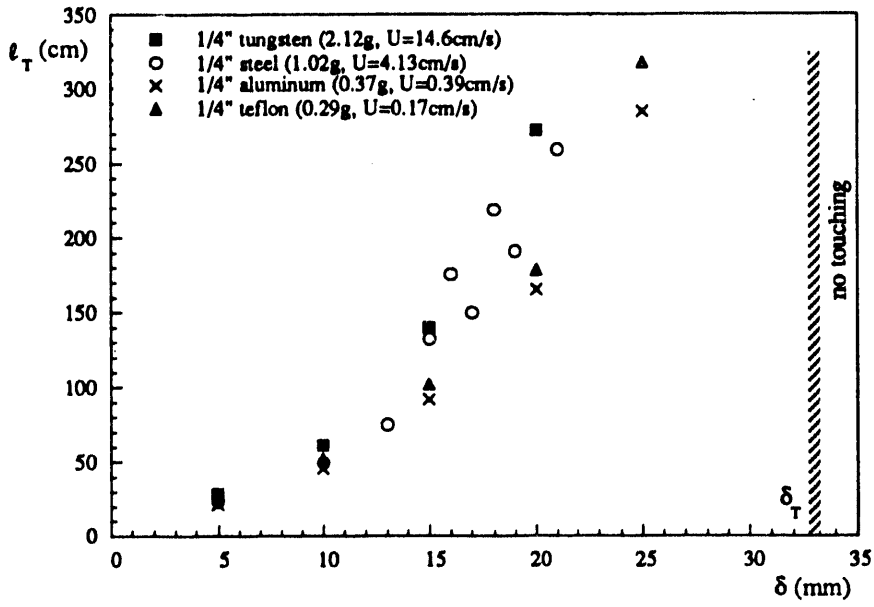

(a)

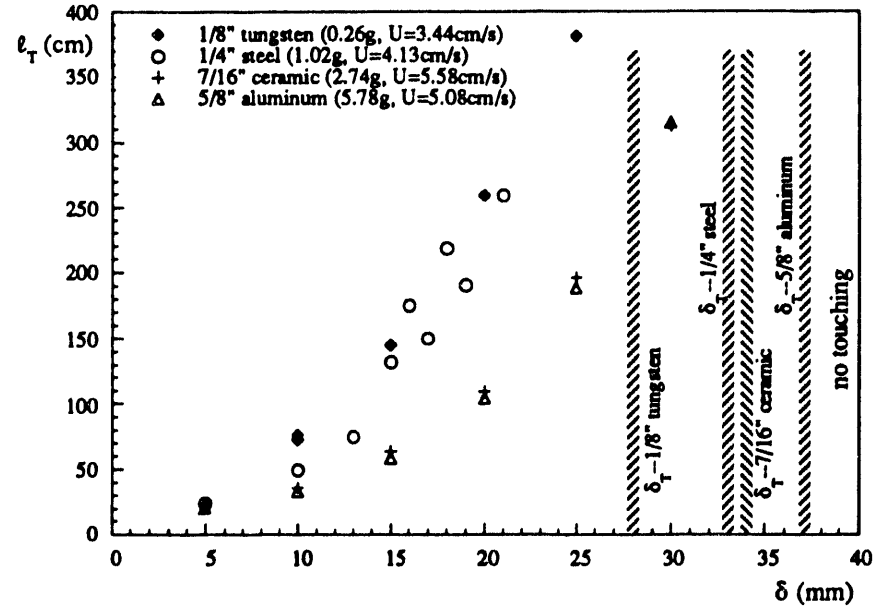

(b)

Fig. 6.6. Interactions between falling spheres and a vertical wall in terms of the vertical distance ℓ_T traveled by the sphere before touching the wall as a function of the initial distance δ between the sphere and the wall in the 1.5% aqueous polyox solution: (a) effect of particle weight; (b) effect of particle size.

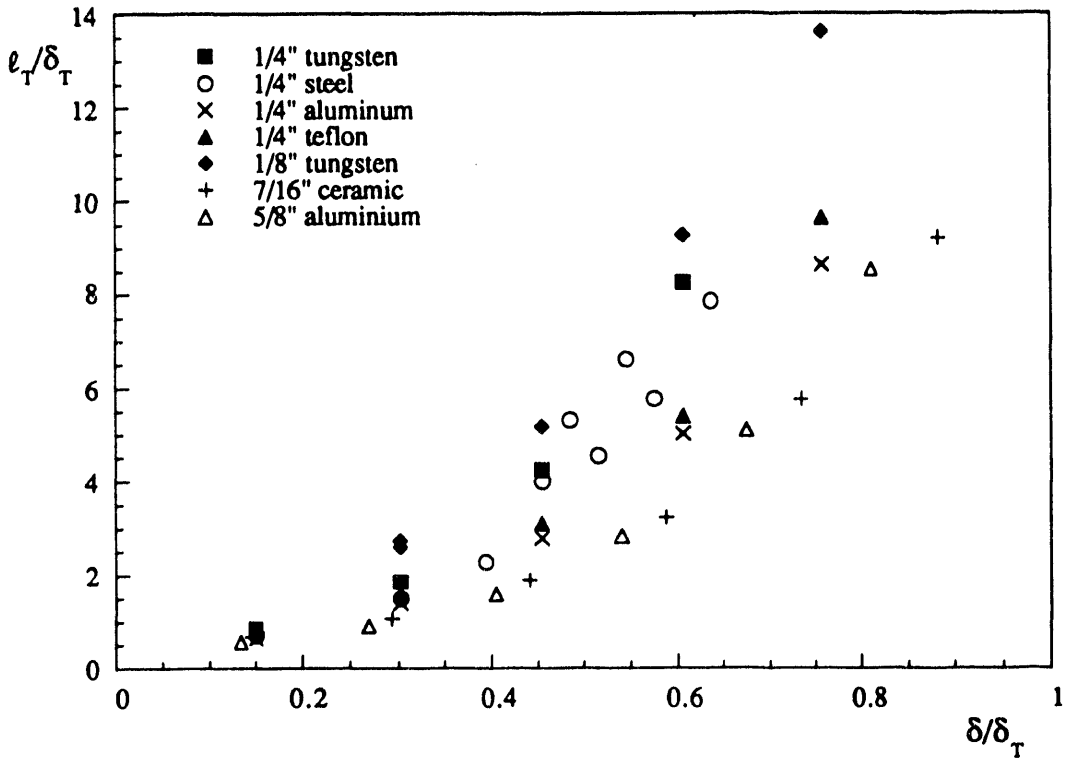

Fig. 6.7. Normalized form of Fig. 6.6.

Interactions between a falling sphere and a wall are expressed in terms of the critical touching distances as a function of the tilt angle in Fig. 6.8. The critical touching distance exists only when the tilt angle of the wall is less than about 2°. The critical angles for most spheres tested were between 1.5° and 2° except for 1/4-in tungsten sphere for which the critical angle was 1°. Most of the spheres tested have similar critical interaction distances in this case, but the critical distances of the 1/4-in tungsten sphere from a tilted wall are much smaller than the others. The experimental results are also summarized in Table 8. The effect of particle size on sphere-wall attraction can also be seen in the case when the wall is tilted through an angle of 1°. Bigger spheres migrate to the wall more rapidly.

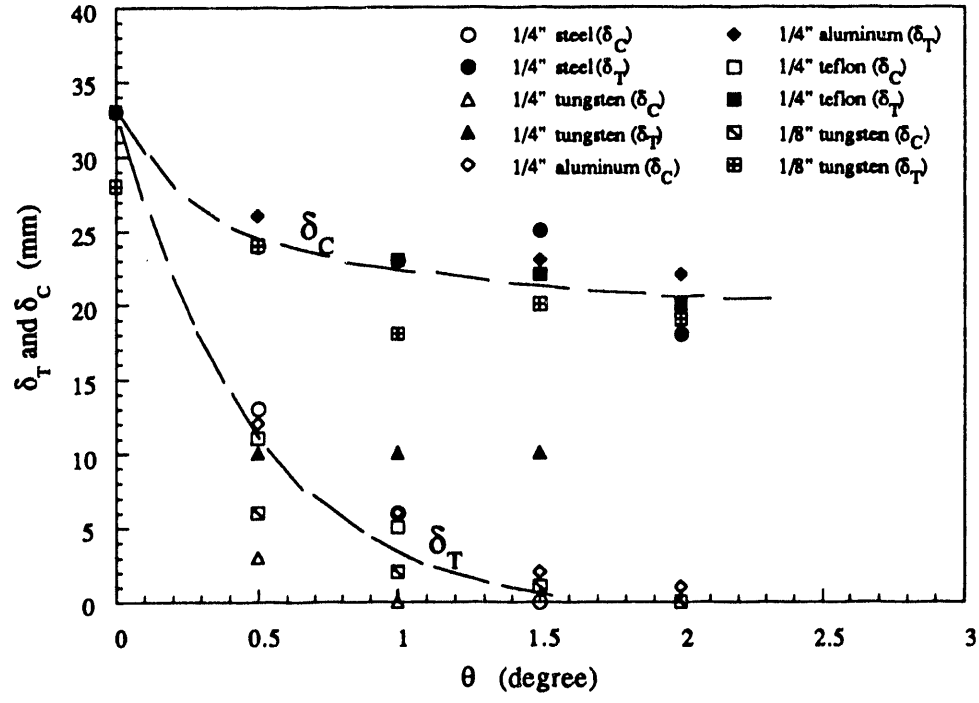

Fig. 6.8. Critical distances vs tilt angle of the wall in a 1.5% aqueous polyox. The results given here are similar to those given in Fig. 6.5.

Sphere	θ (degree)	δ_T (mm)	δ_C (mm)	δ (mm)	ℓ_T (cm)
1/4-in steel	0	33	33	5	23.9
				5	23.6
				10	49.5
				13	74.9
				15	132
				16	175
				17	150
				18	218
				19	191
				21	259
1/4-in tungsten	0	33	33	5	27.9
				10	61
				15	140
				20	272
1/4-in aluminum	0	33	33	5	21.1
				10	45.7
				15	91.4
				20	165
				25	284
1/4-in teflon	0	33	33	5	25.4
				10	52.1
				15	102
				20	178
				25	318
1/8-in tungsten	0	28	28	5	22.9
				10	76.2
				10	72.4
				15	145
				20	259
				25	381
7/16-in ceramic	0	34	34	5	22.9
				10	35.6
				15	63.5
				20	109
				25	196
				30	312
5/8-in aluminum	0	37	37	5	20.3
				10	33
				15	58.4
				20	104
				25	188
				30	315
1/4-in steel	0.5	13	24		
1/4-in tungsten	0.5	3	10		
1/4-in aluminum	0.5	12	26		
1/4-in teflon	0.5	11	24		
1/8-in tungsten	0.5	6	24		
1/4-in steel	1	6	23	5	71.1
1/4-in tungsten	1	0	10		
1/4-in aluminum	1	6	23	5	137
1/4-in teflon	1	5	23		
1/8-in tungsten	1	2	18		
7/16-in ceramic	1	11	22	5	35.6
5/8-in aluminum	1	13	22	5	22.9

1/4-in steel	1.5	0	25		
1/4-in tungsten	1.5	0	10		
1/4-in aluminum	1.5	2	23		
1/4-in teflon	1.5	1	22		
1/8-in tungsten	1.5	1	20		
1/4-in steel	2	0	18		
1/4-in aluminum	2	1	22		
1/4-in teflon	2	0	20		
1/8-in tungsten	2	0	19		

Table 8. Summary of experimental results in the 1.5% aqueous polyox.

7. Discussions and conclusions

We dropped two spheres side-by-side in a sedimentation channel filled with different liquids. In viscoelastic liquids, the spheres will attract when the initial separation distance is small; the line between centers will turn as they attract, until the spheres touch and chain with the line of centers vertical. Close side-by-side settling at slow speeds is unstable in viscoelastic fluids and the dynamics creates stable vertical chains. If the initial side-by-side distance between spheres is large enough, the spheres do not appear to interact, whether or not they are dropped in Newtonian or viscoelastic liquids.

In Newtonian liquids, two spheres launched side-by-side, which are initially separated by a small gap or no gap, will separate. Side-by-side sedimentation is relatively stable or only weakly unstable and spheres will never chain in Newtonian liquids.

Two heavy spheres falling faster than the shear wave speed in a viscoelastic fluid will disperse as in a Newtonian fluid. The phenomenon is the same one that causes long bodies that fall straight down at slow speeds to turn 90° into broadside-cross-the-stream fall at supercritical speeds when inertia dominates viscoelasticity.

In the case of attracting spheres, there are two critical values of the initial distances between spheres. For small values of initial distance below the first critical one, the two spheres will come together in a chain with line of centers vertical. If the initial distance between spheres is larger than the first critical value, the spheres would not come together, and if smaller than the second critical value they will move toward one another, but eventually separate.

Spheres that are initially close to a vertical wall or to a wall tilted slightly in such a way that gravity pulls the sphere away from the wall, will attract falling spheres in a viscoelastic liquid and will repel falling spheres in Newtonian and inelastic liquids. There is a critical separation distance for attraction to a vertical and two critical separation distances, the same ones as for two falling spheres, for the tilted wall. If the angle of tilt is too great (say, greater than 5°) the sphere will always fall away from the wall.

Attraction between spheres and between a sphere and a wall does not depend strongly on the weight or fall velocity of the sphere, but there appears to be a noticeable effect of size, with stronger attractions when the sphere size is larger in the sphere-wall experiments. The effect of changing weight is roughly to change the lateral velocity in proportion to the fall velocity.

Our experiments show that different mechanisms promote aggregation in viscoelastic liquids; more than one property is involved. A possible generalization of our observations is that large values of the elastic stress ratio N_1/τ are sufficient but not necessary for strong aggregation. All of the active viscoelastic liquids (polyox solutions and S1), except 0.3% aqueous Xanthan, have large values of N_1/τ and all the liquids except Xanthan, including STP and Carbopol, are nicely ordered with respect to aggregation behavior by the zero shear coefficient of the elastic stress ratio. The Xanthan solution has no measurable normal stresses and the zero shear coefficient of elastic stress ratio, and the ratio itself are too small to measure, but it has strong properties of aggregation. Xanthan shear-thins strongly and has a large storage modulus. This leads us to believe that shear-thinning plus memory, which creates corridors of reduced viscosity, is also sufficient but not necessary for strong aggregation. In either case the elasticity of the fluid is important. Aggregation seems not to occur in Newtonian fluids or in inelastic fluids with short memory, as in our Carbopol solution or in Boger type fluids with small values of N_1/τ.

Acknowledgments

This work was supported by the NSF, fluid, particulate and hydraulic systems, by the US Army, Mathematics and the Army High Performance Computing Research Center (AHPCRC), and by the DOE, Department of Basic Energy Sciences. We wish to thank Mr. Dave Hultman who made the "clothespin dropper", Ms. A.J. Lin who helped in the experimental measurements with the use of an image processing software, Mr. T. Blomstrom, Mr. M. Arney and Ms. S. Braasch, who measured the rod climbing constants, surface tensions, shear wave speeds and viscosities.

References

1. Y.J. Liu and D.D. Joseph, Sedimentation of particles in polymer solutions, J. Fluid Mech., **255** (1993) 565-595.

2. D.D. Joseph and Y.J. Liu, 1993 Orientation of long bodies falling in a viscoelastic liquid, J. Rheology, **37** (1993) 1-22.

3. D.G. Christopherson and D. Dowson, An example of minimum energy dissipation in viscous flow, Proc. Roy. Soc., A251 (1959) 550-564.

4. R.I. Tanner, End effects in falling-ball viscometer, J. Fluid Mech., **17** (1963) 161-170.

5. B. Caswell, The stability of particle motion near a wall in Newtonian and non-Newtonian fluids, Chem. Eng. Sci., **27** (1972) 373-389.

6. L.G. Leal, The slow motion of slender rod-like particles in a second-order fluid, J. Fluid Mech., **69** (1975) 305-337.

7. L.G. Leal, Particle motions in a viscous fluid, Ann. Rev. Fluid Mech., **12** (1980) 435-476.

8. A.J. Goldman, R.G. Cox and H. Brenner, Slow viscous motion of a sphere parallel to a plane wall. I. Motion through a quiescent fluid, Chem. Engng. Sci., **22** (1967) 637-651.

9. P.A. Bungay and H. Brenner, The motion of a closely-fitting sphere in a fluid-filled tube, Int. J. Multiphase Flow, **1** (1973) 25-26.

10. J.A.C. Humphrey and H. Murata, On the motion of solid spheres falling through viscous fluids in vertical and inclined tubes, ASME 1991 Winter Annual Meeting Paper No. WAM-91-9.

11. D.D. Joseph, J. Nelson, H. Hu and Y.J. Liu, Competition between inertial pressures and normal stresses in the flow induced anisotropy of solid particles, P. Moldenaers and R. Keunings (eds.), Theoretical and Applied Rheology,. Elsvier, Amsterdam, 1992, pp.60-65.

12. Y.J. Liu, J. Nelson, J. Feng and D.D. Joseph, Anomalous rolling of spheres down an inclined plane, J. Non-Newtonian Fluid Mech., **00** (1993) 00-00.

13. D. Sigli and M. Coutanceau, Experimental and theoretical investigations of the motion of a sphere in an elastic-viscous fluid with wall effect, C. Klason and J. Kubat (Eds.), Proc. 7th Int. Cong. Rheol., Swed. Soc. Rheol., Goeteborg, 1974, pp372-373.

14. D. Segli and M. Coutanceau, Effect of finite boundaries on the slow laminar isothermal flow of a viscoelastic fluid around a spherical obstacle, J. Non-Newtonian Fluid Mech., **2** (1977) 1-21.

15. M.J. Riddle, C. Narvaez and R.B. Bird, Interactions between two spheres falling along their line of centers in a viscoelastic fluid, J. Non-Newtonian Fluid Mech., **2** (1977) 23-35.

16. R.B. Bird, R.C. Armstrong and O. Hassager, Dynamics of Polymeric Liquids, John Wiley & Sons, New York, 1987.

17. J. Michele, R. Pätzold and R. Donis, Alignment and aggregation effects in suspensions of spheres in non-Newtonian media, Rheol. Acta, **16** (1977) 317-321.

18. P. Brunn, The slow motion of a rigid particle in a second-order fluid, J. Fluid Mech., **82** (1977) 529-550.

19. H. Giesekus, Die bewegung von teilchen in strömungen nicht-newtonscher flüssigkeiten, ZAMM, **58** (1978) T26-37.

20. B. Van der Brule and G. Gheissary, Vediotape of experiments, (unpublished, 1993).

21. Y.I. Cho and J.P. Hartnett, The falling ball viscometer - A new instrument for viscoelastic fluids, J. Heat Mass Transfer, **6** (1979) 335-342.

22. Y.I. Cho, J.P. Hartnett and W.Y. Lee, Non-Newtonian viscosity measurements in the intermediate shear rate range with the falling ball viscometer, J. Non-Newtonian Fluid Mech., **15** (1984) 61-74.

23. G.S. Beavers and D.D. Joseph, The rotating rod viscometer, J. Fluid Mech., **69** (1975) 475-511.

24. D.D. Joseph, M.S. Arney, G. Gillberg, H. Hu, D. Hultman, C. Verdier and T.M. Vinagre, A spinning drop tensioextensiometer, *J.* Rheology, **36** (1992) 621-662.

25. D.D. Joseph, Fluid Dynamics of Viscoelastic Liquids, Springer-Verlag, New York, 1990.

26. R. Roscoe, The steady elongation of elasto-viscous liquids, Brit. J. Appl. Phys., **16** (1965) 1567-1571.

27. H.A. Barnes, J.F. Hutton and K. Walters, An Introduction to Rheology, Elsevier, 1989.

28. H. Hu, D.D. Joseph and M.J. Crochet, Direct simulation of fluid particle motions, Theoret. & Comput. Fluid Dyn., **3** (1992) 285-306.

29. H. Hu, D.D. Joseph and A.F. Fortes, Experiments and direct simulation of fluid particle motion, Int. Vedio J. of Engng Research, **2** (1992) 17-24.

30. Y. Huang, J. Feng, and D.D. Joseph, The turning couples on an elliptic particle settling in a vertical channel, Submitted to J. Fluid Mech., (see UMSI Research Report 93/55).

31. J. Feng, H. Hu, and D.D. Joseph, Direct simulation of initial value problems for the motion of solid bodies in a Newtonian fluid. Part 1. Sedimentation, Submitted to J. Fluid Mech., (see UMSI Research Report 93/60).

TWO-PHASE POWER-LAW MODELING OF PIPE FLOWS DISPLAYING SHEAR-THINNING PHENOMENA

by
Jianmin Ding, Robert W. Lyczkowski,* and William T. Sha
Argonne National Laboratory
Energy Technology Division
*Energy Systems Division
9700 South Cass Avenue
Argonne, IL 60439

ABSTRACT

This paper describes our work in modeling concentrated liquid-solids flows in pipes. COMMIX-M, a three-dimensional transient and steady-state computer program developed at Argonne National Laboratory, was used to compute velocities and concentrations. Based on our previous analyses, some concentrated liquid-solids suspension flows display shear-thinning rather than Newtonian phenomena. Therefore, we developed a two-phase non-Newtonian power-law model that includes the effect of solids concentration on solids viscosity. With this new two-phase power-law solids-viscosity model, and with constitutive relationships for interfacial drag, virtual mass effect, shear lift force, and solids partial-slip boundary condition at the pipe walls, COMMIX-M is capable of analyzing concentrated three-dimensional liquid-solids flows.

1. Introduction

The behavior of concentrated two-phase liquid-solids suspension flows has been a matter of interest for many years because the processing and transport of these flows are important operations in many industrial applications. This has called attention to the need for a fundamental understanding of the physical phenomena for macroscopic computer simulations of these flows. However, there is as yet no comprehensive theory that accounts for all of the effects in concentrated suspensions, and few computations have been performed for fully three-dimensional two-phase liquid-solids flow.

Argonne National Laboratory (ANL) has initiated research on concentrated two-phase suspension flows (Sekar et al., 1988; Lyczkowski and Wang, 1992; Ding et al., 1992; 1993). A coordinated methodology that involves theory (development of field and constitutive equations), experimentation, and computer modeling is being pursued. ANL anticipates that synergism will be the result when a conscious effort is made to coordinate the extension of this research program, which involves complex and interdisciplinary phenomena that require advances in both a theory and experimentation.

Earlier efforts to study concentrated suspension flow have been reviewed in our previous papers (Ding et al., 1992; 1993). The philosophy of ANL is to use a self-consistent methodology to link micro- and macro-fluid mechanical phenomena. This philosophy will ensure the internal consistency of the design and instrumentation of the experiments, the data acquisition and its processing for use in the development of field and constitutive equations, and computer code validation.

We use the COMMIX-M computer code to analyze the velocities and concentrations of concentrated liquid-solids flows in pipes. COMMIX-M, a three-dimensional transient and steady-state computer program developed at ANL, is capable of analyzing multiphase flow and heat transfer and uses the separated-phases model wherein each phase has its own mass and momentum equations. For a brief description of the COMMIX-M computer code, refer to our previous paper (Ding et al., 1992) and references therein. The COMMIX-M fluid velocities computed with the new two-phase power-law solids viscosity model, together with constitutive relationships for interfacial drag, virtual mass and shear lift forces, and solids partial-slip boundary conditions at the pipe walls, are compared with data obtained by Sinton and Chow (1991) with three-dimensional time-of-flight nuclear magnetic resonance (NMR) imaging techniques. Comparisons are presented in this paper for average solids volume fractions of 21%, 40%, and 52%.

2. Hydrodynamic models

A two-phase, three-dimensional, transient hydrodynamic approach was used to model concentrated liquid-solids flows in pipes. All of the solid particles with identical densities and diameters form a continuum, a particulate phase. Each phase has its own mass and momentum equations. These equations, along with constitutive relations for interfacial drag, were presented in our previous paper (Ding et al., 1992) and are in Table 1 as Eqs. T1-T5 and T8.

In the two-phase momentum equations (Eqs. T4-T8), the shear lift force per unit volume $\mathbf{F}_L$ was extended from Saffman's shear lift force expression (Saffman, 1965; 1968) for a single particle in a simple shear flow to a collection of particles in a general flow field. The expression for $\mathbf{F}_L$ is given by Eq. T6 in Table. 1. When a particle accelerates with respect to the fluid, a virtual mass force that is proportional to the relative acceleration is developed on the particle. The virtual mass force per unit volume $\mathbf{F}_V$ for a collection of particles is given by Eq. T7 in Table. 1. Detailed derivations for these two forces were given by Ding et al.

(1993).

The shear lift and virtual mass forces, represented by Eq. T6 and T7, respectively, were used to perform all the calculations in this paper. These two forces were found to be a secondary effect on the computed fluid velocities and fluid volume fractions because the relative velocity of two phases is small because the Reynolds number is low. Neglect of these two terms was found to produce results that agreed somewhat less with experimental data (Ding et al., 1993). Therefore, it is concluded that these two forces are probably generally necessary to properly describe the solids concentration and velocity fields.

The liquid phase is assumed to be a Newtonian fluid. For isothermal and laminar flow, the liquid viscosity μ_f is constant. For the solids phase, the model for the effective shear viscosity μ_s in two-phase flow is of major concern in this paper. Based on our previous analyses (Ding et al., 1993) and experimental rheological findings (see, for example, Sinton and Chow 1991; Sekar et al, 1988; Lyczkowski and Wang, 1992; Wildman et al; 1992), some concentrated liquid-solids suspension flows display shear-thinning rather than Newtonian phenomena. Such shear-thinning phenomena differ from shear-thickening behavior observed in some rapid gas-solids flow systems, for which a theoretically obtained expression for solids viscosity using a kinetic theory of granular approach was found to be quite successful (Ding and Gidaspow, 1990; Ding and Lyczkowski 1992; Sinclair and Jackson 1989; Pita and Sundaresan, 1991). In rapid gas-solids flow, particle-particle collisions are dominant for momentum transfer, i.e., the duration of two particle contacts is very short compared with a hydrodynamic time scale. Therefore, the kinetic-theory method can be used for rapid gas-solids flow and the solids viscosity obtained is proportional to the shear rate. In slow liquid-solids flows, such as we are studying, the duration of contact between two particles and the fluid lubrication between two particles may play important roles in the rheology. Under such conditions, the kinetic-theory approach may not be applied. When the shear rate of a liquid-solids mixture becomes high enough, the shear-thickening phenomena appear, as shown for example, in the experiments of Sekar et al. (1988).

For modeling the flow of liquid-solids in pipes, we implemented a modified two-phase non-Newtonian power-law model for solids viscosity to account for a resting (static) mixture viscosity. The relative mixture viscosity η can be expressed as

$$\eta = \frac{\epsilon_s \mu_s + \epsilon_f \mu_f}{\mu_f} = m[1 + (\lambda\dot{\gamma})^2]^{\frac{n-1}{2}}, \qquad (1)$$

where m, λ, and n are parameters. Eq. 1 generalizes the model used by Lyczkowski and Wang (1992). We expect that parameters m, λ, and n depend on solids concentration, ratio of particle size to pipe diameter, and density ratio of fluid to solids. From Sinton and Chow's (1991) rheological data, as shown in Fig. 1, the solids concentration affects the rheological properties. At lower solids volume fractions, the flow is Newtonian. As the solids volume fraction increases, shear-thinning behavior becomes significant. For simplicity, we assumed the those parameters in Eq. 1 are a function of solids volume fraction only and used second order polynomial functions to correlate these parameters with one another based

on Sinton and Chow's (1991) measured rheological data. We obtained

$$m = m(\epsilon_s) = 220.7 - 1636.4\epsilon_s + 3024.2\epsilon_s^2 \tag{2a}$$

$$n = n(\epsilon_s) = 1.088 - 0.378\epsilon_s - 0.194\epsilon_s^2 \tag{2b}$$

$$\lambda = \lambda(\epsilon_s) = 1026.3 - 7461.4\epsilon_s + 12257.4\epsilon_s^2 \tag{2c}$$

Equations 1 and 2 are plotted in Fig. 1, together with Sinton and Chow's (1991) data.

To solve the governing equations for fluid-solids flow given in Table 1, we need appropriate initial and boundary conditions for the two-phase velocities, fluid-phase pressure, and volume fraction. The initial conditions depend upon the problem under investigation. The inlet conditions are usually given. The boundary conditions at planes of symmetry demand zero normal gradient of all variables. The no-slip condition was used for the fluid-phase velocity at pipe walls. but this condition cannot always be applied to the solids phase because particles may slip along the wall. The mean solids slip velocity at a solid wall was proposed by Soo (1969) to be

$$v_2|_w = -\lambda_p \frac{\partial v_2}{\partial x_1}|_w, \tag{3}$$

where the x_1 direction is normal to the wall and the x_2 direction is tangential to the wall. The slip parameter λ_p is taken to be the mean distance between particles. Here we used the expression from the work of Ding and Lyczkowski (1992) for λ_p given by

$$\lambda_p = \frac{\sqrt{3\pi}}{24} \frac{d_p}{\epsilon_s g_0}, \tag{4}$$

where

$$g_0 = (1 - \frac{\epsilon_s}{0.65})^{-1.625}. \tag{5}$$

The new two-phase power-law solids-viscosity model, together with constitutive relationships for interfacial drag, virtual mass and shear lift forces, given in Table 1, Eqs. T6-T8, and solids partial-slip boundary condition at the pipe walls, given in Eq. 3, were used to model liquid-solids flow in pipes.

3. Comparison with experimental data

We have analyzed some of the steady-state, fully developed, and isothermal carrier-fluid velocity and solids concentration data of Altobelli et al. (1991) and Sinton and Chow (1991) which were obtained using three-dimensional time-of-flight nuclear magnetic resonance (NMR) imaging techniques (Ding et al., 1992; 1993). NMR imaging is a powerful technique to nonintrusively determine three-dimensional time-dependent velocity and concentration fields to assist development and validation of the constitutive models and the computer programs that

describe concentrated suspensions. These experiments were carefully performed and probably represent the best available data of their kind in the open literature. In this paper, for the purpose of studying shear-thinning phenomena of neutrally buoyant dense suspensions in vertical pipes, we used the models presented in the previous section to analyze the data of Sinton and Chow (1991).

The Sinton and Chow (1991) experiments consisted of a suspension of neutrally buoyant, poly (methylmetkacrylate) spheres (Lucite 47G) with a median volume diameter of 0.131 mm, and a standard deviation of 0.051 mm, flowing in vertical pipes with diameters of 15.2, 25.4, and 50.8 mm and a 500-mm entrance length. Intensity and velocity data were collected over a range of 21 to 52 vol.% plastic spheres and Reynolds numbers ranging from 0.005 to 4.0. The carrier fluid was a mixture of polyether oil (Uncon oil, 75-H-90,000), water and sodium iodide to increase the fluid density to that of the solids having a density of 1190 kg/m^3.

NMR data were taken with a vertically oriented 4.7 T superconducting solenoid by techniques developed by Kose et al. (1985) and Majors et al. (1989). A positive-displacement Moyno pump was used.

Three runs were analyzed: (1) 21 vol.% solids, an average fluid velocity of 22.7 cm/s, and pipe diameter of 2.54 cm; (2) 40 vol.% solids, an average fluid velocity of 17.6 cm/s, and pipe diameter of 1.52 cm; and (3) 52 vol.% solids, an average fluid velocity of 17.5 cm/s, and pipe diameter of 1.52 cm. The pipes were modeled in two dimensions, assuming azimuthal symmetry. A total of 20 nodes were used in the radial direction and 25 in the axial direction.

Fluid velocities computed with both the current model and our Krieger's Newtonian-type solids-viscosity model were compared with the measured data. In our previous analyses (Ding et al 1992; 1993), the solids viscosity μ_s was obtained from Krieger's (1972) empirical expression for the relative viscosity given by

$$\eta = \frac{\epsilon_s \mu_s + \epsilon_f \mu_f}{\mu_f} = (1 - \frac{\epsilon_s}{0.68})^{-1.82}. \tag{6}$$

This expression was used by Phillips et al. (1992) in their analyses of concentrated suspension data. In Eq. 6, the solids viscosity is determined by the solids volume fraction only.

For the case of 21 vol.% solids, as shown in Fig. 1, the relative viscosity is nearly independent of shear rate. Hence, the computed fluid velocities with the new model and Krieger's model for solids viscosity are very close, as shown in Fig. 2. Reasonably good agreement exists between the model predictions and the data. This case exhibited basically Newtonian behavior.

Figure 3 shows the two model predictions and the NMR measured data for the case of 40 vol.% solids. Except near the pipe center, both models agree with the data very well. Because the rheological experiments show a slightly shear-thinning behavior, the new two-phase power-law model gives better agreement with the data near the pipe center.

As can be seen in Figs. 1 and 4, when the solids volume fraction reaches 52%, the shear-thinning phenomena become very prominent. For the case of 52 vol.%, the new two-phase power-law model agrees much better than the Krieger (1972) Newtonian-type model near the pipe center. The data clearly exhibit shear-thinning behavior with a blunted velocity profile. Therefore, the non-Newtonian shear-thinning model is strongly recommended for suspension flows at high solids volume fractions.

Our computer model predictions for these three cases did not show significant nonuniform distributions of solids in the radial direction. Slightly higher solids volume fractions were found in computational nodes away from the pipe walls. This results from particle migration toward the pipe center and is due to the shear lift effect at the wall. It should be also noted that these experiments did not report significant particle migration nor solids concentration distributions.

4. Conclusions

Based upon the agreement between the COMMIX-M computer code predictions and the experimental data, the models proposed in this paper appear to be reasonable and promising. Thus far, no adjustments in the literature model have been made. The parameters in the near empirical shear-thinning model are functions of the physical properties of the fluid and solids concentration. Rheological experiments can be performed to obtained these parameters as input to the computer model and to predict design of dense-suspension flow systems. The rheological properties of suspension flow should be further examined and studied to develop a shear-thinning model that not only includes the effect of solids concentration but also particle size and shape, density ratio of fluid to solids, and carrier fluid velocity and/or velocity gradients. Because some investigations have reported particle migration phenomena (Phillips et al., 1992; and references therein), particle migration mechanisms should also be studied.

Further improvements of the model should increase our confidence in predicting design and processing of concentrated suspension flow systems. Such improvements will be from additional comparisons with a wider data base of experimental measurements and COMMIX-M analyses, which will also serve to more critically evaluate the models.

Acknowledgments

The stimulating and constructive discussions and comments of Drs. T. H. Chien and M. Bottoni (Energy Technology Division), Dr. J. X. Bouillard (Energy Systems Division), Prof. S.-L. Soo (University of Illinois at Urbana-Champaign), and Dr. Z.-Y. Chen (Science Applications International Corp.) are gratefully acknowledged.

The authors acknowledge the encouragement of the program manager, Dr. W. C. Peters (U.S. Department of Energy, Pittsburgh Energy Technology Center) and Dr. S. L. Passman (Sandia National Laboratories).

This study was supported by U.S. Department of Energy, Pittsburgh Energy Technology Center.

Nomenclature

C_d	Drag coefficient
d_p	Particle diameter
$\mathbf{F_L}$	Shear lift force per unit volume
$\mathbf{F_V}$	Virtual mass force per unit volume
$\mathbf{g}$	Acceleration due to gravity
g_0	Radial distribution function
$\overline{\overline{\mathbf{I}}}$	Unit tensor
m	Parameter defined in Eq. 1
n	Parameter defined in Eq. 1
p	Pressure
$\overline{\overline{\mathbf{S}}}$	Deformation rate tensor
t	Time
$\mathbf{u}$	Fluid phase velocity
$\mathbf{v}$	Solids phase velocity

Greek letters

β	Two-phase drag force coefficient
ϵ	Volume fraction
η	Relative mixture viscosity
λ	Parameter defined in Eq. 1
λ_p	Mean distance between particles
μ	Viscosity
ρ	Density
$\overline{\overline{\tau}}$	Stress tensor

Subscripts

f	Fluid phase
s	Solids phase
w	Wall

References

Altobelli, S. A., R. C. Givler, and E. Fukushima, *J. Rheol.* 35 (1991) 721.

Ding, J., and D. Gidaspow, *AIChE J. 36* (1990) 523.

Ding, J., and R. W. Lyczkowski, *Powder Technol. 73* (1992) 127.

Ding, J., R. W. Lyczkowski, W. T. Sha, S. A. Altobelli, and E. Fukushima, *Proc. 4th NSF-DOE Workshop on Flow of Particulates and Fluids* (1992) 281.

Ding, J., R. W. Lyczkowski, W. T. Sha, S. A. Altobelli, and E. Fukushima, *Powder Technol. 77* (1993) 301.

Kose, K., K. Satoh, T. Inouye, and J. Yasuoka, *J. Phys. Soc. Jpn. 54* (1985) 81.

Krieger I. M., *Adv. Colloid Interface Sci. 3* (1972) 111.

Lyczkowski, R. W., and C. S. Wang, *Powder Technol. 69* (1992) 285.

Majors, P. D., R. C. Givler, and E. Fukushima, *J. Magn. Reson. 85* (1989) 235.

Phillips, R. J., R. C. Armstrong, R. A. Brown, A. L. Graham, and J. R. Abbott, *Phys. Fluids A4* (1992) 30.

Pita, J. A., and S. Sundaresan, *AIChE J. 37* (1991) 1009.

Saffman, P. G., *J. Fluid Mech. 22, part 2* (1965) 385; *31* (1968) 624.

Sekar, R. R., C. S. Wang, and U. S. Choi, *Viscosity of Coal/Water Slurries at High Shear Rates*, Argonne National Laboratory Report ANL/CNSV-66, Aug. 1988.

Sinclair, J. L., and R. Jackson, *AIChE J. 35* (1989) 1473.

Sinton, S. W., and A. W. Chow, *J. Rheol. 35* (1991) 735.

Soo, S.L., *Appl. Sci. Res. 21* (1969) 68.

Wildman, D. J., J. M. Ekmann, J. R. Kadambi, and R. C. Chen, *Powder Technol. 73* (1992) 211.

Table 1. GOVERNING EQUATIONS FOR FLUID-SOLIDS SUSPENSION FLOW

CONTINUITY EQUATIONS

Fluid Phase

$$\frac{\partial}{\partial t}(\epsilon\rho_f) + \nabla\cdot(\epsilon\rho_f \mathbf{u}) = 0 \tag{T1}$$

Solids Phase

$$\frac{\partial}{\partial t}(\epsilon_s\rho_p) + \nabla\cdot(\epsilon_s\rho_p \mathbf{v}) = 0 \tag{T2}$$

$$\epsilon_f + \epsilon_s = 1 \tag{T3}$$

MOMENTUM EQUATIONS

Fluid Phase

$$\frac{\partial}{\partial t}(\epsilon_f\rho_f \mathbf{u}) + \nabla\cdot(\epsilon_f\rho_f \mathbf{uu}) = -\epsilon_f \nabla p_f + \epsilon_f\rho_f \mathbf{g} + \nabla\cdot\bar{\bar{\tau}}_f + \beta(\mathbf{v}-\mathbf{u}) - \mathbf{F}_l - \mathbf{F}_v, \tag{T4}$$

where

$$\bar{\bar{\tau}}_f = 2\epsilon_f\mu_f\bar{\bar{\mathbf{S}}}_f \tag{T4a}$$

$$\bar{\bar{\mathbf{S}}}_f = \frac{1}{2}[\nabla\mathbf{u} + (\nabla\mathbf{u})^T] - \frac{1}{3}\nabla\cdot\mathbf{u}\bar{\bar{\mathbf{I}}} \tag{T4b}$$

Solids Phase

$$\frac{\partial}{\partial t}(\epsilon_s\rho_p \mathbf{v}) + \nabla\cdot(\epsilon_s\rho_p \mathbf{vv}) = -\epsilon_s \nabla p_f + \epsilon_s\rho_p \mathbf{g} + \nabla\cdot\bar{\bar{\tau}}_s + \beta(\mathbf{u}-\mathbf{v}) + \mathbf{F}_l + \mathbf{F}_v \tag{T5}$$

where

$$\bar{\bar{\tau}}_s = 2\epsilon_s\mu_s\bar{\bar{\mathbf{S}}}_s \tag{T5a}$$

$$\bar{\bar{\mathbf{S}}}_s = \frac{1}{2}[\nabla\mathbf{v} + (\nabla\mathbf{v})^T] - \frac{1}{3}\nabla\cdot\mathbf{v}\bar{\bar{\mathbf{I}}} \tag{T5b}$$

Shear lift force $\mathbf{F}_l$

$$\mathbf{F}_l = 6.17\epsilon_s(\rho_f\mu_f)^{1/2}(\mathbf{u}-\mathbf{v})\cdot\bar{\bar{\mathbf{S}}}_f(2\bar{\bar{\mathbf{S}}}_f : \bar{\bar{\mathbf{S}}}_f)^{-1/4}/d_p \tag{T6}$$

Virtual mass force

$$\mathbf{F}_v = \frac{1}{2}\epsilon_s\rho_f\left(\frac{D\mathbf{u}}{Dt} - \frac{D\mathbf{v}}{Dt}\right) \tag{T7}$$

Fluid-solids drag coefficeints

For $\epsilon_f < 0.8$, (Ergun equation)

$$\beta = 150\frac{\epsilon_s^2\mu_f}{\epsilon_f d_p^2} + 1.75\frac{\rho_f\epsilon_s|\mathbf{u}-\mathbf{v}|}{d_p} \tag{T8a}$$

For $\epsilon_f > 0.8$, (Wen and Yu's empirical correlation)

$$\beta = \frac{3}{4}C_d\frac{\epsilon_f\epsilon_s\rho_f|\mathbf{u}-\mathbf{v}|}{d_p}\epsilon_f^{-2.65}, \tag{T8b}$$

where

$$C_d = \frac{24}{Re_p}\left[1 + 0.15Re_p^{0.687}\right], \quad For \quad Re_p < 1000 \tag{T8c}$$

$$C_d = 0.44, \quad for \quad Re_p \geq 1000 \tag{T8d}$$

$$Re_p = \frac{\epsilon_f\rho_f|\mathbf{u}-\mathbf{v}|d_p}{\mu_f} \tag{T8e}$$

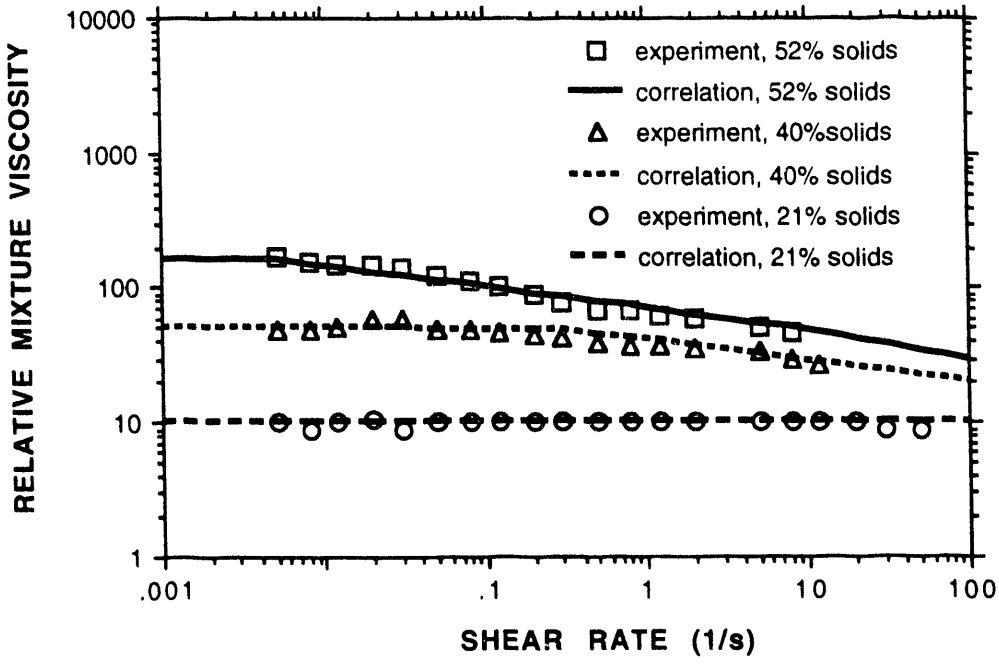

Figure 1. Relative mixture viscosity as a function of shear rate, as calculated by us and experimentally determined by Sinton and Chow (1991)

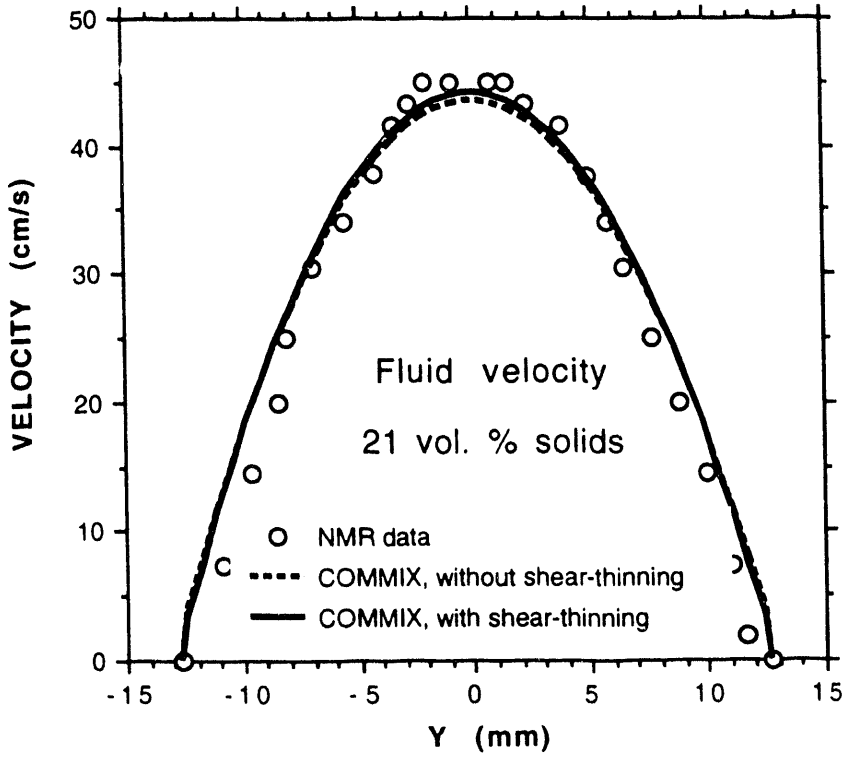

Figure 2. NMR fluid velocity data predicted by COMMIX-M and determined experimentally by Sinton and Chow (1991) for the case of 21 vol.% solids

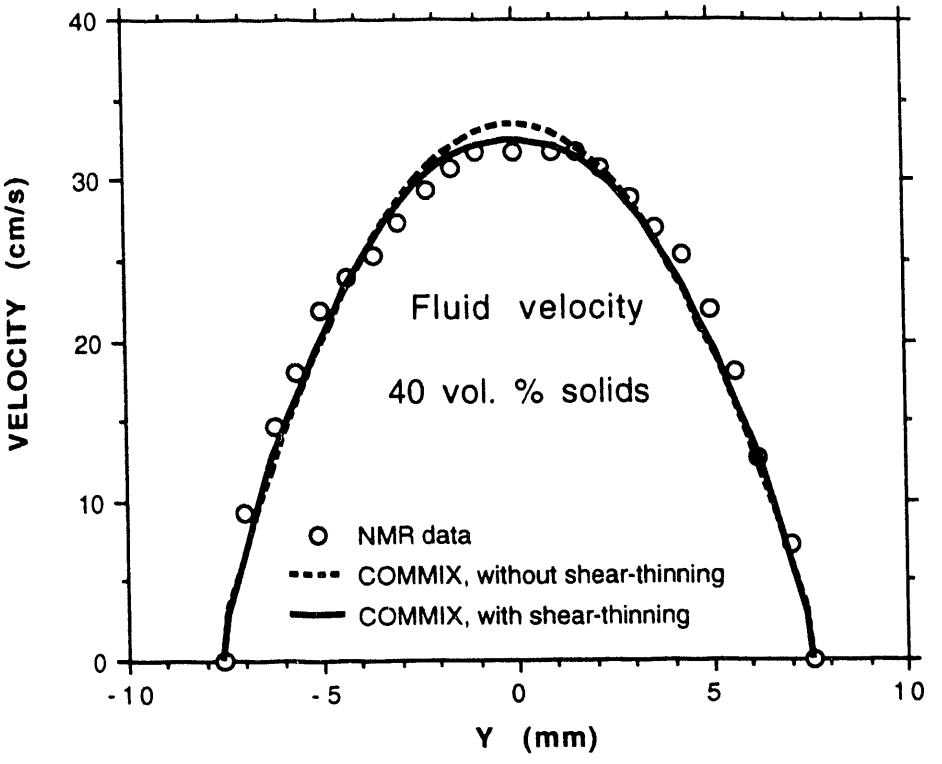

Figure 3. NMR fluid velocity data presented by COMMIX-M and determined experimentally by Sinton and Chow (1991) for the case of 40 vol.% solids

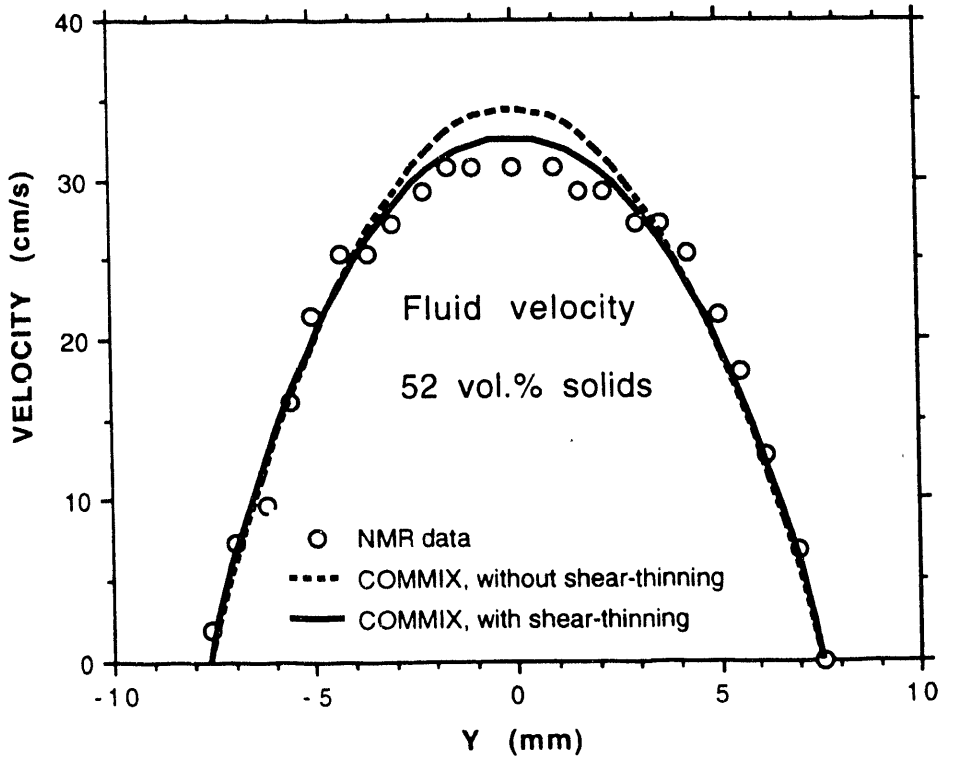

Figure 4. NMR fluid velocity data presented by COMMIX-M and determined experimentally by Sinton and Chow (1991) for the case of 52 vol.% solids

AUTHORS INDEX

AUTHORS INDEX

ATTENDEES LIST

ACRIVOS, ANDREAS
CITY COLLEGE OF CUNY
Levich Institute
T-1M
New York, NY 10031
(212) 590-8159

AIDUN, CYRUS
INSTIT. OF PAPER SCIENCE & TECHNOLOGY
Atlanta, GA 30318
(404) 853-9777

ALTOBELLI, S A
THE LOVELACE INSTITUTES
2425 Ridgecrest Dr SE
Albuquerque, NM 87108
(505) 262-7155

BULTHUIS, HENK
THE JOHNS HOPKINS UNIVERSITY
Charles and 34th St
Baltimore, MD 21218
(410) 516-8525

CAPRIHAN, A
THE LOVELACE INSTITUTES
2425 Ridgecrest Dr SE
Albuquerque, NM 87108
(505) 262-7155

CHEN, ZHONG-YING
SCIENCE APPLICATIONS INT'L CORP
1710 Goodridge Dr
MS 2-2-1
McLean, VA 22102
(703) 442-5692

DAVE, RAJESH
NEW JERSEY INSTITUTE OF TECHNOLOGY
Department of Mechanical & Industrial Engineering
Newark, NJ 07102
(201) 596-3352

DING, JIANMIN
ARGONNE NATIONAL LABORATORY
9700 S Cass Ave
Bldg 308
Argonne, IL 60439
(708) 252-3423

FUKUSHIMA, EIICHI
THE LOVELACE INSTITUTES
2425 Ridgecrest Dr SE
Albuquerque, NM 87108
(505) 262-7155

GILLIES, RANDY
SASKATCHEWAN RESEARCH COUNCIL
15 Innovation Blvd
Saskatoon S7N 2X8 Sask, CANADA
(306) 933-5473

HANES, DANIEL
UNIVERSITY OF FLORIDA
Department of Coastal & Oceanographic Engineering
336 Weil Hall
Gainesville, FL 32611
(904) 392-9801

HETSRONI, GAD
UNIVERSITY OF CALIFORNIA AT SANTA
Department of Chemical And Nuclear Engineering
Santa Barbara, CA 93106
(805) 893-4941

HSIEH, H PHILIP
ALCOA
Alcoa Technical Center
Alcoa Center, PA 15069
(412) 337-5893

HUNT, MELANY
CALTECH
Engineering & Applied Sciences
Pasadena, CA 91125
(818) 395-4231

HURWITZ, MARK F
PALL CORPORATION
Process Equipment Development Dept
3669 State Rt 281
Cortland, NY 13045
(607) 753-6041

JACKSON, ROY
PRINCETON UNIVERSITY
Department of Chemical Engineering
The Engineering Quadrangle
Princeton, NJ 08544-5263
(609) 258-4591

JENKINS, JAMES T
CORNELL UNIVERSITY
Department of Theoretical & Applied Mechanics
Ithaca, NY 14853
(607) 255-7185

JOSEPH, DANIEL D
UNIVERSITY OF MINNESOTA
110 Union St
107 Akerman Hall
Minneapolis, MN 55455
(612) 625-0309

KENKRE, NITANT
UNIVERSITY OF NEW MEXICO
Department of Physics
Albuquerque, NM 87131
(505) 277-4846

KIM, SANGTAE
UNIVERSITY OF WISCONSIN
Department of Chemical Engineering
1415 Johnson Dr
Madison, WI 53706-1691
(608) 262-5921

KUSHNER, MARK J
UNIVERSITY OF ILLINOIS
136 Everitt Laboratory
1406 W Green St
Urbana, IL 61801
(217) 244-5137

LEIGHTON, DAVID
UNIVERSITY OF NOTRE DAME
DEPARTMENT OF CHEMICAL ENGINEERING
NOTRE DAME, IN 46556
(219) 239-6698

LILJEGREN, LUCIA
BATTELLE
Pacific Northwest Laboratories
PO Box 999
Richland, WA 99352
(509) 375-2353

LIU, HENRY
UNIVERSITY OF MISSOURI-COLUMBIA
1047 Engineering Bldg
Columbia, MO 65211
(314) 882-2779

LOUGE, MICHEL Y
CORNELL UNIVERSITY
Upson Hall
Department of Mechanical Engineering
Ithaca, NY 14853
(607) 255-4193

LYCZKOWSKI, ROBERT
ARGONNE NATIONAL LABORATORY
9700 S Cass Ave
Bldg 362
Room C-249
Argonne, IL 60439-4813
(708) 252-5923

MASSOUDI, MEHRDAD
PITTSBURGH ENERGY TECHNOLOGY CENTER
US Department of Energy
PO Box 10940
MS 84-340
Pittsburgh, PA 15236
(412) 892-4975

NELSON, PAUL A
SHELL OIL COMPANY
PO Box 4452
Houston, TX 77210
(713) 493-8159

OFOLI, ROBERT Y
CARNEGIE MELLON UNIVERSITY
Department of Chemical Engineering
Pittsburgh, PA 15213
(412) 268-6428

PASSMAN, STEPHEN L
SANDIA NATIONAL LABORATORIES
Dept 6212
Albuquerque, NM 87185-5800
(505) 844-7686

PETERS, WILLIAM C
PITTSBURGH ENERGY TECHNOLOGY CENTER
US Department of Energy
PO Box 10940
MS 922-300
Pittsburgh, PA 15236
(412) 892-4802

PLASYNSKI, SEAN I
PITTSBURGH ENERGY TECHNOLOGY CENTER
US Department of Energy
PO Box 10940
MS 922-300
Pittsburgh, PA 15236
(412) 892-4867

PROSPERETTI, ANDREA
THE JOHNS HOPKINS UNIVERSITY
Charles and 34th St
Baltimore, MD 21218
(410) 516-8534

RAJAGOPAL, KUMBAKONAM R
UNIVERSITY OF PITTSBURGH
Department of Mechanical Engineering
637 Benedum Hall
Pittsburgh, PA 15261
(412) 624-9799

RAJAGOPALAN, RAJ
UNIVERSITY OF HOUSTON
Department of Chemical Engineering
Houston, TX 77204-4792

REED, ROBERT
PETC/ORAU
PO Box 10940
MS 922-H
Pittsburgh, PA 15236
(412) 892-4794

RICHMAN, MARK W
WORCESTER POLYTECHNIC INSTITUTE
Department of Mechanical Engineering
100 Institute Rd
Worcester, MA 01609
(508) 831-5556

ROCO, MIKE
NATIONAL SCIENCE FOUNDATION
ENGINEERING DIRECTORATE
ROOM 1110
WASHINGTON, DC 20550
(202) 357-9606

ROSATO, ANTHONY
NEW JERSEY INSTITUTE OF TECHNOLOGY
Department of Mechanical & Industrial Engineering
Newark, NJ 07102
(201) 596-5829

SANGANI, A S
SYRACUSE UNIVERSITY
Department of Chemical Engineering
Syracuse, NY 13244
(315) 443-4502

WAGNER, NORMAN
UNIVERSITY OF DELAWARE
Colburn Laboratory
Newark, DE 19716
(302) 831-8079

WALTON, OTIS R
LAWRENCE LIVERMORE NATIONAL LABORATOR
PO Box 808
L-207
Livermore, CA 94550
(510) 422-3947

WALZ, JOHN Y
TULANE UNIVERSITY
Department of Chemical Engineering
New Orleans, LA 70118
(504) 865-5620

ZHANG, DUAN Z
THE JOHNS HOPKINS UNIVERSITY
Charles and 34th St
Baltimore, MD 21218
(410) 516-8525

ZUKOWSKI, CHARLES
UNIVERSITY OF ILLINOIS-URBANA
600 E. Matthews
Urbana, IL 61801
(217) 333-7379

DATE
FILMED
5/19/94
END